Analyses of Aircraft Responses to Atmospheric Turbulence

Analyses of Aircraft Responses to Atmospheric Turbulence

Proefschrift

ter verkrijging van de graad van doctor
aan de Technische Universiteit Delft,
op gezag van de Rector Magnificus prof.dr.ir. J.T. Fokkema,
voorzitter van het College voor Promoties,
in het openbaar te verdedigen op maandag 15 december 2003 om 13.00 uur
door

Willem Hendrik Jan Joseph VAN STAVEREN
ingenieur luchtvaart en ruimtevaart

geboren te Sittard

Dit proefschrift is goedgekeurd door de promotor:
Prof.dr.ir. J.A. Mulder.

Samenstelling promotiecommisie:

Rector Magnificus,	Technische Universiteit Delft, voorzitter
Prof.dr.ir. J.A. Mulder,	Technische Universiteit Delft, promotor
Prof.dr.ir. P.G. Bakker,	Technische Universiteit Delft
Prof.dr.ir. P.M.J. van den Hof,	Technische Universiteit Delft
Prof.dr.ir. Th. van Holten,	Technische Universiteit Delft
Prof.dr.ir. J.H. de Leeuw,	University of Toronto, Ontario, Canada
Prof.dr.-Ing. G. Schänzer,	Technische Universität Braunschweig, Duitsland
Dr.ir. J.C. van der Vaart,	Technische Universiteit Delft
Prof.dr.ir. M.J.L. van Tooren,	Technische Universiteit Delft, reservelid

Dr.ir. J.C. van der Vaart heeft als begeleider in belangrijke mate aan de totstandkoming van het proefschrift bijgedragen.

Published and distributed by: DUP Science

DUP Science is an imprint of
Delft University Press
P.O. Box 98
2600 MG Delft
The Netherlands
Telephone: +31 15 27 85 678
Telefax: +31 15 27 85 706
Email: info@library.tudelft.nl

ISBN 90-407-2453-9

Keywords: aerodynamics / atmospheric flight dynamics / atmospheric turbulence and windshear / Computational Aerodynamics / CFD / elastic aircraft / fixed wing aircraft / flight test / flight dynamics / loads / panel method / parameter identification / potential flow / simulation / system identification / unsteady aerodynamics

Copyright ©2003 by W.H.J.J. van Staveren

All rights reserved. No part of the material protected by this copyright notice may be reproduced or utilized in any form or by any means, electronic or mechanical, including photocopying, recording or by any information storage and retrieval system, whithout written permission from the publisher: Delft University Press

Printed in The Netherlands

Summary

The response of aircraft to stochastic atmospheric turbulence plays an important role in aircraft-design (load calculations), Flight Control System (FCS) design and flight-simulation (handling qualities research and pilot training). In order to simulate these aircraft responses, an accurate mathematical model is required. Two classical models will be discussed in this thesis, that is the Delft University of Technology (DUT) model and the Four Point Aircraft (FPA) model. Although they are well estabilished, their fidelity remains obscure. The cause lies in one of the requirements for system identification; it has always been necessary to relate inputs to outputs to determine, or identify, system dynamic characteristics. From experiments, using both the measured input ánd the measured output, a mathematical model of any system can be obtained. When considering an input-output system such as an aircraft subjected to stochastic atmospheric turbulence, a major problem emerges. During flighttests, no practical difficulty arises measuring the aircraft motion (the output), such as the angle-of-attack, the pitch-angle, the roll-angle, etc.. However, a huge problem arises when the input to the aircraft-system is considered; this input is stochastic atmospheric turbulence in this thesis. Currently, during flighttests it still remains extremely difficult to identify the entire flowfield around an aircraft geometry subjected to a turbulent field of flow; an infinite amount of sensors would be required to identify the atmospheric turbulence velocity component's distribution (the input) over the vehicle geometry.

In an attempt to shed some more light on solving the problem of the response of aircraft to atmospheric turbulence, the subject of this thesis, it depends on the formulation of two distinct models: one of the atmospheric turbulence itself (the atmospheric turbulence model), and the other of the aircraft response to it (the mathematical aircraft model). As concerns atmospheric turbulence, stochastic, stationary, homogeneous, isotropic atmospheric turbulence is considered in this thesis as input to the aircraft model. Models of atmospheric turbulence are well established. As for mathematical aircraft models, many of them have been proposed before. However, verifying these models has always been extremely difficult due to the identification problem indicated above. As part of the mathematical aircraft model, (parametric) aerodynamic models often make use of (quasi-) steady aerodynamic results, that is all steady aerodynamic parameters are estimated using either results obtained from windtunnel experiments, handbook methods, Computational Aerodynamics (CA) which comprises Linearized Potential Flow (LPF) methods, or Computational Fluid Dynamics (CFD) which comprises Full-Potential, Euler and Navier-Stokes methods.

In this thesis the simplest form of fluid-flow modeling is used to calculate the time-dependent aerodynamic forces and moments acting on a vehicle: that is unsteady Linearized Potential Flow (LPF). The fluid-flow model will result in a so called "unsteady panel-method" which will be used as a virtual windtunnel (or virtual flighttest facility) for the example discretized aircraft geometry, also referred to as the "aircraft grid". The application of the method ultimately results in the vehicle's steady and unsteady stability derivatives using harmonic analysis. Similarly, both the steady and unsteady gust derivatives for isolated atmospheric turbulence fields will be calculated. The gust fields will be limited to one-dimensional (1D) longitudinal, lateral and vertical gust fields, as well as two-dimensional (2D) longitudinal and vertical gust fields. The harmonic analysis results in frequency-dependent stability- and gust derivatives which will later be used to obtain an aerodynamic model in terms of constant stability- and gust derivatives. This newly introduced model, the Parametric Computational Aerodynamics (PCA) model, will be compared to the two classical models mentioned earlier, that is the Delft University of Technology (DUT) model and the Four-Point-Aircraft (FPA) model. These three parametric aircraft models are used to calculate both the time- and frequency-domain aerodynamic model and aircraft motion responses to the atmospheric turbulence fields indicated earlier. Also, using the unsteady panel-method the aircraft grid will be flown through spatial-domain 2D stochastic gust fields, resulting in Linearized Potential Flow solutions. Results will be compared to the ones obtained for the parametric models, i.e. the PCA-, DUT- and FPA-model.

From the results presented, it is concluded that the introduced PCA-model is the most accurate for all considered gust fields. Compared to the Linearized Potential Flow solution (which is assumed to be the benchmark, or the model that approximates reality closest) the new parametric model shows increased accuracy over the classical parametric models (the DUT- and FPA-model), especially for the aircraft responses to 2D gust fields. Furthermore, it shows more accuracy in the aircraft responses to 1D longitudinal gust fields. Although results will be presented for a Cessna Ce550 Citation II aircraft only, the theory and methods are applicable to a wide variety of fixed-wing aircraft, that is from the smallest UAV to the largest aircraft (such as the Boeing B747 and the Airbus A380).

As an overview of this thesis, after the introduction given in **chapter 1**, a short summary of the applied atmospheric turbulence model is given in **chapter 2**. Next, the theory of steady incompressible Linearized Potential Flow is given in **chapter 3**. **Chapter 4** continues with a similar treatment as in chapter 3, discussing unsteady incompressible Linearized Potential Flow. Both analytical frequency-response functions (or aerodynamic transfer functions) ánd numerical frequency-response functions for isolated wings will also be discussed in this chapter. In **chapter 5** the definition of specific aircraft motion perturbations and atmospheric turbulence inputs will be given. **Chapter 6** discusses the aircraft grid for the example aircraft. This grid will be used for both steady and unsteady Linearized Potential Flow simulations. For aerodynamic model identification purposes, the aircraft grid defined in chapter 6 is used in **chapter 7** where the numerical symmetrical

aerodynamic frequency-response functions are given for the PCA-model. They are determined with respect to aircraft motions in surge and heave, and to both longitudinal and vertical gusts. All perturbations in aircraft motion and gusts are of harmonic nature. Results of the analytical continuation of frequency-response data for time-domain models will also be given (aerodynamic fits). Next, in this chapter the concept of frequency-dependent stability derivatives and frequency-dependent gust derivatives for complete aircraft configurations is discussed. Furthermore, the steady symmetrical aerodynamic model is defined in this chapter. **Chapter 8** treats, along the same lines as in chapter 7, the numerical asymmetrical frequency-response functions and unsteady asymmetrical aerodynamic model for the PCA-model. The (harmonic) degrees of freedom considered are now with respect to swaying aircraft motions ánd antisymmetrical longitudinal-, asymmetrical lateral- and anti-symmetrical vertical gusts. In **chapter 9** the aircraft grid defined in chapter 6 is flown through 2D spatial-domain gust fields. First, the aerodynamic force and moment coefficients acting on the aircraft geometry are calculated assuming a recti-linear flightpath (no aircraft motions will be considered). Next, additional theory is given for the so-called "coupled-solution", that is the aircraft equations of motion are now coupled with the potential flow solution. **Chapters 10, 11** and **12** discuss the equations of motion of aircraft subjected to both 1D longitudinal, lateral and vertical gusts ánd 2D longitudinal and vertical gusts. In chapter 10 the mathematical aircraft model for the "Parametric Computational Aerodynamics model" (or "PCA-model") is introduced, and it includes the equations of motion using both aerodynamic frequency-response functions (or frequency-dependent stability- and gust derivatives) and an aerodynamic model in terms of constant stability- and gust derivatives. Chapters 11 and 12 will discuss the equations of motion for parametric aerodynamic models in terms of constant stability- and gust derivatives. The aircraft models are based on the Delft University of Technology gust-response theory, the "DUT-model" (chapter 11), and Etkin's "Four-Point-Aircraft model" (or "FPA model", chapter 12). In these chapters, the constant stability derivatives obtained in chapter 10 will be used for simulations. A comparison of results of the PCA-, the DUT- and the FPA-model is given in **chapter 13**. In this chapter both time- and frequency-domain results, given in terms of aerodynamic coefficients, will be compared to the ones obtained from a time-domain Linearized Potential Flow simulation (the LPF-solution). In this case no aircraft motions are taken into account (the aircraft (-grid) is traveling along a prescribed recti-linear flightpath), thus the aerodynamic response is limited to gust fields only. Also, time-domain aircraft motion results will be compared to results obtained for the LPF-solution. First, the PCA-, the DUT- and the FPA-model aircraft motion simulations will be compared to the ones obtained for the LPF-solution. These simulations make use of the gust-induced aerodynamic coefficients obtained for a recti-linear flightpath (excluding aircraft motions). Next, the PCA-, DUT- and FPA-model aircraft motion simulations are compared to results obtained from a Linearized Potential Flow simulation which is coupled to the equations of motion (the so-called "coupled-solution", designated as the LPF-EOM-model). This simulation, in which the aerodynamic grid will be flown through stochastic 2D longitudinal, lateral and vertical gust fields, will be the ultimate test for the parametric models presented in chapters 10, 11 and 12. Chapter 13 is followed by

conclusions and recommendations in **chapter 14**.

Since the research conducted for this thesis involved multiple disciplines, some of them are explained in detail for their educational value. For example, the developed panel-methods are described as a one to one mapping of the applied software codes. Furthermore the recipe for determining the novel PCA-model equations of motion, including its parameters, is outlined in detail.

Contents

1 Introduction **1**
1.1 Goal of this thesis 1
1.2 Outline of this thesis 4

I Atmospheric Turbulence Modeling **7**

2 The atmospheric turbulence model **9**
2.1 Introduction 9
2.2 Atmospheric turbulence modeling assumptions 9
2.2.1 Fundamental atmospheric turbulence correlation functions 14
2.3 The atmospheric turbulence covariance function matrix 15
2.3.1 The general covariance function matrix 15
2.3.2 A 2D spatial separation example 18
2.4 The atmospheric turbulence PSD function matrix 22
2.4.1 The general PSD function matrix 22
2.4.2 Reduced spatial frequency dimension examples 26
2.5 Atmospheric turbulence model parameters 31
2.6 Remarks 31

II Linearized Potential Flow Theory **33**

3 Steady linearized potential flow simulations **35**
3.1 Introduction 35
3.2 Short summary of steady linearized potential flow theory 37
3.2.1 Flow equations 37
3.2.2 Boundary conditions 40
3.2.3 Wake separation and the Kutta condition 41
3.2.4 A general LPF solution 42
3.3 Numerical steady linearized potential flow simulations 42
3.3.1 Body surface discretization 42
3.3.2 Quadri-lateral panels 48

3.3.3 Numerical boundary conditions . . . 50
3.3.4 Wake separation and the numerical Kutta condition . . . 50
3.3.5 General numerical source- and doublet-solutions . . . 51
3.3.6 Velocity perturbation calculations . . . 58
3.3.7 Aerodynamic pressure calculations . . . 61
3.3.8 Aerodynamic loads and aerodynamic coefficients . . . 61
3.4 Remarks . . . 62

4 Unsteady linearized potential flow simulations 63
4.1 Introduction . . . 63
4.2 Analytical unsteady aerodynamics . . . 63
4.2.1 Introduction . . . 63
4.2.2 The Theodorsen function . . . 64
4.2.3 The Sears function . . . 65
4.2.4 The Horlock function . . . 68
4.2.5 The Wagner function . . . 71
4.2.6 The Küssner function . . . 74
4.3 Numerical unsteady linearized potential flow simulations . . . 76
4.3.1 Introduction . . . 76
4.3.2 Kinematics . . . 78
4.3.3 Numerical boundary conditions . . . 79
4.3.4 Unsteady wake-separation and the numerical Kutta condition . . . 79
4.3.5 General numerical source- and doublet-solutions . . . 81
4.3.6 Velocity perturbation calculations . . . 89
4.3.7 Aerodynamic pressure calculations . . . 89
4.3.8 Aerodynamic loads . . . 90
4.4 Examples of numerical unsteady aerodynamic simulations . . . 91
4.4.1 Introduction . . . 91
4.4.2 Theodorsen function simulations . . . 95
4.4.3 Sears function simulations . . . 95
4.4.4 Horlock function simulations . . . 97
4.4.5 Wagner function simulations . . . 99
4.5 Remarks . . . 102

III A Linearized Potential Flow Application 103

5 Aircraft motion perturbations and the atmospheric turbulence inputs 105
5.1 Introduction . . . 105
5.2 Aircraft motion definitions . . . 107
5.2.1 Translational velocity perturbations . . . 107
5.2.2 Rotational velocity perturbations . . . 111
5.3 Atmospheric turbulence input definitions . . . 111
5.3.1 Introduction . . . 111

5.3.2 1D Atmospheric gust fields . . . 112
5.3.3 2D Atmospheric gust fields . . . 114
5.4 (Quasi-) Steady stability derivatives . . . 120
5.5 Aerodynamic frequency-response data . . . 126
5.6 Remarks . . . 128

6 The aircraft grid and steady aerodynamic results 131
6.1 Introduction . . . 131
6.2 Aircraft geometry definition . . . 131
6.3 Wake geometry definition . . . 132
6.4 PCA-model steady-state aerodynamic results . . . 135
6.4.1 A PCA-model steady-state solution . . . 135
6.4.2 (Quasi-) Steady stability derivatives . . . 136
6.4.3 Stability derivatives obtained from flight tests . . . 139
6.5 Unsteady wake geometry definition . . . 141
6.6 Remarks . . . 141

7 PCA-model symmetrical aerodynamic frequency-response functions 153
7.1 Introduction . . . 153
7.2 Generation of frequency-response data . . . 154
7.2.1 Initial condition definitions . . . 154
7.2.2 Time-domain simulations . . . 154
7.2.3 Effect of the discretization time on frequency-response data . . . 155
7.3 Aircraft motion frequency-response results . . . 156
7.3.1 Breakdown of frequency-response data . . . 156
7.3.2 Aerodynamic fitting results . . . 164
7.4 1D Atmospheric turbulence input frequency-response results . . . 166
7.4.1 Breakdown of frequency-response data . . . 166
7.4.2 Aerodynamic fitting results . . . 167
7.5 Frequency-dependent stability- and gust derivatives . . . 167
7.6 Remarks . . . 169

8 PCA-model asymmetrical aerodynamic frequency-response functions 173
8.1 Introduction . . . 173
8.2 Generation of frequency-response data . . . 174
8.2.1 Initial condition definitions . . . 174
8.2.2 Time-domain simulations . . . 174
8.2.3 Effect of the discretization time on frequency-response data . . . 175
8.3 Aircraft motion frequency-response results . . . 176
8.3.1 Breakdown of frequency-response data . . . 176
8.3.2 Aerodynamic fitting results . . . 176
8.4 1D Atmospheric turbulence input frequency-response results . . . 180
8.4.1 Breakdown of frequency-response data . . . 180
8.4.2 Aerodynamic fitting results . . . 180

8.5 2D Atmospheric turbulence input frequency-response results . . . 180
8.5.1 Aerodynamic fitting results . . . 180
8.6 Frequency-dependent stability- and gust derivatives . . . 183
8.7 Remarks . . . 187

IV The Mathematical Aircraft Models 189

9 Time-domain LPF solutions for 2D atmospheric gust fields 191
9.1 Introduction . . . 191
9.2 The time-domain LPF solution for recti-linear flightpaths . . . 192
9.2.1 The initial condition . . . 192
9.2.2 Generation of 2D spatial-domain gust fields . . . 192
9.2.3 The flightpath definition . . . 193
9.2.4 Decomposition of the 2D spatial-domain gust fields . . . 194
9.2.5 gust field interpolations . . . 196
9.2.6 The source definition . . . 196
9.2.7 Application of wake truncation . . . 196
9.2.8 Calculation of aerodynamic coefficients in $\mathcal{F}_{aero}$ and $\mathcal{F}_S$ . . . 198
9.2.9 Effect of the discretization time on the LPF-solution . . . 199
9.3 The time-domain LPF solution for stochastic flightpaths . . . 199
9.3.1 Introduction . . . 199
9.3.2 The LPF-EOM solution . . . 201
9.4 Remarks . . . 203

10 The Parametric Computational Aerodynamics model 205
10.1 Introduction . . . 205
10.2 The trim condition . . . 206
10.3 The atmospheric turbulence PSD-functions . . . 206
10.4 The parametric aircraft model for 1D gust fields . . . 206
10.4.1 Introduction . . . 206
10.4.2 Calculation of the unsteady stability derivatives . . . 208
10.4.3 Calculation of the gust derivatives for 1D gust fields . . . 213
10.5 The parametric aircraft model for 2D gust fields . . . 225
10.5.1 Introduction . . . 225
10.5.2 The frequency-domain aircraft responses to 2D gust fields . . . 226
10.5.3 Calculation of the gust derivatives for 2D gust fields . . . 231
10.6 Remarks . . . 233

11 The Delft University of Technology model 247
11.1 Introduction . . . 247
11.2 Atmospheric turbulence field definitions . . . 248
11.3 Aerodynamic models . . . 249
11.3.1 1D Symmetrical longitudinal gust fields . . . 249

11.3.2 1D Asymmetrical lateral gust fields . . . 250
11.3.3 1D Symmetrical vertical gust fields . . . 254
11.3.4 2D Anti-symmetrical longitudinal gust fields . . . 260
11.3.5 2D Anti-symmetrical vertical gust fields . . . 265
11.4 The atmospheric turbulence PSD-functions . . . 270
11.4.1 1D gust fields . . . 270
11.4.2 2D gust fields . . . 270
11.4.3 Effective 1D PSD-functions for 2D gust fields . . . 271
11.5 Aircraft modeling . . . 274
11.5.1 Aircraft equations of motion for 1D gust fields . . . 274
11.5.2 Aircraft equations of motion for 2D gust fields . . . 276
11.6 Remarks . . . 277

12 The Four Point Aircraft model 283
12.1 Introduction . . . 283
12.2 The FPA-model gust inputs . . . 283
12.2.1 Definition of the gust inputs . . . 283
12.2.2 Correlation functions . . . 284
12.2.3 PSD-functions . . . 289
12.3 Aerodynamic models . . . 292
12.3.1 1D Symmetrical longitudinal gust fields . . . 292
12.3.2 1D Asymmetrical lateral gust fields . . . 295
12.3.3 1D Symmetrical vertical gust fields . . . 295
12.3.4 2D Anti-symmetrical longitudinal gust fields . . . 295
12.3.5 2D Anti-symmetrical vertical gust fields . . . 296
12.4 Aircraft modeling . . . 296
12.4.1 Aircraft equations of motion for 1D gust fields . . . 296
12.4.2 Aircraft equations of motion for 2D gust fields . . . 298
12.5 Remarks . . . 299

V Comparison of Gust Response Calculations 301

13 Comparison of results and discussion 303
13.1 Introduction . . . 303
13.2 Overview of models . . . 304
13.2.1 Introduction . . . 304
13.2.2 The LPF solution . . . 305
13.2.3 The LPF-EOM-solution . . . 305
13.2.4 The PCA-model . . . 306
13.2.5 The DUT-model . . . 307
13.2.6 The FPA-model . . . 308
13.3 Aerodynamic model responses . . . 309
13.3.1 Introduction . . . 309

13.3.2 Time-domain results . . . 312
13.3.3 Frequency-domain results . . . 317
13.4 Aircraft motion responses . . . 334
13.4.1 Introduction . . . 334
13.4.2 Time-domain results . . . 340
13.4.3 Analytical frequency-domain results . . . 341
13.5 LPF-EOM-model simulations . . . 348
13.5.1 Introduction . . . 348
13.5.2 LPF-EOM model responses . . . 354
13.6 Conclusions . . . 365

VI Conclusions and Recommendations 371

14 Conclusions and recommendations 373
14.1 Introduction . . . 373
14.2 Conclusions . . . 374
14.3 Recommendations for future research . . . 376

A Abbreviations and symbols 379

B Reference frames and definitions 387
B.1 Reference frames . . . 387
B.1.1 The Atmosphere-Fixed Frame of Reference $\mathcal{F}_A$ . . . 387
B.1.2 The Aerodynamic Frame of Reference $\mathcal{F}_{aero}$ . . . 387
B.1.3 The Body-Fixed Frame of Reference $\mathcal{F}_B$ . . . 388
B.1.4 The Earth-Fixed Frame of Reference $\mathcal{F}_E$ . . . 388
B.1.5 The Inertial Frame of Reference $\mathcal{F}_I$ . . . 389
B.1.6 The Panel Frame of Reference $\mathcal{F}_P$ . . . 390
B.1.7 The Rig Frame of Reference $\mathcal{F}_{rig}$ . . . 390
B.1.8 The Stability Frame of Reference $\mathcal{F}_S$ . . . 392
B.2 Definitions . . . 393
B.2.1 The Fourier-transform . . . 393
B.2.2 The calculation of frequency-response functions from the state-space representation . . . 394
B.2.3 The output Power Spectral Density function matrix . . . 395

C Quadrilateral source - and doublet elements 397
C.1 Introduction . . . 397
C.2 Quadri-lateral source elements . . . 397
C.3 Quadri-lateral doublet elements . . . 400

D Stability - and gust derivative definitions 403

E Aerodynamic fitting procedures 413
E.1 Introduction . . . 413
E.2 Frequency-response data extraction from time-domain simulations . . . 414
E.3 1D Analytical continuation of frequency-response data . . . 416
E.4 2D Analytical continuation of frequency-response data . . . 417
E.5 PSD-function fits . . . 419

F Aerodynamic fit parameters for 2D atmospheric turbulence inputs 421
F.1 Introduction . . . 421
F.2 Parameter tables . . . 422

G Spatial-domain gust fields, the flightpath definition and aerodynamic model gust inputs 425
G.1 Introduction . . . 425
G.2 The generation of spatial-domain gust fields . . . 426
G.2.1 3D Correlated gust fields . . . 426
G.2.2 2D Uncorrelated gust fields . . . 428
G.2.3 2D Correlated gust fields . . . 430
G.2.4 The numerical simulation of 2D gust fields . . . 431
G.2.5 Verification of the 2D gust fields . . . 432
G.3 Definition of the flightpath and the encountered gust fields . . . 440
G.3.1 Definition of the flightpath . . . 440
G.3.2 Definition of the encountered gust fields . . . 440
G.4 Summary of the definition of the aerodynamic model gust inputs . . . 443
G.5 Remarks . . . 445

H The atmospheric turbulence PSD-functions for the equations of motion 449
H.1 Introduction . . . 449
H.2 2D PSD-functions . . . 450
H.3 1D PSD-functions . . . 451
H.4 FPA-model PSD-functions . . . 452

I The aircraft equations of motion 461
I.1 Introduction . . . 461
I.2 The non-linear equations of motion . . . 462
I.3 The linear time-invariant equations of motion . . . 464
I.3.1 Linearization of the equations of motion . . . 464
I.3.2 Equations of motion in the stability frame of reference . . . 470
I.3.3 Non-dimensional equations of motion . . . 471
I.3.4 The non-dimensional equations of motion in state-space form . . . 473
I.4 The linearized equations of motion in the frequency-domain . . . 475
I.4.1 Introduction . . . 475
I.4.2 Symmetrical equations of motion . . . 476
I.4.3 Asymmetrical equations of motion . . . 476

References **481**

Samenvatting **485**

Acknowledgements **489**

Curriculum vitae **491**

Chapter 1

Introduction

1.1 Goal of this thesis

The response of aircraft to stochastic atmospheric turbulence plays an important role in, for example, aircraft-design (load calculations) and flight-simulation (handling qualities research and pilot training). In order to simulate these aircraft responses, an accurate mathematical model is required. Two classical models will be discussed in this thesis, that is the Delft University of Technology (DUT) model and the Four Point Aircraft (FPA) model. Although they are well estabilished, their fidelity remains obscure. The cause lies in one of the requirements for system identification; it has always been necessary to relate inputs to outputs to determine, or identify, system dynamic characteristics. From experiments, using both the measured input ánd the measured output, a mathematical model of any system can be obtained. When considering an input-output system such as an aircraft subjected to stochastic atmospheric turbulence, a major problem emerges. During flight tests, no practical difficulty arises measuring the aircraft-system's outputs, such as the angle-of-attack, the pitch-angle, the roll-angle, etc.. However, a huge problem arises when the input to the aircraft-system is considered; this input is stochastic atmospheric turbulence in this thesis. Currently, it still remains extremely difficult to identify the entire flowfield around an aircraft's geometry subjected to a turbulent field of flow; an infinite amount of sensors would be required to identify the atmospheric turbulence velocity component's distribution (the input) over it. As a consequence, it is difficult, if not impossible, to identify atmospheric turbulence models from flight tests.

In an attempt to shed some more light on solving the problem of the response of aircraft to atmospheric turbulence, the subject of this thesis, it depends on the formulation of two distinct models: one of the atmospheric turbulence itself (the atmospheric turbulence model), and the other of the aircraft's response to it (the mathematical aircraft model). Regarding atmospheric turbulence modeling, in this thesis stochastic, stationary, homogeneous, isotropic atmospheric turbulence is considered as input to the aircraft model. These models of atmospheric turbulence are well established, see references [2, 35, 1].

As far as mathematical aircraft models are concerned, many of them have been proposed before, see references [4, 5, 35, 25, 30]. However, verifying these models has always been extremely difficult due to the identification problem indicated above. As part of the mathematical aircraft model, (parametric) aerodynamic models often make use of (quasi-) steady aerodynamic results; that is all steady aerodynamic parameters are estimated using either results obtained from windtunnel experiments, handbook methods, Computational Aerodynamics (CA) which comprises Linearized Potential Flow (LPF) methods, or Computational Fluid Dynamics (CFD) which comprises Full-Potential, Euler and Navier-Stokes methods.

Using handbook methods, unsteady aerodynamic effects, such as time-delays and the effect of lift/moment build-up or transients, are usually added to the parametric aerodynamic modeling process later. The fidelity of such models obtained from these methods is usually improved by incorporating the effects of unsteady aerodynamics, that is the effect of aircraft motion unsteady aerodynamics is often incorporated by the use of Theodorsen and Wagner functions. Also, the aerodynamic model's fidelity with respect to atmospheric turbulence is increased by the use of Sears and Küssner functions. Although these analytical mathematical aerodynamic models are enhanced using such functions, they still rely on approximations. The effect of the unsteady wake, for example, is still treated as a steady phenomenon. Furthermore, aerodynamic interactions between aircraft components (such as wing and stabilizer) are neglected.
Presently, however, due to the enormous capabilities in computing power, the numerical simulation of both steady and unsteady airflows over complex vehicle configurations provides a versatile, and hopefully better, tool in estimating both the steady and unsteady aerodynamic parameters of a mathematical aerodynamic model. Simulating the time-dependent pressure distribution over a vehicle's configuration, both the aerodynamic forces and moments acting on the vehicle can now be calculated with adequate precision and with quite reasonable reliability. These simulations include the previously mentioned unsteady aerodynamic effects such as time-delays, unsteady aerodynamic effects regarding the unsteady lift/moment build-up ánd unsteady effects regarding aerodynamic interaction between the vehicle's components (such as wing, horizontal stabilizer, vertical fin, nacelles, etc.).

In this thesis (unsteady) Linearized Potential Flow (LPF) methods, or commonly known as "panel methods", are used to identify both the time-dependent aerodynamic forces and time-dependent moments acting on the aircraft geometry. Using a time-domain approach, the mathematical aircraft model is identified for both aircraft motion and gust-response. Using the steady panel method as a virtual windtunnel (without any windtunnel walls ánd using a true scale vehicle model), the steady Parametric Computational Aerodynamics (PCA) model is identified in terms of stability derivatives. As a test for the reliability of the Linearized Potential Flow method, the steady stability derivatives will be compared to results obtained from flight tests.
Compared to the identification of the steady PCA-model, identifying its unsteady part

with respect to aircraft motion and gusts is quite a different problem and it requires a different approach of identification. In this case the unsteady LPF method is used as a virtual flight test facility, allowing aircraft motions unfeasible during flight test. Initially, from harmonic time-domain simulations, the aerodynamic frequency-response functions with respect to both aircraft motions ánd elementary gust fields are obtained. Using these PCA-model frequency-response functions, which are in fact already models in themselves, the aerodynamic model is given in terms of frequency-dependent aerodynamic parameters, also known as stability derivatives and gust derivatives. Ultimately, using these frequency-dependent stability derivatives and frequency-dependent gust derivatives, the PCA-model in terms of constant (thus independent of frequency) stability- and gust derivatives is obtained.

The promising developments in Computational Aerodynamics (and Computational Fluid Dynamics) provide the necessary tool in identifying both the steady and unsteady aerodynamic models. A distinct advantage over windtunnel experiments and flight tests is the possibility to compute the contribution of every single aircraft part (such as wing, horizontal-stabilizer, fuselage, etc.) to each aerodynamic frequency-response function (or to the stability derivatives and gust derivatives). An advantage which greatly attributes in understanding the shape of PCA-model frequency-responses when plotted in Nyquist-diagrams. Another distinct advantage of Computational Aerodynamics is the possibility to let the considered vehicle perform manoeuvres which are impossible to perform during flight tests (such as isolated surging, swaying and heaving aircraft motions). This last advantage is also used for the simulation of the time-dependent aerodynamic forces and moments due to atmospheric turbulence. Contrary to responses observed during flight tests, the elimination of aircraft motion provides the possibility to simulate aerodynamic responses to isolated atmospheric perturbations. Results of these simulations (the LPF-solutions) will later be compared to results obtained using the "gust derivative approach".

Three parametric mathematical aircraft models are considered in this thesis. The first model is based on simulated aerodynamic frequency-response functions. Using these functions, the constant parameter aerodynamic model is derived. This model is defined as the "PCA-model". Having identified the PCA-model frequency-response functions, and from them the PCA-model in terms of constant stability- ánd gust derivatives, aircraft responses to both one-dimensional (1D) longitudinal, lateral and vertical gusts ánd two-dimensional (2D) longitudinal and vertical gusts are simulated. These simulations will include the frequency-response in terms of Power Spectral Density (PSD) functions of the aircraft's motion variables, as well as the aircraft motion variables' time-domain response. The (classical) second and third model are the so-called Delft Univerity of Technology model ("DUT-model") and Etkin's Four-Point Aircraft model ("FPA-model"), respectively, which are also based on parametric aerodynamic models which rely on constant, thus frequency-independent, parameters. However, the aerodynamic models now rely on stability derivatives only, whith the gust derivatives given as a function of them. The stability derivatives used in these two models are equal to those obtained for the constant parameter

PCA-model. For the DUT- and FPA-model, aircraft responses to both 1D longitudinal, lateral and vertical gusts ánd 2D longitudinal and vertical gusts are simulated as well. Similar to the PCA-model, these simulations will also include the frequency-response in terms of Power Spectral Density (PSD) functions of the aircraft's motion variables, as well as the aircraft motion variables' time-domain response.

1.2 Outline of this thesis

The outline of this thesis is provided in figure 1.1.

After a short summary of the applied atmospheric turbulence model in **chapter 2**, the theory of steady incompressible Linearized Potential Flow is given in **chapter 3**. **Chapter 4** continues with a similar treatment as in chapter 3, discussing unsteady incompressible Linearized Potential Flow. Both analytical frequency-response functions (or aerodynamic transfer functions) ánd numerical frequency-response functions for isolated wings will also be discussed in this chapter. In **chapter 5** the definition of specific aircraft motion perturbations and atmospheric turbulence inputs will be given. **Chapter 6** discusses the aircraft grid for the example aircraft. This grid will be used for both steady and unsteady Linearized Potential Flow simulations. For aerodynamic model identification purposes, the aircraft grid defined in chapter 6 is used in **chapter 7** where the numerical symmetrical aerodynamic frequency-response functions are given for the PCA-model. They are determined with respect to aircraft motions in surge and heave, and to both longitudinal and vertical gusts. All perturbations in aircraft motion and gusts are of harmonic nature. Results of the analytical continuation of frequency-response data for time-domain models will also be given (aerodynamic fits).
Next, in this chapter the concept of frequency-dependent stability derivatives and frequency-dependent gust derivatives for complete aircraft configurations is discussed. Furthermore, the steady symmetrical aerodynamic model is defined in this chapter. **Chapter 8** treats, along the same lines as in chapter 7, the numerical asymmetrical frequency-response functions and unsteady asymmetrical aerodynamic model for the PCA-model. The (harmonic) degrees of freedom considered are now with respect to swaying aircraft motions ánd antisymmetrical longitudinal-, asymmetrical lateral- and anti-symmetrical vertical gusts. In **chapter 9** the aircraft grid defined in chapter 6 is flown through 2D spatial-domain gust fields. First, the aerodynamic force and moment coefficients acting on the aircraft geometry are calculated assuming a recti-linear flightpath (no aircraft motions will be considered). Next, additional theory is given for the so-called "coupled-solution", that is the aircraft equations of motion are now coupled with the potential flow solution.
Chapters 10, 11 and **12** discuss the equations of motion of aircraft subjected to both 1D longitudinal, lateral and vertical gusts ánd 2D longitudinal and vertical gusts. In chapter 10 the mathematical aircraft model for the "Parametric Computational Aerodynamics model" (or "PCA-model") is introduced, and it includes the equations of motion using both aerodynamic frequency-response functions (or frequency-dependent stability- and gust derivatives) and an aerodynamic model in terms of constant stability- and gust

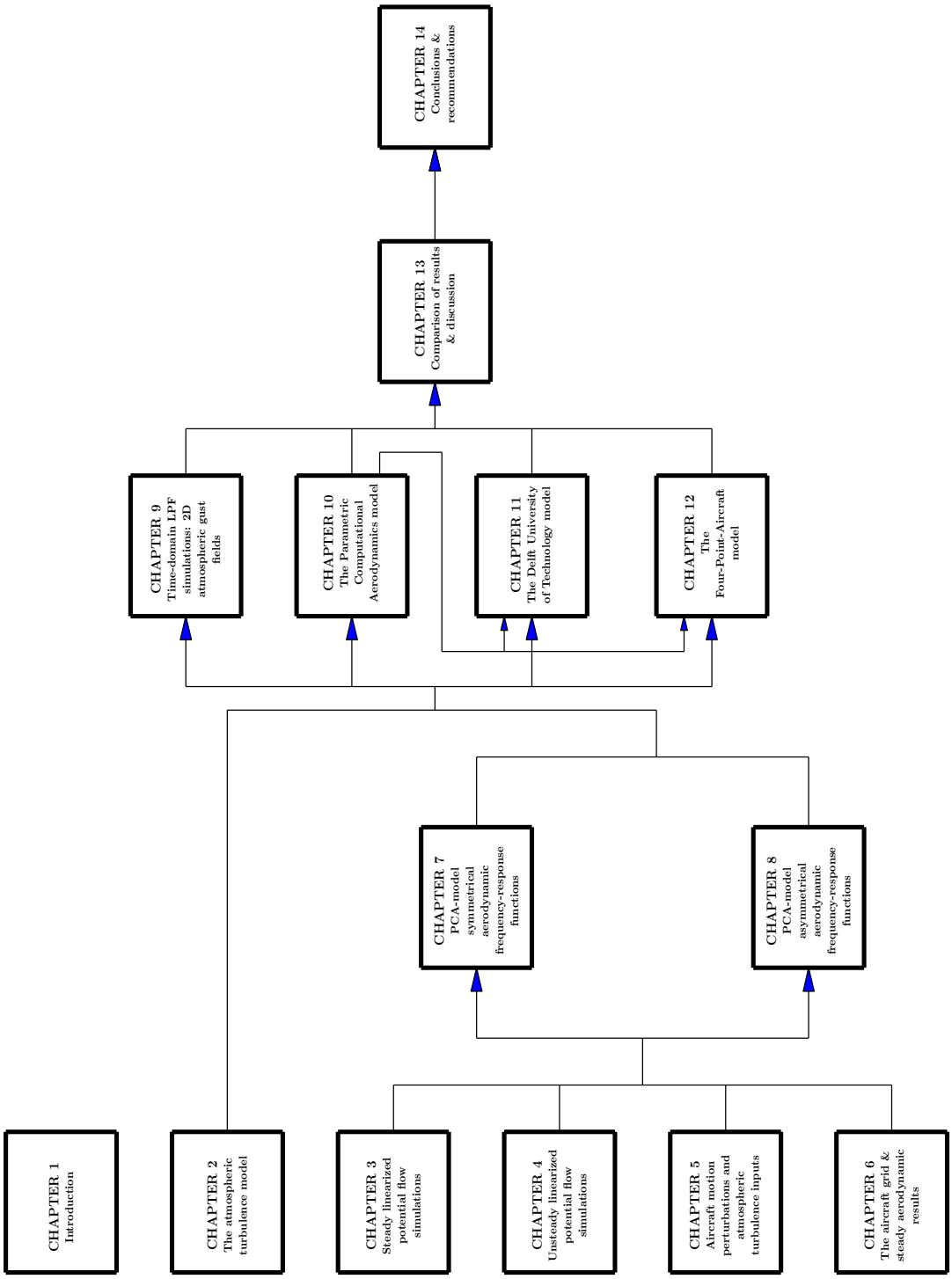


Figure 1.1: This thesis overview.

derivatives. Chapters 11 and 12 will discuss the equations of motion for parametric aerodynamic models in terms of constant stability- and gust derivatives. The aircraft models are based on the Delft University of Technology gust-response theory, the "DUT-model" (chapter 11), and Etkin's "Four-Point-Aircraft model" (or "FPA model", chapter 12). In these chapters, the constant stability derivatives obtained in chapter 10 will be used for simulations. A comparison of results of the PCA-, the DUT- and the FPA-model is given in **chapter 13**. In this chapter both time- and frequency-domain results, given in terms of aerodynamic coefficients, will be compared to the ones obtained from a time-domain Linearized Potential Flow simulation (the LPF-solution). In this case no aircraft motions are taken into account (the aircraft (-grid) is traveling along a prescribed recti-linear flightpath), thus the aerodynamic response is limited to gust fields only. Also, time-domain aircraft motion results will be compared to results obtained for the LPF-solution. First, the PCA-, the DUT- and the FPA-model aircraft motion simulations will be compared to the ones obtained for the LPF-solution. These simulations make use of the gust-induced aerodynamic coefficients obtained for a recti-linear flightpath (excluding aircraft motions). Next, the PCA-, DUT- and FPA-model aircraft motion simulations are compared to results obtained from a Linearized Potential Flow simulation which is coupled to the equations of motion (the so-called "coupled-solution", designated as the LPF-EOM-model). This simulation, in which the aerodynamic grid will be flown through stochastic 2D longitudinal, lateral and vertical gust fields, will be the ultimate test for the parametric models presented in chapters 10, 11 and 12. Chapter 13 is followed by conclusions and recommendations in **chapter 14**.

Since the research conducted for this thesis involved multiple disciplines, some of them are explained in detail for their educational value. For example, the developed panel-methods are described as a one to one mapping of the applied software codes. Furthermore the recipe for determining the novel PCA-model equations of motion, including its parameters, is outlined in detail.

Part I

Atmospheric Turbulence Modeling

Chapter 2

The atmospheric turbulence model

2.1 Introduction

In this chapter the atmospheric turbulence models used in this thesis and their limitations will be discussed. These models are given in terms of atmospheric turbulence velocity components that can be considered as fluctuations superposed on a mean wind. Since mean wind is a problem primarily of importance for navigation and guidance, its effects are not considered and throughout this thesis the mean wind is assumed to be zero.

The theory of atmospheric turbulence modeling is based on the work of Batchelor, see reference [2]. This chapter summarizes the definitions of the atmospheric turbulence covariance function matrix and the atmospheric turbulence Power Spectral Density (PSD) function matrix as they will be used throughout this thesis. Furthermore, it provides the general definition of both the covariance function matrix and the PSD function matrix of three-dimensional (3D), correlated, stationary, homegeneous, isotropic atmospheric turbulence. The atmospheric turbulence models will be used to calculate aircraft responses to random gusts in the following chapters.

The presented atmospheric turbulence model holds for high altitudes (Clear Air Turbulence (CAT)).

2.2 Atmospheric turbulence modeling assumptions

Atmospheric turbulence is a random process which describes the chaotic motion of the air. The gust velocity vector $\underline{u} = [u_1, u_2, u_3]^T$ is a function of the position vector $\underline{r} = [x_1, x_2, x_3]^T$ in the Earth-Fixed Frame of Reference $\mathcal{F}_E$ (which is defined in appendix B) and of time t. The wind velocity vector at an arbitrary point P in $\mathcal{F}_E$ is written as the

vectorial sum of the mean wind and the randomly fluctuating atmospheric turbulence,

$$\underline{u}'(\underline{r},t) = \underline{u}_0 + \underline{u}(\underline{r},t) \tag{2.1}$$

or,

$$\begin{aligned} u_1'(x_1,x_2,x_3,t) &= u_{1_0} + u_1(x_1,x_2,x_3,t) && (2.2)\\ u_2'(x_1,x_2,x_3,t) &= u_{2_0} + u_2(x_1,x_2,x_3,t) && (2.3)\\ u_3'(x_1,x_2,x_3,t) &= u_{3_0} + u_3(x_1,x_2,x_3,t) && (2.4) \end{aligned}$$

Both the mean wind velocity components ($\underline{u}_0 = [u_{1_0}, u_{2_0}, u_{3_0}]^T$) and the atmospheric turbulence velocity components ($\underline{u}(\underline{r},t) = [u_1(x_1,x_2,x_3,t), u_2(x_1,x_2,x_3,t), u_3(x_1,x_2,x_3,t)]^T$) are described in the frame $\mathcal{F}_E$ and are taken positive in respectively the X_E-, Y_E- and Z_E-direction of $\mathcal{F}_E$. The position P in $\mathcal{F}_E$ is given by the coordinates of the position vector $\underline{r} = [x_1, x_2, x_3]^T$.
Since the effect of mean winds are not considered in this thesis, it is assumed that $u_{1_0} = u_{2_0} = u_{3_0} = 0$. Note that the mean wind components are independent of position and time, hence they are both spatially- and time-averaged.

Now, the atmospheric turbulence velocity vector is written as,

$$\begin{aligned} \underline{u}(\underline{r},t) &= [u_1(\underline{r},t), u_2(\underline{r},t), u_3(\underline{r},t)]^T = \\ &= [u_1(x_1,x_2,x_3,t), u_2(x_1,x_2,x_3,t), u_3(x_1,x_2,x_3,t)]^T \end{aligned} \tag{2.5}$$

The atmospheric turbulence velocity vector $\underline{u}$, as defined in equation (2.5), is random and describes a multivariate (u_1, u_2, u_3) and multivariable (x_1, x_2, x_3, t) stochastic process. The purpose is now to obtain a general statistical description of atmospheric turbulence by making use of either the covariance functions or the PSD functions.

When deriving the atmospheric turbulence covariance functions, the relative separation in time τ, instead of absolute time t, and the relative spatial separation vector $\underline{\xi} = [\xi_1, \xi_2, \xi_3]^T$, instead of the absolute position vector $\underline{r} = [x_1, x_2, x_3]^T$, will be defined. Similar to the absolute position vector $\underline{r}$, the spatial separation $\underline{\xi}$ is given in $\mathcal{F}_E$.

Using the spatial separation $\underline{\xi} = [\xi_1, \xi_2, \xi_3]^T$ and time separation τ, the general matrix of covariance functions, $C_{\underline{u}\underline{u}}(\underline{r},t;\underline{r}+\underline{\xi},t+\tau)$ becomes,

$$C_{\underline{u}\underline{u}}(\underline{r},t;\underline{r}+\underline{\xi},t+\tau) = E\left\{\underline{u}(\underline{r},t)\ \underline{u}(\underline{r}+\underline{\xi},t+\tau)\right\} = \tag{2.6}$$

$$= \begin{bmatrix} E\left\{u_1(\underline{r},t)\ u_1(\underline{r}+\underline{\xi},t+\tau)\right\} & E\left\{u_1(\underline{r},t)\ u_2(\underline{r}+\underline{\xi},t+\tau)\right\} & E\left\{u_1(\underline{r},t)\ u_3(\underline{r}+\underline{\xi},t+\tau)\right\} \\ E\left\{u_2(\underline{r},t)\ u_1(\underline{r}+\underline{\xi},t+\tau)\right\} & E\left\{u_2(\underline{r},t)\ u_2(\underline{r}+\underline{\xi},t+\tau)\right\} & E\left\{u_2(\underline{r},t)\ u_3(\underline{r}+\underline{\xi},t+\tau)\right\} \\ E\left\{u_3(\underline{r},t)\ u_1(\underline{r}+\underline{\xi},t+\tau)\right\} & E\left\{u_3(\underline{r},t)\ u_2(\underline{r}+\underline{\xi},t+\tau)\right\} & E\left\{u_3(\underline{r},t)\ u_3(\underline{r}+\underline{\xi},t+\tau)\right\} \end{bmatrix}$$

where $E\{\cdot\}$ denotes the expectation operator.

The Fourier transform, which is defined in appendix B, of the covariance function matrix, equation (2.6), results in the PSD function matrix, $S_{\underline{uu}}(\underline{r}, t; \underline{\Omega}, \omega)$,

$$S_{\underline{uu}}(\underline{r}, t; \underline{\Omega}, \omega) = \int_{-\infty}^{+\infty}\int_{-\infty}^{+\infty}\int_{-\infty}^{+\infty}\int_{-\infty}^{+\infty} C_{\underline{uu}}(\underline{r}, t; \underline{r}+\underline{\xi}, t+\tau)\, e^{-j\left(\underline{\Omega}\cdot\underline{\xi}+\omega\tau\right)} d\xi_1 d\xi_2 d\xi_3 d\tau \tag{2.7}$$

In equation (2.7), four integrals appear due to the four variables ξ_1, ξ_2, ξ_3 and τ. The spatial frequency vector $\underline{\Omega} = [\Omega_1, \Omega_2, \Omega_3]^T$, with (for example) $\Omega_1 = \frac{2\pi}{\lambda_1}$ where λ_1 is the wave length in X_E-direction, naturally arises in the Fourier transformation as the dual of the circular frequency ω belonging to time separation τ.

As an example of an elementary two-dimensional (2D) harmonic atmospheric turbulence field with $\Omega_1 = \frac{2\pi}{\lambda_1}$ and $\Omega_2 = \frac{2\pi}{\lambda_2}$, see figure 2.1. This elementary 2D turbulence field is regarded as one component of the ensemble of an infinite amount of 2D turbulence fields, modulated in amplitude by the atmospheric turbulence PSD function.
Notice that the general expression of the PSD function matrix may differ from point to point ($\underline{r}$) and from time to time (t), and therefore is actually a function of $\underline{r}$ and t. The inverse Fourier transform of the PSD function matrix $S_{\underline{uu}}(\underline{r}, t; \underline{\Omega}, \omega)$ results in the covariance function matrix $C_{\underline{uu}}(\underline{r}, t; \underline{r}+\underline{\xi}, t+\tau)$,

$$C_{\underline{uu}}(\underline{r}, t; \underline{r}+\underline{\xi}, t+\tau) = \frac{1}{(2\pi)^4}\int_{-\infty}^{+\infty}\int_{-\infty}^{+\infty}\int_{-\infty}^{+\infty}\int_{-\infty}^{+\infty} S_{\underline{uu}}(\underline{r}, t; \underline{\Omega}, \omega) e^{+j\left(\underline{\Omega}\cdot\underline{\xi}+\omega\tau\right)} d\Omega_1 d\Omega_2 d\Omega_3 d\omega \tag{2.8}$$

The covariance function matrix, see for example equation (2.6), is a 3x3 matrix where each matrix-element is an ensemble average of the product of two atmospheric turbulence velocity components separated in both space and time.

Next, several assumptions regarding the atmospheric turbulence process are made that will lead to considerable simplifications in both the covariance function matrix and the PSD function matrix:

- **Assumption 1**
  Atmospheric turbulence is a stationary process

  The most general case allows the atmospheric turbulence statistics to vary from point to point and time to time, see equation (2.6). A fact of great practical importance is, however, that the speed of an "air particle" in the atmosphere is constraint to relatively slow fluctuations in time. Now, suppose that an aircraft flies in a turbulent atmosphere. It will then encounter the stochastically fluctuating atmospheric turbulence components u_1, u_2 and u_3. Aircraft usually fly at speeds much greater than the encountered atmospheric turbulence velocities, thus a relatively large patch of atmospheric turbulence can be traversed in a time so short that the atmospheric

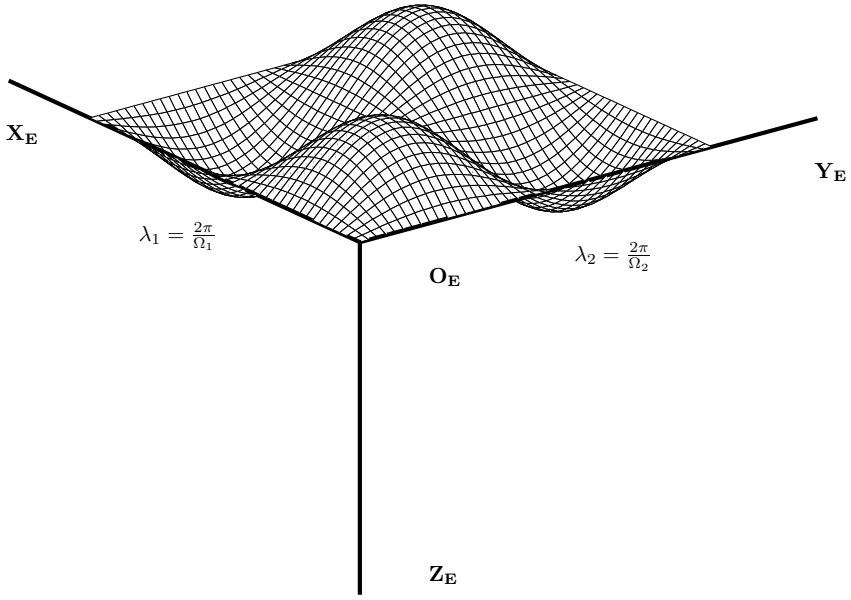


Figure 2.1: An elementary 2D harmonic atmospheric turbulence field in $\mathcal{F}_E$ with $\lambda_1 = \frac{2\pi}{\Omega_1}$ and $\lambda_2 = \frac{2\pi}{\Omega_2}$.

turbulence velocity components shall not change significantly. This amounts to neglecting time t in the argument of $\underline{u}(\underline{r}, t)$, see equation (2.6), that is treating atmospheric turbulence as a "frozen" pattern in the atmosphere (also known as "*Taylor's hypothesis*", see references [1, 30]). The general expressions for the covariance function matrix and the PSD function matrix simplify to, respectively, $C_{\underline{u}\underline{u}}(\underline{r}; \underline{r} + \underline{\xi})$ and $S_{\underline{u}\underline{u}}(\underline{r}; \underline{\Omega})$.

- **Assumption 2**
  Atmospheric turbulence is homogeneous along the flightpath

  At higher altitudes, atmospheric turbulence appears to occur in large patches, each of which can reasonably be considered to be homogeneous although the atmospheric turbulence characteristics may differ from patch to patch, see also reference [30]. Near the earth's surface fairly large changes in the atmospheric turbulence velocity components occur as a function of altitude (induced by vertical windshear). However, for aircraft in nearly horizontal flight, homogenity of atmospheric turbulence along the flight path is a reasonable approximation. As a consequence of this assumption, the dependency of both the covariance function matrix and the PSD function matrix on the position vector $\underline{r}$ vanishes. It is now possible to write the matrices $C_{\underline{u}\underline{u}}(\underline{r}; \underline{r}+\underline{\xi})$ and $S_{\underline{u}\underline{u}}(\underline{r}; \underline{\Omega})$ as $C_{\underline{u}\underline{u}}(\underline{\xi})$ and $S_{\underline{u}\underline{u}}(\underline{\Omega})$, respectively. Notice that when atmospheric turbulence is stationary and homogeneous it is also ergodic, and therefore ensemble averages may be replaced by time averages.

- **Assumption 3**
  Atmospheric turbulence is an isotropic process

  In general, the statistical functions describing atmospheric turbulence depend on the directions of the axes of $\mathcal{F}_E$. This especially is the case in the earth's boundary layer. When this dependency is absent, and there is evidence that this is the case at higher altitudes, atmospheric turbulence is considered to be isotropic, i.e. all statistical properties are independent of the orientation of the axes ($\mathcal{F}_E$), see reference [1, 30]. As a result of isotropy, the three mean-square (variance) atmospheric turbulence velocity components are equal, or,

  $$\sigma_{u_1}^2 = \sigma_{u_2}^2 = \sigma_{u_3}^2 = \sigma^2 \tag{2.9}$$

  with $\sigma_{u_i}^2,\ i = 1 \cdots 3$ the variance of the atmospheric turbulence velocity components. A typical value for the variance at higher altitude is $\sigma^2 = 1\ \left[\frac{m^2}{s^2}\right]$, a value used throughout this thesis. For typical values of $\sigma_{u_1}^2$, $\sigma_{u_2}^2$ and $\sigma_{u_3}^2$ in ground effect, see reference [30].

- **Assumption 4**
  Atmospheric turbulence is a random process with Gaussian distribution

  Although this assumption has no effect on the form of the atmospheric turbulence covariance functions and PSD functions, this assumption is of practical importance for the analysis of atmospheric turbulence fields and the analysis of aircraft responses to them. However, it has been shown from experiments that atmospheric turbulence is not necessarily Gaussian, see reference [6].

- **Assumption 5**
  Atmospheric turbulence velocity components have zero mean

  The assumptions that the atmospheric turbulence process is stationairy and that the atmosphere's mean winds are not considered in this thesis, leads to,

  $$\mu_{u_1} = \mu_{u_2} = \mu_{u_3} = 0 \tag{2.10}$$

  with $\mu_{u_i},\ i = 1 \cdots 3$ the mean of the atmospheric turbulence velocity components.

Using the assumptions indicated above, the covariance function matrix and the PSD function matrix become,

$$C_{\underline{uu}}(\underline{\xi}) \quad = \quad \left[C_{u_i u_j}(\xi_1, \xi_2, \xi_3)\right] = \left[E\left\{u_i(\xi_1, \xi_2, \xi_3) u_j(\xi_1, \xi_2, \xi_3)\right\}\right]$$

$$= \begin{bmatrix} C_{u_1u_1}(\xi_1,\xi_2,\xi_3) & C_{u_1u_2}(\xi_1,\xi_2,\xi_3) & C_{u_1u_3}(\xi_1,\xi_2,\xi_3) \\ C_{u_2u_1}(\xi_1,\xi_2,\xi_3) & C_{u_2u_2}(\xi_1,\xi_2,\xi_3) & C_{u_2u_3}(\xi_1,\xi_2,\xi_3) \\ C_{u_3u_1}(\xi_1,\xi_2,\xi_3) & C_{u_3u_2}(\xi_1,\xi_2,\xi_3) & C_{u_3u_3}(\xi_1,\xi_2,\xi_3) \end{bmatrix}$$

$$= \begin{bmatrix} E\left\{u_1(\underline{0})\ u_1(\underline{\xi})\right\} & E\left\{u_1(\underline{0})\ u_2(\underline{\xi})\right\} & E\left\{u_1(\underline{0})\ u_3(\underline{\xi})\right\} \\ E\left\{u_2(\underline{0})\ u_1(\underline{\xi})\right\} & E\left\{u_2(\underline{0})\ u_2(\underline{\xi})\right\} & E\left\{u_2(\underline{0})\ u_3(\underline{\xi})\right\} \\ E\left\{u_3(\underline{0})\ u_1(\underline{\xi})\right\} & E\left\{u_3(\underline{0})\ u_2(\underline{\xi})\right\} & E\left\{u_3(\underline{0})\ u_3(\underline{\xi})\right\} \end{bmatrix}$$

and,

$$S_{\underline{uu}}(\underline{\Omega}) = \left[S_{u_iu_j}(\Omega_1,\Omega_2,\Omega_3)\right]$$

$$= \begin{bmatrix} S_{u_1u_1}(\Omega_1,\Omega_2,\Omega_3) & S_{u_1u_2}(\Omega_1,\Omega_2,\Omega_3) & S_{u_1u_3}(\Omega_1,\Omega_2,\Omega_3) \\ S_{u_2u_1}(\Omega_1,\Omega_2,\Omega_3) & S_{u_2u_2}(\Omega_1,\Omega_2,\Omega_3) & S_{u_2u_3}(\Omega_1,\Omega_2,\Omega_3) \\ S_{u_3u_1}(\Omega_1,\Omega_2,\Omega_3) & S_{u_3u_2}(\Omega_1,\Omega_2,\Omega_3) & S_{u_3u_3}(\Omega_1,\Omega_2,\Omega_3) \end{bmatrix}$$

with $i = 1,2,3$, $j = 1,2,3$, $\underline{\xi} = [\xi_1,\xi_2,\xi_3]^T$, $\underline{0} = [0,0,0]^T$ and $\underline{\Omega} = [\Omega_1,\Omega_2,\Omega_3]^T$.

Due to the assumptions and simplifications made above, two fundamental one-dimensional (1D) correlation functions can be defined, see references [5, 30, 4, 2] (they will be discussed in section 2.2.1). The general covariance function matrix and the general PSD function matrix will be summarized in sections 2.3 and 2.4, respectively.

2.2.1 Fundamental atmospheric turbulence correlation functions

The atmospheric turbulence velocity components u_1, u_2 and u_3, as given in section 2.2, are parallel to the X_E-, Y_E- and Z_E-axis of $\mathcal{F}_E$, respectively. It should also be noted that with the assumptions made in section 2.2, the atmospheric turbulence velocity components u_1, u_2 and u_3 are written as $u_1(\xi_1,\xi_2,\xi_3)$, $u_2(\xi_1,\xi_2,\xi_3)$ and $u_3(\xi_1,\xi_2,\xi_3)$. The vector $\underline{\xi} = [\xi_1,\xi_2,\xi_3]^T$ is the position (or spatial separation) of an arbitrary point in $\mathcal{F}_E$ with respect to the origin of $\mathcal{F}_E$, O_E, thus relating the atmospheric turbulence velocity components at $[\xi_1,\xi_2,\xi_3]^T$ to the turbulence velocity components present at the origin O_E of the frame $\mathcal{F}_E$.

Due to the simplifications made in section 2.2, two fundamental 1D correlation functions can now be formulated to describe the 1D correlation between atmospheric turbulence velocity components, see also references [4, 1, 30]. They are referred to as "fundamental" as they form the basis for the derivation of the the multi-dimensional correlation functions used throughout this thesis. With $\xi = \left|\underline{\xi}\right|$, these fundamental correlation functions according to Dryden are defined as,

- The 1D longitudinal correlation function $f(\xi)$,

$$f(\xi) = \frac{E\left\{u_{long}(0)u_{long}(\xi)\right\}}{\sigma^2} = e^{-\frac{\xi}{L_g}} \tag{2.11}$$

The longitudinal correlation function $f(\xi)$ describes the correlation of the atmospheric turbulence velocity component along the connection line of two points, with these two points spatially separated over distance ξ, see figure 2.2.

- The 1D lateral correlation function $g(\xi)$,

$$g(\xi) = \frac{E\left\{u_{lat}(0)u_{lat}(\xi)\right\}}{\sigma^2} = e^{-\frac{\xi}{L_g}}\left(1 - \frac{\xi}{2L_g}\right) \tag{2.12}$$

The lateral correlation function $g(\xi)$ describes the correlation of the atmospheric turbulence velocity component perpendicular to the connection line of two points, with these two points spatially separated over distance ξ, see figure 2.3.

In equations (2.11) and (2.12) the variable L_g is given. This variable is also known as the "turbulence scale length" or the "integral scale of turbulence". The relation between the fundamental 1D longitudinal correlation function, $f(\xi)$, and the turbulence scale length L_g is,

$$L_g = \int_0^{+\infty} f(\xi)d\xi = \int_0^{+\infty} e^{-\frac{\xi}{L_g}}d\xi = L_g \int_0^{+\infty} e^{-\frac{\xi}{L_g}}d\frac{\xi}{L_g} = L_g \int_0^{+\infty} e^{-p}dp$$

Bearing in mind that,

$$\int_0^{+\infty} e^{-p}p^n dp = n!$$

and with taking n to be zero, it follows that,

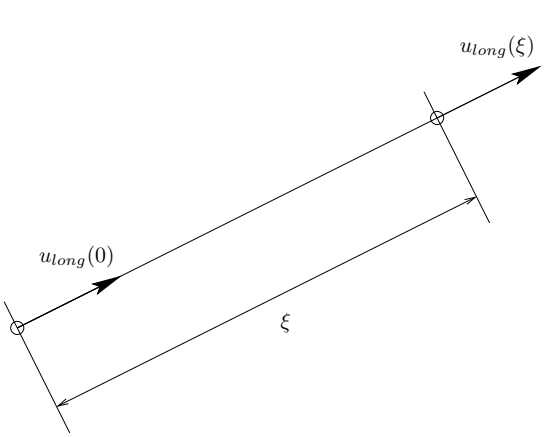
$$L_g = L_g \int_0^{+\infty} e^{-p}dp = L_g \cdot 0! = L_g \tag{2.13}$$

Finally, it should be noted that the atmospheric turbulence velocity component's covariance function is calculated by multiplying the appropriate correlation function by the variance σ^2 of the atmospheric turbulence velocities (see also assumption 3 in section 2.2).

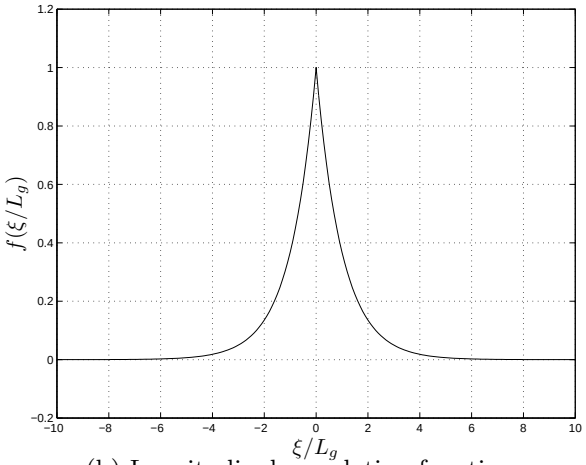
2.3 The atmospheric turbulence covariance function matrix

2.3.1 The general covariance function matrix

In section 2.2.1 the fundamental 1D correlation functions $f(\xi)$ and $g(\xi)$ were summarized. They only hold for spatial separations along a straight line and they are only valid for either separated turbulence velocity components along or perpendicular to the separation line, see for example figure 2.4.

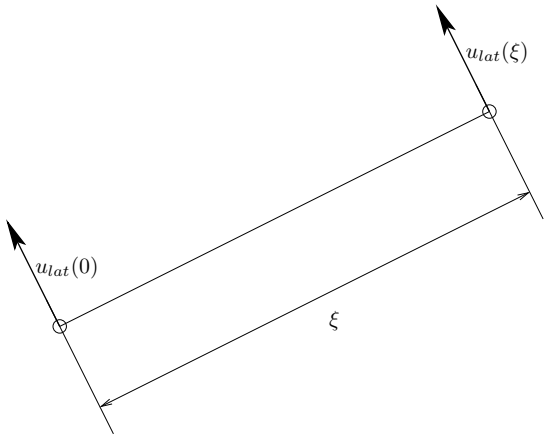


(a) Longitudinal correlation

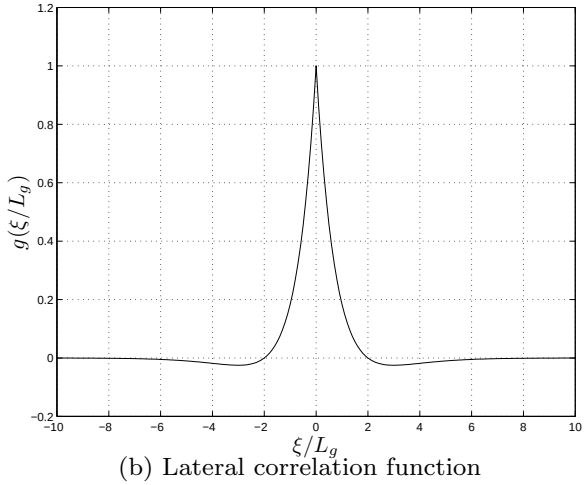


(b) Longitudinal correlation function

Figure 2.2: Longitudinal correlation.



(a) Lateral correlation



(b) Lateral correlation function

Figure 2.3: Lateral correlation.

However, an aircraft's flight path is never exactly aligned with either of the three axes of the frame $\mathcal{F}_E$. Because aerodynamic effects due to the finite dimensions of aircraft flying through the turbulent atmosphere are of importance (see chapters 7 through 12), the covariance function matrix $C_{\underline{u}\underline{u}}(\underline{\xi})$ of the atmospheric turbulence velocity components $[u_1, u_2, u_3]^T$ for the arbitrary spatial separation vector $\underline{\xi} = [\xi_1, \xi_2, \xi_3]^T$ is required. Based on the two fundamental 1D correlation functions, $f(\xi)$ and $g(\xi)$, Batchelor (see reference [2]) introduced a general correlation function matrix for arbitrary spatial separations in three dimensions. The correlation function's matrix elements are written as,

$$R_{u_i u_j}(\underline{\xi}) = \frac{C_{u_i u_j}(\underline{\xi})}{\sigma^2} = \frac{f(|\underline{\xi}|) - g(|\underline{\xi}|)}{|\underline{\xi}|^2}\, \xi_i\, \xi_j + g(|\underline{\xi}|)\, \delta_{ij} \tag{2.14}$$

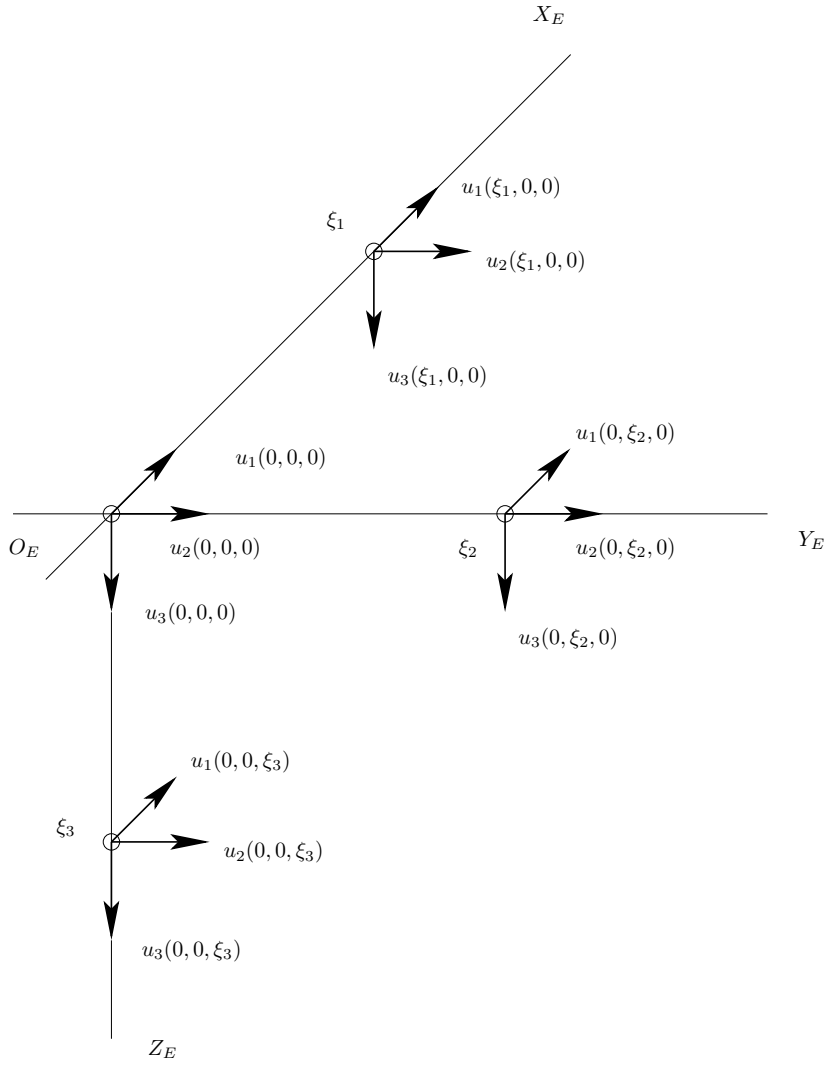


Figure 2.4: Limitations in spatial separation for the fundamental 1D longitudinal ($f(\xi)$) and lateral ($g(\xi)$) correlation functions.

or, for the elements of the covariance function matrix they are written as,

$$C_{u_i u_j}(\underline{\xi}) = \sigma^2 \left(\frac{f(|\underline{\xi}|) - g(|\underline{\xi}|)}{|\underline{\xi}|^2} \, \xi_i \, \xi_j + g(|\underline{\xi}|) \, \delta_{ij} \right) \tag{2.15}$$

with in equations (2.14) and (2.15) the indices, $i = 1, 2, 3$ and $j = 1, 2, 3$, δ_{ij} the Kronecker delta, σ^2 the variance of atmospheric turbulence, $|\underline{\xi}| = \xi = \sqrt{\xi_1^2 + \xi_2^2 + \xi_3^2}$ the spatial separation, and f and g the longitudinal and lateral correlation functions according to Dryden, respectively. The indices i and j define the direction of the spatial separation component ánd they define the direction of the atmospheric turbulence velocity component, so ξ_1, ξ_2 and ξ_3 are spatial separations along, respectively, the X_E-, Y_E- and Z_E-axis, while u_1, u_2 and u_3 are the turbulence velocity components along, respectively, the X_E-, Y_E- and Z_E-axis.

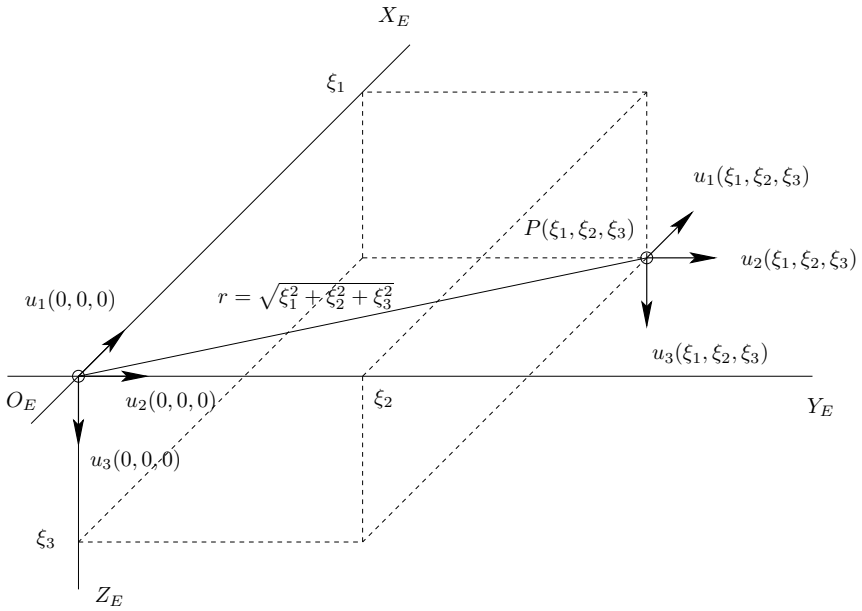


Figure 2.5: Atmospheric turbulence velocity components for two points in $\mathcal{F}_E$, spatially separated in three dimensions.

At first glance, equations (2.14) and (2.15) seem complicated. However, these equations should in fact be considered as a "short-hand" notation for the components of the correlation function matrix and covariance function matrix, since all elements $R_{u_iu_j}(\underline{\xi})$, or $C_{u_iu_j}(\underline{\xi})$, can be derived considering the 3D spatial separation in $\mathcal{F}_E$, see figure 2.5. For example, consider the connection line between the Earth-Fixed Frame of Reference's origin O_E and the arbitrary point $P(\xi_1,\xi_2,\xi_3)$, spatially separated in three dimensions. If the atmospheric turbulence velocity components in origin O_E and point P are decomposed in the direction of this connection line and perpendicular to it, the components of the correlation function matrix $R_{u_iu_j}(\underline{\xi})$ can be derived.

In section 2.3.2 a simple 2D spatial separation example is given. Components of the covariance function matrix $C_{u_iu_j}(\underline{\xi})$, with $i=1,2,3$ $j=1,2,3$ and the spatial separation $\underline{\xi}=[\xi_1,\xi_2,0]^T$, will be derived.

2.3.2 A 2D spatial separation example

As a simple example, a derivation of the atmospheric turbulence covariance function matrix elements $C_{u_iu_j}(\underline{\xi})$ with spatial separation in only two dimensions will be given, see also figure 2.6. Although this example is easily derived from Batchelor's theorem, see reference [2], it is not frequently reported in the literature. For this example only spatial separation in the $O_EX_EY_E$-plane is taken into account, the spatial separation vector becomes $\underline{\xi}=[\xi_1,\xi_2,0]^T$. The derived PSD functions of atmospheric turbulence will be applied in chapters 10, 11 and 12.

For the calculation of the covariance function matrix elements $C_{u_iu_j}(\underline{\xi}) = C_{u_iu_j}(\xi_1, \xi_2, 0)$, consider the connection line between the Earth-Fixed Frame of Reference origin O_E and the arbitrary point $P(\xi_1, \xi_2, 0)$, spatially separated in two dimensions. The atmospheric turbulence covariance function matrix of interest is,

$$\left[C_{u_iu_j}(\underline{\xi})\right] = \begin{bmatrix} C_{u_1u_1}(\xi_1,\xi_2,0) & C_{u_1u_2}(\xi_1,\xi_2,0) & C_{u_1u_3}(\xi_1,\xi_2,0) \\ C_{u_2u_1}(\xi_1,\xi_2,0) & C_{u_2u_2}(\xi_1,\xi_2,0) & C_{u_2u_3}(\xi_1,\xi_2,0) \\ C_{u_3u_1}(\xi_1,\xi_2,0) & C_{u_3u_2}(\xi_1,\xi_2,0) & C_{u_3u_3}(\xi_1,\xi_2,0) \end{bmatrix} \tag{2.16}$$

with for a covariance function matrix element,

$$C_{u_iu_j}(\underline{\xi}) = C_{u_iu_j}(\xi_1, \xi_2, 0) = E\left\{u_i(0,0,0)u_j(\xi_1,\xi_2,0)\right\}$$

Note that the atmospheric turbulence covariance matrix is symmetrical, therefore $C_{u_1u_2}(\underline{\xi}) = C_{u_2u_1}(\underline{\xi})$, $C_{u_1u_3}(\underline{\xi}) = C_{u_3u_1}(\underline{\xi})$ and $C_{u_2u_3}(\underline{\xi}) = C_{u_3u_2}(\underline{\xi})$.

In figure 2.7 a top view of figure 2.6 is presented. This figure shows the atmospheric turbulence velocity components at origin O_E, $u_1(0,0,0)$ and $u_2(0,0,0)$, and at $P(\xi_1, \xi_2, 0)$, $u_1(\xi_1, \xi_2, 0)$ and $u_2(\xi_1, \xi_2, 0)$, decomposed in a direction along the O_EP connection line and decomposed perpendicular to the connection line O_EP. At the origin of $\mathcal{F}_E$ and the spatially separated arbitrary point $P(\xi_1, \xi_2, 0)$, the atmospheric turbulence velocities are written as,

$$\underline{u}(\underline{0}) = \begin{bmatrix} u_1(0,0,0) \\ u_2(0,0,0) \\ u_3(0,0,0) \end{bmatrix}$$

and,

$$\underline{u}(\underline{\xi}) = \begin{bmatrix} u_1(\xi_1,\xi_2,0) \\ u_2(\xi_1,\xi_2,0) \\ u_3(\xi_1,\xi_2,0) \end{bmatrix}$$

respectively.

In order to calculate the elements of the covariance function matrix, see equation (2.16), the atmospheric turbulence velocity components of $\underline{u}(\underline{0})$ and $\underline{u}(\underline{\xi})$ are decomposed in elements along the separation line O_EP and in elements perpendicular to the separation line O_EP, see also figures 2.6 and 2.7. For the origin of the Earth-Fixed Frame of Reference O_E, the three atmospheric turbulence velocity components are written as,

$$\begin{aligned} u_1(0,0,0) &= u_{1_{long}}(0,0,0)\ sin\alpha + u_{1_{lat}}(0,0,0)\ cos\alpha \\ u_2(0,0,0) &= u_{2_{long}}(0,0,0)\ cos\alpha + u_{2_{lat}}(0,0,0)\ sin\alpha \\ u_3(0,0,0) &= u_3(0,0,0) \end{aligned}$$

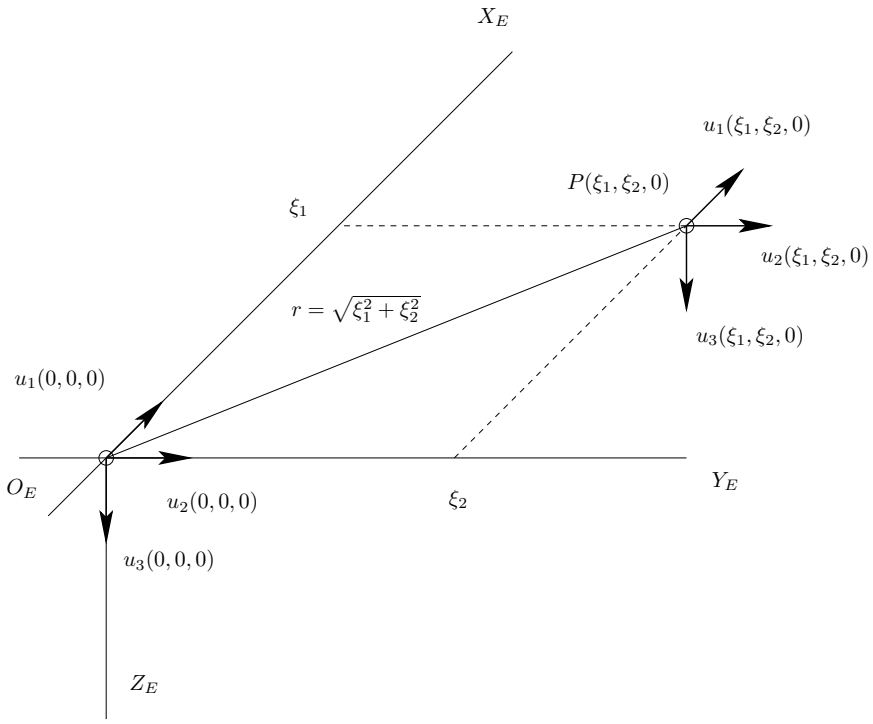


Figure 2.6: Atmospheric turbulence velocity components for two points in $\mathcal{F}_E$, spatially separated in two dimensions in the $O_E X_E Y_E$-plane.

For the arbitrary point $P(\xi_1, \xi_2, 0)$ these three atmospheric turbulence velocity components become,

$$\begin{aligned} u_1(\xi_1,\xi_2,0) &= u_{1_{long}}(\xi_1,\xi_2,0)\ sin\alpha + u_{1_{lat}}(\xi_1,\xi_2,0)\ cos\alpha \\ u_2(\xi_1,\xi_2,0) &= u_{2_{long}}(\xi_1,\xi_2,0)\ cos\alpha + u_{2_{lat}}(\xi_1,\xi_2,0)\ sin\alpha \\ u_3(\xi_1,\xi_2,0) &= u_3(\xi_1,\xi_2,0) \end{aligned}$$

with $sin\alpha = \frac{\xi_1}{r} = \frac{\xi_1}{\sqrt{\xi_1^2+\xi_2^2}}$, $cos\alpha = \frac{\xi_2}{r} = \frac{\xi_2}{\sqrt{\xi_1^2+\xi_2^2}}$ and $r = \sqrt{\xi_1^2+\xi_2^2}$. The atmospheric turbulence velocity components $u_{1_{long}}$ and $u_{1_{lat}}$ are the decompositions of u_1 on the line $O_E P$ and a line perpendicular to it (through origin O_E), respectively. Similar to $u_{1_{long}}$ and $u_{1_{lat}}$, $u_{2_{long}}$ and $u_{2_{lat}}$ are the decompositions of u_2 on the line $O_E P$ and a line perpendicular to it (through point P), respectively.
The elements of the atmospheric turbulence covariance function matrix can be derived by calculating each $C_{u_i u_j}(\underline{\xi}) = C_{u_i u_j}(\xi_1, \xi_2, 0) = E\{u_i(0,0,0)u_j(\xi_1,\xi_2,0)\} = E\left\{u_i(\underline{0})u_j(\underline{\xi})\right\}$. For example, with $\underline{0} = [0,0,0]^T$ and $\underline{\xi} = [\xi_1, \xi_2, 0]^T$, the following expression for $C_{u_1 u_1}(\underline{\xi})$ can be derived,

$$\begin{aligned} C_{u_1 u_1}(\underline{\xi}) &= E\left\{u_1(\underline{0})u_1(\underline{\xi})\right\} \qquad (2.17) \\ &= E\left\{\left(u_{1_{long}}(\underline{0})\ sin\alpha + u_{1_{lat}}(\underline{0})\ cos\alpha\right)\left(u_{1_{long}}(\underline{\xi})\ sin\alpha + u_{1_{lat}}(\underline{\xi})\ cos\alpha\right)\right\} \end{aligned}$$

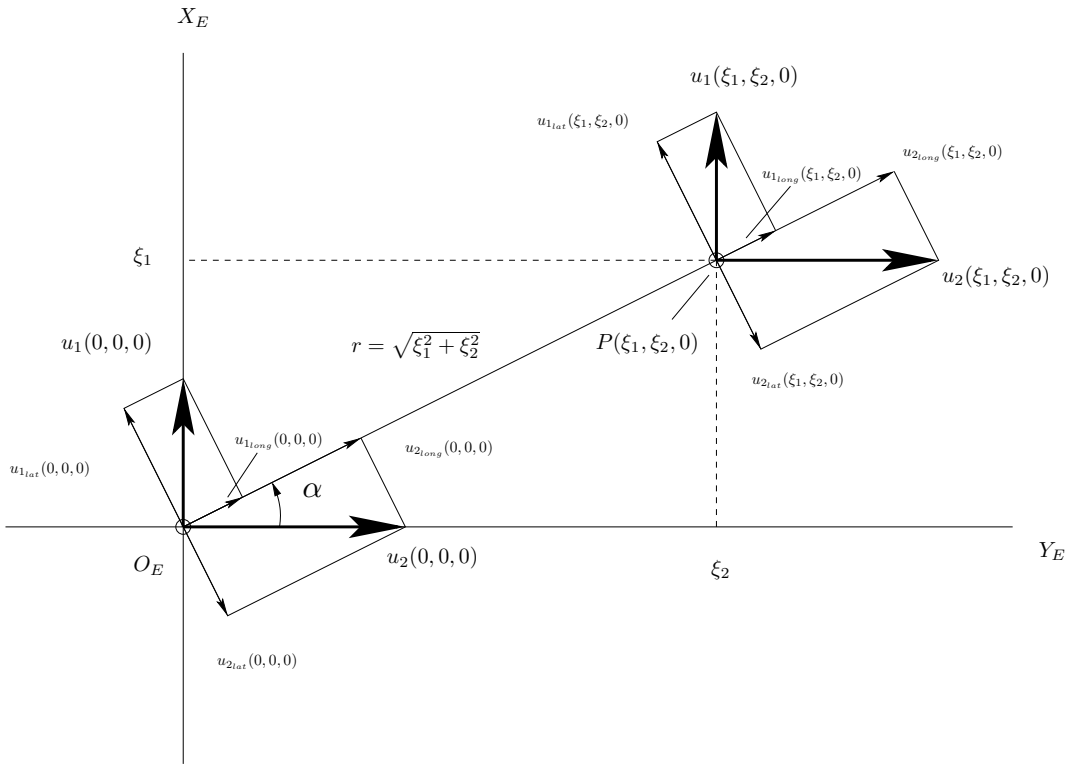


Figure 2.7: Decomposition of atmospheric turbulence velocity components for two points in $\mathcal{F}_E$, spatially separated in two dimensions in the $O_E X_E Y_E$-plane, top view of figure 2.6.

$$
\begin{aligned}
&= E\left\{\left(u_{1_{long}}(\underline{0})\ \frac{\xi_1}{r} + u_{1_{lat}}(\underline{0})\ \frac{\xi_2}{r}\right)\left(u_{1_{long}}(\underline{\xi})\ \frac{\xi_1}{r} + u_{1_{lat}}(\underline{\xi})\ \frac{\xi_2}{r}\right)\right\} \\
&= E\left\{u_{1_{long}}(\underline{0})u_{1_{long}}(\underline{\xi})\left(\frac{\xi_1}{r}\right)^2 + u_{1_{lat}}(\underline{0})u_{1_{lat}}(\underline{\xi})\left(\frac{\xi_2}{r}\right)^2 + \right. \\
&\quad \left. u_{1_{long}}(\underline{0})u_{1_{lat}}(\underline{\xi})\left(\frac{\xi_1\xi_2}{r^2}\right) + u_{1_{lat}}(\underline{0})u_{1_{long}}(\underline{\xi})\left(\frac{\xi_1\xi_2}{r^2}\right)\right\}
\end{aligned}
$$

Considering the atmospheric turbulence modeling assumptions made in section 2.2, which resulted in the application of the fundamental 1D correlation functions $f(\xi)$ and $g(\xi)$, see equations (2.11) and (2.12), the following definitions are used to simplify equation (2.17),

$$
\begin{aligned}
E\left\{u_{1_{long}}(\underline{0})u_{1_{long}}(\underline{\xi})\right\} &= \sigma^2\ f(\xi) \\
E\left\{u_{1_{lat}}(\underline{0})u_{1_{lat}}(\underline{\xi})\right\} &= \sigma^2\ g(\xi) \\
E\left\{u_{1_{long}}(\underline{0})u_{1_{lat}}(\underline{\xi})\right\} &= 0 \\
E\left\{u_{1_{lat}}(\underline{0})u_{1_{long}}(\underline{\xi})\right\} &= 0
\end{aligned}
$$

with $\xi = \sqrt{\xi_1^2 + \xi_2^2}$.

The covariance function $C_{u_1u_1}(\underline{\xi})$ can now be written as,

$$C_{u_1u_1}(\xi_1,\xi_2,0) = \sigma^2\left(f(\xi)\left(\frac{\xi_1}{r}\right)^2 + g(\xi)\left(\frac{\xi_2}{r}\right)^2\right) \tag{2.18}$$

The remaining (auto) covariance functions can be derived in a similar manner, they turn out to be,

$$\begin{aligned} C_{u_2u_2}(\xi_1,\xi_2,0) &= \sigma^2\left(f(\xi)\left(\frac{\xi_2}{r}\right)^2 + g(\xi)\left(\frac{\xi_1}{r}\right)^2\right) \\ C_{u_3u_3}(\xi_1,\xi_2,0) &= \sigma^2 g(\xi) \end{aligned}$$

The remaining (cross) covariance functions are,

$$\begin{aligned} C_{u_1u_2}(\xi_1,\xi_2,0) &= \sigma^2\left(f(\xi)-g(\xi)\right)\frac{\xi_1\xi_2}{r^2} \\ C_{u_1u_3}(\xi_1,\xi_2,0) &= 0 \\ C_{u_2u_3}(\xi_1,\xi_2,0) &= 0 \end{aligned}$$

As an illustration , the covariance functions $C_{u_1u_1}(\xi_1,\xi_2,0)$, $C_{u_2u_2}(\xi_1,\xi_2,0)$, $C_{u_1u_2}(\xi_1,\xi_2,0)$ and $C_{u_3u_3}(\xi_1,\xi_2,0)$ are plotted in figures 2.8, 2.9, 2.10 and 2.11. Note that the variance of the atmospheric turbulence velocity components was chosen as $\sigma^2 = 1\ \left[\frac{m^2}{s^2}\right]$ and that the covariance functions are plotted as a function of the non-dimensional spatial separation $\frac{\xi_1}{L_g}$ and $\frac{\xi_2}{L_g}$, with L_g the gust scale length.

Each of the covariance function matrix elements in equation (2.16) can be calculated by using Batchelor's short-hand notation for the covariance function matrix elements as given by equation (2.15) with $\underline{\xi} = [\xi_1,\xi_2,0]^T$.

2.4 The atmospheric turbulence PSD function matrix

2.4.1 The general PSD function matrix

Similar to the atmospheric turbulence covariance function matrix, $C_{\underline{uu}}(\underline{\xi})$, the atmospheric turbulence PSD matrix is written as,

$$\begin{aligned} S_{\underline{uu}}(\underline{\Omega}) &= \left[S_{u_iu_j}(\Omega_1,\Omega_2,\Omega_3)\right] \\ &= \begin{bmatrix} S_{u_1u_1}(\Omega_1,\Omega_2,\Omega_3) & S_{u_1u_2}(\Omega_1,\Omega_2,\Omega_3) & S_{u_1u_3}(\Omega_1,\Omega_2,\Omega_3) \\ S_{u_2u_1}(\Omega_1,\Omega_2,\Omega_3) & S_{u_2u_2}(\Omega_1,\Omega_2,\Omega_3) & S_{u_2u_3}(\Omega_1,\Omega_2,\Omega_3) \\ S_{u_3u_1}(\Omega_1,\Omega_2,\Omega_3) & S_{u_3u_2}(\Omega_1,\Omega_2,\Omega_3) & S_{u_3u_3}(\Omega_1,\Omega_2,\Omega_3) \end{bmatrix} \end{aligned}$$

with $i = 1,2,3$, $j = 1,2,3$ and $\underline{\Omega} = [\Omega_1,\Omega_2,\Omega_3]^T$.

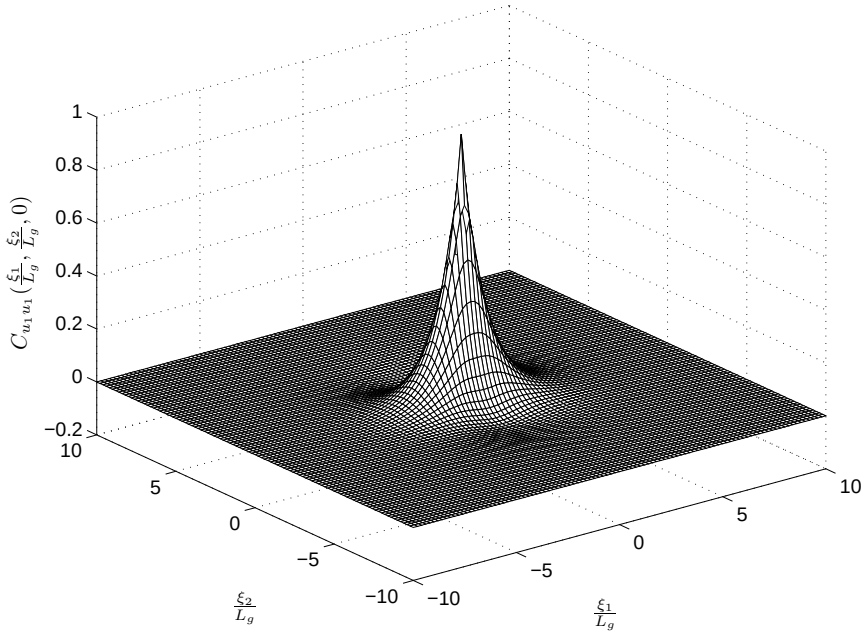


Figure 2.8: 2D Covariance function $C_{u_1u_1}(\frac{\xi_1}{L_g}, \frac{\xi_2}{L_g}, 0)$.

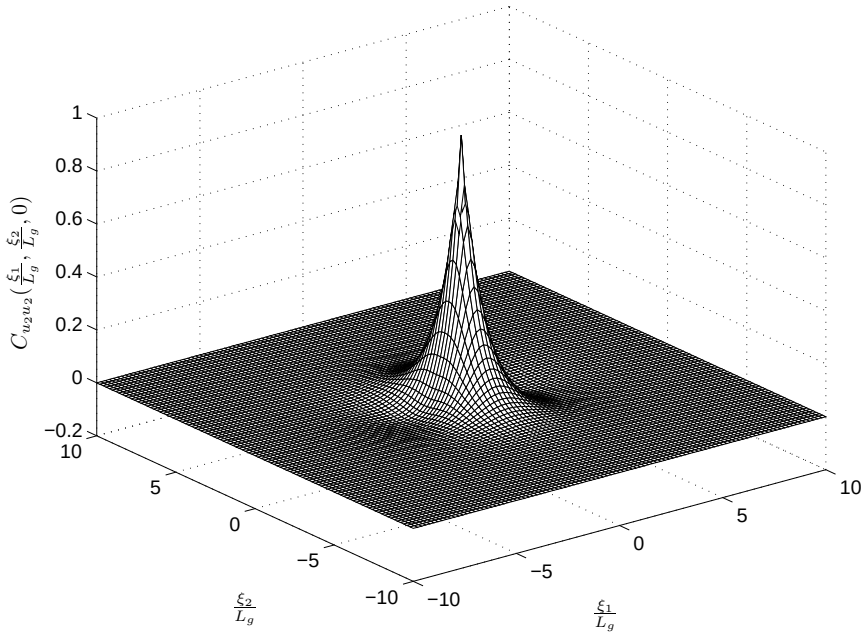


Figure 2.9: 2D Covariance function $C_{u_2u_2}(\frac{\xi_1}{L_g}, \frac{\xi_2}{L_g}, 0)$.

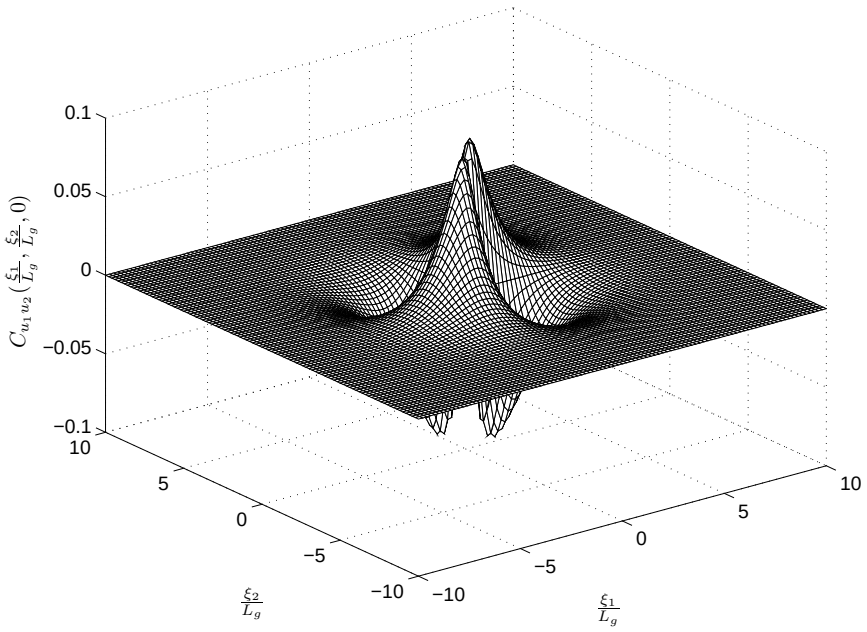


Figure 2.10: 2D Covariance function $C_{u_1u_2}(\frac{\xi_1}{L_g}, \frac{\xi_2}{L_g}, 0)$.

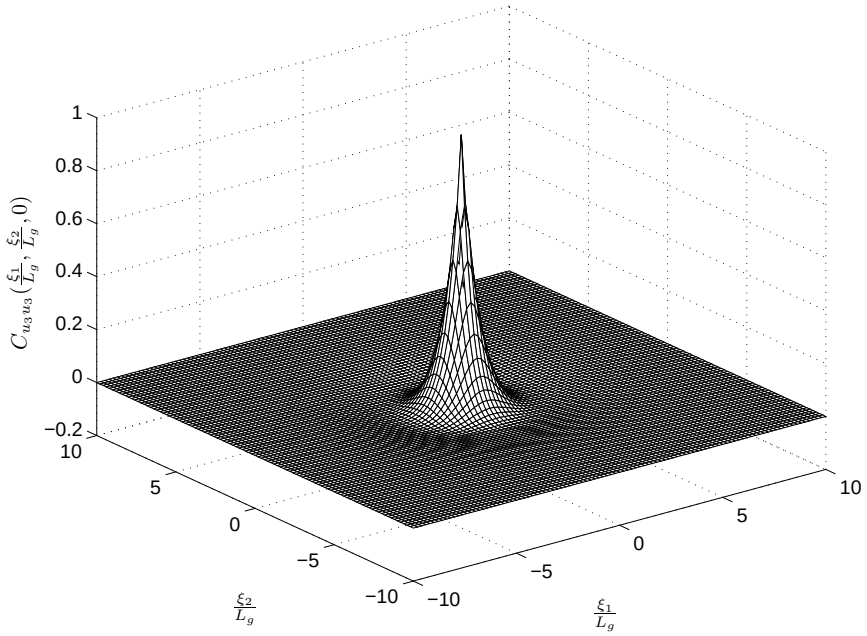


Figure 2.11: 2D Covariance function $C_{u_3u_3}(\frac{\xi_1}{L_g}, \frac{\xi_2}{L_g}, 0)$.

Considering the assumptions made in section 2.2 regarding the modeling of atmospheric turbulence, the PSD function matrix elements for 3D atmospheric turbulence are calculated by Fourier transforming the covariance function matrix elements, equation (2.15),

$$S_{u_i u_j}(\underline{\Omega}) = \int_{-\infty}^{+\infty}\int_{-\infty}^{+\infty}\int_{-\infty}^{+\infty} C_{u_i u_j}(\underline{\xi})\, e^{-j\underline{\Omega}\cdot\underline{\xi}}\, d\underline{\xi} \tag{2.19}$$

or,

$$S_{u_i u_j}(\Omega_1,\Omega_2,\Omega_3) = \int_{-\infty}^{+\infty}\int_{-\infty}^{+\infty}\int_{-\infty}^{+\infty} C_{u_i u_j}(\xi_1,\xi_2,\xi_3)\, e^{-j(\Omega_1\xi_1+\Omega_2\xi_2+\Omega_3\xi_3)}\, d\xi_1\, d\xi_2\, d\xi_3 \tag{2.20}$$

It is customary to use the non-dimensional spatial separation $\frac{\underline{\xi}}{L_g}$ and the non-dimensional spatial frequency $\underline{\Omega} L_g$ in respectively the atmospheric turbulence covariance function matrix and the atmospheric turbulence PSD function matrix, see also references [1, 5], and equations (2.19) and (2.20) become,

$$S_{u_i u_j}(\underline{\Omega} L_g) = \int_{-\infty}^{+\infty}\int_{-\infty}^{+\infty}\int_{-\infty}^{+\infty} C_{u_i u_j}\left(\frac{\underline{\xi}}{L_g}\right)\, e^{-j\underline{\Omega} L_g\cdot\frac{\underline{\xi}}{L_g}}\, d\frac{\underline{\xi}}{L_g} \tag{2.21}$$

or,

$$S_{u_i u_j}(\Omega_1 L_g, \Omega_2 L_g, \Omega_3 L_g) = \tag{2.22}$$

$$= \int_{-\infty}^{+\infty}\int_{-\infty}^{+\infty}\int_{-\infty}^{+\infty} C_{u_i u_j}\left(\frac{\xi_1}{L_g},\frac{\xi_2}{L_g},\frac{\xi_3}{L_g}\right)\, e^{-j(\Omega_1\xi_1+\Omega_2\xi_2+\Omega_3\xi_3)}\, d\frac{\xi_1}{L_g}\, d\frac{\xi_2}{L_g}\, d\frac{\xi_3}{L_g}$$

Note that $S_{u_i u_j}(\Omega_1 L_g, \Omega_2 L_g, \Omega_3 L_g) = \frac{1}{L_g^3} S_{u_i u_j}(\Omega_1,\Omega_2,\Omega_3)$, and that,

$$\begin{aligned} S_{u_i u_j}(\underline{\Omega} L_g) &= \int_{-\infty}^{+\infty}\int_{-\infty}^{+\infty}\int_{-\infty}^{+\infty} C_{u_i u_j}\left(\frac{\underline{\xi}}{L_g}\right)\, e^{-j\underline{\Omega}\cdot\underline{\xi}}\, d\frac{\underline{\xi}}{L_g} = \\ &= \int_{-\infty}^{+\infty}\int_{-\infty}^{+\infty}\int_{-\infty}^{+\infty} C_{u_i u_j}\left(\frac{\underline{\xi}}{L_g}\right)\, e^{-j\underline{\Omega} L_g\cdot\frac{\underline{\xi}}{L_g}}\, d\frac{\underline{\xi}}{L_g} \end{aligned}$$

Similar to equation (2.15), the PSD function matrix elements can be written in a short hand notation,

$$S_{u_i u_j}(\underline{\Omega} L_g) = 16\pi\sigma^2 \frac{\left(\Omega^2 L_g^2 \delta_{ij} - \Omega_i \Omega_j L_g^2\right)}{\left(1+(\Omega L_g)^2\right)^3} \tag{2.23}$$

or,

$$S_{u_i u_j}(\Omega_1 L_g, \Omega_2 L_g, \Omega_3 L_g) = 16\pi\sigma^2 \frac{\left(\left(\Omega_1^2 L_g^2 + \Omega_2^2 L_g^2 + \Omega_3^2 L_g^2\right)\delta_{ij} - \Omega_i \Omega_j L_g^2\right)}{\left(1+\Omega_1^2 L_g^2 + \Omega_2^2 L_g^2 + \Omega_3^2 L_g^2\right)^3} \tag{2.24}$$

with $i = 1, 2, 3$, $j = 1, 2, 3$, δ_{ij} the Kronecker delta, σ^2 the variance of atmospheric turbulence and L_g the turbulence scale length. Integrating equation (2.24) over all non-dimensional spatial frequencies $\Omega_3 L_g$ results in the PSD function matrix elements,

$$S_{u_i u_j}(\Omega_1 L_g, \Omega_2 L_g) = \frac{1}{2\pi} \int_{-\infty}^{+\infty} S_{u_i u_j}(\Omega_1 L_g, \Omega_2 L_g, \Omega_3 L_g)\, d\,(\Omega_3 L_g) \tag{2.25}$$

or in matrix form,

$$S_{\underline{uu}}(\Omega_1 L_g, \Omega_2 L_g) = \begin{bmatrix} S_{u_1 u_1}(\Omega_1 L_g, \Omega_2 L_g) & S_{u_1 u_2}(\Omega_1 L_g, \Omega_2 L_g) & 0 \\ S_{u_2 u_1}(\Omega_1 L_g, \Omega_2 L_g) & S_{u_2 u_2}(\Omega_1 L_g, \Omega_2 L_g) & 0 \\ 0 & 0 & S_{u_3 u_3}(\Omega_1 L_g, \Omega_2 L_g) \end{bmatrix} \tag{2.26}$$

Similarly, integrating equation (2.26) over all non-dimensional spatial frequencies $\Omega_2 L_g$ results in the PSD function matrix,

$$S_{\underline{uu}}(\Omega_1 L_g) = \frac{1}{2\pi} \int_{-\infty}^{+\infty} S_{\underline{uu}}(\Omega_1 L_g, \Omega_2 L_g)\, d\,(\Omega_2 L_g) \tag{2.27}$$

with,

$$S_{\underline{uu}}(\Omega_1 L_g) = \begin{bmatrix} S_{u_1 u_1}(\Omega_1 L_g) & 0 & 0 \\ 0 & S_{u_2 u_2}(\Omega_1 L_g) & 0 \\ 0 & 0 & S_{u_3 u_3}(\Omega_1 L_g) \end{bmatrix} \tag{2.28}$$

Finally, integrating equation (2.28) over all non-dimensional spatial frequencies $\Omega_1 L_g$ results in the covariance function matrix,

$$C_{\underline{uu}}(\underline{0}) = \frac{1}{2\pi} \int_{-\infty}^{+\infty} S_{\underline{uu}}(\Omega_1 L_g)\, d\,(\Omega_1 L_g) \tag{2.29}$$

with,

$$C_{\underline{uu}}(\underline{0}) = \begin{bmatrix} \sigma^2 & 0 & 0 \\ 0 & \sigma^2 & 0 \\ 0 & 0 & \sigma^2 \end{bmatrix} \tag{2.30}$$

2.4.2 Reduced spatial frequency dimension examples

Reduced spatial frequency dimension PSD examples are derived by integrating over non-dimensional spatial frequencies $\Omega_i L_g$ with $i = 1, 2, 3$. For the calculation of these PSD matrices, the atmospheric turbulence PSD matrix elements, equation (2.24), are written in matrix form,

$$S_{\underline{uu}}(\Omega_1 L_g, \Omega_2 L_g, \Omega_3 L_g) = \tag{2.31}$$

$$= \frac{16\pi\sigma^2}{(1+\Omega_1^2L_g^2+\Omega_2^2L_g^2+\Omega_3^2L_g^2)^3}\begin{bmatrix} \Omega_2^2L_g^2+\Omega_3^2L_g^2 & -\Omega_1\Omega_2L_g^2 & -\Omega_1\Omega_3L_g^2 \\ -\Omega_2\Omega_1L_g^2 & \Omega_1^2L_g^2+\Omega_3^2L_g^2 & -\Omega_2\Omega_3L_g^2 \\ -\Omega_3\Omega_1L_g^2 & -\Omega_3\Omega_2L_g^2 & \Omega_1^2L_g^2+\Omega_2^2L_g^2 \end{bmatrix}$$

In the following, two examples of reduced spatial frequency dimension atmospheric turbulence will be given. The first example considers 3D atmospheric turbulence in the $O_EX_EY_E$-plane of the frame $\mathcal{F}_E$, while the second example considers 3D atmospheric turbulence along the X_E-axis of $\mathcal{F}_E$.

A 2D spatial frequency example

Integrating equation (2.31) over all non-dimensional spatial frequencies Ω_3L_g results in,

$$S_{\underline{uu}}(\Omega_1L_g,\Omega_2L_g) = \frac{1}{2\pi}\int_{-\infty}^{+\infty} S_{\underline{uu}}(\Omega_1L_g,\Omega_2L_g,\Omega_3L_g)\,d\,(\Omega_3L_g) \tag{2.32}$$

or,

$$S_{\underline{uu}}(\Omega_1L_g,\Omega_2L_g) = \tag{2.33}$$

$$= \frac{\pi\sigma^2}{(1+\Omega_1^2L_g^2+\Omega_2^2L_g^2)^{5/2}}\begin{bmatrix} 1+\Omega_1^2L_g^2+4\Omega_2^2L_g^2 & -3\Omega_1\Omega_2L_g^2 & 0 \\ -3\Omega_2\Omega_1L_g^2 & 1+4\Omega_1^2L_g^2+\Omega_2^2L_g^2 & 0 \\ 0 & 0 & 3\left(\Omega_1^2L_g^2+\Omega_2^2L_g^2\right) \end{bmatrix}$$

As an illustration, the PSD function matrix elements $S_{u_1u_1}(\Omega_1L_g,\Omega_2L_g)$, $S_{u_2u_2}(\Omega_1L_g,\Omega_2L_g)$, $S_{u_1u_2}(\Omega_1L_g,\Omega_2L_g)$ and $S_{u_3u_3}(\Omega_1L_g,\Omega_2L_g)$, see equation (2.33), are plotted in figures 2.12, 2.13, 2.14 and 2.15, respectively. Again, the variance of the atmospheric turbulence velocity components is taken to be $\sigma^2 = 1\ \left[\frac{m^2}{s^2}\right]$ and the PSD function matrix elements are plotted as a function of the non-dimensional spatial frequency Ω_1L_g and Ω_2L_g.

A 1D spatial frequency example

Integrating equation (2.33) over all non-dimensional spatial frequencies Ω_2L_g results in,

$$S_{\underline{uu}}(\Omega_1L_g) = \frac{1}{2\pi}\int_{-\infty}^{+\infty} S_{\underline{uu}}(\Omega_1L_g,\Omega_2L_g)\,d\,(\Omega_2L_g) \tag{2.34}$$

or,

$$S_{\underline{uu}}(\Omega_1L_g) = \frac{\sigma^2}{\left(1+\Omega_1^2L_g^2\right)^2}\begin{bmatrix} 2\left(1+\Omega_1^2L_g^2\right) & 0 & 0 \\ 0 & 1+3\Omega_1^2L_g^2 & 0 \\ 0 & 0 & 1+3\Omega_1^2L_g^2 \end{bmatrix} \tag{2.35}$$

As an illustration, the PSD function matrix elements $S_{u_1u_1}(\Omega_1L_g)$, $S_{u_2u_2}(\Omega_1L_g)$ and $S_{u_3u_3}(\Omega_1L_g)$, see equation (2.35), are shown in figures 2.16, 2.17 and 2.18. The variance of the atmospheric turbulence velocity components is again chosen to be $\sigma^2 = 1\ \left[\frac{m^2}{s^2}\right]$ and that the PSD function matrix elements are plotted as a function of the non-dimensional spatial frequency Ω_1L_g.

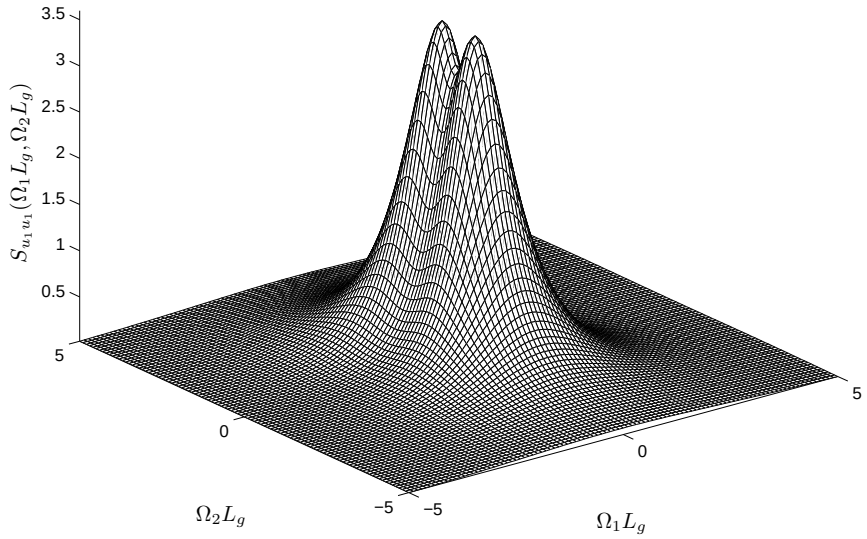


Figure 2.12: The 2D PSD function $S_{u_1u_1}(\Omega_1 L_g, \Omega_2 L_g)$.

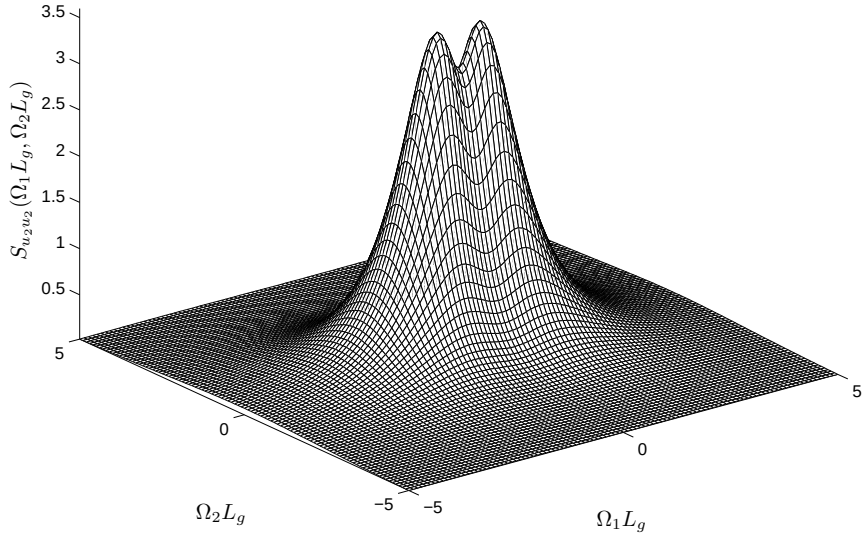


Figure 2.13: The 2D PSD function $S_{u_2u_2}(\Omega_1 L_g, \Omega_2 L_g)$.

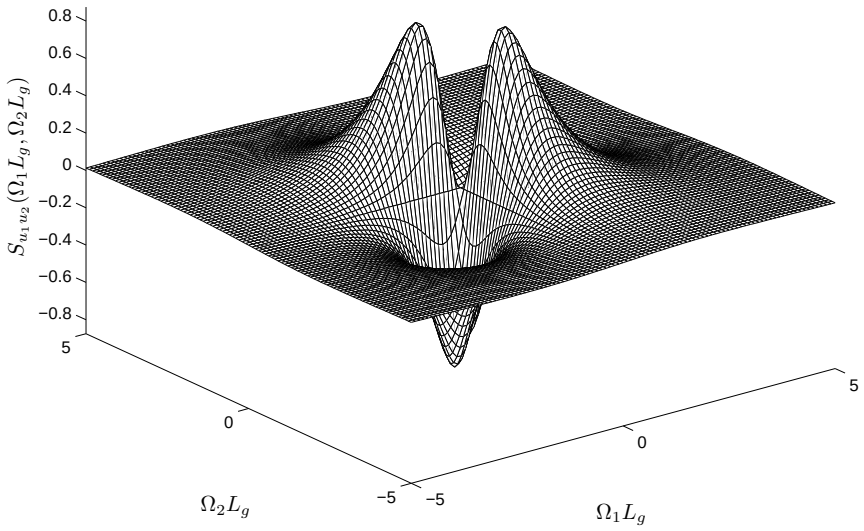


Figure 2.14: The 2D PSD function $S_{u_1u_2}(\Omega_1 L_g, \Omega_2 L_g)$.

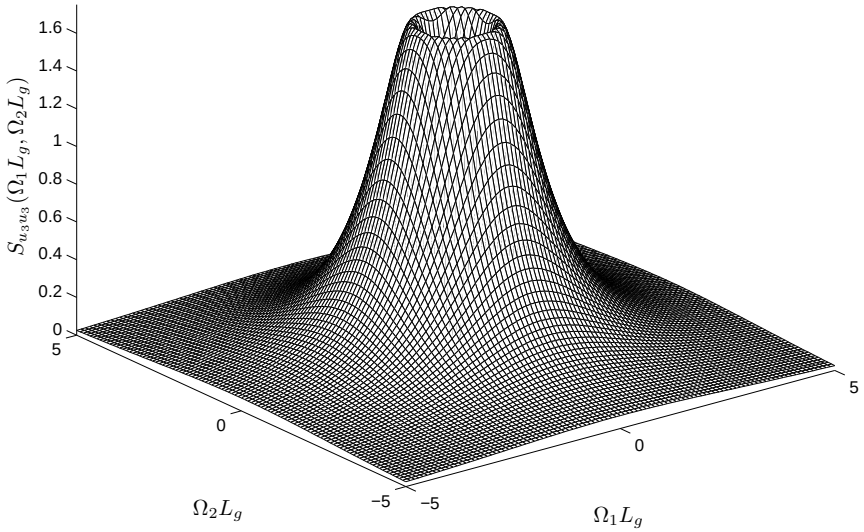


Figure 2.15: The 2D PSD function $S_{u_3u_3}(\Omega_1 L_g, \Omega_2 L_g)$.

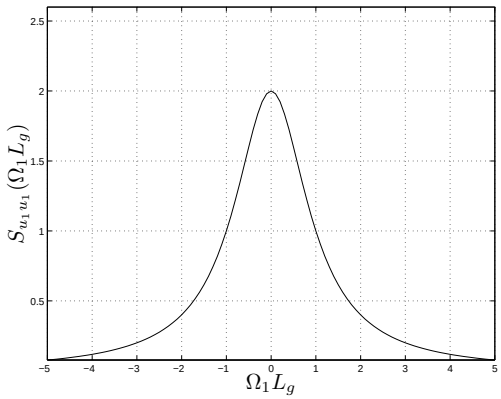


Figure 2.16: The 1D PSD function $S_{u_1u_1}(\Omega_1 L_g)$.

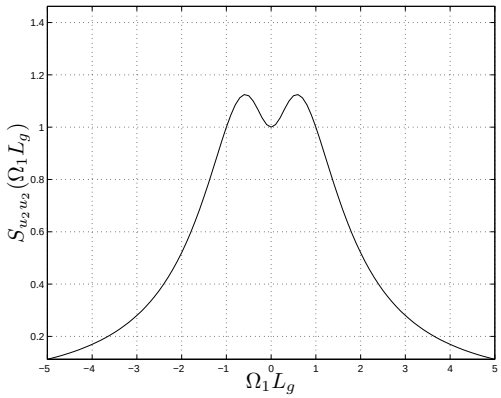


Figure 2.17: The 1D PSD function $S_{u_2u_2}(\Omega_1 L_g)$.

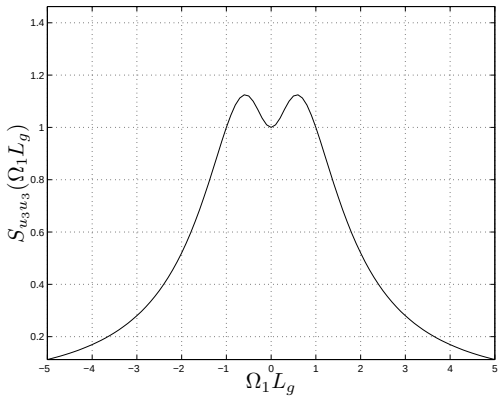


Figure 2.18: The 1D PSD function $S_{u_3u_3}(\Omega_1 L_g)$.

Classification	$\sigma\ [\frac{m}{s}]$	$\sigma^2\ [\frac{\mathrm{m}^2}{\mathrm{s}^2}]$
light turbulence, clean air	1.22	1.49
moderate turbulence, cumulous cloud	2.43	5.90
severe turbulence, thunderstorm	4.86	23.62

Table 2.1: Classification of the atmospheric turbulence intensity given in terms of the standard deviation and the variance, taken from reference [3].

2.5 Atmospheric turbulence model parameters

Throughout this thesis the gust scale length L_g is chosen as $L_g = 300$ [m], a value representative for high altitude atmospheric turbulence, see references [1, 3, 30]. Furthermore, the variance of the atmospheric turbulence velocity components is chosen to equal $\sigma^2 = 1\ \frac{\mathrm{m}^2}{\mathrm{s}^2}$, and by this value it is classified as less than light turbulence, see table 2.1.

2.6 Remarks

In chapters 7 and 8 (panel) aircraft models will be flown through both elementary symmetrical and elementary anti-symmetrical atmospheric turbulence fields in order to determine the aerodynamic forces and moments acting upon them. After the aircraft model identification process is completed, the parametric aircraft models will be used to calculate the aircraft's response to atmospheric turbulence. As presented in this chapter, the atmospheric turbulence PSD functions will be used as input for these parametric aircraft models. Aircraft responses to the atmospheric turbulence models are given in chapters 10 through 13.

Part II

Linearized Potential Flow Theory

Chapter 3

Steady linearized potential flow simulations

3.1 Introduction

Aside the atmospheric turbulence models defined in chapter 2 a mathematical aircraft model is required for aircraft motion simulations. This model in turn requires an aerodynamic model describing how both aircraft motions ánd atmospheric turbulence velocity components result in aerodynamic forces and moments acting on the aircraft configuration. For the estimation of these aerodynamic forces and moments several methods may be used, e.g. flight tests, windtunnel experiments, handbook methods and Computational Aerodynamics (CA) techniques may be selected. An important disadvantage of flight tests and windtunnel experiments is that they are both extremely costly and time-consuming. A disadvantage of handbook methods, for example, is that they do not accurately capture aerodynamic interference phenomena, which results in incorrect aerodynamic moment estimations, see reference [7].

Once the aerodynamic forces and moments due to all known perturbations have been calculated/simulated, an aerodynamic model can be derived. This can be formulated as a parametric model in terms of aerodynamic model parameters, i.e. stability derivatives.
One major advantage of the Computational Aerodynamics approach over other methods, such as the use of parametric models, is that it provides the identification of the entire flowfield in both pressure and local airspeed, including the pressure acting on the configuration. Integrating the on-body surface pressure distribution ultimately results in the aerodynamic forces and moments acting on the configuration submerged in an airflow. Given sufficient computer power, the aerodynamic model may also be considered as the simulation of a discretized aircraft model submerged in a turbulent airflow. Over this discretized aircraft model the flow equations are then solved resulting in aerodynamic forces and moments acting on the aircraft. From these simulations, parametric aerodynamic

models are then obtained. From both the simulated aerodynamic forces and moments ánd the known perturbations a mathematical aerodynamic model can be constructed.
For the purpose of determining the aerodynamic model parameters, a numerical simulation method has been developed. The flow equations to be solved are based on Linearized Potential Flow (LPF) formulations, see also references [11, 12]. These formulations only hold for inviscid, irrotational, incompressible flow.

In estimating the aerodynamic forces and moments, however, the Computational Aerodynamics approach does have its limitations, they are governed by the fluid flow model.
Starting at the highest level of fluid flow modeling, the basic equations of motion describing a fluid flow are the so-called Navier-Stokes equations. They include viscosity effects, compressibility effects and heat transfer, and, in principle, hold for incompressible, subsonic, transonic, supersonic and hypersonic airflows. Neglecting viscosity and heat transfer phenomena, the fluid flow's equations of motion result in the Euler equations. If the fluid flow model is limited to irrotational flow, the Full Potential equations are derived. Omitting both the transsonic and supersonic speed range, and thus omitting the shock capturing capability of the Full Potential equations, the fluid flow model is further simplified to the Linearized Potential fluid flow equations. Finally, if airflow compressibility effects are neglected as well, the fluid flow equations of motion for inviscid, incompressible flow will result in Laplace's equation which will be used in this thesis. One of the consequences of these assumptions is that viscous drag is not considered.
The motivation for using the Linearized Potential Flow model is that, contrary to the Navier-Stokes, Euler and Full Potential solvers, this method does not require a volume grid for the numerical solution of the airflow. The reduction of the 3D computational domain into a two-dimensional (2D) one results in much less execution time (flow-solving). Furthermore, the LPF model reduces pre-processing time (grid-generation) and post-processing time (checking the flowfield and the on-body pressure distribution). Still, this model remains highly adequate to capture large flow features.

As mentioned earlier in chapter 1, the goal of this thesis is to compare three calculation methods for aircraft subjected to atmospheric turbulence. In chapter 10 (Parametric Computational Aircraft Model) a parametric model model based on aerodynamic transfer functions is given, while in chapter 11 (Single Point Aircraft Model, or DUT-model) and chapter 12 (Four Point Aircraft Model) parametric models in terms of constant stability derivatives are given. In chapter 13 a comparison of results is provided, including results of a Computational Aerodynamics simulation. Both one- (1D) and 2D atmospheric turbulence fields will be considered.

The present chapter provides a limited overview of the theory and application of the (numerical) steady, incompressible Linearized Potential Flow model. With some alterations, the formulations are based on references [11, 12]; the mathematical expressions will be briefly summarized while details of alterations of the original expressions are presented in appendix C. For the LPF model's numerical solution, two singularity elements are used,

the quadri-lateral doublet-panel and the quadri-lateral source panel. Both the doublet-strength (μ) and the source-strength (σ) are taken to be constant over a panel. Therefore, the panel-method used in this thesis is a "low-order" panel method, see also references [8, 9, 10, 11, 12]. The steady Linearized Potential Flow model, as used in this chapter, will be extended to an unsteady Linearized Potential flow model in chapter 4.

3.2 Short summary of steady linearized potential flow theory

3.2.1 Flow equations

In this section a short summary of the applied Linearized Potential Flow theory will be given. The fluid flow equations hold for the solution over a configuration submerged in potential flow.
Starting with the general time-dependent differential form of the conservation of mass in a Cartesian coordinate system,

$$\frac{\partial \rho}{\partial t} + \frac{\partial \rho u}{\partial x} + \frac{\partial \rho v}{\partial y} + \frac{\partial \rho w}{\partial z} = 0 \tag{3.1}$$

with ρ the fluid's (air) density, u, v, w the fluid's velocity components and t time, the continuity equation (3.1) is written for incompressible airflow (ρ = constant) as,

$$\frac{\partial u}{\partial x} + \frac{\partial v}{\partial y} + \frac{\partial w}{\partial z} = 0 \tag{3.2}$$

Introducing the velocity potential Φ (thus assuming irrotational flow) with,

$$\frac{\partial \Phi}{\partial x} = u \qquad \frac{\partial \Phi}{\partial y} = v \qquad \frac{\partial \Phi}{\partial z} = w \tag{3.3}$$

or,

$$\nabla \Phi = \begin{bmatrix} \frac{\partial \Phi}{\partial x} \\ \frac{\partial \Phi}{\partial y} \\ \frac{\partial \Phi}{\partial z} \end{bmatrix} = \begin{bmatrix} u \\ v \\ w \end{bmatrix}$$

and substituting equations (3.3) in equation (3.2), Laplace's equation is derived, see also references [11, 12].
In order to solve Laplace's equation with given boundary conditions, LPF theory is used. In the case of steady LPF methods, the configuration of interest is at rest and is submerged in a moving airflow. The configuration may be considered as a 3D aircraft, or a 3D wing, in a flow domain of interest. This configuration is described in an Aerodynamic Frame of Reference $\mathcal{F}_{aero}$ of which details are given in Appendix B. This frame of reference remains fixed to the configuration.

In figure 3.2 a configuration submerged in a fluid flow is schematically depicted for a 2D aerofoil. It is considered as a cross-section of a 3D wing to which the LPF theory is applied. In this figure the aerofoil's contour, or the configuration's surface, is indicated by S_B, while its upper and lower wake-surfaces are indicated by $S_{W_{upper}}$ and $S_{W_{lower}}$ respectively. The contour S_∞ encloses the flow domain of interest and defines the outer flow region, see reference [8, 9]. The aerofoil's contour, or wing's surface, defines a fictitious inner flow region. Both the potential in the outer region, defined as Φ, and the potential in the inner region, defined as Φ_i, are assumed to satisfy Laplace's equation. For the outer flow region, Laplace's equation becomes,

$$\nabla^2\Phi = \frac{\partial^2\Phi}{\partial x^2} + \frac{\partial^2\Phi}{\partial y^2} + \frac{\partial^2\Phi}{\partial z^2} = 0 \tag{3.4}$$

where Φ is the outer flow region's potential and x, y and z denote Cartesian ordinates in the frame $\mathcal{F}_{aero}$. For the inner flow region, Laplace's equation becomes,

$$\nabla^2\Phi_i = \frac{\partial^2\Phi_i}{\partial x^2} + \frac{\partial^2\Phi_i}{\partial y^2} + \frac{\partial^2\Phi_i}{\partial z^2} = 0 \tag{3.5}$$

where Φ_i is the inner flow region's potential and x, y and z also denote Cartesian ordinates in the frame $\mathcal{F}_{aero}$. Note that the free-stream potential, designated as Φ_∞,

$$\Phi_\infty = U_\infty x + V_\infty y + W_\infty z \tag{3.6}$$

with U_∞, V_∞ and W_∞ the undisturbed velocity components of the velocity vector $\underline{Q}_\infty = [U_\infty, V_\infty, W_\infty]^T$ at infinity, always is a solution to both equations (3.4) and (3.5). The velocity components U_∞, V_∞, W_∞ are taken to be positive along the X_{aero}-, Y_{aero}- and Z_{aero}-axis, respectively. See also figure 3.1 where the frame $\mathcal{F}_{aero}$ is given, including the definition of the undisturbed velocity components $[U_\infty, V_\infty, W_\infty]^T$ in it.
With respect to the boundary conditions, for the submerged configuration the airflow velocity is tangential to the configuration. Therefore, the airflow's velocity component normal to the surface of the configuration equals zero (see also figure 3.2). This so-called Neumann boundary condition (see references [11, 12]), is written as,

$$\nabla\Phi \cdot \underline{n} = 0|_{S_B} \tag{3.7}$$

with $\nabla\Phi$ the airflow's velocity components and $\underline{n}$ the configuration's local normal vector (both given in the frame $\mathcal{F}_{aero}$). Another boundary condition is that the potential flow's velocity disturbance created by the configuration should diminish for $r = \sqrt{x^2 + y^2 + z^2}$ far from the configuration in $\mathcal{F}_{aero}$ (see also figure 3.2), or,

$$\lim_{r\to\infty} \left(\nabla\Phi - \underline{Q}_\infty \right) = \underline{0} \tag{3.8}$$

with $\underline{Q}_\infty = [U_\infty, V_\infty, W_\infty]^T$, the vector of undisturbed velocity components at infinity.
The general solution to equations (3.4) and (3.5) is given as a combination of source (σ) and doublet (μ) strength distributions on S_B, $S_{W_{upper}}$, $S_{W_{lower}}$ and S_∞, see references

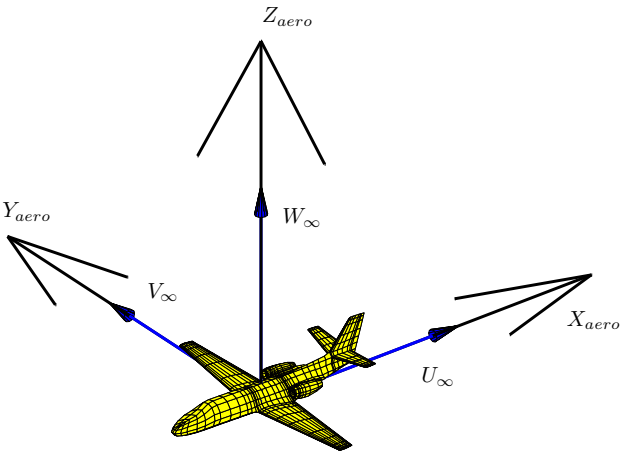


Figure 3.1: The Aerodynamic Frame of Reference $\mathcal{F}_{aero}$, including the undisturbed velocity components $[U_\infty, V_\infty, W_\infty]^T$ of $\underline{Q}_\infty$.

[11, 12, 8, 9]. The velocity potential solution Φ at an arbitrarily chosen point $P = (x, y, z)$ yields,

$$\Phi(P) = \frac{1}{4\pi} \left\{ \int\limits_{S_B+S_W+S_\infty} \mu \, \underline{n} \cdot \nabla \left(\frac{1}{r}\right) \, dS - \int\limits_{S_B+S_W+S_\infty} \sigma \left(\frac{1}{r}\right) \, dS \right\} \tag{3.9}$$

with S_W containing both the upper and lower wake-surfaces, or $S_{W_{upper}}$ and $S_{W_{lower}}$, respectively. Referring to figure 3.2, the integrals appearing in equation (3.9) hold for a sphere at infinity (S_∞), the configuration submerged in the airflow (S_B) and the configuration's wake ($S_W = S_{W_{upper}} + S_{W_{lower}}$). To simplify equation (3.9), two assumptions are made.

Considering the sphere at infinity, the local velocity there is assumed to equal the undisturbed or free-stream velocity $\underline{Q}_\infty$. It is assumed that the on-body source- and doublet-elements' influence has decayed to zero, see also equation (3.8). Therefore, the velocity potential at infinity ($\Phi(P)$) is essentially equal to $\Phi_\infty = U_\infty x + V_\infty y + W_\infty z$, see equation (3.6). This leads to the exclusion of the surface S_∞ in the integral as given in equation (3.9). However, the term Φ_∞ now has to be added to equation (3.9).

The second assumption is that the wake's thickness is infinitesimally small, thus making $S_W = S_{W_{upper}} = S_{W_{lower}}$. If crossflows through the configuration's wake are not present (the configuration's wake for non-seperated airflow follows local streamlines), the thin wake-representation is excluded from source-distributions in the LPF model. Therefore, only doublet-elements will represent the configuration's wake.

With these two assumptions, equation (3.9) now becomes,

$$\Phi(P) = \frac{1}{4\pi} \int\limits_{S_B+S_W} \mu \, \underline{n} \cdot \nabla \left(\frac{1}{r}\right) \, dS - \frac{1}{4\pi} \int\limits_{S_B} \sigma \left(\frac{1}{r}\right) \, dS + \Phi_\infty(P) \tag{3.10}$$

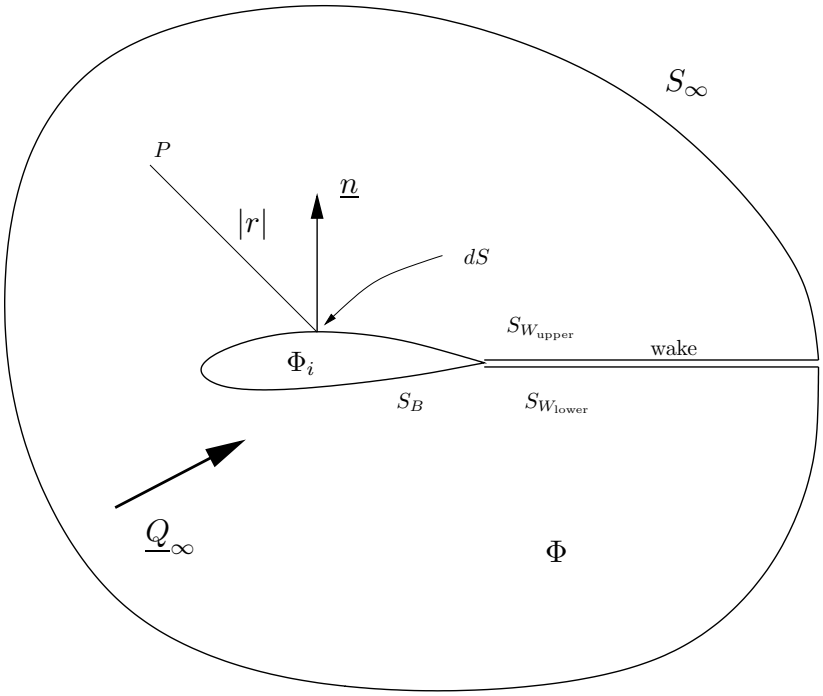


Figure 3.2: General sectional idealized potential flow model, see reference [8, 9].

or,

$$\Phi(P) = \Phi_{dist}(P) + \Phi_\infty(P) \tag{3.11}$$

where Φ_{dist} represents the disturbance potential due to both source- and doublet- distributions on the configuration ánd to doublet-distributions on the configuration's wake. Equation (3.10) leads to the following LPF model: the configuration of interest is distributed by both sources and doublets, while the configuration's wake is distributed by doublets only. This LPF model is represented in figure 3.3 where a cross-section of a 3D wing is given in the frame $\mathcal{F}_{aero}$. Equation (3.10) will form the basis for the numerical LPF simulations.

3.2.2 Boundary conditions

Boundary conditions for the Linearized Potential flow model have already been mentioned in section 3.2.1. The first condition included a fundamental solution of Laplace's equation, specifying the flow condition at infinity, see equation (3.6). The second condition specified the zero-flow through the configuration condition, see equation (3.7). The condition as given in equation (3.8), which specifies the singularities' disturbance influence at infinity, is inherently fulfilled by using both source- and doublet-distributions on the configuration of interest.

The condition specifying the zero-flow through the configuration, see equation (3.7), is also known as the Neumann boundary condition. Similar to this "zero-flow through the

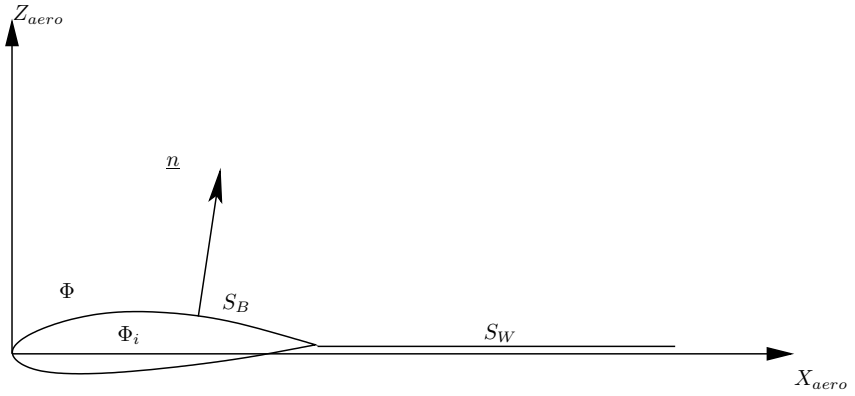


Figure 3.3: Sectional idealized potential flow model in the Aerodynamic Frame of Reference $\mathcal{F}_{aero}$.

configuration condition", the Dirichlet boundary condition can be specified. It specifies the configuration's internal potential Φ_i (see figure 3.3),

$$\Phi_i = \text{constant} \tag{3.12}$$

The internal potential Φ_i may be set to an arbitrary constant. Throughout this thesis the Dirichlet boundary condition will be used for numerical LPF simulations, with the internal (disturbance) potential, Φ_{dist_i}, set to zero,

$$\Phi_{dist_i} = 0 \tag{3.13}$$

Referring to equation (3.10), the disturbance potential only contains the contribution of the configuration's on-body source- and doublet-distribution as well as the contribution of the wake-doublet distribution. The wake's doublet-distribution will be discussed in the following section.

3.2.3 Wake separation and the Kutta condition

The wake model is defined by considering two distinct conditions. First, both the wake's location and shape have to be defined, and, secondly, the wake's doublet-distribution has to be determined.
The configuration's wake originates at prescribed on-body wake-shedding lines and it is convected downstream to infinity, see figure 3.3. The wake will be shed from lifting surfaces' trailing edges so that it will counteract the configuration's induced circulation. To counteract this induced circulation, the wake's singularity distribution will consist of doublets only, see also section 3.2.1.
The wake's doublet-strength is determined from the Kutta condition, which prescribes the airflow to leave an aerofoil's sharp trailing edge smoothly of finite velocity, see also references [11, 12]. The Kutta condition eventually leads to a definition of the wake's doublet-strength,

$$\mu_{wake} = \mu_{up_{te}} - \mu_{low_{te}} \tag{3.14}$$

where μ_{wake} is the wake's doublet-strength, and $\mu_{up_{te}}$ and $\mu_{low_{te}}$ are the corresponding aerofoil's upper and lower doublet-strengths at the trailing edge, respectively. This Kutta condition will also be applied to arbitrary 3D configurations.

3.2.4 A general LPF solution

Using the Dirichlet boundary condition, equation (3.12), and both equations (3.10) and (3.11), a general LPF solution can be formulated. However, at this stage the number of solutions remains infinite (see references [11, 12, 8, 9]). A step closer to a unique LPF solution is obtained by either prescribing the source- or the doublet-strength distribution. In references [11, 12, 8, 9] a prescribed source-strength distribution σ is suggested for numerical solutions,

$$\sigma = -\underline{n} \cdot \underline{Q}_{\infty} \tag{3.15}$$

with $\underline{n}$ the configuration's normal and $\underline{Q}_{\infty} = [U_{\infty}, V_{\infty}, W_{\infty}]^T$ the vector of undisturbed velocity components at infinity. Here, contrary to references [11, 12], the configuration's normal $\underline{n}$ points out of the configuration, see figure 3.3. The motivation for using this source-strength distribution is that it provides for most of the configuration's normal velocity component as required for the "zero-flow through the configuration condition". With this prescribed source-strength distribution a solution for the doublet-strength distribution is obtained.

Finally, considering both the Dirichlet boundary condition ánd the combination of the configuration's on-body source/doublet-strength distribution, a prescription of both the shape ánd position of the configuration's wake will lead to a unique solution of the LPF model (including lift). In principle, both the position ánd shape of the wake (that is the definition of wake-shedding lines on the configuration) will define the airflow's stagnation lines at the trailing edges of lift generating configuration elements, and, therefore, it will determine the amount of the configuration's circulation (or lift). The configuration's wake-doublet-strength will be related to the configuration's on-body doublet-strength at the prescribed wake-shedding lines.

In section 3.3 the numerical equivalent for the general LPF solution will be given.

3.3 Numerical steady linearized potential flow simulations

3.3.1 Body surface discretization

The numerical solution of Laplace's equation requires a discretization of the continuous surface description of the configuration over wich the airflow has to be solved. From the several software packages available, MATLAB was chosen to generate the required surface discretization for its easy coding/debugging, pre/post-processing, well documentation and

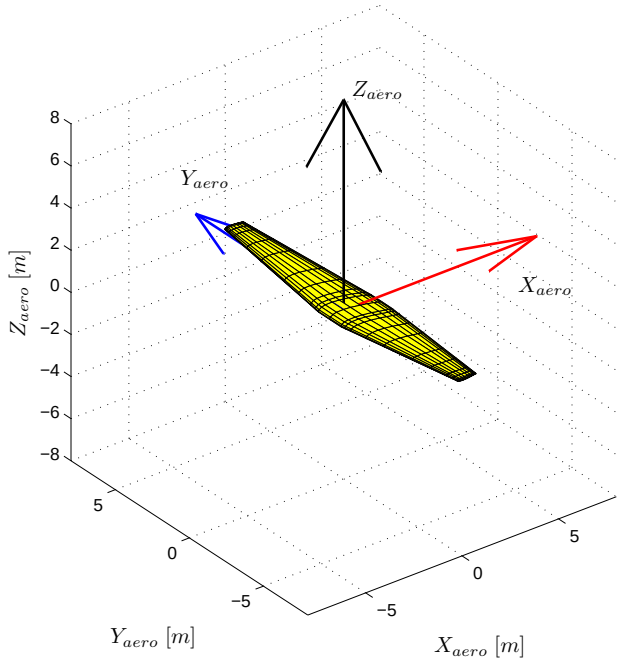


Figure 3.4: An example wing configuration in the Aerodynamic Frame of Reference $\mathcal{F}_{aero}$.

accessibility for both students and engineers. The MATLAB software will also be used for the solution of the Laplace equation and for post-processing of results.

The aerodynamic frame of reference $\mathcal{F}_{aero}$

For the simulation of airflows over an arbitrary configuration, the configuration is modeled in an orthonormal right-handed Aerodynamic Frame of Reference $\mathcal{F}_{aero}$, of which details can be found in appendix B. In figure 3.4 the frame $\mathcal{F}_{aero}$ with an example wing configuration (resembling the Cessna Ce550 Citation II wing) is given. The X_{aero}-axis is pointing aft in the vertical plane of symmetry, (for example) parallel to the airflow's direction at infinity $\underline{Q}_\infty$ (effectively resulting in $W_\infty = V_\infty = 0$), the Y_{aero}-axis is pointing to the right perpendicular to the vertical plane of symmetry, and the Z_{aero}-axis is pointing up, perpendicular to the $O_{aero}X_{aero}Y_{aero}$-plane. The origin O_{aero} is located at the configuration's center of gravity.

The numerical simulation of the airflow requires the continuous surface description of the configuration to be discretized in panels, with each panel having four corner points, e.g. for configuration panel k (with $k = 1 \cdots N_B$ and N_B the total number of configuration panels) $[x_{1_k}, y_{1_k}, z_{1_k}]^T$, $[x_{2_k}, y_{2_k}, z_{2_k}]^T$, $[x_{3_k}, y_{3_k}, z_{3_k}]^T$ and $[x_{4_k}, y_{4_k}, z_{4_k}]^T$ in $\mathcal{F}_{aero}$. The orientation of these four corner points is shown in figure 3.5. These corner points will define each panel's collocation point and they will also be used to define a local Panel Frame of Reference $\mathcal{F}_P$ of which details are also given in appendix B. The frame $\mathcal{F}_P$ will be used to evaluate each panel's contribution to the disturbance potential, see also appendix C.

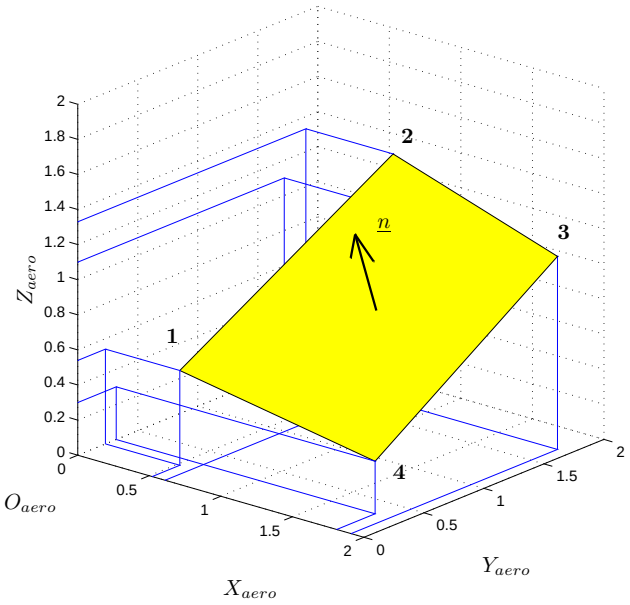


Figure 3.5: Orientation of the panel corner points $[x_i, y_i, z_i]^T$, with $i = 1, 2, 3, 4$, and the panel's normal, $\underline{n}$, in the Aerodynamic Frame of Reference $\mathcal{F}_{aero}$.

Collocation points

The collocation points are defined as those points of the configuration where the numerical flow is actually solved. For each panel k, both the doublet-strength (μ_k) and source-strength (σ_k) are defined in this point. Also, in these points the flow is defined with respect to the computed pressure p_k and both the source- and doublet-induced velocity components $[u_{ind}, v_{ind}, w_{ind}]^T$. The doublet-strength μ_k, the source-strength σ_k and the pressure p_k are assumed to be constant over configuration panel k.
In the frame $\mathcal{F}_{aero}$ the position of the collocation points $[x_{col_k}, y_{col_k}, z_{col_k}]^T$ is defined as,

$$\left.\begin{array}{rcl} x_{col_k} & = & \frac{1}{4}\left(x_{1_k} + x_{2_k} + x_{3_k} + x_{4_k}\right) \\ y_{col_k} & = & \frac{1}{4}\left(y_{1_k} + y_{2_k} + y_{3_k} + y_{4_k}\right) \\ z_{col_k} & = & \frac{1}{4}\left(z_{1_k} + z_{2_k} + z_{3_k} + z_{4_k}\right) \end{array}\right\} \tag{3.16}$$

with $k = 1 \cdots N_B$ and N_B the total number of configuration panels. In figure 3.6 a part of the left hand side of the configuration presented in figure 3.4 is given. In this figure the configuration's collocation points are given, as well as the panel corner points for an isolated panel.

The panel frame of reference $\mathcal{F}_P$

For each individual panel with corner points $[x_{1_k}, y_{1_k}, z_{1_k}]^T$, $[x_{2_k}, y_{2_k}, z_{2_k}]^T$, $[x_{3_k}, y_{3_k}, z_{3_k}]^T$ and $[x_{4_k}, y_{4_k}, z_{4_k}]^T$, a Panel Frame of Reference $\mathcal{F}_P$ is established in the frame $\mathcal{F}_{aero}$. In figure 3.7 this (local) reference frame is given for a part of the left hand side of the configuration presented in figure 3.4. In figure 3.7 $\mathcal{F}_P$ is also shown for an isolated panel. The reference frame $\mathcal{F}_P$ is a right-handed orthonormal frame of reference, with its origin

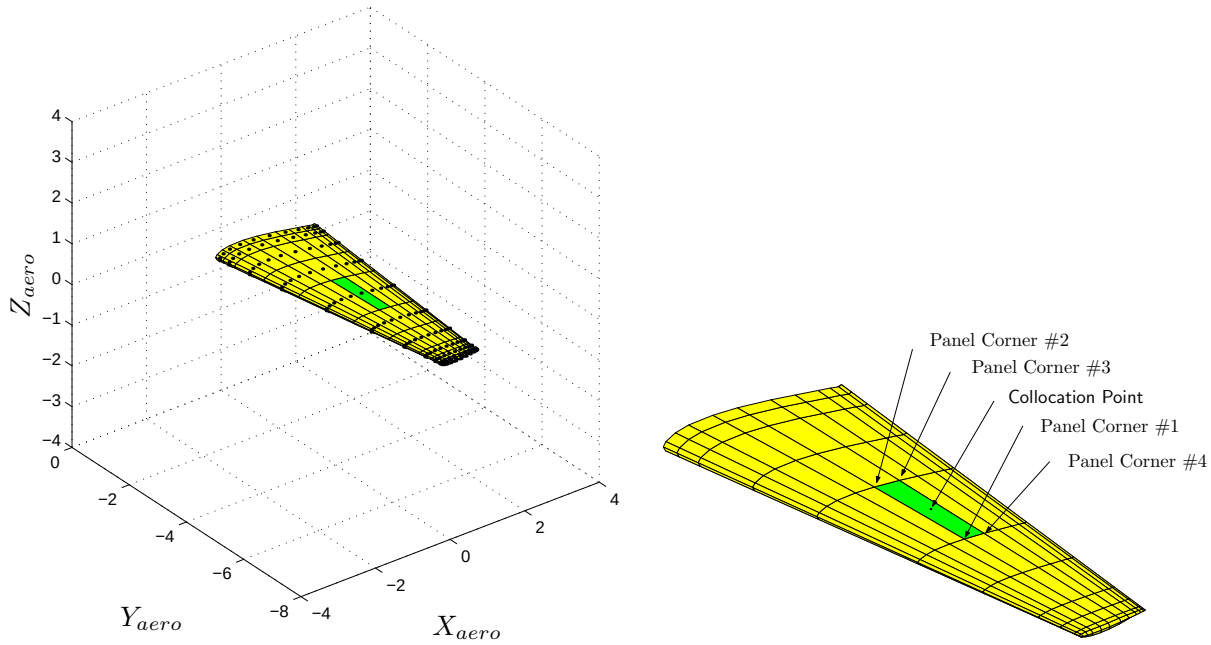


Figure 3.6: Position of collocation points $[x_{col_k}, y_{col_k}, z_{col_k}]^T$ (left) and a magnification of a single panel's collocation point including its panel corner points #1, #2, #3 and #4 in the Aerodynamic Frame of Reference $\mathcal{F}_{aero}$ (right).

O_P located in the panel's collocation point $[x_{col_k}, y_{col_k}, z_{col_k}]^T$. Details of the frame $\mathcal{F}_P$ are given in appendix B. For each panel, the location of its collocation point is given by equation (3.16). The three unit vectors along, respectively, the X_P-, Y_P- and Z_P-axis of $\mathcal{F}_P$ are designated in $\mathcal{F}_{aero}$ for an isolated panel k as $\underline{e}_{1_k} = [x_{e_{1_k}}, y_{e_{1_k}}, z_{e_{1_k}}]^T$, $\underline{e}_{2_k} = [x_{e_{2_k}}, y_{e_{2_k}}, z_{e_{2_k}}]^T$ and $\underline{e}_{3_k} = \underline{n}_k = [x_{e_{3_k}}, y_{e_{3_k}}, z_{e_{3_k}}]^T$.
With respect to the configuration's surface, for each panel the Z_P-axis of $\mathcal{F}_P$ always points outwards and its orientation is determined by the four panel corner points. To determine the orientation of this axis, first the diagonal $\underline{d}_{1_k}$ between corner points $[x_{1_k}, y_{1_k}, z_{1_k}]^T$ and $[x_{3_k}, y_{3_k}, z_{3_k}]^T$ is calculated. Second, the diagonal $\underline{d}_{2_k}$ between corner points $[x_{4_k}, y_{4_k}, z_{4_k}]^T$ and $[x_{2_k}, y_{2_k}, z_{2_k}]^T$ is calculated. The two diagonal vectors $\underline{d}_{1_k}$ and $\underline{d}_{2_k}$ are, respectively,

$$\underline{d}_{1_k} = \begin{bmatrix} x_{3_k} \\ y_{3_k} \\ z_{3_k} \end{bmatrix} - \begin{bmatrix} x_{1_k} \\ y_{1_k} \\ z_{1_k} \end{bmatrix} \tag{3.17}$$

$$\underline{d}_{2_k} = \begin{bmatrix} x_{2_k} \\ y_{2_k} \\ z_{2_k} \end{bmatrix} - \begin{bmatrix} x_{4_k} \\ y_{4_k} \\ z_{4_k} \end{bmatrix} \tag{3.18}$$

From these two diagonals the panel's normal unit vector $\underline{e}_{3_k} = \underline{n}_k = [x_{e_{3_k}}, y_{e_{3_k}}, z_{e_{3_k}}]^T$, pointing in the positive Z_P-axis direction, is constructed by taking the vector product between $\underline{d}_{1_k}$ and $\underline{d}_{2_k}$, and normalizing it (see figure 3.8),

$$\underline{n}_k = \underline{e}_{3_k} = \frac{\underline{d}_{1_k} \times \underline{d}_{2_k}}{\left|\underline{d}_{1_k} \times \underline{d}_{2_k}\right|} \tag{3.19}$$

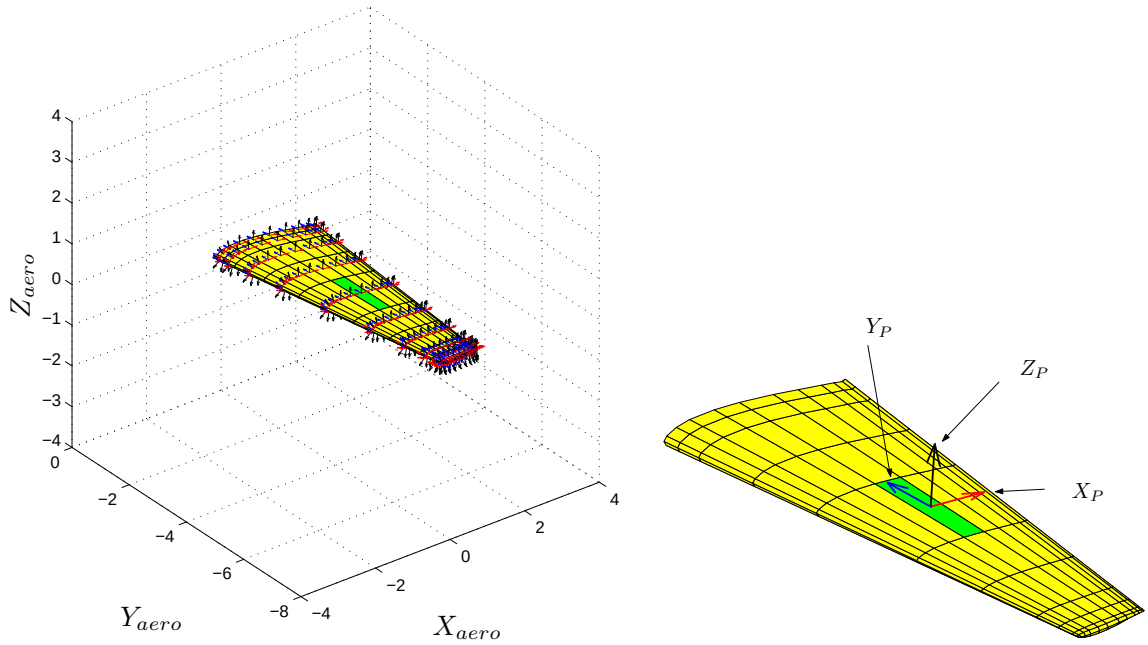


Figure 3.7: The local Panel Frame of Reference $\mathcal{F}_P$ in $\mathcal{F}_{aero}$ (left) and a magnification of a single panel's local frame with origin at the panel's collocation point (right), also in $\mathcal{F}_{aero}$.

Using equations (3.17) and (3.18), the panel's surface area ΔS_{P_k} is defined as,

$$\Delta S_{P_k} = \frac{1}{2} \left| \underline{d}_{1_k} \times \underline{d}_{2_k} \right| \tag{3.20}$$

For each panel, the X_P-axis of $\mathcal{F}_P$ points aft and is constructed by the corner points $[x_{3_k}, y_{3_k}, z_{3_k}]^T$ and $[x_{4_k}, y_{4_k}, z_{4_k}]^T$, by the normal vector $\underline{n}_k = \underline{e}_{3_k} = [x_{e_{3_k}}, y_{e_{3_k}}, z_{e_{3_k}}]^T$ and by the collocation point $[x_{col_k}, y_{col_k}, z_{col_k}]^T$, which is the origin of $\mathcal{F}_P$. The unit vector $\underline{e}_{1_k} = [x_{e_{1_k}}, y_{e_{1_k}}, z_{e_{1_k}}]^T$, pointing in the positive X_P-axis direction, is constructed by first defining a flat plane through the collocation point which, in $\mathcal{F}_{aero}$, has a normal vector $\underline{n}_k = \underline{e}_{3_k} = [x_{e_{3_k}}, y_{e_{3_k}}, z_{e_{3_k}}]^T$,

$$K_{pan_k} = x_{e_{3_k}}\ x_{col_k} + y_{e_{3_k}}\ y_{col_k} + z_{e_{3_k}}\ z_{col_k} \tag{3.21}$$

Then, the elements $x^*_{e_{1_k}}$ and $y^*_{e_{1_k}}$ are calculated by,

$$x^*_{e_{1_k}} = \frac{1}{2} \left(x_{3_k} + x_{4_k} \right)$$
$$y^*_{e_{1_k}} = \frac{1}{2} \left(y_{3_k} + y_{4_k} \right)$$

Using equation (3.21), the element $z^*_{e_{1_k}}$ becomes,

$$z^*_{e_{1_k}} = \frac{1}{z_{e_{3_k}}} \left(K_{pan_k} - x_{e_{3_k}}\ x^*_{e_{1_k}} - y_{e_{3_k}}\ y^*_{e_{1_k}} \right) \tag{3.22}$$

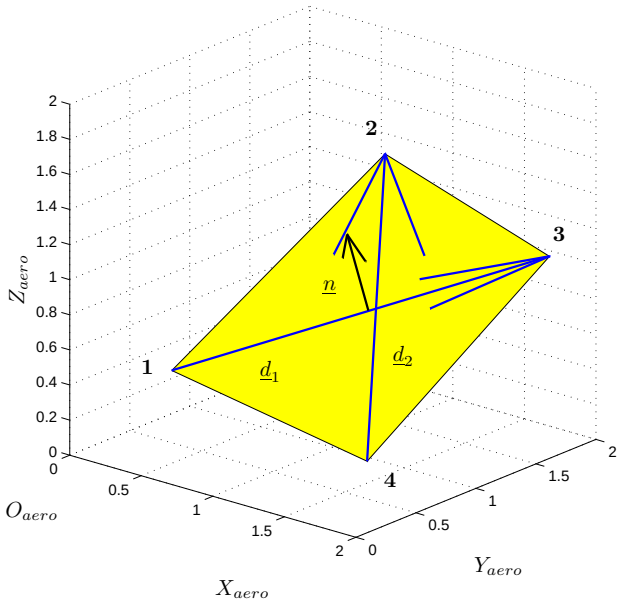


Figure 3.8: Orientation of the panel corner points $[x_i, y_i, z_i]^T$, with $i = 1, 2, 3, 4$, the panel's diagonal vectors $\underline{d}_1$ and $\underline{d}_2$, and the panel's normal, $\underline{n}$, in the Aerodynamic Frame of Reference $\mathcal{F}_{aero}$.

If the absolute value of $z_{e_{3_k}}$ becomes too small (smaller than the order of $O(-5)$), $z^*_{e_{1_k}}$ becomes,

$$z^*_{e_{1_k}} = \frac{1}{2}\left(z_{3_k} + z_{4_k}\right)$$

In $\mathcal{F}_{aero}$, the elements of vector $\underline{e}'_{1_k} = [x'_{e_{1_k}}, y'_{e_{1_k}}, z'_{e_{1_k}}]^T$ become,

$$\begin{aligned} x'_{e_{1_k}} &= x^*_{e_{1_k}} - x_{col_k} \\ y'_{e_{1_k}} &= y^*_{e_{1_k}} - y_{col_k} \\ z'_{e_{1_k}} &= z^*_{e_{1_k}} - z_{col_k} \end{aligned}$$

Finally, vector $\underline{e}'_{1_k}$ becomes the unit vector $\underline{e}_{1_k} = [x_{e_{1_k}}, y_{e_{1_k}}, z_{e_{1_k}}]^T$ by normalizing it with its length $\left|\underline{e}'_{1_k}\right|$,

$$\begin{aligned} x_{e_{1_k}} &= \frac{x'_{e_{1_k}}}{\sqrt{x'^2_{e_{1_k}} + y'^2_{e_{1_k}} + z'^2_{e_{1_k}}}} \\ y_{e_{1_k}} &= \frac{y'_{e_{1_k}}}{\sqrt{x'^2_{e_{1_k}} + y'^2_{e_{1_k}} + z'^2_{e_{1_k}}}} \\ z_{e_{1_k}} &= \frac{z'_{e_{1_k}}}{\sqrt{x'^2_{e_{1_k}} + y'^2_{e_{1_k}} + z'^2_{e_{1_k}}}} \end{aligned}$$

Having identified both the orientation ánd magnitude of the unit vectors $\underline{e}_{1_k}$ and $\underline{e}_{3_k}$ in X_P- and Z_P-direction, respectively, the orientation and magnitude of $\underline{e}_{2_k}$ follows from the

vector product between the unit vectors $\underline{e}_{3_k}$ and $\underline{e}_{1_k}$,

$$\underline{e}_{2_k} = \underline{e}_{3_k} \times \underline{e}_{1_k} \tag{3.23}$$

or with $\underline{e}_{2_k} = [x_{e_{2_k}}, y_{e_{2_k}}, z_{e_{2_k}}]^T$, the seperate elements become,

$$\begin{aligned} x_{e_{2_k}} &= y_{e_{3_k}} z_{e_{1_k}} - y_{e_{1_k}} z_{e_{3_k}} \\ y_{e_{2_k}} &= z_{e_{3_k}} x_{e_{1_k}} - z_{e_{1_k}} x_{e_{3_k}} \\ z_{e_{2_k}} &= x_{e_{3_k}} y_{e_{1_k}} - x_{e_{1_k}} y_{e_{3_k}} \end{aligned}$$

Note that $\underline{e}_{2_k} = [x_{e_{2_k}}, y_{e_{2_k}}, z_{e_{2_k}}]^T$ is a unit vector, so $\left|\underline{e}_{2_k}\right| = \left|\underline{e}_{1_k}\right| = \left|\underline{e}_{3_k}\right| = 1$.
For an isolated panel k, the frame $\mathcal{F}_P$ with its origin in the panel's collocation point and the orthonormal vectors $\underline{e}_{1_k}$, $\underline{e}_{2_k}$ and $\underline{e}_{3_k}$, defined in the frame $\mathcal{F}_{aero}$, will later be used to calculate a panel's induced disturbance potential Φ_{dist}.

3.3.2 Quadri-lateral panels

For the Linearized Potential Flow model simulations, both the source- ánd doublet-panels are modeled as quadri-lateral panels, so as flat surfaces with four straight lines. The motivation for transforming both the configuration ánd wake-panels to their quadri-lateral equivalents is that the constant strength source- and doublet-panel influence formulae as presented in appendix C only hold for quadri-lateral panels.
For each individual panel the four corner points are translated into a plane through its collocation point and perpendicular to its normal. In the frame $\mathcal{F}_{aero}$ the plane perpendicular to the panel's normal $\underline{n}_k = \underline{e}_{3_k} = [x_{e_{3_k}}, y_{e_{3_k}}, z_{e_{3_k}}]^T$ is given by equation (3.21),

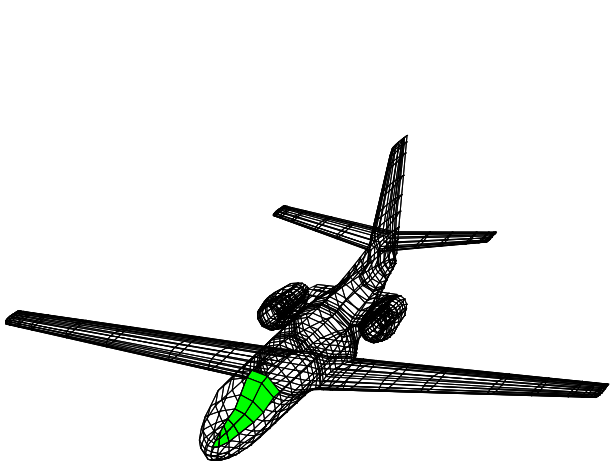
$$K_{pan_k} = x_{e_{3_k}}\ x_{col_k} + y_{e_{3_k}}\ y_{col_k} + z_{e_{3_k}}\ z_{col_k}$$

For each panel's corner point position in $\mathcal{F}_{aero}$ the x and y component is kept equal, however, the z component is altered to make sure all four (quadri-lateral) panel corner points are located in a flat plane. For all four quadri-lateral panel corner points equations similar to equation (3.21) are used to calculate their new z component. For an individual panel the quadri-lateral panel's z components become,

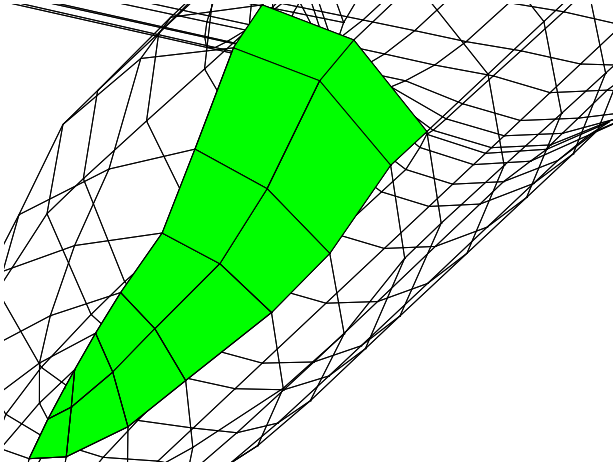
$$\begin{aligned} K_{pan_k} &= x_{e_{3_k}}\ x_{1_k} + y_{e_{3_k}}\ y_{1_k} + z_{e_{3_k}}\ z_{1_{quad_k}} \\ K_{pan_k} &= x_{e_{3_k}}\ x_{2_k} + y_{e_{3_k}}\ y_{2_k} + z_{e_{3_k}}\ z_{2_{quad_k}} \\ K_{pan_k} &= x_{e_{3_k}}\ x_{3_k} + y_{e_{3_k}}\ y_{3_k} + z_{e_{3_k}}\ z_{3_{quad_k}} \\ K_{pan_k} &= x_{e_{3_k}}\ x_{4_k} + y_{e_{3_k}}\ y_{4_k} + z_{e_{3_k}}\ z_{4_{quad_k}} \end{aligned}$$

or,

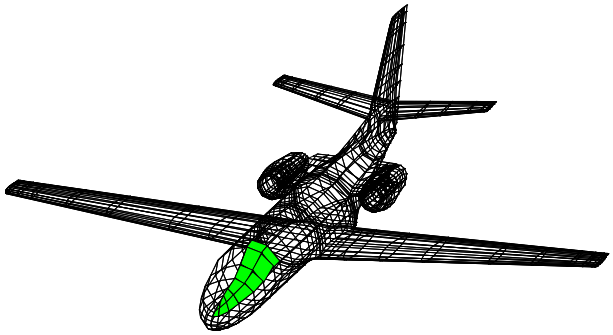
$$\begin{aligned} z_{1_{quad_k}} &= \frac{1}{z_{e_{3_k}}} \left(K_{pan_k} - x_{e_{3_k}}\ x_{1_k} - y_{e_{3_k}}\ y_{1_k} \right) \\ z_{2_{quad_k}} &= \frac{1}{z_{e_{3_k}}} \left(K_{pan_k} - x_{e_{3_k}}\ x_{2_k} - y_{e_{3_k}}\ y_{2_k} \right) \end{aligned}$$



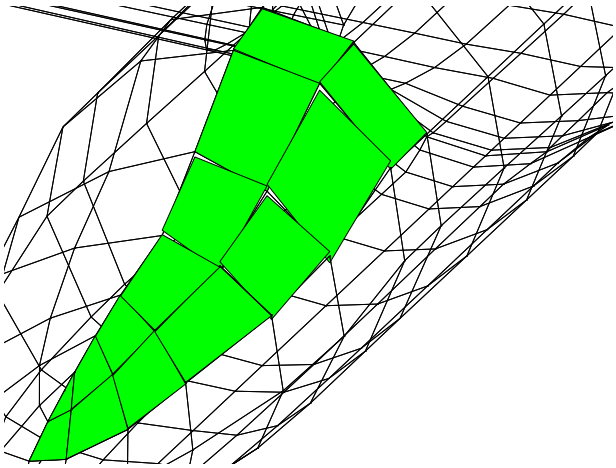
(a) Configuration panels



(b) Configuration panels (magnification)



(c) Quadri-lateral panels



(d) Quadri-lateral panels (magnification)

Figure 3.9: Configuration panels (both top figures) and their quadri-lateral equivalents (both bottom figures).

$$z_{3_{quad_k}} = \frac{1}{z_{e_{3_k}}} \left(K_{pan_k} - x_{e_{3_k}} \, x_{3_k} - y_{e_{3_k}} \, y_{3_k} \right)$$

$$z_{4_{quad_k}} = \frac{1}{z_{e_{3_k}}} \left(K_{pan_k} - x_{e_{3_k}} \, x_{4_k} - y_{e_{3_k}} \, y_{4_k} \right)$$

with $z_{1_{quad_k}}$, $z_{2_{quad_k}}$, $z_{3_{quad_k}}$ and $z_{4_{quad_k}}$ the new position of panel corner points #1, #2, #3 and #4, respectively, along the Z_{aero}-axis in $\mathcal{F}_{aero}$. Now, the quadri-lateral panel's four corner points $[x_{1_k}, y_{1_k}, z_{1_{quad_k}}]^T$, $[x_{2_k}, y_{2_k}, z_{2_{quad_k}}]^T$, $[x_{3_k}, y_{3_k}, z_{3_{quad_k}}]^T$ and $[x_{4_k}, y_{4_k}, z_{4_{quad_k}}]^T$ are located in a flat plane, and, obviously, the panel does not contain any twist. In figure 3.9 an example of the difference between configuration panels and their quadri-lateral equivalents is given.

The contributions of a quadri-lateral source- or doublet-panel to the disturbance potential Φ_{dist} are given in references [11, 12] and they have been summarized in appendix C. These

contributions are given in the local frame $\mathcal{F}_P$, with the origin O_P located in the collocation point of the panel.
Similar to the configuration panels, the wake-panels are also transformed to their quadri-lateral equivalents. The derivations of $z_{wake_{1_{quad_k}}}$, $z_{wake_{2_{quad_k}}}$, $z_{wake_{3_{quad_k}}}$ and $z_{wake_{4_{quad_k}}}$ are similar to the ones for $z_{1_{quad_k}}$, $z_{2_{quad_k}}$, $z_{3_{quad_k}}$ and $z_{4_{quad_k}}$, respectively.

3.3.3 Numerical boundary conditions

The numerical boundary condition employed in this thesis is the Dirichlet boundary condition. It requires the internal disturbance potential to equal a constant (and is selected as zero, see reference [11]). For this purpose, each collocation point (now located inside the configuration, slightly below the surface) is scanned and the sum of the disturbance potential of all configuration and all wake-panels is calculated. The motivation for calculating the disturbance potential slightly below the configuration's outer surface contours is to ensure that the internal disturbance potential Φ_{dist_i} is indeed calculated. For this purpose, the configuration's collocation points are translated into the configuration,

$$\begin{aligned} x^*_{col_k} &= x_{col_k} - \varepsilon * x_{e_{3_k}} \\ y^*_{col_k} &= y_{col_k} - \varepsilon * y_{e_{3_k}} \\ z^*_{col_k} &= z_{col_k} - \varepsilon * z_{e_{3_k}} \end{aligned}$$

with $[x_{col_k}, y_{col_k}, z_{col_k}]^T$ the position of the configuration's collocation points in the frame $\mathcal{F}_{aero}$ according to equation (3.16), $\underline{n_k} = [x_{e_{3_k}}, y_{e_{3_k}}, z_{e_{3_k}}]^T$ the panel's normal vector components in $\mathcal{F}_{aero}$, ε an extremely small constant (with ε of the order of $\varepsilon = O(e-10)$) and $[x^*_{col_k}, y^*_{col_k}, z^*_{col_k}]^T$ the position of the configuration's translated collocation point, also in $\mathcal{F}_{aero}$.

3.3.4 Wake separation and the numerical Kutta condition

The wake consists of a number of quadri-lateral doublet-panels. Similar to the configuration's panels, they also have four corner points which are designated for an isolated wake-panel j $[x_{w_{1_j}}, y_{w_{1_j}}, z_{w_{1_j}}]^T$, $[x_{w_{2_j}}, y_{w_{2_j}}, z_{w_{2_j}}]^T$, $[x_{w_{3_j}}, y_{w_{3_j}}, z_{w_{3_j}}]^T$ and $[x_{w_{4_j}}, y_{w_{4_j}}, z_{w_{4_j}}]^T$ in $\mathcal{F}_{aero}$, with $j = 1 \cdots N_W$ and N_W the total number of wake-panels.
The configuration's wake is determined by sets of user defined wake-shedding lines. When considering attached flows only, these wake-shedding panels are located at the trailing edges of lift-generating configuration components or panels from which a wake is desired (separation). In figure 3.10 the (truncated) wake of a part of the left hand side of the configuration presented in figure 3.4 is given. The wake-shedding lines on the configuration define the position of wake-panel corner points #1 and #2. The wake-panels extend downstream to a prescribed location defining the position of wake-panel corner points #3 and #4 along the X_{aero}-axis. Throughout this thesis this downstream location is set at 100 times the span of the configuration, $L_{wake} = 100\ b_{ref}$, with b_{ref} a reference length taken to be the configuration's span. The position of the downstream wake-panel corner

points #3 and #4 along the Y_{aero}- and Z_{aero}-axis are set equal to the position of wake-panel corner points #2 and #1, respectively.

Similar to the configuration panels, the wake-panels also have a collocation point and a local frame $\mathcal{F}_P$, see section 3.3.1. The wake's local frame $\mathcal{F}_P$ in $\mathcal{F}_{aero}$ is given in figure 3.11. The wake's collocation points are defined as,

$$\left.\begin{array}{rcl} x_{w_{col_j}} & = & \frac{1}{4}\left(x_{w_{1_j}} + x_{w_{2_j}} + x_{w_{3_j}} + x_{w_{4_j}}\right) \\ y_{w_{col_j}} & = & \frac{1}{4}\left(y_{w_{1_j}} + y_{w_{2_j}} + y_{w_{3_j}} + y_{w_{4_j}}\right) \\ z_{w_{col_j}} & = & \frac{1}{4}\left(z_{w_{1_j}} + z_{w_{2_j}} + z_{w_{3_j}} + z_{w_{4_j}}\right) \end{array}\right\} \tag{3.24}$$

with $j = 1 \cdots N_W$.
The definition of the wake-panels local frame $\mathcal{F}_P$ is similar to that of the configuration panels local frame, see section 3.3.1.
The singularity distribution on the wake-panels consists of doublets only. Similar to the wake doublet-strength definition in section 3.2.3, the wake panels' doublet-strength μ_{wake} is determined by specifying the wake-separation lines, thus defining the upper and lower wake-shedding panels on the configuration, see also figure 3.12. Similar to the analytical Kutta condition given in equation (3.14), the wake-panels' doublet-strength μ_{wake} is determined by (omitting subscripts),

$$\mu_{wake} = \mu_{up} - \mu_{low} \tag{3.25}$$

where μ_{wake} is the wake-panel's doublet-strength, and μ_{up} and μ_{low} are the corresponding upper and lower configuration-panel's doublet-strength at the wing's trailing edge, respectively. Although a wake-rollup option is available in this panel-method, throughout this thesis the wake-geometry remains planar since only small disturbances in aircraft motion and atmospheric turbulence velocity components (both with respect to airspeed $Q_\infty = \left|\underline{Q}_\infty\right|$) will be considered.

3.3.5 General numerical source- and doublet-solutions

Now, the configuration submerged in a fluid flow is considered to be discretized in N_B (quadri-lateral) configuration panels while the wake is divided into N_W (quadri-lateral) wake-panels. Assuming that all N_B panel corner points of the discretized configuration in $\mathcal{F}_{aero}$, as well as all N_W panel corner points of the discretized wake configuration in $\mathcal{F}_{aero}$, are known, a solution for the potential flow problem is derived. Furthermore, assuming that the configuration panels contain both constant strength source and constant strength doublet-distributions and that the wake-panels only contain constant strength doublet-distributions, the Dirichlet boundary condition for each of the N_B collocation points can be evaluated. The internal disturbance potential Φ_{dist_i} at each collocation point k (with $k = 1 \cdots N_B$) now located inside the configuration, equals the sum of the disturbance potential due to both the configuration source and configuration doublet-panels ($i = 1 \cdots N_B$) ánd the sum of the disturbance potential due to the wake-doublet-panels ($j = 1 \cdots N_W$). Referring also to equation (3.10), this disturbance potential Φ_{dist_i}

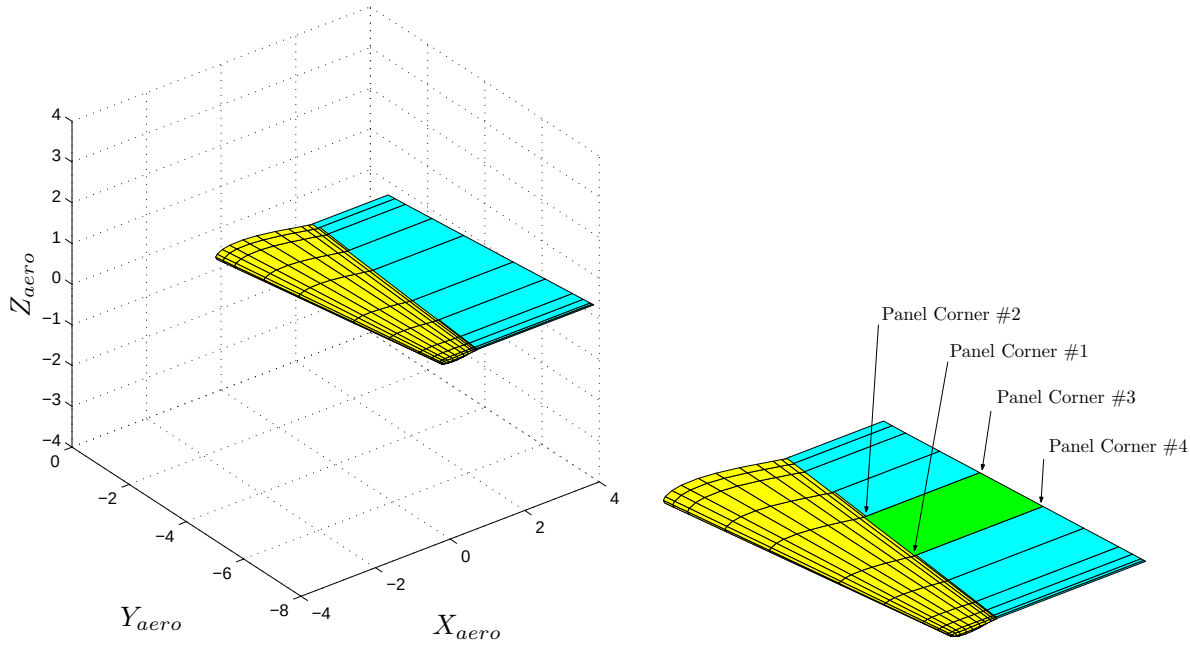


Figure 3.10: Configuration and (truncated) wake-definition (left) and a magnification of a single wake-panel including its panel corner points #1, #2, #3 and #4 in the Aerodynamic Frame of Reference $\mathcal{F}_{aero}$ (right).

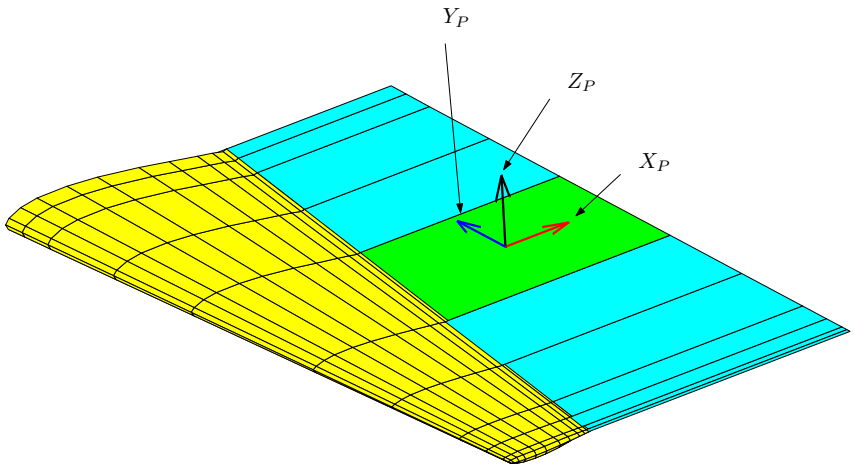


Figure 3.11: Configuration and the (truncated) wake-definition including the wake's local Panel Frame of Reference $\mathcal{F}_P$ in $\mathcal{F}_{aero}$.

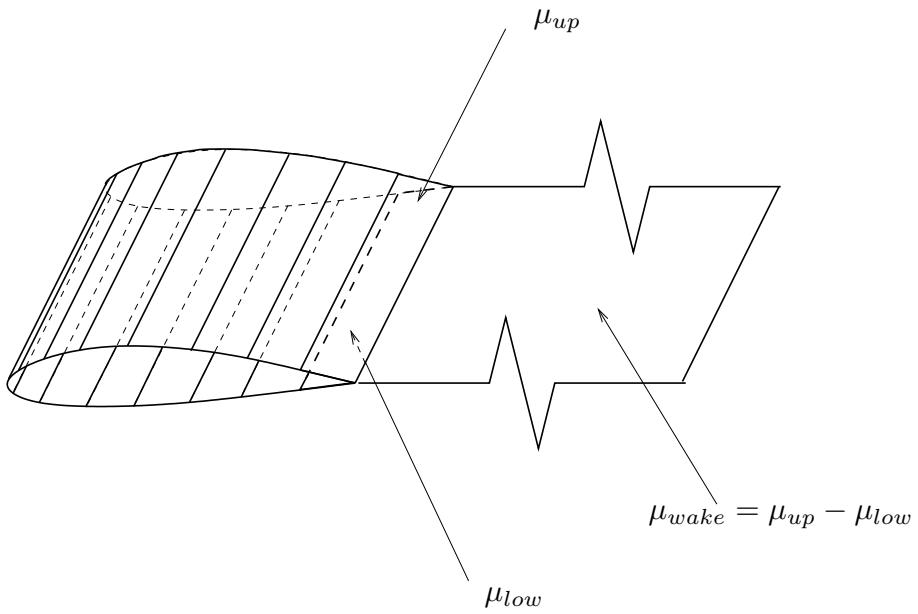


Figure 3.12: Calculation of the wake-doublet-strength μ_{wake}.

equals zero,

$$- \sum_{i=1}^{N_B} \frac{1}{4\pi} \int\limits_{body-panel_i} \sigma \left(\frac{1}{r}\right) dS + \sum_{i=1}^{N_B} \frac{1}{4\pi} \int\limits_{body-panel_i} \mu \, \underline{n} \cdot \nabla \left(\frac{1}{r}\right) dS +$$

$$+ \sum_{j=1}^{N_W} \frac{1}{4\pi} \int\limits_{wake-panel_j} \mu \, \underline{n} \cdot \nabla \left(\frac{1}{r}\right) dS = 0 \Big|_{\text{collocation point } k} \tag{3.26}$$

with $r = \sqrt{x^2 + y^2 + z^2}$ in $\mathcal{F}_{aero}$. In equation (3.26) a single collocation point k is evaluated and the influence of all $i = 1 \cdots N_B$ configuration panels and the influence of all $j = 1 \cdots N_W$ wake-panels at that collocation point is summed, see figure 3.13.

Reference frame transformation $\mathcal{T}^P_{aero}$

When calculating the disturbance potential of a quadri-lateral panel i on configuration panel k's collocation point, it is determined by transforming the panel corner points of panel i to its local frame $\mathcal{F}_P$. Also the collocation point of panel k is transformed to $\mathcal{F}_P$ of panel i. The disturbance potential due to both a unit strength doublet-panel and a unit strength source-panel is now calculated. For constant panel k, all panels $i = 1 \cdots N_B$ are scanned and the disturbance potential due to all configuration panels is calculated. Similarly, the influence of all wake-panels to the disturbance potential at collocation point k is determined.
For the transformation from the frame $\mathcal{F}_{aero}$ to panel i's local frame $\mathcal{F}_P$, denoted as $\mathcal{T}^P_{aero}$, the three unit vectors $\underline{e}_{1_i}$, $\underline{e}_{2_i}$ and $\underline{e}_{3_i} = \underline{n}_i$ describing panel i's unit vectors of $\mathcal{F}_P$ in $\mathcal{F}_{aero}$

are used. The transformation matrix $\mathcal{T}^P_{aero}$ is used for the transformation from reference frame $\mathcal{F}_{aero}$ to reference frame $\mathcal{F}_P$ by,

$$\begin{bmatrix} x_P \\ y_P \\ z_P \end{bmatrix} = \mathcal{T}^P_{aero} \begin{bmatrix} x_{aero} \\ y_{aero} \\ z_{aero} \end{bmatrix} \tag{3.27}$$

with $[x_P, y_P, z_P]^T$ a vector in $\mathcal{F}_P$ and $[x_{aero}, y_{aero}, z_{aero}]^T$ a vector in $\mathcal{F}_{aero}$.
The elements of transformation matrix $\mathcal{T}^P_{aero}$ are obtained by first defining the (unknown) transformation matrix $\mathcal{T}^P_{aero}$ as,

$$\mathcal{T}^P_{aero} = \begin{bmatrix} t_{11} & t_{12} & t_{13} \\ t_{21} & t_{22} & t_{23} \\ t_{31} & t_{32} & t_{33} \end{bmatrix} \tag{3.28}$$

For each panel i the unknown matrix elements t_{rs}, with $r = 1 \cdots 3$ and $s = 1 \cdots 3$, in equation (3.28) are obtained from expressions similar to equation (3.27); each of the unit vectors $\underline{e}_{1_i}$, $\underline{e}_{2_i}$ and $\underline{e}_{3_i} = \underline{n}_i$ in $\mathcal{F}_{aero}$ will eventually be transformed to unit vectors $[1,0,0]^T$, $[0,1,0]^T$ and $[0,0,1]^T$ in $\mathcal{F}_P$, respectively. Starting with panel i's normal vector $\underline{e}_{3_i} = \underline{n}_i$, equation (3.27) is written as,

$$\begin{bmatrix} t_{11_i} & t_{12_i} & t_{13_i} \\ t_{21_i} & t_{22_i} & t_{23_i} \\ t_{31_i} & t_{32_i} & t_{33_i} \end{bmatrix} \begin{bmatrix} x_{e_{3_i}} \\ y_{e_{3_i}} \\ z_{e_{3_i}} \end{bmatrix} = \begin{bmatrix} 0 \\ 0 \\ 1 \end{bmatrix} \tag{3.29}$$

For the unit vectors $\underline{e}_{2_i}$ and $\underline{e}_{1_i}$, equation (3.29) becomes,

$$\begin{bmatrix} t_{11_i} & t_{12_i} & t_{13_i} \\ t_{21_i} & t_{22_i} & t_{23_i} \\ t_{31_i} & t_{32_i} & t_{33_i} \end{bmatrix} \begin{bmatrix} x_{e_{2_i}} \\ y_{e_{2_i}} \\ z_{e_{2_i}} \end{bmatrix} = \begin{bmatrix} 0 \\ 1 \\ 0 \end{bmatrix} \tag{3.30}$$

and,

$$\begin{bmatrix} t_{11_i} & t_{12_i} & t_{13_i} \\ t_{21_i} & t_{22_i} & t_{23_i} \\ t_{31_i} & t_{32_i} & t_{33_i} \end{bmatrix} \begin{bmatrix} x_{e_{1_i}} \\ y_{e_{1_i}} \\ z_{e_{1_i}} \end{bmatrix} = \begin{bmatrix} 1 \\ 0 \\ 0 \end{bmatrix} \tag{3.31}$$

respectively.

From equations (3.29), (3.30) and (3.31), for each panel i the unknown matrix elements t_{rs} of $\mathcal{T}^P_{aero}$ are calculated from,

$$\left[\begin{array}{ccc|ccc|ccc} x_{e_{3_i}} & y_{e_{3_i}} & z_{e_{3_i}} & 0 & 0 & 0 & 0 & 0 & 0 \\ 0 & 0 & 0 & x_{e_{3_i}} & y_{e_{3_i}} & z_{e_{3_i}} & 0 & 0 & 0 \\ 0 & 0 & 0 & 0 & 0 & 0 & x_{e_{3_i}} & y_{e_{3_i}} & z_{e_{3_i}} \\ \hline x_{e_{2_i}} & y_{e_{2_i}} & z_{e_{2_i}} & 0 & 0 & 0 & 0 & 0 & 0 \\ 0 & 0 & 0 & x_{e_{2_i}} & y_{e_{2_i}} & z_{e_{2_i}} & 0 & 0 & 0 \\ 0 & 0 & 0 & 0 & 0 & 0 & x_{e_{2_i}} & y_{e_{2_i}} & z_{e_{2_i}} \\ \hline x_{e_{1_i}} & y_{e_{1_i}} & z_{e_{1_i}} & 0 & 0 & 0 & 0 & 0 & 0 \\ 0 & 0 & 0 & x_{e_{1_i}} & y_{e_{1_i}} & z_{e_{1_i}} & 0 & 0 & 0 \\ 0 & 0 & 0 & 0 & 0 & 0 & x_{e_{1_i}} & y_{e_{1_i}} & z_{e_{1_i}} \end{array}\right] \left[\begin{array}{c} t_{11_i} \\ t_{12_i} \\ t_{13_i} \\ \hline t_{21_i} \\ t_{22_i} \\ t_{23_i} \\ \hline t_{31_i} \\ t_{32_i} \\ t_{33_i} \end{array}\right] = \left[\begin{array}{c} 0 \\ 0 \\ 1 \\ \hline 0 \\ 1 \\ 0 \\ \hline 1 \\ 0 \\ 0 \end{array}\right] \tag{3.32}$$

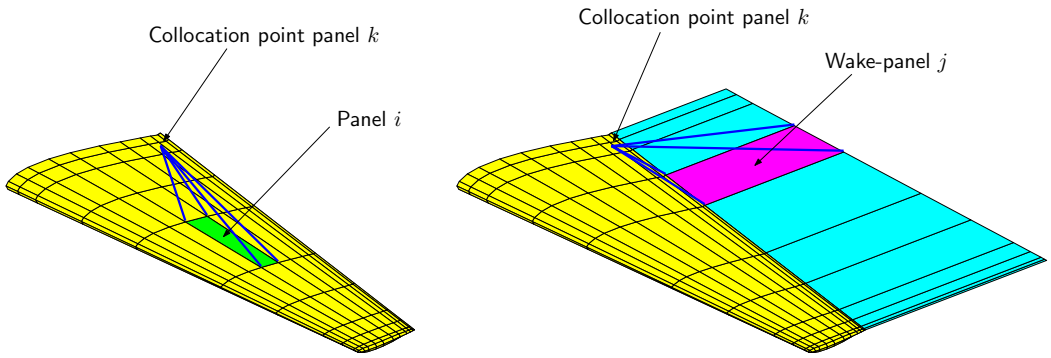


Figure 3.13: Influence of configuration panel i on configuration panel k (left), and the influence of wake-panel j on configuration panel k (right).

The unknown matrix elements of transformation matrix $\mathcal{T}^P_{aero}$, equation (3.28), are obtained from equation (3.32) by,

$$\begin{bmatrix} t_{11_i} \\ t_{12_i} \\ t_{13_i} \\ \hline t_{21_i} \\ t_{22_i} \\ t_{23_i} \\ \hline t_{31_i} \\ t_{32_i} \\ t_{33_i} \end{bmatrix} = \left[\begin{array}{ccc|ccc|ccc} x_{e_{3_i}} & y_{e_{3_i}} & z_{e_{3_i}} & 0 & 0 & 0 & 0 & 0 & 0 \\ 0 & 0 & 0 & x_{e_{3_i}} & y_{e_{3_i}} & z_{e_{3_i}} & 0 & 0 & 0 \\ 0 & 0 & 0 & 0 & 0 & 0 & x_{e_{3_i}} & y_{e_{3_i}} & z_{e_{3_i}} \\ \hline x_{e_{2_i}} & y_{e_{2_i}} & z_{e_{2_i}} & 0 & 0 & 0 & 0 & 0 & 0 \\ 0 & 0 & 0 & x_{e_{2_i}} & y_{e_{2_i}} & z_{e_{2_i}} & 0 & 0 & 0 \\ 0 & 0 & 0 & 0 & 0 & 0 & x_{e_{2_i}} & y_{e_{2_i}} & z_{e_{2_i}} \\ \hline x_{e_{1_i}} & y_{e_{1_i}} & z_{e_{1_i}} & 0 & 0 & 0 & 0 & 0 & 0 \\ 0 & 0 & 0 & x_{e_{1_i}} & y_{e_{1_i}} & z_{e_{1_i}} & 0 & 0 & 0 \\ 0 & 0 & 0 & 0 & 0 & 0 & x_{e_{1_i}} & y_{e_{1_i}} & z_{e_{1_i}} \end{array}\right]^{-1} \begin{bmatrix} 0 \\ 0 \\ 1 \\ \hline 0 \\ 1 \\ 0 \\ \hline 1 \\ 0 \\ 0 \end{bmatrix} \tag{3.33}$$

Aerodynamic influence coefficient matrix calculation

Now that the transformation matrix $\mathcal{T}^P_{aero}$ is known, the Aerodynamic Influence Coefficient matrix (AIC) is calculated. To derive the AIC matrix, unit singularity strengths $\sigma_i = 1$, $\mu_i = 1$ and $\mu_{wake_j} = 1$ are assumed for all configuration and wake-panels. The integrals appearing in equation (3.26) now become a function of the quadri-lateral panel geometry only. The influence of an i-th unit strength source-panel on an arbitrary collocation point k is written as,

$$-\frac{1}{4\pi} \int\limits_{body-panel_i} \sigma \left(\frac{1}{r}\right) dS = -\frac{1}{4\pi} \int\limits_{body-panel_i} \left(\frac{1}{r}\right) dS \equiv B_i \tag{3.34}$$

while the influence of an i-th unit strength doublet-panel on an arbitrary collocation point k is written as,

$$\frac{1}{4\pi} \int\limits_{body-panel_i} \mu\, \underline{n} \cdot \nabla \left(\frac{1}{r}\right) dS = \frac{1}{4\pi} \int\limits_{body-panel_i} \frac{\partial}{\partial n} \left(\frac{1}{r}\right) dS \equiv C_i \tag{3.35}$$

and the influence of a j-th unit strength doublet wake-panel on an arbitrary collocation point k is written as,

$$\frac{1}{4\pi} \int\limits_{wake-panel_j} \mu \, \underline{n} \cdot \nabla \left(\frac{1}{r} \right) dS = \frac{1}{4\pi} \int\limits_{wake-panel_j} \frac{\partial}{\partial n} \left(\frac{1}{r} \right) dS \equiv D_j \tag{3.36}$$

Evaluating the influence of all configuration panels ánd all wake-panels at each configuration's panel collocation point, the equivalent of the Dirichlet boundary condition, equation (3.26), for each internal collocation point is written as,

$$\sum_{i=1}^{N_B} B_i \sigma_i + \sum_{i=1}^{N_B} C_i \mu_i + \sum_{j=1}^{N_W} D_j \mu_{wake_j} = 0 \Bigg|_{\text{collocation point } k} \tag{3.37}$$

or,

$$\sum_{i=1}^{N_B} C_i \mu_i + \sum_{j=1}^{N_W} D_j \mu_{wake_j} = - \sum_{i=1}^{N_B} B_i \sigma_i \Bigg|_{\text{collocation point } k} \tag{3.38}$$

or, for an arbitrary configuration collocation point k,

$$\sum_{i=1}^{N_B} C_{ki} \mu_i + \sum_{j=1}^{N_W} D_{kj} \mu_{wake_j} = - \sum_{i=1}^{N_B} B_{ki} \sigma_i \tag{3.39}$$

with C_{ki} the disturbance velocity potential influence of unit strength doublet configuration panel i on configuration panel collocation point k, D_{kj} the disturbance velocity potential influence of unit strength doublet wake-panel j on configuration panel collocation point k, and B_{ki} the disturbance velocity potential influence of unit strength source configuration panel i on configuration panel collocation point k, respectively.

Wake-panel doublet-strength definition

For the ease of programming, the wake-panels, different from reference [11], are considered as individual panels, also having unit doublet-strength. The wake-panels' doublet-strength, however, is related to the configuration panels' doublet-strength and is dependent of the doublet-strength of the upper and lower wake-shedding panels, see section 3.3.4. The wake-panels' doublet-strength is determined by equation (3.25),

$$\mu_{wake} = \mu_{up} - \mu_{low}$$

or,

$$\mu_{up} - \mu_{low} - \mu_{wake} = 0 \tag{3.40}$$

Aerodynamic influence coefficient matrix definition

Using matrix notation, equation (3.39) is written as,

$$\left[\begin{array}{cccc|cccc} C_{11} & C_{12} & \cdots & C_{1N_B} & D_{11} & D_{12} & \cdots & D_{1N_W} \\ C_{21} & C_{22} & \cdots & C_{2N_B} & D_{21} & D_{22} & \cdots & D_{2N_W} \\ \vdots & \vdots & \ddots & \vdots & \vdots & \vdots & \ddots & \vdots \\ C_{N_B1} & C_{N_B2} & \cdots & C_{N_BN_B} & D_{N_B1} & D_{N_B2} & \cdots & D_{N_BN_W} \\ \hline \multicolumn{4}{c|}{E_{N_W \times N_B}} & \multicolumn{4}{c}{E_{N_W \times N_W}} \end{array}\right] \left[\begin{array}{c} \mu_1 \\ \mu_2 \\ \vdots \\ \mu_{N_B} \\ \hline \mu_{wake_1} \\ \mu_{wake_2} \\ \vdots \\ \mu_{wake_{N_W}} \end{array}\right]$$

$$= - \left[\begin{array}{cccc} B_{11} & B_{12} & \cdots & B_{1N_B} \\ B_{21} & B_{22} & \cdots & B_{2N_B} \\ \vdots & \vdots & \ddots & \vdots \\ B_{N_B1} & B_{N_B2} & \cdots & B_{N_BN_B} \\ \hline \multicolumn{4}{c}{O_{N_W \times N_B}} \end{array}\right] \left[\begin{array}{c} \sigma_1 \\ \sigma_2 \\ \vdots \\ \sigma_{N_B} \\ \hline O_{N_W \times 1} \end{array}\right] \tag{3.41}$$

with both matrices $E_{N_W \times N_B}$ ánd $E_{N_W \times N_W}$ defining the wake-panels' strength related to the configuration panels' doublet-strength similar to equation (3.40). Both matrices $O_{N_W \times N_B}$ and $O_{N_W \times 1}$ are zero matrices of order $N_W \times N_B$ and $N_W \times 1$, respectively. Using the numerical equivalent of equation (3.15),

$$\sigma_k = -\underline{n}_k \cdot \underline{Q}_\infty \tag{3.42}$$

equation (3.41) is written as,

$$[AIC] \left[\begin{array}{c} \underline{\mu} \\ \underline{\mu}_{wake} \end{array}\right] = RHS \tag{3.43}$$

From equation (3.43), both the unknown configuration panels' doublet- strength $\underline{\mu}$,

$$\underline{\mu} = [\mu_1, \mu_2, \cdots, \mu_{N_B}]^T$$

ánd the unknown wake-panels' doublet-strength, $\underline{\mu}_{wake}$,

$$\underline{\mu}_{wake} = [\mu_{wake_1}, \mu_{wake_2}, \cdots, \mu_{wake_{N_W}}]^T$$

are calculated from,

$$\left[\begin{array}{c} \underline{\mu} \\ \underline{\mu}_{wake} \end{array}\right] = \left[AIC^{-1}\right] RHS \tag{3.44}$$

3.3.6 Velocity perturbation calculations

Once the configuration panels' doublet-strength μ_k is known from equation (3.44), the perturbation velocity components, designated as $[q_{l_k}, q_{m_k}, q_{n_k}]^T$ in the frame $\mathcal{F}_P$, are calculated. The local frame $\mathcal{F}_P$ axes (X_P, Y_P, Z_P) are now given as (l, m, n). The two tangential perturbation velocities q_{l_k} and q_{m_k} are obtained by local differentiation in a direction tangential ((l, m) in $\mathcal{F}_P$) to the surface,

$$q_{l_k} = -\frac{\partial \mu_k}{\partial l} \tag{3.45}$$

$$q_{m_k} = -\frac{\partial \mu_k}{\partial m} \tag{3.46}$$

while the normal perturbation velocity becomes q_{n_k},

$$q_{n_k} = \sigma \tag{3.47}$$

Similar to references [11, 12], the local differentiation is performed using local panel coordinates (in $\mathcal{F}_P$), see also figures 3.14 and 3.16. In these figures the local axes of the frame $\mathcal{F}_P$ are denoted as (l, m, n). If for an arbitrary collocation point all neighboring panels *neighbor*1, *neighbor*2, *neighbor*3 and *neighbor*4 are known, a numerical differentiation is performed to calculate both q_{l_k} and q_{m_k}. Instead of a local first order differentiation (as used in references [11, 12]), similar to reference [8, 9] in this thesis first a local second order fit of the known doublet-strengths μ_k is performed. From this second order fit, the local velocity perturbations q_{l_k} and q_{m_k} are calculated.
For example, referring to figure 3.14, for the calculation of q_l (omitting the subscript k for simplicity) the local second order fit along the X_P-axis in $\mathcal{F}_P$ becomes,

$$\mu(s) = a_2 s^2 + a_1 s + a_0 \tag{3.48}$$

with s the local independent variable tangential to the configuration's surface. The local velocity perturbation along the X_P-axis in $\mathcal{F}_P$ becomes,

$$q_l = -\frac{\partial \mu(s)}{\partial s} = -2a_2 s - a_1 \tag{3.49}$$

Referring to figure 3.15, determining q_l for collocation point #2, for the local numerical differentiation the local independent variable s is decomposed in distances s_1, s_2, s_3 and s_4, with s_1 the distance from collocation point #1 to panel #1's side edge, s_2 the distance from panel #1's side edge to collocation point #2, s_3 the distance from collocation point #2 to panel #2's side edge and s_4 the distance from panel #2's side edge to collocation point #3. With the origin located at the collocation point of panel #1, the numerical equivalent of equation (3.48) becomes,

$$\begin{aligned}
\mu_1 &= a_2 0^2 + a_1 0 + a_0 \\
\mu_2 &= a_2 (s_1 + s_2)^2 + a_1 (s_1 + s_2) + a_0 \\
\mu_3 &= a_2 (s_1 + s_2 + s_3 + s_4)^2 + a_1 (s_1 + s_2 + s_3 + s_4) + a_0
\end{aligned}$$

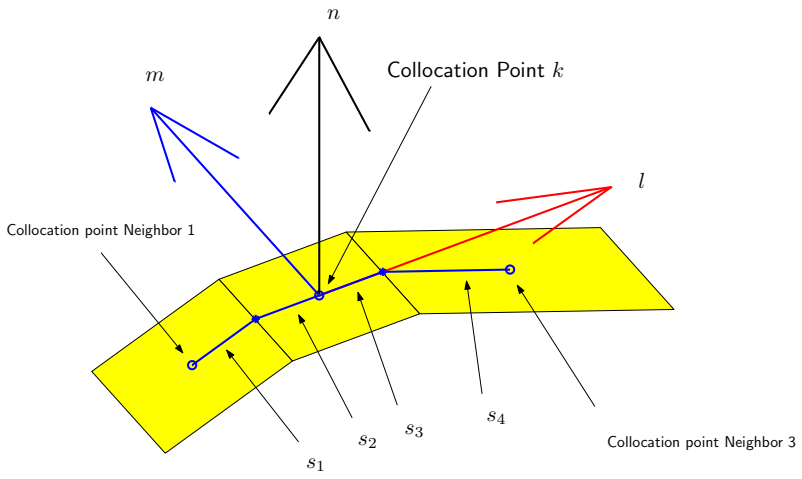


Figure 3.14: The configuration's local Panel Frame of Reference $\mathcal{F}_P$ designated as (l, m, n), including the definition of distances s_1, s_2, s_3 and s_4 for local numerical differentiation (estimation of q_l).

or,

$$\begin{bmatrix} 0 & 0 & 1 \\ (s_1+s_2)^2 & (s_1+s_2) & 1 \\ (s_1+s_2+s_3+s_4)^2 & (s_1+s_2+s_3+s_4) & 1 \end{bmatrix} \begin{bmatrix} a_2 \\ a_1 \\ a_0 \end{bmatrix} = \begin{bmatrix} \mu_1 \\ \mu_2 \\ \mu_3 \end{bmatrix} \tag{3.50}$$

with μ_1, μ_2 and μ_3 the doublet-strengths' of panel #1, #2 and #3, respectively. From equation (3.50) the unknown parameters a_2, a_1 and a_0, are obtained by,

$$\begin{bmatrix} a_2 \\ a_1 \\ a_0 \end{bmatrix} = \begin{bmatrix} 0 & 0 & 1 \\ (s_1+s_2)^2 & (s_1+s_2) & 1 \\ (s_1+s_2+s_3+s_4)^2 & (s_1+s_2+s_3+s_4) & 1 \end{bmatrix}^{-1} \begin{bmatrix} \mu_1 \\ \mu_2 \\ \mu_3 \end{bmatrix} \tag{3.51}$$

Using equation (3.49), the local velocity perturbation q_l in $\mathcal{F}_P$ at the collocation point of interest k is obtained by,

$$q_l = -\left.\frac{\partial \mu(s)}{\partial s}\right|_{\text{collocation point \#2}} = -2a_2(s_1+s_2) - a_1$$

Similar to the derivation of the velocity perturbation q_l in $\mathcal{F}_P$, the velocity perturbation q_m is derived. Should any of the panel's neighbours *neighbor*1, *neighbor*2, *neighbor*3 or *neighbor*4 be unknown, either a left- or right-hand side numerical differentiation (depending on the unknown neighbour panel) is performed using panel neighbours *neighbor*5, *neighbor*6, *neighbor*7 or *neighbor*8, see figure 3.16.

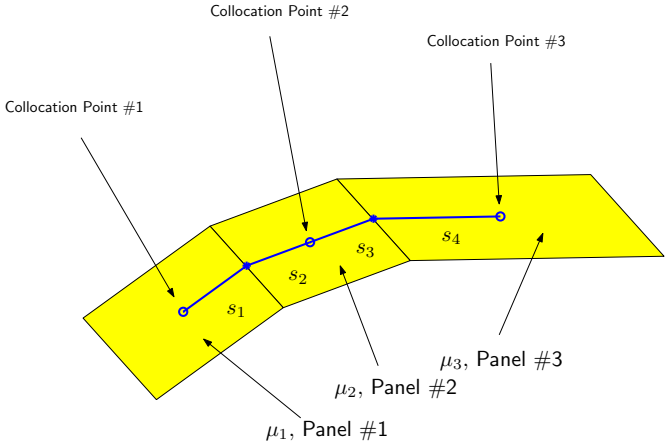


Figure 3.15: The panels' doublet-strength including the definition of distances s_1, s_2, s_3 and s_4 for local numerical differentiation in l (X_P) direction of the local Panel Frame of Reference $\mathcal{F}_P$.

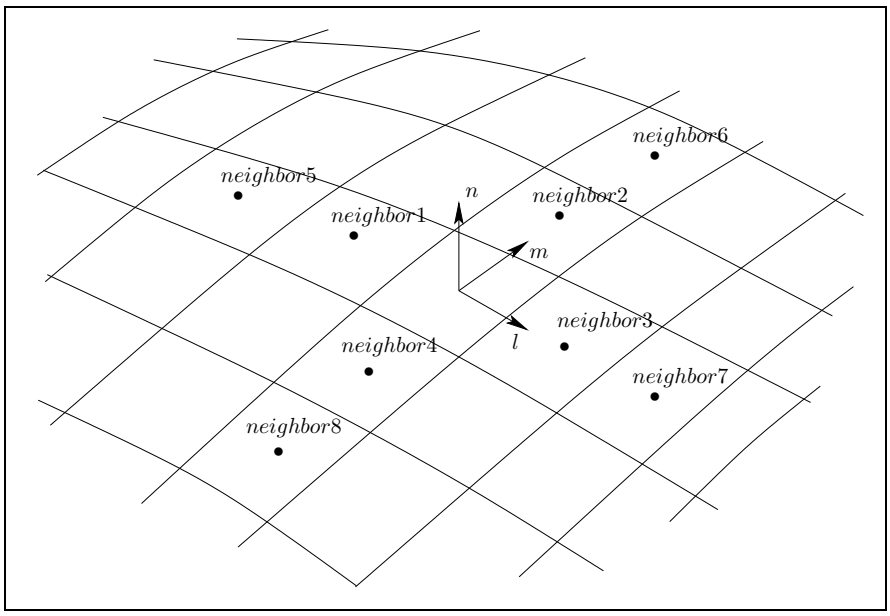


Figure 3.16: Neighbor panel definition for numerical differentiation.

3.3.7 Aerodynamic pressure calculations

The aerodynamic pressure calculations are also performed in the frame $\mathcal{F}_P$. To derive the total local velocity at an arbitrary collocation point k, first the undisturbed velocity at infinity, which is perceived by the configuration's panels', $\underline{Q}_\infty = [U_\infty, V_\infty, W_\infty]^T$, is decomposed in $\mathcal{F}_P$. The decomposition of $\underline{Q}_\infty$ in $\mathcal{F}_P$ is denoted as $[Q_{\infty_l}, Q_{\infty_m}, Q_{\infty_n}]^T$, and it is performed using the transformation from $\mathcal{F}_{aero}$ to $\mathcal{F}_P$ ($\mathcal{T}^P_{aero}$) as mentioned in section 3.3.5,

$$\begin{bmatrix} Q_{\infty_l} \\ Q_{\infty_m} \\ Q_{\infty_n} \end{bmatrix} = \mathcal{T}^P_{aero} \begin{bmatrix} U_\infty \\ V_\infty \\ W_\infty \end{bmatrix}$$

For an arbitrary collocation point k, the total local velocity $\underline{Q}_{local_k}$ in $\mathcal{F}_P$ is calculated by,

$$\underline{Q}_{local_k} = \begin{bmatrix} Q_{\infty_{l_k}} \\ Q_{\infty_{m_k}} \\ Q_{\infty_{n_k}} \end{bmatrix} + \begin{bmatrix} q_{l_k} \\ q_{m_k} \\ q_{n_k} \end{bmatrix} \tag{3.52}$$

The non-dimensional pressure coefficient C_{p_k} for panel k is calculated by (see references [11, 12, 8, 9]),

$$C_{p_k} = 1 - \frac{\left|\underline{Q}_{local_k}\right|^2}{Q^2_\infty} \tag{3.53}$$

with $Q_\infty = \left|\underline{Q}_\infty\right|$. Note that $Q_\infty = \sqrt{U^2_\infty + V^2_\infty + W^2_\infty} = \sqrt{Q^2_{\infty_l} + Q^2_{\infty_m} + Q^2_{\infty_n}}$, since all frames of reference are taken to be unit reference frames.

3.3.8 Aerodynamic loads and aerodynamic coefficients

Once the configuration's non-dimensional pressure coefficient C_{p_k} distribution is known, the aerodynamic forces and moments in the frame $\mathcal{F}_{aero}$ acting on the configuration are calculated. The aerodynamic forces acting on configuration panel k become,

$$\begin{aligned} \Delta F_{x_k} &= -C_{p_k}\, \frac{1}{2}\rho\, Q^2_\infty\, \Delta S_{P_k}\, x_{e_{3_k}} \\ \Delta F_{y_k} &= -C_{p_k}\, \frac{1}{2}\rho\, Q^2_\infty\, \Delta S_{P_k}\, y_{e_{3_k}} \\ \Delta F_{z_k} &= -C_{p_k}\, \frac{1}{2}\rho\, Q^2_\infty\, \Delta S_{P_k}\, z_{e_{3_k}} \end{aligned}$$

with C_{p_k} the panel's non-dimenional pressure coefficient according to equation (3.53), ρ the air's density, $Q_\infty = \left|\underline{Q}_\infty\right|$, ΔS_{P_k} the panel's surface area according to equation (3.20) and $x_{e_{3_k}}$, $y_{e_{3_k}}$, $z_{e_{3_k}}$ the panel's normal components ($\underline{e}_{3_k} = \underline{n}_k = [x_{e_{3_k}}, y_{e_{3_k}}, z_{e_{3_k}}]^T$) in $\mathcal{F}_{aero}$.

Panel k's contribution to the aerodynamic moments with respect to a reference point, which is taken to be $[0,0,0]^T$ in $\mathcal{F}_{aero}$, becomes,

$$\begin{aligned}\Delta M_{x_k} &= \Delta F_{z_k}\ y_{col_k} - \Delta F_{y_k}\ z_{col_k}\\ \Delta M_{y_k} &= \Delta F_{x_k}\ z_{col_k} - \Delta F_{z_k}\ x_{col_k}\\ \Delta M_{z_k} &= \Delta F_{y_k}\ x_{col_k} - \Delta F_{x_k}\ y_{col_k}\end{aligned}$$

with x_{col_k}, y_{col_k} and z_{col_k} the components of collocation point k in $\mathcal{F}_{aero}$.
Both the total aerodynamic forces and moments acting on the configuration are obtained by summation of all the configuration panels' contribution to them,

$$F_x = \sum_{k=1}^{N_B} F_{x_k} \qquad F_y = \sum_{k=1}^{N_B} F_{y_k} \qquad F_z = \sum_{k=1}^{N_B} F_{z_k}$$

and,

$$M_x = \sum_{k=1}^{N_B} M_{x_k} \qquad M_y = \sum_{k=1}^{N_B} M_{y_k} \qquad M_z = \sum_{k=1}^{N_B} M_{z_k}$$

Finally, the non-dimensional aerodynamic force and moment coefficients in $\mathcal{F}_{aero}$ become,

$$C_X = \frac{F_x}{\frac{1}{2}\rho\ Q_\infty^2\ S_{ref}} \qquad C_Y = \frac{F_y}{\frac{1}{2}\rho\ Q_\infty^2\ S_{ref}} \qquad C_Z = \frac{F_z}{\frac{1}{2}\rho\ Q_\infty^2\ S_{ref}}$$

and,

$$C_\ell = \frac{M_x}{\frac{1}{2}\rho\ Q_\infty^2\ S_{ref}\ b_{ref}} \qquad C_m = \frac{M_y}{\frac{1}{2}\rho\ Q_\infty^2\ S_{ref}\ c_{ref}} \qquad C_n = \frac{M_z}{\frac{1}{2}\rho\ Q_\infty^2\ S_{ref}\ b_{ref}}$$

with b_{ref} and c_{ref} taken to be the configuration's span and mean aerodynamic chord, respectively.

3.4 Remarks

In chapter 4 the steady Linearized Potential Flow model is extended to allow the calculation of both unsteady aerodynamic forces and moments due to arbitrary aircraft motion. Also, it will allow the calculation of both unsteady aerodynamic forces and moments to 1D and 2D atmospheric turbulence fields.

Chapter 4

Unsteady linearized potential flow simulations

4.1 Introduction

As a continuation of chapter 3, in this chapter the steady Linearized Potential Flow (LPF) method is extended to the unsteady LPF method. The motivation for this extension is that it allows the time-domain simulation of aircraft responses in terms of aerodynamic forces and moments caused by aircraft motions and atmospheric gusts. From the time-dependent aircraft responses, and the prescribed aircraft motions and gust inputs, parametric aerodynamic models are obtained, the goal of this thesis.

First a brief overview of analytical unsteady aerodynamic theory is given. The theory will discuss an aerofoil's lift due to heaving motions. Also, it will discuss the lift due to both longitudinal ánd vertical atmospheric turbulence gusts.
Second, the theory of the used unsteady LPF model will be discussed. It is an extension of the steady LPF model given in chapter 3, and it will allow the calculation of time-domain unsteady aerodynamic forces and moments due to aircraft motions, as well as those due to atmospheric gust fields.
Finally, the unsteady LPF method will be verified by analytical unsteady aerodynamic results obtained by Theodorsen, Sears and Horlock, see references [24, 22, 14], respectively. A comparison between time-domain unsteady LPF results and time-domain analytical results by R.T. Jones, see references [16, 17], will also be made.

4.2 Analytical unsteady aerodynamics

4.2.1 Introduction

In this section a short summary of the theory of analytical unsteady aerodynamics is given and well-known functions, such as Theodorsen's function $C(k)$ and Sears' function $S(k)$

will be briefly discussed, see references [24, 22]. These functions, dependent of the reduced frequency $k = \frac{\omega \bar{c}}{2Q_\infty}$, describe the dynamics of an aerofoil's aerodynamic lift caused by heaving motions and vertical gusts, respectively.
Less known in the area of flight-dynamics, Horlock's function $T(k)$ will be briefly discussed as well, see reference [14]. Similar to the Sears function, this function describes the dynamics of an aerofoil's aerodynamic lift as a function of horizontal gust inputs. Similar to Theodorsen's and Sears' function, Horlock's function is also dependent of the reduced frequency k.

4.2.2 The Theodorsen function

For wings with an infinite aspect-ratio, Theodorsen introduced the lift deficiency function $C(k)$, see reference [24]. It describes the dynamics of an aerofoil's aerodynamic lift due to both harmonic angle-of-attack perturbations (or plunging motion, see figure 4.1) and pitching motions, as a function of the reduced frequency $k = \frac{\omega \bar{c}}{2Q_\infty}$. The unsteady lift holds for inviscid, incompressible, irrotational flow only. Furthermore, the function holds for aerofoils of zero-thickness only.
Consider, as an example, harmonic plunging motions only. The unsteady aerodynamic lift L of an aerofoil due to harmonically varying heaving motions with amplitude h is written as, see references [24, 31],

$$L = \pi\ \rho\ \left\{\frac{\bar{c}}{2}\right\}^2 \left\{\ddot{h}\right\}\ +\ 2\ \pi\rho\ Q_\infty\ \frac{\bar{c}}{2}\ C(k) \left\{\dot{h}\right\} \tag{4.1}$$

with ρ air density, $\bar{c}$ the (mean) aerodynamic chord, h vertical translation distance, $C(k)$ Theodorsen's lift deficiency function, Q_∞ airspeed and k the reduced frequency.
Considering harmonic plunging motions only, that is $h = h_0\ e^{j\omega t}$, and defining $\alpha = \frac{\dot{h}}{Q_\infty}$, $\dot{\alpha} = \frac{\ddot{h}}{Q_\infty}$ and the non-dimensional aerodynamic lift-coefficient $C_l = \frac{L}{\frac{1}{2}\rho\ Q_\infty^2\ \bar{c}}$, equation (4.1) becomes,

$$C_l = \pi\ \frac{\dot{\alpha}\bar{c}}{2Q_\infty}\ +\ 2\pi\ C(k)\ \alpha \tag{4.2}$$

Writing Theodorsen's function as the combination of its real and imaginary parts, $C(k) = F(k)\ +\ j\ G(k)$, equation (4.2) becomes, also see reference [5],

$$\begin{aligned} C_l &= 2\pi F(k)\ \alpha\ +\ \left\{2\pi\frac{G(k)}{k} + \pi\right\}\frac{\dot{\alpha}\bar{c}}{2Q_\infty} = \\ &= 2\pi\left\{F(k)\ \alpha\ +\ \frac{G(k)}{k}\frac{\dot{\alpha}\bar{c}}{2Q_\infty}\right\} + \pi\frac{\dot{\alpha}\bar{c}}{2Q_\infty} = \\ &= C_{l_1}\ +\ C_{l_2} \end{aligned}$$

The lift-coefficient C_{l_2} is usually referred to as the "additional mass effect" and acts at the semi-chord point of the aerofoil. The lift-coefficient C_{l_1} is associated with the circulation around the aerofoil and acts at the $\frac{1}{4}$ chord point. In terms of stability parameters, the lift-coefficient is also often given as, see reference [5],

$$C_l = 2\pi F(k)\ \alpha\ +\ \left\{2\pi\frac{G(k)}{k} + \pi\right\}\frac{\dot{\alpha}\bar{c}}{2Q_\infty} = C_{l_\alpha}\ \alpha\ +\ C_{l_{\dot{\alpha}}}\ \frac{\dot{\alpha}\bar{c}}{2Q_\infty} \tag{4.3}$$

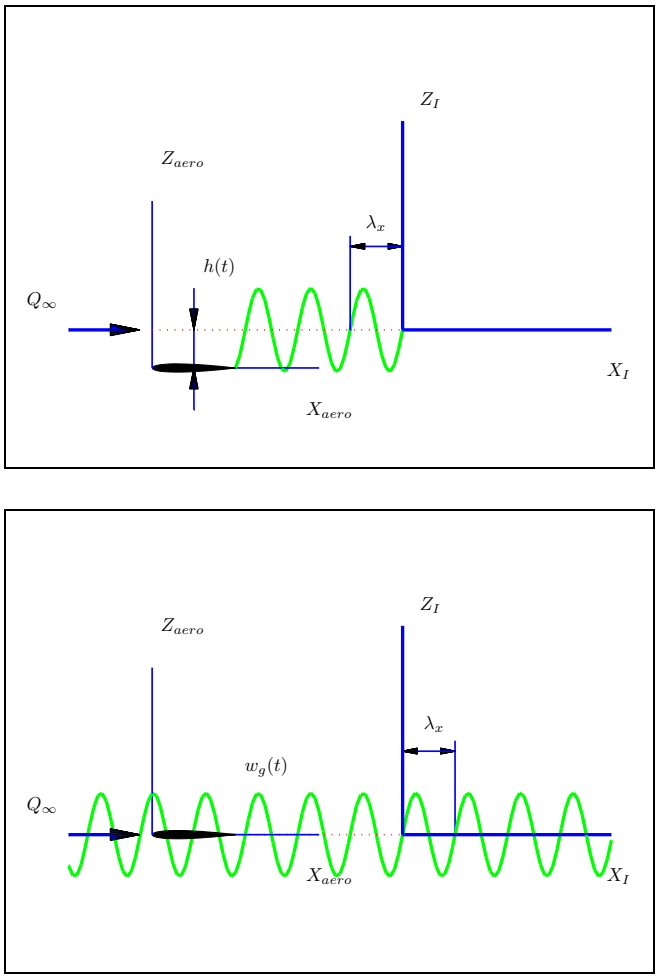


Figure 4.1: An aerofoil during a harmonically varying plunging motion, $h(t)$, in the Inertial Frame of Reference $\mathcal{F}_I$ (top), and an aerofoil encountering a harmonically varying vertical gust, $w_g(t)$, in the frame $\mathcal{F}_I$ (bottom). The aerofoil itself is decribed in the Aerodynamic Frame of Reference $\mathcal{F}_{aero}$.

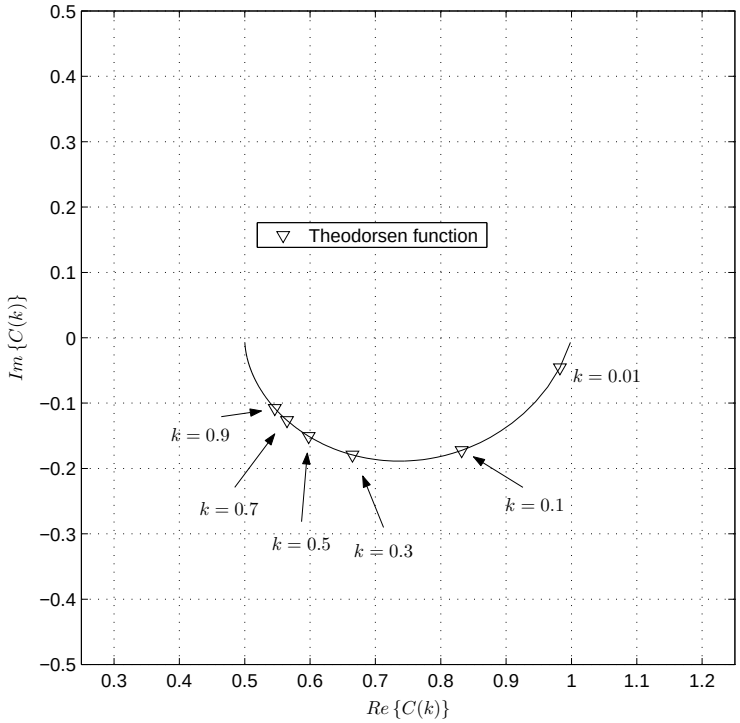
The aerodynamic derivatives C_{l_α} and $C_{l_{\dot\alpha}}$ in equation (4.3) are frequency-dependent and they are defined as,

$$\begin{aligned} C_{l_\alpha} &= 2\pi\, F(k) \\ C_{l_{\dot\alpha}} &= 2\pi \frac{G(k)}{k} + \pi \end{aligned}$$

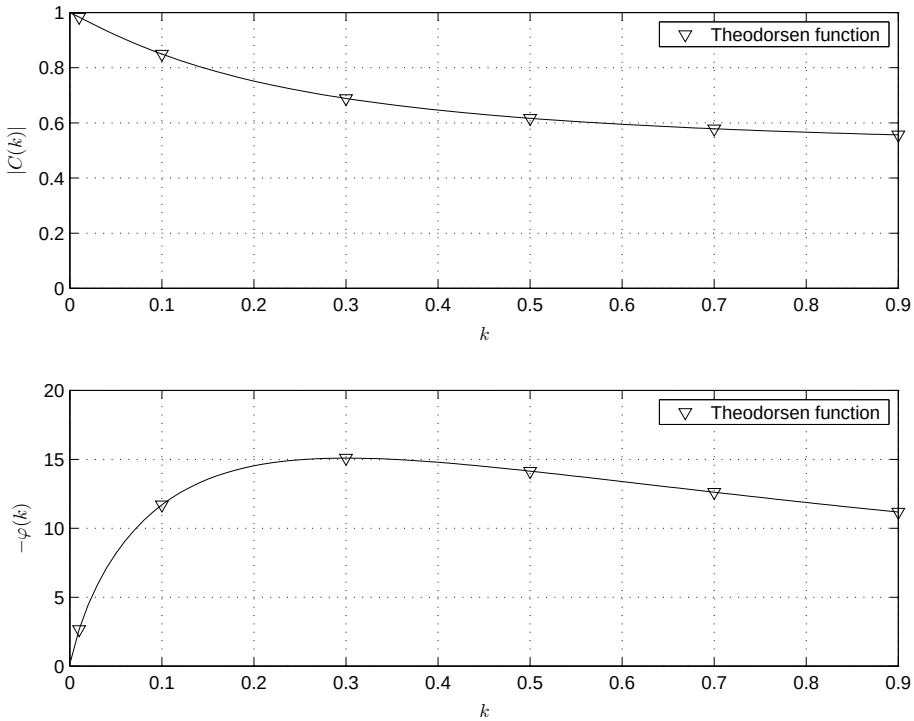
Theodorsen's function, $C(k)$, is tabulated in table 4.1, and also given in figures 4.2.

4.2.3 The Sears function

For infinite aspect-ratio wings a lift deficiency function $S(k)$ was introduced by Sears, see reference [22]. It describes the dynamics of the aerodynamic lift of an aerofoil of zero-thickness due to harmonically varying vertical gusts (see figure 4.1), as a function of the reduced frequency $k = \frac{\omega \bar{c}}{2Q_\infty}$. The gust field is given in the frame $\mathcal{F}_I$, through which the aerofoil is traveling along the negative X_I-axis. As a function of time the position of the



(a) Theodorsen's function



(b) Magnitude and (minus) phase of Theodorsen's function

Figure 4.2: Theodorsen's function $C(k)$ (top) and both its magnitude $|C(k)|$ ánd (minus) phase $-\varphi$ (bottom).

k	$C(k)$	$\|C(k)\|$	φ [Deg.]
1.0000e-002	9.8242e-001 -j4.5652e-002	9.8348e-001	-2.6606e+000
1.0000e-001	8.3192e-001 -j1.7230e-001	8.4958e-001	-1.1701e+001
3.0000e-001	6.6497e-001 -j1.7932e-001	6.8872e-001	-1.5092e+001
5.0000e-001	5.9794e-001 -j1.5071e-001	6.1664e-001	-1.4147e+001
7.0000e-001	5.6476e-001 -j1.2642e-001	5.7874e-001	-1.2617e+001
9.0000e-001	5.4593e-001 -j1.0785e-001	5.5648e-001	-1.1175e+001

Table 4.1: Theodorsen's function $C(k)$ including its magnitude $|C(k)|$ and phase φ as a function of the reduced frequency $k = \frac{\omega c}{2Q_\infty}$.

aerofoil changes, although the gust field remains frozen in terms of both magnitude and position. Noted that, contrary to heaving motions, the vertical gust is allowed to vary over the aerofoil's chord.
The aerodynamic lift of an aerofoil in inviscid, incompressible, irrotational flow due to a harmonically varying vertical gust w_g, is written as, see reference [31],

$$L_g \; = 2\pi \; \rho \, Q_\infty \; \frac{\bar{c}}{2} \; S(k) \; \{w_g\} \tag{4.4}$$

with ρ air density, $\bar{c}$ the (mean) aerodynamic chord, w_g the harmonically varying vertical gust velocity, $S(k)$ Sears' function, and k the reduced frequency.
Defining $\alpha_g = \frac{w_g}{Q_\infty}$ and the non-dimensional aerodynamic lift-coefficient, $C_{l_g} = \frac{L_g}{\frac{1}{2}\rho \, Q_\infty^2 \, \bar{c}}$, equation (4.4) becomes,

$$C_{l_g} = 2\pi \; S(k) \; \alpha_g \tag{4.5}$$

Writing Sears' function as the combination of its real and imaginary parts, using the notation as in reference [31], $S(k) = F_G(k) \; + \; j \; G_G(k)$, equation (4.5) is written as,

$$C_{l_g} = 2\pi F_G(k) \; \alpha_g \; + \; 2\pi \frac{G_G(k)}{k} \frac{\dot{\alpha}_g \bar{c}}{2Q_\infty} \tag{4.6}$$

Since in Sears' analysis the aerofoil is not in motion, there is no "additional mass effect" and the aerodynamic forces and moments are only due to circulation around the aerofoil. Also, the aerodynamic lift always acts at the $\frac{1}{4}$ chord point. In terms of stability parameters, the lift-coefficient is also often given as, see reference [5],

$$C_{l_g} = 2\pi F_G(k) \; \alpha_g \; + \; 2\pi \frac{G_G(k)}{k} \frac{\dot{\alpha}_g \bar{c}}{2Q_\infty} = C_{l_{\alpha_g}} \; \alpha_g \; + \; C_{l_{\dot{\alpha}_g}} \frac{\dot{\alpha}_g \bar{c}}{2Q_\infty} \tag{4.7}$$

The stability parameters $C_{l_{\alpha_g}}$ and $C_{l_{\dot{\alpha}_g}}$ in equation (4.7) are frequency-dependent and are defined as,

$$\begin{aligned} C_{l_{\alpha_g}} &= 2\pi \; F_G(k) \\ C_{l_{\dot{\alpha}_g}} &= 2\pi \frac{G_G(k)}{k} \end{aligned}$$

k	$S(k)$	$\|S(k)\|$	φ [Deg.]
1.0000e-002	9.8217e-001 -j4.5563e-002	9.8322e-001	-2.6561e+000
1.0000e-001	8.2124e-001 -j1.6348e-001	8.3735e-001	-1.1258e+001
3.0000e-001	6.2350e-001 -j1.2562e-001	6.3602e-001	-1.1391e+001
5.0000e-001	5.2463e-001 -j4.4029e-002	5.2648e-001	-4.7972e+000
7.0000e-001	4.5608e-001 +j3.1792e-002	4.5718e-001	3.9875e+000
9.0000e-001	3.9707e-001 +j9.7239e-002	4.0880e-001	1.3760e+001

Table 4.2: Sears' function $S(k)$ including its magnitude $|S(k)|$ and phase φ as a function of the reduced frequency $k = \frac{\omega c}{2Q_\infty}$.

k	$S_{mod}(k)$	$\|S_{mod}(k)\|$	φ [Deg.]
1.0000e-002	9.8166e-001 -j5.5382e-002	9.8322e-001	-3.2290e+000
1.0000e-001	8.0082e-001 -j2.4465e-001	8.3735e-001	-1.6988e+001
3.0000e-001	5.5853e-001 -j3.0426e-001	6.3602e-001	-2.8580e+001
5.0000e-001	4.3930e-001 -j2.9016e-001	5.2648e-001	-3.3445e+001
7.0000e-001	3.6931e-001 -j2.6950e-001	4.5718e-001	-3.6120e+001
9.0000e-001	3.2299e-001 -j2.5059e-001	4.0880e-001	-3.7806e+001

Table 4.3: The Modified Sears function $S_{mod}(k)$ including its magnitude $|S_{mod}(k)|$ and phase φ as a function of the reduced frequency $k = \frac{\omega c}{2Q_\infty}$ ($\Delta x = -\frac{c}{2}$).

Contrary to the case where harmonic plunging motions were considered (Theodorsen), the position of the center of gravity, or the choice of the coordinate system (in this case the Aerodynamic Frame of Reference $\mathcal{F}_{aero}$), is extremely important when considering atmospheric turbulence. Note that Sears' function only holds for the origin located at the semi-chord point. This origin is the point which prescribes a gust to phase-lead or phase-lag in distance from it (and has zero phase-shift at the origin). If the origin is chosen to differ from the semi-chord point, Sears' function is multiplied by $e^{jk\frac{2x_0}{c}}$, resulting in the so-called Modified Sears function $S_{mod}(k)$, see reference [13],

$$S_{mod}(k) = S(k)\, e^{jk\frac{2x_0}{c}}$$

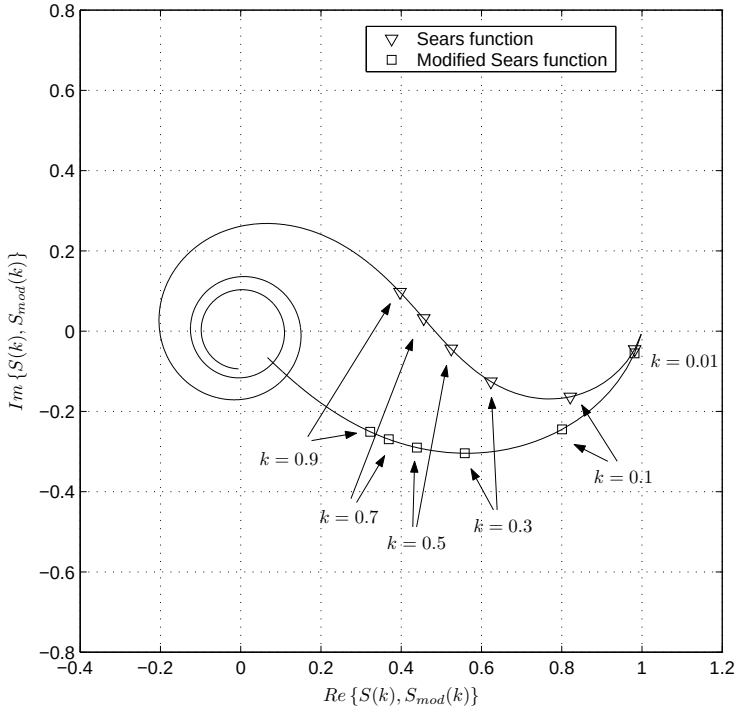
with x_0 the origin's location positive downstream. For the origin located at the aerofoil's leading-edge, x_0 becomes $x_0 = -\frac{\bar{c}}{2}$, and the Modified Sears function is written as,

$$S_{mod}(k) = S(k)\, e^{-jk} \tag{4.8}$$

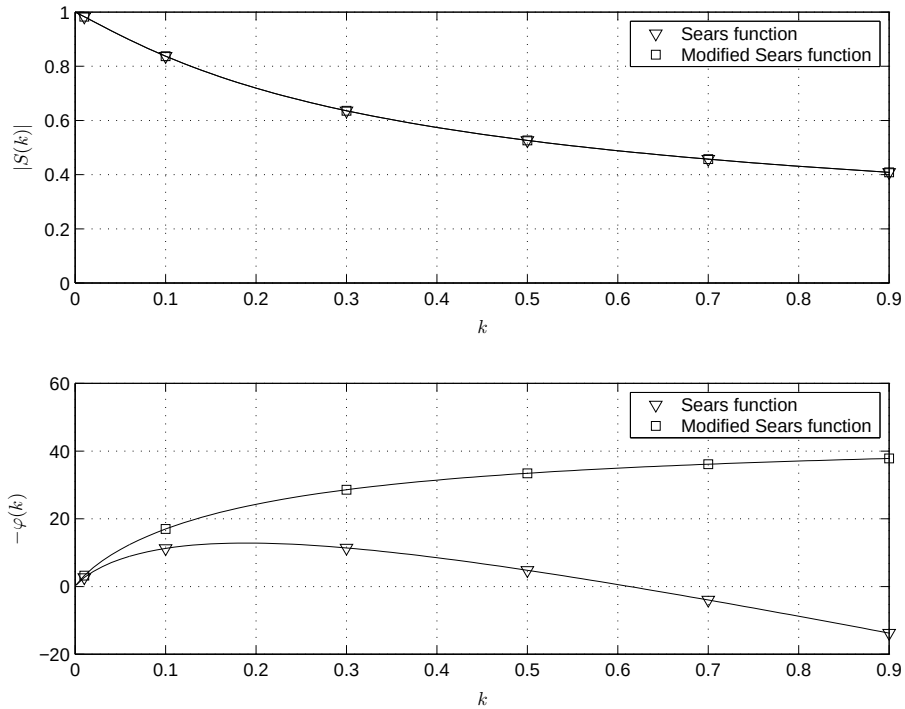
Both the Sears function $S(k)$ ánd the Modified Sears function $S_{mod}(k)$ are tabulated in tables 4.2 and 4.3, respectively. The functions are also shown in figures 4.3.

4.2.4 The Horlock function

Similar to the analysis by Sears, see reference [22], for infinite aspect-ratio wings a lift deficiency function $T(k)$ was introduced by Horlock, see reference [14]. This function



(a) Sears' function and the Modified Sears function



(b) Magnitude and (minus) phase of both Sears' function and the Modified Sears function

Figure 4.3: Sears' function $S(k)$ and the Modified Sears function $S_{mod}(k)$ ($\Delta x = -\frac{c}{2}$), (top), and both its magnitude $|S(k)|$, $|S_{mod}(k)|$ ánd (minus) phase $-\varphi$ (bottom).

describes the dynamics of the aerodynamic lift of an aerofoil of zero-thickness due to harmonically varying horizontal gusts, also as a function of reduced frequency $k = \frac{\omega \bar{c}}{2Q_\infty}$. In figure 4.4, a (finite-thickness) aerofoil is depicted encountering harmonically varying horizontal gusts u_g, with spatial wave-length λ_x. Contrary to figures 4.1, the frame $\mathcal{F}_I$ is not given in figure 4.4, however, similar to figures 4.1 the origin of $\mathcal{F}_{aero}$ is assumed to travel along the negative X_I-axis. Similar to Sears' analysis, the gust field is given in the frame $\mathcal{F}_I$, and as a function of time it remains frozen in terms of both magnitude and position. Note here that, contrary to surging motions, the horizontal gust is allowed to vary over the aerofoil's chord.
The lift of an aerofoil in inviscid, incompressible, irrotational flow due to a harmonically varying horizontal gust is written as,

$$L_g = 2\pi\ \rho\ Q_\infty\ \alpha\ \frac{\bar{c}}{2}\ T(k)\ \{u_g\} \tag{4.9}$$

with α the aerofoil's angle-of-attack, ρ air density, $\bar{c}$ the (mean) aerodynamic chord, u_g the harmonically varying horizontal gust velocity, $T(k)$ Horlock's function, and k the reduced frequency. Although no characteristic length is mentioned in reference [14], for an analogy with the analysis of Sears the term $\frac{\bar{c}}{2}$ was added in equation (4.9).
Defining $\hat{u}_g = \frac{u_g}{Q_\infty}$ and the non-dimensional aerodynamic lift-coefficient $C_{l_g} = \frac{L_g}{\frac{1}{2}\rho\ Q_\infty^2\ \bar{c}}$, equation (4.9) becomes,

$$C_{l_g} = 2\pi\ \alpha\ T(k)\ \hat{u}_g \tag{4.10}$$

Writing Horlock's function as the combination of its real and imaginary parts, $T(k) = X_G(k)\ +\ j\ Y_G(k)$, equation (4.10) is written as,

$$C_{l_g} = 2\pi\alpha\ X_G(k)\ \hat{u}_g\ +\ 2\pi\alpha\ \frac{Y_G(k)}{k}\frac{\dot{\hat{u}}_g \bar{c}}{2Q_\infty} \tag{4.11}$$

In terms of stability parameters, the lift-coefficient may also be written as,

$$C_{l_g} = 2\pi\alpha\ X_G(k)\ \hat{u}_g\ +\ 2\pi\alpha\ \frac{Y_G(k)}{k}\frac{\dot{\hat{u}}_g \bar{c}}{2Q_\infty} = C_{l_{\hat{u}_g}}\ \hat{u}_g\ +\ C_{l_{\dot{\hat{u}}_g}}\frac{\dot{\hat{u}}_g \bar{c}}{2Q_\infty} \tag{4.12}$$

The stability parameters $C_{l_{\hat{u}_g}}$ and $C_{l_{\dot{\hat{u}}_g}}$ in equation (4.12) are frequency-dependent and are defined as,

$$\begin{aligned} C_{l_{\hat{u}_g}} &= 2\pi\alpha\ X_G(k) \\ C_{l_{\dot{\hat{u}}_g}} &= 2\pi\alpha\ \frac{Y_G(k)}{k} \end{aligned}$$

Similar to Sears' analysis, the position of the center of gravity, or the choice of the coordinate system (in this case the frame $\mathcal{F}_{aero}$), is again extremely important when considering atmospheric turbulence. Horlock's function only holds for the origin located at the aerofoil's semi-chord point. If the origin is chosen to differ from the semi-chord point, Horlock's function is multiplied by $e^{jk\frac{2x_0}{\bar{c}}}$, resulting in the so-called Modified Horlock function $T_{mod}(k)$,

$$T_{mod}(k) = T(k)\ e^{jk\frac{2x_0}{\bar{c}}}$$

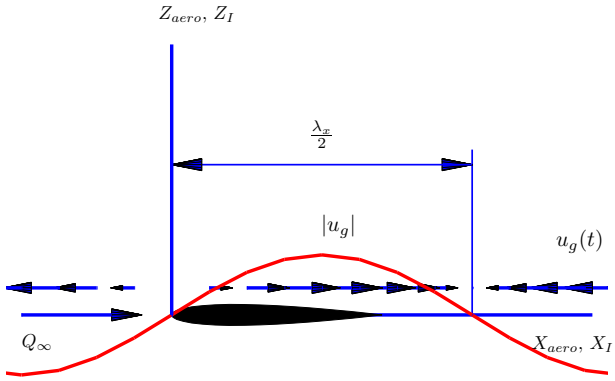


Figure 4.4: An aerofoil encountering a harmonically varying horizontal gust $u_g(t)$ for the initial condition when $\mathcal{F}_{aero}$ and $\mathcal{F}_I$ coincide. The aerofoil itself is decribed in the Aerodynamic Frame of Reference $\mathcal{F}_{aero}$.

k	$T(k)$	$\|T(k)\|$	φ [Deg.]
1.0000e-002	1.9821e+000 -j4.0563e-002	1.9826e+000	-1.1724e+000
1.0000e-001	1.8187e+000 -j1.1354e-001	1.8223e+000	-3.5722e+000
3.0000e-001	1.6011e+000 +j2.2703e-002	1.6013e+000	8.1236e-001
5.0000e-001	1.4631e+000 +j1.9824e-001	1.4765e+000	7.7162e+000
7.0000e-001	1.3373e+000 +j3.6079e-001	1.3851e+000	1.5099e+001
9.0000e-001	1.2046e+000 +j5.0319e-001	1.3055e+000	2.2672e+001

Table 4.4: Horlock's function $T(k)$ including its magnitude $|T(k)|$ and phase φ as a function of the reduced frequency $k = \frac{\omega c}{2Q_\infty}$.

with x_0 the origin's location positive downstream. For the origin located at the aerofoil's leading-edge, x_0 becomes $x_0 = -\frac{\bar{c}}{2}$, and the Modified Horlock function is written as,

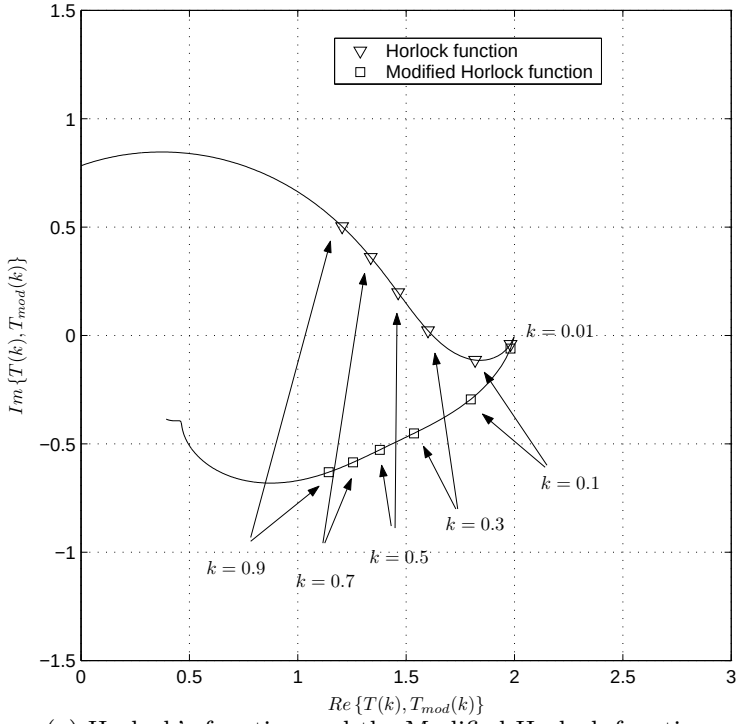
$$T_{mod}(k) = T(k)\, e^{-jk} \tag{4.13}$$

Both Horlock's function $T(k)$ ánd the Modified Horlock function $T_{mod}(k)$, are tabulated in tables 4.4 and 4.5, respectively. The functions are also shown in figures 4.5.

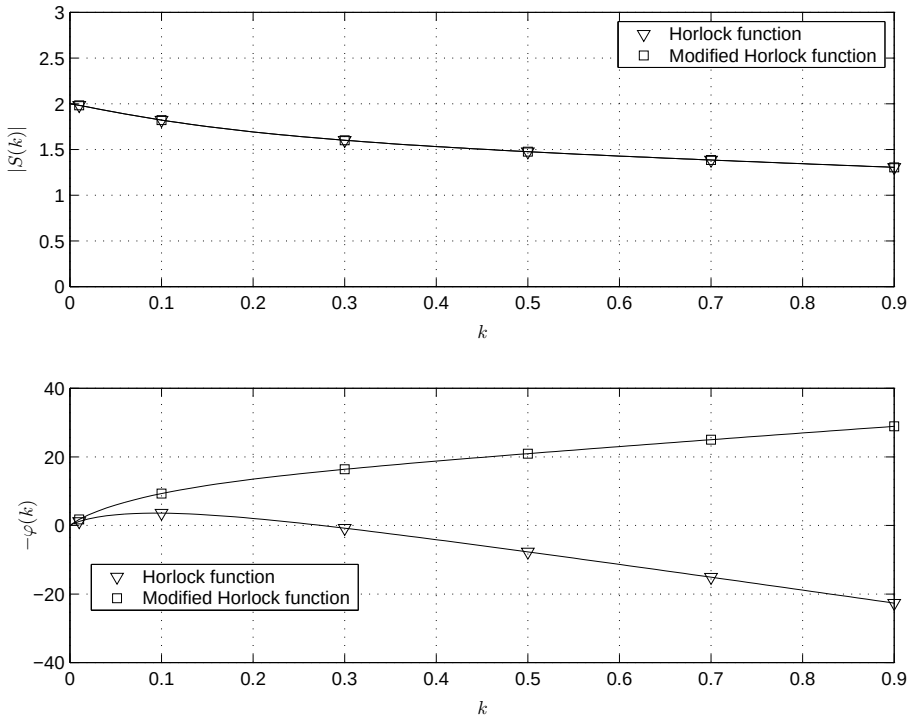
4.2.5 The Wagner function

Contrary to the harmonic analysis of Theodorsen, see reference [24], for the time-domain a non-dimensional indicial function for the aerodynamic lift due to a step-wise increase in angle-of-attack has been given by Wagner, see reference [26]. In figure 4.6, an example is given for an aerofoil of zero-thickness during a step-wise change in angle-of-attack. Similar to Theodorsen's function, Wagner's function also holds for inviscid, incompressible, irrotational flow.

Wagner's function is written as $\Phi(s)$, with s non-dimensional time in terms of semi-chord distance traveled by the aerofoil, $s = \frac{2Q_\infty t}{c}$, and Q_∞ the undisturbed velocity at infinity, t



(a) Horlock's function and the Modified Horlock function



(b) Magnitude and (minus) phase of both Horlock's function and the Modified Horlock function

Figure 4.5: Horlock's function $T(k)$ and the Modified Horlock function $T_{mod}(k)$ ($\Delta x = -\frac{c}{2}$), (top), and both its magnitude $|T(k)|$, $|T_{mod}(k)|$ and (minus) phase $-\varphi$ (bottom).

k	$T_{mod}(k)$	$\|T_{mod}(k)\|$	φ [Deg.]
1.0000e-002	1.9816e+000 -j6.0382e-002	1.9826e+000	-1.7453e+000
1.0000e-001	1.7983e+000 -j2.9454e-001	1.8223e+000	-9.3018e+000
3.0000e-001	1.5363e+000 -j4.5148e-001	1.6013e+000	-1.6376e+001
5.0000e-001	1.3790e+000 -j5.2748e-001	1.4765e+000	-2.0932e+001
7.0000e-001	1.2552e+000 -j5.8555e-001	1.3851e+000	-2.5009e+001
9.0000e-001	1.1429e+000 -j6.3080e-001	1.3055e+000	-2.8895e+001

Table 4.5: The Modified Horlock function $T_{mod}(k)$ including its magnitude $|T_{mod}(k)|$ and phase φ as a function of the reduced frequency $k = \frac{\omega c}{2Q_\infty}$ ($\Delta x = -\frac{c}{2}$).

time and c the aerodynamic chord of the aerofoil. The non-dimensional lift-coefficient, C_l, of a zero-thickness aerofoil subjected to a step-wise change in angle-of-attack, is written as, see reference [21],

$$C_l(s) = \frac{\pi c}{2Q_\infty}\delta(s) + 2\pi\ \alpha\ \Phi(s) \tag{4.14}$$

with $C_l(s)$ the aerofoil's non-dimensional lift-coefficient, $\delta(s)$ Dirac's delta function, α the magnitude of the step-wise change in angle-of-attack, $\Phi(s)$ Wagner's function, s the semi-chord distance traveled by the aerofoil $s = \frac{2Q_\infty t}{c}$, and 2π the steady-state lift-curve slope for a zero-thickness aerofoil. The term including Dirac's delta function in equation (4.14) represents the "additional mass effect", also described by Theodorsen, see reference [24]. Although known exactly, Wagner's function is not provided in a closed analytical form. The approximation by R.T. Jones, see references [16, 17], is often referred to in the literature. This approximation of Wagner's function, $\Phi(s)$, is written as a series of exponentials,

$$\Phi(s) \approx 1 + \sum_{k=1}^{N} B_k e^{-\beta_k s} \tag{4.15}$$

or, for R.T. Jones' approximation of Wagner's function,

$$\Phi(s) \approx 1 - 0.165e^{-0.0455s} - 0.335e^{-0.3s} \tag{4.16}$$

Noted that this approximation of Wagner's function does not include the "additional mass effect" as described by Theodorsen, see reference [24], and it only includes the circulatory lift. R.T. Jones' approximation of Wagner's function is shown in figure 4.7.

For an analysis in the frequency-domain, Wagner's function may be transformed to it. Similar to Theodorsen's function, a Fourier analysis of Jones' approximation of Wagner's function ultimately results in a frequency-response function which holds for arbitrary sinusoidal angle-of-attack motions. Whereas the Jones approximation of Wagner's function only holds for a step-wise change in angle-of-attack, the transformed Jones function can be written in terms of a frequency-response similar to Theodorsen's function.
For example, equation (4.15), which holds for a step-wise change in angle-of-attack, is

transformed to the (non-dimensional) frequency-domain for sinusoidal inputs. As a function of reduced frequency, $k = \frac{\omega \bar{c}}{2Q_\infty}$, the Jones' approximation in terms of frequency-response, is written as a series of lag-functions,

$$\Phi(k) \approx 1 + \sum_{k=1}^{N} B_k \frac{jk}{jk + \beta_k} \tag{4.17}$$

or, specifically for R.T. Jones' approximation of Wagner's function,

$$\Phi(k) \approx 1 - 0.165 \, \frac{jk}{jk + 0.0455} - 0.335 \, \frac{jk}{jk + 0.3} \tag{4.18}$$

The frequency-response function as given in equation (4.18) only includes the effect of circulatory lift. Both Theodorsen's function $C(k)$ ánd Jones' approximation of it $\Phi(k)$ are shown in figure 4.8.

4.2.6 The Küssner function

Similar to the analysis of Wagner's function, and contrary to the harmonic analysis of Sears, see reference [22], for the time-domain a non-dimensional indicial function for the aerodynamic lift due to a sharp-edged penetrating vertical gust has been given by Küssner, see reference [20]. In figure 4.6, an example is given for an aerofoil of zero-thickness encountering a sharp-edged vertical gust-front. Note that the origin of the frame $\mathcal{F}_{aero}$ is located at the leading-edge of aerofoil. Similar to Sears' function, Küssner's function also holds for inviscid, incompressible, irrotational flow only.

Küssner's function is written as $\Psi(s)$, with s non-dimensional time in terms of semi-chord distance traveled by the aerofoil $s = \frac{2Q_\infty t}{c}$ and Q_∞ the undisturbed velocity at infinity, t time and c the aerodynamic chord of the aerofoil. The non-dimensional lift-coefficient C_l of a zero-thickness aerofoil encountering a vertical gust front, is written as, see reference [21],

$$C_l(s) = 2\pi \; \alpha_g \; \Psi(s) \tag{4.19}$$

with $\alpha_g = \frac{w_g}{Q_\infty}$ the magnitude of the vertical gust-induced change in angle-of-attack, w_g the vertical gust component, s the semi-chord distance traveled by the aerofoil and 2π the steady-state lift-curve slope for a zero-thickness aerofoil. Note that, contrary to the Theodorsen/Wagner analysis, in this case of atmospheric turbulence responses no "additional mass effect" is present in equation (4.19).
Similar to Wagner's function, Küssner's function is known exactly, albeit not in a closed analytical form. An approximation of Küssner's function is given by Sears and Sparks, see reference [23]. Similar to Jones' approximation of Wagner's function, this approximation of Küssner's function, $\Psi(s)$, is written as a series of exponentials similar to equation (4.15). Sears' approximation of Küssner's function is written as,

$$\Psi(s) \approx 1 - 0.5e^{-0.13s} - 0.5e^{-1.0s} \tag{4.20}$$

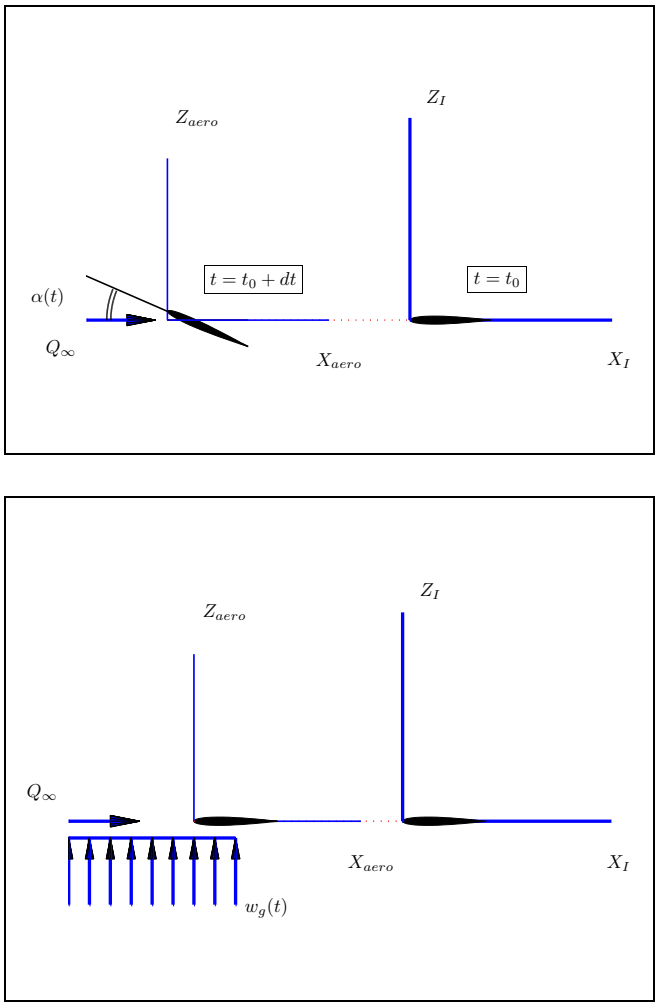


Figure 4.6: An aerofoil during a step change in angle-of-attack $\alpha(t)$ in the Inertial Frame of Reference $\mathcal{F}_I$ (top), and an aerofoil encountering a sharp-edged vertical gust $w_g(t)$, also in the frame $\mathcal{F}_I$ (bottom). The aerofoil is decribed in the Aerodynamic Frame of Reference $\mathcal{F}_{aero}$.

Sears' approximation of Küssner's function is shown in figure 4.7.
Similar to the frequency-domain results of Jones' function, a frequency-response function of the Sears approximation of Küssner's function can be obtained. As a function of reduced frequency $k = \frac{\omega \bar{c}}{2Q_\infty}$ the Sears approximation in terms of frequency-response, becomes,

$$\Psi(k) \approx 1 - 0.5\,\frac{jk}{jk + 0.13} - 0.5\,\frac{jk}{jk + 1.0} \tag{4.21}$$

The frequency-response function as given in equation (4.21) only includes the effect of circulatory lift. Both the Modified Sears function $S_{mod}(k)$ and Sears and Sparks' approximation of it $\Psi(k)$ are shown in figure 4.8.

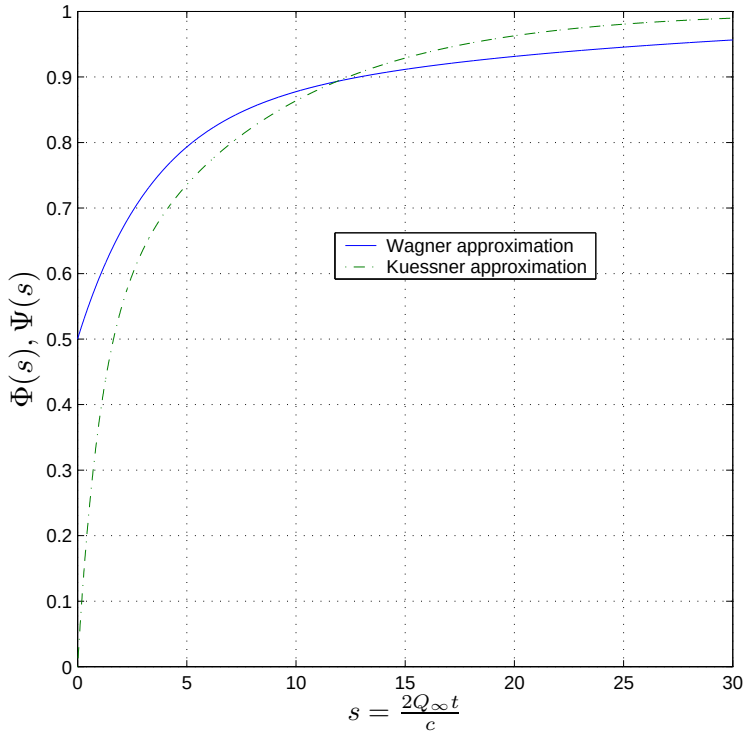


Figure 4.7: R.T. Jones' Wagner function approximation $\Phi(s)$ for a step-wise change in angle-of-attack and Sears & Sparks' approximation of Küssner's function $\Psi(s)$, for the penetration of a sharp-edged vertical gust, see also figures 4.6.

4.3 Numerical unsteady linearized potential flow simulations

4.3.1 Introduction

In this section, the steady LPF method, as described in chapter 3, will be extended to allow the calculation of unsteady aerodynamic forces and moments due to arbitrary motions and atmospheric turbulence inputs. Also this unsteady LPF method assumes that the flow is irrotational, inviscid and incompressible.

The basic formulation of the unsteady LPF method also relies on the solution of Laplace's equation, discussed in chapter 3. By means of time-dependent boundary conditions, the flow becomes a function of time while still using the initial flow-solver theory. Also, the unsteady flow will be solved in the frame $\mathcal{F}_{aero}$ and the unsteady LPF method also requires a discretized representation of the configuration of interest using quadri-lateral panels, see sections 3.3.1 and 3.3.2.
The extension to the steady LPF method is based on references [11, 12]. With respect to the steady LPF formulation presented in chapter 3, the main differences will include the addition of an unsteady wake model. The unsteady wake will be defined in the frame $\mathcal{F}_I$ in which the frame $\mathcal{F}_{aero}$ is traveling along a pre-described flightpath. Since the flow is solved in $\mathcal{F}_{aero}$, the wake's position in $\mathcal{F}_I$ will be transformed to $\mathcal{F}_{aero}$ for each discrete

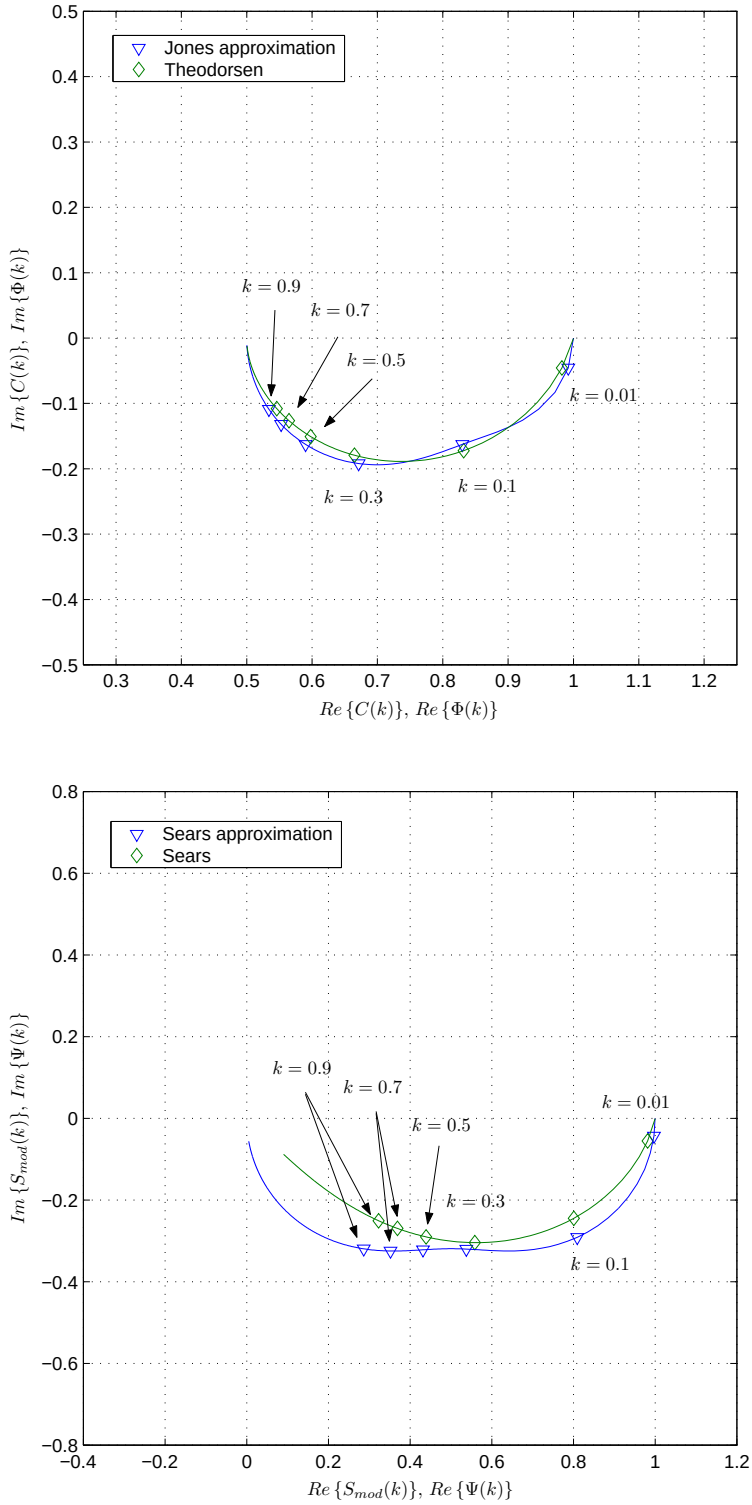


Figure 4.8: Theodorsen's function $C(k)$ and Jones' approximation (top) and the Modified Sears function $S_{mod}(k)$ and Sears' & Sparks' approximation (bottom).

time-step. The unsteady LPF method requires some adjustments for the calculation of the on-body pressure distribution in order to include the unsteady part of it.
Although the unsteady LPF method solution given in references [11, 12] considers arbitrary aircraft motions, here the aircraft's response in terms of both atmospheric forces and moments to perturbations is limited to recti-linear flightpaths. In this chapter, these perturbations will include both surging- and heaving motions, as well as atmospheric turbulence inputs including both longitudinal (u_g) ánd vertical gusts (w_g).

4.3.2 Kinematics

In references [11, 12] a formulation for the unsteady LPF method is given, resulting in a solution for the time-dependent simulation of both aerodynamic forces and moments. The method requires a definition of the flightpath along which the configuration of interest is traveling.
In figure 4.9 both the frame $\mathcal{F}_I$ and the frame $\mathcal{F}_{aero}$ are given. The figure also includes the definition of $\mathcal{F}_{aero}$'s translational degrees of freedom $[U(t), V(t), W(t)]^T$ as well as its rotational degrees of freedom $[p(t), q(t), r(t)]^T$. The angles of rotation $[\Psi(t), \theta(t), \varphi(t)]^T$ are also shown in this figure.
Since the flow over the configuration is solved in $\mathcal{F}_{aero}$, its position is required in $\mathcal{F}_I$. For arbitrary motions, the position of $\mathcal{F}_{aero}$'s origin O_{aero} is given as,

$$\underline{R}_0(t) = \begin{bmatrix} X_0(t) \\ Y_0(t) \\ Z_0(t) \end{bmatrix} \tag{4.22}$$

with $\underline{R}_0(t)$ the position of $\mathcal{F}_{aero}$'s origin in $\mathcal{F}_I$, and $X_0(t)$, $Y_0(t)$ and $Z_0(t)$ its components. The instantaneous orientation of $\mathcal{F}_{aero}$ is given as,

$$\underline{\Theta}(t) = \begin{bmatrix} \Psi(t) \\ \theta(t) \\ \varphi(t) \end{bmatrix} \tag{4.23}$$

with $\underline{\Theta}(t)$ the orientation of $\mathcal{F}_{aero}$, and $\Psi(t)$, $\theta(t)$ and $\varphi(t)$ its components. The motivation for including equations (4.22) and (4.23) is that they are required for the definition of the configuration's position in $\mathcal{F}_I$. Similar to chapter 3, this position is required to model a time-dependent wake which eminates from prescribed wake-separation lines [1]. Although the configuration's wake initially is defined in $\mathcal{F}_I$, the flow is actually solved in $\mathcal{F}_{aero}$. Therefore, both the configuration's position and its wake, are required in $\mathcal{F}_{aero}$. For a fixed arbitrary point $[x, y, z]^T$ in $\mathcal{F}_{aero}$, and with its known position $[X(t), Y(t), Z(t)]^T$ in $\mathcal{F}_I$, the transformation is written as,

$$\begin{bmatrix} x \\ y \\ z \end{bmatrix} = \mathcal{T}_\varphi \mathcal{T}_\theta \mathcal{T}_\psi \begin{bmatrix} X(t) - X_0(t) \\ Y(t) - Y_0(t) \\ Z(t) - Z_0(t) \end{bmatrix} \tag{4.24}$$

[1] Note that in chapter 3 $\mathcal{F}_{aero}$ and $\mathcal{F}_I$ always coincide

with the transformation matrices $\mathcal{T}_\psi$, $\mathcal{T}_\theta$ and $\mathcal{T}_\varphi$, given as,

$$\mathcal{T}_\psi = \begin{bmatrix} cos\ \psi(t) & sin\ \psi(t) & 0 \\ -sin\ \psi(t) & cos\ \psi(t) & 0 \\ 0 & 0 & 1 \end{bmatrix} \tag{4.25}$$

$$\mathcal{T}_\theta = \begin{bmatrix} cos\ \theta(t) & 0 & -sin\ \theta(t) \\ 0 & 1 & 0 \\ sin\ \theta(t) & 0 & cos\ \theta(t) \end{bmatrix} \tag{4.26}$$

$$\mathcal{T}_\varphi = \begin{bmatrix} 1 & 0 & 0 \\ 0 & cos\ \varphi(t) & sin\ \varphi(t) \\ 0 & -sin\ \varphi(t) & cos\ \varphi(t) \end{bmatrix} \tag{4.27}$$

The inverse of the transformation given in equation (4.24) is also used for unsteady LPF simulations, and it is written as,

$$\begin{bmatrix} X(t) \\ Y(t) \\ Z(t) \end{bmatrix} = \begin{bmatrix} X_0(t) \\ Y_0(t) \\ Z_0(t) \end{bmatrix} + [\mathcal{T}_\varphi \mathcal{T}_\theta \mathcal{T}_\psi]^{-1} \begin{bmatrix} x \\ y \\ z \end{bmatrix} \tag{4.28}$$

The transformation given in equation (4.28) is used to generate the unsteady wake. From the trailing-edges of the configuration's lift-generating elements the wake is shedded. The position of these trailing-edges is known in $\mathcal{F}_{aero}$, and using equation (4.28), the position of them is also known in $\mathcal{F}_I$. In section 4.3.4 the procedure of unsteady wake-shedding will be further discussed.

4.3.3 Numerical boundary conditions

Similar to chapter 3, the boundary condition employed for unsteady LPF simulations is the Dirichlet boundary condition. For time-domain simulations, it also requires the internal disturbance potential to equal a constant (and is selected as zero, see references [11, 12]). For this purpose, each collocation point (located inside the configuration, slightly below the surface) is scanned and the sum of the disturbance potential of all configuration and all wake-panels is calculated.

4.3.4 Unsteady wake-separation and the numerical Kutta condition

For the time-dependent simulations, initially a steady-state condition is assumed. This condition has been described in chapter 3 and will be referred to as the "trim condition". This trim condition is given using a pre-defined angle-of-attack, side-slip-angle, angular-velocities $[p, q, r]^T$ and free-stream velocity $\underline{Q}_\infty$ (or, for non-zero side-slip-angle and angle-of-attack, its components $\underline{Q}_\infty = [U_\infty, V_\infty, W_\infty]^T$).

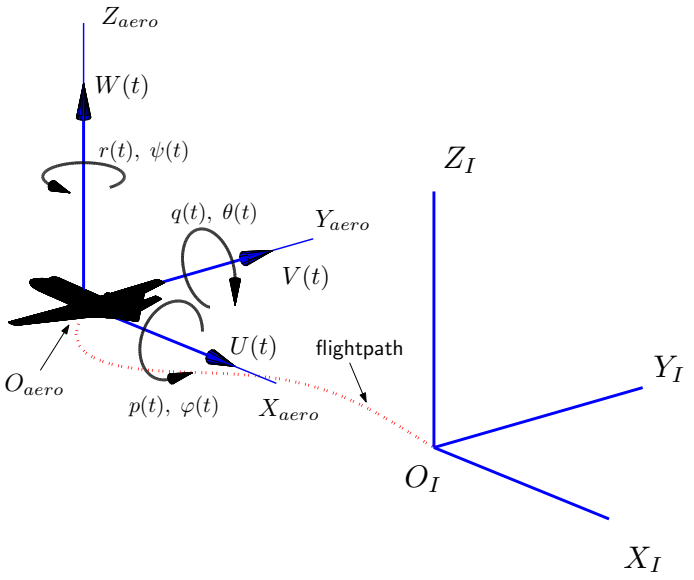


Figure 4.9: The Inertial Frame of Reference $\mathcal{F}_I$ and the Aerodynamic Frame of Reference $\mathcal{F}_{aero}$ during unsteady motion, including the motion variables' definitions.

For the trim condition, both $\mathcal{F}_{aero}$ and $\mathcal{F}_I$ coincide. Starting from this trim condition, the numerical time-domain unsteady LPF simulations will only consider translations along the negative X_I-axis of $\mathcal{F}_I$. With the free-stream velocity vector $\underline{Q}_\infty$ defined as $\underline{Q}_\infty = [U_\infty, 0, 0]^T$, for each consecutive time-step, $t_n = n\Delta t$, with $n = 0 \cdots N_{time}$, Δt the discretization time and N_{time} the number of time-steps, a number of wake-panels is shed from the trailing edges of lift-generating configuration elements or prescribed separation-lines.
For example, in figure 4.10 the wake-development for an aerofoil is given. At $t = t_0$ the frames $\mathcal{F}_{aero}$ and $\mathcal{F}_I$ coincide. At $t_1 = \Delta t$ the aerofoil's trailing-edge has traveled along the negative X_I-axis over a distance equalling $|X_0| = U_\infty \Delta t$. During this first time-step, the aerofoil has shed a new wake-element to counteract the aerofoil's variation of circulation caused by any perturbations (also known as the Kelvin condition, which states that the time rate of change of circulation around a closed curve, including the configuration and its wake, equals zero, see reference [11]). The aerofoil's time-dependent trailing-edge position in $\mathcal{F}_I$ is known from equation (4.28). The position of the leading-edge of the newly shed wake-element is equal to the aerofoils' trailing-edge position at $t_1 = \Delta t$. Similarly, the position of the trailing-edge of the new wake-element is equal to the position of the leading-edge of the shedded wake-panel one time-step earlier (which is the leading-edge of the steady wake for $t_1 = \Delta t$). For additional time-steps the wake-shedding procedure is similar. The wake-development for additional time-steps is shown in figure 4.10.

Although the wake-development given in figure in figure 4.10 is quite straightforward, in references [11, 12] it is suggested to place the trailing-edge of the newly shed wake-panel

closer to the aerofoil's trailing-edge, see also figure 4.11. The suggestion is to place the trailing-edge of the newly shed wake-panel within $0.2 - 0.3$ of the distance covered by the aerofoil's trailing-edge (which equals $|U_\infty \Delta t|$). Throughout this thesis, the trailing-edge of the latest shed wake-panel is translated to a position equalling $0.25 \cdot |U_\infty \Delta t|$ from the aerofoil's trailing-edge, see also figure 4.12. Both the leading- and trailing-edges of the previously shed wake-panels are also translated over the same distance ($0.25 \cdot |U_\infty \Delta t|$) closer to the aerofoil's trailing-edge. Although the time-dependent wake-development has been described for an aerofoil, for arbitrary three-dimensional (3D) configurations the procedure is similar. As an example, for a 3D wing the time-dependent wake-development (omitting the steady-state wake) is given in figure 4.13.

Similar to chapter 3, the time-dependent wake consists of a number of quadri-lateral doublet-panels. The configuration's wake is also determined by sets of user defined wake-shedding or separation lines. When considering attached flows only, the wake-shedding panels are located at the trailing-edges of lift-generating configuration elements (or panels) from which a wake is desired (separation). Furthermore, the time-dependent wake-panels also have a collocation point and a local Panel Frame of Reference $\mathcal{F}_P$, see also sections 3.3.1 and 3.3.3.
The definition of the newly shed wake-panels' local frame $\mathcal{F}_P$ is similar to that of the configuration panels' local Panel Frame of Reference definition defined in section 3.3.1. Furthermore, the singularity distribution on the newly shed wake-panels consists of doublets only. Referring to chapter 3, the wake-panels' doublet-strength μ_{wake} is determined by specifying the wake-separation lines, thus defining the upper and lower wake-shedding panels on the configuration. Similar to the Kutta condition given in equation (3.14), which requires that the vorticity at the aerofoil's trailing-edge remains zero, the continuous-time-dependent wake-panels' doublet-strength $\mu_{wake}(t)$ is also determined by,

$$\mu_{wake}(t) = \mu_{up}(t) - \mu_{low}(t) \tag{4.29}$$

where $\mu_{up}(t)$ and $\mu_{low}(t)$ are the corresponding upper and lower configuration-panel doublet-strength at the aerofoil's trailing-edge, respectively. Contrary to chapter 3, see section 3.3.4, the wake-panel doublet-strength now becomes a function of time. According to Kelvin's condition, the wake-panels are now used to counteract any change in circulation. In the numerical scheme, or for discrete-time simulations, the doublet-strength of the newly shed wake-panels is now related to the corresponding upper and lower configuration-panel's doublet-strength at the aerofoil's trailing-edge at the previous time-step. The numerical equivalent of equation (4.29) becomes,

$$\mu_{wake}(t_n) = \mu_{up}(t_{n-1}) - \mu_{low}(t_{n-1}) \tag{4.30}$$

with both $t_{n-1} = (n-1)\Delta t$ and $t_n = n\Delta t$ consecutive discrete time-steps.

4.3.5 General numerical source- and doublet-solutions

Similar to section 3.3.5, the unsteady flow-solution holds for the frame $\mathcal{F}_{aero}$. For the unsteady LPF method, both the configuration and its wake are also discretized in a number

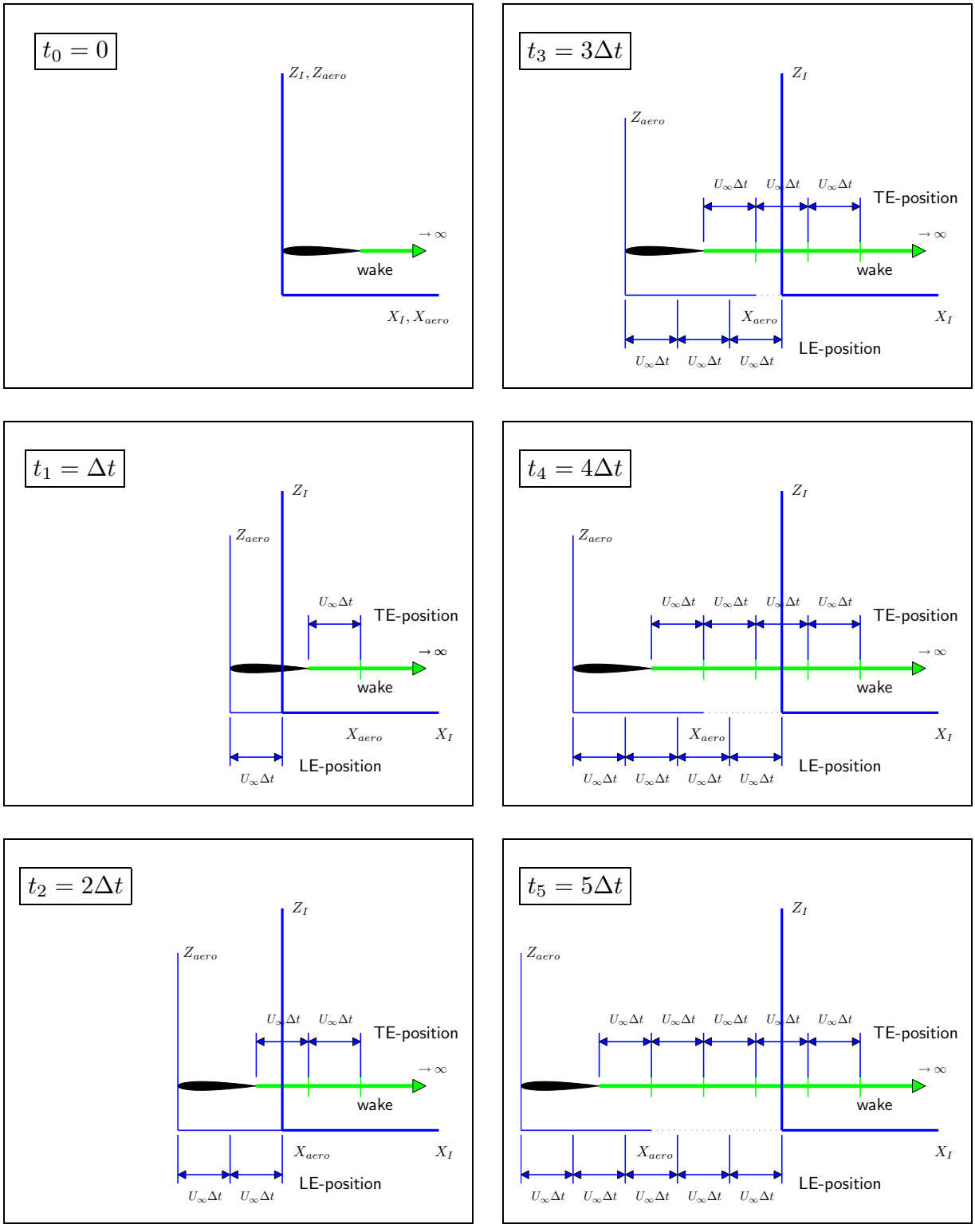


Figure 4.10: Wake-development and position of an aerofoil during unsteady motion in the Inertial Frame of Reference $\mathcal{F}_I$.

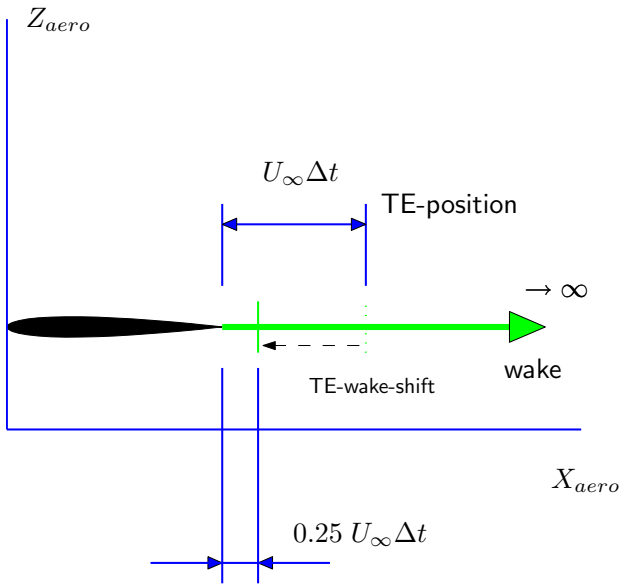


Figure 4.11: Shift of the trailing-edge of the latest shed wake-panel closer to the aerofoil's trailing-edge.

of quadri-lateral panels. Similar to chapter 3, the method uses N_B configuration panels (which include both doublet- and source-elements), and N_W wake doublet-elements, with N_B the number of configuration panels and N_W the number of wake-panels.

A steady-state solution

With reference to figure 4.12, at time $t = t_0$ the frames $\mathcal{F}_{aero}$ and $\mathcal{F}_I$ coincide. Referring to chapter 3, for this steady-state condition the LPF method uses the Dirichlet boundary-condition. This condition states that in each collocation point the sum of the perturbation velocity potential due to both the configuration- and wake-panels equals zero (with the configuration-panels containing both doublet- and source-elements, while the wake-panels consist of doublet-elements only). Considering an arbitrary configuration's collocation point k, for the steady-state condition the Dirichlet boundary condition is now written as, similar to equation (3.39),

$$\sum_{i=1}^{N_B} C_{ki}\mu_i + \sum_{j=1}^{N_W} D_{kj}\mu_{wake_j} + \sum_{i=1}^{N_B} B_{ki}\sigma_i = 0 \Bigg|_{t=t_0} \tag{4.31}$$

with C_{ki} the disturbance velocity potential influence of a unit-strength configuration doublet-panel i on the configuration-panel's collocation point k, D_{kj} the disturbance velocity potential influence of a unit-strength wake doublet-panel j on the configuration-panel's collocation point k, and B_{ki} the disturbance velocity potential influence of a unit-strength configuration source-panel i on the configuration-panel's collocation point k, respectively.

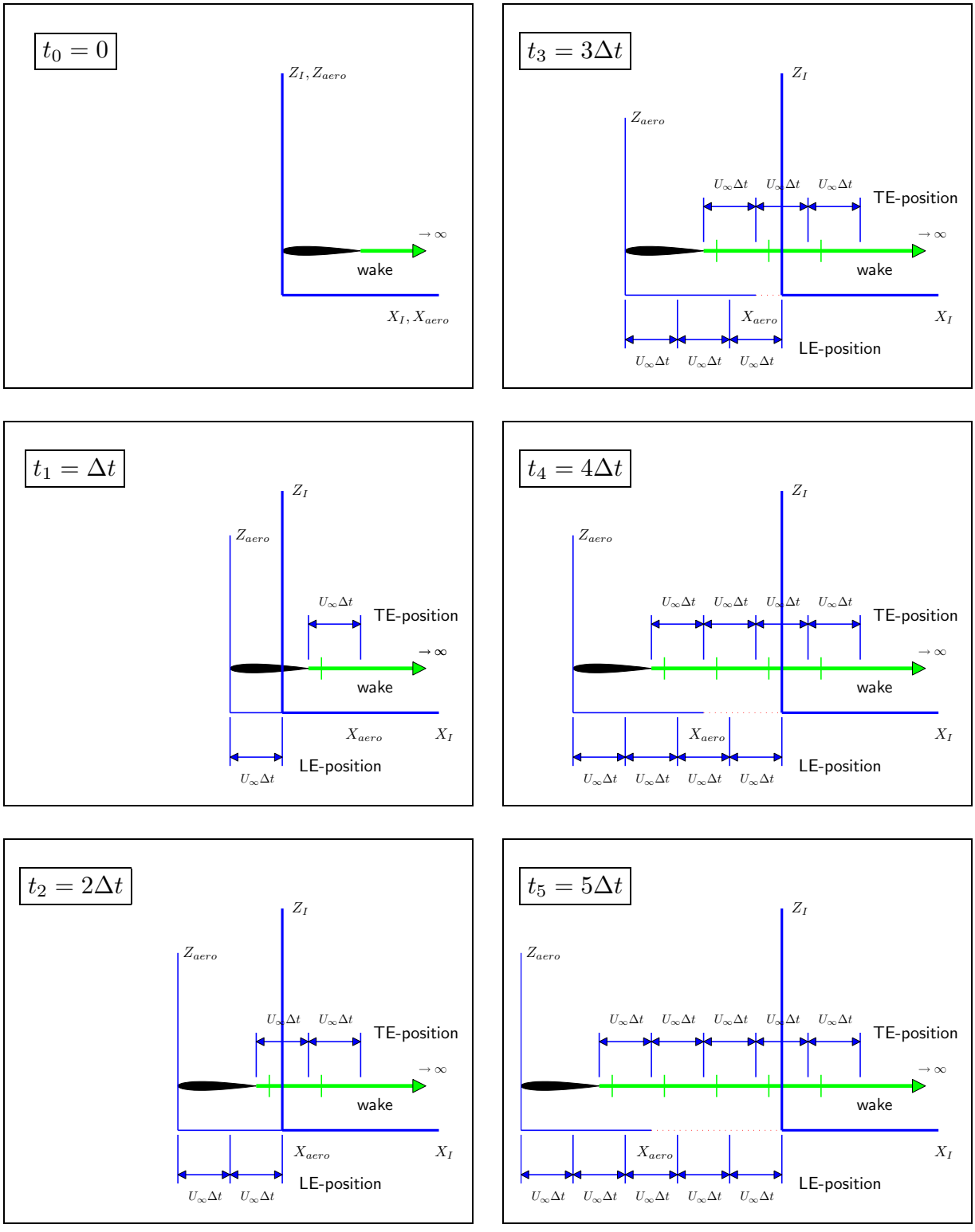


Figure 4.12: Corrected wake-development and position of an aerofoil during unsteady motion in the Inertial Frame of Reference $\mathcal{F}_I$.

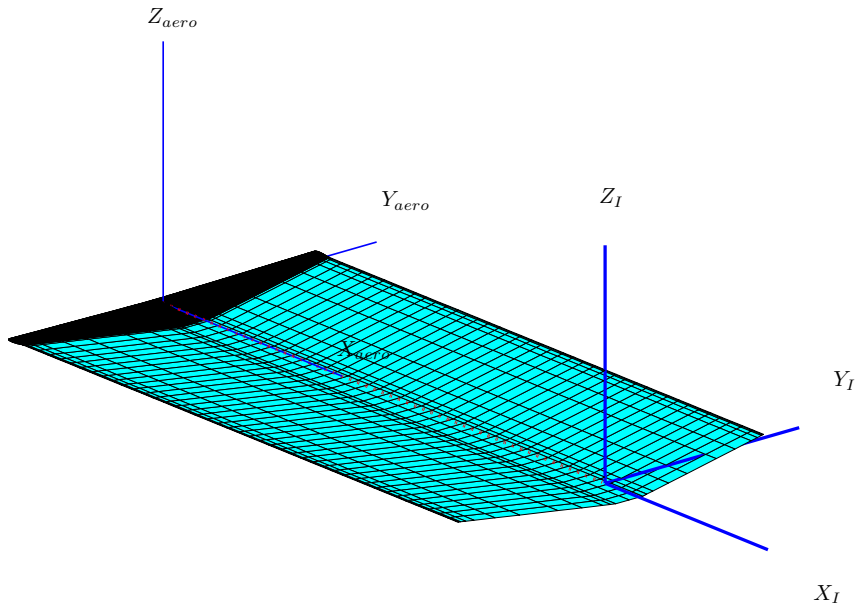


Figure 4.13: A finite wing configuration, the planar unsteady wake along a recti-linear flightpath, the Aerodynamic Frame of Reference $\mathcal{F}_{aero}$ and the Inertial Frame of Reference $\mathcal{F}_I$.

For the steady-state condition, the wake's doublet-strength μ_{wake} is related to the doublet-strength of the configuration's upper (μ_{up}) and lower panels (μ_{low}) at the wake-separation lines, see also equation (3.40),

$$\mu_{up} - \mu_{low} - \mu_{wake} = 0$$

Furthermore, for the steady LPF method the configuration-panels' prescribed source-strength σ is given by equation (3.42),

$$\sigma_k = -\underline{n}_k \cdot \underline{Q}_\infty$$

with $k = 1 \cdots N_B$, $\underline{n}_k$ the panel k's normal and $\underline{Q}_\infty$ the vector of free-stream flow components at infinity. In this thesis, for the steady-state condition this vector is given as $\underline{Q}_\infty = [U_\infty, 0, 0]^T$. Finally, the solution of the unknown doublet-strength distribution on both the configuration and wake is obtained from equation (3.43),

$$[AIC] \begin{bmatrix} \underline{\mu} \\ \underline{\mu}_{wake} \end{bmatrix} = RHS$$

A time-dependent solution

For time-domain simulations, the configuration travels along the negative X_I-axis of $\mathcal{F}_I$ with velocity $\underline{Q}_\infty = [U_\infty, 0, 0]^T$, see figure 4.12. Similar to references [11, 12], for these unsteady simulations at each time-step (with discretization time Δt) a number of wake-panels is being shed. These new wake-panels make sure that the Kelvin condition is fullfilled for

all time-steps. Basically, these newly shed wake-panels counteract the variation of circulation caused by any perturbations such as aircraft motion and atmospheric turbulence inputs. The time-dependent flow is solved in $\mathcal{F}_{aero}$, although the time-dependent wake is generated in $\mathcal{F}_I$. The wake-panels' corner points are transformed to $\mathcal{F}_{aero}$ using the transformation given in equation (4.24).

For the solution of the time-dependent doublet-strenght distribution of both the configuration ánd its wake, a formulation similar to equation (4.31) is used. Also, for the time-domain simulation the Dirichlet boundary condition is used. This boundary condition requires that at each collocation point the sum of the disturbance velocity potential of the configuration's source- and doublet-panels, as well as the disturbance velocity potential of all the wake-doublet-panels, equals zero. In the case of unsteady time-dependent simulations, the wake-geometry includes wake-panels shed at previous time-steps. For an arbitrary collocation point k and at time $t = t_n$, the equivalent of equation (4.31) is given as,

$$\sum_{i=1}^{N_B} C_{ki}\mu_i + \sum_{m=0}^{n}\sum_{j=1}^{N_W} D_{kjm}\mu_{wake_{jm}} + \sum_{i=1}^{N_B} B_{ki}\sigma_i = 0 \Bigg|_{t=t_n} \tag{4.32}$$

with C_{ki} the disturbance velocity potential influence of unit-strength doublet configuration panel i on configuration panel collocation point k, D_{kjm} the disturbance velocity potential influence of unit-strength doublet-wake-panel j on configuration panel collocation point k at $t = t_m$, and B_{ki} the disturbance velocity potential influence of unit-strength source configuration panel i on configuration panel collocation point k, respectively. Similar to equation (4.31), the configuration's doublet strength at time $t = t_n$ is written as μ_i with $i = 1 \cdots N_B$, the configuration's source-strength at time $t = t_n$ is written as σ_i with $i = 1 \cdots N_B$ and the wake-panels' doublet-strength at time $t = t_n$ is written as $\mu_{wake_{jm}}$ with $j = 1 \cdots N_W$, $m = 0 \cdots n$ and with $n = 0 \cdots N_{time}$ with N_{time} the number of time-steps.
Equation (4.32) holds for time-step $t = t_n$ while for all previous time-steps $t = t_0 \cdots t_{n-1}$ the wake-doublet-strength $\mu_{wake_{jm}}$ is known from equation (4.30). For an arbitrary wake-panel with counter j at intermediate time-step $t = t_m$, this equation is written as,

$$\mu_{wake_{jm}}(t_m) = \mu_{up}(t_{m-1}) - \mu_{low}(t_{m-1}) \tag{4.33}$$

Using equation (4.33), for an arbitrary collocation point k and for $t = t_n$, equation (4.32) is written as,

$$\sum_{i=1}^{N_B} C_{ki}\mu_i + \sum_{m=n}^{n}\sum_{j=1}^{N_W} D_{kjm}\mu_{wake_{jm}} = -\sum_{i=1}^{N_B} B_{ki}\sigma_i - \sum_{m=0}^{n-1}\sum_{j=1}^{N_W} D_{kjm}\mu_{wake_{jm}} \Bigg|_{t=t_n} \tag{4.34}$$

Similar to equation (3.42), the time-dependent source-strength $\sigma(t_n)$ is known. According to references [11, 12], for an arbitrary collocation point k, the prescribed source-strength,

$\sigma_k(t_n)$, is generally given as,

$$\sigma_k(t_n) = -\underline{n}_k \cdot \left(\begin{bmatrix} U(t_n) \\ V(t_n) \\ W(t_n) \end{bmatrix} + \underline{\Omega}(t_n) \times \begin{bmatrix} x_{col_k} \\ y_{col_k} \\ z_{col_k} \end{bmatrix} \right) \tag{4.35}$$

with $U(t_n)$, $V(t_n)$ and $W(t_n)$ the translational velocity components along the X_{aero}-, Y_{aero}- and Z_{aero}-axis, respectively, $\underline{\Omega}(t_n)$ the vector of rotational velocity components $[p(t_n), q(t_n), r(t_n)]^T$ along the X_{aero}-, Y_{aero}- and Z_{aero}-axis, respectively, and $[x_{col_k}, y_{col_k}, z_{col_k}]^T$ the position of the k-th collocation point in $\mathcal{F}_{aero}$. See figure 4.9 for the definition of both the translational and rotational velocity components.
In this thesis, only perturbations along a recti-linear flightpath are considered with constant translational velocity components $U(t_n) = U_\infty = |\underline{Q}_\infty|$, $V(t_n) = 0$ and $W(t_n) = 0$. Furthermore, for the estimation of stability derivatives only quasi-steady perturbations for the rotational velocity components are considered, thus $p(t_n) = p$, $q(t_n) = q$ and $r(t_n) = r$. If atmospheric turbulence inputs are considered along the recti-linear flightpath, equation (4.35) is written as,

$$\sigma_k(t_n) = -\underline{n}_k \cdot \left(\begin{bmatrix} U_\infty \\ 0 \\ 0 \end{bmatrix} + \begin{bmatrix} u_g(t_n) \\ v_g(t_n) \\ w_g(t_n) \end{bmatrix} \right) \tag{4.36}$$

with $u_g(t_n)$, $v_g(t_n)$ and $w_g(t_n)$ the longitudinal, lateral and vertical atmospheric turbulence velocity components along the X_{aero}-, Y_{aero}- and Z_{aero}-axis, respectively. See also figure 4.14 for the definition of the atmospheric turbulence velocity components. In chapter 5, the definition of isolated aircraft motion perturbations and isolated atmospheric turbulence inputs is given in terms of the prescribed source-strength.
Once the prescribed time-dependent source-strength has been defined, and using equation (3.40) for the row of latest shed wake-panels, equation (4.34) is written in a form similar to equation (3.43),

$$[AIC] \begin{bmatrix} \underline{\mu}(t_n) \\ \underline{\mu}_{wake}(t_n) \end{bmatrix} = RHS \Big|_{t=t_n} \tag{4.37}$$

with $\underline{\mu}(t_n) = [\mu_1(t_n), \cdots, \mu_{N_B}(t_n)]^T$ the unknown configuration doublet-strength distribution at $t = t_n$, $\underline{\mu}_{wake}(t_n) = [\mu_{wake_1}(t_n), \cdots, \mu_{wake_{N_W}}(t_n)]^T$ the unknown wake-doublet-strength distribution at $t = t_n$ and AIC the aerodynamic influence coefficient matrix according to,

$$AIC = \left[\begin{array}{cccc|cccc} C_{11} & C_{12} & \cdots & C_{1N_B} & D_{11} & D_{12} & \cdots & D_{1N_W} \\ C_{21} & C_{22} & \cdots & C_{2N_B} & D_{21} & D_{22} & \cdots & D_{2N_W} \\ \vdots & \vdots & \ddots & \vdots & \vdots & \vdots & \ddots & \vdots \\ C_{N_B1} & C_{N_B2} & \cdots & C_{N_BN_B} & D_{N_B1} & D_{N_B2} & \cdots & D_{N_BN_W} \\ \hline \multicolumn{4}{c|}{E_{N_W \times N_B}} & \multicolumn{4}{c}{E_{N_W \times N_W}} \end{array}\right] \tag{4.38}$$

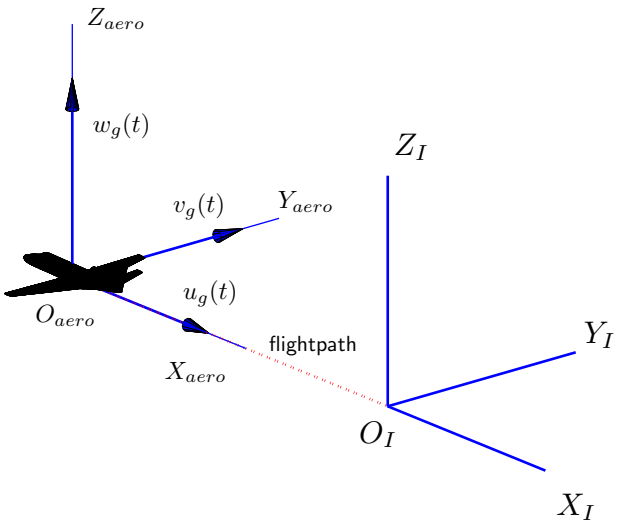


Figure 4.14: The Inertial Frame of Reference $\mathcal{F}_I$ and the Aerodynamic Frame of Reference $\mathcal{F}_{aero}$ for the aircraft motion along a recti-linear flightpath, including the atmospheric turbulence velocity component definitions.

with both matrices $E_{N_W \times N_B}$ and $E_{N_W \times N_W}$ defining the wake-panels' strength related to the configuration panels' doublet-strength similar to equation (3.40). Referring to equation (3.39), the matrix elements C_{ki} and D_{kj} in equation (4.38) represent the disturbance velocity potential influence due to a unit-strength doublet configuration panel i on configuration panel collocation point k, and the disturbance velocity potential influence of the latest shed unit-strength doublet-wake-panel j on configuration panel collocation point k, respectively. The vector RHS in equation (4.37) is defined as,

$$RHS = \left[\frac{RHS_k}{O_{N_W \times 1}} \right] \tag{4.39}$$

with $k = 1 \cdots N_B$, N_B the number of configuration panels, the vector $O_{N_W \times 1}$ a zero vector with N_W the number of wake-panels, and RHS_k defined as,

$$RHS_k = -\sum_{i=1}^{N_B} B_{ki}\sigma_i - \sum_{m=0}^{n-1}\sum_{j=1}^{N_W} D_{kjm}\mu_{wake_{jm}} \tag{4.40}$$

with D_{kjm} the disturbance velocity potential influence of a unit-strength wake doublet-panel j (at intermediate time-step $t = t_m$) on configuration panel collocation point k, B_{ki} the disturbance velocity potential influence of unit-strength source configuration panel i on configuration panel collocation point k, and σ_i the prescribed source-strength, respectively. The unknown configuration doublet-strength at $t = t_n$, $\underline{\mu}(t_n)$, and the unknown wake-doublet-strength of the latest shed wake-panels at $t = t_n$, $\underline{\mu}_{wake}(t_n)$, follows from equation (4.37) by matrix inversion.

4.3.6 Velocity perturbation calculations

Similar to chapter 3, section 3.3.6, from the known configuration's doublet-strength, μ_k, with $k = 1 \cdots N_B$, the time-dependent perturbation velocity components, now designated as $[q_{l_k}(t_n), q_{m_k}(t_n), q_{n_k}(t_n)]^T$ in the frame $\mathcal{F}_P$, are calculated. The procedure for calculating these velocity components is equal to the procedure given in chapter 3, section 3.3.6.

4.3.7 Aerodynamic pressure calculations

The procedure for calculating the aerodynamic pressure coefficient acting on a configuration-panel, is similar to the one presented in section 3.3.7. The aerodynamic pressure coefficient calculations are also performed in $\mathcal{F}_P$. To derive the total local velocity at an arbitrary collocation point k, first the configuration-panels' time-dependent perceived velocity, $\underline{Q}_p(t_n)$, in $\mathcal{F}_{aero}$ is given. For arbitrary motions as well as atmospheric turbulence inputs, the perceived velocity vector at time $t = t_n$ is given as,

$$\underline{Q}_p(t_n) = \begin{bmatrix} U_p(t_n) \\ V_p(t_n) \\ W_p(t_n) \end{bmatrix} = \begin{bmatrix} U(t_n) \\ V(t_n) \\ W(t_n) \end{bmatrix} + \underline{\Omega} \times \begin{bmatrix} x_{col_k} \\ y_{col_k} \\ z_{col_k} \end{bmatrix} + \begin{bmatrix} u_g(t_n) \\ v_g(t_n) \\ w_g(t_n) \end{bmatrix} \tag{4.41}$$

with $U(t_n)$, $V(t_n)$ and $W(t_n)$ the translational velocity components along the X_{aero}-, Y_{aero}- and Z_{aero}-axis, respectively, $\underline{\Omega}(t_n)$ the vector of rotational velocity components $[p(t_n), q(t_n), r(t_n)]^T$ along the X_{aero}-, Y_{aero}- and Z_{aero}-axis, respectively, the position of the k-th collocation point in $\mathcal{F}_{aero}$ given as $[x_{col_k}, y_{col_k}, z_{col_k}]^T$, and $u_g(t_n)$, $v_g(t_n)$ and $w_g(t_n)$ the longitudinal, lateral and vertical atmospheric turbulence velocity components along the X_{aero}-, Y_{aero}- and Z_{aero}-axis, respectively. See also figures 4.9 and 4.14 for the translational, rotational and atmospheric turbulence velocity component definitions. The time-dependent perceived velocity vector $\underline{Q}_p(t_n)$ is decomposed in $\mathcal{F}_P$, and its decomposition in $\mathcal{F}_P$ is denoted as $[Q_{p_l}(t_n), Q_{p_m}(t_n), Q_{p_n}(t_n)]^T$. The decomposition makes use of the transformation from $\mathcal{F}_{aero}$ to $\mathcal{F}_P$ ($\mathcal{T}^P_{aero}$) given in section 3.3.5,

$$\begin{bmatrix} Q_{p_l}(t_n) \\ Q_{p_m}(t_n) \\ Q_{p_n}(t_n) \end{bmatrix} = \mathcal{T}^P_{aero} \begin{bmatrix} U_p(t_n) \\ V_p(t_n) \\ W_p(t_n) \end{bmatrix}$$

For an arbitrary collocation point k, the total time-dependent local velocity $\underline{Q}_{local_k}(t_n)$ in $\mathcal{F}_P$ is calculated by,

$$\underline{Q}_{local_k}(t_n) = \begin{bmatrix} Q_{p_{l_k}}(t_n) \\ Q_{p_{m_k}}(t_n) \\ Q_{p_{n_k}}(t_n) \end{bmatrix} + \begin{bmatrix} q_{l_k}(t_n) \\ q_{m_k}(t_n) \\ q_{n_k}(t_n) \end{bmatrix} \tag{4.42}$$

The time-dependent non-dimensional pressure coefficient $C_{p_k}(t_n)$ for panel k is calculated by, see references [11, 12, 8, 9],

$$C_{p_k}(t_n) = 1 - \frac{\left|\underline{Q}_{local_k}(t_n)\right|^2}{Q^2_\infty} + 2\frac{\mu_k(t_n) - \mu_k(t_{n-1})}{\Delta t\, Q^2_\infty} \tag{4.43}$$

with $\mu_k(t_n)$ panel k's doublet-strength at $t = t_n$, $\mu_k(t_{n-1})$ panel k's doublet-strength at the previous time-step $t = t_{n-1}$, $Q_\infty = \left|\underline{Q}_\infty\right| = \sqrt{U_\infty^2 + V_\infty^2 + W_\infty^2}$ and Δt the discretization time.

Concluding this section, it should be noted that the perturbations described in equation (4.41) will not occur simultaneously. In chapter 5, all (isolated) aircraft motion perturbations and (isolated) atmospheric turbulence inputs will be defined.

4.3.8 Aerodynamic loads

Once the configuration's time-dependent non-dimensional pressure coefficient distribution $C_{p_k}(t_n)$ is known, the aerodynamic forces and moments acting on the configuration are calculated in $\mathcal{F}_{aero}$. Similar to section 3.3.8, the aerodynamic forces acting on configuration panel k become,

$$\begin{aligned}
\Delta F_{x_k}(t_n) &= -C_{p_k}(t_n)\,\frac{1}{2}\rho\, Q_\infty^2\, \Delta S_{P_k}\, x_{e_{3_k}} \\
\Delta F_{y_k}(t_n) &= -C_{p_k}(t_n)\,\frac{1}{2}\rho\, Q_\infty^2\, \Delta S_{P_k}\, y_{e_{3_k}} \\
\Delta F_{z_k}(t_n) &= -C_{p_k}(t_n)\,\frac{1}{2}\rho\, Q_\infty^2\, \Delta S_{P_k}\, z_{e_{3_k}}
\end{aligned}$$

with $C_{p_k}(t_n)$ the time-dependent panel's non-dimenional pressure coefficient according to equation (4.43), ρ the air density, $Q_\infty = \left|\underline{Q}_\infty\right|$, ΔS_{P_k} the panel's surface area according to equation (3.20) and $x_{e_{3_k}}$, $y_{e_{3_k}}$, $z_{e_{3_k}}$ the panel normal components ($\underline{e}_{3_k} = \underline{n}_k = [x_{e_{3_k}}, y_{e_{3_k}}, z_{e_{3_k}}]^T$) in $\mathcal{F}_{aero}$.

Panel k's contribution to the time-dependent aerodynamic moments with respect to a reference point, which is taken to be $[0,0,0]^T$ in $\mathcal{F}_{aero}$, becomes,

$$\begin{aligned}
\Delta M_{x_k}(t_n) &= \Delta F_{z_k}(t_n)\, y_{col_k} - \Delta F_{y_k}(t_n)\, z_{col_k} \\
\Delta M_{y_k}(t_n) &= \Delta F_{x_k}(t_n)\, z_{col_k} - \Delta F_{z_k}(t_n)\, x_{col_k} \\
\Delta M_{z_k}(t_n) &= \Delta F_{y_k}(t_n)\, x_{col_k} - \Delta F_{x_k}(t_n)\, y_{col_k}
\end{aligned}$$

with x_{col_k}, y_{col_k} and z_{col_k} the components of the position of collocation point k in $\mathcal{F}_{aero}$. The time-dependent total aerodynamic forces and moments acting on the configuration are obtained by summation of all the configuration panels' contribution to them,

$$F_x(t_n) = \sum_{k=1}^{N_B} F_{x_k}(t_n) \qquad F_y(t_n) = \sum_{k=1}^{N_B} F_{y_k}(t_n) \qquad F_z(t_n) = \sum_{k=1}^{N_B} F_{z_k}(t_n)$$

and,

$$M_x(t_n) = \sum_{k=1}^{N_B} M_{x_k}(t_n) \qquad M_y(t_n) = \sum_{k=1}^{N_B} M_{y_k}(t_n) \qquad M_z(t_n) = \sum_{k=1}^{N_B} M_{z_k}(t_n)$$

Finally, the time-dependent non-dimensional aerodynamic force and moment coefficients in $\mathcal{F}_{aero}$ become,

$$C_X(t_n) = \frac{F_x(t_n)}{\frac{1}{2}\rho\, Q_\infty^2\, S_{ref}} \qquad C_Y(t_n) = \frac{F_y(t_n)}{\frac{1}{2}\rho\, Q_\infty^2\, S_{ref}} \qquad C_Z(t_n) = \frac{F_z(t_n)}{\frac{1}{2}\rho\, Q_\infty^2\, S_{ref}}$$

and,

$$C_\ell(t_n) = \frac{M_x(t_n)}{\frac{1}{2}\rho\, Q_\infty^2\, S_{ref}\, b_{ref}} \qquad C_m(t_n) = \frac{M_y(t_n)}{\frac{1}{2}\rho\, Q_\infty^2\, S_{ref}\, c_{ref}} \qquad C_n(t_n) = \frac{M_z(t_n)}{\frac{1}{2}\rho\, Q_\infty^2\, S_{ref}\, b_{ref}}$$

with b_{ref} and c_{ref} the configuration's span and the (mean) aerodynamic chord, respectively.

4.4 Examples of numerical unsteady aerodynamic simulations

4.4.1 Introduction

In this section, several examples of numerical results will be given for the verification of the unsteady LPF method used in this thesis. The example configuration for which the numerical simulations are given is a (finite) wing with Aspect-Ratio $AR = 100$ with a NACA 0002 aerofoil. For three different aerodynamic grids the configuration is given in figure 4.15; a configuration with 6 span-wise elements and 10 chord-wise elements (top), a configuration with 6 span-wise elements and 25 chord-wise elements (middle), and a configuration with 6 span-wise elements and 50 chord-wise elements (bottom). Note that the origin O_{aero} of $\mathcal{F}_{aero}$ is located on the wing's leading-edge.

The frequency-domain aerodynamic results will be given in terms of the simulated Theodorsen function, the simulated (Modified) Sears function and the simulated (Modified) Horlock function. Although the simulations will use a finite Aspect-Ratio wing with finite thickness, the results are assumed to be representative for results of an aerofoil of zero thickness. The simulations will be compared to analytical results provided by Theodorsen, Sears and Horlock, see references [24, 22, 14] and see section 4.2.
Time-domain results will include simulated indicial responses. These responses to a step-wise change in angle-of-attack will be compared to analytical results obtained by R.T. Jones, see also references [16, 17].

Harmonic perturbation definitions

For all simulations the wing is traveling along the negative X_I-axis with velocity vector $\underline{Q}_\infty = [U_\infty, 0, 0]^T$. For the simulation of Theodorsen's, Sears' and Horlock's function, the harmonic perturbations will include heaving motions, vertical gust inputs and longitudinal gust inputs with velocities $w(t_n)$, $w_g(t_n)$ and $u_g(t_n)$, respectively. As a function of time, an arbitrary perturbation $z(t_n)$ is written as,

$$z(t_n) = z_{max}\ sin(\omega\ t_n) \tag{4.44}$$

with $z(t_n)$ either the perturbation $w(t_n)$, $w_g(t_n)$ or $u_g(t_n)$, z_{max} the amplitude of the perturbation (with $\frac{z_{max}}{Q_\infty} << 1$), t_n time and ω the perturbation circular frequency (in $[Rad/sec]$). For the time-domain simulations presented in this thesis, the reduced frequency k is used to define the frequency of the perturbations. Equation (4.44) is rewritten as,

$$z(t_n) = z_{max}\ sin\left(\frac{\omega\bar{c}}{2Q_\infty}\frac{2Q_\infty t_n}{\bar{c}}\right) = z_{max}\ sin\left(k\frac{2Q_\infty t_n}{\bar{c}}\right) \tag{4.45}$$

Equation (4.45) will be used to define the perturbation velocity at each collocation point. For aircraft motion perturbations, $z(t_n)$ is equal for all collocation points i, $i = 1 \cdots N_B$, resulting in,

$$z_i(t_n) = z_{max}\ sin\left(k\frac{2Q_\infty t_n}{\bar{c}}\right) = -z_{max}\ sin\left(k\frac{2X_0}{\bar{c}}\right) \tag{4.46}$$

with $X_0 = -Q_\infty t_n = -U_\infty t_n$, the position of the origin of $\mathcal{F}_{aero}$ given along the negative X_I-axis of $\mathcal{F}_I$ and i equal to $i = 1 \cdots N_B$. For atmospheric turbulence perturbations, $z(t_n)$ will differ for all collocation points i, $i = 1 \cdots N_B$, resulting in,

$$z_i(t_n) = z_{max}\ sin\left(k\frac{2X_{col_i}}{\bar{c}}\right) \tag{4.47}$$

with X_{col_i} the time-dependent position of all collocation points in $\mathcal{F}_I$ and i equal to $i = 1 \cdots N_B$. The transformation of the position of collocation point i in $\mathcal{F}_{aero}$ ($[x_{col_i}, y_{col_i}, z_{col_i}]^T$) to its position in $\mathcal{F}_I$ ($[X_{col_i}, Y_{col_i}, Z_{col_i}]^T$), is given in equation (4.28).

Frequency-response data calculations

The results provided by Theodorsen, Sears and Horlock are given in the frequency-domain. In order to obtain frequency-domain results from the unsteady LPF method, for a number of reduced frequencies $k = \frac{\omega\bar{c}}{2Q_\infty} = [0.01, 0.1, 0.3, 0.5, 0.7, 0.9]^T$ the non-dimensional lift-coefficient was calculated as a function of time using harmonically varying inputs. Using the input ("the perturbation") and the output ($C_L(t)$, which is equal to $C_Z(t)$ in $\mathcal{F}_{aero}$), the results are transformed to the frequency-domain for each reduced frequency k. The procedure for transforming the time-domain results to the frequency-domain is given in appendix E. This procedure eventually results in frequency-response data, given as $\frac{C_L}{\alpha}(k)$, $\frac{C_L}{\alpha_g}(k)$ and $\frac{C_L}{\hat{u}_g}(k)$, with $\alpha = \frac{w}{Q_\infty}$, $\alpha_g = \frac{w_g}{Q_\infty}$ and $\hat{u}_g = \frac{u_g}{Q_\infty}$, the non-dimensional heaving motion perturbation, the non-dimensional vertical gust input and the non-dimensional longitudinal gust input, respectively.
The aerodynamic frequency-response data are written in a parametric form which is similar to the one used in equation (4.3). For example, for the time-domain the simulated lift-coefficient due to harmonic angle-of-attack perturbations is written as,

$$C_L = C_{L_\alpha}\ \alpha\ +\ C_{L_{\dot{\alpha}}}\ \frac{\dot{\alpha}\bar{c}}{2Q_\infty} \tag{4.48}$$

The stability parameters C_{L_α} and $C_{L_{\dot\alpha}}$ in equation (4.48) are frequency-dependent, and are known from the procedure given in appendix E. The frequency-domain equivalent of equation (4.48) is written as,

$$C_L(k) = C_{L_\alpha}(k)\ \alpha\ +\ C_{L_{\dot\alpha}}(k)\ \frac{j\omega\alpha\bar{c}}{2Q_\infty} = C_{L_\alpha}(k)\ \alpha\ +\ C_{L_{\dot\alpha}}(k)\ jk\ \alpha \tag{4.49}$$

with k the reduced frequency $k = \frac{\omega\bar{c}}{2Q_\infty}$. The known stability parameters C_{L_α} and $C_{L_{\dot\alpha}}$ can now be compared to the stability parameters C_{l_α} and $C_{l_{\dot\alpha}}$ as given in equation (4.3). From both equations (4.49) ánd (4.3) the simulated Theodorsen function $C_{sim}(k) = F_{sim}(k)\ +\ j\ G_{sim}(k)$ is derived.
Similarly, from the simulated frequency-response functions $\frac{C_L}{\alpha_g}(k)$ and $\frac{C_L}{\hat{u}_g}(k)$, and using the frequency-domain equivalents of equations (4.7) and (4.12), the simulated (Modified) Sears function, $S_{sim}(k) = F_{G_{sim}}(k)\ +\ j\ G_{G_{sim}}(k)$, and the simulated (Modified) Horlock function, $T_{sim}(k) = X_{G_{sim}}(k)\ +\ j\ Y_{G_{sim}}(k)$, are derived.

Time-domain simulations

In this chapter, all time-domain simulations are performed over three cycles with 25 time-steps per cycle. The discretization-time Δt for the simulations is taken to be a function of the reduced frequency $k = \frac{\omega\bar{c}}{2Q_\infty}$. In order to calculate Δt from the prescribed reduced frequency k, the circular frequency is calculated first from,

$$\omega = \frac{2\ k\ Q_\infty}{\bar{c}}$$

Using this expression for ω, the frequency f in cycles per second (or Hz) becomes,

$$f = \frac{2\ k\ Q_\infty}{2\pi\ \bar{c}}$$

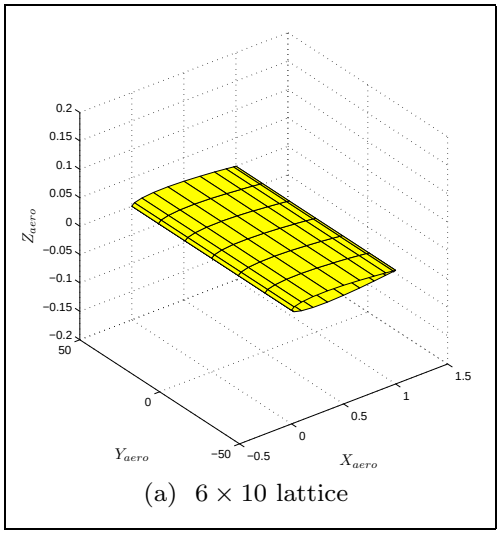
from which the period T [sec.] follows,

$$T = \frac{2\pi\ \bar{c}}{2\ k\ Q_\infty}$$

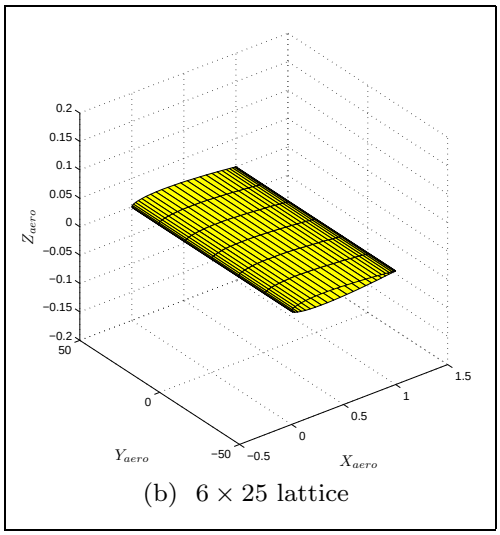
Assuming that one period of a sine function is approximated by a number of $N_{samples}$ samples (that is $N_{samples} = 25$), the discretization-time Δt [sec.] is defined as,

$$\Delta t = \frac{2\pi\ \bar{c}}{2\ k\ Q_\infty\ N_{samples}} \tag{4.50}$$

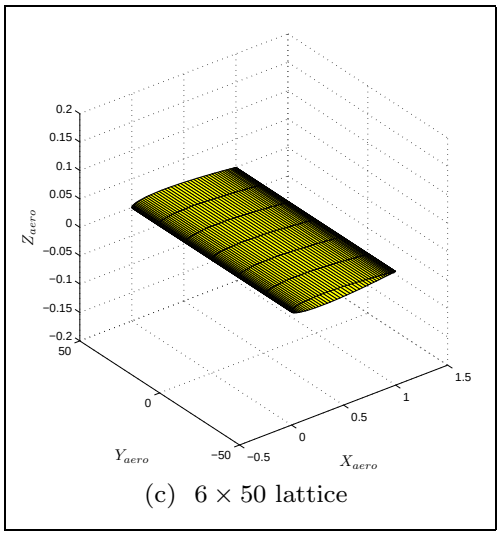
Thus, the discretization-time Δt is determined from the reduced frequency k and the number of samples $N_{samples}$ to describe a single oscillation of the harmonically varying aircraft motion perturbations or the atmospheric turbulence inputs.



(a) 6×10 lattice



(b) 6×25 lattice



(c) 6×50 lattice

Figure 4.15: Aspect-Ratio $AR = 100$ wings with a NACA 0002 aerofoil for several aerodynamic grids, as used for LPF simulations.

4.4.2 Theodorsen function simulations

Theodorsen's function $C(k)$ describes the dynamics of the aerodynamic lift of an aerofoil of zero-thickness due to harmonically varying heaving motions as a function of the reduced frequency $k = \frac{\omega \bar{c}}{2Q_\infty}$, see also section 4.2.2. The unsteady LPF simulations are performed using a steady-state angle-of-attack equal to $\alpha_0 = 0^o$.

For the simulation of Theodorsen's function the prescribed source-strength of panel i is similar to equation (4.35) and it is given as,

$$\sigma_i(t_n) = -\underline{n}_i \cdot \left(\begin{bmatrix} U_\infty \\ 0 \\ w_i(t_n) \end{bmatrix} \right) \tag{4.51}$$

while, similar to equation (4.41), the perceived velocity vector of panel i now becomes,

$$\underline{Q}_{p_i}(t_n) = \begin{bmatrix} U_{p_i}(t_n) \\ V_{p_i}(t_n) \\ W_{p_i}(t_n) \end{bmatrix} = \begin{bmatrix} U_\infty \\ 0 \\ w_i(t_n) \end{bmatrix} \tag{4.52}$$

In equations (4.51) and (4.52), the perturbation velocity $w_i(t_n)$ is similar to equation (4.46),

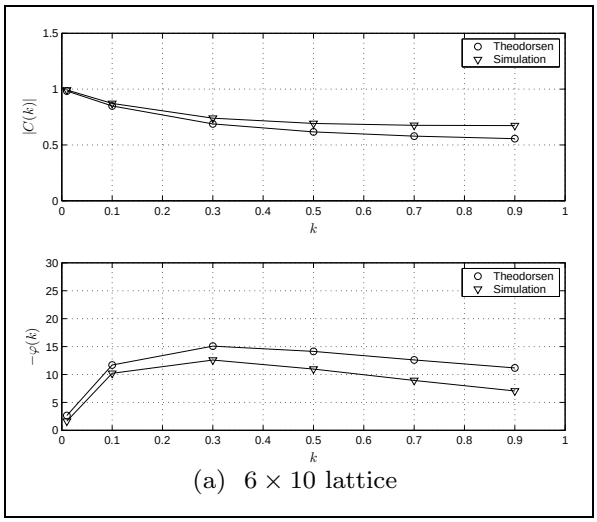
$$w_i(t_n) = w_{max}\ sin\left(k\frac{2X_0}{\bar{c}}\right) \tag{4.53}$$

with X_0 the position of the origin O_{aero} of $\mathcal{F}_{aero}$ in $\mathcal{F}_I$, and i equal to $i = 1 \cdots N_B$.
Both Theodorsen's function $C(k)$ and the simulated Theodorsen function $C_{sim}(k)$ are shown in figure 4.16. For all configurations both the simulated magnitude ánd the simulated phase show good correlation with the analytical results. Especially for the more dense aerodynamic grids, both the magnitude ánd phase of the simulated Theodorsen function show excellent agreement with the analytical results.

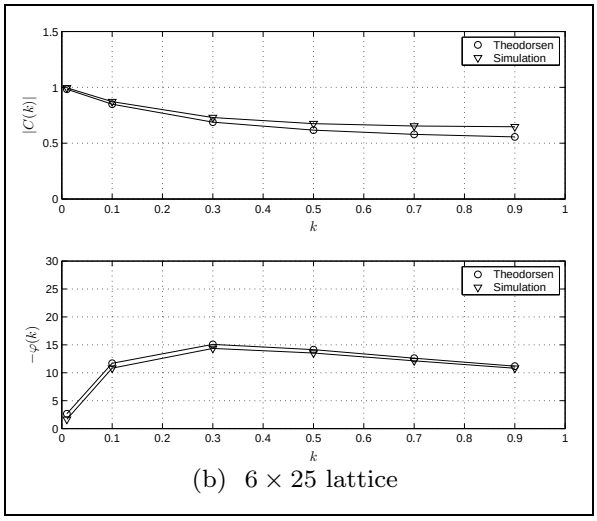
4.4.3 Sears function simulations

Sears' function $S(k)$ describes the dynamics of the aerodynamic lift of an aerofoil of zero-thickness due to harmonically varying vertical gusts as a function of the reduced frequency $k = \frac{\omega \bar{c}}{2Q_\infty}$, see also section 4.2.3. The unsteady LPF simulations are performed using a steady-state angle-of-attack equal to $\alpha_0 = 0^o$. Note that (see figure 4.15) the origin of $\mathcal{F}_{aero}$ is located at the leading-edge of the wing, resulting in Modified Sears function simulations. For the simulation of the Modified Sears function the prescribed source-strength of panel i is similar to equation (4.36) and it is given as,

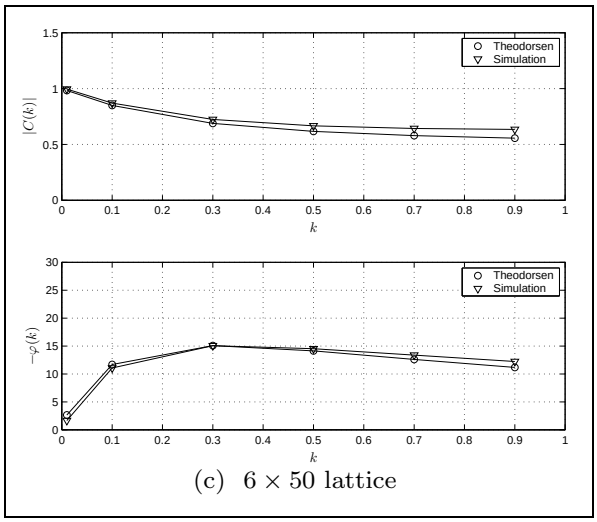
$$\sigma_i(t_n) = -\underline{n}_i \cdot \left(\begin{bmatrix} U_\infty \\ 0 \\ w_{g_i}(t_n) \end{bmatrix} \right) \tag{4.54}$$



(a) 6×10 lattice



(b) 6×25 lattice



(c) 6×50 lattice

Figure 4.16: Magnitude and phase of Theodorsen's function, and the magnitude and phase of the simulated Theodorsen function for an AR=100 wing, NACA 0002 aerofoil, for several aerodynamic grids.

while, similar to equation (4.41), the perceived velocity vector of panel i now becomes,

$$\underline{Q}_{p_i}(t_n) = \begin{bmatrix} U_{p_i}(t_n) \\ V_{p_i}(t_n) \\ W_{p_i}(t_n) \end{bmatrix} = \begin{bmatrix} U_\infty \\ 0 \\ w_{g_i}(t_n) \end{bmatrix} \tag{4.55}$$

In equations (4.54) and (4.55), the perturbation velocity $w_{g_i}(t_n)$ is similar to equation (4.47),

$$w_{g_i}(t_n) = w_{g_{max}}\ sin\left(k\frac{2X_{col_i}}{\bar{c}}\right) \tag{4.56}$$

with X_{col_i} the position of all collocation points in $\mathcal{F}_I$ and i equal to $i = 1 \cdots N_B$.
Both the Modified Sears function $S_{mod}(k)$ and the simulated Modified Sears function $S_{mod_{sim}}(k)$ are presented in figure 4.17. For all configurations, both the simulated magnitude ánd the simulated phase show good correlation with the analytical results. Especially for the more dense aerodynamic grids, both the magnitude ánd phase of the simulated Modified Sears function show excellent agreement with the analytical results.

4.4.4 Horlock function simulations

Horlock's function $T(k)$ describes the dynamics of the aerodynamic lift of an aerofoil of zero-thickness due to harmonically varying longitudinal gusts as a function of the reduced frequency $k = \frac{\omega\bar{c}}{2Q_\infty}$, see also section 4.2.4. The unsteady LPF simulations are performed using a steady-state angle-of-attack equal to $\alpha_0 = 2.5^o$. Note that (see figure 4.15) the origin of $\mathcal{F}_{aero}$ is located at the leading-edge of the wing, resulting in Modified Horlock function simulations.

For the simulation of the Modified Horlock function the prescribed source-strength of panel i is similar to equation (4.36) and it is given as,

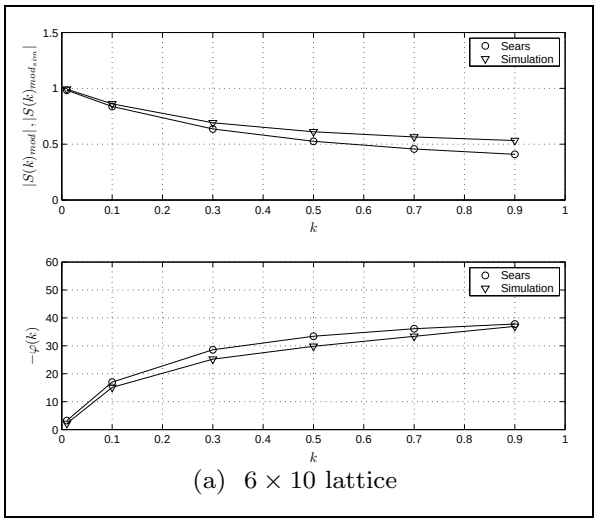
$$\sigma_i(t_n) = -\underline{n}_i \cdot \left(\begin{bmatrix} U_\infty + u_{g_i}(t_n) \\ 0 \\ 0 \end{bmatrix}\right) \tag{4.57}$$

while, similar to equation (4.41), the perceived velocity vector of panel i now becomes,

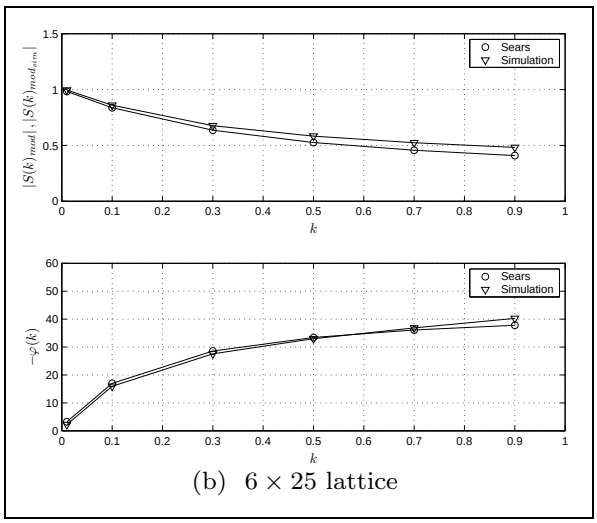
$$\underline{Q}_{p_i}(t_n) = \begin{bmatrix} U_{p_i}(t_n) \\ V_{p_i}(t_n) \\ W_{p_i}(t_n) \end{bmatrix} = \begin{bmatrix} U_\infty + u_{g_i}(t_n) \\ 0 \\ 0 \end{bmatrix} \tag{4.58}$$

In equations (4.57) and (4.58), the perturbation velocity $u_{g_i}(t_n)$ is similar to equation (4.47),

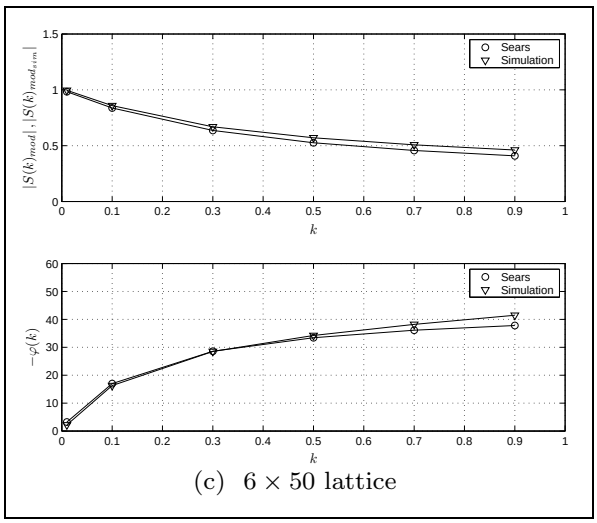
$$u_{g_i}(t_n) = u_{g_{max}}\ sin\left(k\frac{2X_{col_i}}{\bar{c}}\right) \tag{4.59}$$



(a) 6×10 lattice



(b) 6×25 lattice



(c) 6×50 lattice

Figure 4.17: Magnitude and phase of the Modified Sears function ($\Delta x = -\frac{c}{2}$), and the magnitude and phase of the simulated Modified Sears function for an AR=100 wing, NACA 0002 aerofoil, for several aerodynamic grids.

with X_{col_i} the position of all collocation points in $\mathcal{F}_I$ and i equal to $i = 1 \cdots N_B$.
Both the Modified Horlock function $T_{mod}(k)$ and the simulated Modified Horlock function $T_{mod_{sim}}(k)$ are presented in figure 4.18. Especially for the more dense aerodynamic grids, both the magnitude and the phase of the simulated Modified Horlock function show excellent agreement with the analytical results.

4.4.5 Wagner function simulations

For a verification of the unsteady LPF method in the time-domain, in this section simulations of Wagner's function $\Phi(s)$ are given. Wagner's function describes the response of the aerodynamic lift of an aerofoil of zero-thickness due to a step-wise change in angle-of-attack and it is given as a function of the semi-chord distance traveled $s = \frac{2Q_\infty t}{\bar{c}}$, see also section 4.2.5. The unsteady LPF simulations are performed using a step-change in angle-of-attack equal to $\alpha_{step} = 2.5^o$, with the initial angle-of-attack equal to $\alpha_0 = 0^o$. The simulated indicial-functions have been obtained using a prescribed source-strength for configuration-panel i equal to,

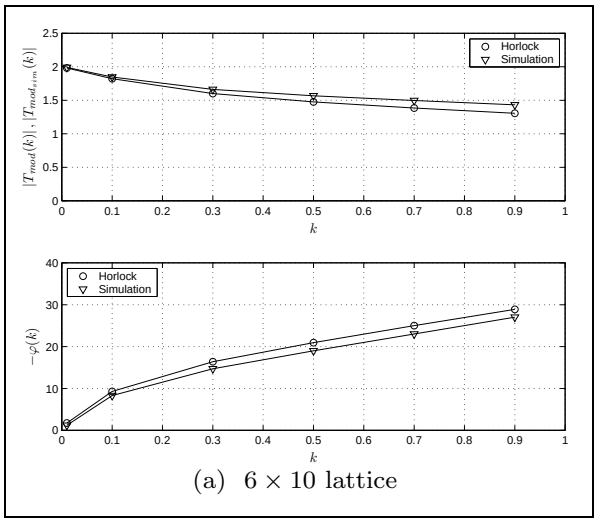
$$\sigma_i(t_n) = -\underline{n}_i \cdot \left(\begin{bmatrix} U_\infty \\ 0 \\ w \end{bmatrix} \right) \tag{4.60}$$

with $w = Q_\infty \, sin(\alpha_{step})$ and α_{step} the step-wise change in angle-of-attack. The perceived velocity vector of panel i becomes,

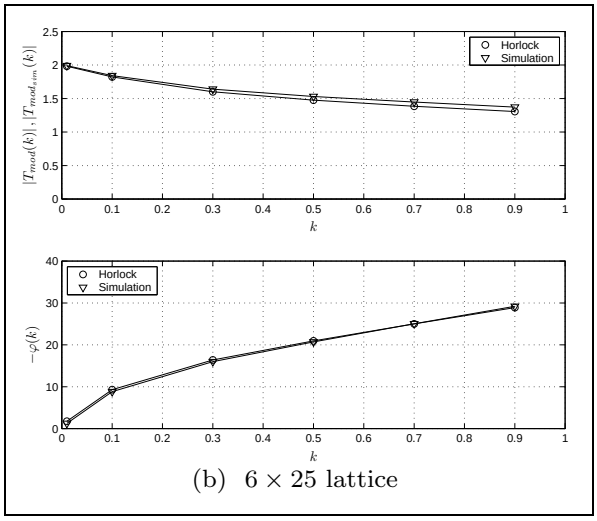
$$\underline{Q}_{p_i}(t_n) = \begin{bmatrix} U_{p_i}(t_n) \\ V_{p_i}(t_n) \\ W_{p_i}(t_n) \end{bmatrix} = \begin{bmatrix} U_\infty \\ 0 \\ w \end{bmatrix} \tag{4.61}$$

In both equations (4.60) and (4.61), the perturbation velocity w is constant.

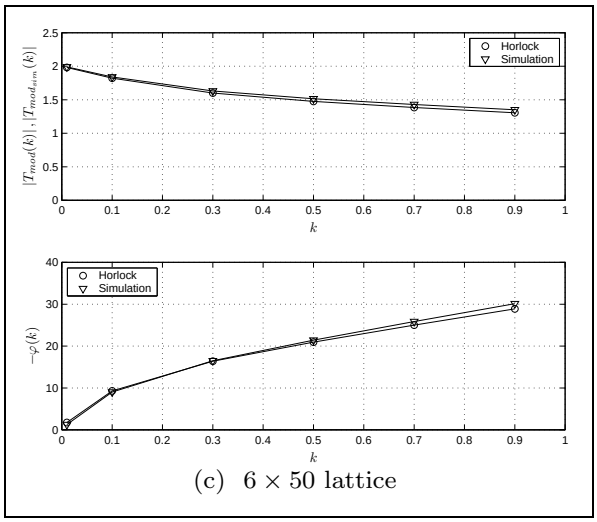
The time-domain result of the non-dimensional lift-coefficient $C_L(t)$ is divided by the steady-state coefficient $C_L(t \to \infty)$ to obtain the simulated Wagner function, or $\Phi_{sim}(t) = \left. \frac{C_L(t)}{C_L(t \to \infty)} \right|_{t>0}$. Note that Wagner's function is usually given as a function of non-dimensional time, or in semi-chords traveled $s = \frac{2Q_\infty t}{\bar{c}}$, or $\Phi_{sim}(s)$. In figure 4.19 for several discretization times Δt the simulated indicial responses are shown for the aerodynamic grids depicted in figure 4.15. Also, R.T. Jones' approximation of Wagner's function (see references [16, 17]) is presented in figure 4.19. The analytical result of R.T. Jones' approximation of Wagner's function is given in equation (4.16). For all configurations the simulated indicial-functions show a good correlation with the analytical result provided by R.T. Jones for $t > 0$. Also note that, contrary to the Jones approximation, the unsteady LPF method simulates the "added mass" effect, resulting in large values of the simulated Wagner function $\Phi_{sim}(s)$ for $s = 0$.



(a) 6×10 lattice

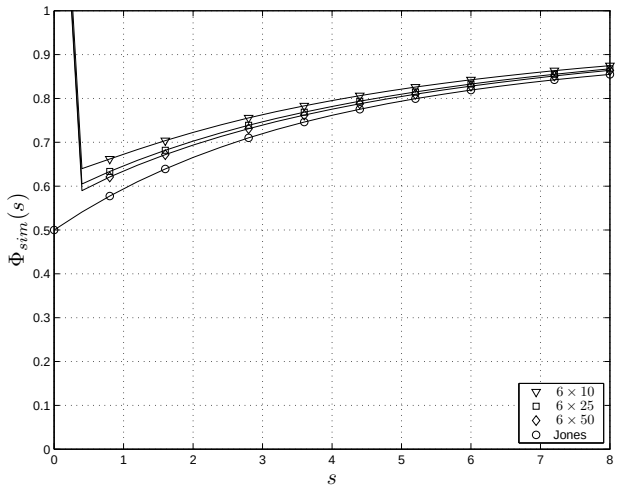


(b) 6×25 lattice

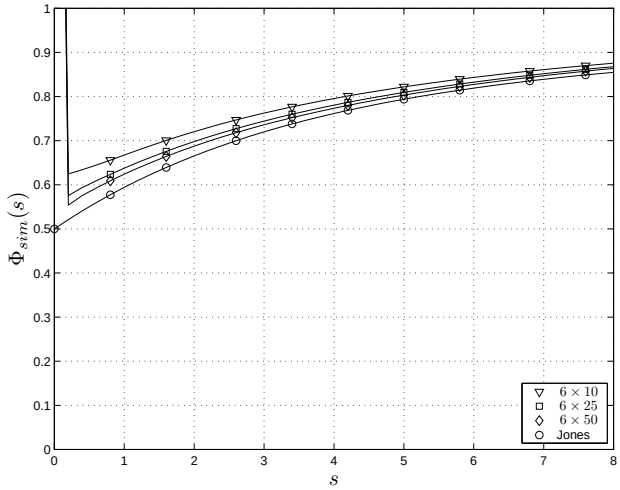


(c) 6×50 lattice

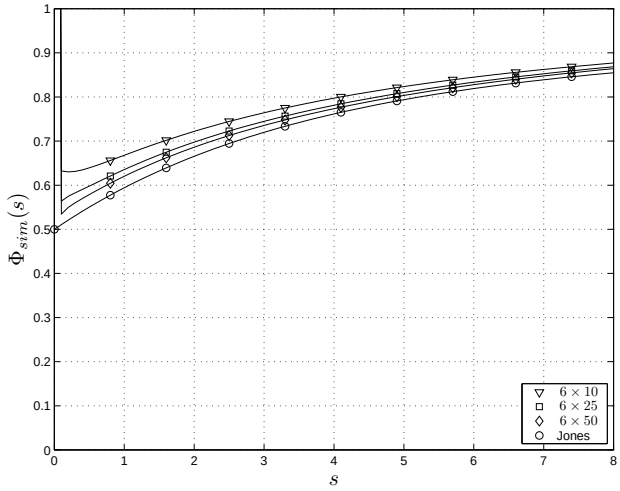
Figure 4.18: Magnitude and phase of the Modified Horlock function, and the magnitude and phase of the simulated Modified Horlock function for an AR=100 wing, NACA 0002 aerofoil, for several aerodynamic grids.



(a) $\Delta t = 0.2 \ \frac{c}{Q_\infty}$



(b) $\Delta t = 0.1 \ \frac{c}{Q_\infty}$



(c) $\Delta t = 0.05 \ \frac{c}{Q_\infty}$

Figure 4.19: Simulated indicial functions $\Phi_{sim}(s)$ for several discretization times Δt and several aerodynamic grids, including Jones approximation of Wagner's function.

4.5 Remarks

In this chapter, it has been shown that the unsteady LPF method captures the analytical functions according to Theodorsen, Sears, Horlock and Wagner. The theory will now be used to simulate aircraft responses in terms of both non-dimensional aerodynamic forces and moments due to both arbitrary aircraft motions and atmospheric turbulence inputs. In chapter 5, the aircraft motion perturbations will be defined, as well as both the one- and two-dimensional atmospheric turbulence inputs. For these perturbations, the prescribed source-strength and the configuration panels' perceived velocity vector will be given. Furthermore, the procedure for calculating both stability- and gust derivatives will be given. These derivatives will hold for the Stability Frame of Reference $\mathcal{F}_S$.

Part III

A Linearized Potential Flow Application

Chapter 5

Aircraft motion perturbations and the atmospheric turbulence inputs

5.1 Introduction

In chapters 3 and 4 the Linearized Potential Flow (LPF) method and the unsteady LPF method for simulating the (time-dependent) aerodynamic forces and moments acting on an arbitrary configuration have been discussed, respectively. In this chapter, the definition of specific aircraft motion perturbations and atmospheric turbulence inputs for the simulation of these aerodynamic forces and moments is given.

The aerodynamic response will be given in terms of non-dimensional aerodynamic force and moment coefficients. The steady aerodynamic response to stationary aircraft motion perturbations will eventually result in the so-called "steady stability derivatives". These derivatives are valid for the Stability Frame of Reference $\mathcal{F}_S$ in which the equations of motion are modeled, see appendix I. The considered stability derivatives are given with respect to the aircraft motion degrees of freedom, which include stationary perturbations in airspeed, side-slip-angle, angle-of-attack, roll-rate, pitch-rate and yaw-rate. For an assumed trim condition (see chapter 6), these steady stability derivatives are constant.

Next to the steady stability derivatives, the so-called "unsteady stability derivatives" are required for the simulation of the aircraft's equations of motion. Estimating these unsteady stability derivatives, such as $C_{Z_{\dot{\alpha}}}$, $C_{m_{\dot{\alpha}}}$, $C_{Y_{\dot{\beta}}}$, $C_{\ell_{\dot{\beta}}}$ and $C_{n_{\dot{\beta}}}$, requires a time-domain approach. These derivatives are obtained from time-domain simulations resulting in the time-dependent response of aerodynamic force and moment coefficients due to isolated, and prescribed, harmonically varying inputs such as angle-of-attack and side-slip-angle. For a number of reduced frequencies, the time-dependent aerodynamic force and moment

coefficients will be calculated due to these inputs. From both the outputs (the aerodynamic force and moment responses) and the inputs (the harmonically varying angle-of-attack or side-slip-angle) for each reduced frequency the frequency-dependent steady and frequency-dependent unsteady stability derivative is obtained using a least squares fit (see appendix E). These derivatives allow the aerodynamic forces and moments' response to inputs to be given as frequency-response data.
Next to the unsteady stability derivatives, the calculation of both steady and unsteady gust derivatives will also be described in this chapter. These derivatives are also obtained from time-domain simulations resulting in the time-dependent response of aerodynamic force and moment coefficients due to isolated, and prescribed, harmonically varying gust inputs. These gust derivatives also allow the aerodynamic forces and moments' response to gust inputs to be given as a frequency-response.

As an overview of this chapter, in section 5.2 the aircraft motion perturbations are described for the Aerodynamic Frame of Reference $\mathcal{F}_{aero}$. They will include stationary perturbations and harmonic perturbations as a function of the reduced frequency $k = \frac{\omega \bar{c}}{2Q_\infty}$. Simulating both the stationary and the unsteady aerodynamic response to aircraft motions, the degrees of freedom considered here will include translational perturbations such as surge, sway and heave. The stationary simulations will also include rotational perturbations such as rolling, pitching and yawing motions. In addition to chapters 3 and 4, the aircraft motion perturbations in the frame $\mathcal{F}_{aero}$ will be defined in terms of the configuration panel perceived velocity vector, $\underline{Q}_{p_i}$, and its corresponding prescribed source-strength distribution, $\sigma_i = -\underline{n}_i \cdot \underline{Q}_{p_i}$, with $\underline{n}_i$ the i-th panel normal vector, $i = 1 \cdots N_B$, and N_B the number of configuration panels.
In section 5.3 the (harmonic) atmospheric turbulence inputs will be defined for the frame $\mathcal{F}_{aero}$. They are also given as a function of the reduced frequency k and will include atmospheric turbulence velocity components along $\mathcal{F}_{aero}$'s axes, that is longitudinal gusts, lateral gusts and vertical gusts. Both one-dimensional (1D) atmospheric turbulence (for which the atmospheric turbulence velocity components are only allowed to vary along the aircraft's recti-linear flightpath) and two-dimensional (2D) gust inputs (for which the atmospheric turbulence velocity components are allowed to vary both along the aircraft's recti-linear flightpath and its span) will be considered. In addition to chapters 3 and 4, the atmospheric turbulence inputs in the frame $\mathcal{F}_{aero}$ will also be defined in terms of the configuration panels perceived velocity vector, $\underline{Q}_{p_i}$, and its corresponding prescribed source-strength distribution, $\sigma_i = -\underline{n}_i \cdot \underline{Q}_{p_i}$.
Using the aircraft motion perturbations and atmospheric turbulence inputs given in sections 5.2 and 5.3, the aerodynamic responses due to these perturbations and inputs will initially result in aerodynamic derivatives and aerodynamic gust derivatives (in frame $\mathcal{F}_{aero}$), respectively. Using both the prescribed perturbations for aircraft motions and the prescribed atmospheric turbulence inputs, in section 5.4 the theory for transforming the derivatives to stability and gust derivatives is given. These stability and gust derivatives are given for the frame $\mathcal{F}_S$. Details of both the frames $\mathcal{F}_{aero}$ and $\mathcal{F}_S$ are given in appendix B.

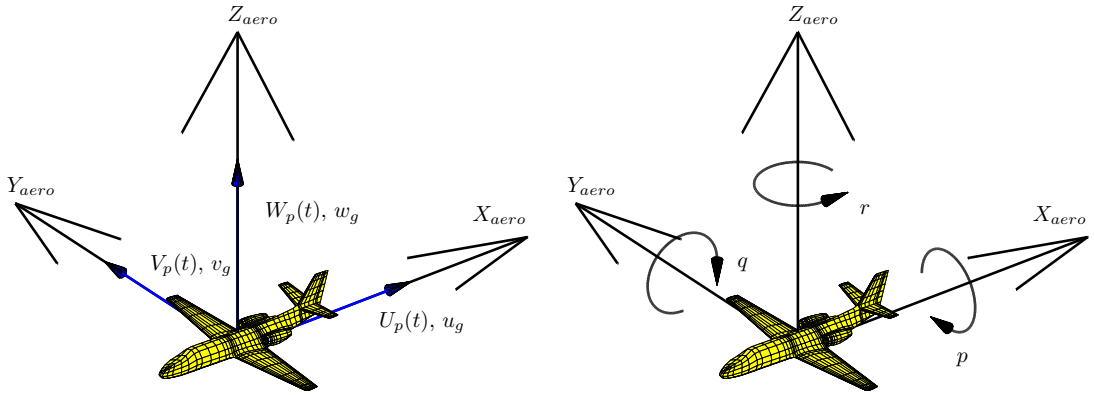


Figure 5.1: The Aerodynamic Frame of Reference $\mathcal{F}_{aero}$, including the positive directions of the perceived aircraft motion velocity vector components $U_p(t)$, $V_p(t)$ and $W_p(t)$, the positive directions of atmospheric turbulence input velocity vector components u_g, v_g and w_g (left), and the Aerodynamic Frame of Reference $\mathcal{F}_{aero}$, including the positive directions of the rotational velocity vector components p, q and r (right).

In section 5.5 the theory for calculating aerodynamic frequency-response data is given. Furthermore, the definitions of the frequency-dependent stability- and gust derivatives is provided.

5.2 Aircraft motion definitions

5.2.1 Translational velocity perturbations

In the frame $\mathcal{F}_{aero}$ the considered translational aircraft motion perturbations include isolated surging, swaying and heaving motions along the X_{aero}-, Y_{aero}- and Z_{aero}-axis, respectively. The definition of the perceived translational velocity components U_p, V_p and W_p along the X_{aero}-, Y_{aero}- and Z_{aero}-axis, respectively, is shown in figure 5.1.
The aerodynamic forces and moments will ultimately be defined as functions of the non-dimensional perturbations $\hat{u} = \frac{u}{Q_\infty}$, $\beta = \frac{v}{Q_\infty}$ and $\alpha = \frac{w}{Q_\infty}$, with u, v and w the perturbation velocity components along the X_{aero}-, Y_{aero}- and Z_{aero}-axis, respectively, and Q_∞ the free stream's velocity magnitude with $Q_\infty = \left|\underline{Q}_\infty\right| = \left|[U_\infty, 0, 0]^T\right|$.

Stationary perturbations

The aerodynamic response to stationary aircraft motion perturbations involves surge, sway and heave. The surging motion along the X_{aero}-axis results in a perturbation velocity vector component u which is constant for all configuration panels. The configuration panels perceived velocity components U_p, V_p and W_p along the X_{aero}-, Y_{aero}- and Z_{aero}-

axis, respectively, become for surging motions,

$$\underline{Q}_{p_i} = \begin{bmatrix} U_{p_i} \\ V_{p_i} \\ W_{p_i} \end{bmatrix} = \begin{bmatrix} Q_\infty + u \\ 0 \\ 0 \end{bmatrix} \tag{5.1}$$

with Q_∞ the magnitude of the undisturbed (free-stream) velocity and $i = 1 \cdots N_B$ with N_B the number of configuration panels.
The swaying motion along the Y_{aero}-axis results in the configuration panels perceived velocity vector components U_p, V_p and W_p along the X_{aero}-, Y_{aero}- and Z_{aero}-axis, respectively, according to,

$$\underline{Q}_{p_i} = \begin{bmatrix} U_{p_i} \\ V_{p_i} \\ W_{p_i} \end{bmatrix} = \begin{bmatrix} Q_\infty \, cos\beta \\ Q_\infty \, sin\beta \\ 0 \end{bmatrix} \tag{5.2}$$

with β the side-slip angle.
Finally, the heaving motion along the Z_{aero}-axis results in the configuration panels perceived velocity vector components U, V and W along the X_{aero}-, Y_{aero}- and Z_{aero}-axis, respectively, according to,

$$\underline{Q}_{p_i} = \begin{bmatrix} U_{p_i} \\ V_{p_i} \\ W_{p_i} \end{bmatrix} = \begin{bmatrix} Q_\infty \, cos\alpha \\ 0 \\ Q_\infty \, sin\alpha \end{bmatrix} \tag{5.3}$$

with α the angle-of-attack.

For the surging, swaying and heaving motion, the prescribed source-strength for LPF simulations results in $\sigma_i = -\underline{n}_i \cdot \underline{Q}_{p_i}$, with $\underline{n}_i$ configuration panel i-th normal in $\mathcal{F}_{aero}$, and $\underline{Q}_{p_i}$ according to equation (5.1), (5.2) or 5.3).

Unsteady perturbations

One of the major advantages using Computational Aerodynamics (CA) techniques for the estimation of both aerodynamic forces and moments due to prescribed perturbations is the decoupling of motions; contrary to flight tests the unsteady aerodynamic response to isolated perturbations along the X_{aero}-, Y_{aero}- and Z_{aero}-axis can be performed.
For the calculation of these unsteady aerodynamic forces and moments, recti-linear flight is assumed; initially the Inertial Frame of Reference $\mathcal{F}_I$ and the frame $\mathcal{F}_{aero}$ coincide. As shown in figure 5.2, the aircraft center of gravity is traveling along the negative X_I-axis with constant airspeed of magnitude $Q_\infty = \left|\underline{Q}_\infty\right| = \left|[U_\infty, V_\infty, W_\infty]^T\right|$, which equals U_∞ with $V_\infty = W_\infty = 0$.

The time-dependent velocity components for unsteady surging motions, swaying motions and heaving motions along the X_{aero}-, Y_{aero}- and Z_{aero}-axis, respectively, are now denoted

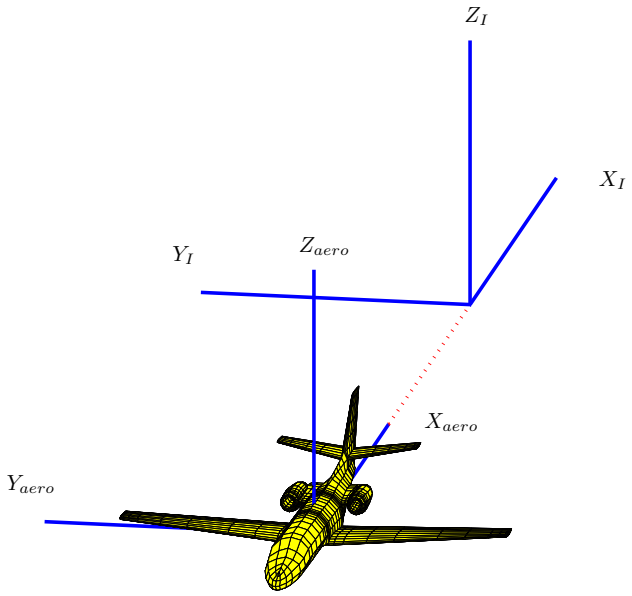


Figure 5.2: The Aerodynamic Frame of Reference $\mathcal{F}_{aero}$ and the Inertial Frame of Reference $\mathcal{F}_I$ as used for recti-linear flightpath simulations.

as $u(t)$, $v(t)$ and $w(t)$. These time-dependent components are harmonic and, for example, an arbitrary perturbation $p(t)$ is written as,

$$p(t) = p_{max}\ sin\,(\omega\ t) \tag{5.4}$$

with p_{max} the perturbation's amplitude, ω the perceived circular frequency in $[Rad/sec]$ and t time. Writing equation (5.4) as a function of the reduced frequency $k = \frac{\omega \bar{c}}{2Q_\infty}$, yields,

$$p(t) = p_{max}\ sin\left(\frac{\omega \bar{c}}{2Q_\infty}\frac{2Q_\infty t}{\bar{c}}\right) = p_{max}\ sin\left(k\frac{2Q_\infty t}{\bar{c}}\right) \tag{5.5}$$

with $\bar{c}$ the mean aerodynamic chord. Since the aircraft is assumed to travel along the negative X_I-axis with constant airspeed of magnitude Q_∞, the position of the origin of $\mathcal{F}_{aero}$ in the frame $\mathcal{F}_I$ is written as $X_0(t) = -Q_\infty t = -U_\infty t$, and equation (5.5) becomes,

$$p(t) = -p_{max}\ sin\left(k\frac{2X_0(t)}{\bar{c}}\right) \tag{5.6}$$

Equation (5.6) is used for the definition of a configuration panel perceived velocity vector. For the aircraft motion perturbations, the resulting configuration panels' perceived time-dependent velocity vector components $U_p(t)$, $V_p(t)$ and $W_p(t)$ in the frame $\mathcal{F}_{aero}$ become for surging motions,

$$\underline{Q}_{p_i}(t) = \begin{bmatrix} U_{p_i}(t) \\ V_{p_i}(t) \\ W_{p_i}(t) \end{bmatrix} = \begin{bmatrix} Q_\infty + u(t) \\ 0 \\ 0 \end{bmatrix} \tag{5.7}$$

for the swaying motion,

$$\underline{Q}_{p_i}(t) = \begin{bmatrix} U_{p_i}(t) \\ V_{p_i}(t) \\ W_{p_i}(t) \end{bmatrix} = \begin{bmatrix} Q_\infty \\ v(t) \\ 0 \end{bmatrix} \tag{5.8}$$

and, for the heaving motion,

$$\underline{Q}_{p_i}(t) = \begin{bmatrix} U_{p_i}(t) \\ V_{p_i}(t) \\ W_{p_i}(t) \end{bmatrix} = \begin{bmatrix} Q_\infty \\ 0 \\ w(t) \end{bmatrix} \tag{5.9}$$

The perturbation velocity components $u(t)$, $v(t)$ and $w(t)$ are harmonic, and for discrete-time simulations they are given as, similar to equation (5.6),

$$u_i(t_n) = u_{max}\ sin\left(k\frac{2X_0(t_n)}{\bar{c}}\right) \tag{5.10}$$

$$v_i(t_n) = v_{max}\ sin\left(k\frac{2X_0(t_n)}{\bar{c}}\right) \tag{5.11}$$

and,

$$w_i(t_n) = w_{max}\ sin\left(k\frac{2X_0(t_n)}{\bar{c}}\right) \tag{5.12}$$

respectively, with $t_n = n\Delta t$ discrete-time, $k = \frac{\omega\bar{c}}{2Q_\infty}$ the reduced frequency, $X_0(t_n)$ the time-dependent position of the origin of $\mathcal{F}_{aero}$, O_{aero}, in the frame $\mathcal{F}_I$, i equal to $i = 1 \cdots N_B$ with N_B the number of configuration panels, and u_{max}, v_{max} and w_{max} the amplitude of $u_i(t_n)$, $v_i(t_n)$ and $w_i(t_n)$, respectively. Note that the aircraft motion perturbation velocity components are constant over the aircraft dimensions.
It should be noted that, contrary to the calculation of the steady aerodynamic forces and moments, the total velocity is not kept constant for the unsteady harmonic simulations. The harmonic velocity component perturbations $u(t)$, $v(t)$ and $w(t)$ are kept small with respect to the magnitude of the (free stream) trim airspeed Q_∞, that is $u(t) << Q_\infty$, $v(t) << Q_\infty$ and $w(t) << Q_\infty$, respectively.

The definition of the unsteady perceived translational velocity components $U_p(t)$, $V_p(t)$ and $W_p(t)$ along the X_{aero}-, Y_{aero}- and Z_{aero}-axis, respectively, is given in figure 5.1. Similar to the steady source-strength definition for steady perturbations, for the unsteady perturbations the prescribed source-strength for unsteady LPF simulations results in $\sigma_i(t) = -\underline{n}_i \cdot \underline{Q}_{p_i}(t)$, with $\underline{n}_i$ configuration panel i-th normal in the frame $\mathcal{F}_{aero}$ and $\underline{Q}_{p_i}(t)$ according to equation (5.7), (5.8) or (5.9).

5.2.2 Rotational velocity perturbations

For the simulation of the (quasi-) steady aerodynamic forces and moments due to rotational velocity perturbations, the aircraft configuration is again assumed to travel along a recti-linear flightpath with velocity Q_∞. The translational velocity components become,

$$\underline{Q}_{p_i} = \begin{bmatrix} U_{p_i} \\ V_{p_i} \\ W_{p_i} \end{bmatrix} = \begin{bmatrix} Q_\infty \\ 0 \\ 0 \end{bmatrix} \tag{5.13}$$

Including rotational effects, equation (5.13) is written as,

$$\underline{Q}_{p_i} = \begin{bmatrix} U_{p_i} \\ V_{p_i} \\ W_{p_i} \end{bmatrix} = \begin{bmatrix} Q_\infty \\ 0 \\ 0 \end{bmatrix} + \underline{\Omega} \times \begin{bmatrix} x_{col_i} \\ y_{col_i} \\ z_{col_i} \end{bmatrix} \tag{5.14}$$

with $\underline{\Omega}$ the vector of (isolated) rotational velocity components $\underline{\Omega} = [p, 0, 0]^T$, $\underline{\Omega} = [0, q, 0]^T$, or $\underline{\Omega} = [0, 0, r]^T$, and $[x_{col_i}, y_{col_i}, z_{col_i}]^T$ the panel collocation point position in the frame $\mathcal{F}_{aero}$ with $i = 1 \cdots N_B$ and N_B the number of configuration panels.

The definition of the rotational velocity components p, q and r along the X_{aero}-, Y_{aero}- and Z_{aero}-axis, respectively, is shown in figure 5.1. It should be noted that the rotational velocity components are constant, resulting in quasi-steady aerodynamic results.

Similar to the source-strength definition for steady perturbations, for the rotational velocity perturbations the prescribed source-strength for LPF simulations results in $\sigma_i = -\underline{n}_i \cdot \underline{Q}_{p_i}$, with $\underline{n}_i$ configuration panel i-th normal in $\mathcal{F}_{aero}$ and $\underline{Q}_{p_i}$ according to equation (5.14).

5.3 Atmospheric turbulence input definitions

5.3.1 Introduction

For the simulation of the time-dependent aerodynamic response to isolated atmospheric turbulence inputs, the configuration is also assumed to travel along a recti-linear flightpath, see also figure 5.2. The aircraft center of gravity is traveling along the negative X_I-axis with constant speed $Q_\infty = U_\infty$, and $V_\infty = W_\infty = 0$. The atmospheric turbulence inputs will include isolated longitudinal gusts u_g, lateral gusts v_g, and vertical gusts w_g, along the X_{aero}-, Y_{aero}- and Z_{aero}-axis, respectively. The definition of the perceived gust velocity components u_g, v_g and w_g in the frame $\mathcal{F}_{aero}$, is shown in figure 5.1.

The (isolated) atmospheric turbulence-fields will be harmonic and are fixed in the frame $\mathcal{F}_I$, with the aircraft traveling through them. As an example, in figure 5.3 the situation is given for a 1D harmonic vertical gust field with spatial wave-length λ_x. At $t = 0$ both the frames $\mathcal{F}_{aero}$ and $\mathcal{F}_I$ coincide. For time-steps $t > 0$ the aircraft is traveling along the

negative X_I-axis encountering the prescribed harmonic gust field. Although the situation is depicted for a 1D harmonic vertical gust field, it is representative for all atmospheric turbulence inputs, both 1D and 2D, considered in this thesis.

5.3.2 1D Atmospheric gust fields

The 1D atmospheric turbulence inputs will include isolated longitudinal gusts, u_g, lateral gusts, v_g, and vertical gusts, w_g, along the X_{aero}-, Y_{aero}- and Z_{aero}-axis, respectively. As an example, both a 1D vertical gust field and a 1D lateral gust field with spatial wave-length λ_x are presented in figure 5.4. In this figure the vertical gust w_g and the lateral gust v_g are only allowed to vary along the flightpath and they are assumed constant over the wingspan. Furthermore, it should be noted that the 1D vertical gust field is representative for 1D longitudinal gust fields u_g. Also, figure 5.4 is representative for the situation at $t = 0$ whith both the frames $\mathcal{F}_I$ and $\mathcal{F}_{aero}$ coinciding. For a series of the spatial wave-length values λ_x, in figure 5.5 1D vertical gust fields and 1D lateral gust fields are shown.

For longitudinal gusts u_g the resulting configuration panel perceived time-dependent velocity components $U_{p_i}(t)$, $V_{p_i}(t)$ and $W_{p_i}(t)$ in the frame $\mathcal{F}_{aero}$ become,

$$\underline{Q}_{p_i}(t) = \begin{bmatrix} U_{p_i}(t) \\ V_{p_i}(t) \\ W_{p_i}(t) \end{bmatrix} = \begin{bmatrix} Q_\infty + u_g(t) \\ 0 \\ 0 \end{bmatrix} \tag{5.15}$$

For lateral gusts v_g these perceived velocity components become,

$$\underline{Q}_{p_i}(t) = \begin{bmatrix} U_{p_i}(t) \\ V_{p_i}(t) \\ W_{p_i}(t) \end{bmatrix} = \begin{bmatrix} Q_\infty \\ v_g(t) \\ 0 \end{bmatrix} \tag{5.16}$$

Finally, for vertical gusts w_g these perceived velocity components become,

$$\underline{Q}_{p_i}(t) = \begin{bmatrix} U_{p_i}(t) \\ V_{p_i}(t) \\ W_{p_i}(t) \end{bmatrix} = \begin{bmatrix} Q_\infty \\ 0 \\ w_g(t) \end{bmatrix} \tag{5.17}$$

Similar to the aircraft motion unsteady velocity component perturbations $u(t)$, $v(t)$ and $w(t)$, the 1D atmospheric turbulence velocity components $u_g(t)$, $v_g(t)$ and $w_g(t)$ are harmonic. However, contrary to the aircraft motion perturbations, these 1D atmospheric turbulence velocity components $u_g(t)$, $v_g(t)$ and $w_g(t)$ vary along the aircraft flightpath (but are constant over the wingspan) and, similar to equation (5.6), they are given as,

$$u_{g_i}(t_n) = u_{g_{max}} \; sin\left(k\frac{2X_{col_i}(t_n)}{\bar{c}}\right) \tag{5.18}$$

$$v_{g_i}(t_n) = v_{g_{max}} \; sin\left(k\frac{2X_{col_i}(t_n)}{\bar{c}}\right) \tag{5.19}$$

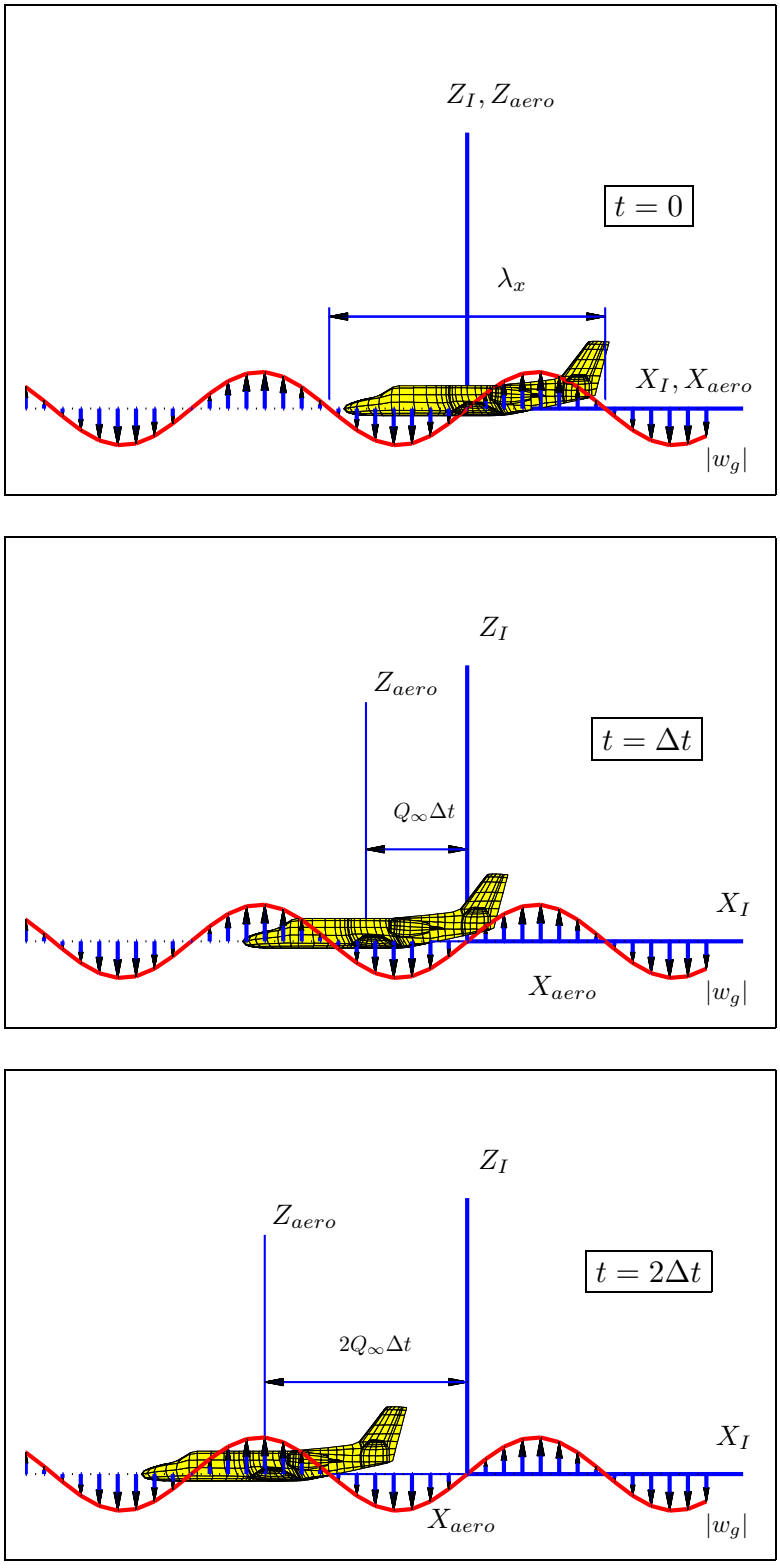


Figure 5.3: An aircraft traveling through a harmonically varying vertical gust field as a function of time.

and,

$$w_{g_i}(t_n) = w_{g_{max}}\ sin\left(k\frac{2X_{col_i}(t_n)}{\bar{c}}\right) \tag{5.20}$$

respectively, with $t_n = n\Delta t$ discrete-time, $k = \frac{\omega\bar{c}}{2Q_\infty}$ the reduced frequency, $X_{col_i}(t_n)$ the time-dependent position of all collocation points in the frame $\mathcal{F}_I$, i equal to $i = 1 \cdots N_B$ with N_B the number of configuration panels, and $u_{g_{max}}$, $v_{g_{max}}$ and $w_{g_{max}}$ the amplitude of $u_g(t_n)$, $v_g(t_n)$ and $w_g(t_n)$, respectively. It should be noted that the perceived circular frequency ω can be written as $\omega = \frac{\Omega_x}{Q_\infty}$, with $\Omega_x = \frac{2\pi}{\lambda_x}$ the atmospheric turbulence input spatial frequency along the X_I-axis. Using this relationship, the definition of the reduced frequency k for atmospheric turbulence simulations becomes,

$$k = \frac{\omega\bar{c}}{2Q_\infty} = \frac{\Omega_x\bar{c}}{2} \tag{5.21}$$

For time-domain simulations, the harmonic atmospheric turbulence velocity components $u_g(t)$, $v_g(t)$ and $w_g(t)$ are kept small with respect to the magnitude of the free-stream trim airspeed Q_∞, that is $u_g(t) << Q_\infty$, $v_g(t) << Q_\infty$ and $w_g(t) << Q_\infty$, respectively.

Similar to the source-strength definition for the unsteady aircraft motion perturbations, for the unsteady atmospheric turbulence input simulations it becomes $\sigma_i(t) = -\underline{n}_i \cdot \underline{Q}_{p_i}(t)$ with $\underline{n}_i$ the $i-th$ configuration panel normal in the frame $\mathcal{F}_{aero}$ and $\underline{Q}_{p_i}(t)$ according to equation (5.15), (5.16) or (5.17).

The atmospheric turbulence-induced aerodynamic forces and moments will ultimately be defined as functions of the non-dimensional inputs $\hat{u}_g = \frac{u_g}{Q_\infty}$, $\beta_g = \frac{v_g}{Q_\infty}$ and $\alpha_g = \frac{w_g}{Q_\infty}$, with u_g, v_g and w_g the atmospheric turbulence velocity components along the X_{aero}-, Y_{aero}- and Z_{aero}-axis, respectively, and Q_∞ the free stream velocity magnitude.

5.3.3 2D Atmospheric gust fields

In this thesis 2D isolated longitudinal gusts u_g, lateral gusts v_g, and vertical gusts w_g, are considered as well. The definition of the perceived gust velocity components u_g, v_g and w_g along the X_{aero}-, Y_{aero}- and Z_{aero}-axis, respectively, is shown in figure 5.1.
As an example, both a symmetrical 2D vertical gust field ánd an anti-symmetrical 2D vertical gust field w_g with spatial wave-length values λ_x and λ_y are depicted in figure 5.6. The vertical gust field is allowed to vary both along the flightpath and over the wingspan. Furthermore, it should be noted that the depicted 2D vertical gust field is representative for both 2D longitudinal gust fields u_g and 2D lateral gust fields v_g. Also, figure 5.6 is representative for the situation at $t = 0$ whith both the frames $\mathcal{F}_I$ and $\mathcal{F}_{aero}$ coinciding. For a series of the spatial wave-length values λ_y in figure 5.7 the magnitude of both symmetrical and anti-symmetrical 2D vertical gust fields are shown.

The expressions for the resulting configuration panel perceived time-dependent velocity components $U_p(t)$, $V_p(t)$ and $W_p(t)$ in $\mathcal{F}_{aero}$ are similar to the ones obtained previously

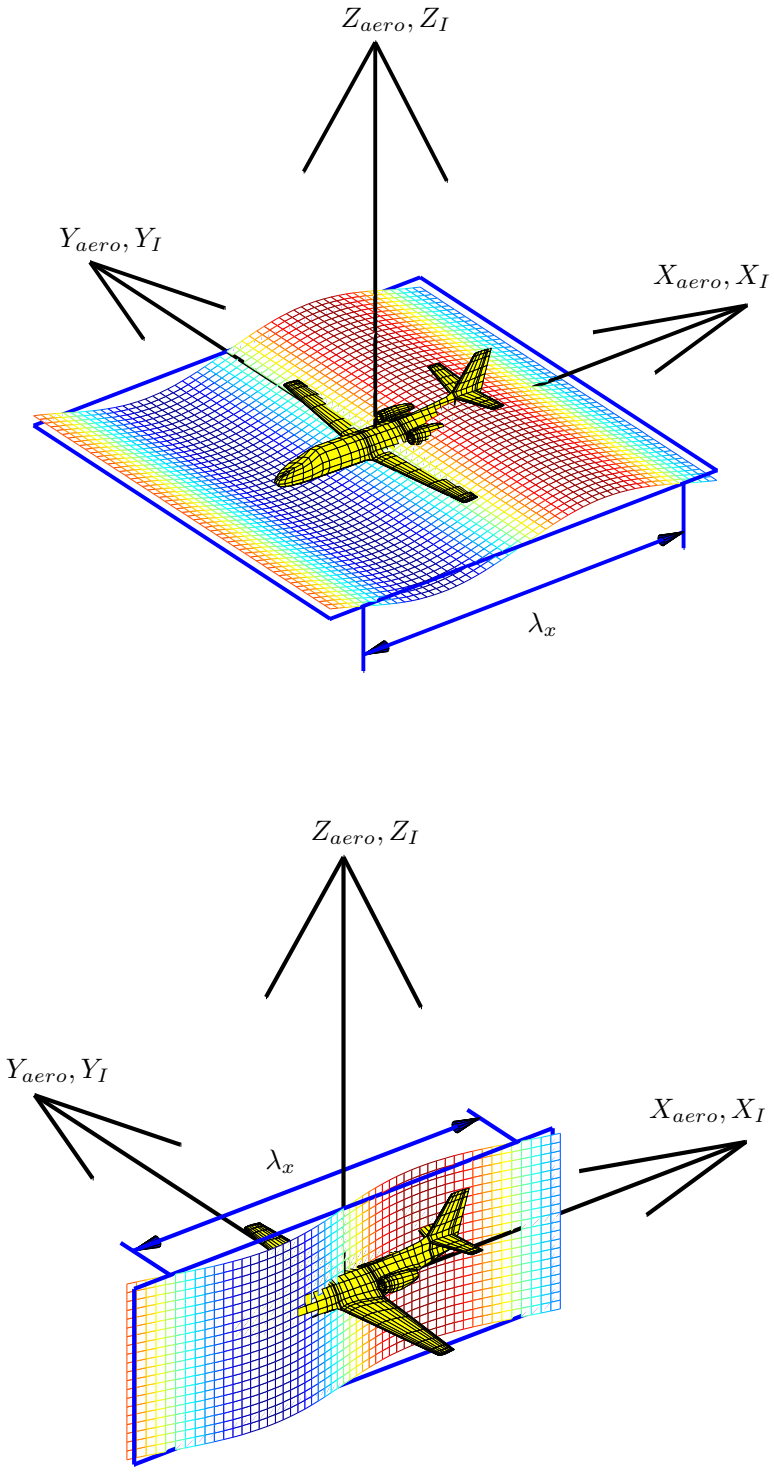


Figure 5.4: A symmetrical harmonic 1D gust field w_g (top), and an asymmetrical harmonic 1D gust field v_g (bottom), with both reference frames $\mathcal{F}_{aero}$ and $\mathcal{F}_I$ coinciding at $t = 0$.

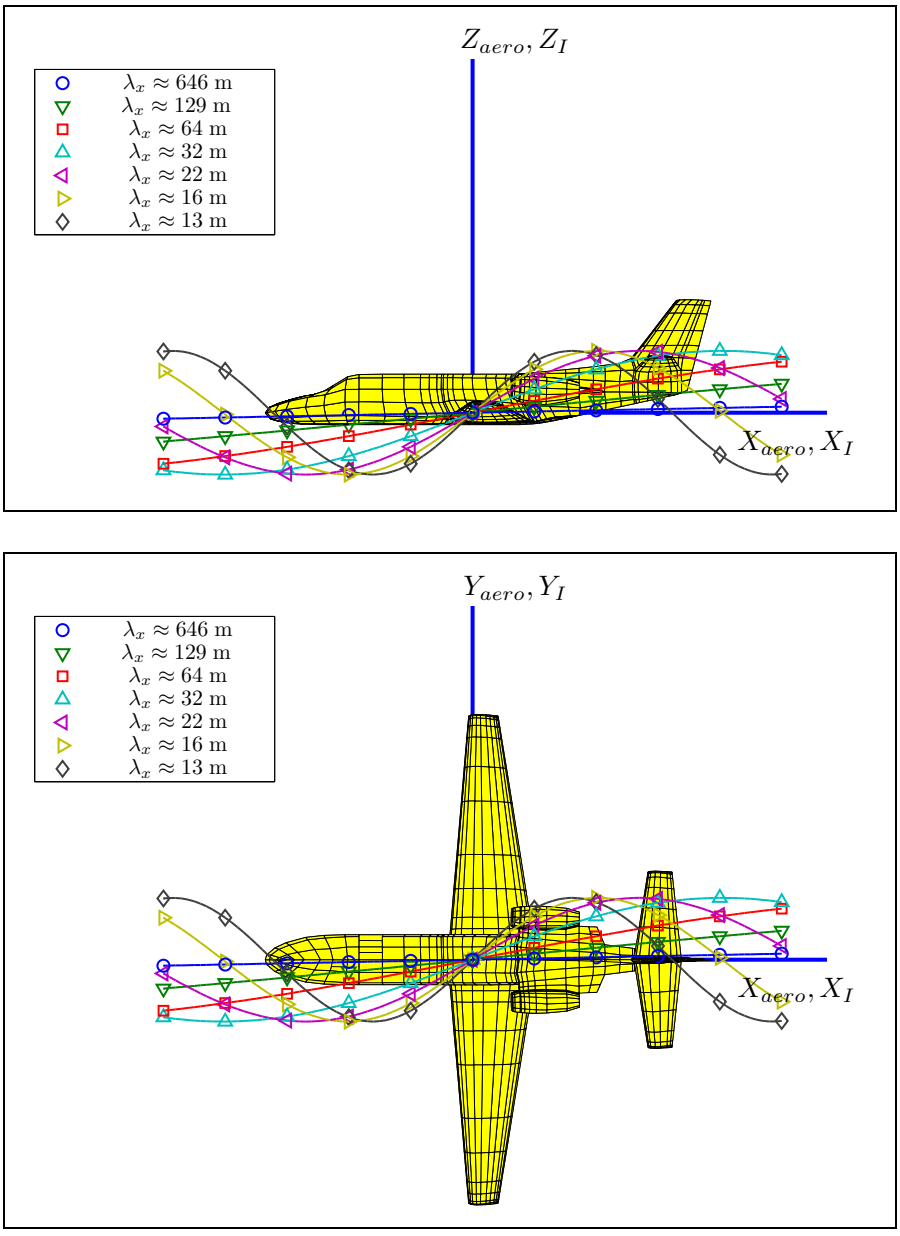


Figure 5.5: Magnitude of both a symmetrical harmonic 1D gust field w_g (top), and an asymmetrical harmonic 1D gust field v_g (bottom), for gust fields of several spatial wave-length values λ_x, with both reference frames $\mathcal{F}_{aero}$ and $\mathcal{F}_I$ coinciding at $t = 0$.

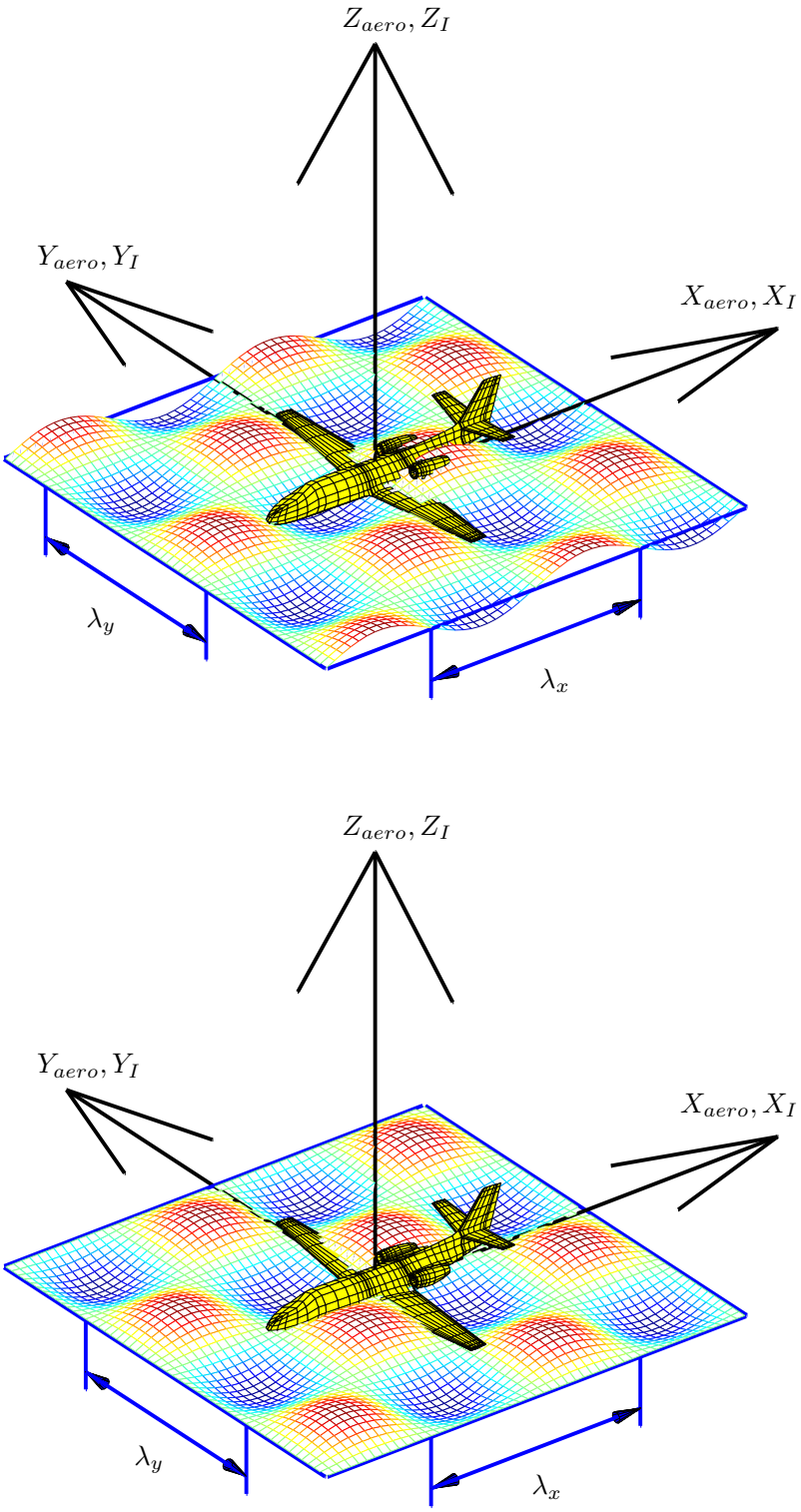


Figure 5.6: A symmetrical harmonic 2D gust field w_g (top) and an anti-symmetrical harmonic 2D gust field w_g (bottom), with both reference frames $\mathcal{F}_{aero}$ and $\mathcal{F}_I$ coinciding at $t = 0$.

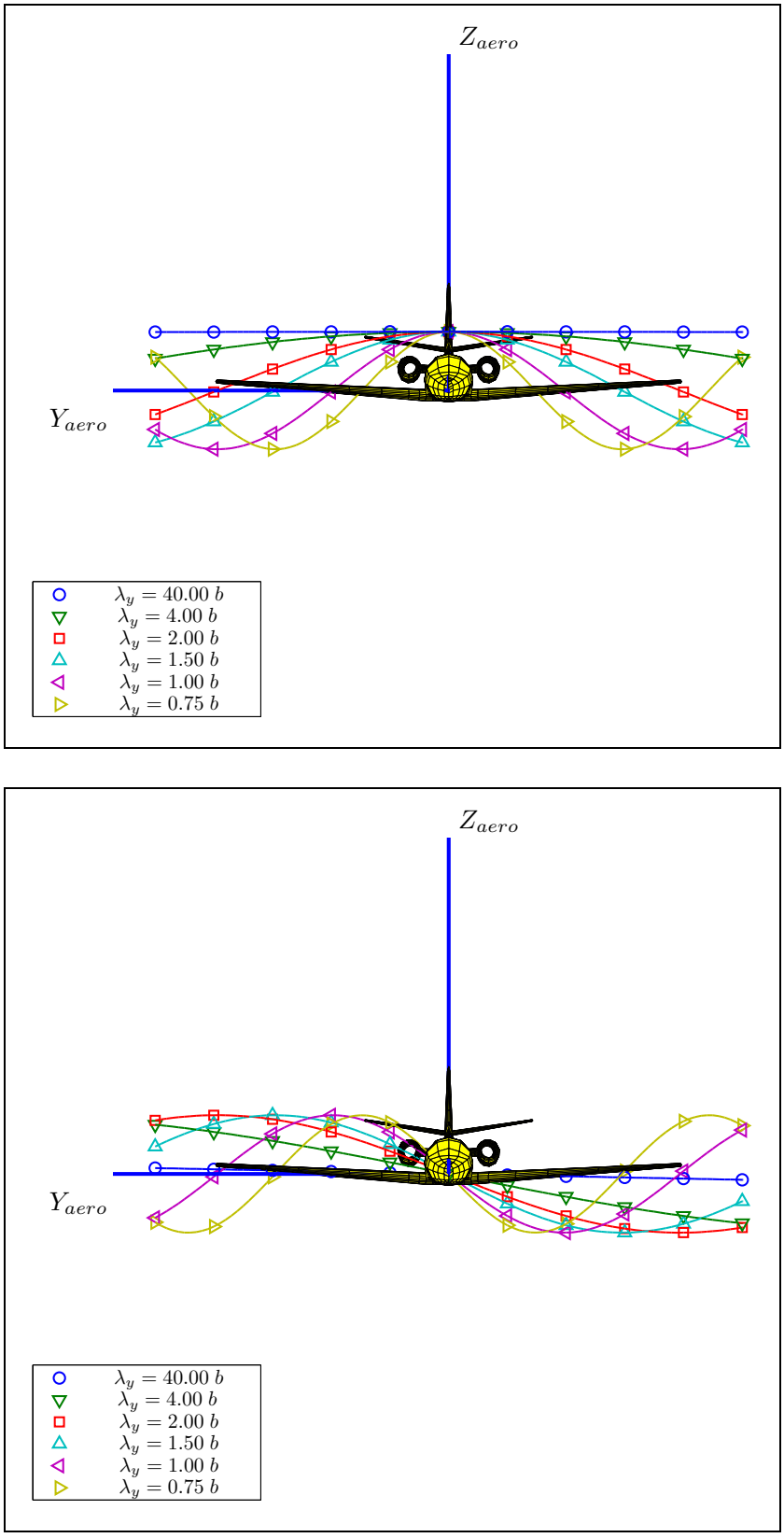


Figure 5.7: Magnitude of both a symmetrical harmonic 2D gust field w_g (top), and an anti-symmetrical harmonic 2D gust field w_g (bottom), for gust fields of several spatial wave-length values λ_y.

for 1D atmospheric turbulence, see equations (5.15), (5.16) and (5.17). For the calculation of both the aerodynamic forces and moments, the 2D atmospheric turbulence velocity components $u_g(t,\Omega_y)$, $v_g(t,\Omega_y)$ and $w_g(t,\Omega_y)$ are also harmonic, with $\Omega_y = \frac{2\pi}{\lambda_y}$ the spatial frequency along the Y_I-axis. Thus, these velocity components now vary both along the aircraft flightpath and over the wingspan. For symmetrical 2D gust fields the components are written as,

$$u_{g_{sym_i}}(t_n,\Omega_y) = u_{g_{max}}\ sin\left(k\frac{2X_{col_i}(t_n)}{\bar{c}}\right)\ cos\left(\Omega_y\ Y_{col_i}(t_n)\right) \tag{5.22}$$

$$v_{g_{sym_i}}(t_n,\Omega_y) = v_{g_{max}}\ sin\left(k\frac{2X_{col_i}(t_n)}{\bar{c}}\right)\ sin\left(\Omega_y\ Y_{col_i}(t_n)\right) \tag{5.23}$$

and,

$$w_{g_{sym_i}}(t_n,\Omega_y) = w_{g_{max}}\ sin\left(k\frac{2X_{col_i}(t_n)}{\bar{c}}\right)\ cos\left(\Omega_y\ Y_{col_i}(t_n)\right) \tag{5.24}$$

while for anti-symmetrical 2D gust fields they are given as,

$$u_{g_{asym_i}}(t_n,\Omega_y) = u_{g_{max}}\ sin\left(k\frac{2X_{col_i}(t_n)}{\bar{c}}\right)\ sin\left(\Omega_y\ Y_{col_i}(t_n)\right) \tag{5.25}$$

$$v_{g_{asym_i}}(t_n,\Omega_y) = v_{g_{max}}\ sin\left(k\frac{2X_{col_i}(t_n)}{\bar{c}}\right)\ cos\left(\Omega_y\ Y_{col_i}(t_n)\right) \tag{5.26}$$

and,

$$w_{g_{asym_i}}(t_n,\Omega_y) = w_{g_{max}}\ sin\left(k\frac{2X_{col_i}(t_n)}{\bar{c}}\right)\ sin\left(\Omega_y\ Y_{col_i}(t_n)\right) \tag{5.27}$$

with in equations (5.22) to (5.27), $t_n = n\Delta t$ discrete-time, $k = \frac{\omega\bar{c}}{2Q_\infty} = \frac{\Omega_x\bar{c}}{2}$ the reduced frequency, $\Omega_x = \frac{2\pi}{\lambda_x}$ the spatial frequency along the X_I-axis and $\Omega_y = \frac{2\pi}{\lambda_y}$ the spatial frequency along the Y_I-axis. Further, both $X_{col_i}(t_n)$ and $Y_{col_i}(t_n)$ the time-dependent x and y components of the position of all collocation points in $\mathcal{F}_I$, $i = 1\cdots N_B$ with N_B the number of configuration panels, and $u_{g_{max}}$, $v_{g_{max}}$ and $w_{g_{max}}$ the amplitude of the atmospheric turbulence components $u_{g_{(a)sym}}(t_n,\Omega_y)$, $v_{g_{(a)sym}}(t_n,\Omega_y)$ and $w_{g_{(a)sym}}(t_n,\Omega_y)$, respectively. For the steady-state condition at $t = 0$, in figures 5.8, 5.9 and 5.10 the definition is given of both symmetrical and anti-symmetrical 2D gust fields for the longitudinal, lateral and vertical gust-components, respectively.

Similar to the source-strength definition for the 1D atmospheric turbulence input simulations, it becomes $\sigma_i(t_n,\Omega_y) = -\underline{n}_i \cdot \underline{Q}_{p_i}(t_n,\Omega_y)$ with $\underline{n}_i$ configuration panel i-th normal in $\mathcal{F}_{aero}$ and $\underline{Q}_{p_i}(t_n,\Omega_y)$ similar to equation (5.15), (5.16) or (5.17) and with the now 2D atmospheric turbulence inputs according to equations (5.22) through (5.27).

Also for the 2D atmospheric turbulence inputs, the induced aerodynamic forces and moments will ultimately be defined as functions of the non-dimensional inputs $\hat{u}_g = \frac{u_g}{Q_\infty}$,

$\beta_g = \frac{v_g}{Q_\infty}$ and $\alpha_g = \frac{w_g}{Q_\infty}$, with u_g, v_g and w_g the atmospheric turbulence velocity components along the X_{aero}-, Y_{aero}- and Z_{aero}-axis, respectively, and Q_∞ the free stream velocity magnitude. Similar to the 1D atmospheric turbulence inputs, the 2D atmospheric turbulence velocity components are kept small with respect to the free stream velocity magnitude, thus $u_g(t) << Q_\infty$, $v_g(t) << Q_\infty$ and $w_g(t) << Q_\infty$.

5.4 (Quasi-) Steady stability derivatives

Throughout this thesis the aircraft equations of motion given in the Stability Frame of Reference $\mathcal{F}_S$ are used. Details of the frame $\mathcal{F}_S$ are provided in appendix B, while details concerning the aircraft equations of motion are given in appendix I. The definition of all stability derivatives in the frame $\mathcal{F}_S$ is given in appendix A.
In order to obtain the (quasi-) steady stability derivatives required for the equations of motion, the results obtained in the frame $\mathcal{F}_{aero}$ have to be transformed to the frame $\mathcal{F}_S$. In this section this transformation is given for both translational and rotational perturbations, resulting in the definition of the (quasi-) steady stability derivatives.

Using the theory of chapter 3 and the definitions of the (quasi-) steady aircraft motion perturbations given in section 5.2, aerodynamic derivatives are calculated. These aerodynamic derivatives originally hold for the frame $\mathcal{F}_{aero}$ and they describe the aerodynamic effects in terms of aerodynamic force and moment coefficients due to isolated prescribed aircraft motion perturbations. Aerodynamic derivatives with respect to these stationary perturbations in (non-dimensional) airspeed ($\hat{u} = \frac{u}{Q_\infty}$), side-slip angle ($\beta = \frac{v}{Q_\infty}$), angle-of-attack ($\alpha = \frac{w}{Q_\infty}$), roll-rate ($\frac{pb}{2Q_\infty}$), pitch-rate ($\frac{q\bar{c}}{2Q_\infty}$) and yaw-rate ($\frac{rb}{2Q_\infty}$) will be given. The aerodynamic derivatives for the frame $\mathcal{F}_{aero}$ are calculated by first assuming an initial, or trim-, condition, for which the non-dimensional aerodynamic forces and moments coefficients, $\left[C^a_{X_{trim}}, C^a_{Y_{trim}}, C^a_{Z_{trim}}, C^a_{\ell_{trim}}, C^a_{m_{trim}}, C^a_{n_{trim}}\right]^T$ are calculated, see also chapter 3 (note that the superscript ^{a} refers to Aerodynamic Frame of Reference $\mathcal{F}_{aero}$ results). For a stationary prescribed isolated perturbation, the new aerodynamic coefficients, $[C^a_X, C^a_Y, C^a_Z, C^a_\ell, C^a_m, C^a_n]^T$, are calculated. For example, consider the aerodynamic force coefficient C^a_Z in the frame $\mathcal{F}_{aero}$ due to an angle-of-attack perturbation $\Delta\alpha = \frac{\Delta w}{Q_\infty}$. The aerodynamic derivative is calculated from,

$$C^a_{Z_\alpha} = \frac{\partial C^a_Z}{\partial \alpha} = \frac{C^a_{Z_{pert.}} - C^a_{Z_{trim}}}{\Delta\alpha} \tag{5.28}$$

with $C^a_{Z_\alpha}$ the aerodynamic derivative in the frame $\mathcal{F}_{aero}$, $C^a_{Z_{pert.}}$ the aerodynamic coefficient due to perturbation $\Delta\alpha$ in $\mathcal{F}_{aero}$ and $C^a_{Z_{trim}}$ the aerodynamic coefficient for the trim condition in $\mathcal{F}_{aero}$. From this aerodynamic derivative a stability derivative is obtained which holds for the frame $\mathcal{F}_S$. See also chapter 6, where the stability derivatives for an example aircraft are given.

If aircraft rotations along the axes of reference frames $\mathcal{F}_S$ and $\mathcal{F}_{aero}$ are left out of consideration, the definition of the perturbation velocity components u, v and w (or for that

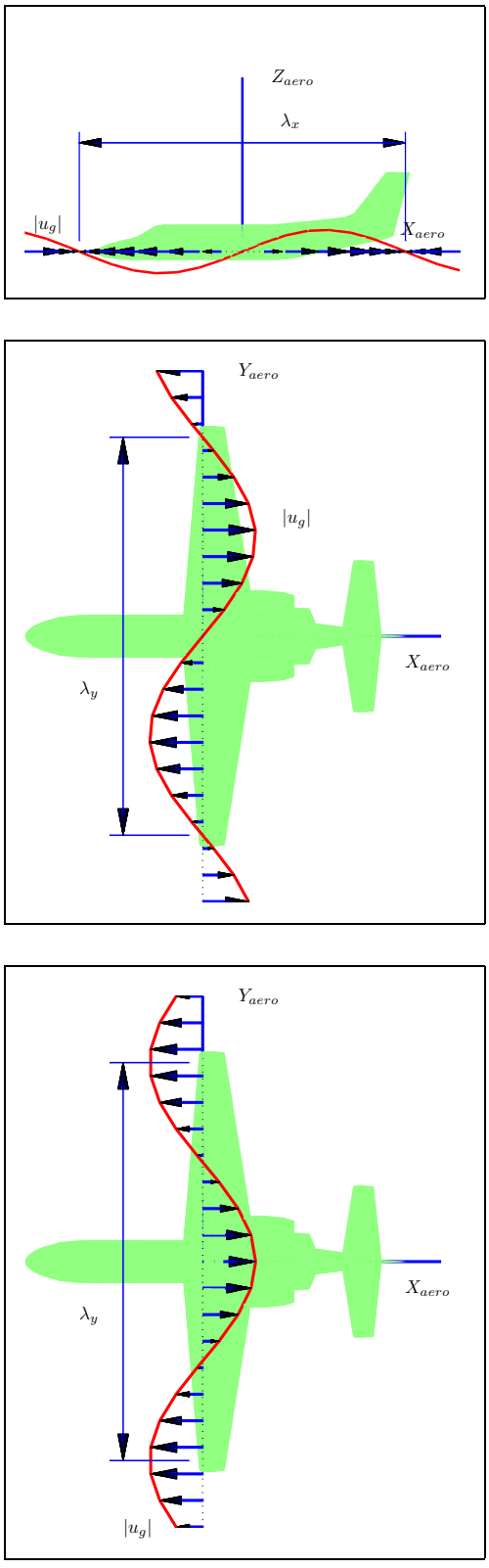


Figure 5.8: An elementary harmonic 2D longitudinal gust field (u_g) varying in the flightpath's direction (top), the magnitude of an anti-symmetrical gust field varying along the Y_{aero}-axis (middle), and the magnitude of a symmetrical gust field varying along the Y_{aero}-axis (bottom).

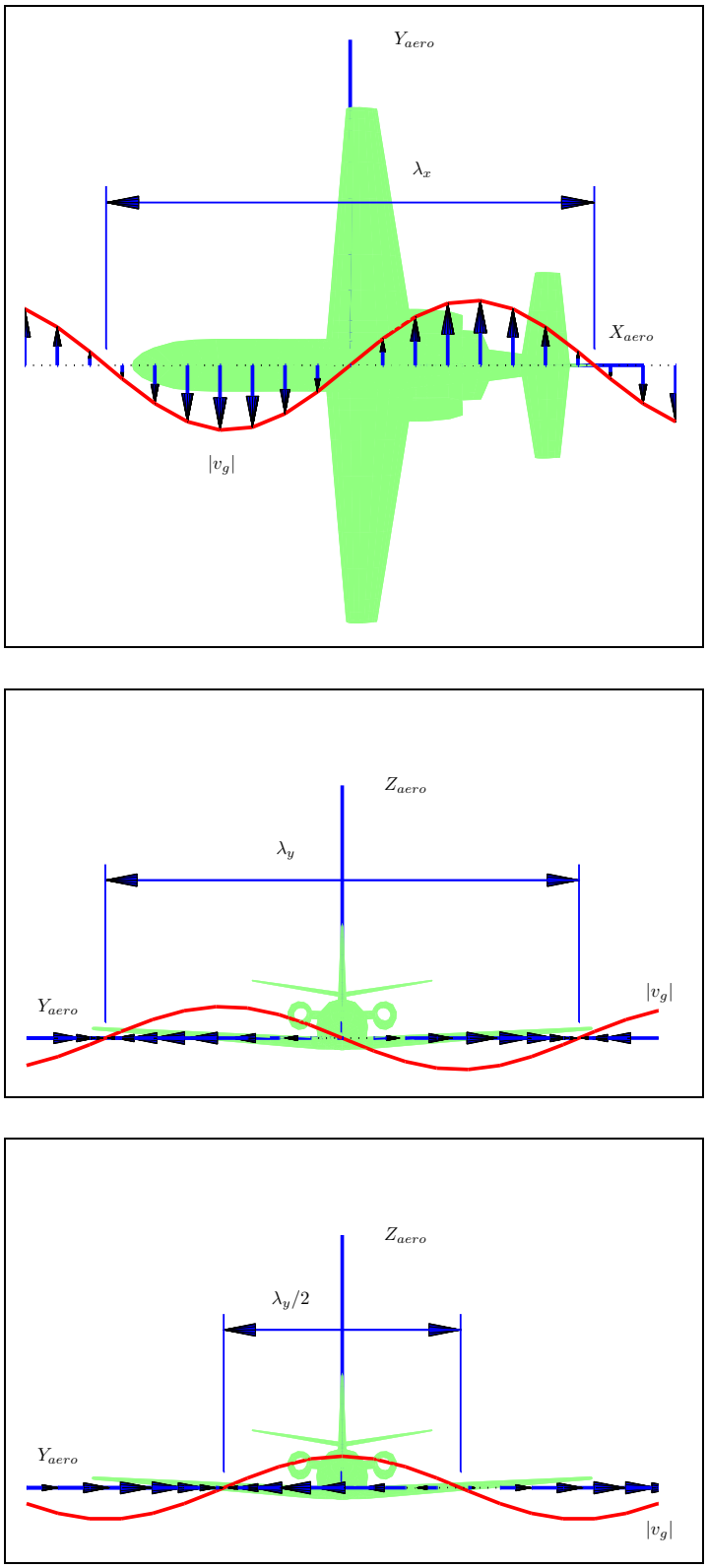


Figure 5.9: An elementary harmonic 2D lateral gust field (v_g) varying in the flightpath's direction (top), the magnitude of a symmetrical gust field varying along the Y_{aero}-axis (middle), and the magnitude of an anti-symmetrical gust field varying along the Y_{aero}-axis (bottom).

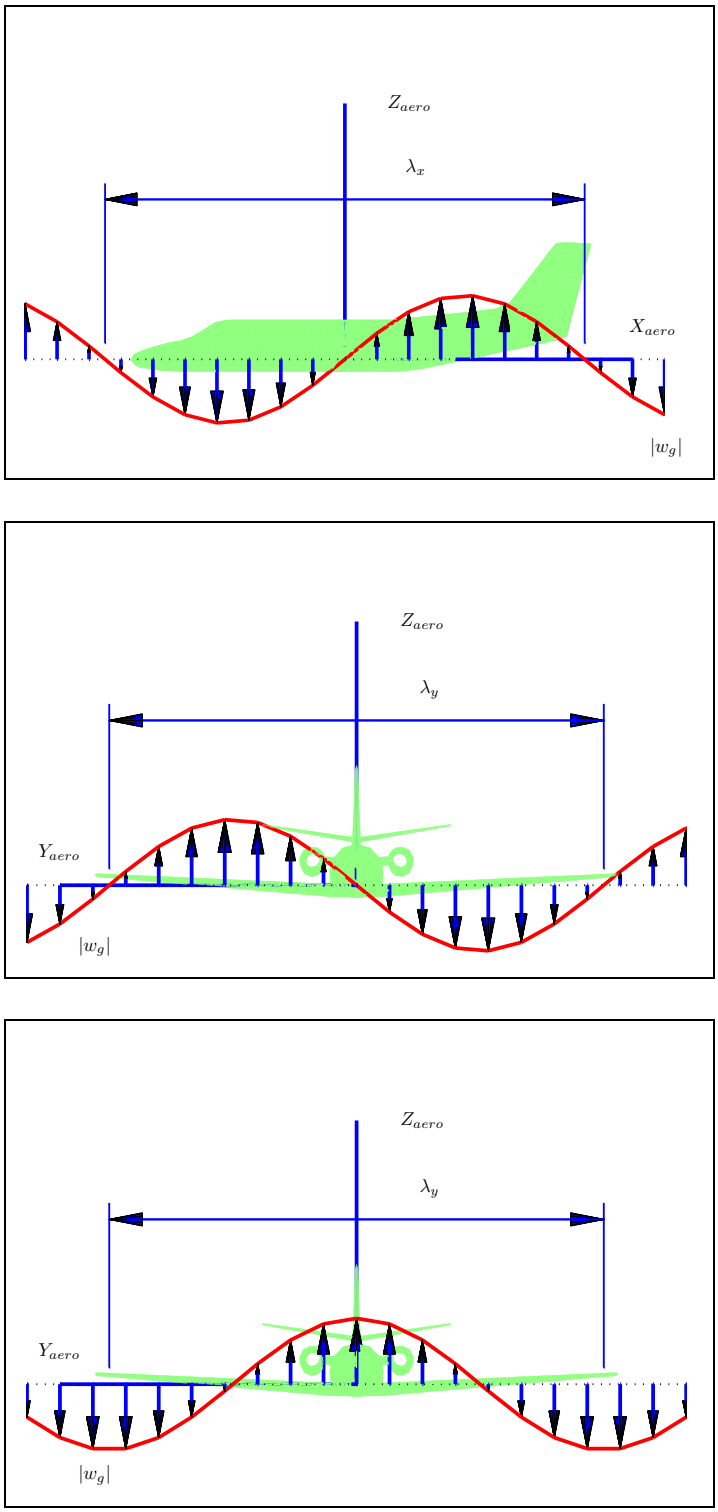


Figure 5.10: An elementary harmonic 2D vertical gust field (w_g) varying in the flightpath's direction (top), the magnitude of an anti-symmetrical gust field varying along the Y_{aero}-axis (middle), and the magnitude of a symmetrical gust field varying along the Y_{aero}-axis (bottom).

matter $\hat{u}$, β and α) along the X_S-, Y_S- and Z_S-axis of the frame $\mathcal{F}_S$, respectively, is shown in figure 5.11. In this figure the definition of the perceived velocity components U_p, V_p and W_p along the X_{aero}-, Y_{aero}- and Z_{aero}-axis of the frame $\mathcal{F}_{aero}$, respectively, is given as well. The perceived velocity components include the perturbation velocity components, see section 5.2. In figure 5.12 the definition of the rotational velocity components p, q and r for both reference frames $\mathcal{F}_S$ and $\mathcal{F}_{aero}$ is given.
Comparing the frame $\mathcal{F}_{aero}$ to the frame $\mathcal{F}_S$, two major differences should be noted. The first is the orientation of the axes; the X_{aero}- and X_S-axes point in opposite direction, resulting in $C_X|_{\mathcal{F}_S} = -C_X^a$. Similarly, the Z_{aero}- and Z_S-axes also point in opposite direction, resulting in $C_Z|_{\mathcal{F}_S} = -C_Z^a$. The Y_{aero}- and Y_S-axis coincide, thus $C_Y|_{\mathcal{F}_S} = C_Y^a$. Both frames of reference $\mathcal{F}_{aero}$ and $\mathcal{F}_S$ have their origin at the aircraft center of gravity.
The second difference between the two reference frames is the definition of both translational and rotational velocity perturbations along their axes. Also, the translational velocity perturbation components u, v and w along the X_S-, Y_S- and Z_S-axis, respectively, are in fact velocity perturbations of the frame of reference $\mathcal{F}_S$ with respect to a steady-state trim speed, while the perturbed velocity components U, V and W are actually perceived velocity components along the X_{aero}-, Y_{aero}- and Z_{aero}-axis, respectively, in the frame $\mathcal{F}_{aero}$. For example, in terms of the aircraft pressure distribution, a positive velocity perturbation u along the X_S-axis in $\mathcal{F}_S$ will result in an equal pressure distribution caused by a positive velocity perturbation u along the X_{aero}-axis in $\mathcal{F}_{aero}$. A similar conclusion can be made for the translational velocity perturbation w and the rotational velocity perturbation q. However, the aerodynamic effect in terms of the pressure distribution caused by a positive velocity perturbation v along the Y_S-axis in $\mathcal{F}_S$ leads to an opposite aerodynamic effect as compared to a positive velocity perturbation v along the Y_{aero}-axis in $\mathcal{F}_{aero}$, with a similar conclusion for both the rotational velocity perturbations p and r.

As an example, in the frame $\mathcal{F}_S$ the aerodynamic derivative, equation (5.28), becomes the stability derivative according to,

$$C_{Z_\alpha}|_{\mathcal{F}_{stab}} = -C_{Z_\alpha}^a \tag{5.29}$$

For both symmetric and asymmetric aircraft motions, the definition of all stability derivatives (which hold for the frame $\mathcal{F}_S$) in terms of the corresponding aerodynamic derivatives (which hold for the frame $\mathcal{F}_{aero}$) is summarized in appendix D, see tables D.1 and D.2. In terms of partial derivatives, the stability derivatives are defined in appendix A, however, they are also summarized in tables D.11 and D.12. Similarly, for both symmetric and asymmetric 1D gust-inputs, the definition of the gust derivatives for the frame $\mathcal{F}_S$ in terms of the corresponding aerodynamic derivatives for $\mathcal{F}_{aero}$ is summarized in tables D.3 and D.4. In terms of partial derivatives, the gust derivatives are defined in tables D.13 and D.14.

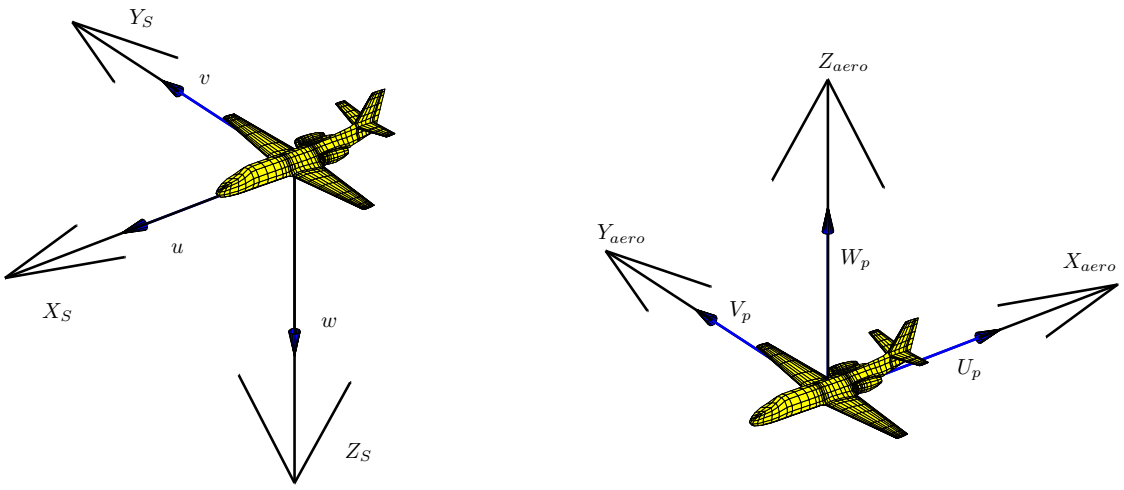


Figure 5.11: The Stability Frame of Reference $\mathcal{F}_S$, including perturbation velocity components $[u, v, w]^T$ (left), and the Aerodynamic Frame of Reference $\mathcal{F}_{aero}$, including the perceived velocity components $[U_p, V_p, W_p]^T$ (right).

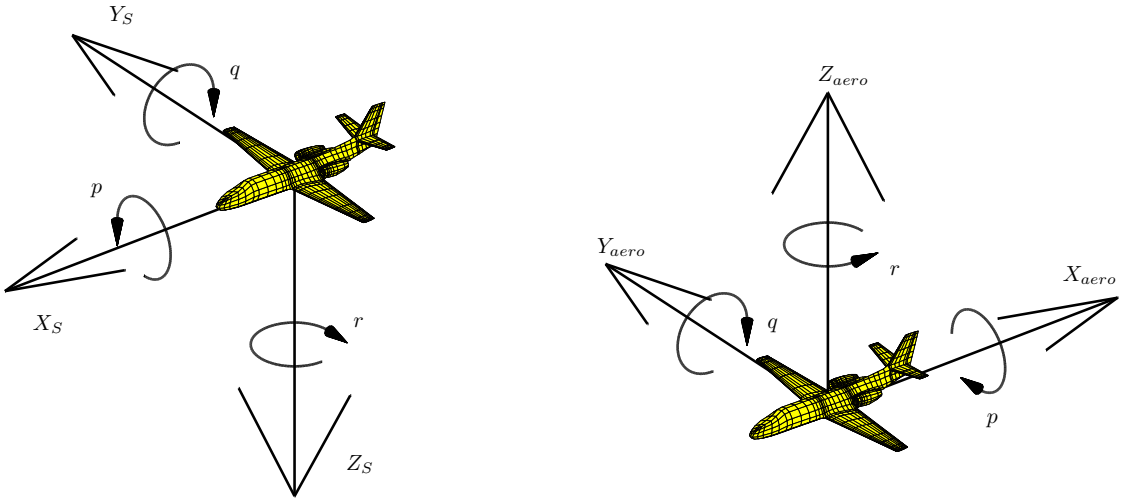


Figure 5.12: The Stability Frame of Reference $\mathcal{F}_S$ (left) and the Aerodynamic Frame of Reference $\mathcal{F}_{aero}$ (right), including the definition of perturbation rotational velocity components $[p, q, r]^T$ (right).

5.5 Aerodynamic frequency-response data

In this thesis, the aircraft time-dependent response in terms of aerodynamic coefficients due to harmonically varying perturbations is considered. These perturbations include surge, sway and heave for the aircraft motions. For atmospheric turbulence inputs they will include responses to both 1D and 2D longitudinal, lateral and vertical gust fields.
For all time-dependent simulations considered in this thesis the aircraft is traveling along a recti-linear flightpath, which is chosen to be along the negative X_I-axis of the Inertial Frame of Reference $\mathcal{F}_I$, see also figure 5.2. For these simulations the steady-state velocity vector in $\mathcal{F}_{aero}$ is written as $\underline{Q}_\infty = [U_\infty, 0, 0]^T$, resulting in $Q_\infty = \left|\underline{Q}_\infty\right| = U_\infty$, with aircraft motion perturbations according to equations (5.10), (5.11), and (5.12). As the 1D atmospheric turbulence inputs are concerned, the perturbations according to equations (5.18), (5.19) and (5.20) are used, while for 2D atmospheric turbulence inputs the perturbations according to equations (5.22) through (5.27) are used.
For a series of the reduced frequency k, the time-dependent response of the aerodynamic coefficients $[C^a_X(t), C^a_Y(t), C^a_Z(t), C^a_\ell(t), C^a_m(t), C^a_n(t)]^T$ due to prescribed harmonically varying aircraft motion perturbations and to prescribed harmonically varying atmospheric turbulence inputs is simulated. For each isolated input (being either an aircraft motion perturbation or a turbulence input) the so-called "Aerodynamic Frequency-Response" is calculated for the aerodynamic force and moment coefficients. Using the harmonically varying input (the perturbation) and the harmonically varying output (the force or moment coefficient, corrected for the result obtained for the trim condition), for each reduced frequency k the results are transformed to the frequency-domain using a least-squares fit-routine. The procedure for transforming the time-domain results to the frequency-domain is given in appendix E. It eventually results in frequency-dependent aerodynamic derivatives.
As an example, the time-domain simulation of the response of the aerodynamic force coefficient $C^a_Z(t)$ due to a harmonically varying isolated aircraft motion perturbation along the Z_{aero}-axis $\alpha(t) = \frac{w(t)}{Q_\infty}$ is considered. Using the procedure from appendix E, for each considered reduced frequency the frequency-response of the aerodynamic force coefficient $C^a_Z(k)$ due the isolated aircraft motion perturbation $\alpha(k) = \frac{w(k)}{Q_\infty}$ is calculated,

$$C^a_Z(k) = \mathcal{C}^a_{\mathcal{Z}_\alpha}(k)\ \alpha(k)\ +\ \mathcal{C}^a_{\mathcal{Z}_{\dot\alpha}}(k)\ \frac{j\omega\alpha(k)\bar{c}}{2Q_\infty} = \mathcal{C}^a_{\mathcal{Z}_\alpha}(k)\ \alpha(k)\ +\ \mathcal{C}^a_{\mathcal{Z}_{\dot\alpha}}(k)\ jk\ \alpha(k) \quad (5.30)$$

with k the reduced frequency $k = \frac{\omega\bar{c}}{2Q_\infty}$, and both $\mathcal{C}^a_{\mathcal{Z}_\alpha}(k)$ and $\mathcal{C}^a_{\mathcal{Z}_{\dot\alpha}}(k)$ the frequency-dependent "*steady aerodynamic derivative*" and the frequency-dependent "*unsteady aerodynamic derivative*", respectively, according to,

$$\mathcal{C}^a_{\mathcal{Z}_\alpha}(k) = \frac{\partial C^a_Z}{\partial\alpha}(k)$$

and,

$$\mathcal{C}^a_{\mathcal{Z}_{\dot\alpha}}(k) = \frac{\partial C^a_Z}{\partial\frac{\dot\alpha\bar{c}}{2Q_\infty}}(k)$$

Note that the aerodynamic derivative $C^a_{Z_\alpha}$ is constant, while the aerodynamic derivative $\mathcal{C}^a_{\mathcal{Z}_\alpha}(k)$ is frequency-dependent. Both the frequency-dependent steady and unsteady aerodynamic derivatives are known from the procedure given in appendix E. The aerodynamic frequency-response is obtained from equation 5.30),

$$H^a_{Z\alpha}(k) = \frac{C^a_Z}{\alpha}(k) = \mathcal{C}^a_{\mathcal{Z}_\alpha}(k) \; + \; \mathcal{C}^a_{\mathcal{Z}_{\dot\alpha}}(k) \; \frac{j\omega\bar{c}}{2Q_\infty} = \mathcal{C}^a_{\mathcal{Z}_\alpha}(k) \;\; + \; \mathcal{C}^a_{\mathcal{Z}_{\dot\alpha}}(k) \; jk \tag{5.31}$$

A similar analysis can be performed for the aerodynamic coefficients' frequency-response to both 1D and 2D atmospheric turbulence inputs. For example, the frequency-response of the aerodynamic force coefficient $C^a_{Z_g}$ due to isolated 2D vertical atmospheric turbulence inputs, $\alpha_g(k,\Omega_y) = \frac{w_g(k,\Omega_y)}{Q_\infty}$, for each reduced frequency k the coefficient $C^a_{Z_g}(k,\Omega_y)$ is written as,

$$C^a_{Z_g}(k,\Omega_y) = \mathcal{C}^a_{\mathcal{Z}_{\alpha_g}}(k,\Omega_y) \; \alpha_g(k,\Omega_y) \; + \; \mathcal{C}^a_{\mathcal{Z}_{\dot\alpha_g}}(k,\Omega_y) \; \frac{j\omega\alpha_g(k,\Omega_y)\bar{c}}{2Q_\infty}$$

or,

$$C^a_{Z_g}(k,\Omega_y) = \mathcal{C}^a_{\mathcal{Z}_{\alpha_g}}(k,\Omega_y) \; \alpha_g(k,\Omega_y) \; + \; \mathcal{C}^a_{\mathcal{Z}_{\dot\alpha_g}}(k,\Omega_y) \; jk \; \alpha_g(k,\Omega_y) \tag{5.32}$$

with $k = \frac{\omega\bar{c}}{2Q_\infty}$ the reduced frequency, $\Omega_y = \frac{2\pi}{\lambda_y}$ the spatial frequency along the Y_I-axis, λ_y the spatial wave-length along the Y_I-axis, $\alpha_g(k,\Omega_y) = \frac{w_g(k,\Omega_y)}{Q_\infty}$ the vertical gust-induced angle-of-attack, $\mathcal{C}^a_{\mathcal{Z}_{\alpha_g}}(k,\Omega_y)$ the frequency-dependent "*steady aerodynamic gust derivative*" and $\mathcal{C}^a_{\mathcal{Z}_{\dot\alpha_g}}(k,\Omega_y)$ the frequency-dependent "*unsteady aerodynamic gust derivative*". Both the steady and unsteady aerodynamic gust derivatives are also known from the procedure given in appendix E, and they are defined as,

$$\mathcal{C}^a_{\mathcal{Z}_{\alpha_g}}(k,\Omega_y) = \frac{\partial C^a_{Z_g}}{\partial \alpha_g}(k,\Omega_y)$$

and,

$$\mathcal{C}^a_{\mathcal{Z}_{\dot\alpha_g}}(k,\Omega_y) = \frac{\partial C^a_{Z_g}}{\partial \frac{\dot\alpha_g \bar{c}}{2Q_\infty}}(k,\Omega_y)$$

From equation (5.32) the aerodynamic frequency-response data is obtained,

$$H^a_{Z\alpha_g}(k,\Omega_y) = \frac{C^a_Z}{\alpha_g}(k,\Omega_y) = \mathcal{C}^a_{\mathcal{Z}_{\alpha_g}}(k,\Omega_y) \; + \; \mathcal{C}^a_{\mathcal{Z}_{\dot\alpha_g}}(k,\Omega_y) \; \frac{j\omega\bar{c}}{2Q_\infty}$$

or,

$$H^a_{Z\alpha_g}(k,\Omega_y) = \mathcal{C}^a_{\mathcal{Z}_{\alpha_g}}(k,\Omega_y) \;\; + \; \mathcal{C}^a_{\mathcal{Z}_{\dot\alpha_g}}(k,\Omega_y) \; jk \tag{5.33}$$

Similar to the definition of the constant stability derivatives for the frame $\mathcal{F}_S$, as listed in tables D.1 and D.2, the definition of the frequency-dependent symmetrical stability derivatives for the frame $\mathcal{F}_S$ in terms of the calculated aerodynamic derivatives in $\mathcal{F}_{aero}$ is given in table D.5. The definition of the frequency-dependent asymmetrical stability

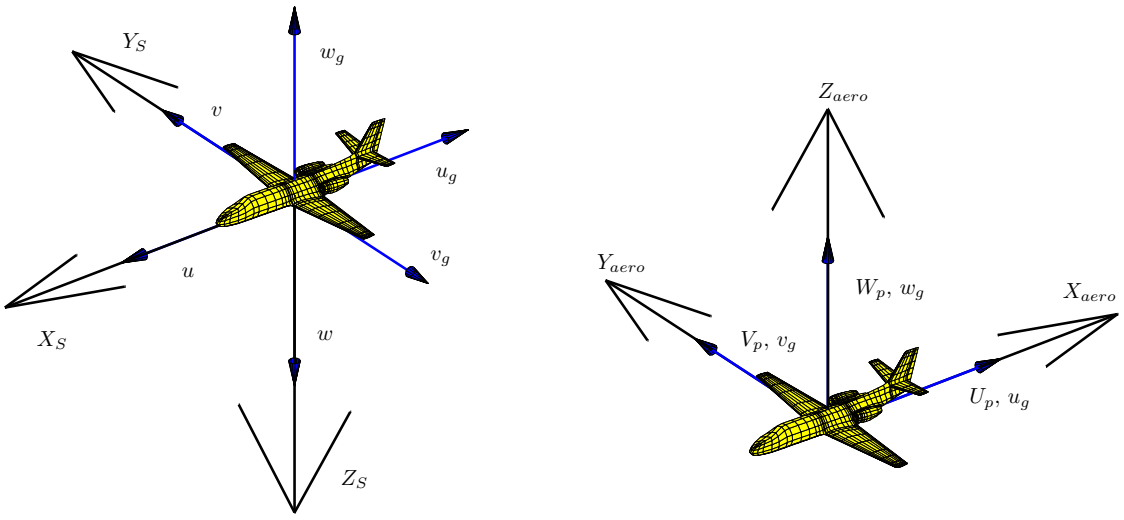


Figure 5.13: The Stability Frame of Reference $\mathcal{F}_S$, including perturbation velocity components $[u, v, w]^T$ and atmospheric turbulence velocity component inputs $[u_g, v_g, w_g]^T$ (left), and the Aerodynamic Frame of Reference $\mathcal{F}_{aero}$, including the perceived velocity components $[U_p, V_p, W_p]^T$ and atmospheric turbulence velocity component inputs $[u_g, v_g, w_g]^T$ (right).

derivatives for $\mathcal{F}_S$ in terms of the calculated aerodynamic derivatives in $\mathcal{F}_{aero}$ is given in table D.6, while a similar definition of the frequency-dependent gust derivatives is given in tables D.7 and D.8 for 1D atmospheric turbulence gust fields, and tables D.9 and D.10 for 2D atmospheric turbulence gust fields.
In terms of partial derivatives, the frequency-dependent stability derivatives are also defined in appendix A. They are also summarized in tables D.15 and D.16. In terms of partial derivatives, the frequency-dependent gust derivatives are also summarized in tables D.17 and D.18 for 1D turbulence. For 2D turbulence they are summarized in tables D.19 and D.20.

5.6 Remarks

The definition of the stationary aircraft motion perturbations will be used in chapter 6 to calculate the stability derivatives of an example aircraft. The calculated stability derivatives will be compared to results obtained from flight tests.
In chapters 7 and 8 for a series of the reduced frequency the aerodynamic frequency-response will be calculated for this example aircraft. The data are obtained for the harmonically varying unsteady aircraft motion perturbations and the harmonically varying atmospheric turbulence inputs (both 1D and 2D), as defined in this chapter. These aerodynamic frequency-response data will also hold for the Stability Frame of Reference $\mathcal{F}_S$.
In chapter 10 the constant unsteady stability derivatives $C_{Z_{\dot{\alpha}}}$, $C_{m_{\dot{\alpha}}}$, $C_{Y_{\dot{\beta}}}$, $C_{\ell_{\dot{\beta}}}$ and $C_{n_{\dot{\beta}}}$ are estimated using the aerodynamic frequency-response data. With the estimation of these (constant) unsteady stability derivatives, a complete constant-parameter aerody-

namic model is obtained. This model is required for the equations of motion described in the Stability Frame of Reference $\mathcal{F}_S$ as given in appendix I, and it will be used in chapters 11 and 12 for the simulation of aircraft responses to both 1D and 2D atmospheric turbulence.

Chapter 6

The aircraft grid and steady aerodynamic results

6.1 Introduction

In this chapter the aircraft grid (also referred to as the "aerodynamic grid") of the example aircraft geometry and its wake grid will be given. The example aircraft geometry is that of a Cessna Ce550 Citation II aircraft. The geometry-wake configuration will be used to calculate both the steady ánd the time-dependent aerodynamic forces and moments due to harmonic aircraft motion perturbations, i.e. in u, v and w. Also, it will be used to determine the responses to both harmonic one- (1D) and two-dimensional (2D) gust fields (u_g, v_g and w_g).

In this chapter the Linearized Potential Flow (LPF) method will primarily be used as a virtual windtunnel. The obtained (quasi-) steady perturbations result in aerodynamic force and moment coefficient responses which will be used to determine the (quasi-) steady stability derivatives. These derivatives will be determined for the trim condition, and they will be referred to as the (constant parameter) Parametric Computational Aerodynmics (PCA) model. The trim condition is taken to be recti-linear flight at an angle-of-attack of $\alpha_0 = 1.5^o$.

6.2 Aircraft geometry definition

The example aircraft geometry represents a low-winged aircraft with two turbofan engines located aft of the wing and connected to the fuselage by pylons. The turbofan jets issuing from the engines are not modeled and the nacelles are treated as ring-wings, thus allowing the air to flow through the nacelles. However, since the nacelles are modeled as ring wings they shed a wake and, therefore, they will generate both lift and drag.
The original aerodynamic grid is provided in the aircraft manufacturer rig-frame $\mathcal{F}_{rig}$

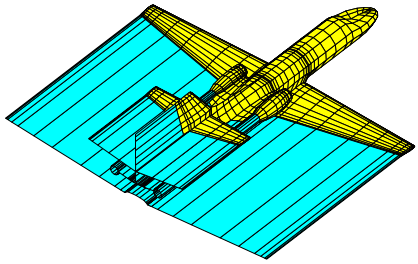


Figure 6.1: The aircraft geometry including its (truncated) total planar wake convected downstream.

($O_{rig}X_{rig}Y_{rig}Z_{rig}$). The definition of the frame $\mathcal{F}_{rig}$ is given in appendix B, see also figure B.6. The grid was provided by the aircraft manufacturer for Euler Computational Fluid Dynamics (CFD) simulations, however, for LPF simulations it was reduced to a limited number of panels.

The aerodynamic calculations are performed in the Aerodynamic Frame of Reference $\mathcal{F}_{aero}$ ($O_{aero}X_{aero}Y_{aero}Z_{aero}$). The definition of this frame is given in appendix B, see also . figure B.1.
When unsteady simulations are considered, the motion of the frame $\mathcal{F}_{aero}$ is described in an Inertial Frame of Reference $\mathcal{F}_I$ ($O_IX_IY_IZ_I$). In the steady-state, or initial, condition, both the origin of the frame $\mathcal{F}_{aero}$ and the origin of the frame $\mathcal{F}_I$ coincide, so $O_{aero} = O_I$. When time-dependent perturbations are considered, the aircraft's center of gravity travels along the negative X_I-axis. Details of the frame $\mathcal{F}_I$ are given in appendix B.

6.3 Wake geometry definition

Before any time-domain simulations can be performed a steady-state initial condition has to be defined, prescribing the position and size of the steady wake. The steady-state wake is taken to be planar and no wake roll-up is modeled. Also, as described in chapter 4, in time-stepping mode the wake remains planar, hence assuming small disturbances. Of the considered aircraft geometry only lift generating elements are modeled as shedding a wake.
In the case of the example aircraft configuration, the aircraft's wake geometry in itself is quite complex, since it consists of wake segments connected to the wing, horizontal stabilizer, vertical stabilizer, nacelles, pylons and fuselage, each of which will be discussed in the following. All wake segments, being shed from lifting surfaces, are convected downstream and are modeled to have a length of $l_{wake} = 100\ b$, or 100 times the aircraft wingspan. The wake model for the total aircraft configuration is shown in figure 6.1.

In figures 6.2 to 6.7 the details of the aircraft wake are presented. In figure 6.2 the planar wake doublet panels connected to the trailing edge of the wing are given. Note that the side edges of the wake doublet panels may be considered as vortex lines (since the equivalent of a doublet panel is a vortex ring, see references [11, 12]).
Figure 6.3 shows the fuselage wake. Similar to the wake generation of both the pylons and the horizontal stabilizer, careful modeling is required for the wing's wake connected to the fuselage. In principle isolated wake vortex lines are present in the airflow, very near to the fuselage, if additional wake vortex elements are not modeled, see also figure 6.2. Normally, these kind of wake vortex lines only originate from wing tips. For instance, the wing wake vortex originating at the root of the wing contains circulation opposite in direction to the wing-tip vortex. This wing wake vortex line at the wing-fuselage junction must be modeled carefully, see references [9, 11, 12], since it may affect the airflow over the entire aircraft configuration. To avoid the effect of this particular wing wake vortex, the wing's wake is modeled up to the fuselage and is butted to it (see the bottom view of the fuselage wake panels being shed from the aft fuselage in figure 6.3). The doublet strength of all added fuselage wake panels is equal to the doublet strength of the wing's wake panel element being shed at the trailing edge nearest to the wing-fuselage junction.
In figure 6.4 the planar wake connected to the trailing edge of the horizontal stabilizer is depicted. Similar to the wing's wake modeling, additional wake elements are modeled near the vertical stabilizer. The horizontal stabilizer's wake is connected to the vertical stabilizer to prevent the occurence of isolated vortex lines near it, see figure 6.4 (bottom) where the additional wake panels are marked. Similar to the fuselage's wake strength definition, the doublet strength of added vertical stabilizer wake panels is equal to the doublet strength of the horizontal stabilizer's wake panel element being shed at it's trailing edge nearest to the vertical stabilizer-horizontal stabilizer junction.
In figure 6.5 the planar wake of the vertical stabilizer is given. Just as for the wing, these wake elements are connected to the trailing edge of the vertical stabilizer.
In figures 6.6 the pylon's wake is given. The pylons are considered to act as lifting surfaces, hence they also shed a wake. The pylons' wake is connected to the trailing edges. Just as for the wing and the horizontal stabilizer, the pylon's wake is connected, or butted, to the fuselage to prevent the occurence of isolated wake vortex lines near the fuselage. Also, in this case the additional wake elements' doublet strength is equal to the doublet strength of the wake panel being shed closest to the fuselage.
Figure 6.7 shows the nacelles' wake, connected to the nacelle trailing edges. Since these nacelles are modeled as open ring-wings, in this case the wake is non-planar and is tubular shaped.

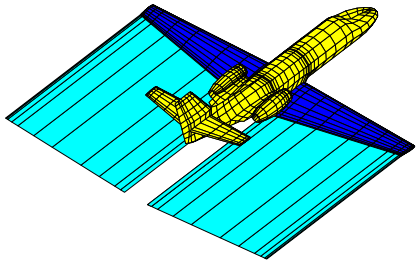


Figure 6.2: The aircraft geometry including the (truncated) planar steady wake being shed from the wings.

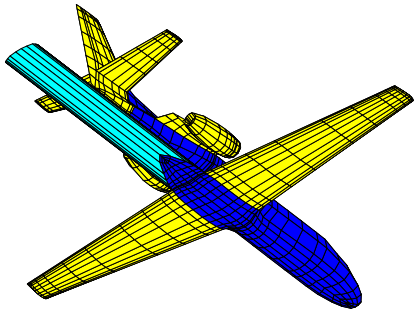
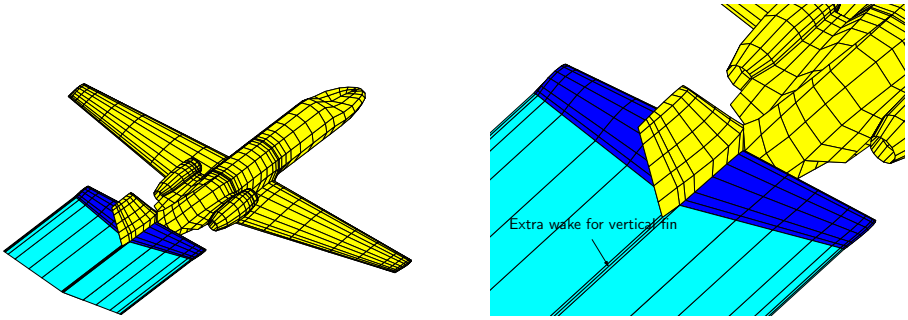


Figure 6.3: The aircraft geometry including the (truncated) planar steady wake being shed from the fuselage.



(a) Horizontal stabilizers' wake

(b) Magnification of the horizontal stabilizers' wake

Figure 6.4: The aircraft geometry including the (truncated) planar steady wake being shed from the horizontal stabilizer (left). The additional (truncated) wake elements shed from the vertical stabilizer are marked in the right figure, which is a magnification of the left figure.

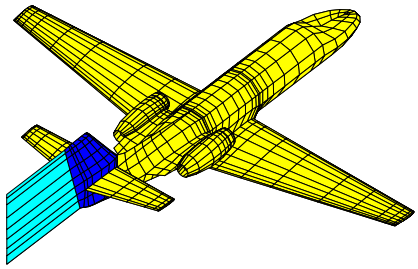
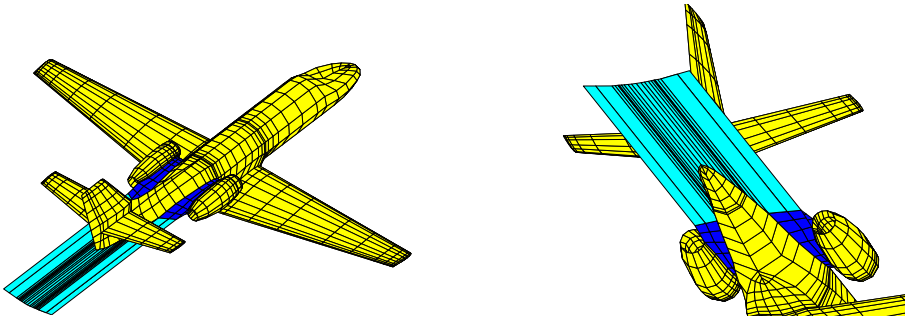


Figure 6.5: The aircraft geometry including the (truncated) planar steady wake being shed from the vertical stabilizer.



(a) Pylons' wake

(b) Magnification of the pylons' wake

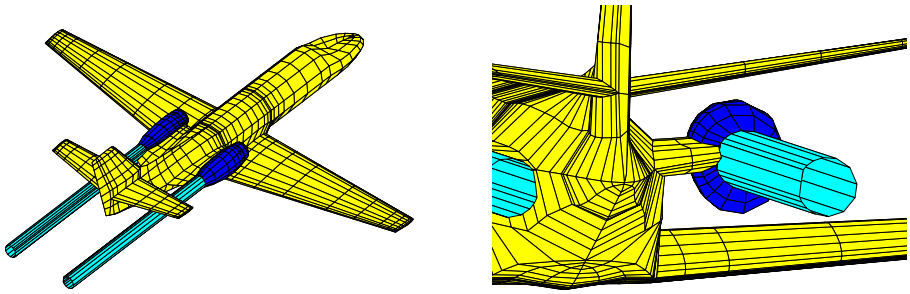
Figure 6.6: The aircraft geometry including the (truncated) planar wake being shed from the pylons and fuselage (left), and a bottom view magnification (right).

6.4 PCA-model steady-state aerodynamic results

6.4.1 A PCA-model steady-state solution

In this section a steady-state LPF solution is given for the aircraft-wake geometry discussed previously. The aircraft configuration is a discrete model of the continuous surface description of a Cessna Ce550 Citation II. The number of body panels is $N_{panels} = 1966$, while the number of wake panels is $N_{wake-panels} = 112$, which are both sufficient according to previous studies, see reference [7]. The configuration used showed a good correlation in terms of simulated stability derivatives with other simulation methods. In figure 6.1 both the discretized aircraft model and its wake are given.

In table 6.1 several PCA-model parameters specific for the aircraft configuration are given.



(a) Nacelles' wake

(b) Magnification of the nacelles' wake

Figure 6.7: The aircraft geometry including the (truncated) tubular shaped steady wake being shed from the nacelles (left), and magnification (right).

The chosen steady-state, or initial, flight condition is given in table 6.2. It will be considered as the initial condition for all unsteady simulations throughout this thesis. The center of gravity position (including its limits, reference [28]) are also given in figure 6.8.

The LPF boundary conditions posed on the discretized aircraft-wake geometry are determined by the initial flight condition (see also chapter 3) and they result in a steady-state solution. For both angles-of attack $\alpha_0 = 0.0^o$ and $\alpha_0 = 1.5^o$, the prescribed body source distribution ($\sigma = -\underline{n} \cdot \underline{Q}_\infty$) is given in figure 6.9 (top), while the calculated body doublet distribution for both angles-of-attack is given in figure 6.9 (middle). For both angles-of-attack, the non-dimensional pressure distributions are calculated from the on-body doublet, and thus, airspeed distribution, and are given in figure 6.9 (bottom). Referring to chapter 3, integrating the non-dimensional pressure distribution eventually results in the aerodynamic force and moment coefficients in the frame $\mathcal{F}_{aero}$, see table 6.3. These results are also given for the aerodynamic force and moment coefficients in the Stability Frame of Reference $\mathcal{F}_S$, see table 6.4. Details of the frame $\mathcal{F}_S$ are given in appendix B.

6.4.2 (Quasi-) Steady stability derivatives

In estimating the PCA-model (quasi-) steady stability derivatives, the aircraft-wake geometry is perturbed in airspeed, angle-of-attack, side-slip-angle, roll-rate, pitch-rate and yaw-rate. These aerodynamic derivatives hold in the frame $\mathcal{F}_S$. Note that both the X_S-axis and Z_S-axis of the frame $\mathcal{F}_S$ are taken to be positive in the opposite directions of X_{aero} and Z_{aero} of the frame $\mathcal{F}_{aero}$, and that the Y_S-axis and Y_{aero}-axis coincide. See also section 5.4.

In figures 6.11 to 6.16 the calculated aerodynamic force and moment coefficients are given with respect to the Stability Frame of Reference. These coefficients are defined

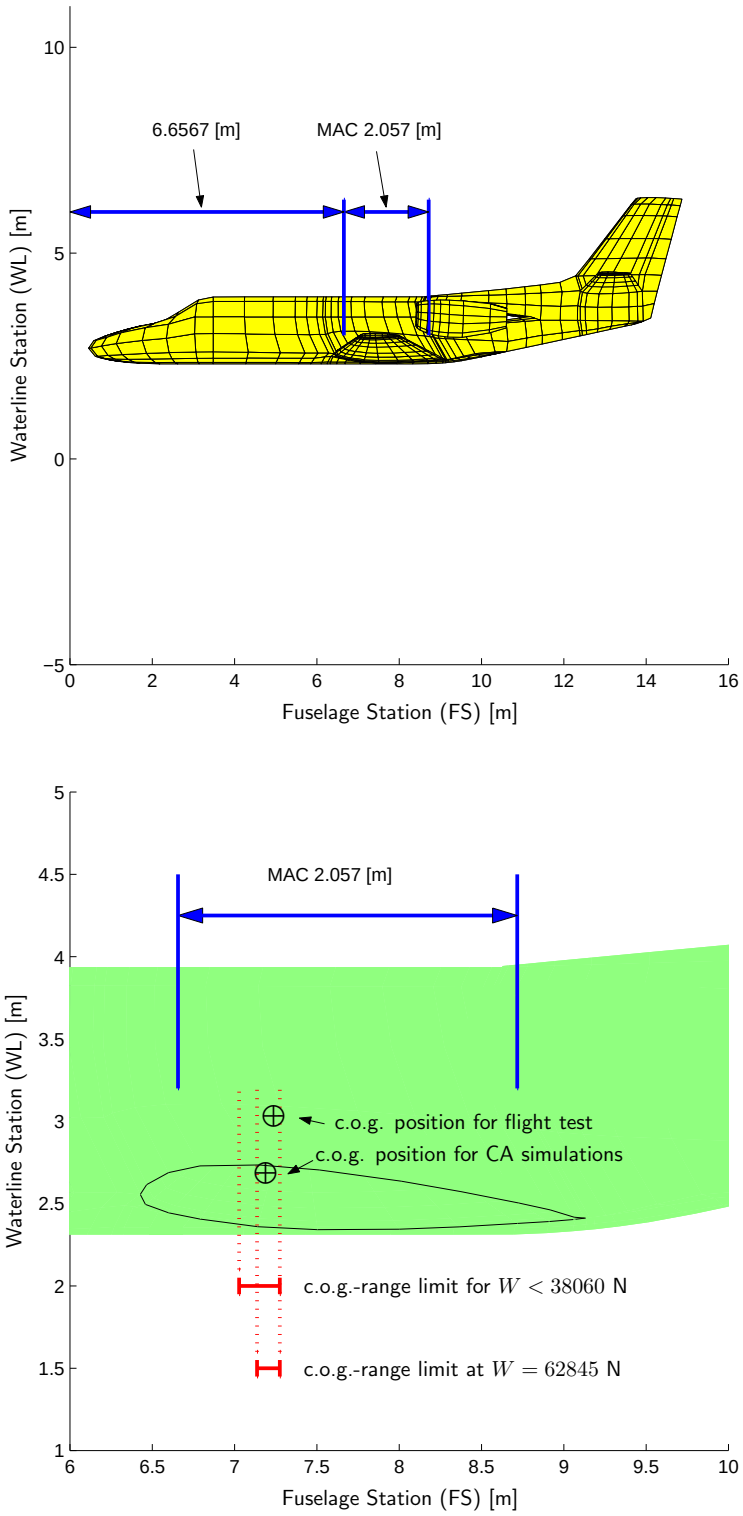
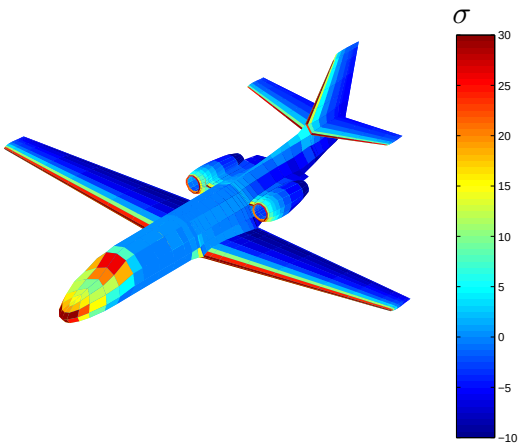
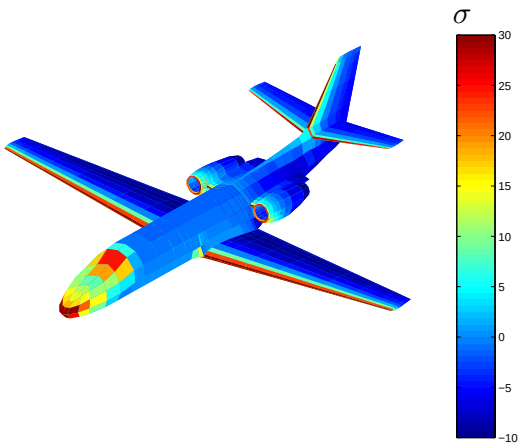


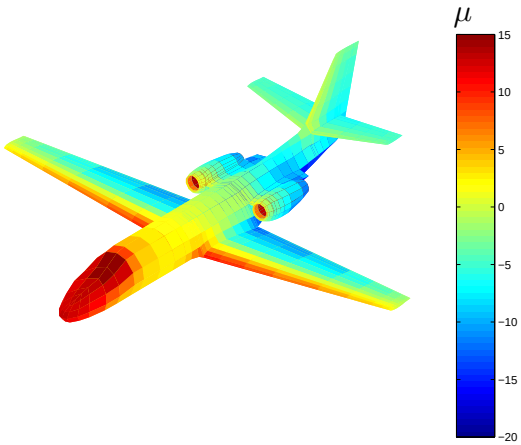
Figure 6.8: The position of the mean aerodynamic chord (MAC) in the aircraft manufacturer's rig-frame $\mathcal{F}_{rig}$ (top), and the position of the center of gravity (including its range limits) used for Computational Aerodynamics (CA) experiments (bottom), also in the frame $\mathcal{F}_{rig}$. This data has been taken from reference [28].



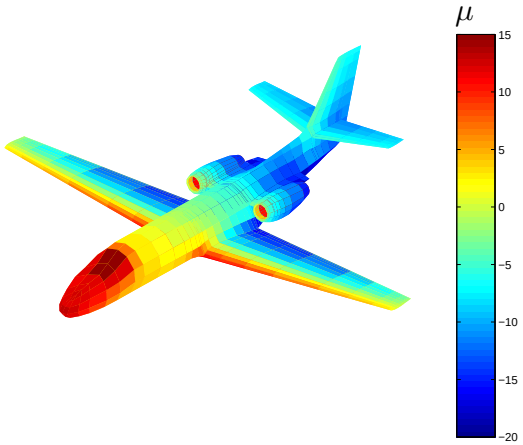
(a) Prescribed source strength distribution σ for $\alpha = 0.0^o$



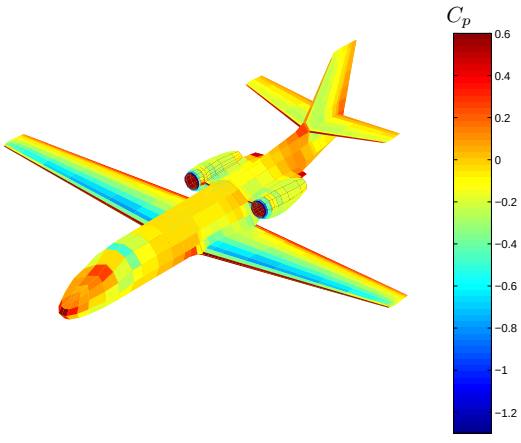
(b) Prescribed source strength distribution σ for $\alpha = 1.5^o$



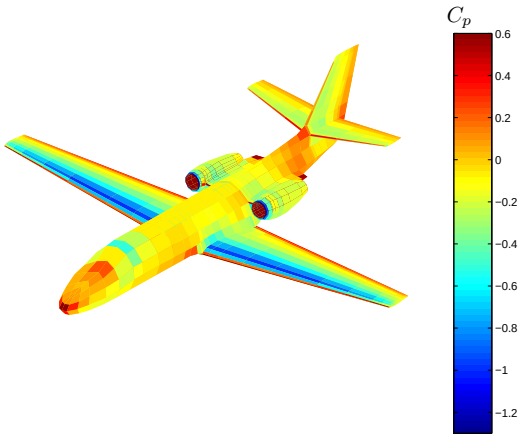
(c) Calculated doublet strength distribution μ for $\alpha = 0.0^o$



(d) Calculated doublet strength distribution μ for $\alpha = 1.5^o$



(e) Calculated pressure distribution C_p for $\alpha = 0.0^o$



(f) Calculated pressure distribution C_p for $\alpha = 1.5^o$

Figure 6.9: The prescribed source strength distribution σ (top), the calculated doublet strength distribution μ (middle) and the calculated non-dimensional pressure distribution C_p (bottom), over the aircraft configuration, for $\alpha = 0.0^o$ (left) and $\alpha = 1.5^o$ (right).

as $C_X = \frac{X}{\frac{1}{2}\rho Q_\infty^2 S}$, $C_Y = \frac{Y}{\frac{1}{2}\rho Q_\infty^2 S}$, $C_Z = \frac{Z}{\frac{1}{2}\rho Q_\infty^2 S}$, $C_\ell = \frac{L}{\frac{1}{2}\rho Q_\infty^2 Sb}$, $C_m = \frac{M}{\frac{1}{2}\rho Q_\infty^2 S\bar{c}}$ and $C_n = \frac{N}{\frac{1}{2}\rho Q_\infty^2 Sb}$. The airspeed perturbations u range from $u = -5$ m/s to $u = +5$ m/s, while the perturbations for both the angle-of-attack α and the side-slip angle β range from -10^o to $+10^o$. The roll-rate, pitch-rate and yaw-rate perturbations range from $-\frac{\pi}{3}$ to $+\frac{\pi}{3}$ [Rad./sec.]. In these figures, all aerodynamic force and moment coefficients are plotted against their non-dimensional perturbations $\hat{u} = \frac{u}{Q_\infty}$, α, β, $\frac{pb}{2Q_\infty}$, $\frac{q\bar{c}}{2Q_\infty}$ and $\frac{rb}{2Q_\infty}$ (all in [Rad.]).
In these figures, a breakdown of the contribution of isolated aircraft parts to the aerodynamic responses is shown as well, with the sum of all aircraft part contributions to the considered aerodynamic force and moment coefficient data equalling the total aircraft's aerodynamic response. In figures 6.10 the definition of these aircraft parts is given as "wing", "horizontal stabilizer", "pylons", "fuselage", "vertical fin" and "nacelles".

From the results presented in figures 6.11 to 6.16, the PCA-model's stability derivatives are calculated by taking the gradient of the aerodynamic force or moment coefficient to the respective non-dimensional perturbation. For this purpose, first, a second order function is fitted locally through the aerodynamic forces' or moments' data-points with the considered perturbation being the independent variable. Secondly, using this function, its first order derivative with respect to the independent variable (the perturbation) produces the sought stability derivative.
The definition of all PCA-model's stability derivatives is given in appendix A. The calculated PCA-model's symmetric and asymmetric stability derivatives are summarized in tables 6.5 and 6.6, respectively. A breakdown of the symmetric and asymmetric stability derivatives into aircraft part contributions is given in tables 6.10 and 6.11, respectively.

6.4.3 Stability derivatives obtained from flight tests

For comparison, the symmetric quasi-steady stability derivatives as obtained from flight tests are given in table 6.9, taken from reference [27]. Both aircraft parameters ánd the definition of the trim condition are given in tables 6.7 and 6.8, respectively. The given parameters for the short-period data set only include the short-period stability derivatives. Note that the center-of-gravity location during flight tests was different from its position during LPF simulations, see figure 6.8, and for comparison, Parametric Computational Aerodynamics results taking the center of gravity position equal to the one used during the flight test, are also given in table 6.9. It should be noted that the LPF-based calculation of the stability derivatives holds for inviscid, incompressible and irrotational flow, which explains the difference in magnitude of the stability derivatives presented in table 6.9. These differences are mainly attributed to compressibility (Mach) and viscosity (Reynolds) effects. Especially the stability derivative C_{Z_α} shows a good correlation with the result obtained from LPF simulations. Although the center of gravity position during flight tests was estimated from weight and balance sheets, see reference [28], similar to the stability derivative C_{Z_α}, the derivative C_{m_α} again shows a good correlation with the result obtained from LPF simulations. Furthermore, the stability derivative C_{m_q} obtained during flight

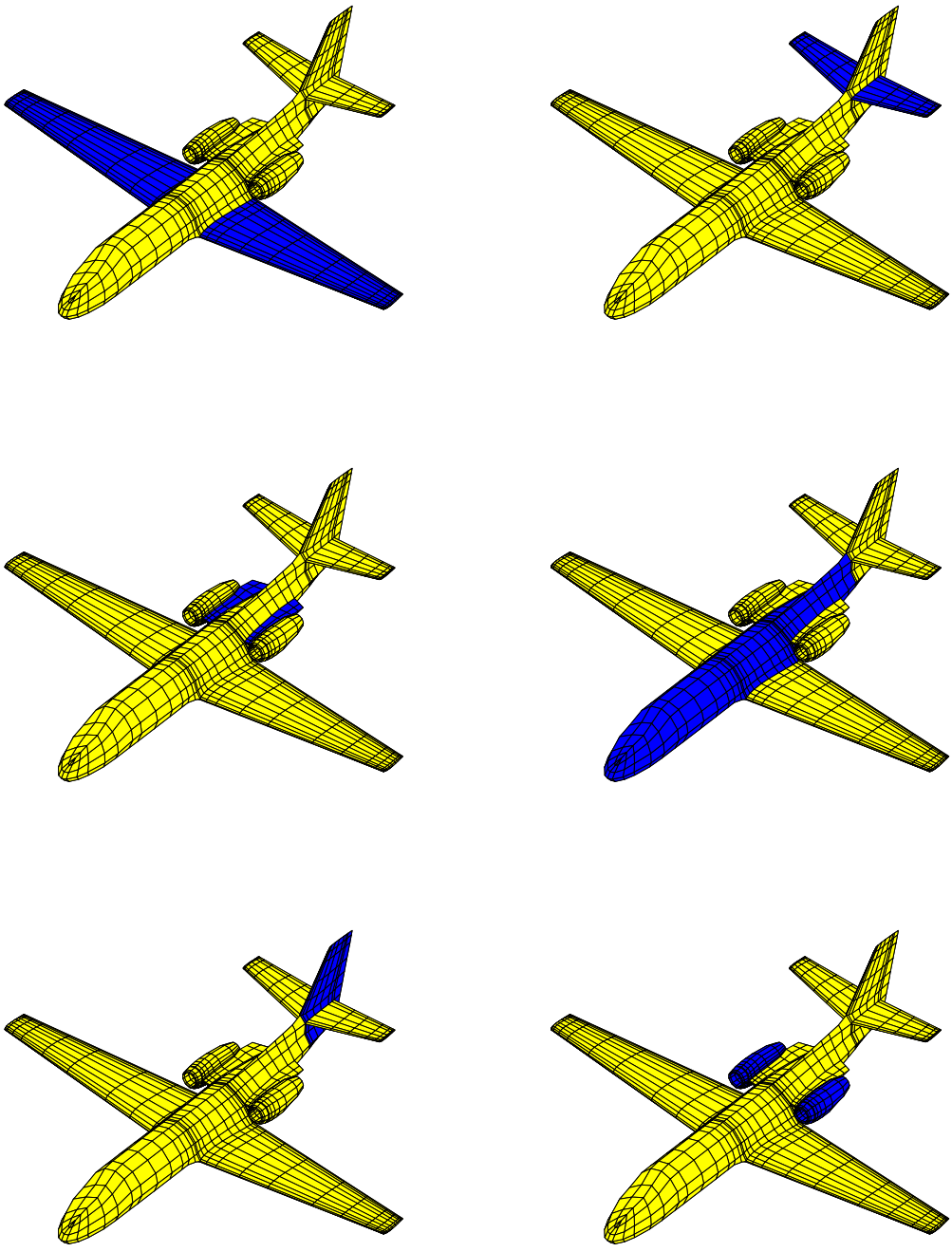


Figure 6.10: The definition of aircraft parts “wing” and “horizontal stabilizer” (top), “pylons” and “fuselage” (middle), “vertical fin” and “nacelles” (bottom) for the Cessna Ce550 “Citation II” model.

tests shows well correlation as well, taking into account that this derivative is actually the sum of stability derivatives $C_{m_{\dot{\alpha}}}$ and C_{m_q}. However, as expected, the stability derivative of the aerodynamic force coefficient C_X with respect to α shows a poor correlation with the LPF model results. This poor correlation is attributed to the elimination of viscous drag effects in the LPF model.

6.5 Unsteady wake geometry definition

Once the initial condition has been established, all wake elements have been defined, and all flow data are known, the time-dependent aerodynamic forces and moments due to harmonic aircraft motion and due to harmonic atmospheric turbulence can be simulated, see also chapters 7 and 8. For identification purposes, in these chapters the time-dependent aerodynamic force and moment coefficients $(C_X, C_Y, C_Z, C_\ell, C_m, C_n)$ due to harmonic aircraft motions (surging, swaying and heaving motions) are simulated. Also, the time-dependent aerodynamic force and moment coefficients $(C_{X_g}, C_{Y_g}, C_{Z_g}, C_{\ell_g}, C_{m_g}, C_{n_g})$ due to harmonic atmospheric turbulence are calculated. Finally, from both these harmonic excitations and the harmonic responses the aerodynamic frequency-response functions are calculated. From these functions the frequency dependent stability- and gust derivatives are derived.
Using the initial condition's flowfield and the prescribed perturbations on it, the aerodynamic forces and moments are solved in the time-domain by time-stepping, as discussed in chapter 4. Initially, at $t = t_0 = 0$, the frames $\mathcal{F}_{aero}$ and $\mathcal{F}_I$ coincide. When harmonic perturbations are considered, the aircraft's center of gravity travels along a recti-linear flightpath in the direction of the negative X_I-axis, see figure 6.17. The position of the center of gravity in $\mathcal{F}_I$ is given as,

$$X_0 = -Q_\infty t$$

with X_0 the position of the aircraft center of gravity in $\mathcal{F}_I$, Q_∞ the airspeed (with $\underline{Q}_\infty = [U_\infty, V_\infty, W_\infty]^T = [U_\infty, 0, 0]^T$), and t time.

6.6 Remarks

In this chapter the aircraft geometry and its wake configuration have been described for the (un)steady Linearized Potential Flow simulations. Also, the steady-state, or initial, condition for all future simulations has been defined. For the trim condition, the calculated PCA-model parameters were the (quasi-steady) stability derivatives. For several stability derivatives the LPF/PCA results correlated well with results obtained from flight tests, and, therefore, the LPF method will be extended to perform simulations for both unsteady aircraft motion and atmospheric gust-response.
In chapter 7 PCA-model results will be presented of time-domain simulations for the given aircraft-wake geometry subjected to harmonic symmetrical aircraft motion perturbations ánd harmonic symmetrical atmospheric turbulence.

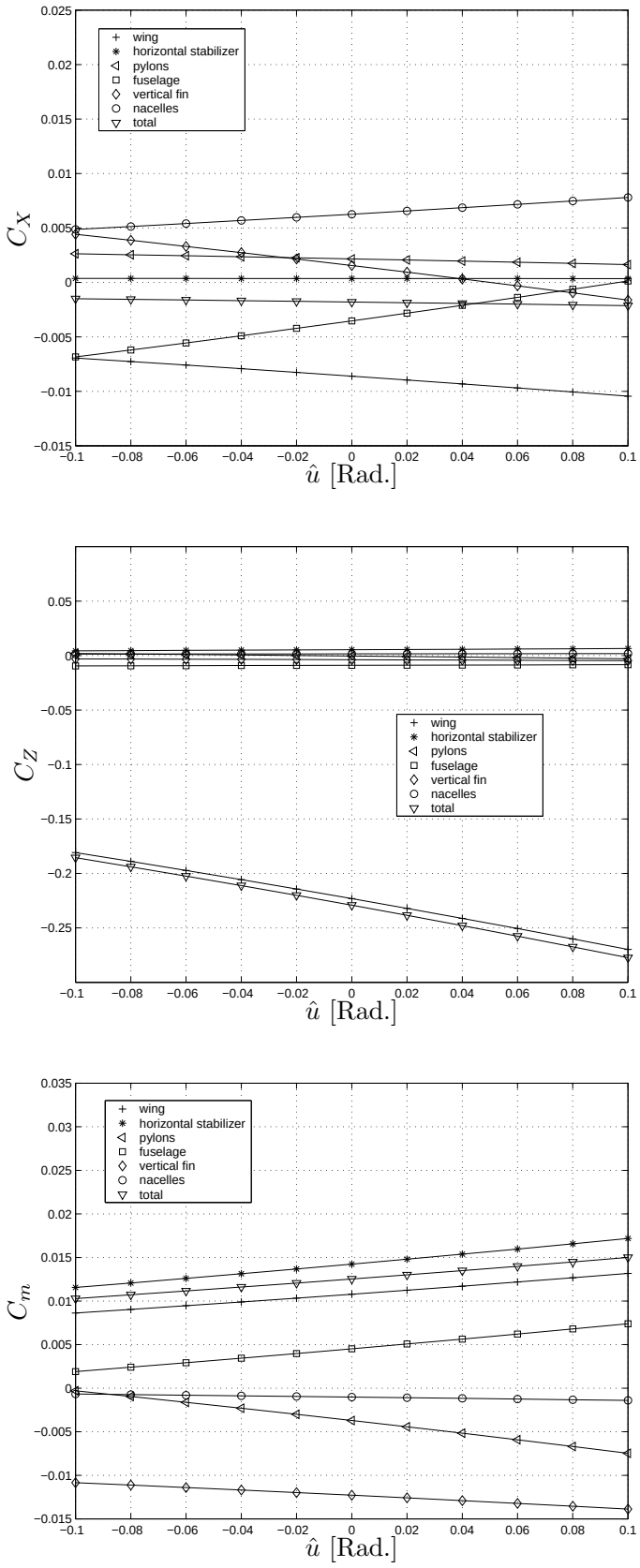


Figure 6.11: The calculated aerodynamic force coefficients C_X and C_Z and the aerodynamic moment coefficient C_m in $\mathcal{F}_S$ due to perturbations in non-dimensional airspeed $\hat{u} = \frac{u}{Q_\infty}$, for the trim condition $\alpha_0 = 1.5^o$.

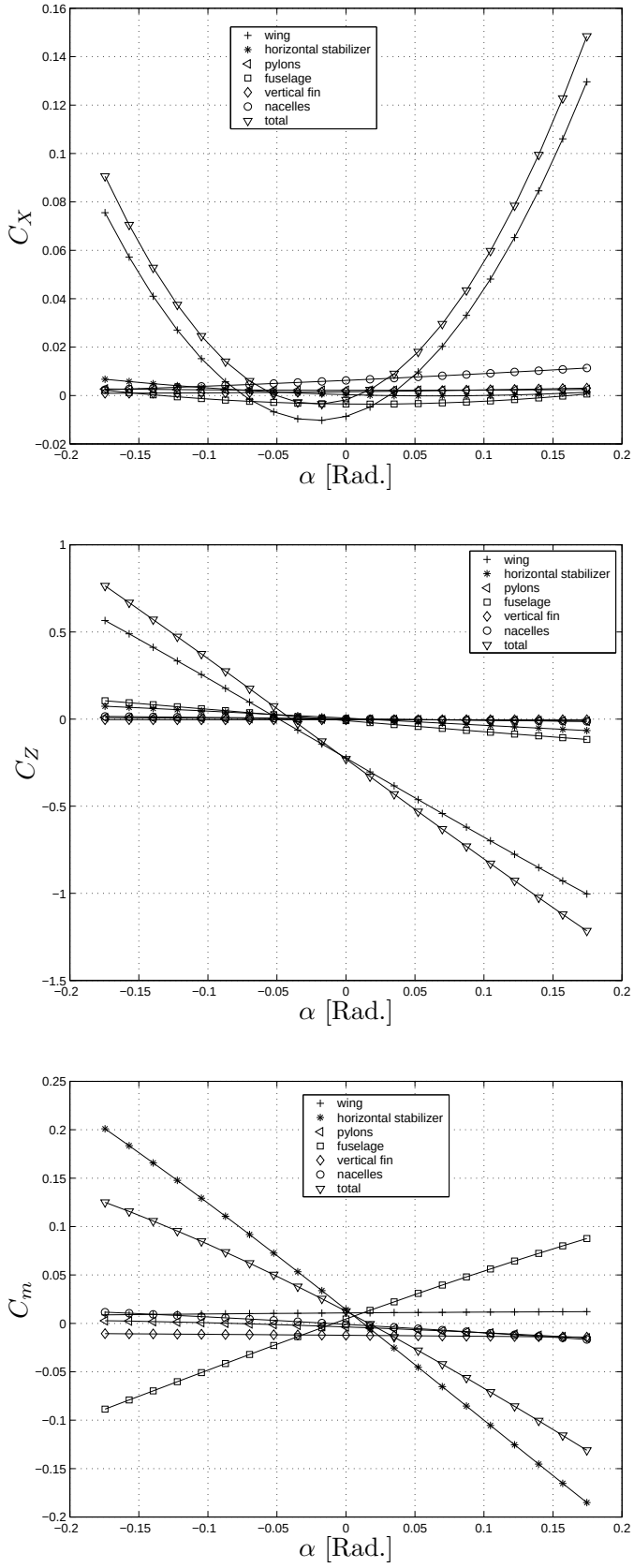


Figure 6.12: The calculated aerodynamic force coefficients C_X and C_Z and the aerodynamic moment coefficient C_m in $\mathcal{F}_S$ due to perturbations in angle-of-attack α, for the trim condition $\alpha_0 = 1.5^o$.

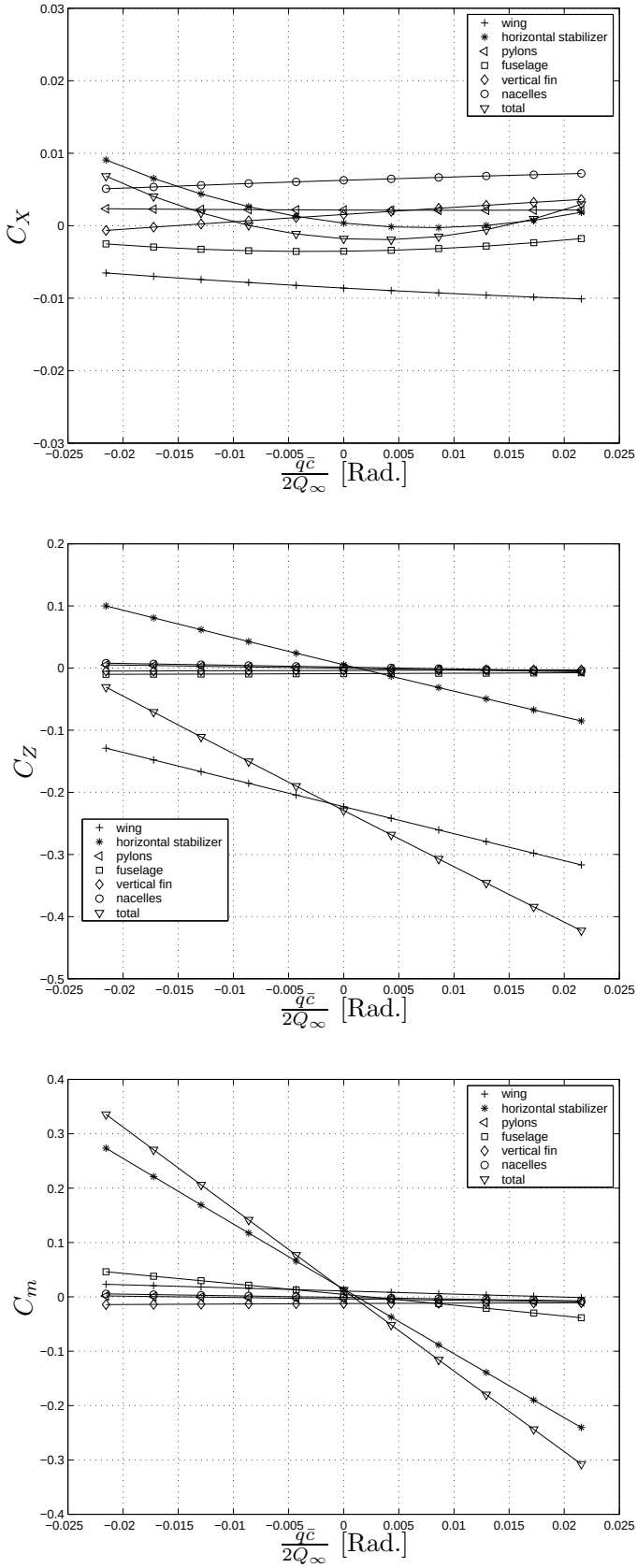


Figure 6.13: The calculated aerodynamic force coefficients C_X and C_Z and the aerodynamic moment coefficient C_m in $\mathcal{F}_S$ due to perturbations in non-dimensional pitch-rate $\frac{q\bar{c}}{2Q_\infty}$, for the trim condition $\alpha_0 = 1.5^o$.

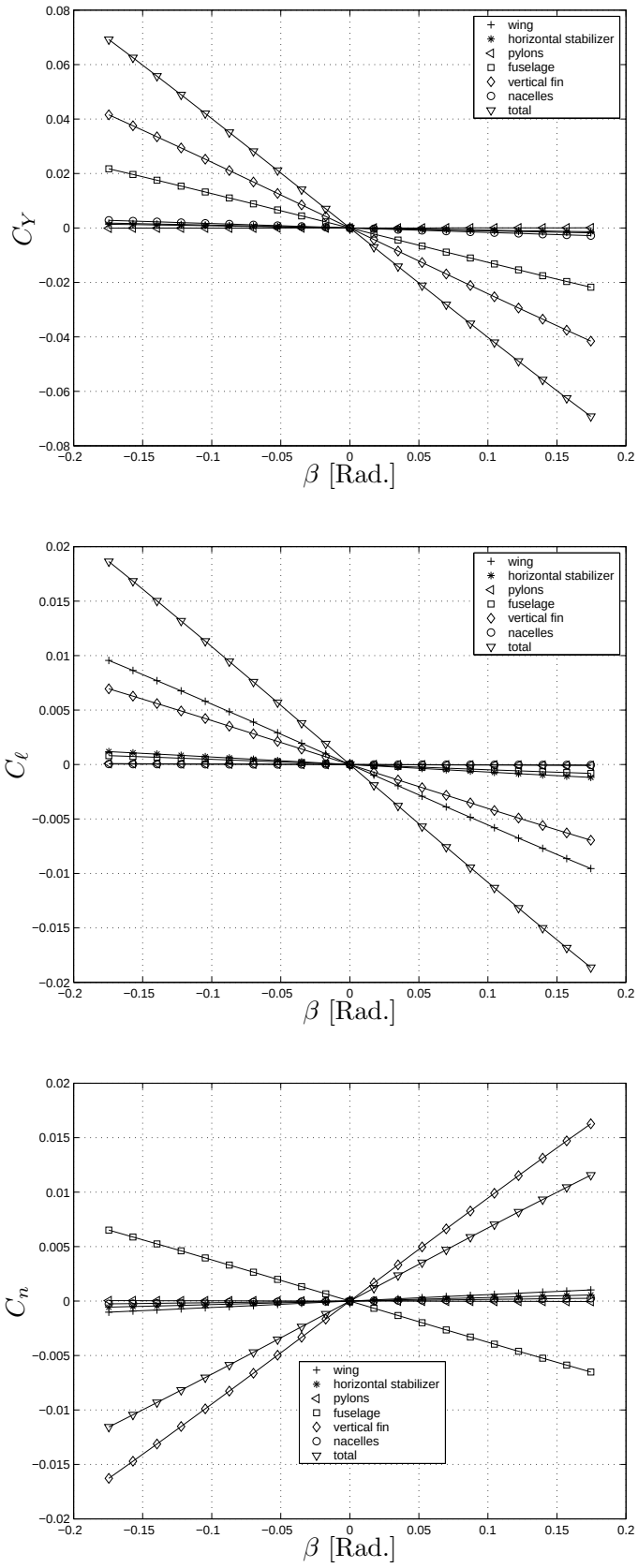


Figure 6.14: The calculated aerodynamic force coefficient C_Y and the aerodynamic moment coefficients C_ℓ and C_n in $\mathcal{F}_S$ due to perturbations in side-slip-angle β, for the trim condition $\alpha_0 = 1.5^o$.

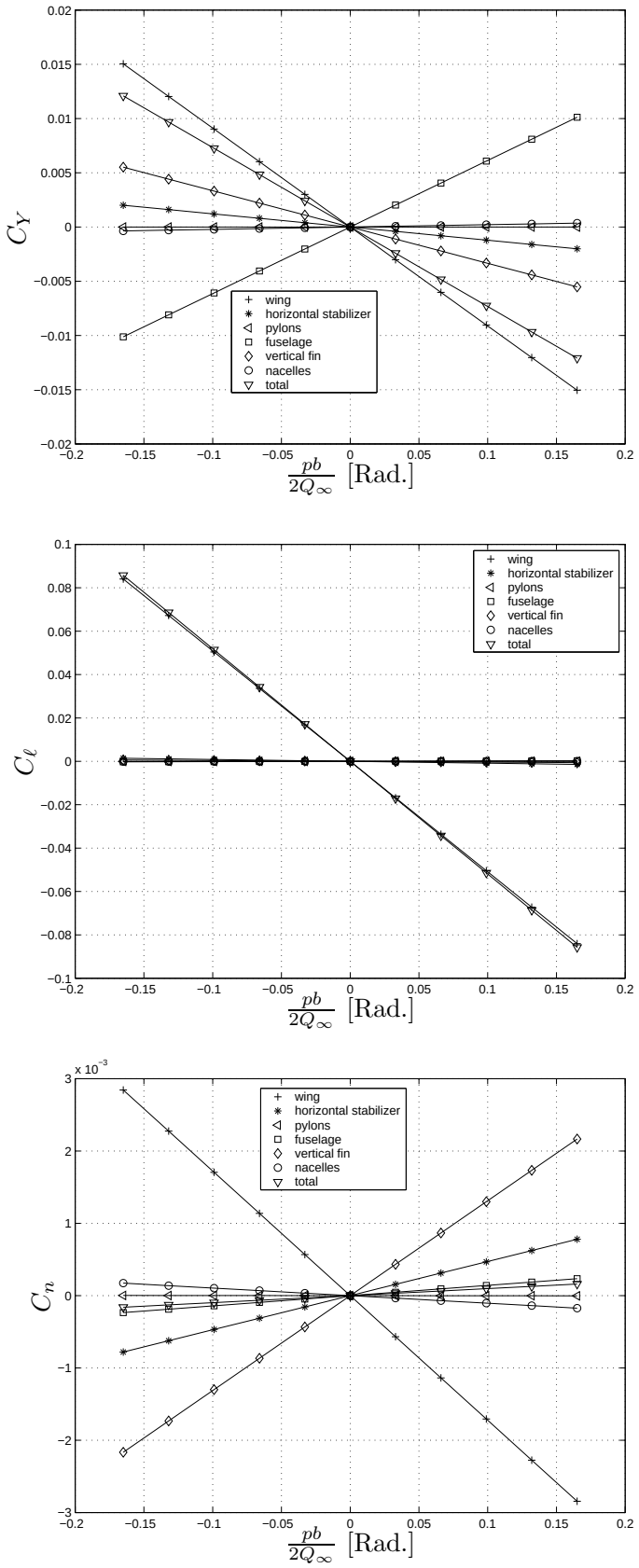


Figure 6.15: The calculated aerodynamic force coefficient C_Y and the aerodynamic moment coefficients C_ℓ and C_n in $\mathcal{F}_S$ due to perturbations in non-dimensional roll-rate $\frac{pb}{2Q_\infty}$, for the trim condition $\alpha_0 = 1.5^o$.

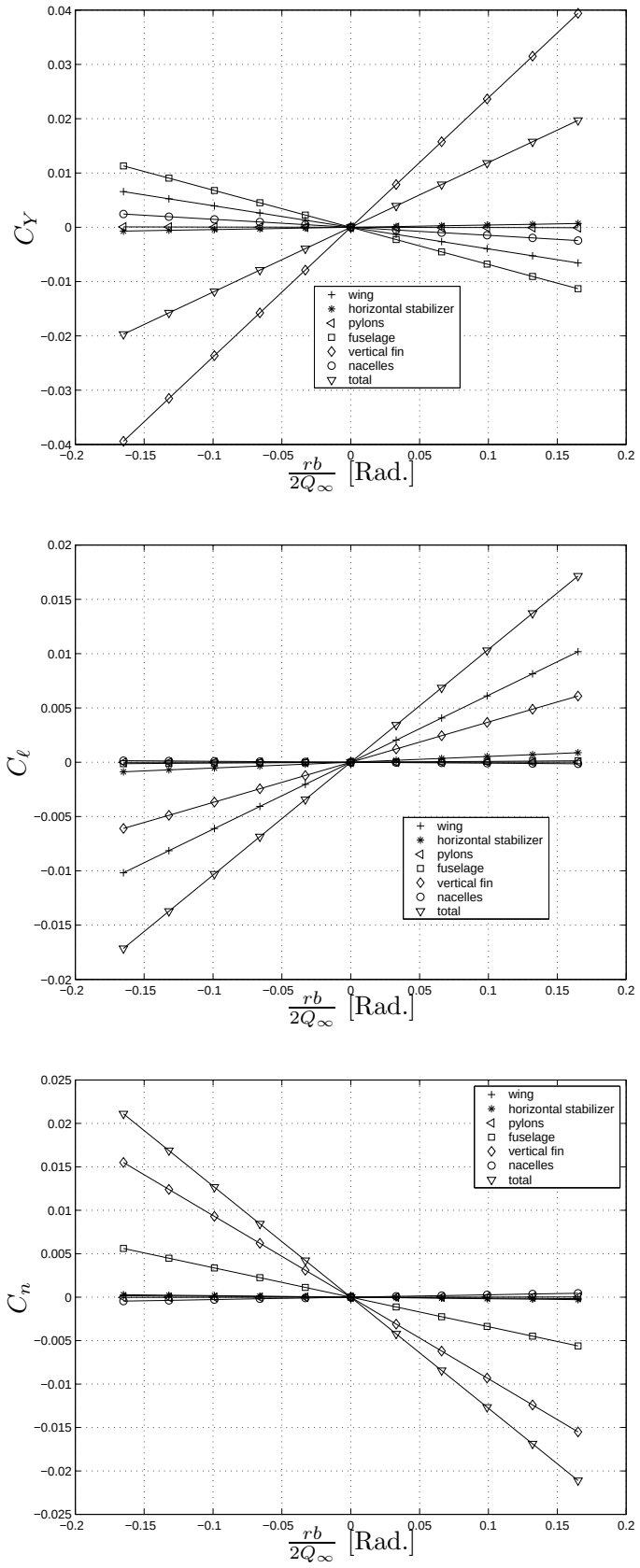


Figure 6.16: The calculated aerodynamic force coefficient C_Y and the aerodynamic moment coefficients C_ℓ and C_n in $\mathcal{F}_S$ due to perturbations in non-dimensional yaw-rate $\frac{rb}{2Q_\infty}$, for the trim condition $\alpha_0 = 1.5^o$.

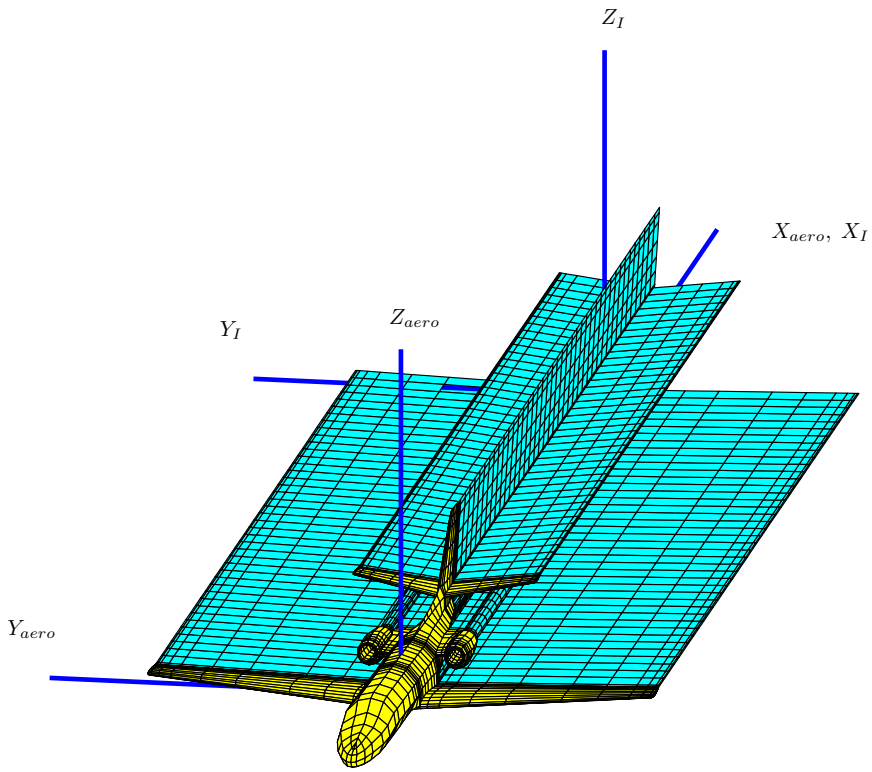


Figure 6.17: The aircraft configuration, the planar unsteady wake along a recti-linear flightpath, the frame $\mathcal{F}_{aero}$ and the frame $\mathcal{F}_I$.

Similar to chapter 7, in chapter 8 PCA-model results will be presented of time-domain simulations for the aircraft-wake geometry subjected to harmonic asymmetrical aircraft motion perturbations ánd both harmonic asymmetrical ánd anti-symmetrical atmospheric turbulence.

x_{cg}	=	7.158	m
y_{cg}	=	0	m
z_{cg}	=	2.695	m
span b	=	15.762	m
m.a.c. $\bar{c}$	=	2.057	m
wing-area S	=	30.000	m^2

Table 6.1: The aircraft center of gravity position in the frame $\mathcal{F}_{rig}$ and aircraft geometry parameters for LPF/PCA simulations.

Airspeed Q_∞	=	50.0	m/sec.
Angle-of-attack α_0	=	1.5	Deg.
Angle of side-slip β	=	0.0	Deg.
flightpath angle γ_0	=	0.0	Deg.
Angle of pitch θ_0	=	1.5	Deg.
Air-density ρ	=	1.000	kg m^{-3}
Roll-rate p	=	0.0	Rad/sec.
Pitch-rate q	=	0.0	Rad/sec.
Yaw-rate r	=	0.0	Rad/sec.

Table 6.2: The initial state parameters for LPF/PCA simulations.

α	C_{X_0}	C_{Y_0}	C_{Z_0}	C_{ℓ_0}	C_{m_0}	C_{n_0}
0.0	0.0015	0.0000	0.0782	0.0000	0.0321	0.0000
1.5	0.0018	0.0000	0.2292	0.0000	0.0125	0.0000

Table 6.3: PCA-model steady aerodynamic force and moment coefficients in the frame $\mathcal{F}_{aero}$ for $\alpha = 0^o$ and $\alpha = 1.5^o$.

α	C_{X_0}	C_{Y_0}	C_{Z_0}	C_{ℓ_0}	C_{m_0}	C_{n_0}
0.0	-0.0015	0.0000	-0.0782	0.0000	0.0321	0.0000
1.5	-0.0018	0.0000	-0.2292	0.0000	0.0125	0.0000

Table 6.4: PCA-model steady aerodynamic force and moment coefficients in the frame $\mathcal{F}_S$ for $\alpha = 0^o$ and $\alpha = 1.5^o$.

C_{X_0}	=	-0.0018	C_{Z_0}	=	-0.2292	C_{m_0}	=	0.0125
C_{X_u}	=	-0.0032	C_{Z_u}	=	-0.4592	C_{m_u}	=	0.0236
C_{X_α}	=	0.1692	C_{Z_α}	=	-5.7874	C_{m_α}	=	-0.7486
C_{X_q}	=	-0.0900	C_{Z_q}	=	-9.0997	C_{m_q}	=	-14.9294

Table 6.5: The PCA-model steady symmetric stability derivatives in $\mathcal{F}_S$ for the trim condition $\alpha_0 = 1.5^o$.

C_{Y_0}	=	0	C_{ℓ_0}	=	0	C_{n_0}	=	0
C_{Y_β}	=	-0.4046	C_{ℓ_β}	=	-0.1090	C_{n_β}	=	0.0676
C_{Y_p}	=	-0.0733	C_{ℓ_p}	=	-0.5194	C_{n_p}	=	0.0010
C_{Y_r}	=	0.1193	C_{ℓ_r}	=	0.1039	C_{n_r}	=	-0.1279

Table 6.6: The PCA-model steady asymmetric stability derivatives in $\mathcal{F}_S$ for the trim condition $\alpha_0 = 1.5^o$.

x_{cg}	=	7.2059	m (estimated)
y_{cg}	=	0	m
z_{cg}	=	3.0450	m (estimated)
span b	=	15.762	m
m.a.c. $\bar{c}$	=	2.057	m
wing-area S	=	30.000	m^2

Table 6.7: The aircraft center of gravity position in $\mathcal{F}_{rig}$ and aircraft geometry parameters used for flight test data analysis (see reference [27]).

Mass m	=	6042.3	kg
Moment of inertia I_y	=	35028.9680	kg m^2
Airspeed Q_∞	=	90.6550	m/sec
Angle-of-attack α	=	6.0075	Deg.
Angle of side-slip β	=	0.0000	Deg.
Angle of pitch θ_0	=	3.2659	Deg.
Air-density ρ	=	0.7734	kg m^{-3}
Roll-rate p	=	0.0000	Rad/sec
Pitch-rate q	=	0.0100	Rad/sec
Yaw-rate r	=	0.0000	Rad/sec

Table 6.8: The initial state parameters used for flight test data analysis (see reference [27]).

flight test Results						**LPF Results**		
Parameter			Standard deviation			Parameter		
C_{X_0}	=	0.0119	$\sigma_{C_{X_0}}$	=	0.00303	C_{X_0}	=	-0.0018
C_{Z_0}	=	-0.2267	$\sigma_{C_{Z_0}}$	=	0.02925	C_{Z_0}	=	-0.2292
C_{m_0}	=	0.0138	$\sigma_{C_{m_0}}$	=	0.00255	C_{m_0}	=	0.0186
C_{X_u}	=	N.A.		⋯		C_{X_u}	=	-0.0032
C_{Z_u}	=	N.A.		⋯		C_{Z_u}	=	-0.4592
C_{m_u}	=	N.A.		⋯		C_{m_u}	=	0.0358
C_{X_α}	=	-0.5563	$\sigma_{C_{X_\alpha}}$	=	0.03665	C_{X_α}	=	0.1692
C_{Z_α}	=	-5.8450	$\sigma_{C_{Z_\alpha}}$	=	0.02370	C_{Z_α}	=	-5.7874
C_{m_α}	=	-0.4763	$\sigma_{C_{m_\alpha}}$	=	0.00495	C_{m_α}	=	-0.5595
C_{X_q}	=	N.A.		⋯		C_{X_q}	=	-0.1004
C_{Z_q}	=	N.A.		⋯		C_{Z_q}	=	-8.9342
C_{m_q} (1)	=	-17.6698	$\sigma_{C_{m_q}}$	=	1.45690	C_{m_q}	=	-14.6492

Table 6.9: The steady symmetric stability derivatives, including their standard deviation σ, in $\mathcal{F}_S$ obtained from flight test data analysis (taken from reference [27]), and the steady symmetric stability derivatives in $\mathcal{F}_S$ obtained from LPF simulations using the center of gravity position as used in reference [27], $\alpha_0 = 1.5^o$. ($^{(1)}$ note that C_{m_q} obtained from flight tests includes $C_{m_{\dot{\alpha}}}$)

	The contribution of aircraft parts to the symmetrical stability derivatives						
	wing	horizontal stabilizer	pylons	fuselage	vertical fin	nacelles	total configuration (sum)
C_{X_u}	-1.7476e-002	-7.1116e-005	-4.9633e-003	3.4861e-002	-3.0171e-002	1.4661e-002	-3.1594e-003
C_{Z_u}	-4.4486e-001	1.0463e-002	-2.4250e-002	5.4842e-003	-8.2687e-003	2.1936e-003	-4.5923e-001
C_{m_u}	2.2717e-002	2.8091e-002	-3.5845e-002	2.7468e-002	-1.5185e-002	-3.6709e-003	2.3575e-002
C_{X_α}	1.5800e-001	-1.5733e-002	-6.2383e-004	-4.7126e-003	6.1040e-003	2.6137e-002	1.6918e-001
C_{Z_α}	-4.5865e+000	-4.0859e-001	-5.9114e-002	-6.4846e-001	-1.8752e-003	-8.2821e-002	-5.7874e+000
C_{m_α}	9.4989e-003	-1.1285e+000	-5.1828e-002	5.1499e-001	-1.0345e-002	-8.2443e-002	-7.4865e-001
C_{X_q}	-8.3212e-002	-1.6797e-001	-4.3286e-003	1.7162e-002	9.9314e-002	4.9046e-002	-8.9984e-002
C_{Z_q}	-4.3561e+000	-4.2990e+000	-2.5710e-001	5.8978e-002	4.6102e-002	-2.9252e-001	-9.0997e+000
C_{m_q}	-5.6751e-001	-1.1928e+001	-2.5051e-001	-1.9646e+000	7.8669e-002	-2.9791e-001	-1.4929e+001

Table 6.10: The contribution of aircraft parts to the symmetrical stability derivatives, $\alpha_0 = 1.5^o$.

	The contribution of aircraft parts to the asymmetrical stability derivatives						
	wing	horizontal stabilizer	pylons	fuselage	vertical fin	nacelles	total configuration (sum)
C_{Y_β}	-1.0491e-002	-8.0155e-003	3.5297e-004	-1.2713e-001	-2.4288e-001	-1.6391e-002	-4.0455e-001
C_{ℓ_β}	-5.5867e-002	-6.9378e-003	-4.9662e-004	-4.7858e-003	-4.0610e-002	-2.5664e-004	-1.0895e-001
C_{n_β}	5.9554e-003	3.2743e-003	-2.2980e-004	-3.8082e-002	9.5189e-002	1.5098e-003	6.7617e-002
C_{Y_p}	-9.1178e-002	-1.2166e-002	9.4863e-006	6.1341e-002	-3.3447e-002	2.1759e-003	-7.3264e-002
C_{ℓ_p}	-5.0926e-001	-8.6281e-003	2.7291e-004	1.3027e-003	-3.7174e-003	6.0791e-004	-5.1943e-001
C_{n_p}	-1.7228e-002	4.7232e-003	-1.3672e-005	1.4180e-003	1.3120e-002	-1.0475e-003	9.7275e-004
C_{Y_r}	-3.9775e-002	4.2072e-003	-4.4781e-004	-6.8549e-002	2.3872e-001	-1.4820e-002	1.1934e-001
C_{ℓ_r}	6.1648e-002	5.3276e-003	3.4076e-005	7.9752e-004	3.6974e-002	-8.7607e-004	1.0391e-001
C_{n_r}	-1.0267e-003	-1.7439e-003	1.4099e-004	-3.4004e-002	-9.3962e-002	2.7416e-003	-1.2785e-001

Table 6.11: The contribution of aircraft parts to the asymmetrical stability derivatives, $\alpha_0 = 1.5^o$.

Chapter 7

PCA-model symmetrical aerodynamic frequency-response functions

7.1 Introduction

In this chapter the Parametric Computational Aerodynamics (PCA) model symmetrical aerodynamic frequency-response functions for the aircraft configuration defined in chapter 6 will be given. In the time-domain the aerodynamic force and moment coefficients' response ("the output") due to harmonically varying aircraft motions and atmospheric turbulence inputs ("the input") will be calculated. From the input and the output the so-called frequency-dependent stability derivatives are obtained for aircraft motion perturbations. Similarly, the so-called frequency-dependent gust derivatives are obtained for atmospheric turbulence inputs. From these derivatives, the so-called aerodynamic frequency-response data are obtained, see also appendix E. The data will be calculated for a selected range of reduced frequencies using the unsteady Linearized Potential Flow (LPF) simulation method presented in chapter 4. From the aerodynamic frequency-response data the aerodynamic frequency-response functions are calculated. They approximate the frequency-domain data using functions which include rational filters (this procedure is known as "analytical continuation"), see also appendix E. The presented PCA-model aerodynamic frequency-response data and the aerodynamic frequency-response functions will be given for the Stability Frame of Reference $\mathcal{F}_S$. As a function of the reduced frequency $k = \frac{\omega \bar{c}}{2Q_\infty}$, with ω [Rad/sec] the circular frequency of the considered perturbation (being either an isolated aircraft motion perturbation or an isolated atmospheric turbulence input), Q_∞ [m/s] the airspeed and $\bar{c}$ [m] the mean aerodynamic chord, in this chapter the aerodynamic frequency-response functions include the response of the aerodynamic force and moment coefficients $C_X(k)$, $C_Z(k)$ and $C_m(k)$ due to non-dimensional aircraft motion perturbations $\hat{u}(k) = \frac{u(k)}{Q_\infty}$ and $\alpha(k) = \frac{w(k)}{Q_\infty}$. Also, they will include the response due to one-dimensional

	C_X	C_Z	C_m
$\hat{u}(k) = \frac{u(k)}{Q_\infty}$	$\frac{C_X}{\hat{u}}(k)$	$\frac{C_Z}{\hat{u}}(k)$	$\frac{C_m}{\hat{u}}(k)$
$\alpha(k) = \frac{w(k)}{Q_\infty}$	$\frac{C_X}{\alpha}(k)$	$\frac{C_Z}{\alpha}(k)$	$\frac{C_m}{\alpha}(k)$
$\hat{u}_g(k) = \frac{u_g(k)}{Q_\infty}$	$\frac{C_X}{\hat{u}_g}(k)$	$\frac{C_Z}{\hat{u}_g}(k)$	$\frac{C_m}{\hat{u}_g}(k)$
$\alpha_g(k) = \frac{w_g(k)}{Q_\infty}$	$\frac{C_X}{\alpha_g}(k)$	$\frac{C_Z}{\alpha_g}(k)$	$\frac{C_m}{\alpha_g}(k)$

Table 7.1: Symmetrical aerodynamic frequency-response functions for the frame $\mathcal{F}_S$ as a function of the reduced frequency $k = \frac{\omega \bar{c}}{2Q_\infty}$ with respect to aircraft motions ánd 1D atmospheric turbulence inputs.

(1D) atmospheric turbulence inputs given as $\hat{u}_g(k) = \frac{u_g(k)}{Q_\infty}$ and $\alpha_g(k) = \frac{w_g(k)}{Q_\infty}$. The definition of the aircraft motion perturbations and the atmospheric turbulence inputs is given in chapter 5. The aerodynamic frequency-response functions for the frame $\mathcal{F}_S$ are summarized in table 7.1.
The aerodynamic frequency-response of $C_X(k)$ with respect to both the aircraft motion perturbation $\alpha(k) = \frac{w(k)}{Q_\infty}$ and the 1D atmospheric turbulence input $\alpha_g(k) = \frac{w_g(k)}{Q_\infty}$ is left out of consideration since they show non-linear behaviour. The non-linearity of these frequency-response functions will be further discussed in sections 7.3 and 7.4.

7.2 Generation of frequency-response data

7.2.1 Initial condition definitions

For the simulations presented in this chapter, use is made of the initial condition given in chapter 6, which assumes steady, straight, symmetric flight with a steady-state angle-of-attack $\alpha_0 = 1.5^o$ and the steady-state airspeed $Q_\infty = 50$ [m/s], with $\underline{Q}_\infty = [U_\infty, 0, 0]^T$. Also, for the presented simulations, the aerodynamic grid as defined in chapter 6 is used. The definitions of the harmonically varying aircraft motion perturbations and the harmonically varying atmospheric turbulence inputs are given in chapter 5.

7.2.2 Time-domain simulations

In terms of the aerodynamic force and moment coefficient responses, the results of the time-domain simulations are assumed to be due to small perturbations with respect to the initial condition. Also, these time-domain simulations will be performed over slightly more than two cycles to obtain a stationary aerodynamic response. From these simulations it

was concluded that the number of two cycles for time-domain simulations was sufficient enough to obtain a stationary response by checking the minimum and maximum values of the last cycle's unsteady aerodynamic force and moment coefficient responses.
During these simulations the aircraft travels along the negative X_I-axis of the Inertial Frame of Reference $\mathcal{F}_I$. The aerodynamic response (in terms of the aerodynamic force and moment coefficients due to the prescribed perturbations) obtained from the last simulation cycle is used for the determination of the frequency-dependent stability- and gust derivatives.

The symmetrical aircraft motion perturbations u and w are defined according to equations (5.10) and (5.12), while the symmetrical 1D atmospheric turbulence inputs u_g and w_g are defined according to equations (5.18) and (5.20), respectively. The amplitude of the aircraft motion perturbations as well as the atmospheric turbulence inputs is chosen as 1 [m/s] resulting with $Q_\infty = 50$ [m/s] in small perturbations $\hat{u} = \frac{u}{Q_\infty}$, $\alpha = \frac{w}{Q_\infty}$, $\hat{u}_g = \frac{u_g}{Q_\infty}$ and $\alpha_g = \frac{w_g}{Q_\infty}$.

7.2.3 Effect of the discretization time on frequency-response data

Similar to the results presented in chapter 4, the discretization-time Δt for the time-domain simulations is taken to be a function of the reduced frequency $k = \frac{\omega \bar{c}}{2Q_\infty}$. In order to calculate the discretization-time Δt from the prescribed reduced frequency k, the circular frequency is calculated first from,

$$\omega = \frac{2\ k\ Q_\infty}{\bar{c}}$$

Using this expression for ω, the frequency f in cycles per second (or Hz) becomes,

$$f = \frac{2\ k\ Q_\infty}{2\pi\ \bar{c}}$$

from which the period T [sec.] follows,

$$T = \frac{2\pi\ \bar{c}}{2\ k\ Q_\infty}$$

Assuming that a sine function is approximated by a number of $N_{samples}$ samples, the discretization-time Δt is defined as,

$$\Delta t = \frac{2\pi\ \bar{c}}{2\ k\ Q_\infty\ N_{samples}} \tag{7.1}$$

with Δt given in [sec.].
Thus, the discretization-time Δt is determined from the reduced frequency k and the number of samples $N_{samples}$ to describe a single oscillation of the harmonically varying aircraft motion perturbations or the atmospheric turbulence inputs.

In figures 7.1 and 7.2 the time-domain aerodynamic force and moment coefficients $C_X(t)$, $C_Z(t)$ and $C_m(t)$ are presented for the last simulation cycle for a series of the reduced frequency. For these figures the discretization-time Δt according to equation (7.1) is used with $N_{samples} = 30$.
Using the aerodynamic fitting procedures given in appendix E, and the definition of the aircraft motion perturbations and the atmospheric turbulence inputs given in chapter 5, as a function of the discretization-time Δt the symmetrical aerodynamic frequency-response data are shown in figures 7.3 and 7.4. The aerodynamic frequency-response data of the force and moment coefficients C_X, C_Z and C_m are given with respect to symmetrical aircraft motions and symmetrical 1D atmospheric turbulence inputs. They are also shown as a function of the discretization-time Δt given in terms of the parameter $N_{samples}$, which is taken to be $N_{samples} = 10$, $N_{samples} = 20$ and $N_{samples} = 30$. Although the frequency-response data do not vary significantly in terms of magnitude, they do differ considerably in terms of dynamics or in frequency-response. The effect of the discretization-time on the aerodynamic frequency-response is attributed to the wake model since variations in the aircraft circulation are counteracted by the aircraft's wake[1].
The wake-history is given as a function of $N_{samples}$ in figures 7.5, 7.6 and 7.7 for a single simulation cycle for reduced frequencies $k = 0.05$, $k = 0.3$ and $k = 0.5$. It can be seen that the wake discretization in the vicinity of the horizontal stabilizer is too coarse for small reduced frequencies k and discretization-times Δt related to $N_{samples} = 10$. Referring to figures 7.3 and 7.4, the effect of a coarse wake-representation near the horizontal stabilizer on the aerodynamic frequency-responses is highly noticeable, especially for frequency-responses for which the horizontal stabilizer's contribution is dominant (as, for example, for the aerodynamic frequency-response of C_m with respect to longitudinal gust $\hat{u}_g$ and vertical gust α_g).
Providing the most dense wake discretization, thus assuming to result in the most accurate time-domain aerodynamic results, the simulation data for $N_{samples} = 30$ will be used throughout this thesis. Consequently, for time-domain simulations the discretization time Δt related to the $N_{samples} = 30$ condition is used, see also equation (7.1).
For the discretization time Δt related to the $N_{samples} = 30$ condition, in the following sections the aerodynamic frequency-responses are given with respect to aircraft motion perturbations and atmospheric turbulence inputs. The contributions of several aircraft parts, such as the horizontal stabilizer, to these frequency-responses will be discussed.

7.3 Aircraft motion frequency-response results

7.3.1 Breakdown of frequency-response data

In figures 6.10 the definition of these parts is given. The aircraft parts considered include the definitions "wing", "horizontal stabilizer", "pylons", "fuselage", "vertical fin" and "nacelles". Using these definitions, a breakdown of the aerodynamic frequency-response functions in these aircraft parts' contributions is performed, similar to the breakdown of

[1] Which is known as Kelvin's condition, see also chapter 4

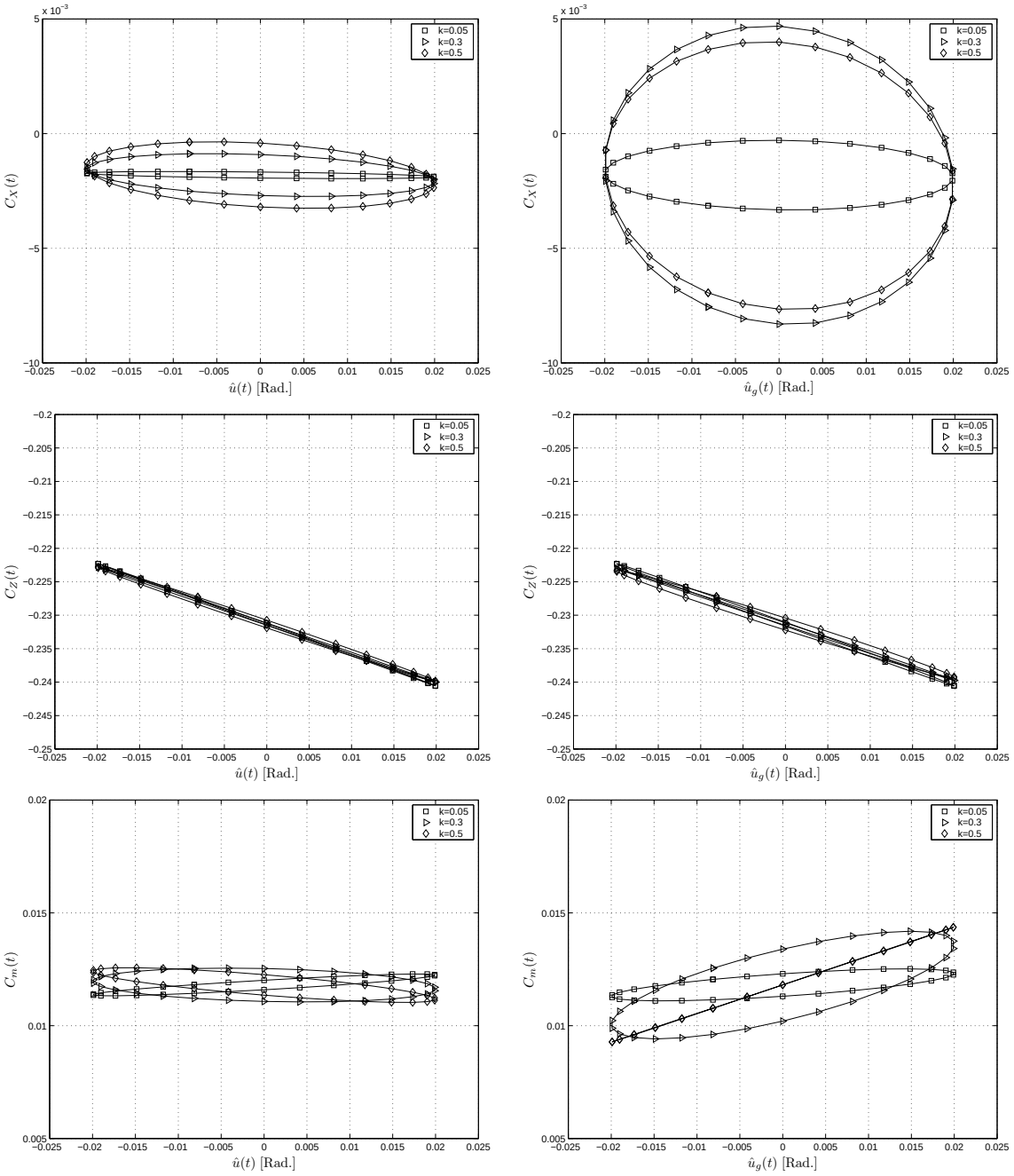


Figure 7.1: Simulated time-dependent aerodynamic force and moment coefficients $C_X(t)$, $C_Z(t)$ and $C_m(t)$ with respect to harmonically varying $\hat{u}(t)$ and $\hat{u}_g(t)$ for the frame $\mathcal{F}_S$, with Δt related to $N_{samples} = 30$, for the Cessna Ce550 Citation II complete aircraft configuration, with $\alpha_0 = 1.5^o$.

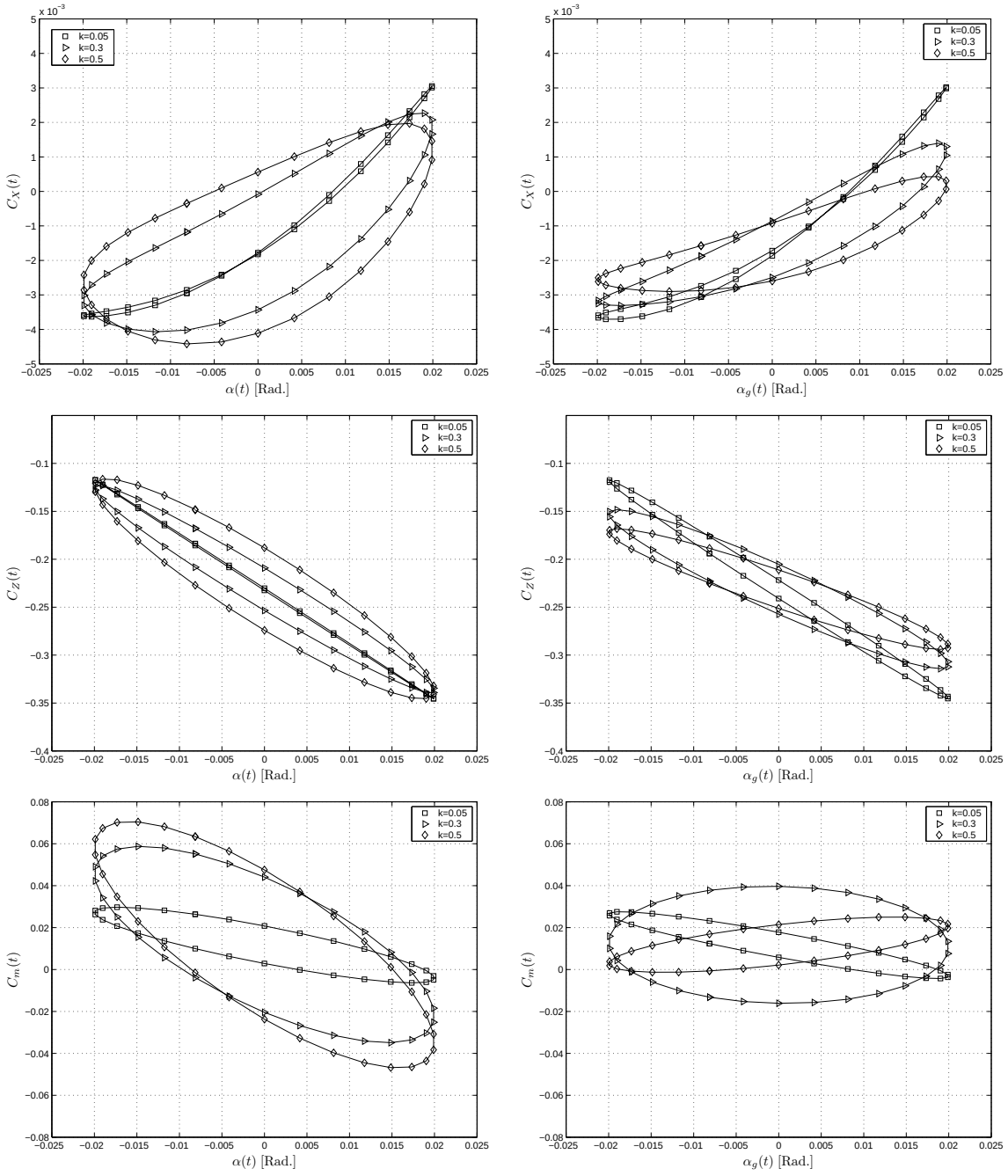


Figure 7.2: Simulated time-dependent aerodynamic force and moment coefficients $C_X(t)$, $C_Z(t)$ and $C_m(t)$ with respect to harmonically varying $\alpha(t)$ and $\alpha_g(t)$ for the frame $\mathcal{F}_S$, with Δt related to $N_{samples} = 30$, for the Cessna Ce550 Citation II complete aircraft configuration, with $\alpha_0 = 1.5^o$.

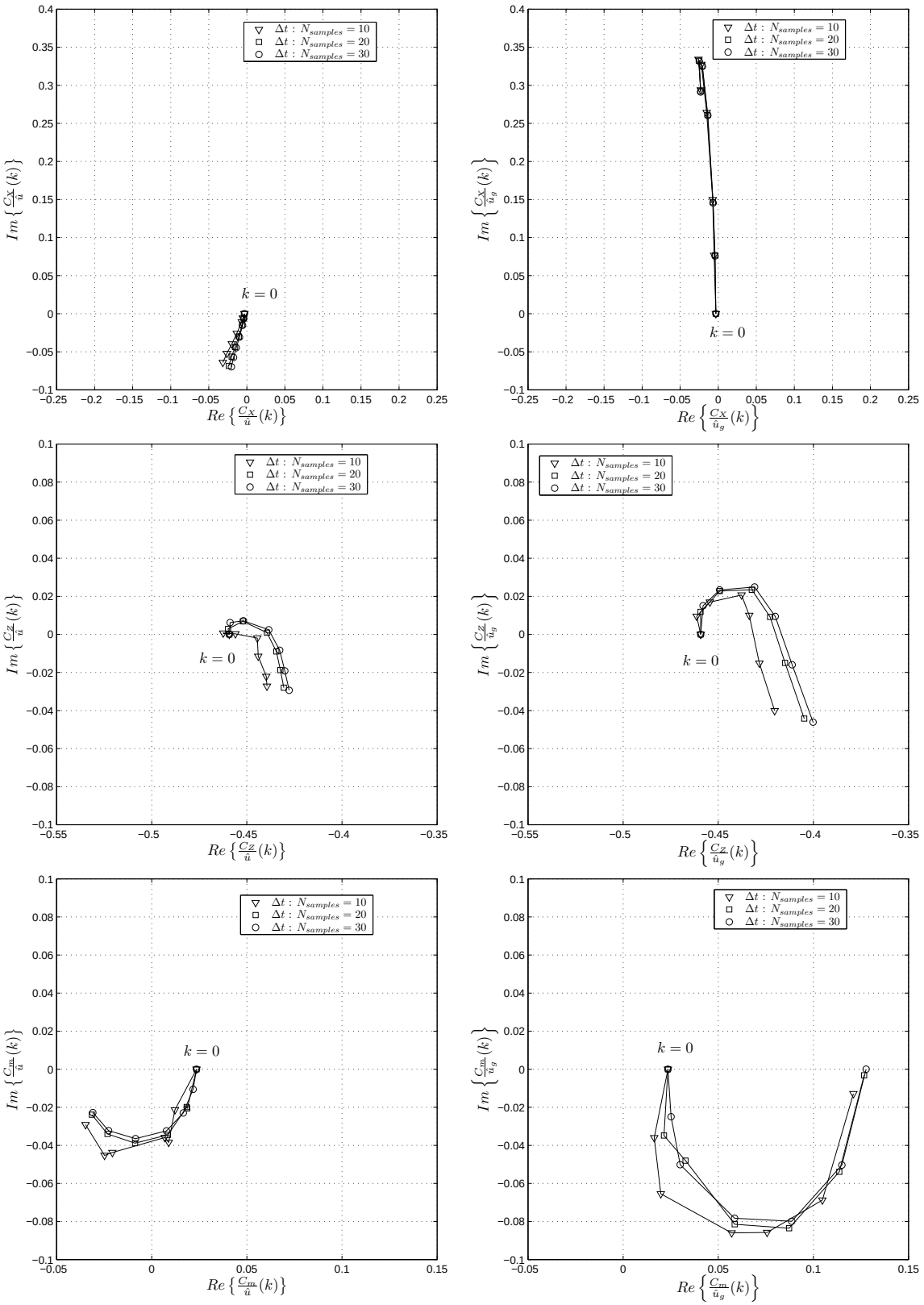


Figure 7.3: Simulated symmetrical aerodynamic frequency-response data in the frame $\mathcal{F}_S$ with respect to $\hat{u}$ and $\hat{u}_g$ as a function of discretization-times Δt related to $N_{samples} = 10$, $N_{samples} = 20$ and $N_{samples} = 30$, for the Cessna Ce550 Citation II complete aircraft configuration, with $\alpha_0 = 1.5^o$.

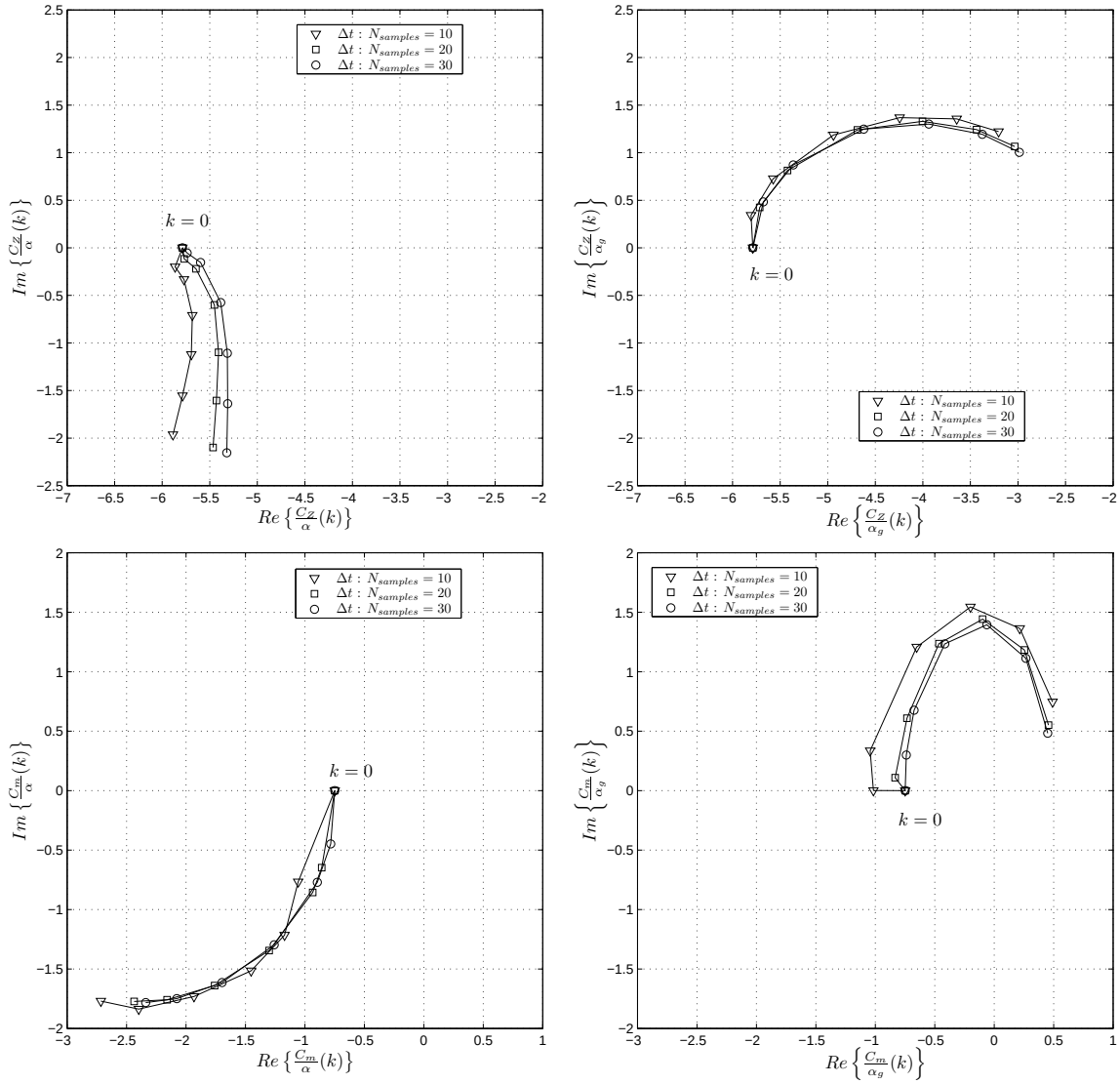
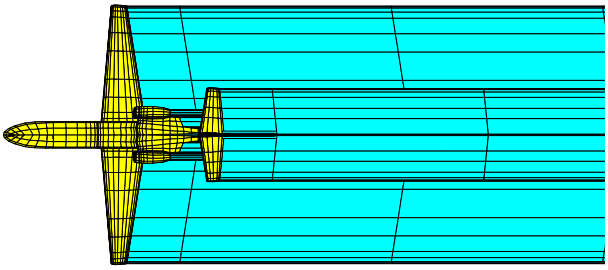
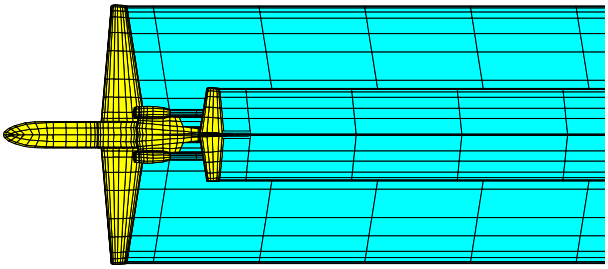


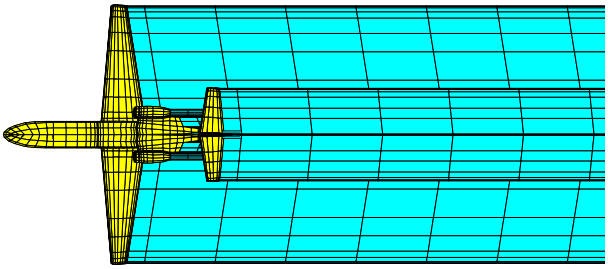
Figure 7.4: Simulated symmetrical aerodynamic frequency-response data in the frame $\mathcal{F}_S$ with respect to α and α_g as a function of discretization-times Δt related to $N_{samples} = 10$, $N_{samples} = 20$ and $N_{samples} = 30$, for the Cessna Ce550 Citation II complete aircraft configuration, with $\alpha_0 = 1.5^o$.



(a) $k = 0.05$, $N_{samples} = 10$

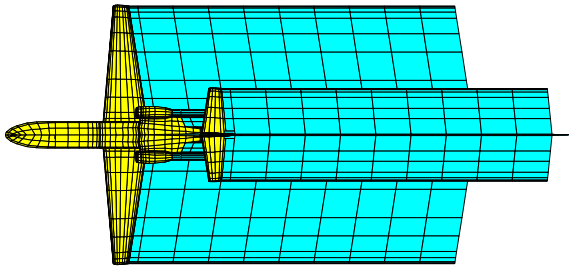


(b) $k = 0.05$, $N_{samples} = 20$

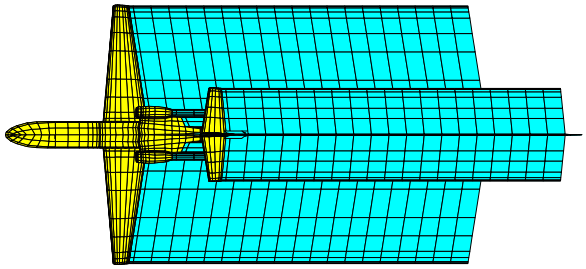


(c) $k = 0.05$, $N_{samples} = 30$

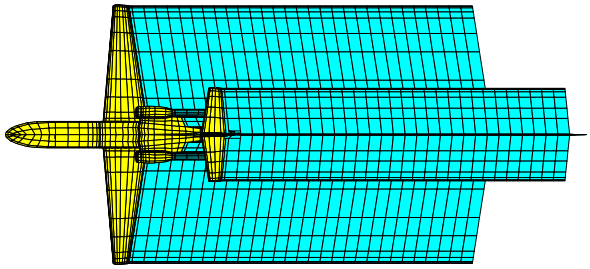
Figure 7.5: Wake history for a single simulation cycle with reduced frequency $k = 0.05$ and discretization-times Δt related to $N_{samples} = 10$, $N_{samples} = 20$ and $N_{samples} = 30$.



(a) $k = 0.3$, $N_{samples} = 10$

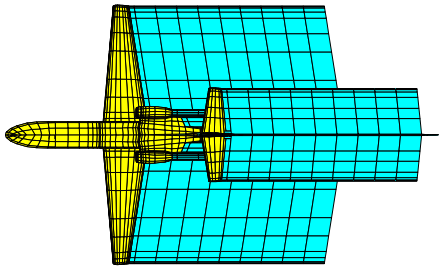


(b) $k = 0.3$, $N_{samples} = 20$

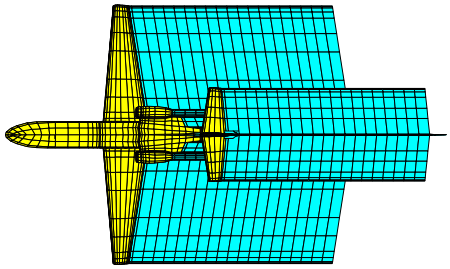


(c) $k = 0.3$, $N_{samples} = 30$

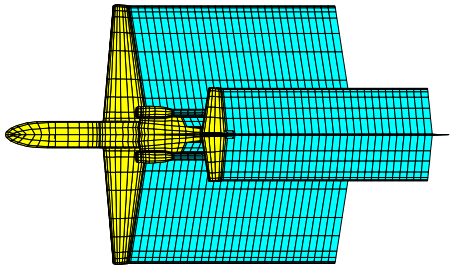
Figure 7.6: Wake history for a single simulation cycle with reduced frequency $k = 0.3$ and discretization-times Δt related to $N_{samples} = 10$, $N_{samples} = 20$ and $N_{samples} = 30$.



(a) $k = 0.5$, $N_{samples} = 10$



(b) $k = 0.5$, $N_{samples} = 20$



(c) $k = 0.5$, $N_{samples} = 30$

Figure 7.7: Wake history for a single simulation cycle with reduced frequency $k = 0.5$ and discretization-times Δt related to $N_{samples} = 10$, $N_{samples} = 20$ and $N_{samples} = 30$.

contributions with respect to the steady stability derivatives, see also chapter 6.

In figures 7.8 and 7.9 the breakdown in aircraft part contributions to the aerodynamic frequency-response data is given for a discretization-time Δt related to $N_{samples} = 30$. In these figures the aircraft configuration's frequency-response is shown as well, which is the sum of all aircraft part contributions to the considered frequency-response data. The calculated aerodynamic frequency-response data is given for the reduced frequencies $k = 0, 0.05, 0.1, 0.2, 0.3, 0.4, 0.5$.
From these figures it is concluded that the aerodynamic frequency-response data of the aerodynamic force and moment coefficients C_X, C_Z and C_m with respect to harmonically varying aircraft surging motions $\hat{u} = \frac{u}{Q_\infty}$ are primarily governed by the contributions of the wing, horizontal-stabilizer and the fuselage. The aerodynamic frequency-response data of the aerodynamic force and moment coefficients C_Z and C_m with respect to harmonically varying aircraft plunging motions $\alpha = \frac{w}{Q_\infty}$ are also primarily governed by the contributions of the wing, horizontal-stabilizer and the fuselage.

7.3.2 Aerodynamic fitting results

Since the aerodynamic frequency-response data are limited to only seven reduced frequencies, the data are approximated by an analytical function. For the aircraft configuration aerodynamic frequency-response, the data are approximated using the function, see also appendix E,

$$\hat{H}(k) = A_0 + A_1\, jk + A_2\, (jk)^2 + \sum_{i=1}^{i=N} B_i \frac{jk}{jk + \beta_i} \tag{7.2}$$

with $\hat{H}(k)$ the estimated analytical frequency-response function for either $\frac{C_X}{\hat{u}}(k)$, $\frac{C_Z}{\hat{u}}(k)$, $\frac{C_m}{\hat{u}}(k)$, $\frac{C_Z}{\alpha}(k)$, $\frac{C_m}{\alpha}(k)$, and A_0, A_1, A_2 the so-called "aerodynamic stiffness", "aerodynamic damping" and "aerodynamic inertia" parameters, respectively. The parameters B_i, $i = 1 \cdots N$, are the gains of the so-called "aerodynamic lag-functions" $\frac{jk}{jk+\beta_i}$, with β_i, $i = 1 \cdots N$, the poles of these functions, and N the number of lag-functions, see also reference [36]. In this thesis for all aerodynamic frequency-response functions the number of lag-functions is chosen as $N = 3$.
Using the aerodynamic fitting procedure given in appendix E, the unknown parameters A_i with $i = 0, 1, 2$, and both B_j and β_j with $j = 1, 2, 3$, are obtained for each aerodynamic frequency-response function. The parameters for each function are summarized in table 7.2. Note that all poles for all the aerodynamic frequency-response functions with respect to the aircraft motions are stable.

In figures 7.10 and 7.11 all aerodynamic frequency-response data are given, including their frequency-response data-fit. The data-fits are given for an increased number of reduced frequency points in order to check that no intermediate oscillations between the calculated frequency-response data occur. It should be noted that the aerodynamic frequency-response function of C_X with respect to both α and α_g are not considered in this thesis,

Aerodynamic function-fit coefficients Aircraft motions			
	A_0	A_1	A_2
$\frac{C_X}{\hat{\mu}}(k)$	-3.1594e-003	-3.6461e-001	1.7074e-001
$\frac{C_Z}{\hat{\mu}}(k)$	-4.5923e-001	-6.1119e-001	1.9494e-001
$\frac{C_m}{\hat{\mu}}(k)$	2.3575e-002	1.1704e+000	-3.9364e-001
$\frac{C_Z}{\alpha}(k)$	-5.7874e+000	-4.7457e+000	7.7100e-001
$\frac{C_m}{\alpha}(k)$	-7.4865e-001	-2.2633e+000	-1.4684e+000
	B_1	B_2	B_3
$\frac{C_X}{\hat{\mu}}(k)$	3.0083e-003	-4.5716e-001	7.7958e-001
$\frac{C_Z}{\hat{\mu}}(k)$	1.5172e-001	-1.9360e-001	1.2446e+000
$\frac{C_m}{\hat{\mu}}(k)$	-1.6229e-002	-1.5822e-001	-3.5033e+000
$\frac{C_Z}{\alpha}(k)$	-9.7144e-001	1.6971e+000	-5.5835e-003
$\frac{C_m}{\alpha}(k)$	-2.8737e-001	-5.1098e+000	1.1030e+001
	β_1	β_2	β_3
$\frac{C_X}{\hat{\mu}}(k)$	1.2936e-001	6.8431e-001	9.0842e-001
$\frac{C_Z}{\hat{\mu}}(k)$	2.7405e-001	4.0314e-001	1.8962e+000
$\frac{C_m}{\hat{\mu}}(k)$	2.1144e-001	6.5135e-001	3.2574e+000
$\frac{C_Z}{\alpha}(k)$	1.2685e-001	1.4500e-001	4.6405e-001
$\frac{C_m}{\alpha}(k)$	1.4526e-001	6.1374e-001	2.7549e+000

Table 7.2: Calculated coefficients for the aerodynamic function-fit (given in equation (7.2)) for longitudinal and vertical aircraft motions.

since the simulated time-dependent response of the aerodynamic force coefficient $C_X(t)$ due to both harmonically varying $\alpha(t)$ and $\alpha_g(t)$ could not be fitted using equation (E.1). For example, for the input $\alpha(t)$ it is written,

$$\hat{C_X}(t) = \mathcal{C}_{\mathcal{X}_\alpha}(k)\ \alpha(t) + \mathcal{C}_{\mathcal{X}_{\dot{\alpha}}}(k)\ \frac{\dot{\alpha}(t)\bar{c}}{2Q_\infty}$$

with $\hat{C_X}(t)$ the model response, $\dot{\alpha}(t)$ the time derivative of the input $\alpha(t)$, and both $\mathcal{C}_{\mathcal{X}_\alpha}(k)$ and $\mathcal{C}_{\mathcal{X}_{\dot{\alpha}}}(k)$ the frequency-dependent steady and unsteady stability derivatives, respectively. Since the response of C_X to both α and α_g shows a non-linear character (due to induced drag, see also figures 7.2), the parameters $\mathcal{C}_{\mathcal{X}_\alpha}(k)$ and $\mathcal{C}_{\mathcal{X}_{\dot{\alpha}}}(k)$ inaccurately modeled the C_X response for all reduced frequencies.

Aerodynamic function-fit coefficients 1D atmospheric turbulence inputs			
	A_0	A_1	A_2
$\frac{C_X}{\hat{u}_g}(k)$	-3.1594e-003	-2.0746e+002	2.8256e+001
$\frac{C_Z}{\hat{u}_g}(k)$	-4.5923e-001	-1.4692e+001	3.6039e+000
$\frac{C_m}{\hat{u}_g}(k)$	2.3575e-002	7.5891e+001	-1.8804e+001
$\frac{C_Z}{\alpha_g}(k)$	-5.7874e+000	-1.6448e+000	-2.7660e+000
$\frac{C_m}{\alpha_g}(k)$	-7.4865e-001	-1.8882e+001	1.8660e+001
	B_1	B_2	B_3
$\frac{C_X}{\hat{u}_g}(k)$	1.1302e+003	-6.5091e+002	1.6767e+003
$\frac{C_Z}{\hat{u}_g}(k)$	5.3975e-002	8.5292e+001	-8.5876e+001
$\frac{C_m}{\hat{u}_g}(k)$	-1.7061e+002	3.9741e+001	-1.4314e+002
$\frac{C_Z}{\alpha_g}(k)$	8.3051e+000	3.2859e+001	-5.5972e+000
$\frac{C_m}{\alpha_g}(k)$	3.0469e+001	-1.3890e+001	-1.0527e-001
	β_1	β_2	β_3
$\frac{C_X}{\hat{u}_g}(k)$	3.4466e+000	2.9893e+000	1.6985e+001
$\frac{C_Z}{\hat{u}_g}(k)$	2.0291e-001	4.7518e+000	2.6593e+001
$\frac{C_m}{\hat{u}_g}(k)$	3.4974e+000	1.6462e+000	2.7680e+000
$\frac{C_Z}{\alpha_g}(k)$	2.5738e-001	2.2310e+001	2.5745e-001
$\frac{C_m}{\alpha_g}(k)$	9.6940e-001	2.6943e+000	7.0000e-002

Table 7.3: Calculated coefficients for the aerodynamic function-fit (given in equation (7.2)) for both 1D longitudinal and vertical atmospheric turbulence inputs.

7.4 1D Atmospheric turbulence input frequency-response results

7.4.1 Breakdown of frequency-response data

Similar to section 7.3.1, a breakdown of aerodynamic results into aircraft parts contributions is performed for the aerodynamic frequency-response data with respect to both 1D longitudinal gusts and 1D vertical gusts. Also similar to section 7.3.1, in figures 7.8 and 7.9 the breakdown in aircraft part contributions to the aerodynamic frequency-response data is given for a discretization-time Δt related to $N_{samples} = 30$, with the aerodynamic frequency-response given for the reduced frequencies used earlier. From these figures it is concluded that the aerodynamic frequency-response data of the aerodynamic force coefficient C_X with respect to 1D harmonically varying longitudinal gusts $\hat{u}_g = \frac{u_g}{Q_\infty}$ are primarily governed by the contributions of the fuselage, wing and vertical-fin. For this

atmospheric turbulence input, the aerodynamic frequency-response data of the aerodynamic force coefficient C_Z is primarily governed by contributions of the fuselage, wing and pylons. Finally, for the considered gust input the aerodynamic frequency-response data of the aerodynamic moment coefficient C_m is primarily governed by contributions of the fuselage, horizontal stabilizer, wing, pylons and vertical fin. The aerodynamic frequency-response data of the aerodynamic force coefficient C_Z with respect to 1D harmonically varying vertical gusts, given as $\alpha = \frac{w}{Q_\infty}$, are primarily governed by the contributions of the wing and the horizontal-stabilizer, while the aerodynamic moment coefficient C_m with respect to the input is primarily governed by contributions of the horizontal stabilizer and fuselage.

7.4.2 Aerodynamic fitting results

Similar to section 7.3.2 the aerodynamic frequency-response data with respect to 1D longitudinal as well as 1D vertical gusts are approximated by equation (7.2). The frequency-response data and the frequency-response data-fit of the functions $\frac{C_X}{\hat{u}_g}(k)$, $\frac{C_Z}{\hat{u}_g}(k)$, $\frac{C_m}{\hat{u}_g}(k)$, $\frac{C_Z}{\alpha_g}(k)$ and $\frac{C_m}{\alpha_g}(k)$ are given in figures 7.10 and 7.11.
Similar to the aircraft motion results, using the aerodynamic fitting procedure given in appendix E the unknown parameters A_i with $i = 0, 1, 2$, and both B_j and β_j with $j = 1, 2, 3$, are calculated for each aerodynamic frequency-response function. The parameters for each function are summarized in table 7.3. Note that also for the aerodynamic frequency-response functions with respect to 1D atmospheric turbulence inputs, all poles are stable.

7.5 Frequency-dependent stability- and gust derivatives

Once the analytical frequency-response functions have been obtained, they are decomposed in the so-called frequency-dependent steady derivatives and frequency-dependent unsteady derivatives. For example, consider the aerodynamic frequency-response function of the aerodynamic force coefficient C_Z with respect to the 1D vertical atmospheric turbulence input $\alpha_g(k) = \frac{w_g(k)}{Q_\infty}$, written as $\frac{C_Z}{\alpha_g}(k)$ with k the reduced frequency. Obviously, the frequency-response $\frac{C_Z}{\alpha_g}(k)$ is complex valued and it is written as,

$$\frac{C_Z}{\alpha_g}(k) = Re\left\{\frac{C_Z}{\alpha_g}(k)\right\} + j\ Im\left\{\frac{C_Z}{\alpha_g}(k)\right\} = \mathcal{C}_{\mathcal{Z}_{\alpha_g}}(k) + jk\,\mathcal{C}_{\mathcal{Z}_{\dot{\alpha}_g}}(k) \tag{7.3}$$

with the frequency-dependent gust derivatives $\mathcal{C}_{\mathcal{Z}_{\alpha_g}}(k)$ and $\mathcal{C}_{\mathcal{Z}_{\dot{\alpha}_g}}(k)$ given as,

$$\mathcal{C}_{\mathcal{Z}_{\alpha_g}}(k) = Re\left\{\frac{C_Z}{\alpha_g}(k)\right\} \tag{7.4}$$

and,

$$\mathcal{C}_{\mathcal{Z}_{\dot{\alpha}_g}}(k) = \frac{1}{k} Im\left\{\frac{C_Z}{\alpha_g}(k)\right\} \tag{7.5}$$

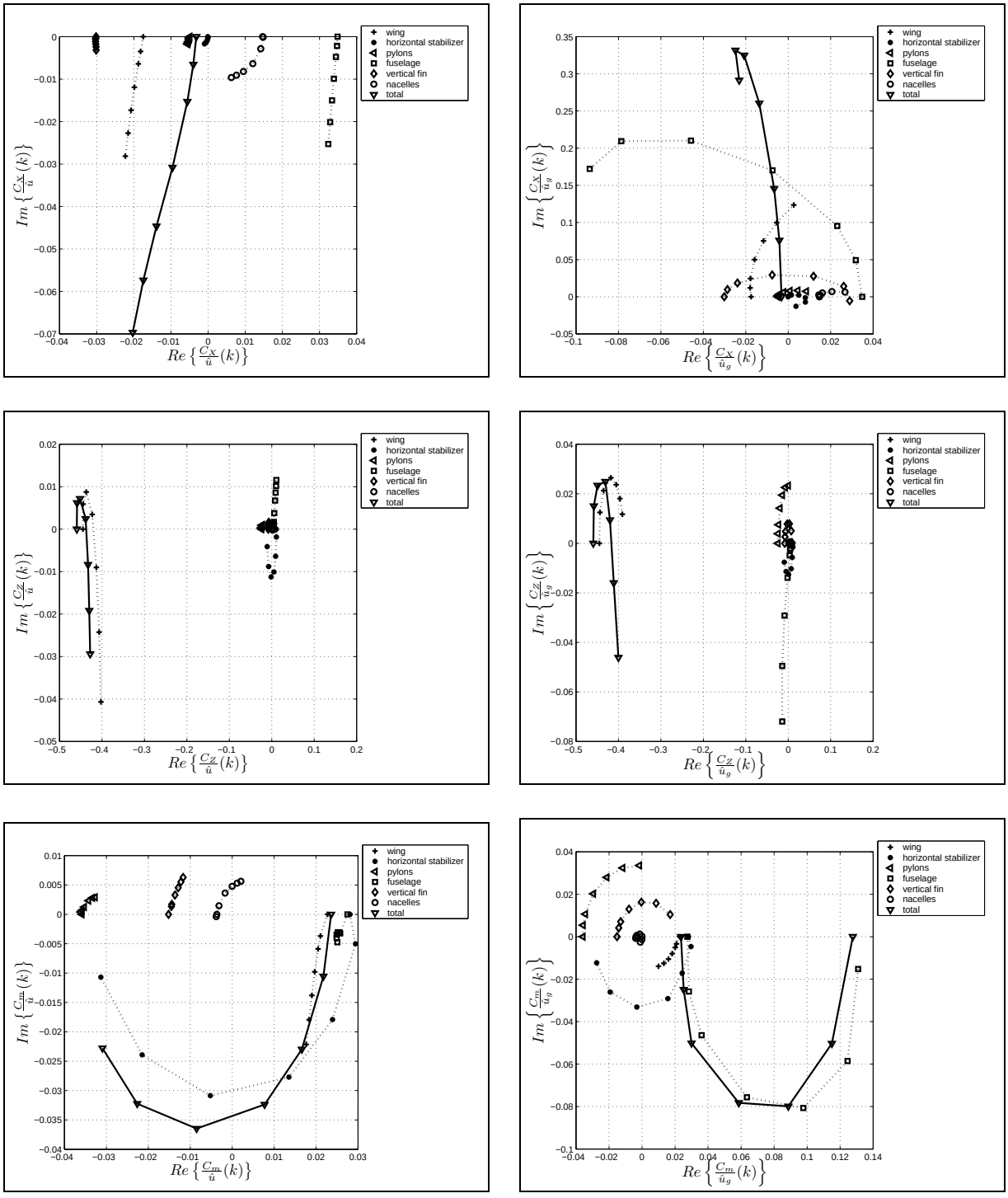


Figure 7.8: Breakdown of the simulated symmetrical aerodynamic frequency-response data in the frame$\mathcal{F}_S$ with respect to $\hat{u}$ and $\hat{u}_g$ in aircraft part contributions, for the Cessna Ce550 Citation II complete aircraft configuration, with $\alpha_0 = 1.5^o$.

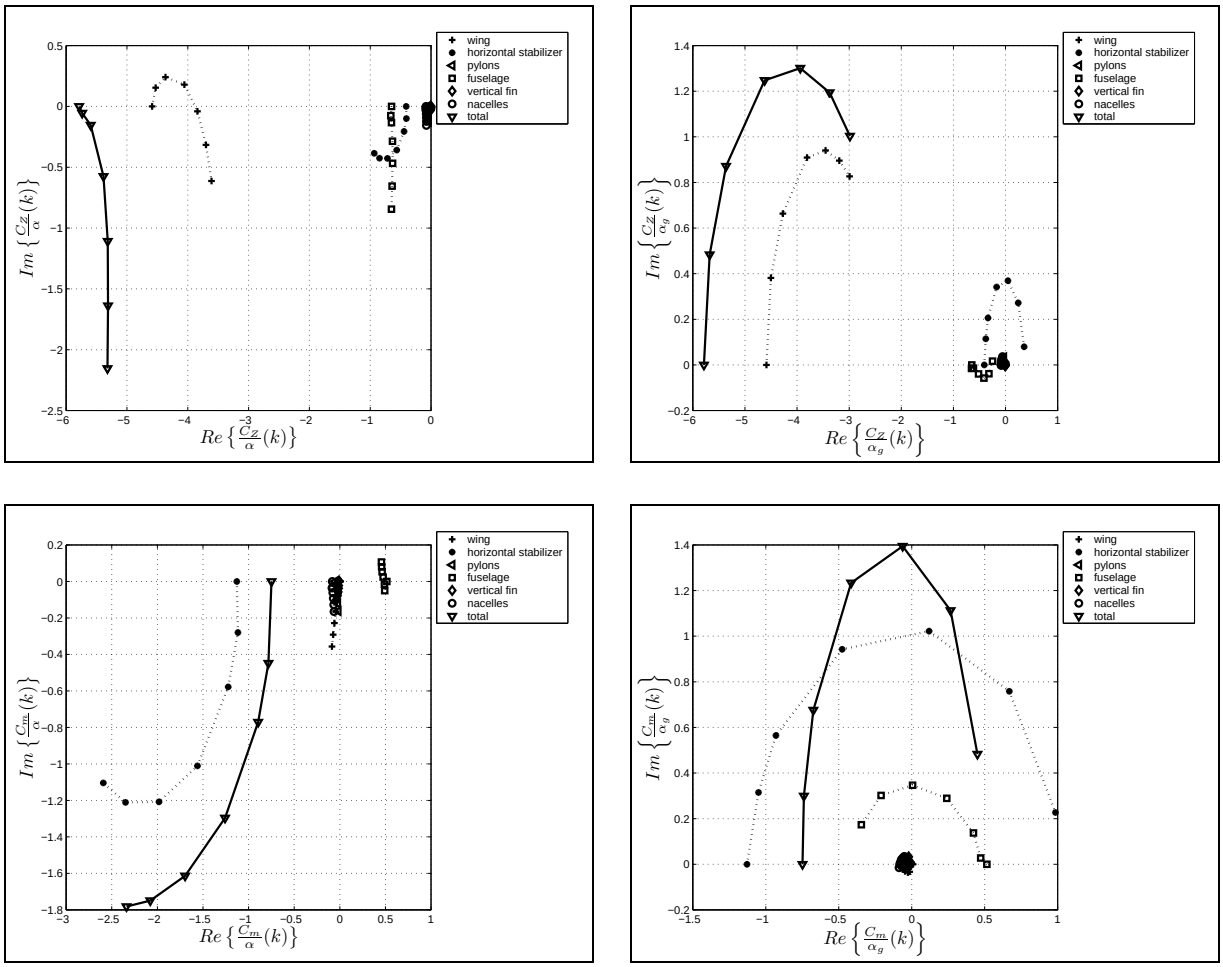


Figure 7.9: Breakdown of the simulated symmetrical aerodynamic frequency-response data in the frame$\mathcal{F}_S$ with respect to α and α_g in aircraft part contributions, for the Cessna Ce550 Citation II complete aircraft configuration, with $\alpha_0 = 1.5^o$.

The definition of the frequency-dependent steady stability derivatives and the frequency-dependent unsteady stability derivatives is summarized in table 7.4, including the definitions of the 1D frequency-dependent steady gust derivatives and the 1D frequency-dependent unsteady gust derivatives. These frequency-dependent stability- and gust derivatives are required in chapter 10 where they will be used for the frequency-domain simulations of the equations of motions.

7.6 Remarks

In this chapter the aerodynamic frequency-response functions for symmetrical aircraft motions and symmetrical atmospheric turbulence inputs have been given. The considered aerodynamic frequency-response functions have been determined for the aerodynamic force and moment coefficients C_X, C_Z and C_m with respect to the symmetrical aircraft motions $\hat{u}(k)$ and $\alpha(k)$ and the symmetrical 1D turbulence inputs $\hat{u}_g(k)$ and $\alpha_g(k)$. The frequency-response functions were obtained by approximating the aerodynamic frequency-response

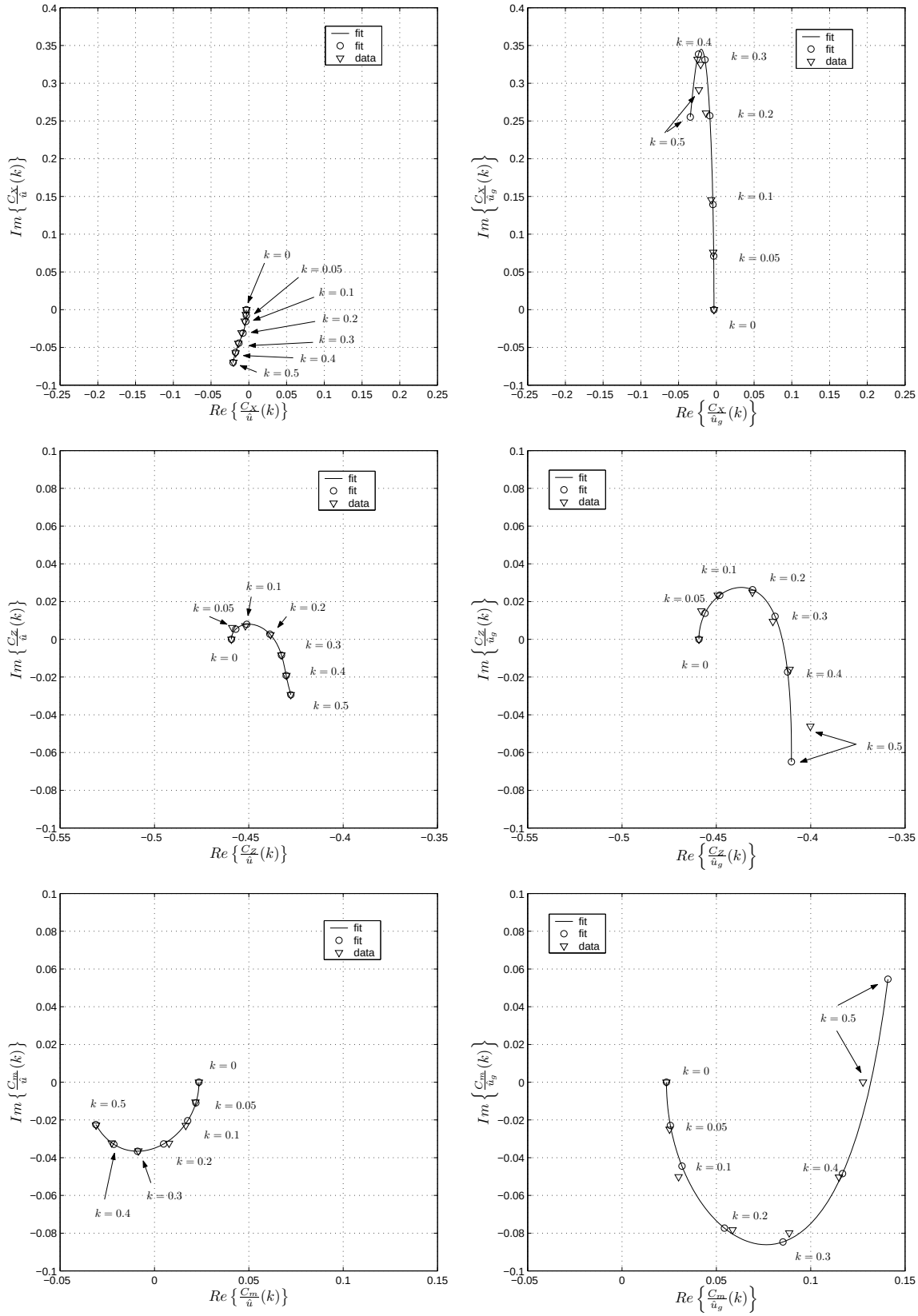


Figure 7.10: Simulated 1D symmetrical aerodynamic frequency-response data in the frame $\mathcal{F}_S$ with respect to $\hat{u}$ and $\hat{u}_g$, including the aerodynamic frequency-response data-fit, for the Cessna Ce550 Citation II complete aircraft configuration, with $\alpha_0 = 1.5^o$.

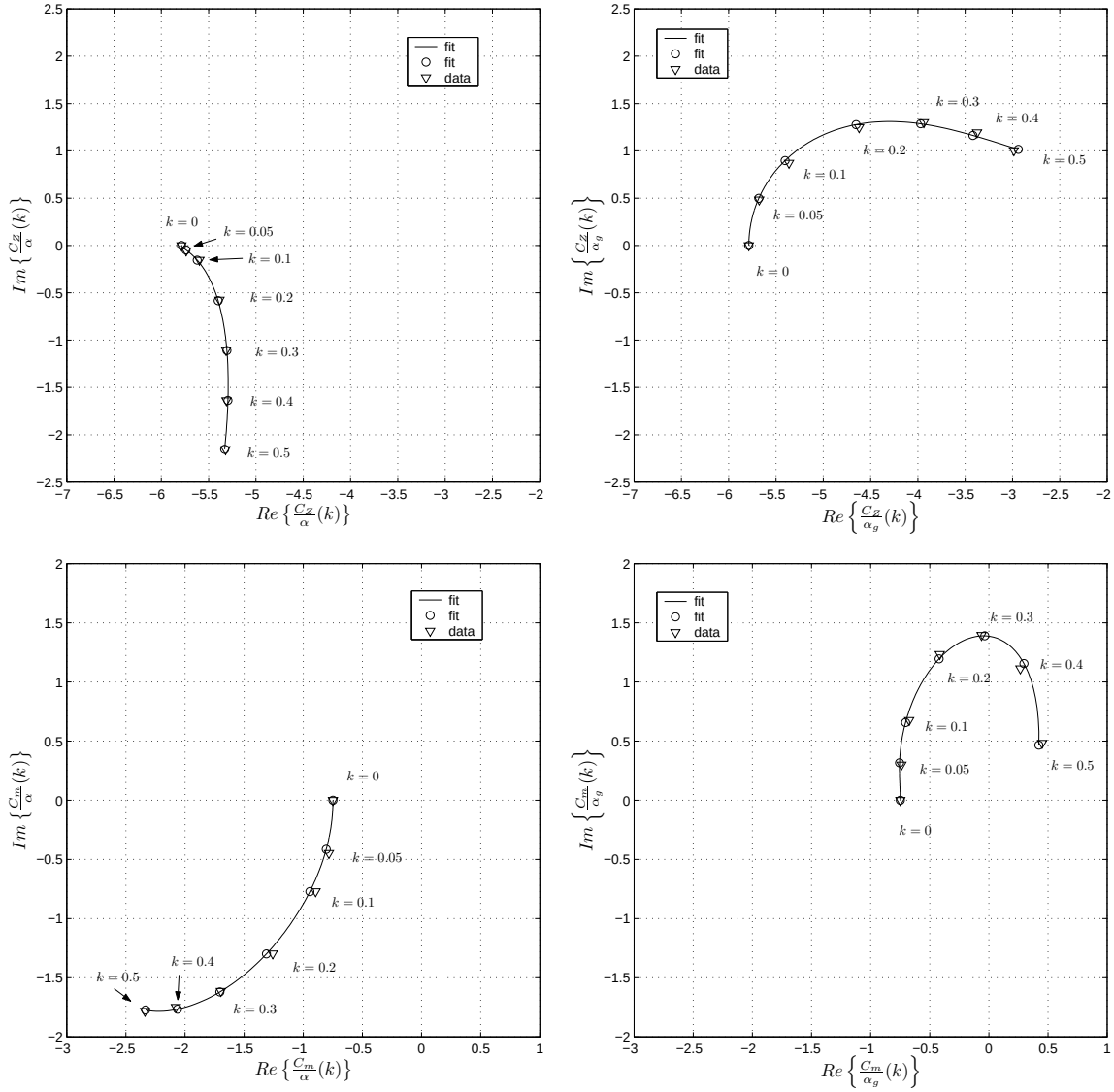


Figure 7.11: Simulated 1D symmetrical aerodynamic frequency-response data in the frame $\mathcal{F}_S$ with respect to α and α_g, including the aerodynamic frequency-response data-fit, for the Cessna Ce550 Citation II complete aircraft configuration, with $\alpha_0 = 1.5^o$.

	Frequency dependent stability- and 1D gust derivatives		
	C_X	C_Z	C_m
$\hat{u}$	$\mathcal{C}_{\mathcal{X}_u}(k) = Re\left\{\frac{C_X}{\hat{u}}(k)\right\}$	$\mathcal{C}_{\mathcal{Z}_u}(k) = Re\left\{\frac{C_Z}{\hat{u}}(k)\right\}$	$\mathcal{C}_{m_u}(k) = Re\left\{\frac{C_m}{\hat{u}}(k)\right\}$
$\frac{\dot{\hat{u}}\bar{c}}{2Q_\infty}$	$\mathcal{C}_{\mathcal{X}_{\dot{u}}}(k) = \frac{1}{k} Im\left\{\frac{C_X}{\hat{u}}(k)\right\}$	$\mathcal{C}_{\mathcal{Z}_{\dot{u}}}(k) = \frac{1}{k} Im\left\{\frac{C_Z}{\hat{u}}(k)\right\}$	$\mathcal{C}_{m_{\dot{u}}}(k) = \frac{1}{k} Im\left\{\frac{C_m}{\hat{u}}(k)\right\}$
α	$\mathcal{C}_{\mathcal{X}_\alpha}(k) = Re\left\{\frac{C_X}{\alpha}(k)\right\}$	$\mathcal{C}_{\mathcal{Z}_\alpha}(k) = Re\left\{\frac{C_Z}{\alpha}(k)\right\}$	$\mathcal{C}_{m_\alpha}(k) = Re\left\{\frac{C_m}{\alpha}(k)\right\}$
$\frac{\dot{\alpha}\bar{c}}{2Q_\infty}$	$\mathcal{C}_{\mathcal{X}_{\dot{\alpha}}}(k) = \frac{1}{k} Im\left\{\frac{C_X}{\alpha}(k)\right\}$	$\mathcal{C}_{\mathcal{Z}_{\dot{\alpha}}}(k) = \frac{1}{k} Im\left\{\frac{C_Z}{\alpha}(k)\right\}$	$\mathcal{C}_{m_{\dot{\alpha}}}(k) = \frac{1}{k} Im\left\{\frac{C_m}{\alpha}(k)\right\}$
$\hat{u}_g$	$\mathcal{C}_{\mathcal{X}_{u_g}}(k) = Re\left\{\frac{C_X}{\hat{u}_g}(k)\right\}$	$\mathcal{C}_{\mathcal{Z}_{u_g}}(k) = Re\left\{\frac{C_Z}{\hat{u}_g}(k)\right\}$	$\mathcal{C}_{m_{u_g}}(k) = Re\left\{\frac{C_m}{\hat{u}_g}(k)\right\}$
$\frac{\dot{\hat{u}}_g\bar{c}}{2Q_\infty}$	$\mathcal{C}_{\mathcal{X}_{\dot{u}_g}}(k) = \frac{1}{k} Im\left\{\frac{C_X}{\hat{u}_g}(k)\right\}$	$\mathcal{C}_{\mathcal{Z}_{\dot{u}_g}}(k) = \frac{1}{k} Im\left\{\frac{C_Z}{\hat{u}_g}(k)\right\}$	$\mathcal{C}_{m_{\dot{u}_g}}(k) = \frac{1}{k} Im\left\{\frac{C_m}{\hat{u}_g}(k)\right\}$
α_g	$\mathcal{C}_{\mathcal{X}_{\alpha_g}}(k) = Re\left\{\frac{C_X}{\alpha_g}(k)\right\}$	$\mathcal{C}_{\mathcal{Z}_{\alpha_g}}(k) = Re\left\{\frac{C_Z}{\alpha_g}(k)\right\}$	$\mathcal{C}_{m_{\alpha_g}}(k) = Re\left\{\frac{C_m}{\alpha_g}(k)\right\}$
$\frac{\dot{\alpha}_g\bar{c}}{2Q_\infty}$	$\mathcal{C}_{\mathcal{X}_{\dot{\alpha}_g}}(k) = \frac{1}{k} Im\left\{\frac{C_X}{\alpha_g}(k)\right\}$	$\mathcal{C}_{\mathcal{Z}_{\dot{\alpha}_g}}(k) = \frac{1}{k} Im\left\{\frac{C_Z}{\alpha_g}(k)\right\}$	$\mathcal{C}_{m_{\dot{\alpha}_g}}(k) = \frac{1}{k} Im\left\{\frac{C_m}{\alpha_g}(k)\right\}$

Table 7.4: Definition of the symmetrical frequency-dependent stability derivatives and the symmetrical frequency-dependent 1D gust derivatives for the frame $\mathcal{F}_S$ given as a function of the reduced frequency $k = \frac{\omega\bar{c}}{2Q_\infty}$, as calculated from symmetrical aerodynamic frequency-response functions.

data by analytical functions.

In chapter 8 the aerodynamic frequency-response functions for asymmetrical aircraft motions will be given. These functions will be given for both asymmetrical and anti-symmetrical atmospheric turbulence inputs as well.
The results presented in chapters 7 and 8 will be used for the computational aerodynamics model presented in chapter 10. Also, in the latter chapter both the constant unsteady stability- and the constant unsteady gust derivatives will be calculated. In conjunction with the constant stability derivatives calculated in chapter 6, the constant parameter aerodynamic model is then completely determined.

Chapter 8

PCA-model asymmetrical aerodynamic frequency-response functions

8.1 Introduction

In this chapter the Parametric Computational Aerodynamics (PCA) model asymmetrical aerodynamic frequency-response functions for the aircraft configuration defined in chapter 6 will be given. Also, the frequency-dependent stability derivatives are obtained with respect to asymmetrical aircraft motions in terms of the side-slip-angle β. Furthermore, the gust derivatives are obtained for the asymmetrical atmospheric turbulence input β_g and both the anti-symmetrical longitudinal $\hat{u}_g$ and vertical α_g inputs. From these derivatives, the aerodynamic frequency-response data are obtained, see appendix E.
The frequency-response data will be calculated over a selected range of reduced frequencies using the unsteady Linearized Potential Flow (LPF) simulation method presented in chapter 4. From the aerodynamic frequency-response data the aerodynamic frequency-response functions are calculated. These functions approximate the frequency-domain data using functions which include rational filters, see also appendix E.

The PCA-model aerodynamic frequency-response data and the aerodynamic frequency-response functions presented will be given for the Stability Frame of Reference $\mathcal{F}_S$. The aerodynamic frequency-response functions include the response of the aerodynamic force and moment coefficients $C_Y(k)$, $C_\ell(k)$ and $C_n(k)$ due to the non-dimensional aircraft motion perturbation $\beta = \frac{v(k)}{Q_\infty}$. Also, they include the response due to the one-dimensional (1D) atmospheric turbulence input given as $\beta_g = \frac{v_g(k)}{Q_\infty}$. Finally, the aerodynamic frequency-response functions include the response of the aerodynamic force and moment coefficients $C_Y(k,\Omega_y)$, $C_\ell(k,\Omega_y)$ and $C_n(k,\Omega_y)$ due to anti-symmetrical two-dimensional (2D) atmospheric turbulence inputs given as $\hat{u}_g(k,\Omega_y) = \frac{u_g(k,\Omega_y)}{Q_\infty}$ and $\alpha_g(k,\Omega_y) = \frac{w_g(k,\Omega_y)}{Q_\infty}$. The

	C_Y	C_ℓ	C_n
$\beta(k) = \frac{v(k)}{Q_\infty}$	$\frac{C_Y}{\beta}(k)$	$\frac{C_\ell}{\beta}(k)$	$\frac{C_n}{\beta}(k)$
$\beta_g(k) = \frac{v_g(k)}{Q_\infty}$	$\frac{C_Y}{\beta_g}(k)$	$\frac{C_\ell}{\beta_g}(k)$	$\frac{C_n}{\beta_g}(k)$
$\hat{u}_g(k,\Omega_y) = \frac{u_g(k,\Omega_y)}{Q_\infty}$	$\frac{C_Y}{\hat{u}_g}(k,\Omega_y)$	$\frac{C_\ell}{\hat{u}_g}(k,\Omega_y)$	$\frac{C_n}{\hat{u}_g}(k,\Omega_y)$
$\alpha_g(k,\Omega_y) = \frac{w_g(k,\Omega_y)}{Q_\infty}$	$\frac{C_Y}{\alpha_g}(k,\Omega_y)$	$\frac{C_\ell}{\alpha_g}(k,\Omega_y)$	$\frac{C_n}{\alpha_g}(k,\Omega_y)$

Table 8.1: Both asymmetrical and anti-symmetrical aerodynamic frequency-response functions for the frame $\mathcal{F}_S$ as a function of the reduced frequency $k = \frac{\omega \bar{c}}{2Q_\infty}$ and the spatial frequency Ω_y with respect to aircraft motions ánd both 1D and 2D atmospheric turbulence inputs.

definitions of the aircraft motion perturbations and the atmospheric turbulence inputs are given in chapter 5. The aerodynamic frequency-response functions for the frame $\mathcal{F}_S$ are summarized in table 8.1.

8.2 Generation of frequency-response data

8.2.1 Initial condition definitions

Similar to chapter 7, here use is made of the initial condition given in chapter 6. This condition assumes steady, straight, symmetric flight with the steady-state angle-of-attack $\alpha_0 = 1.5^o$ and the steady-state airspeed $Q_\infty = 50$ [m/s], with $\underline{Q}_\infty = [U_\infty, 0, 0]^T$. The aerodynamic grid as defined in chapter 6 is also used here. Definitions of the harmonically varying aircraft motion perturbations and the harmonically varying atmospheric turbulence inputs are given in chapter 5.

8.2.2 Time-domain simulations

Again, the aerodynamic force and moment coefficients response, as resulting from the time-domain simulations are assumed to be caused by small perturbations with respect to the initial condition. Also, the time-domain simulations presented in this chapter will be performed over slightly more than two cycles in order to obtain a stationary aerodynamic response. During these simulations the aircraft travels along the negative X_I-axis of the Inertial Frame of Reference $\mathcal{F}_I$. The aerodynamic response (in terms of the aerodynamic force and moment coefficients due to the prescribed disturbances) obtained from the last

simulation cycle is used for the estimation of the frequency-dependent stability- and gust derivatives.

The asymmetrical aircraft motion perturbation v is defined according to equation (5.11), whereas the asymmetrical 1D atmospheric turbulence input v_g is defined according to equation (5.19). The anti-symmetrical 2D atmospheric turbulence inputs u_g and w_g are defined according to equations (5.25) and (5.27), respectively. The amplitude of the aircraft motion perturbation and the atmospheric turbulence inputs are chosen as 1 [m/s] resulting with $Q_\infty = 50$ [m/s] in small perturbations $\beta = \frac{v}{Q_\infty}$, $\hat{u}_g = \frac{u_g}{Q_\infty}$, $\beta_g = \frac{v_g}{Q_\infty}$ and $\alpha_g = \frac{w_g}{Q_\infty}$.

8.2.3 Effect of the discretization time on frequency-response data

Similar to section 7.2.3, the discretization-time Δt is determined from the reduced frequency k and the number of samples $N_{samples}$ to describe a single oscillation of the harmonically varying aircraft motion perturbations as well as the atmospheric turbulence inputs.

In figure 8.1 the time-domain aerodynamic force and moment coefficients $C_Y(t)$, $C_\ell(t)$ and $C_n(t)$ are presented for the last simulation cycle for a number of reduced frequencies ($k = 0.05, 0.3, 0.5$). Here the used discretization-time Δt is according to equation (7.1) with $N_{samples} = 30$. From these time-domain results the frequency-dependent stability and gust derivatives are calculated which eventually result in aerodynamic frequency-response data, see also appendix E.
Using the aerodynamic fitting procedures and both the definition of the aircraft motion perturbations ánd the atmospheric turbulence inputs given in chapter 5, the asymmetrical aerodynamic frequency-response data are shown in figures 8.2 as a function of the discretization-time Δt. The aerodynamic frequency-response data of the force and moment coefficients C_Y, C_ℓ and C_n are given with respect to the asymmetrical aircraft motion β and the asymmetrical 1D atmospheric turbulence input β_g. They are also shown as a function of the discretization-time Δt given in terms of the parameter $N_{samples}$, which is taken to be $N_{samples} = 10$, $N_{samples} = 20$ and $N_{samples} = 30$.

Contrary to the symmetrical aerodynamic frequency-response data presented in chapter 7, the asymmetrical frequency-response data do not vary significantly in terms of magnitude or dynamics (or in frequency-response). The reduced-dependency of the aerodynamic frequency-response data with respect to the discretization-time Δt is explained from the aircraft parts' dominating contributions to these data. Therefore, in the following sections the aerodynamic frequency-responses are given with respect to the aircraft motion perturbation β and the asymmetrical atmospheric turbulence input β_g. In these sections the contributions of several aircraft parts, such as the horizontal stabilizer, to these frequency-responses will be discussed as well.

All aerodynamic frequency-response data will be given for a discretization time Δt related to $N_{samples} = 30$, see also equation (7.1), while the reduced frequencies considered include $k = 0, 0.05, 0.1, 0.2, 0.3, 0.4, 0.5$.

8.3 Aircraft motion frequency-response results

8.3.1 Breakdown of frequency-response data

In figures 6.10 the definition of isolated aircraft parts is given with the aircraft parts considered, including the definitions “wing”, “horizontal stabilizer”, “pylon”, “nacelles”, “vertical fin” and “fuselage”.

Similar to section 7.3.1, in figures 8.3 the breakdown in aircraft part contributions is given for a discretization-time Δt related to $N_{samples} = 30$. The total aircraft configuration's frequency-response is given as well, the sum of all aircraft part contributions to the considered frequency-response data. The calculated aerodynamic frequency-response data is given for reduced frequencies $k = 0, 0.05, 0.1, 0.2, 0.3, 0.4, 0.5$.
From these figures it is evident that the aerodynamic frequency-response data of the aerodynamic force and moment coefficients C_Y, C_ℓ and C_n with respect to harmonically varying aircraft swaying motions $\beta = \frac{v}{Q_\infty}$ are primarily governed by the contributions of the fuselage and the vertical fin.

8.3.2 Aerodynamic fitting results

Also in this chapter, the aerodynamic frequency-response data are limited to a number of reduced frequencies. The data are approximated by an analytical function given by equation (7.2).
In figures 8.4 all total aircraft configuration aerodynamic frequency-response data are given, including their frequency-response data-fits. The data-fits are also given for an increased number of reduced frequency points in order to check that no intermediate oscillations between the calculated frequency-response data occur.
Using the aerodynamic fitting procedure given in appendix E, the unknown parameters in equation (7.2), A_i with $i = 0, 1, 2$, and both B_j and β_j with $j = 1, 2, 3$ are calculated for each aerodynamic frequency-response function, and they are summarized in table 8.2. Note that all poles for all the aerodynamic frequency-response functions with respect to aircraft motions are stable.

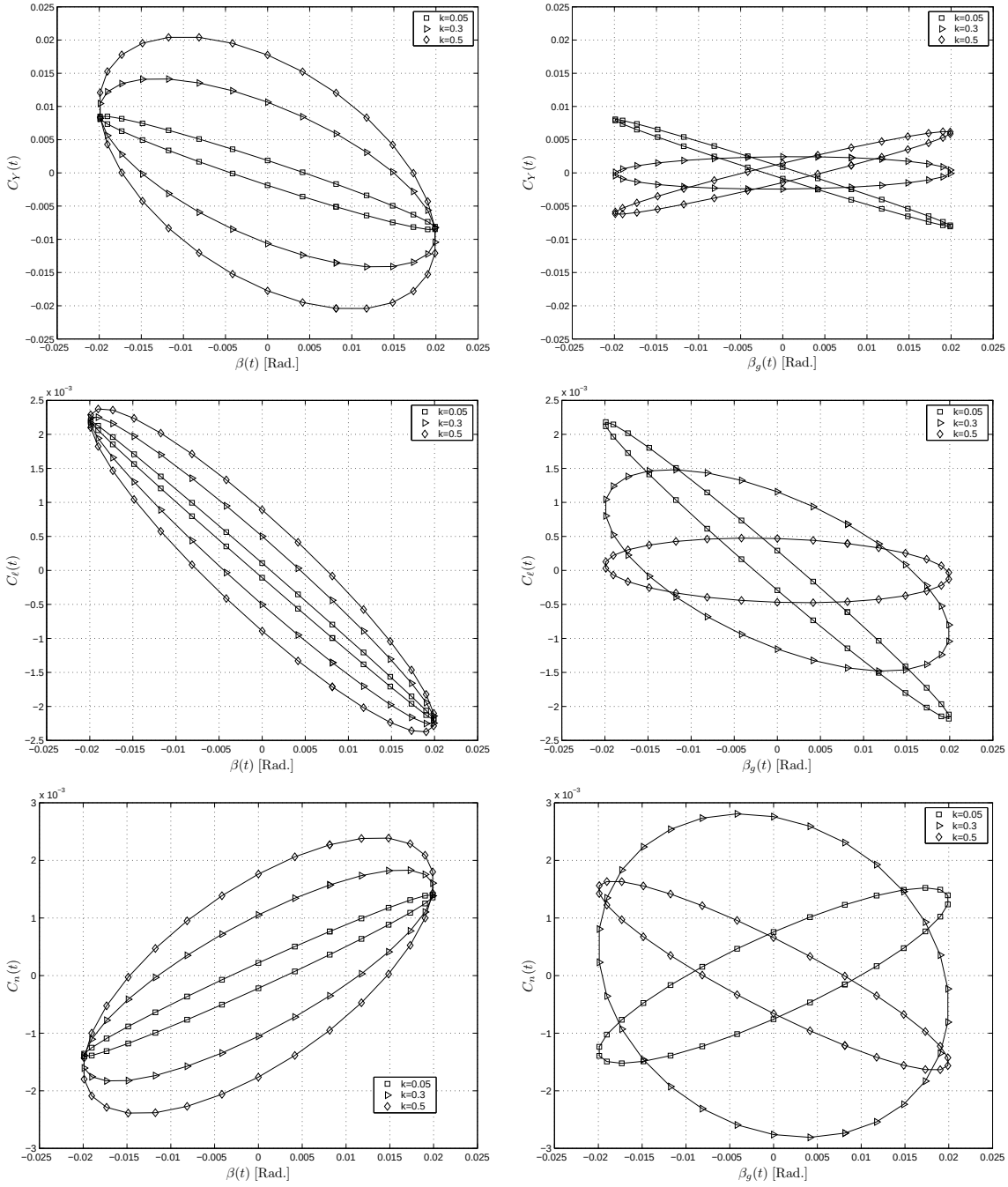


Figure 8.1: Simulated time-dependent aerodynamic force and moment coefficients $C_Y(t)$, $C_\ell(t)$ and $C_n(t)$ with respect to harmonically varying $\beta(t)$ and $\beta_g(t)$ for the frame $\mathcal{F}_S$, with Δt related to $N_{samples} = 30$, for the Cessna Ce550 Citation II complete aircraft configuration, with $\alpha_0 = 1.5^o$.

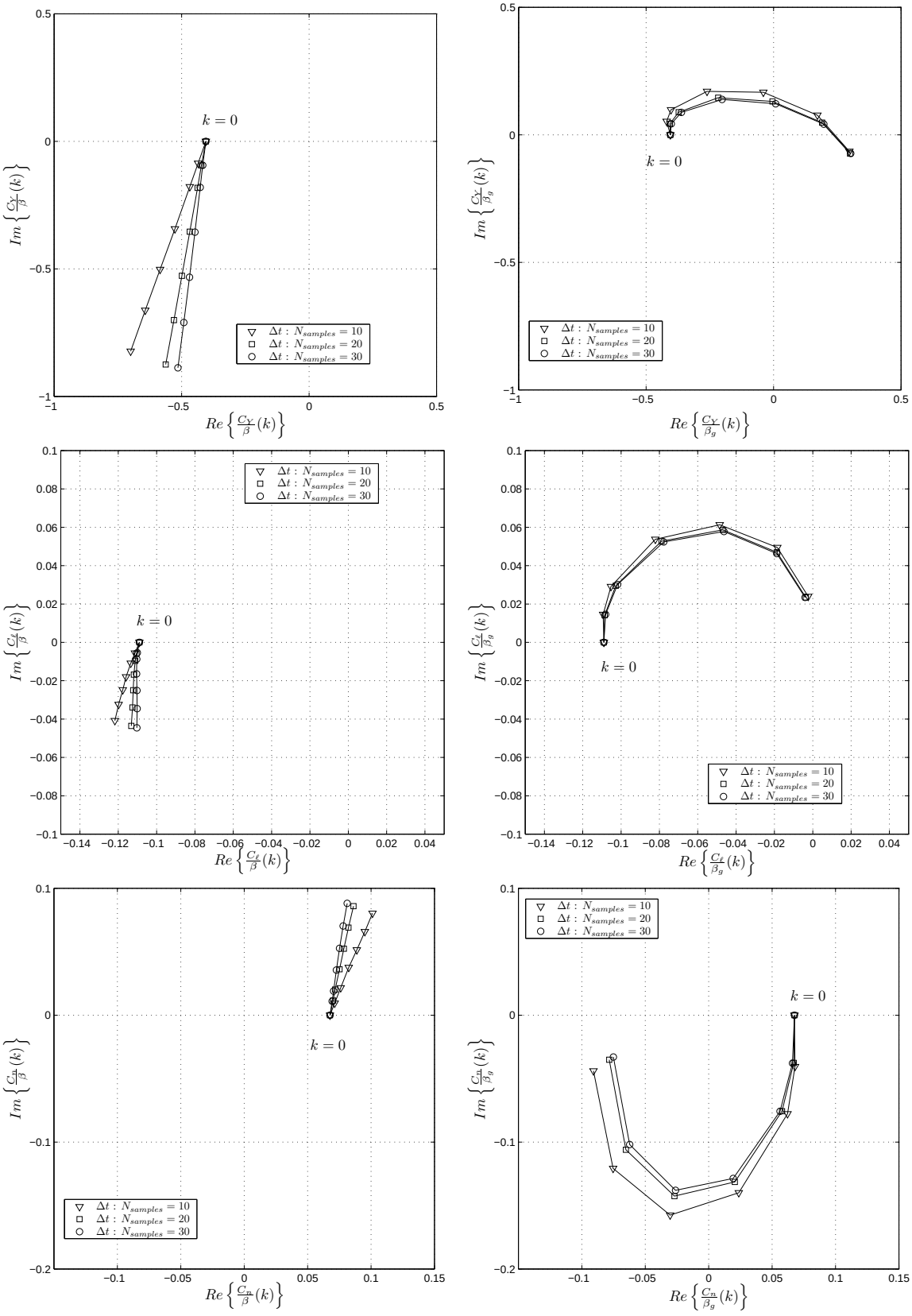


Figure 8.2: Simulated asymmetrical aerodynamic frequency-response data for the frame $\mathcal{F}_S$ with respect to β and β_g as a function of the discretization-times Δt related to $N_{samples} = 10$, $N_{samples} = 20$ and $N_{samples} = 30$, for the Cessna Ce550 Citation II complete aircraft configuration, with $\alpha_0 = 1.5^o$.

Aerodynamic function-fit coefficients Aircraft motion			
	A_0	A_1	A_2
$\frac{C_Y}{\beta}(k)$	-4.0455e-001	2.2525e+000	-1.9185e-001
$\frac{C_\ell}{\beta}(k)$	-1.0895e-001	1.3608e-002	-7.4757e-003
$\frac{C_n}{\beta}(k)$	6.7617e-002	3.3226e-001	-7.9952e-002
	B_1	B_2	B_3
$\frac{C_Y}{\beta}(k)$	-1.5404e-001	1.2892e+001	-2.7125e+001
$\frac{C_\ell}{\beta}(k)$	-2.7429e-003	1.4189e-001	-4.3750e-001
$\frac{C_n}{\beta}(k)$	-1.0537e+000	1.0576e+000	-6.1113e-001
	β_1	β_2	β_3
$\frac{C_Y}{\beta}(k)$	3.2653e-001	1.5678e+000	2.2792e+000
$\frac{C_\ell}{\beta}(k)$	5.7321e-002	1.0222e+000	1.9117e+000
$\frac{C_n}{\beta}(k)$	9.2307e-002	9.2123e-002	3.8338e+000

Table 8.2: Calculated coefficients for the aerodynamic function-fit (given in equation (7.2)) for lateral aircraft motions.

Aerodynamic function-fit coefficients 1D atmospheric turbulence input			
	A_0	A_1	A_2
$\frac{C_Y}{\beta_g}(k)$	-4.0455e-001	6.8114e+001	-1.8628e+001
$\frac{C_\ell}{\beta_g}(k)$	-1.0895e-001	-4.3933e-002	5.1162e-002
$\frac{C_n}{\beta_g}(k)$	6.7617e-002	2.6698e+000	-1.8048e+000
	B_1	B_2	B_3
$\frac{C_Y}{\beta_g}(k)$	1.9933e+002	-3.7048e+002	-4.6623e+002
$\frac{C_\ell}{\beta_g}(k)$	-7.1088e-002	-3.5733e-001	4.3788e-001
$\frac{C_n}{\beta_g}(k)$	7.7907e-003	-1.5923e+000	-4.9390e+000
	β_1	β_2	β_3
$\frac{C_Y}{\beta_g}(k)$	1.4421e+000	1.8459e+000	1.0000e+002
$\frac{C_\ell}{\beta_g}(k)$	2.3254e-001	9.8861e-001	4.3416e-001
$\frac{C_n}{\beta_g}(k)$	1.5779e-001	7.1927e-001	3.9069e+000

Table 8.3: Calculated coefficients for the aerodynamic function-fit (given in equation (7.2)) for 1D lateral atmospheric turbulence inputs.

8.4 1D Atmospheric turbulence input frequency-response results

8.4.1 Breakdown of frequency-response data

Similar to section 7.4.1, a breakdown of aerodynamic results into aircraft part contributions is performed for the aerodynamic frequency-response data with respect to 1D lateral gusts. Also similar to section 7.4.1, in figure 8.3 the breakdown in aircraft part contributions to the aerodynamic frequency-response data is given for a discretization-time Δt related to $N_{samples} = 30$, with the aerodynamic frequency-response given for the reduced frequencies $k = 0, 0.05, 0.1, 0.2, 0.3, 0.4, 0.5$.
From these figures it is concluded that the aerodynamic frequency-response data of the aerodynamic force coefficient C_Y with respect to 1D harmonically varying lateral gusts $\beta_g = \frac{v_g}{Q_\infty}$ are primarily governed by the contributions of the fuselage and vertical fin. For this atmospheric turbulence input, the aerodynamic frequency-response data of the aerodynamic force coefficient C_ℓ is primarily governed by contributions of the vertical fin, wing and horizontal stabilizer. Finally, for the considered gust input the aerodynamic frequency-response data of the aerodynamic moment coefficient C_n is primarily governed by contributions of the fuselage and the vertical fin.

8.4.2 Aerodynamic fitting results

Similar to section 7.4.2 the aerodynamic frequency-response data with respect to 1D lateral gusts are approximated by equation (7.2). The frequency-response data and data-fit of the functions $\frac{C_Y}{\beta_g}(k)$, $\frac{C_\ell}{\beta_g}(k)$ and $\frac{C_n}{\beta_g}(k)$ are given in figures 8.4.
Similar to the aircraft motion fitting results, using the aerodynamic fitting procedure given in appendix E, equation (7.2)'s unknown parameters A_i with $i = 0, 1, 2$, and both B_j and β_j with $j = 1, 2, 3$ are calculated for each aerodynamic frequency-response function, and they are summarized in table 8.3. Note again that also for the aerodynamic frequency-response functions with respect to 1D atmospheric turbulence inputs, all poles are stable.

8.5 2D Atmospheric turbulence input frequency-response results

8.5.1 Aerodynamic fitting results

The aerodynamic frequency-response data of the aerodynamic force and moment coefficients C_Y, C_ℓ and C_n with respect to both (2D) anti-symmetrical longitudinal $\hat{u}_g(k, \Omega_y)$ and vertical gusts $\alpha_g(k, \Omega_y)$ are also considered here (see also chapter 5).
Since the number of aerodynamic frequency-response data-points is limited with respect to the non-dimensional reduced frequencies $k = 0, 0.05, 0.1, 0.2, 0.3, 0.4, 0.5$ and the spatial frequencies $\Omega_y = \frac{2\pi}{40b}, \frac{2\pi}{4b}, \frac{2\pi}{2b}, \frac{2\pi}{1.5b}, \frac{2\pi}{1b}, \frac{2\pi}{0.75b}$, the data are approximated by the analytical

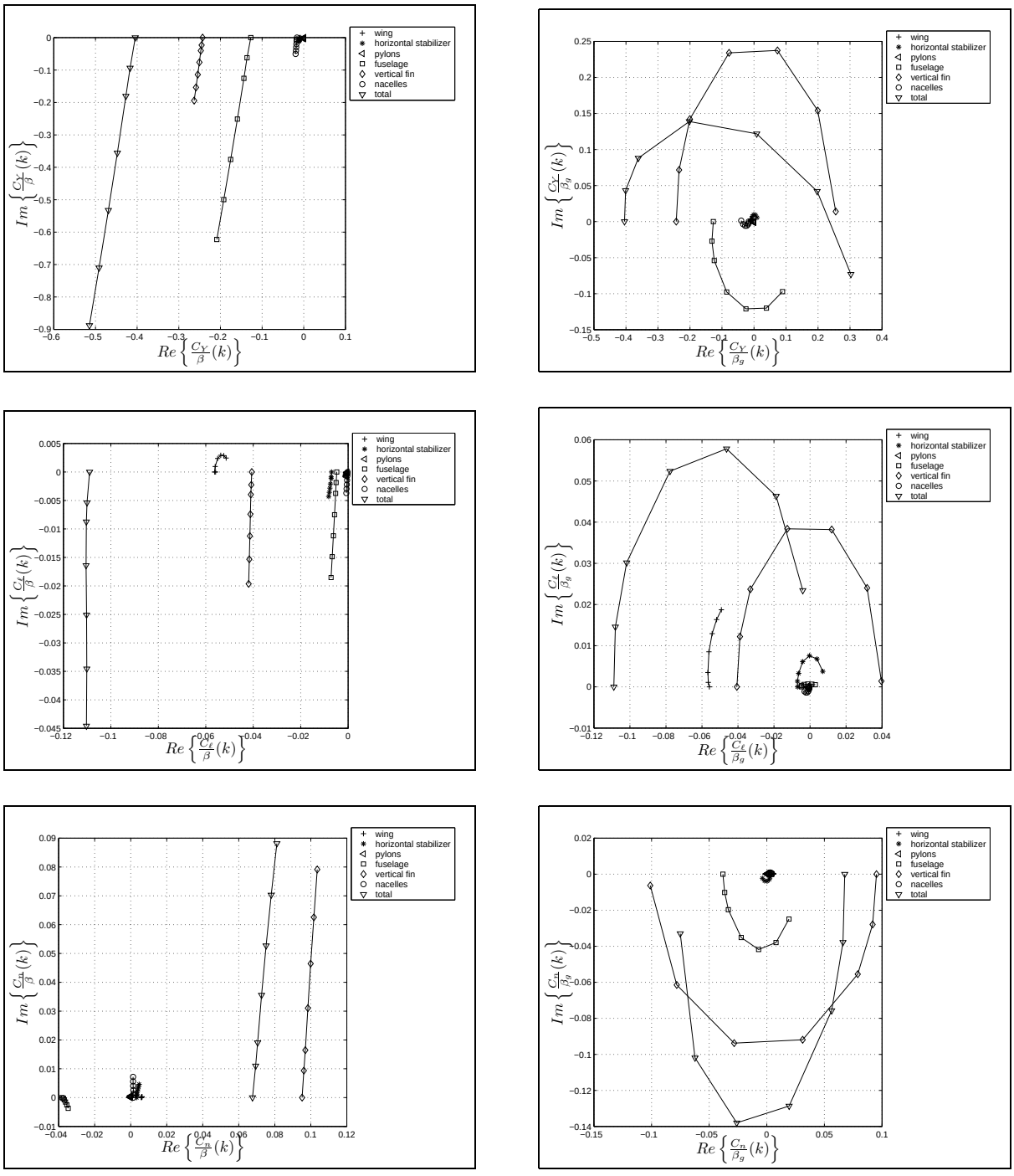


Figure 8.3: Breakdown in aircraft part contributions of the simulated anti-symmetrical aerodynamic frequency-response data with respect to β and β_g in the frame $\mathcal{F}_S$ for the Cessna Ce550 Citation II complete aircraft configuration, $\alpha_0 = 1.5^o$.

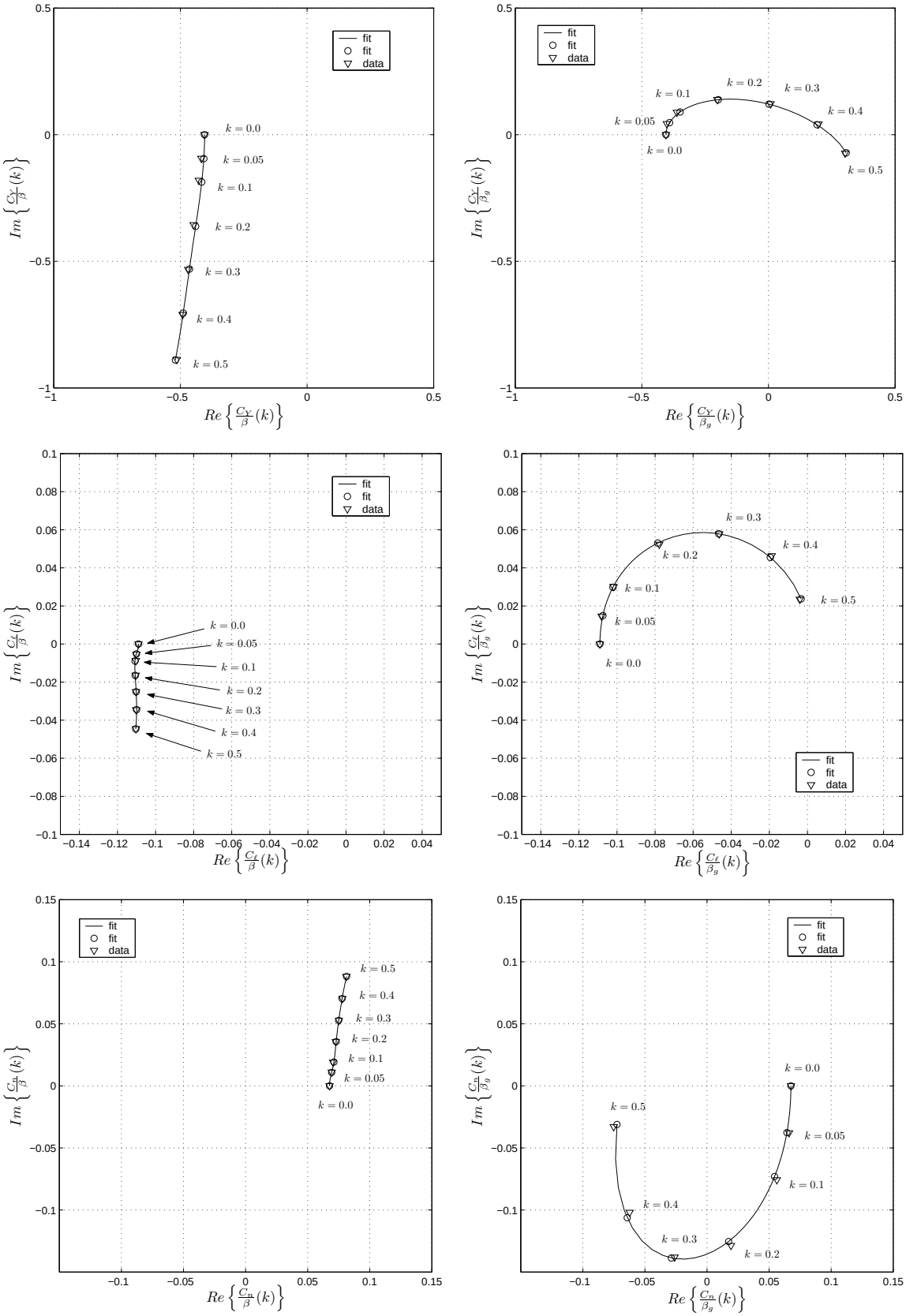


Figure 8.4: Simulated anti-symmetrical aerodynamic frequency-response functions with respect to β and β_g in the frame $\mathcal{F}_S$, including the aerodynamic frequency-response fit, for the Cessna Ce550 Citation II complete aircraft configuration, $\alpha_0 = 1.5^o$.

function, see also appendix E,

$$\hat{H}(k,\Omega_y) = A_0(\Omega_y) + A_1(\Omega_y)(jk) + A_2(\Omega_y)(jk)^2 + \sum_{i=1}^{i=N} B_i(\Omega_y)\frac{jk}{jk+\beta_i(\Omega_y)} \tag{8.1}$$

with $\hat{H}(k,\Omega_y)$ the estimated analytical frequency-response function for either $\frac{C_Y}{\hat{u}_g}(k,\Omega_y)$, $\frac{C_\ell}{\hat{u}_g}(k,\Omega_y)$, $\frac{C_n}{\hat{u}_g}(k,\Omega_y)$, $\frac{C_Y}{\alpha_g}(k,\Omega_y)$, $\frac{C_\ell}{\alpha_g}(k,\Omega_y)$ or $\frac{C_n}{\alpha_g}(k,\Omega_y)$, N the number of lag-terms, the parameters $A_0(\Omega_y)$, $A_1(\Omega_y)$ and $A_2(\Omega_y)$ given by,

$$\begin{aligned}
A_0(\Omega_y) &= A_{00} + A_{01}(\Omega_y) + A_{02}(\Omega_y)^2 + A_{03}(\Omega_y)^3 + A_{04}(\Omega_y)^4 \\
A_1(\Omega_y) &= A_{10} + A_{11}(\Omega_y) + A_{12}(\Omega_y)^2 + A_{13}(\Omega_y)^3 + A_{14}(\Omega_y)^4 \\
A_2(\Omega_y) &= A_{20} + A_{21}(\Omega_y) + A_{22}(\Omega_y)^2 + A_{23}(\Omega_y)^3 + A_{24}(\Omega_y)^4
\end{aligned}$$

and the parameters $B_i(\Omega_y)$ and $\beta_i(\Omega_y)$ given by,

$$B_i(\Omega_y) = B_{i0} + B_{i1}(\Omega_y) + B_{i2}(\Omega_y)^2 + B_{i3}(\Omega_y)^3 + B_{i4}(\Omega_y)^4$$

and,

$$\beta_i(\Omega_y) = \beta_{i0} + \beta_{i1}(\Omega_y) + \beta_{i2}(\Omega_y)^2 + \beta_{i3}(\Omega_y)^3 + \beta_{i4}(\Omega_y)^4$$

respectively. It should be noted that the lag-functions are not required to be stable, that is the poles of equation (8.1) are not required to be negative, since the main goal of the aerodynamic frequency-response data-fits is the generation of data in between calculated aerodynamic frequency-response points.
In figures 8.5 to 8.10 both the 2D aerodynamic frequency-response data and their aerodynamic frequency-response function fits $\frac{C_Y}{\hat{u}_g}(k,\Omega_y)$, $\frac{C_\ell}{\hat{u}_g}(k,\Omega_y)$, $\frac{C_n}{\hat{u}_g}(k,\Omega_y)$, $\frac{C_Y}{\alpha_g}(k,\Omega_y)$, $\frac{C_\ell}{\alpha_g}(k,\Omega_y)$ and $\frac{C_n}{\alpha_g}(k,\Omega_y)$, are shown.

8.6 Frequency-dependent stability- and gust derivatives

Similar to section 7.5, the aerodynamic frequency-response functions are decomposed in the so-called frequency-dependent steady derivatives and frequency-dependent unsteady derivatives. Following the procedure given in section 7.5, the frequency-dependent stability- and gust derivatives are obtained for the asymmetrical aircraft motion and the anti-symmetrical atmospheric turbulence inputs. The definitions of the frequency-dependent steady stability derivatives and the frequency-dependent unsteady stability derivatives are summarized in table 8.4, including the definitions of the 1D frequency-dependent steady gust derivatives and the 1D frequency-dependent unsteady gust derivatives. In table 8.5 the definitions of the 2D frequency-dependent steady gust derivatives and the 2D frequency-dependent unsteady gust derivatives are given. These derivatives are required in chapter 10 where they will be used for the frequency-domain simulations of the equations of motions.

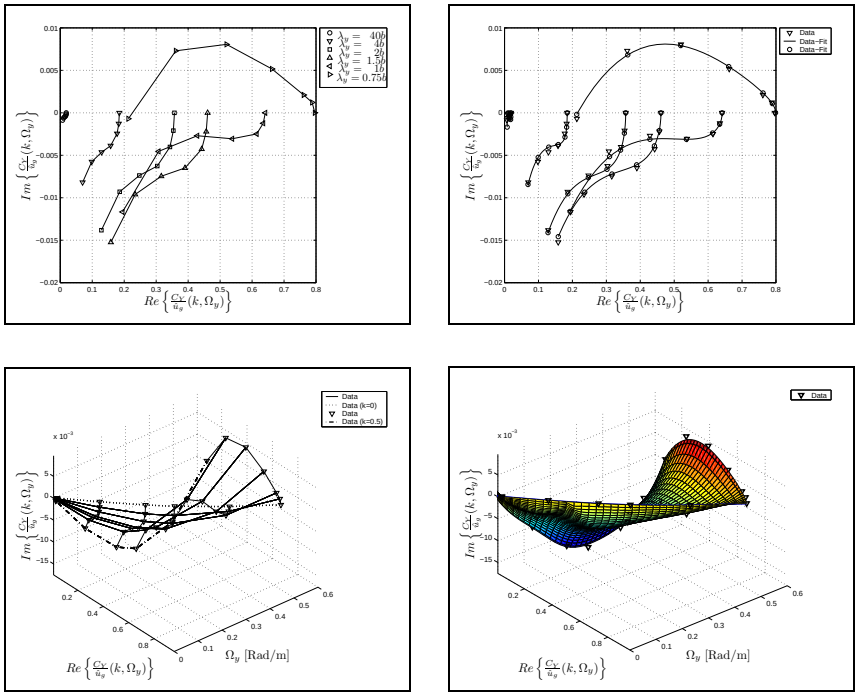


Figure 8.5: Aerodynamic frequency-response data (left top and left bottom) and its function fit (right top and right bottom) of C_Y with respect to the anti-symmetrical gust field input $\hat{u}_g(k,\Omega_y)$, $\frac{C_Y}{\hat{u}_g}(k,\Omega_y)$ in $\mathcal{F}_S$, for the Cessna Ce550 Citation II aircraft configuration, $\alpha_0 = 1.5^o$.

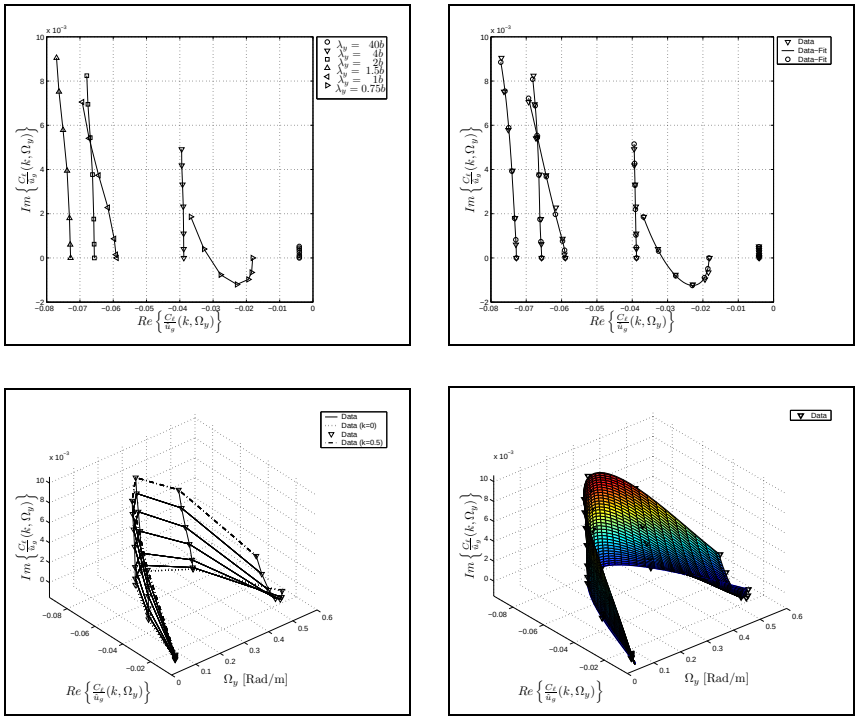


Figure 8.6: Aerodynamic frequency-response data (left top and left bottom) and its function fit (right top and right bottom) of C_ℓ with respect to the anti-symmetrical gust field input $\hat{u}_g(k,\Omega_y)$, $\frac{C_\ell}{\hat{u}_g}(k,\Omega_y)$ in $\mathcal{F}_S$, for the Cessna Ce550 Citation II aircraft configuration, $\alpha_0 = 1.5^o$.

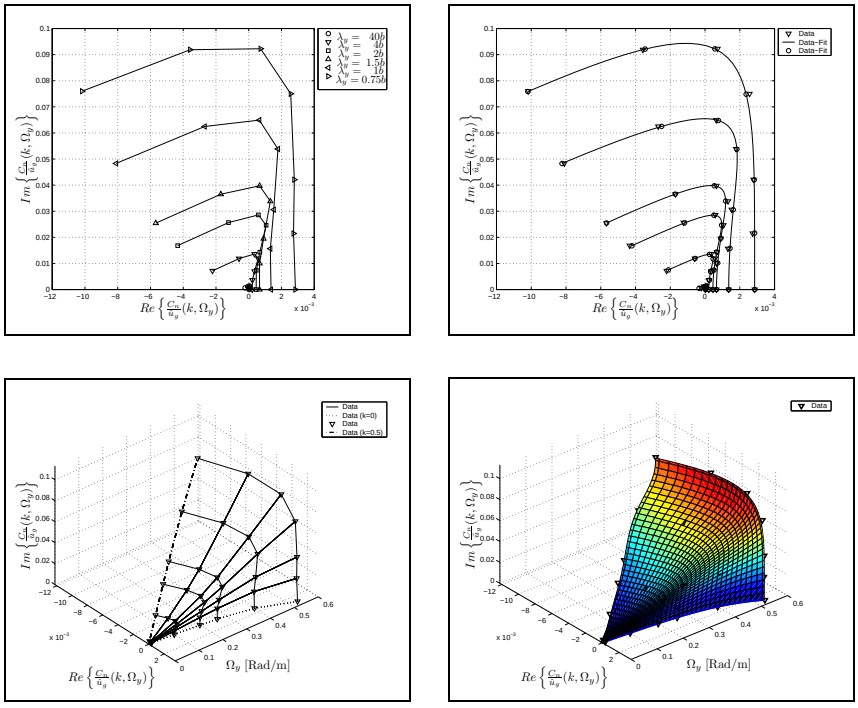


Figure 8.7: Aerodynamic frequency-response data (left top and left bottom) and its function fit (right top and right bottom) of C_n with respect to the anti-symmetrical gust field input $\hat{u}_g(k,\Omega_y)$, $\frac{C_n}{\hat{u}_g}(k,\Omega_y)$ in $\mathcal{F}_S$, for the Cessna Ce550 Citation II aircraft configuration, $\alpha_0 = 1.5^o$.

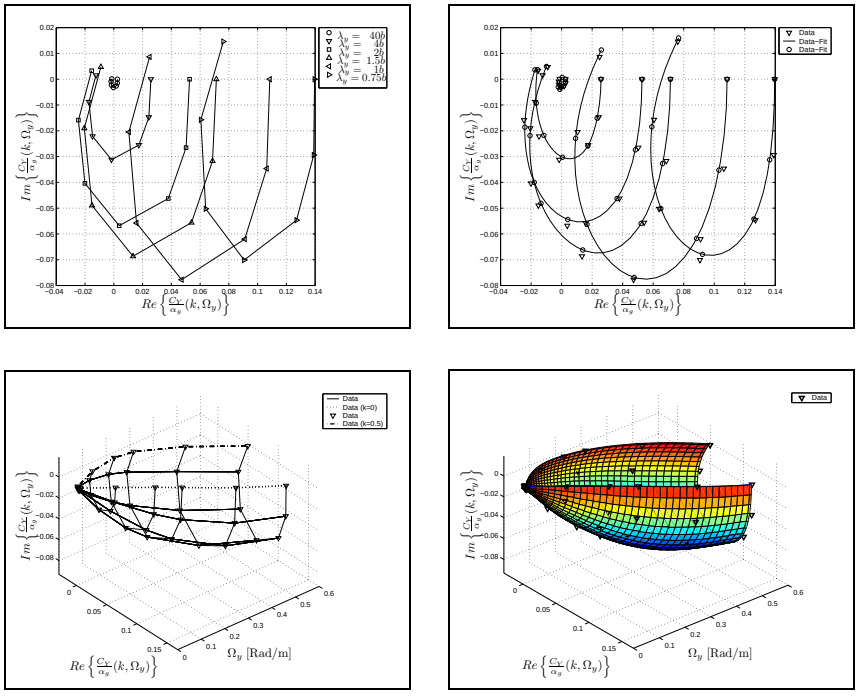


Figure 8.8: Aerodynamic frequency-response data (left top and left bottom) and its function fit (right top and right bottom) of C_Y with respect to the anti-symmetrical gust field input $\alpha_g(k,\Omega_y)$, $\frac{C_Y}{\alpha_g}(k,\Omega_y)$ in $\mathcal{F}_S$, for the Cessna Ce550 Citation II aircraft configuration, $\alpha_0 = 1.5^o$.

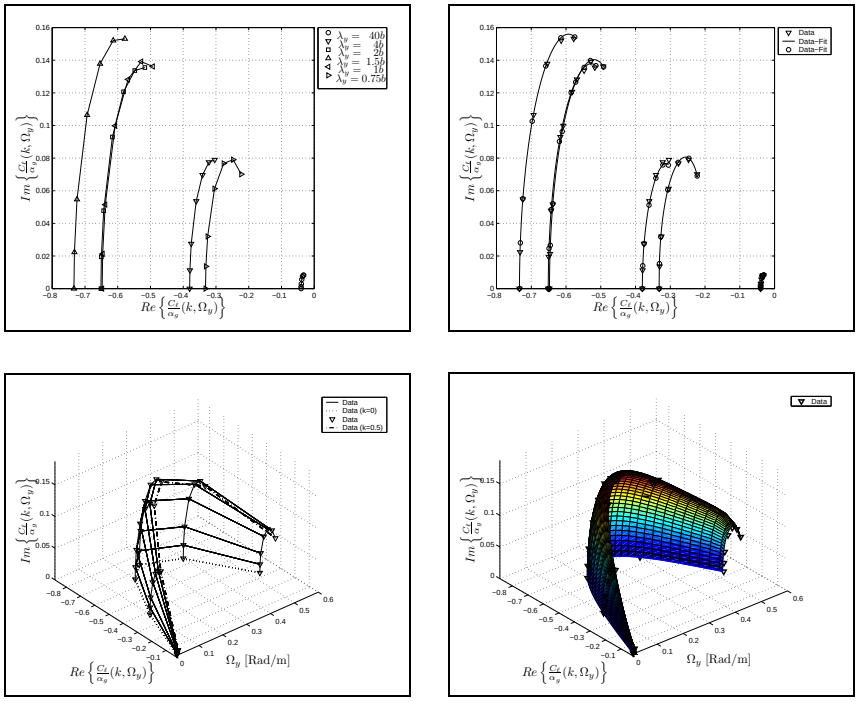


Figure 8.9: Aerodynamic frequency-response data (left top and left bottom) and its function fit (right top and right bottom) of C_ℓ with respect to the anti-symmetrical gust field input $\alpha_g(k,\Omega_y)$, $\frac{C_\ell}{\alpha_g}(k,\Omega_y)$ in $\mathcal{F}_S$, for the Cessna Ce550 Citation II aircraft configuration, $\alpha_0 = 1.5^o$.

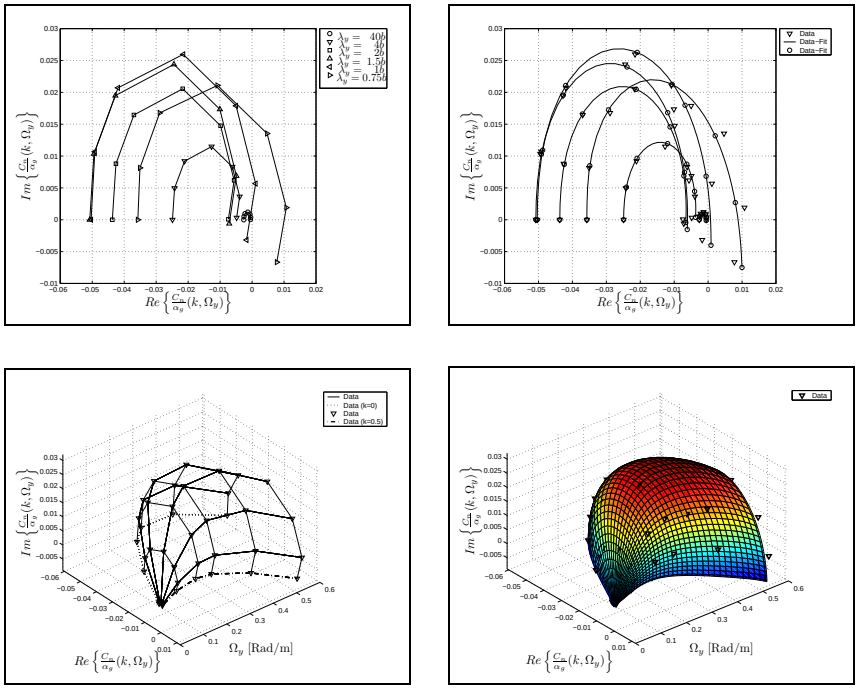


Figure 8.10: Aerodynamic frequency-response data (left top and left bottom) and its function fit (right top and right bottom) of C_n with respect to the anti-symmetrical gust field input $\alpha_g(k,\Omega_y)$, $\frac{C_n}{\alpha_g}(k,\Omega_y)$ in $\mathcal{F}_S$, for the Cessna Ce550 Citation II aircraft configuration, $\alpha_0 = 1.5^o$.

	Frequency dependent stability- and gust derivatives		
	C_Y	C_ℓ	C_n
β	$\mathcal{C}_{\mathcal{Y}_\beta}(k) = Re\left\{\frac{C_Y}{\beta}(k)\right\}$	$\mathcal{C}_{\ell_\beta}(k) = Re\left\{\frac{C_\ell}{\beta}(k)\right\}$	$\mathcal{C}_{n_\beta}(k) = Re\left\{\frac{C_n}{\beta}(k)\right\}$
$\frac{\dot{\beta}\bar{c}}{2Q_\infty}$	$\mathcal{C}_{\mathcal{Y}_{\dot{\beta}}}(k) = \frac{1}{k}Im\left\{\frac{C_Y}{\beta}(k)\right\}$	$\mathcal{C}_{\ell_{\dot{\beta}}}(k) = \frac{1}{k}Im\left\{\frac{C_\ell}{\beta}(k)\right\}$	$\mathcal{C}_{n_{\dot{\beta}}}(k) = \frac{1}{k}Im\left\{\frac{C_n}{\beta}(k)\right\}$
β_g	$\mathcal{C}_{\mathcal{Y}_{\beta_g}}(k) = Re\left\{\frac{C_Y}{\beta_g}(k)\right\}$	$\mathcal{C}_{\ell_{\beta_g}}(k) = Re\left\{\frac{C_\ell}{\beta_g}(k)\right\}$	$\mathcal{C}_{n_{\beta_g}}(k) = Re\left\{\frac{C_n}{\beta_g}(k)\right\}$
$\frac{\dot{\beta}_g\bar{c}}{2Q_\infty}$	$\mathcal{C}_{\mathcal{Y}_{\dot{\beta}_g}}(k) = \frac{1}{k}Im\left\{\frac{C_Y}{\beta_g}(k)\right\}$	$\mathcal{C}_{\ell_{\dot{\beta}_g}}(k) = \frac{1}{k}Im\left\{\frac{C_\ell}{\beta_g}(k)\right\}$	$\mathcal{C}_{n_{\dot{\beta}_g}}(k) = \frac{1}{k}Im\left\{\frac{C_n}{\beta_g}(k)\right\}$

Table 8.4: Definition of both the asymmetrical frequency-dependent stability - and 1D gust derivatives for the frame $\mathcal{F}_S$, given as a function of the reduced frequency $k = \frac{\omega\bar{c}}{2Q_\infty}$, as calculated from asymmetrical aerodynamic frequency-response functions.

8.7 Remarks

In this chapter the aerodynamic frequency-response functions for the asymmetrical aircraft motions have geen given, similar to the ones for the asymmetrical and anti-symmetrical atmospheric turbulence inputs. The aerodynamic frequency-response functions considered here are given for the aerodynamic force and moment coefficients C_Y, C_ℓ and C_n with respect to the asymmetrical aircraft motion $\beta(k)$, the asymmetrical 1D turbulence input $\beta_g(k)$, and the anti-symmetrical 2D atmospheric turbulence inputs $\hat{u}_g(k, \Omega_y)$ and $\alpha_g(k, \Omega_y)$. The frequency-response functions have been obtained by approximating the aerodynamic frequency-response data by analytical functions, see also appendix E.

The results presented in chapters 7 and 8 will be used for the computational aerodynamics model presented in chapter 10. Also, in chapter 10 both the constant unsteady stability- and the constant unsteady gust derivatives will be calculated. In conjunction with the constant stability derivatives calculated in chapter 6, the constant parameter aerodynamic model is then completely determined.

	Frequency dependent 2D gust derivatives		
	C_Y	C_ℓ	C_n
$\hat{u}_g$	$\mathcal{C}_{\mathcal{Y}_{u_g}}(k,\Omega_y) = Re\left\{\frac{C_Y}{\hat{u}_g}(k,\Omega_y)\right\}$	$\mathcal{C}_{\ell_{u_g}}(k,\Omega_y) = Re\left\{\frac{C_\ell}{\hat{u}_g}(k,\Omega_y)\right\}$	$\mathcal{C}_{n_{u_g}}(k,\Omega_y) = Re\left\{\frac{C_n}{\hat{u}_g}(k,\Omega_y)\right\}$
$\frac{\dot{\hat{u}}_g \bar{c}}{2Q_\infty}$	$\mathcal{C}_{\mathcal{Y}_{\dot{u}_g}}(k,\Omega_y) = \frac{1}{k} Im\left\{\frac{C_Y}{\hat{u}_g}(k,\Omega_y)\right\}$	$\mathcal{C}_{\ell_{\dot{u}_g}}(k,\Omega_y) = \frac{1}{k} Im\left\{\frac{C_\ell}{\hat{u}_g}(k,\Omega_y)\right\}$	$\mathcal{C}_{n_{\dot{u}_g}}(k,\Omega_y) = \frac{1}{k} Im\left\{\frac{C_n}{\hat{u}_g}(k,\Omega_y)\right\}$
α_g	$\mathcal{C}_{\mathcal{Y}_{\alpha_g}}(k,\Omega_y) = Re\left\{\frac{C_Y}{\alpha_g}(k,\Omega_y)\right\}$	$\mathcal{C}_{\ell_{\alpha_g}}(k,\Omega_y) = Re\left\{\frac{C_\ell}{\alpha_g}(k,\Omega_y)\right\}$	$\mathcal{C}_{n_{\alpha_g}}(k,\Omega_y) = Re\left\{\frac{C_n}{\alpha_g}(k,\Omega_y)\right\}$
$\frac{\dot{\alpha}_g \bar{c}}{2Q_\infty}$	$\mathcal{C}_{\mathcal{Y}_{\dot{\alpha}_g}}(k,\Omega_y) = \frac{1}{k} Im\left\{\frac{C_Y}{\alpha_g}(k,\Omega_y)\right\}$	$\mathcal{C}_{\ell_{\dot{\alpha}_g}}(k,\Omega_y) = \frac{1}{k} Im\left\{\frac{C_\ell}{\alpha_g}(k,\Omega_y)\right\}$	$\mathcal{C}_{n_{\dot{\alpha}_g}}(k,\Omega_y) = \frac{1}{k} Im\left\{\frac{C_n}{\alpha_g}(k,\Omega_y)\right\}$

Table 8.5: Definition of the anti-symmetrical frequency-dependent 2D gust derivatives for the frame $\mathcal{F}_S$ given as a function of both the reduced frequency $k = \frac{\omega \bar{c}}{2Q_\infty}$ and the spatial frequency Ω_y, as calculated from anti-symmetrical aerodynamic frequency-response functions.

Part IV

The Mathematical Aircraft Models

Chapter 9

Time-domain LPF solutions for 2D atmospheric gust fields

9.1 Introduction

This chapter treats additional theory for the time-domain Linearized Potential Flow (LPF) simulations. Here, the unsteady LPF method will primarily be used as a virtual flighttest facility to determine the time-dependent aerodynamic force and moment coefficients acting on the aircraft. The aircraft grid, as defined in chapter 6, is used again, but it is now flown through random (isolated) two-dimensional (2D) gust fields.

To set the scene for this chapter, section 9.2 discusses some aspects of LPF simulations with respect to 2D stochastic atmospheric turbulence. Recti-linear flightpaths will be considered only in this section. The initial flight-condition is treated first; this trim condition is given in terms of the aircraft mass, the airspeed, the angle-of-attack, the side-slip angle, and the angular rates p, q and r. Next, the generation of 2D spatial-domain gust fields is shortly discussed. This discussion is followed by the definition of both the aircraft's flightpath ánd the encountered symmetrical and anti-symmetrical gust fields. Further, the gust field interpolation procedure for the time-domain LPF simulations is given. The application of a truncated wake to reduce simulation time is explained next. Also, the transformation of the aerodynamic force and moment coefficients (given in the Aerodynamic Frame of Reference $\mathcal{F}_{aero}$) to the Stability Frame of Reference $\mathcal{F}_S$ is given. Finally, the effect of the discretization time Δt on the numerically obtained LPF-solution is discussed. The LPF-solution is given in terms of encountered turbulence velocity component simulations and the aerodynamic force and moment responses in the frame $\mathcal{F}_S$.
Next, in section 9.3 the LPF simulation is coupled with the aircraft equations of motion. Here, contrary to section 9.2, both the flightpath and the aircraft (-grid) orientation become stochastic variables. For these simulations, the 2D gust-fields obtained in section 9.2 are used.

Throughout this chapter, results will be given for a series of the gust scale length L_g. However, for the gust scale length $L_g = 300$ [m] only, both the one-dimensional (1D) and 2D atmospheric turbulence fields will be used for illustrations and discussion throughout this thesis.

9.2 The time-domain LPF solution for recti-linear flight-paths

9.2.1 The initial condition

The aircraft initial (or trim) condition is given similar to the one provided in chapter 6. The center of gravity position of the example aircraft in the Rig Frame of Reference $\mathcal{F}_{rig}$, along with other aircraft geometry parameters, is given in table 6.1.
The initial condition for which both the steady stability derivatives (see chapter 6) and the aerodynamic frequency-response functions have been calculated (see chapters 7 and 8) is presented in chapter 6 (table 6.2), and it is also used in this chapter. However, for the time-domain LPF simulations in this chapter the airspeed now has been increased to $Q_\infty = 125.675$ [m/s]. The motivation for altering the airspeed is to obtain an equilibrium loading condition for which both mass and inertia data are available from references. These data have been obtained from reference [7] and they will be used throughout this thesis. In this reference both mass and moment of inertia data are given for the Body-Fixed Frame of Reference $\mathcal{F}_B$ and they will be used to calculate the moments of inertia for the frame $\mathcal{F}_S$, see also appendix I, section I.3.2.

Regarding the aforementioned loading condition, for the trim condition in the frame $\mathcal{F}_S$ the aerodynamic lift-coefficient C_L cancels the non-dimensional weight given as C_{Z_0} in the equations of motion (see also appendix I). The parameter C_{Z_0} is defined as,

$$C_{Z_0} = \frac{-W\ cos\ \theta_0}{\frac{1}{2}\rho Q_\infty^2 S} \tag{9.1}$$

with W the aircraft weight, θ_0 the pitch-angle, ρ the air-density and S the (reference) wing surface area. From equation (9.1), and using the C_L value obtained from LPF simulations, the new airspeed $Q_\infty = 125.675$ [m/s] was determined from the aircraft mass (taken from reference [7]). Similar to table 6.2, the flight-condition parameters are summarized in table 9.1.

9.2.2 Generation of 2D spatial-domain gust fields

The spatial-domain longitudinal (u_g), lateral (v_g) and vertical (w_g) 2D gust fields are obtained using the theory given in appendix G. As an example, for the gust scale length $L_g = 300$ [m] and variance $\sigma^2 = 1$ $[\frac{\mathrm{m}^2}{\mathrm{s}^2}]$ the vertical atmospheric turbulence velocity component w_g [m/s] is given in figure 9.1 using the simulation parameters (that is spatial sampling and spatial dimensions) given in appendix G. As an illustration, for the gust

Mass m	=	5535.0	kg
Airspeed Q_∞	=	125.675	m/sec.
Angle-of-attack α_0	=	1.5	Deg.
Angle of side-slip β	=	0.0	Deg.
flightpath angle γ_0	=	0.0	Deg.
Angle of pitch θ_0	=	1.5	Deg.
Air-density ρ	=	1.000	kg m^{-3}
Roll-rate p	=	0.0	Rad/sec.
Pitch-rate q	=	0.0	Rad/sec.
Yaw-rate r	=	0.0	Rad/sec.
Lift-coefficient C_L	=	0.2292	

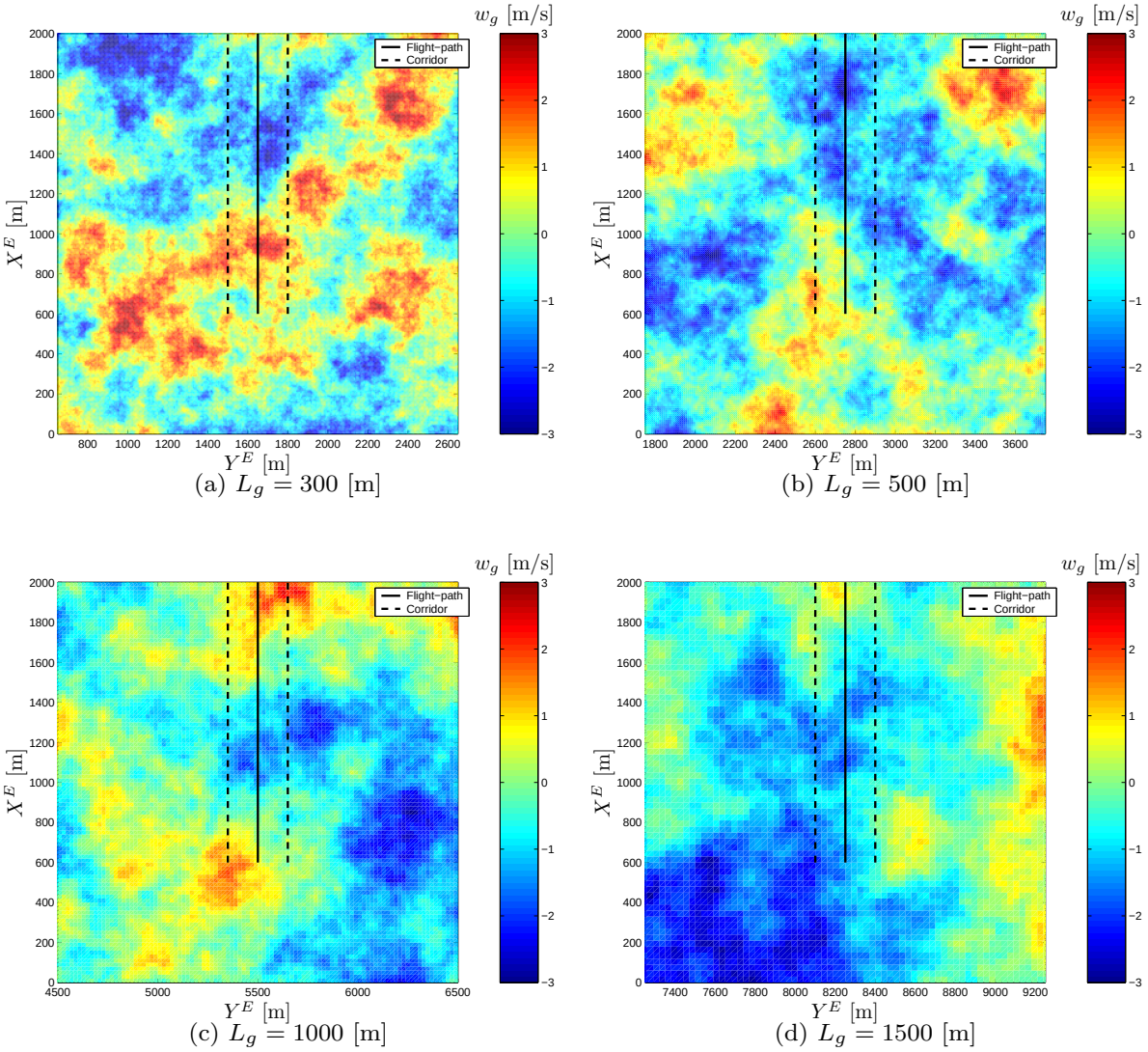
Table 9.1: Aircraft's initial state parameters for Linearized Potential Flow simulations.

scale lengths $L_g = 500$ [m], $L_g = 1000$ [m] and $L_g = 1500$ [m], the gust velocity component is shown in figure 9.1 as well. These results are given for a 2000×2000 [m^2] grid, with the spatial sampling $\Delta X^E = \Delta Y^E = 6$ [m], $\Delta X^E = \Delta Y^E = 10$ [m], $\Delta X^E = \Delta Y^E = 20$ [m] and $\Delta X^E = \Delta Y^E = 30$ [m], for the gust scale lengths $L_g = 300$ [m], $L_g = 500$ [m], $L_g = 1000$ [m] and $L_g = 1500$ [m], respectively (with the variance $\sigma^2 = 1$ [$\frac{\text{m}^2}{\text{s}^2}$]), and ΔX^E and ΔY^E the spatial sampling along the X_E- and Y_E-axis of the Earth Fixed Frame of Reference $\mathcal{F}_E$, respectively. These plots are magnifications of simulations resulting from the theory given in appendix G (for example, compare the $L_g = 300$ [m] result shown in figure 9.1 with the results given in figure G.4 where the "full-scale" spatial simulation of the vertical gust velocity component w_g is given).
For the gust scale length $L_g = 300$ [m], in appendix G the atmospheric turbulence velocity component's correlation functions are given as well. They are obtained from the ensemble average of the entire 2D gust field. Compared to the analytical correlation functions given in chapter 2, the numerically obtained correlation functions show good agreement, see also figures G.5 through G.12.

9.2.3 The flightpath definition

For the calculation of the LPF time-domain aerodynamic responses to 2D gust fields, thus excluding aircraft motions, a flightpath in the frame $\mathcal{F}_E$ has to be defined. As shown in figure 4.14, for the calculation of the aerodynamic forces and moments the aircraft will travel along the negative X_I-axis of the frame $\mathcal{F}_I$ (this figure includes the atmospheric turbulence velocity component definition for $\mathcal{F}_{aero}$, see also chapters 4 and 5).

The origin of the frame $\mathcal{F}_I$ is now placed in the frame $\mathcal{F}_E$ at an arbitrary point, chosen to be $\left[X_0^E, Y_0^E, Z_0^E\right]^T = [600, 1650, 0]^T$ [m] (for the $L_g = 300$ [m] gust field). See also figure 9.2 where the reference frame $\mathcal{F}_I$ is given in the frame $\mathcal{F}_E$, including the definition of the



(a) $L_g = 300$ [m] (b) $L_g = 500$ [m]

(c) $L_g = 1000$ [m] (d) $L_g = 1500$ [m]

Figure 9.1: Physical representations of the 2D gust field $w_g(X^E, Y^E)$ [m/s] for the gust scale lengths $L_g = 300$ [m], $L_g = 500$ [m], $L_g = 1000$ [m] and $L_g = 1500$ [m], including the definitions of both the flightpath and the flightpath corridor.

aircraft's flightpath. The aircraft's recti-linear motion is described in the frame $\mathcal{F}_I$ which (during the motion) remains connected to $\mathcal{F}_E$ (note that the origin (O_I) of the frame $\mathcal{F}_I$ equals $\left[X_0^E, Y_0^E, Z_0^E\right]^T$ in the frame $\mathcal{F}_E$).

9.2.4 Decomposition of the 2D spatial-domain gust fields

Once the definition of the flightpath has been established, a "flightpath corridor" is defined. This corridor is used for the calculation of the time-domain aerodynamic forces and moments. Also, using the corridor (which is chosen to be 300 [m] wide), the 2D atmospheric turbulence velocity component fields are decomposed into symmetrical - and anti-symmetrical gust fields. The procedure for the decomposition of the 2D gust fields is outlined in appendix G, section G.3.2.

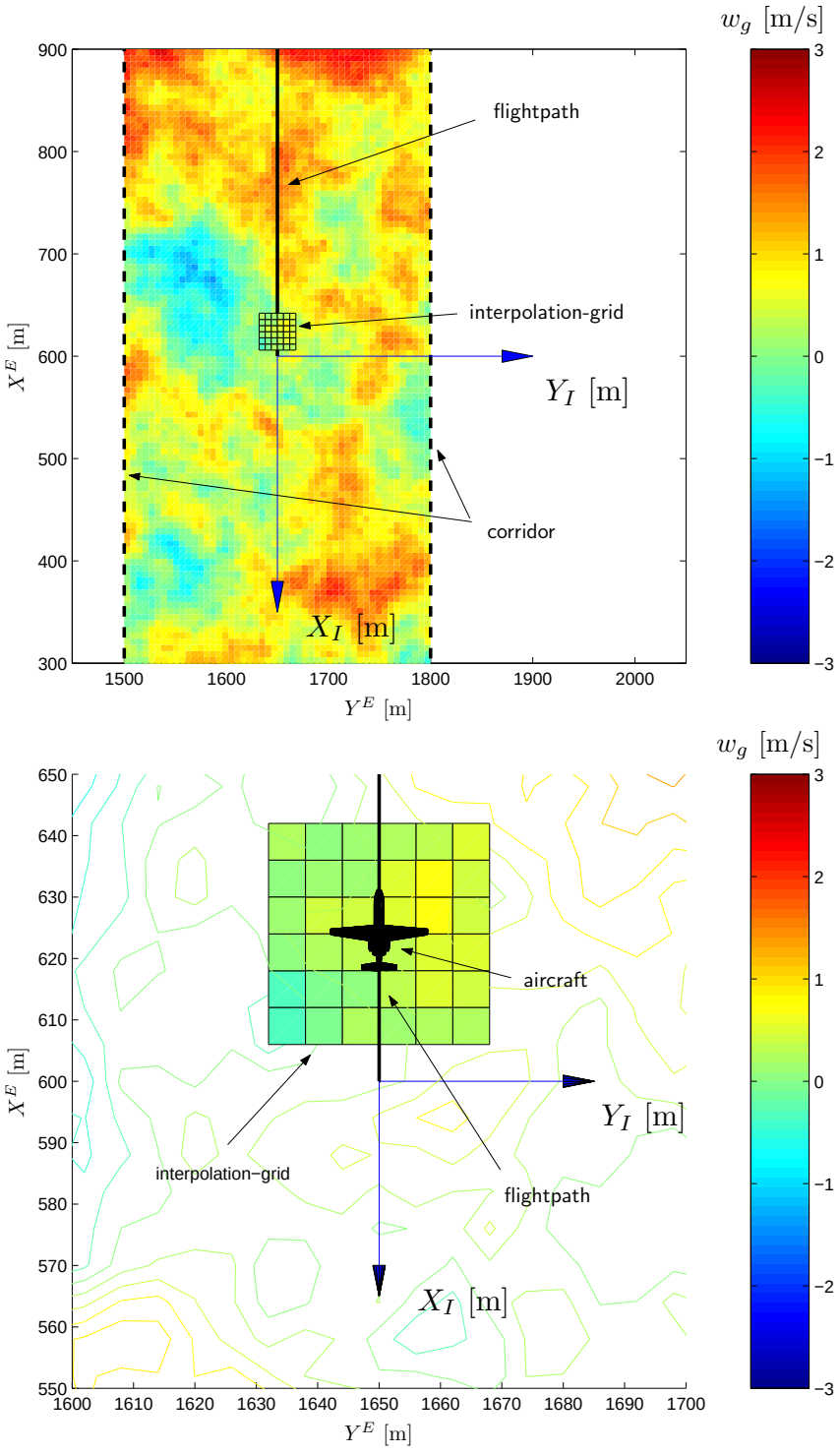


Figure 9.2: The 2D gust field $w_g(X^E, Y^E)$ [m/s] for the gust scale length $L_g = 300$ [m], including the definitions of the frame $\mathcal{F}_I$, the flightpath, the gust field interpolation-grid and the flightpath corridor (top), and a magnification of the gust field (given as a contour plot) including the Cessna Ce550 Citation II dimensions given in the interpolation-grid (bottom).

The time-domain LPF simulation to 2D stochastic gust fields is now divided into responses to symmetrical and anti-symmetrical gust fields. Similar to figure 9.1, plots for the atmospheric turbulence velocity components u_g, v_g and w_g are shown in appendix G. The decomposed gust fields are also given in this appendix, see figures G.13 through G.16.

9.2.5 gust field interpolations

During the time-domain LPF simulations the aircraft is surrounded by a 2D interpolation-grid which travels along the negative X_I-axis while keeping the aircraft's center of gravity close to the center of the grid, see also figures 9.2. The grid is required to generate the gust velocity components at the aircraft configuration's collocation points for each time-step. As an example, for the aircraft encountering the simulated 2D vertical gust field w_g this interpolation-grid is given in the bottom figure of figure 9.2. Using this grid, the vertical gust velocity component w_g is calculated at each collocation point applying a cubic splining to the data-points in the interpolation-grid. For the gust scale length $L_g = 300$ [m], the applied grid covers 36×36 [m^2] while its spatial sampling equals the one used for the generation of the 2D gust fields for the gust scale length $L_g = 300$ [m] ($\Delta X^E = \Delta Y^E = 6$ [m], see also appendix G).

9.2.6 The source definition

Using the local interpolation-grid defined in section 9.2.5, for the example vertical gust component the time-dependent source-strength $\sigma_k(t_n)$ (see also chapter 4) is calculated similar to equation (4.36),

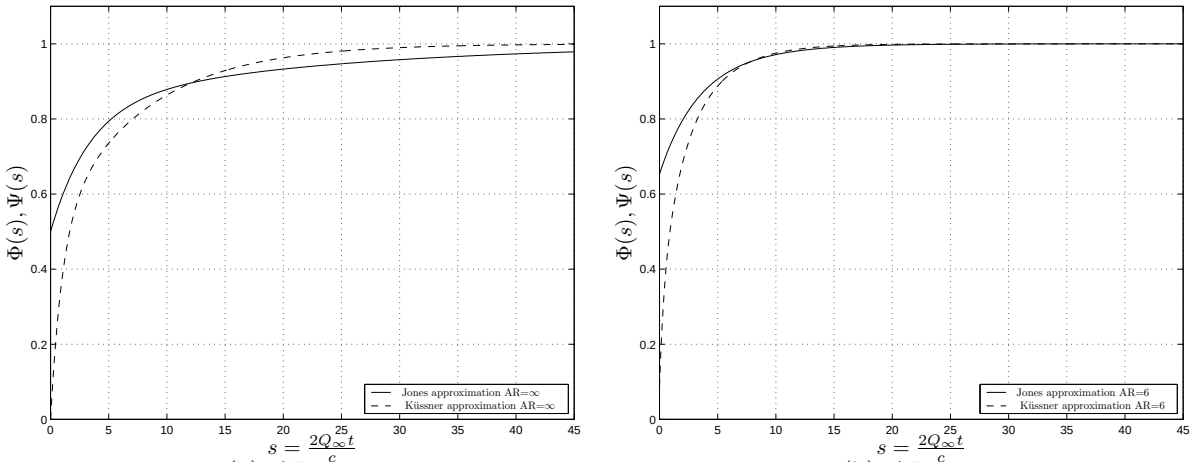
$$\sigma_k(t_n) = -\underline{n}_k \cdot \left(\begin{bmatrix} U_\infty \\ 0 \\ 0 \end{bmatrix} + \begin{bmatrix} 0 \\ 0 \\ w_{g_k}(t_n) \end{bmatrix} \right) \tag{9.2}$$

with $w_{g_k}(t_n)$ the vertical atmospheric turbulence velocity component (being either symmetrical or anti-symmetrical) for each collocation point k (it should be noted that contrary to equation (4.36) the gust velocity component w_g is now allowed to vary along the Y_{aero}-axis as well), $k = 1 \cdots N_B$ with N_B the number of body-panels, $t_n = n\Delta t$ discrete-time with n the time-counter, the vector $\underline{n}_k$ the configuration normal vector for panel k and $U_\infty = Q_\infty = \left| \underline{Q}_\infty \right|$.

The prescribed source-strength for the 2D symmetrical and anti-symmetrical gust fields $u_g(X^E, Y^E)$ and $v_g(X^E, Y^E)$ is similar to equation (9.2).

9.2.7 Application of wake truncation

For each time-step during the time-domain LPF simulations a new row of wake-elements is generated. The influence of the newly shed wake-elements is evaluated at each body-panel of the aircraft grid, and therefore the CPU-time increases as time progresses (see



(a) $AR = \infty$ (b) $AR = 6$

Figure 9.3: Jones' Wagner function approximation (see references [16, 17]), $\Phi(s)$, for a step-wise change in angle-of-attack and Sears & Sparks' (see reference [23]) approximation of Küssner's function, $\Psi(s)$, for the penetration of a sharp-edged vertical gust (see also figures 4.6 and 4.7) for the wing aspect-ratios AR=∞ (left) and AR=6 (right).

also chapter 4). To reduce the CPU-time, a truncated wake model is used. The length of the truncated wake is limited to three times the aircraft wingspan (ranging from the configuration wake-separation lines extending downstream), or $l_{wake} = 3b$ with b the aircraft wingspan. The wake-length l_{wake} was chosen by reviewing Küssner's function in chapter 4. The Sears approximation (see reference [23]) of Küssner's lift deficiency function for sharp-edged vertical gusts, as already given in figure 4.7, is duplicated in figure 9.3. However, here the Sears approximation is given for an increased length of the semi-chord distance traveled $s = \frac{2Q_\infty t_n}{\bar{c}}$. From this figure it follows that at $s = 45$ Küssner's function $\Psi(s)$ equals $\Psi(45) = 0.9986$. If the gust field is considered to be a sharp-edged gust, the effect of the unsteady wake on the lift deficiency function $\Psi(s)$ is almost negligible for $s > 45$ (that is a steady response is obtained). Or, in other words, at $s = 45$ the wake contains most of the history of the airflow leading to the transient response given in figure 9.3. Although these findings are only applicable for 2D airflow, it is assumed that for both three-dimensional (3D) airflow ánd stochastic gust inputs a wake-length equalling $s = 45$ is sufficient to describe the airflow's time-dependent behaviour. As an example, for the aspect-ratio AR=6 the Sears approximation of Küssner's lift deficiency function is also given in figure 9.3. For this finite-dimensional wing it appears that at $s = 20$ the wake contains most of the history of the airflow (that is $\Psi(s) \approx 1$).

Summarizing, for the AR=∞ (or 2D) wing the semi-chord distance traveled $s = 45$ results in the truncated wake-length definition of three times the aircraft wingspan, or $3b$ (note that $\frac{3b}{\bar{c}/2} \approx 46$ for the Cessna Ce550). Similar conclusions may be drawn for aircraft motions (see also figure 9.3 where Jones' approximation for Wagner's function is given, see also chapter 4 and reference [17]). Obviously, for the finite Aspect Ratio wing (AR=6) the truncated wake-length l_{wake} equalling three times the aircraft wingspan is sufficient.

9.2.8 Calculation of aerodynamic coefficients in $\mathcal{F}_{aero}$ and $\mathcal{F}_S$

With the known time-dependent source-strength for the isolated gust fields (see equation 9.2), the procedure for calculating the time-dependent aerodynamic force- and moment-coefficients in the frame $\mathcal{F}_{aero}$ is outlined in chapter 4. Similarly, the aerodynamic coefficients for the frame $\mathcal{F}_S$ are obtained following the same lines as given in chapter 4. Using the definition of the atmospheric turbulence velocity components and the aerodynamic force and moment coefficients in the frames $\mathcal{F}_{aero}$ and $\mathcal{F}_S$ (see also chapter 5, figure 5.13), the time-domain aerodynamic force and moment coefficients for the frame $\mathcal{F}_S$ are given in terms of the coefficients obtained for the frame $\mathcal{F}_{aero}$, or, for example for the longitudinal gust velocity component u_g,

$$\left.\begin{array}{rcl} C_X(u_g(t)) &=& -C_X^a(u_g^a(t) \\ C_Y(u_g(t)) &=& C_Y^a(u_g^a(t) \\ C_Z(u_g(t)) &=& -C_Z^a(u_g^a(t) \\ \\ C_\ell(u_g(t)) &=& -C_\ell^a(u_g^a(t) \\ C_m(u_g(t)) &=& C_m^a(u_g^a(t) \\ C_n(u_g(t)) &=& -C_n^a(u_g^a(t) \end{array}\right\} \tag{9.3}$$

with $u_g(t)$ and $u_g^a(t)$ the definition of the longitudinal gust velocity component given in the frames $\mathcal{F}_S$ and $\mathcal{F}_{aero}$, respectively, and the superscript ^{a} denoting the coefficients for $\mathcal{F}_{aero}$. Similar expressions are obtained for the coefficients with respect to the lateral gust velocity component v_g and the vertical gust velocity component w_g. For the sake of completeness, similar to equation (9.3) the aerodynamic coeffcients for the v_g gust field are summarized as,

$$\left.\begin{array}{rcl} C_X(v_g(t)) &=& C_X^a(v_g^a(t) \\ C_Y(v_g(t)) &=& -C_Y^a(v_g^a(t) \\ C_Z(v_g(t)) &=& C_Z^a(v_g^a(t) \\ \\ C_\ell(v_g(t)) &=& C_\ell^a(v_g^a(t) \\ C_m(v_g(t)) &=& -C_m^a(v_g^a(t) \\ C_n(v_g(t)) &=& C_n^a(v_g^a(t) \end{array}\right\} \tag{9.4}$$

with $v_g(t)$ and $v_g^a(t)$ the definition of the lateral gust velocity component given in the frames $\mathcal{F}_S$ and $\mathcal{F}_{aero}$, respectively. The aerodynamic coeffcients for the w_g gust field are summarized as,

$$\left.\begin{array}{rcl} C_X(w_g(t)) &=& -C_X^a(w_g^a(t) \\ C_Y(w_g(t)) &=& C_Y^a(w_g^a(t) \\ C_Z(w_g(t)) &=& -C_Z^a(w_g^a(t) \\ \\ C_\ell(w_g(t)) &=& -C_\ell^a(w_g^a(t) \\ C_m(w_g(t)) &=& C_m^a(w_g^a(t) \\ C_n(w_g(t)) &=& -C_n^a(w_g^a(t) \end{array}\right\} \tag{9.5}$$

with $w_g(t)$ and $w_g^a(t)$ the definition of the vertical gust velocity component given in the frames $\mathcal{F}_S$ and $\mathcal{F}_{aero}$, respectively. Similar to equation (9.3), in equations (9.4) and (9.5) the superscript ^{a} denotes the coefficients for $\mathcal{F}_{aero}$.

9.2.9 Effect of the discretization time on the LPF-solution

In section 9.2.2 the generation of the spatial-domain 2D gust fields has been discussed. Using the now known gust fields, the aircraft grid defined in chapter 6 is flown through these fields to obtain the time-dependent aerodynamic forces and moments acting upon it. These LPF-simulations make use of the discretization time Δt, which is given in terms of the aircraft's mean aerodynamic chord $\bar{c}$ and the airspeed Q_∞, or,

$$\Delta t = K_{\Delta t} \frac{\bar{c}}{Q_\infty} \tag{9.6}$$

with $K_{\Delta t}$ the LPF-simulation discretization-time factor. Note that if $K_{\Delta t}$ equals 1, for each time-step the aircraft configuration travels along the negative X_I-axis of $\mathcal{F}_I$ over a distance equalling 1 times the mean aerodynamic chord.

As an example, as a function of the distance traveled along the X_E-axis in $\mathcal{F}_E$, the vertical gust velocity component w_g at the position of the center of gravity as obtained from spatial-domain simulations is given in figure 9.4, along with the LPF-model simulation's interpolated vertical gust velocity component for the discretization-time factors $K_{\Delta t} = 0.5$, $K_{\Delta t} = 1$ and $K_{\Delta t} = 2$.
Similarly, however now given as a function of time, examples of the response of the aerodynamic coefficients (given for $\mathcal{F}_{aero}$) $C_Z^a(w_g(t))$ and $C_\ell^a(w_g(t))$ are shown in figure 9.5. Also these results are given for the discretization-time factors $K_{\Delta t} = 0.5$, $K_{\Delta t} = 1$ and $K_{\Delta t} = 2$.
From the results presented above, for all the considered discretization-time factors $K_{\Delta t}$ the time-domain responses show good agreement.

9.3 The time-domain LPF solution for stochastic flightpaths

9.3.1 Introduction

In the previous section the procedure for determining the gust-induced aerodynamic force and moment coefficients for recti-linear flightpaths was outlined. Here, the procedure is extended for stochastic flightpaths, that is the potential flow solution is now coupled to the aircraft equations of motion (details of the equations of motion can be found in appendix I). For each time-step, the solution of the potential flow method is now used to steer the equations of motion resulting in both a new aircraft (-grid) position and a new orientation in the reference frame $\mathcal{F}_I$. In the following, the (coupled) LPF - and Equations of Motion (EOM) solution will be designated as the LPF-EOM-model.

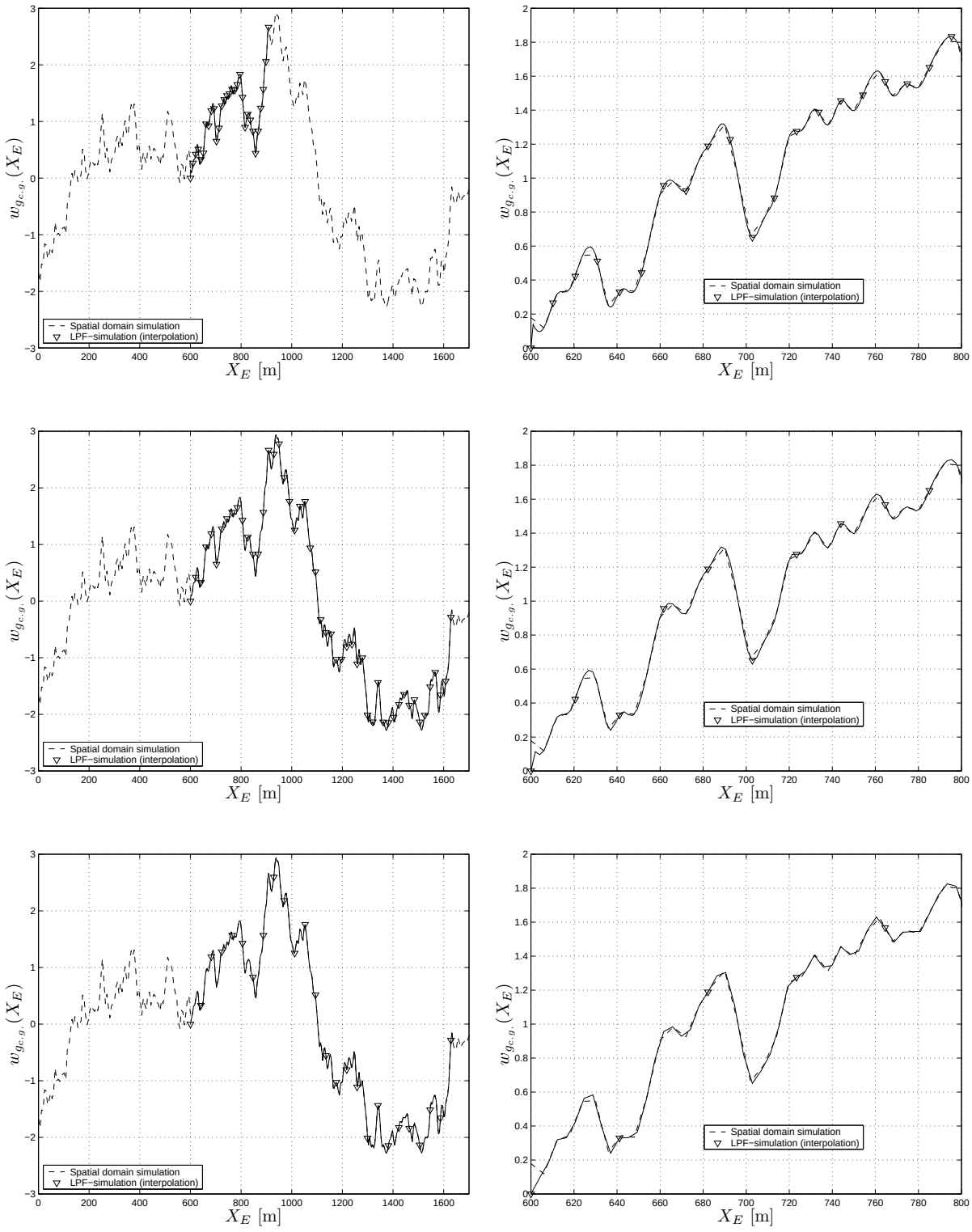


Figure 9.4: The vertical gust velocity component w_g encountered by the center of gravity obtained from spatial-domain simulations ($L_g = 300$ [m]), and obtained from LPF-model simulations (interpolation) for the discretization-time factors $K_{\Delta t} = 0.5$ (top), $K_{\Delta t} = 1$ (middle) and $K_{\Delta t} = 2$ (bottom), given in $\mathcal{F}_E$ (the right-hand-side figures are a magnification of the left-hand-side figures).

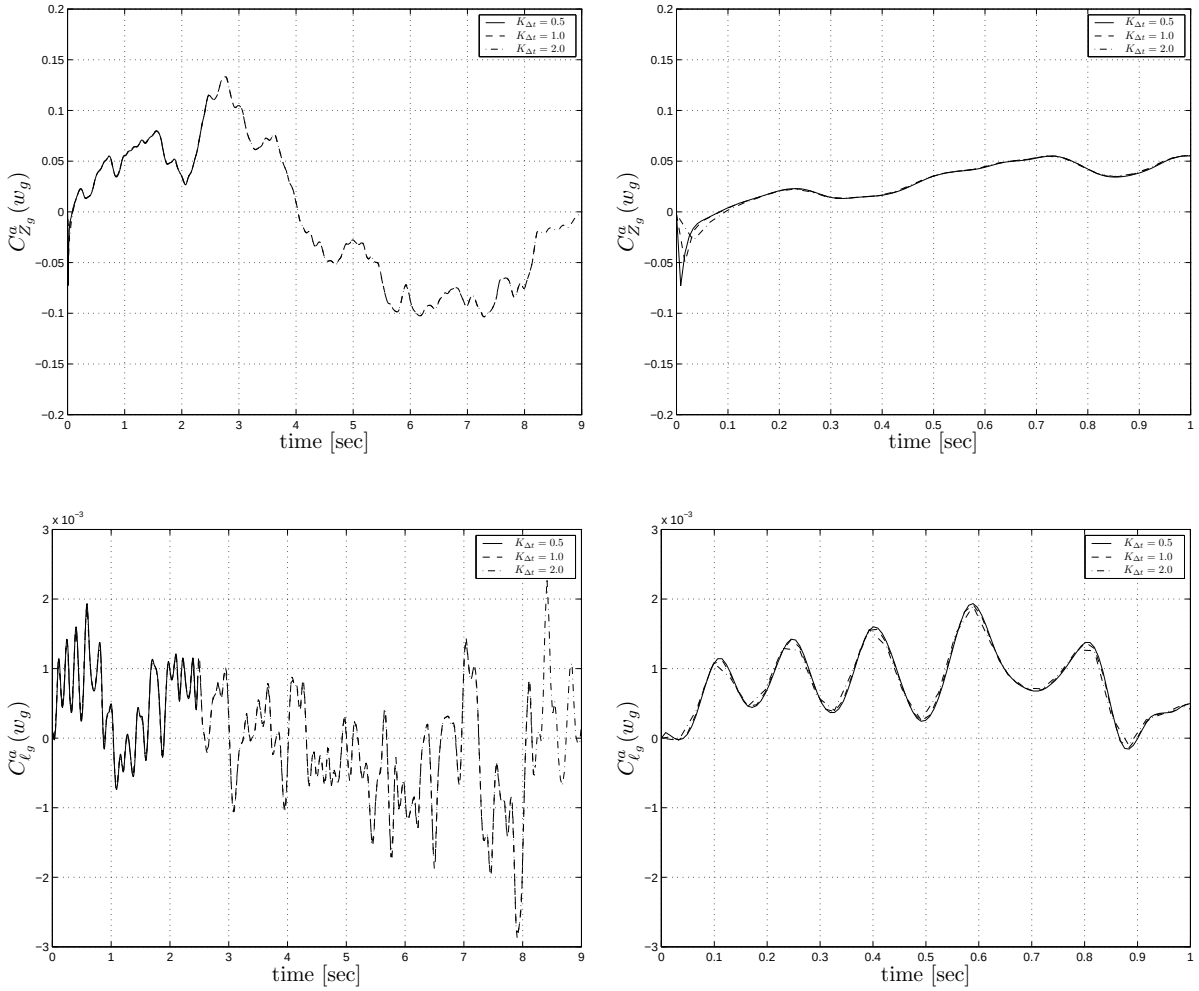


Figure 9.5: Both the aerodynamic force coefficient's response $C^a_{Z_g}(w_g)$ and the aerodynamic rolling moment coefficient's response $C^a_{\ell_g}(w_g)$ (given for the frame $\mathcal{F}_{aero}$) as a function of the discretization-time factor $K_{\Delta t} = 0.5$, $K_{\Delta t} = 1$ and $K_{\Delta t} = 2$. The results are valid for the gust scale length $L_g = 300$ [m]. The right-hand-side figures are a magnification of the left-hand-side figures.

9.3.2 The LPF-EOM solution

In figure 9.6 a flow chart for calculating the LPF-EOM-model aircraft responses to 2D gust fields is shown. Similar to the recti-linear flightpath simulations, as discussed in section 9.2, the aircraft grid is placed into the 2D gust-field of interest. Here, however, the potential flow solution is coupled to the aircraft equations of motion, resulting in both stochastic flightpaths ánd aircraft orientations which are given in terms of the Euler angles $[\Psi, \theta, \varphi]^T$. For each time-step the flow over the aircraft grid is solved (see chapter 4), resulting in the aerodynamic forces and moments acting upon it. Integrating the equations of motions results in both a new position and orientation of the aircraft grid in the reference frame $\mathcal{F}_I$. Similar to the recti-linear flightpath simulations, the aircraft responses to either symmetrical -, asymmetrical - or anti-symmetrical gust fields will be considered only. These gust fields are calculated (and shown) in appendix G.

The LPF-EOM-model aircraft motion responses are calculated using the Stability Frame of Reference $\mathcal{F}_S$. For the calculation of these responses the following set of equations of motion is used (see also appendix I, equations (I.11) and (I.12)),

$$\left.\begin{array}{rcc} \dot{u}(t) & = & \left(X(t) - W\ cos\theta_0 \cdot \theta(t)\right)/m \\ \dot{v}(t) & = & \left(Y(t) + W\ cos\theta_0 \cdot \varphi(t)\right)/m - r(t)\ Q_\infty \\ \dot{w}(t) & = & \left(Z(t) - W\ sin\theta_0 \cdot \theta(t)\right)/m + q(t)\ Q_\infty \\ & & \\ I_x\ \dot{p}(t) - J_{xz}\ \dot{r}(t) & = & L(t) \\ I_y\ \dot{q}(t) & = & M(t) \\ -J_{xz}\ \dot{p}(t) + I_z\ \dot{r}(t) & = & N(t) \\ & & \\ \dot{\Psi}(t) & = & \frac{r(t)}{cos\theta_0} \\ \dot{\theta}(t) & = & q(t) \\ \dot{\varphi}(t) & = & p(t) + r(t)\ tg\theta_0 \end{array}\right\} \tag{9.7}$$

with $[u(t), v(t), w(t)]^T$ the velocity component perturbations, $[p(t), q(t), r(t)]^T$ the rotational velocity component perturbations, $[\Psi(t), \theta(t), \varphi(t)]^T$ the Euler angles, m the aircraft mass, $W = mg$ the aircraft weight (with g the Earth gravitational acceleration), Q_∞ the airspeed and θ_0 the pitch-angle for the trim condition. Further, the aerodynamic forces and moments, $[X(t), Y(t), Z(t)]^T$ and $[L(t), M(t), N(t)]^T$, respectively, are obtained from the unsteady potential flow method and they are corrected for their values for the trim condition.
The time-dependent position of (for example) the center of gravity in the reference frame $\mathcal{F}_I$, $[X_0(t), Y_0(t), Z_0(t)]^T$, is calculated using an initial position $[X_0^{init}(t), Y_0^{init}(t), Z_0^{init}(t)]^T$ and $[\dot{X}_0(t), \dot{Y}_0(t), \dot{Z}_0(t)]^T$, or,

$$\left.\begin{array}{l} X_0(t) = X_0^{init}(t) + \int^t \dot{X}_0(t)\ dt \\ \\ Y_0(t) = Y_0^{init}(t) + \int^t \dot{Y}_0(t)\ dt \\ \\ Z_0(t) = Z_0^{init}(t) + \int^t \dot{Z}_0(t)\ dt \end{array}\right\} \tag{9.8}$$

with,

$$\begin{bmatrix} \dot{X}_0(t) \\ \dot{Y}_0(t) \\ \dot{Z}_0(t) \end{bmatrix} = [\mathcal{T}_\varphi \mathcal{T}_\theta \mathcal{T}_\psi]^{-1} \begin{bmatrix} Q_\infty + u(t) \\ v(t) \\ w(t) \end{bmatrix} \tag{9.9}$$

and the matrices $\mathcal{T}_\psi$, $\mathcal{T}_\theta$ and $\mathcal{T}_\varphi$ equal to the ones given in equations (4.25), (4.26) and (4.27), respectively. Both equations (9.8) and (9.9) are used to determine the aircraft grid position in the frame $\mathcal{F}_I$.

Contrary to the recti-linear flightpath simulations (the LPF-solution), it should be noted that for the LPF-EOM simulations the gust fields, given in the frame $\mathcal{F}_E$, are now decomposed in the frame $\mathcal{F}_S$ for each aircraft position (and orientation) given in the frame $\mathcal{F}_I$. The decomposition is similar to the one given in equation (9.9), and it becomes, taking for example the vertical gust field w_g in $\mathcal{F}_E$,

$$\begin{bmatrix} u_g^S \\ v_g^S \\ w_g^S \end{bmatrix} = [\mathcal{T}_\varphi \mathcal{T}_\theta \mathcal{T}_\psi] \begin{bmatrix} 0 \\ 0 \\ w_g^E \end{bmatrix} \tag{9.10}$$

with w_g^E the vertical gust velocity component in the frame $\mathcal{F}_E$ and u_g^S, v_g^S and w_g^S the decomposed gust velocity components for the frame $\mathcal{F}_S$.

In this thesis the LPF-EOM simulations are restricted in the aircraft motion degrees of freedom; that is the aircraft motion responses are either symmetrical or asymmetrical. For the simulations to both the symmetrical longitudinal - and the symmetrical vertical gust fields, the flightpath deviations are limited to the $X_I O_I Z_I$-plane. For the simulation with respect to asymmetrical lateral - and both anti-symmetrical longitudinal - and vertical gust fields, only flightpath deviations in the $X_I O_I Y_I$-plane in $\mathcal{F}_I$ are allowed.

The LPF-EOM-model aircraft responses are summarized and discussed in chapter 13.

9.4 Remarks

In terms of both aerodynamic coefficient - and aircraft motion responses due to symmetrical and anti-symmetrical gust fields, results of the LPF-model simulations are summarized in chapter 13 where they will be compared to results obtained for the Parametric Computational Aerodynamics (PCA) -, the Delft University of Technology (DUT) - and the Four-Point-Aircraft (FPA) model (details of these models can be found in chapters 10, 11 and 12, respectively). The LPF-model simulation results will be given for the frame $\mathcal{F}_S$, and they will be shown for the discretization-time factor $K_{\Delta t} = 2$ only.

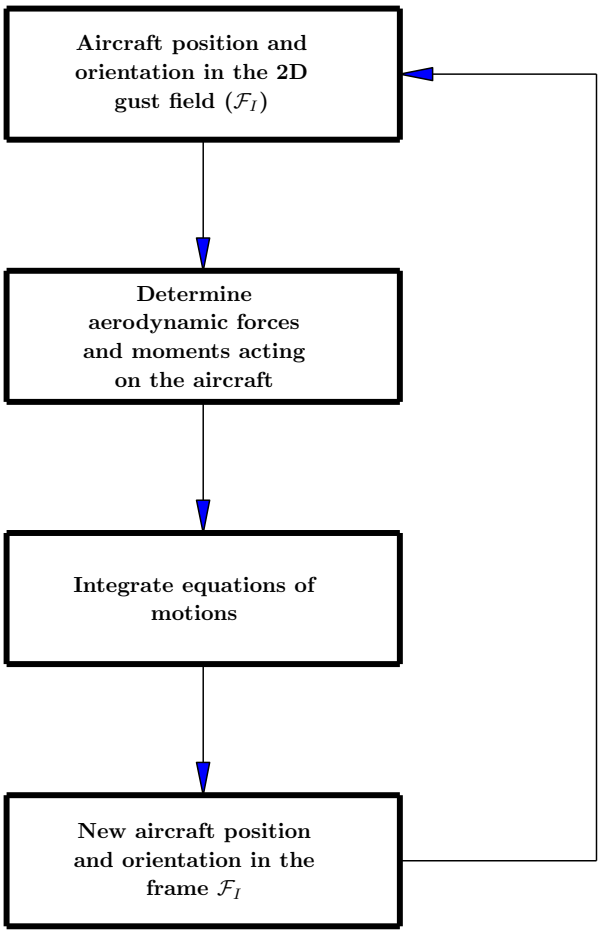


Figure 9.6: The LPF-EOM simulation procedure for the calculation of aircraft responses to 2D atmospheric turbulence fields.

Chapter 10

The Parametric Computational Aerodynamics model

10.1 Introduction

In this chapter the Parametric Computational Aerodynamics (PCA) gust-response theory is introduced. It relies on the results presented in chapters 7 and 8 where the aerodynamic frequency-response functions with respect to aircraft motions and both one- (1D) and two-dimensional (2D) atmospheric gust fields have been calculated. The theory for obtaining these functions has been presented in chapters 3 to 6.
The aircraft responses to atmospheric turbulence inputs, in this chapter, are limited to 1D longitudinal - (u_g), lateral - (v_g) and vertical gust inputs (w_g). These gusts are assumed to be representative for gust fields being constant over the aircraft's span while they vary over the aircraft's longitudinal axis X_S of the Stability Frame of Reference $\mathcal{F}_S$. Also, the aircraft responses to both 2D anti-symmetrical longitudinal - (u_g) and vertical gusts (w_g) will be considered. In this case the atmospheric turbulence velocity components are allowed to vary over the aircraft's wingspan and along the aircraft's longitudinal axis X_S.
Similar to both the Delft University of Technology (DUT) - and the Four-Point-Aircraft (FPA) model (which are presented in chapters 11 and 12, respectively), the PCA mathematical aircraft model relies on an aerodynamic model in terms of constant stability derivatives. In this chapter these derivatives are obtained from aircraft motion frequency-response functions with respect to 1D atmospheric turbulence inputs. From these functions, the aircraft motion resonance frequencies will be used to calculate the derivatives. Similarly, as a function of the gust scale length L_g, both the 1D- and 2D constant gust derivatives are also obtained from resonance frequencies. These frequencies are obtained from aircraft motion gust-responses given in terms of Power Spectral Density (PSD) functions.
For the time-domain aircraft motion simulations to the atmospheric turbulence inputs indicated above, use will be made of the FPA-model gust inputs. Details of this model are given in chapter 12 and appendix G. Furthermore, for these simulations use is made

of stochastic 2D gust fields of which both the model characteristics and the generation details are given in appendix G.
For the frequency-domain aircraft motion simulations use is made of parametric aircraft models and the atmospheric turbulence input PSD-functions given in chapter 12 and appendix H.

10.2 The trim condition

In chapter 6 the numerical values for the steady (constant) stability derivatives have been calculated. In table 6.2 the trim condition for these derivatives is given, while the numerical values for both the steady symmetrical and asymmetrical stability derivatives are listed in tables 6.5 and 6.6, respectively. In chapters 7 and 8 the aerodynamic frequency-response functions with respect to both aircraft motions and atmospheric turbulence inputs are given as well for this trim condition.
The initial condition, for which these aerodynamic frequency-response functions have been calculated, is presented in chapter 6 (table 6.2), and it is also used in this chapter. However, for the simulations presented in this chapter the airspeed now has been increased to $Q_\infty = 125.675$ [m/s], see also chapter 9, section 9.2.1. The new airspeed $Q_\infty = 125.675$ [m/s] was calculated from the aircraft mass (taken from reference [7]) and it is given in table 10.1 along with other flight-condition parameters. In this table the mass and moments of inertia data for both the Body Fixed Frame of reference $\mathcal{F}_B$ and the frame $\mathcal{F}_S$ are summarized as well. The moments of inertia for the frame $\mathcal{F}_S$ are obtained from the available data for the frame $\mathcal{F}_B$, and they are calculated using the transformation equations given in appendix I, section I.3.2.

10.3 The atmospheric turbulence PSD-functions

The PSD-functions for the longitudinal, lateral and vertical atmospheric turbulence velocity components, u_g, v_g and w_g, respectively, are summarized in appendix H. The PSD-functions are given in terms of the non-dimensional gust velocity component $\hat{u}_g = \frac{u_g}{Q_\infty}$, the gust-induced side-slip-angle $\beta_g = \frac{v_g}{Q_\infty}$ and the gust-induced angle-of-attack $\alpha_g = \frac{w_g}{Q_\infty}$, and they are given for both 1D and 2D gust fields.

10.4 The parametric aircraft model for 1D gust fields

10.4.1 Introduction

In this thesis the parametric aircraft model for 1D gust fields is based on the aircraft equations of motion presented in references [29, 30, 35]. In these references the equations are given for a constant parameter aerodynamic model, see also appendix I. The aerodynamic model is given in terms of constant steady and unsteady stability derivatives. For both the PCA-model symmetrical and asymmetrical equations of motion the constant steady

Mass m	=	5535.0	kg
Moment of inertia $I_x\|_{\mathcal{F}_B}$	=	19520.0	kg m^2
Moment of inertia $I_y\|_{\mathcal{F}_B}$	=	35120.0	kg m^2
Moment of inertia $I_z\|_{\mathcal{F}_B}$	=	51879.0	kg m^2
Product of inertia $J_{xz}\|_{\mathcal{F}_B}$	=	2339.0	kg m^2
Moment of inertia $I_x\|_{\mathcal{F}_S}$	=	19419.8	kg m^2
Moment of inertia $I_y\|_{\mathcal{F}_S}$	=	35120.0	kg m^2
Moment of inertia $I_z\|_{\mathcal{F}_S}$	=	51979.2	kg m^2
Product of inertia $J_{xz}\|_{\mathcal{F}_S}$	=	1489.0	kg m^2
Airspeed Q_∞	=	125.675	m/sec.
Angle-of-attack $\alpha_0\|_{\mathcal{F}_B}$	=	1.5	Deg.
Angle of side-slip $\beta_0\|_{\mathcal{F}_B}$	=	0.0	Deg.
flightpath angle $\gamma_0\|_{\mathcal{F}_B}$	=	0.0	Deg.
Angle of pitch $\theta_0\|_{\mathcal{F}_B}$	=	1.5	Deg.
Angle-of-attack $\alpha\|_{\mathcal{F}_S}$	=	0.0	Deg.
Angle of side-slip $\beta_0\|_{\mathcal{F}_S}$	=	0.0	Deg.
flightpath angle $\gamma_0\|_{\mathcal{F}_S}$	=	0.0	Deg.
Angle of pitch $\theta_0\|_{\mathcal{F}_S}$	=	0.0	Deg.
Roll-rate p	=	0.0	Rad/sec.
Pitch-rate q	=	0.0	Rad/sec.
Yaw-rate r	=	0.0	Rad/sec.
Air-density ρ	=	1.0	kg m^{-3}
Lift-coefficient C_L	=	0.2292	

Table 10.1: The aircraft's initial state parameters used for both Parametric Computational Aerodynamics (PCA) data analysis and simulation in the frame $\mathcal{F}_S$ (original mass and inertia data for the frame $\mathcal{F}_B$ was taken from reference [7]).

stability derivatives are given in chapter 6. For the identification of the PCA-model's constant unsteady stability derivatives use is made of resonance frequencies in the aircraft motions frequency-response functions with respect to the 1D atmospheric turbulence velocity components u_g, v_g and w_g.
Similarly, for the estimation of the constant unsteady gust derivatives use is made of resonance frequencies obtained from aircraft motion output PSD-functions for a series of the gust scale length L_g. In this section these derivatives are given for 1D atmospheric turbulence fields only, that is the gust velocity components do not vary along the Y_S-axis of $\mathcal{F}_S$.

10.4.2 Calculation of the unsteady stability derivatives

For the estimation of the constant unsteady stability derivatives use is made of the results presented in chapters 7 and 8. In these chapters the aerodynamic frequency-response functions with respect to aircraft motions and 1D atmospheric turbulence fields are given. The results of these frequency-response functions will be incorporated in the aircraft's equations of motion in terms of frequency-dependent stability- and gust derivatives. Using these derivatives, the equations of motion are given in terms of (real-valued) frequency-dependent matrices $P(\omega)$, $Q(\omega)$ and $R(\omega)$ (see also appendix I),

$$P(\omega)\ j\omega\ \underline{x} = Q(\omega)\ \underline{x} + R(\omega)\ \underline{u} \tag{10.1}$$

with for the symmetrical aircraft motions the aircraft state defined as $\underline{x} = \left[\hat{u}, \alpha, \theta, \frac{q\bar{c}}{Q_\infty}\right]^T$, and the input defined as $\underline{u} = \left[\hat{u}_g(\omega),\ \frac{j\omega\hat{u}_g(\omega)\bar{c}}{Q_\infty},\ \alpha_g(\omega),\ \frac{j\omega\alpha_g(\omega)\bar{c}}{Q_\infty}\right]^T$. For the asymmetrical aircraft motions the aircraft state is defined as $\underline{x} = \left[\beta, \varphi, \frac{pb}{2Q_\infty}, \frac{rb}{2Q_\infty}\right]^T$, while the input is defined as $\underline{u} = \left[\beta_g(\omega),\ \frac{j\omega\beta_g(\omega)b}{Q_\infty}\right]^T$.

Calculation of the frequency-dependent stability- and gust derivatives

The aerodynamic frequency-response functions given in chapters 7 and 8 are now transformed into frequency-dependent stability- and gust derivatives (these derivatives will be used in equation (10.1)). For example, the frequency-dependent steady and unsteady stability derivatives $\mathcal{C}_{\mathcal{Z}_\alpha}(\omega)$ and $\mathcal{C}_{\mathcal{Z}_{\dot{\alpha}}}(\omega)$ are calculated from the frequency-response function $\frac{C_Z}{\alpha}(k)$ according to (see also section 7.5),

$$\frac{C_Z}{\alpha}(k) = Re\left\{\frac{C_Z}{\alpha}(k)\right\} + j\ Im\left\{\frac{C_Z}{\alpha}(k)\right\} = \mathcal{C}_{\mathcal{Z}_\alpha}(k) + jk\ \mathcal{C}_{\mathcal{Z}_{\dot{\alpha}}}(k) \tag{10.2}$$

with the frequency-dependent stability derivatives $\mathcal{C}_{\mathcal{Z}_\alpha}(k)$ and $\mathcal{C}_{\mathcal{Z}_{\dot{\alpha}}}(k)$ given as,

$$\mathcal{C}_{\mathcal{Z}_\alpha}(k) = Re\left\{\frac{C_Z}{\alpha}(k)\right\} \tag{10.3}$$

and,

$$\mathcal{C}_{\mathcal{Z}_{\dot{\alpha}}}(k) = \frac{1}{k} Im\left\{\frac{C_Z}{\alpha}(k)\right\} \tag{10.4}$$

respectively, with the reduced frequency $k = \frac{\omega \bar{c}}{2Q_\infty}$, ω the circular frequency in [Rad/sec.], $\bar{c}$ the mean aerodynamic chord in [m] and Q_∞ the airspeed in [m/s]. For the symmetrical equations of motion, however, all unsteady derivatives are defined with respect to the reduced frequency $\frac{\omega \bar{c}}{Q_\infty}$. Therefore, equation (10.4) now becomes,

$$\mathcal{C}_{\mathcal{Z}_{\dot{\alpha}}}(k) = \frac{1}{2k} Im\left\{\frac{C_Z}{\alpha}(k)\right\} \tag{10.5}$$

Similar to equations (10.3) and (10.5), all other frequency-dependent steady and unsteady stability derivatives (given as a function of the circular frequency ω) are calculated. Also similar to these equations, all frequency-dependent steady and unsteady gust derivatives are calculated. It should be noted that the frequency-dependent unsteady stability- and gust derivatives for the asymmetrical equations of motion are defined with respect to the reduced frequency $\frac{\omega b}{Q_\infty}$, with b the aircraft wingspan in [m]. The definition of all frequency-dependent stability- and gust derivatives (as used in both the symmetrical and asymmetrical equations of motion) is summarized in tables 10.6 and 10.7.

The frequency-domain equations of motion system matrices

For the symmetrical equations of motion the matrices $P(\omega)$, $Q(\omega)$ and $R(\omega)$ in equation (10.1) are given as,

$$P_s(\omega) = \frac{\bar{c}}{Q_\infty} \begin{bmatrix} \{\mathcal{C}_{\mathcal{X}_{\dot{u}}}(\omega) - 2\mu_c\} & \mathcal{C}_{\mathcal{X}_{\dot{\alpha}}}(\omega) & 0 & 0 \\ \mathcal{C}_{\mathcal{Z}_{\dot{u}}}(\omega) & \{\mathcal{C}_{\mathcal{Z}_{\dot{\alpha}}}(\omega) - 2\mu_c\} & 0 & 0 \\ 0 & 0 & -1 & 0 \\ \mathcal{C}_{m_{\dot{u}}}(\omega) & \mathcal{C}_{m_{\dot{\alpha}}}(\omega) & 0 & -2\mu_c K_Y^2 \end{bmatrix} \tag{10.6}$$

and,

$$Q_s(\omega) = \begin{bmatrix} -\mathcal{C}_{\mathcal{X}_u}(\omega) & -\mathcal{C}_{\mathcal{X}_\alpha}(\omega) & -C_{Z_0} & -C_{X_q} \\ -\mathcal{C}_{\mathcal{Z}_u}(\omega) & -\mathcal{C}_{\mathcal{Z}_\alpha}(\omega) & C_{X_0} & -\left(C_{Z_q} + 2\mu_c\right) \\ 0 & 0 & 0 & -1 \\ -\mathcal{C}_{m_u}(\omega) & -\mathcal{C}_{m_\alpha}(\omega) & 0 & -C_{m_q} \end{bmatrix} \tag{10.7}$$

and,

$$R_s(\omega) = \begin{bmatrix} -\mathcal{C}_{\mathcal{X}_{u_g}}(\omega) & -\mathcal{C}_{\mathcal{X}_{\dot{u}_g}}(\omega) & -\mathcal{C}_{\mathcal{X}_{\alpha_g}}(\omega) & -\mathcal{C}_{\mathcal{X}_{\dot{\alpha}_g}}(\omega) \\ -\mathcal{C}_{\mathcal{Z}_{u_g}}(\omega) & -\mathcal{C}_{\mathcal{Z}_{\dot{u}_g}}(\omega) & -\mathcal{C}_{\mathcal{Z}_{\alpha_g}}(\omega) & -\mathcal{C}_{\mathcal{Z}_{\dot{\alpha}_g}}(\omega) \\ 0 & 0 & 0 & 0 \\ -\mathcal{C}_{m_{u_g}}(\omega) & -\mathcal{C}_{m_{\dot{u}_g}}(\omega) & -\mathcal{C}_{m_{\alpha_g}}(\omega) & -\mathcal{C}_{m_{\dot{\alpha}_g}}(\omega) \end{bmatrix} \tag{10.8}$$

respectively, and for equations (10.6), (10.7) and (10.8) the definition of the frequency-dependent derivatives summarized in table 10.6. In table I.5 the definition of the constant

symmetrical stability- and 1D gust derivatives for the frame $\mathcal{F}_S$ is given, while in table I.1 the definition of the mass and inertia terms is provided.
Similar to the symmetrical equations of motion, for the asymmetrical equations of motion the matrices $P(\omega)$, $Q(\omega)$ and $R(\omega)$ in equation (10.1) are given as,

$$P_a(\omega) = \frac{b}{Q_\infty} \begin{bmatrix} \left\{\mathcal{C}_{\mathcal{Y}_{\dot{\beta}}}(\omega) - 2\mu_b\right\} & 0 & 0 & 0 \\ 0 & -\frac{1}{2} & 0 & 0 \\ \mathcal{C}_{\ell_{\dot{\beta}}}(\omega) & 0 & -4\mu_b K_X^2 & 4\mu_b K_{XZ} \\ \mathcal{C}_{n_{\dot{\beta}}}(\omega) & 0 & 4\mu_b K_{XZ} & -4\mu_b K_Z^2 \end{bmatrix} \tag{10.9}$$

and,

$$Q_a(\omega) = \begin{bmatrix} -\mathcal{C}_{\mathcal{Y}_\beta}(\omega) & -C_L & -C_{Y_p} & -\left(C_{Y_r} - 4\mu_b\right) \\ 0 & 0 & -1 & 0 \\ -\mathcal{C}_{\ell_\beta}(\omega) & 0 & -C_{\ell_p} & -C_{\ell_r} \\ -\mathcal{C}_{n_\beta}(\omega) & 0 & -C_{n_p} & -C_{n_r} \end{bmatrix} \tag{10.10}$$

and,

$$R_a(\omega) = \begin{bmatrix} -\mathcal{C}_{\mathcal{Y}_{\beta_g}}(\omega) & -\mathcal{C}_{\mathcal{Y}_{\dot{\beta}_g}}(\omega) \\ 0 & 0 \\ -\mathcal{C}_{\ell_{\beta_g}}(\omega) & -\mathcal{C}_{\ell_{\dot{\beta}_g}}(\omega) \\ -\mathcal{C}_{n_{\beta_g}}(\omega) & -\mathcal{C}_{n_{\dot{\beta}_g}}(\omega) \end{bmatrix} \tag{10.11}$$

respectively, and for equations (10.9), (10.10) and (10.11) the definition of the frequency-dependent derivatives summarized in table 10.7. In table I.6 the definition of the constant asymmetrical stability- and 1D gust derivatives for the frame $\mathcal{F}_S$ is given, while in table I.3 the definition of the mass and inertia terms is provided.

Equations of motion used for frequency-domain simulations

Similar to the mathematical aircraft models presented in references [29, 30, 35], the unsteady stability derivatives with respect to the non-dimensional airspeed perturbation $\hat{u}$ are not taken into account. Only the constant (steady) stability derivatives with respect to $\hat{u}$ will be used (these derivatives have been calculated in chapter 6).
Also, the unsteady stability derivative $C_{X_{\dot{\alpha}}}$ is neglected, resulting in the elimination of the derivative $\mathcal{C}_{\mathcal{X}_{\dot{\alpha}}}(\omega)$. The constant stability derivative C_{X_α} will be retained only.
The frequency-dependent matrices given in equations (10.6) and (10.7) now become,

$$P_s(\omega) = \frac{\bar{c}}{Q_\infty} \begin{bmatrix} -2\mu_c & 0 & 0 & 0 \\ 0 & \{\mathcal{C}_{\mathcal{Z}_{\dot{\alpha}}}(\omega) - 2\mu_c\} & 0 & 0 \\ 0 & 0 & -1 & 0 \\ 0 & \mathcal{C}_{m_{\dot{\alpha}}}(\omega) & 0 & -2\mu_c K_Y^2 \end{bmatrix} \tag{10.12}$$

and,

$$Q_s(\omega) = \begin{bmatrix} -C_{X_u} & -C_{X_\alpha} & -C_{Z_0} & -C_{X_q} \\ -C_{Z_u} & -\mathcal{C}_{Z_\alpha}(\omega) & C_{X_0} & -\left(C_{Z_q} + 2\mu_c\right) \\ 0 & 0 & 0 & -1 \\ -C_{m_u} & -\mathcal{C}_{m_\alpha}(\omega) & 0 & -C_{m_q} \end{bmatrix} \tag{10.13}$$

while the matrix $R_s(\omega)$ given in equation (10.8) remains unchanged.

For the frequency-domain simulation of the symmetrical equations of motions use will be made of equations (10.12), (10.13) and (10.8), while for the frequency-domain simulation of the asymmetrical equations of motions use will be made of equations (10.9), (10.10) and (10.11).

The aircraft motion Frequency-Response Functions

Since the unsteady stability derivatives with respect to the airspeed perturbation u are neglected (as is $C_{X_{\dot\alpha}}$), the constant unsteady derivatives to be determined are $C_{Y_{\dot\beta}}$, $C_{\ell_{\dot\beta}}$, $C_{n_{\dot\beta}}$, $C_{Z_{\dot\alpha}}$ and $C_{m_{\dot\alpha}}$. For the estimation of these constant parameters, use is made of aircraft motion Frequency-Response Functions (FRF's). From selected aircraft motion variable resonance peaks, the resonance frequency is determined. Using this frequency, the sought unsteady stability derivative is obtained from the corresponding aerodynamic frequency-response function.
The calculation of the aircraft motion FRF's is performed using equation (10.1), see also appendix B,

$$P(\omega)\ j\omega\ \underline{x} = Q(\omega)\ \underline{x} + R(\omega)\ \underline{u}$$

with the matrices $P(\omega)$, $Q(\omega)$ and $R(\omega)$ according to equations (10.12), (10.13) and (10.8), respectively, for the symmetrical equations of motion. For the asymmetrical equations of motion these matrices are given in equations (10.9), (10.10) and (10.11), respectively.
Using the program package MATLAB, the aircraft motion FRF's are calculated.

In figures 10.10 the FRF's of the aircraft state $\underline{x} = \left[\hat{u}, \alpha, \theta, \frac{q\bar{c}}{Q_\infty}\right]^T$ due to the 1D longitudinal gust input $\hat{u}_g$ are shown. In these figures results are given for the Computational Aerodynamics model (CA-model) which makes use of both frequency-dependent stability- and gust derivatives. In each of the state-variable's responses the results clearly show the phugoid-mode resonance frequency at $\omega_{ph} = 0.1146$ [Rad/sec.], with ω_{ph} the phugoid mode resonance frequency.
Similar to figures 10.10, in figures 10.11 the FRF's of the aircraft state $\underline{x} = \left[\beta, \varphi, \frac{pb}{2Q_\infty}, \frac{rb}{2Q_\infty}\right]^T$ due to the 1D lateral gust input β_g are shown. In these figures results are shown for the Computational Aerodynamics model (CA-model) which also makes use of both frequency-dependent stability- and gust derivatives. The resonance peaks are attributed to the badly damped dutch-roll mode and they are evident at the frequency $\omega_{dr} = 2.2224$ [Rad/sec.], with ω_{dr} the dutch-roll mode resonance frequency.

Finally, in figures 10.12 the FRF's of the aircraft state $\underline{x} = \left[\hat{u}, \alpha, \theta, \frac{q\bar{c}}{Q_\infty}\right]^T$ due to the 1D vertical gust input α_g are shown. In these figures results are given for the Computational Aerodynamics model (CA-model) which also makes use of both frequency-dependent stability- and gust derivatives. The resonance peak in the response of the FRF $\left|H_{q\alpha_g}(\omega)\right|$ is evident at frequency $\omega_{sp} = 3.8929$ [Rad/sec.], with ω_{sp} the short-period mode resonance frequency.

Calculation of the constant unsteady stability derivatives

The resonance frequencies of both the dutch-roll and the short-period mode are now used to calculate the constant unsteady stability derivatives $C_{Y_{\dot\beta}}$, $C_{\ell_{\dot\beta}}$, $C_{n_{\dot\beta}}$, $C_{Z_{\dot\alpha}}$ and $C_{m_{\dot\alpha}}$.
Using the resonance frequency for the dutch-roll mode and the frequency-response functions given in chapter 8, for example the unsteady stability derivative $C_{Y_{\dot\beta}}$ is calculated from,

$$\frac{C_Y}{\beta}(k_{dr}) = C_{Y_\beta} + C_{Y_{\dot\beta}} j k_{dr} = C_{Y_\beta} + \frac{\bar{c}}{2b} C'_{Y_{\dot\beta}} j \frac{\omega_{dr} b}{Q_\infty} = C_{Y_\beta} + C_{Y_{\dot\beta}} j \frac{\omega_{dr} b}{Q_\infty} \tag{10.14}$$

with $\frac{C_Y}{\beta}(k_{dr})$ the aerodynamic frequency-response for the reduced frequency $k = \frac{\omega\bar{c}}{2Q_\infty} = k_{dr}$, C_{Y_β} the constant steady stability derivative determined in chapter 6,
$C'_{Y_{\dot\beta}} = \frac{1}{k_{dr}} Im\left\{\frac{C_Y}{\beta}(k_{dr})\right\}$ the constant unsteady stability derivative obtained from the aerodynamic frequency-response function at $\omega = \omega_{dr}$ ánd with respect to the reduced frequency $k_{dr} = \frac{\omega_{dr}\bar{c}}{2Q_\infty}$, $C_{Y_{\dot\beta}}$ the constant unsteady stability derivative obtained from the aerodynamic frequency-response function at $\omega = \omega_{dr}$ ánd with respect to the reduced frequency $k_{dr} = \frac{\omega_{dr} b}{Q_\infty}$, $\bar{c}$ the mean aerodynamic chord, b the aircraft's span, and Q_∞ the airspeed. In chapter 8 the aerodynamic frequency-response functions for the swaying motion β were calculated as a function of the reduced frequency $k = \frac{\omega\bar{c}}{2Q_\infty}$, which explains the factor $\frac{\bar{c}}{2b}$ in equation (10.14). The definition of the asymmetrical unsteady stability derivatives $C_{Y_{\dot\beta}}$, $C_{\ell_{\dot\beta}}$ and $C_{n_{\dot\beta}}$ is summarized in table 10.7. See also appendix I for the definition of the equations of motion and the definition of its parameters.
In figure 10.1 the asymmetrical frequency-dependent stability derivatives are shown, while the constant unsteady stability derivatives are summarized in table 10.5.

The unsteady stability derivatives $C_{Z_{\dot\alpha}}$ and $C_{m_{\dot\alpha}}$ are calculated in a similar manner as used for the calculation of the unsteady derivatives $C_{Y_{\dot\beta}}$. The symmetrical aerodynamic frequency-response functions given in chapter 7 were calculated as a function of the reduced frequency $k = \frac{\omega\bar{c}}{2Q_\infty}$. For the calculation of, for example, the unsteady derivative $C_{Z_{\dot\alpha}}$, use is made of the short-period mode resonance frequency ω_{sp}, and it becomes,

$$\frac{C_Z}{\alpha}(k_{sp}) = C_{Z_\alpha} + C_{Z_{\dot\alpha}} j k_{sp} = C_{Z_\alpha} + \frac{1}{2} C'_{Z_{\dot\alpha}} j \frac{\omega_{sp}\bar{c}}{Q_\infty} = C_{Z_\alpha} + C_{Z_{\dot\alpha}} j \frac{\omega_{sp}\bar{c}}{Q_\infty} \tag{10.15}$$

with $\frac{C_Z}{\alpha}(k_{sp})$ the aerodynamic frequency-response for the reduced frequency $k = \frac{\omega\bar{c}}{2Q_\infty} = k_{sp}$, C_{Z_α} the constant steady stability derivative determined in chapter 6,
$C'_{Z_{\dot\alpha}} = \frac{1}{k_{sp}} Im\left\{\frac{C_Z}{\alpha}(k_{sp})\right\}$ the constant unsteady stability derivative obtained from the

aerodynamic frequency-response function at $\omega = \omega_{sp}$ ánd with respect to the reduced frequency $k_{sp} = \frac{\omega_{sp}\bar{c}}{2Q_\infty}$, $C_{Z_{\dot{\alpha}}}$ the constant unsteady stability derivative obtained from the aerodynamic frequency-response function at $\omega = \omega_{sp}$ ánd with respect to the reduced frequency $k_{sp} = \frac{\omega_{sp}\bar{c}}{Q_\infty}$, $\bar{c}$ the mean aerodynamic chord and Q_∞ the airspeed. In chapter 7 the aerodynamic frequency-response functions for the heaving motion α were calculated as a function of the reduced frequency $k = \frac{\omega\bar{c}}{2Q_\infty}$, which explains the factor $\frac{1}{2}$ in equation (10.15). The definition of the symmetrical unsteady stability derivatives $C_{Z_{\dot{\alpha}}}$ and $C_{m_{\dot{\alpha}}}$ is summarized in table 10.6. See also appendix I for the definition of the equations of motion and the definition of its parameters.
In figure 10.2 the symmetrical frequency-dependent stability derivatives are shown, while the constant unsteady stability derivatives are summarized in table 10.4.

10.4.3 Calculation of the gust derivatives for 1D gust fields

Similar to the calculation of the unsteady stability derivatives, the unsteady gust derivatives for 1D gust fields are calculated from resonance frequencies. These resonance frequencies, however, are now obtained from aircraft motion responses using the atmospheric turbulence input PSD-functions for the gust input considered. The aircraft motion frequency-response functions are used to calculate the output PSD-function according to, see also appendix B,

$$S_{yy}(\omega) = |H_{yu}(\omega)|^2 \, S_{uu}(\omega) \tag{10.16}$$

with $S_{uu}(\omega)$ the input PSD-function of either the (non-dimensional) 1D longitudinal, lateral or vertical gust input, $\hat{u}_g$, β_g, α_g, respectively, $H_{yu}(\omega)$ the aerodynamic frequency-response function of the output (being either the symmetrical or asymmetrical state) and $S_{yy}(\omega)$ the output PSD-function. For all frequency-domain aircraft motion results the aerodynamic frequency-response functions are obtained from equation (10.1). The aerodynamic model makes use of frequency-dependent stability derivatives and frequency-dependent gust derivatives. The definition of the unsteady gust derivatives is similar to the ones given in equations (10.14) and (10.15), and it is summarized in tables 10.6 and 10.7. Furthermore, the frequency-dependent gust derivatives are shown as a function of the circular frequency in figures 10.3, 10.4 and 10.5.

For a series of the atmospheric turbulence gust scale length,

$$L_g = [30, 150, 300, 500, 1000, 1500]^T$$

the input PSD-functions for 1D non-dimensional longitudinal, lateral and vertical gusts, $S_{\hat{u}_g\hat{u}_g}(\omega)$, $S_{\beta_g\beta_g}(\omega)$ and $S_{\alpha_g\alpha_g}(\omega)$, respectively, are given in figures 10.6. The symmetrical aircraft state output PSD-functions due to the longitudinal gust $\hat{u}_g$ are shown in figures 10.7. These figures clearly show the badly damped phugoid-mode resonance peak for all the aircraft state variables. Similar to the calculation of the unsteady stability derivatives, the resonance frequency is used to calculate the constant unsteady gust derivatives. The constant steady gust derivatives are taken equal to the corresponding stability derivative,

or in this case $C_{X_{u_g}} = C_{X_u}$, $C_{Z_{u_g}} = C_{Z_u}$ and $C_{m_{u_g}} = C_{m_u}$. As a function of the gust scale length L_g, both the steady and unsteady gust derivatives, $C_{X_{u_g}}$, $C_{Z_{u_g}}$, $C_{m_{u_g}}$, and $C_{X_{\dot{u}_g}}$, $C_{Z_{\dot{u}_g}}$ and $C_{m_{\dot{u}_g}}$, respectively, are summarized in table 10.2. In this table the phugoid-mode resonance frequency is given as well. Due to both the phugoid-mode's low damping and its low resonance frequency, the unsteady gust derivatives are independent of L_g.
Similar to the responses for the longitudinal gust $\hat{u}_g$, the asymmetrical aircraft state output PSD-functions due to the lateral gust β_g are shown in figure 10.8. These results also show a badly damped mode, that is the dutch-roll mode. For all the aircraft-state variables a resonance peak is present at approximately ω_{dr}, with ω_{dr} the dutch-roll mode's resonance frequency. Again, similar to the calculation of the unsteady stability derivatives, the resonance frequency is used to calculate the constant unsteady gust derivatives. The constant steady gust derivatives are taken to be equal to the corresponding stability derivative, which are in this case $C_{Y_{\beta_g}} = C_{Y_\beta}$, $C_{\ell_{\beta_g}} = C_{\ell_\beta}$ and $C_{n_{\beta_g}} = C_{n_\beta}$. As a function of the gust scale length L_g, both the steady and unsteady gust derivatives, $C_{Y_{\beta_g}}$, $C_{\ell_{\beta_g}}$, $C_{n_{\beta_g}}$, and $C_{Y_{\dot{\beta}_g}}$, $C_{\ell_{\dot{\beta}_g}}$ and $C_{n_{\dot{\beta}_g}}$, respectively, are summarized in table 10.3. In this table the dutch-roll mode resonance frequency is given as well. Quite similar to the results obtained for the 1D longitudinal gust $\hat{u}_g$, due to the dutch-roll mode's low damping the unsteady gust derivatives are independent of L_g.
Finally, the symmetrical aircraft state output PSD-functions to the vertical gust α_g are shown in figures 10.9. Since the short-period mode is well damped, for the estimation of its resonance frequency the output PSD-function $S_{qq}(\omega, L_g)$ is used. Also here the resonance frequency is used to calculate the constant unsteady gust derivatives. The constant steady gust derivatives are taken equal to the corresponding stability derivative, or in this case $C_{X_{\alpha_g}} = C_{X_\alpha}$, $C_{Z_{\alpha_g}} = C_{Z_\alpha}$ and $C_{m_{\alpha_g}} = C_{m_\alpha}$. As a function of the gust scale length L_g, both the steady and unsteady gust derivatives, $C_{X_{\alpha_g}}$, $C_{Z_{\alpha_g}}$, $C_{m_{\alpha_g}}$, and $C_{X_{\dot{\alpha}_g}}$, $C_{Z_{\dot{\alpha}_g}}$ and $C_{m_{\dot{\alpha}_g}}$, respectively, are summarized in table 10.2 (with the unsteady gust derivative $C_{X_{\dot{\alpha}_g}}$ taken to be zero for all L_g). In the table the short-period mode resonance frequency is given as well. Now, due to the short-period mode's relatively high resonance frequency, the unsteady gust derivatives are dependent of L_g (see also figures 10.6). With respect to a mean value (taken to be the results for $L_g = 300$ [m]), the variation of the unsteady gust derivatives is relatively small (less than 1%). Therefore, the unsteady gust derivatives for the gust scale length $L_g = 300$ [m] will be used for all simulations, irrespective of the true gust scale length.

All constant steady and unsteady gust derivatives are summarized in tables 10.4 and 10.5 for the symmetric and asymmetric gust inputs, respectively. Using these derivatives, the aerodynamic models are written as (using non-dimensional gust inputs for all the 1D symmetrical gust fields u_g and w_g, and the asymmetrical 1D gust field v_g),

$$\left.\begin{aligned} C_{X_g} &= C_{X_{u_g}}\ \hat{u}_g + C_{X_{\dot{u}_g}}\ \frac{\dot{\hat{u}}_g \bar{c}}{Q_\infty} \\ C_{Z_g} &= C_{Z_{u_g}}\ \hat{u}_g + C_{Z_{\dot{u}_g}}\ \frac{\dot{\hat{u}}_g \bar{c}}{Q_\infty} \\ C_{m_g} &= C_{m_{u_g}}\ \hat{u}_g + C_{m_{\dot{u}_g}}\ \frac{\dot{\hat{u}}_g \bar{c}}{Q_\infty} \end{aligned}\right\} \qquad (10.17)$$

with $\hat{u}_g = \frac{u_g}{Q_\infty}$, $\bar{c}$ the mean aerodynamic chord and Q_∞ the airspeed.
The aerodynamic model for the vertical gust field becomes,

$$\left.\begin{array}{rcl} C_{X_g} & = & C_{X_{\alpha_g}}\ \alpha_g + C_{X_{\dot{\alpha}_g}}\ \frac{\dot{\alpha}_g \bar{c}}{Q_\infty} \\ C_{Z_g} & = & C_{Z_{\alpha_g}}\ \alpha_g + C_{Z_{\dot{\alpha}_g}}\ \frac{\dot{\alpha}_g \bar{c}}{Q_\infty} \\ C_{m_g} & = & C_{m_{\alpha_g}}\ \alpha_g + C_{m_{\dot{\alpha}_g}}\ \frac{\dot{\alpha}_g \bar{c}}{Q_\infty} \end{array}\right\} \tag{10.18}$$

with $\alpha_g = \frac{w_g}{Q_\infty}$.
Similarly, the aerodynamic model for the 1D asymmetrical gust field (v_g) written in non-dimensional form is given as,

$$\left.\begin{array}{rcl} C_{Y_g} & = & C_{Y_{\beta_g}}\ \beta_g + C_{Y_{\dot{\beta}_g}}\ \frac{\dot{\beta}_g b}{Q_\infty} \\ C_{\ell_g} & = & C_{\ell_{\beta_g}}\ \beta_g + C_{\ell_{\dot{\beta}_g}}\ \frac{\dot{\beta}_g b}{Q_\infty} \\ C_{n_g} & = & C_{n_{\beta_g}}\ \beta_g + C_{n_{\dot{\beta}_g}}\ \frac{\dot{\beta}_g b}{Q_\infty} \end{array}\right\} \tag{10.19}$$

with $\beta_g = \frac{v_g}{Q_\infty}$, b the aircraft wingspan and Q_∞ the airspeed.

Comparison of PCA-models

Now all constant, both steady and unsteady, stability- and gust derivatives are known for all 1D gust inputs, the equations of motion are written as,

$$P^c\ j\omega\ \underline{x} = Q^c\ \underline{x} + R^c\ \underline{u} \tag{10.20}$$

with for the symmetrical equations of motion the P^c, Q^c and R^c matrices equal to,

$$P_s^c = \frac{\bar{c}}{Q_\infty} \begin{bmatrix} -2\mu_c & 0 & 0 & 0 \\ 0 & (C_{Z_{\dot{\alpha}}} - 2\mu_c) & 0 & 0 \\ 0 & 0 & -1 & 0 \\ 0 & C_{m_{\dot{\alpha}}} & 0 & -2\mu_c K_Y^2 \end{bmatrix} \tag{10.21}$$

and,

$$Q_s^c = \begin{bmatrix} -C_{X_u} & -C_{X_\alpha} & -C_{Z_0} & -C_{X_q} \\ -C_{Z_u} & -C_{Z_\alpha} & C_{X_0} & -\left(C_{Z_q} + 2\mu_c\right) \\ 0 & 0 & 0 & -1 \\ -C_{m_u} & -C_{m_\alpha} & 0 & -C_{m_q} \end{bmatrix} \tag{10.22}$$

and,

$$R_s^c = \begin{bmatrix} -C_{X_{u_g}} & -C_{X_{\dot{u}_g}} & -C_{X_{\alpha_g}} & -C_{X_{\dot{\alpha}_g}} \\ -C_{Z_{u_g}} & -C_{Z_{\dot{u}_g}} & -C_{Z_{\alpha_g}} & -C_{Z_{\dot{\alpha}_g}} \\ 0 & 0 & 0 & 0 \\ -C_{m_{u_g}} & -C_{m_{\dot{u}_g}} & -C_{m_{\alpha_g}} & -C_{m_{\dot{\alpha}_g}} \end{bmatrix} \tag{10.23}$$

respectively, the aircraft state $\underline{x} = \left[\hat{u}, \alpha, \theta, \frac{q\bar{c}}{Q_\infty}\right]^T$, the input $\underline{u} = \left[\hat{u}_g(\omega),\ \frac{j\omega\hat{u}_g(\omega)\bar{c}}{Q_\infty},\ \alpha_g(\omega),\ \frac{j\omega\alpha_g(\omega)\bar{c}}{Q_\infty}\right]^T$, and the definition of all derivatives given in appendix I, table I.5.

For the asymmetrical equations of motion, the matrices P^c, Q^c and R^c in equation (10.20) become,

$$P_a^c = \frac{b}{Q_\infty}\begin{bmatrix} \left(C_{Y_{\dot{\beta}}} - 2\mu_b\right) & 0 & 0 & 0 \\ 0 & -\frac{1}{2} & 0 & 0 \\ C_{\ell_{\dot{\beta}}} & 0 & -4\mu_b K_X^2 & 4\mu_b K_{XZ} \\ C_{n_{\dot{\beta}}} & 0 & 4\mu_b K_{XZ} & -4\mu_b K_Z^2 \end{bmatrix} \tag{10.24}$$

and,

$$Q_a^c = \begin{bmatrix} -C_{Y_\beta} & -C_L & -C_{Y_p} & -\left(C_{Y_r} - 4\mu_b\right) \\ 0 & 0 & -1 & 0 \\ -C_{\ell_\beta} & 0 & -C_{\ell_p} & -C_{\ell_r} \\ -C_{n_\beta} & 0 & -C_{n_p} & -C_{n_r} \end{bmatrix} \tag{10.25}$$

and,

$$R_a^c = \begin{bmatrix} -C_{Y_{\beta_g}} & -C_{Y_{\dot{\beta}_g}} \\ 0 & 0 \\ -C_{\ell_{\beta_g}} & -C_{\ell_{\dot{\beta}_g}} \\ -C_{n_{\beta_g}} & -C_{n_{\dot{\beta}_g}} \end{bmatrix} \tag{10.26}$$

respectively, the aircraft state $\underline{x} = \left[\beta, \varphi, \frac{pb}{2Q_\infty}, \frac{rb}{2Q_\infty}\right]^T$, the input $\underline{u} = \left[\beta_g(\omega),\ \frac{j\omega\beta_g(\omega)b}{Q_\infty}\right]^T$, and the definition of all derivatives also given in appendix I, table I.6.

Using the numerical results presented in tables 10.4 and 10.5 for the symmetrical and asymmetrical equations of motion, respectively, the Constant Parameter model (CP) Bode plots of the state variables are given in figures 10.10, 10.11 and 10.12, as well. As is shown, for all the state-variable frequency-response functions the results of both the CA- and the CP-model coincide over a wide frequency-range.
As an illustration, the results of the Computational Aerodynamics Parametric stability derivative (or CAP)-model are also shown in these figures. The CAP-model makes use of constant stability derivatives, while the gust derivatives are kept frequency-dependent. Also for this model, the frequency-response functions coincide over a wide frequency-range as compared to the results obtained for the CA- and CP-model.
From these results it is concluded that for the example aircraft the aircraft motion frequency-response functions are accurately simulated using both constant stability- and gust derivatives.

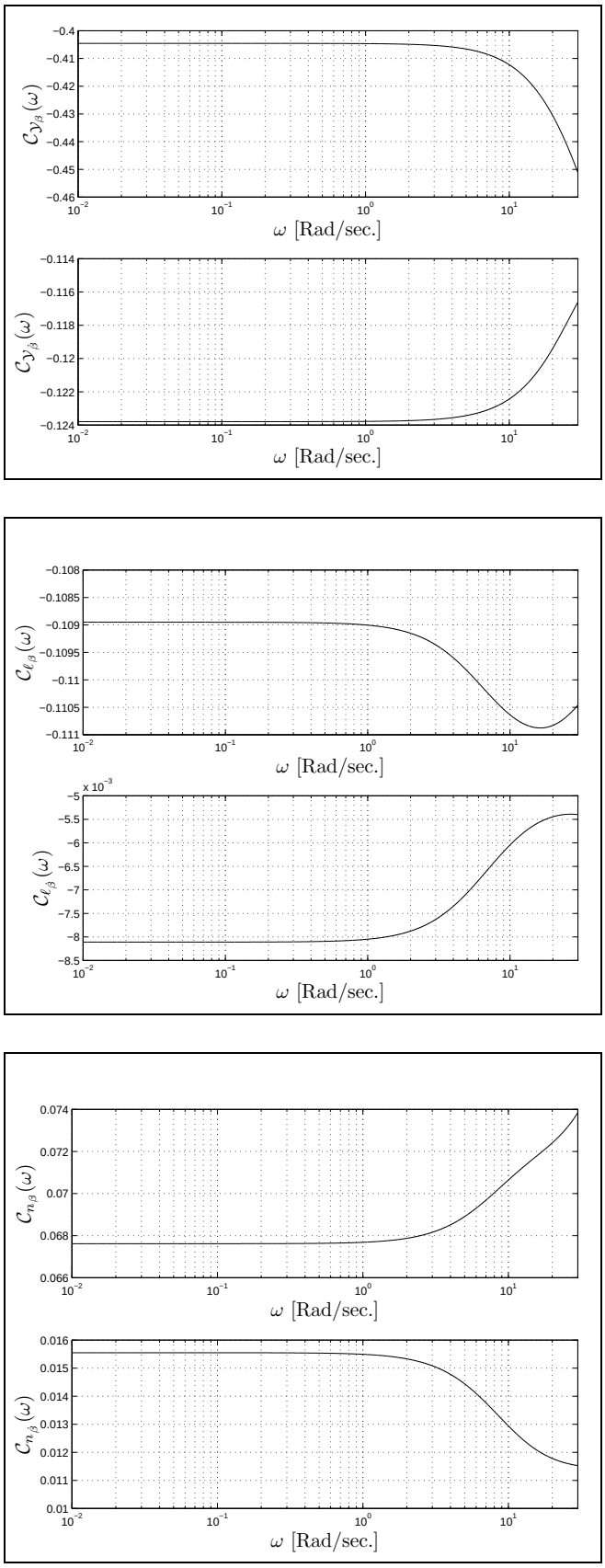


Figure 10.1: The frequency-dependent asymmetrical stability derivatives $\mathcal{C}_{\mathcal{Y}_\beta}(\omega)$ and $\mathcal{C}_{\mathcal{Y}_{\dot\beta}}(\omega)$ (top), $\mathcal{C}_{\ell_\beta}(\omega)$ and $\mathcal{C}_{\ell_{\dot\beta}}(\omega)$ (center), and $\mathcal{C}_{n_\beta}(\omega)$ and $\mathcal{C}_{n_{\dot\beta}}(\omega)$ (bottom).

Gust scale length L_g **[m]**	**Phugoid resonance frequency** [Rad/sec]	$C_{X_{u_g}}(L_g)$	$C_{X_{\dot{u}_g}}(L_g)$	$C_{Z_{u_g}}(L_g)$	$C_{Z_{\dot{u}_g}}(L_g)$	$C_{m_{u_g}}(L_g)$	$C_{m_{\dot{u}_g}}(L_g)$
3.0000e+001	1.1464e-001	-3.1594e-003	7.1449e-001	-4.5923e-001	1.4698e-001	2.3575e-002	-2.3148e-001
1.5000e+002	1.1464e-001	-3.1594e-003	7.1449e-001	-4.5923e-001	1.4698e-001	2.3575e-002	-2.3148e-001
3.0000e+002	1.1464e-001	-3.1594e-003	7.1449e-001	-4.5923e-001	1.4698e-001	2.3575e-002	-2.3148e-001
5.0000e+002	1.1464e-001	-3.1594e-003	7.1449e-001	-4.5923e-001	1.4698e-001	2.3575e-002	-2.3148e-001
1.0000e+003	1.1464e-001	-3.1594e-003	7.1449e-001	-4.5923e-001	1.4698e-001	2.3575e-002	-2.3148e-001
1.5000e+003	1.1464e-001	-3.1594e-003	7.1449e-001	-4.5923e-001	1.4698e-001	2.3575e-002	-2.3148e-001
Gust scale length L_g **[m]**	**Short-period resonance frequency** [Rad/sec]	$C_{X_{\alpha_g}}(L_g)$	$C_{X_{\dot{\alpha}_g}}(L_g)$	$C_{Z_{\alpha_g}}(L_g)$	$C_{Z_{\dot{\alpha}_g}}(L_g)$	$C_{m_{\alpha_g}}(L_g)$	$C_{m_{\dot{\alpha}_g}}(L_g)$
3.0000e+001	3.6222e+000	1.6920e-001	0.0000e+000	-5.7874e+000	5.1088e+000	-7.4865e-001	3.0451e+000
1.5000e+002	2.4782e+000	1.6920e-001	0.0000e+000	-5.7874e+000	5.1453e+000	-7.4865e-001	2.9966e+000
3.0000e+002	2.1455e+000	1.6920e-001	0.0000e+000	-5.7874e+000	5.1534e+000	-7.4865e-001	2.9846e+000
5.0000e+002	1.9867e+000	1.6920e-001	0.0000e+000	-5.7874e+000	5.1569e+000	-7.4865e-001	2.9793e+000
1.0000e+003	1.8664e+000	1.6920e-001	0.0000e+000	-5.7874e+000	5.1593e+000	-7.4865e-001	2.9755e+000
1.5000e+003	1.8338e+000	1.6920e-001	0.0000e+000	-5.7874e+000	5.1600e+000	-7.4865e-001	2.9745e+000

Table 10.2: The PCA-model 1D symmetrical gust derivatives obtained from frequency-domain simulations given as a function of the gust scale length L_g [m].

Gust scale length L_g **[m]**	**Dutch-roll resonance frequency** [Rad/sec]	$C_{Y_{\beta_g}}(L_g)$	$C_{Y_{\dot{\beta}_g}}(L_g)$	$C_{\ell_{\beta_g}}(L_g)$	$C_{\ell_{\dot{\beta}_g}}(L_g)$	$C_{n_{\beta_g}}(L_g)$	$C_{n_{\dot{\beta}_g}}(L_g)$
3.0000e+001	2.2511e+000	-4.0455e-001	6.3349e-002	-1.0895e-001	1.9411e-002	6.7617e-002	-4.9518e-002
1.5000e+002	2.2083e+000	-4.0455e-001	6.3349e-002	-1.0895e-001	1.9411e-002	6.7617e-002	-4.9518e-002
3.0000e+002	2.1977e+000	-4.0455e-001	6.3349e-002	-1.0895e-001	1.9411e-002	6.7617e-002	-4.9518e-002
5.0000e+002	2.1977e+000	-4.0455e-001	6.3349e-002	-1.0895e-001	1.9411e-002	6.7617e-002	-4.9518e-002
1.0000e+003	2.1977e+000	-4.0455e-001	6.3349e-002	-1.0895e-001	1.9411e-002	6.7617e-002	-4.9518e-002
1.5000e+003	2.1941e+000	-4.0455e-001	6.3349e-002	-1.0895e-001	1.9411e-002	6.7617e-002	-4.9518e-002

Table 10.3: The PCA-model 1D asymmetrical gust derivatives obtained from frequency-domain simulations given as a function of the gust scale length L_g [m].

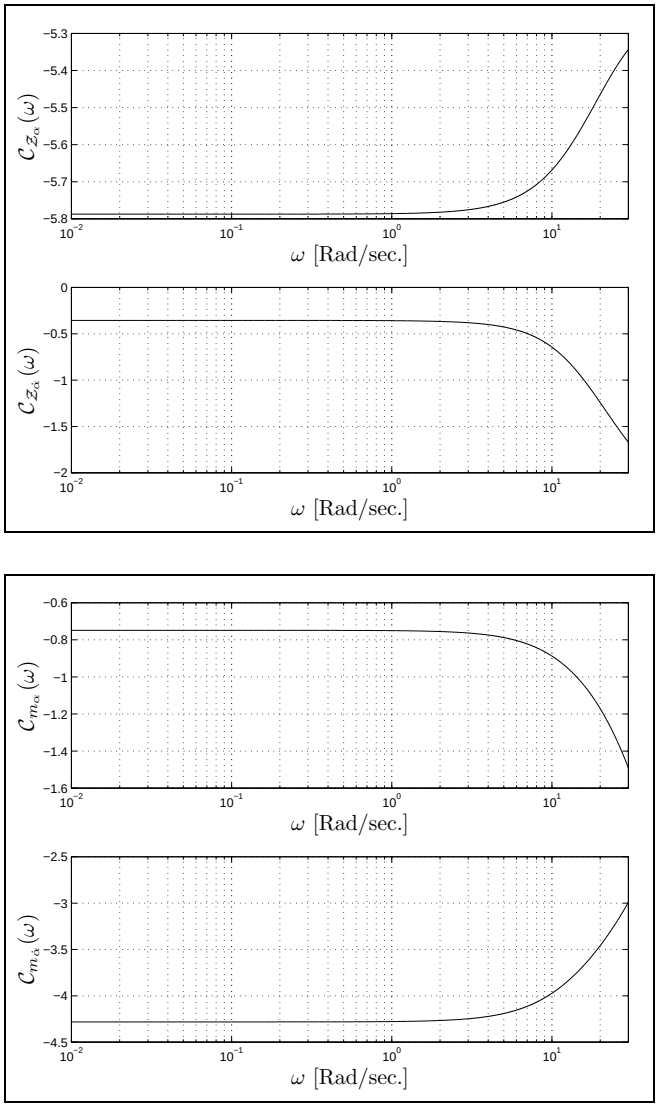


Figure 10.2: The frequency-dependent symmetrical stability derivatives $\mathcal{C}_{\mathcal{Z}_\alpha}(\omega)$ and $\mathcal{C}_{\mathcal{Z}_{\dot\alpha}}(\omega)$ (top), and $\mathcal{C}_{m_\alpha}(\omega)$ and $\mathcal{C}_{m_{\dot\alpha}}(\omega)$ (bottom).

C_{X_0}	=	0.0	C_{Z_0}	=	-0.2292	C_{m_0}	=	0.0
C_{X_u}	=	-0.0032	C_{Z_u}	=	-0.4592	C_{m_u}	=	0.0236
$C_{X_{\dot u}}$	=	0.0	$C_{Z_{\dot u}}$	=	0.0	$C_{m_{\dot u}}$	=	0.0
C_{X_α}	=	0.1692	C_{Z_α}	=	-5.7874	C_{m_α}	=	-0.7486
$C_{X_{\dot\alpha}}$	=	0	$C_{Z_{\dot\alpha}}$	=	-0.3980	$C_{m_{\dot\alpha}}$	=	-4.2255
C_{X_q}	=	-0.0450	C_{Z_q}	=	-4.5499	C_{m_q}	=	-7.4647
$C_{X_{u_g}}$	=	-0.0032	$C_{Z_{u_g}}$	=	-0.4592	$C_{m_{u_g}}$	=	0.0236
$C_{X_{\dot u_g}}$	=	0.7145	$C_{Z_{\dot u_g}}$	=	0.1470	$C_{m_{\dot u_g}}$	=	-0.2315
$C_{X_{\alpha_g}}$	=	0.1692	$C_{Z_{\alpha_g}}$	=	-5.7874	$C_{m_{\alpha_g}}$	=	-0.7486
$C_{X_{\dot\alpha_g}}$	=	0	$C_{Z_{\dot\alpha_g}}$	=	5.1534	$C_{m_{\dot\alpha_g}}$	=	2.9846

Table 10.4: The (constant) symmetric stability- and 1D gust derivatives for the PCA-model equations of motion in the frame $\mathcal{F}_S$, with the gust scale length $L_g = 300$ [m].

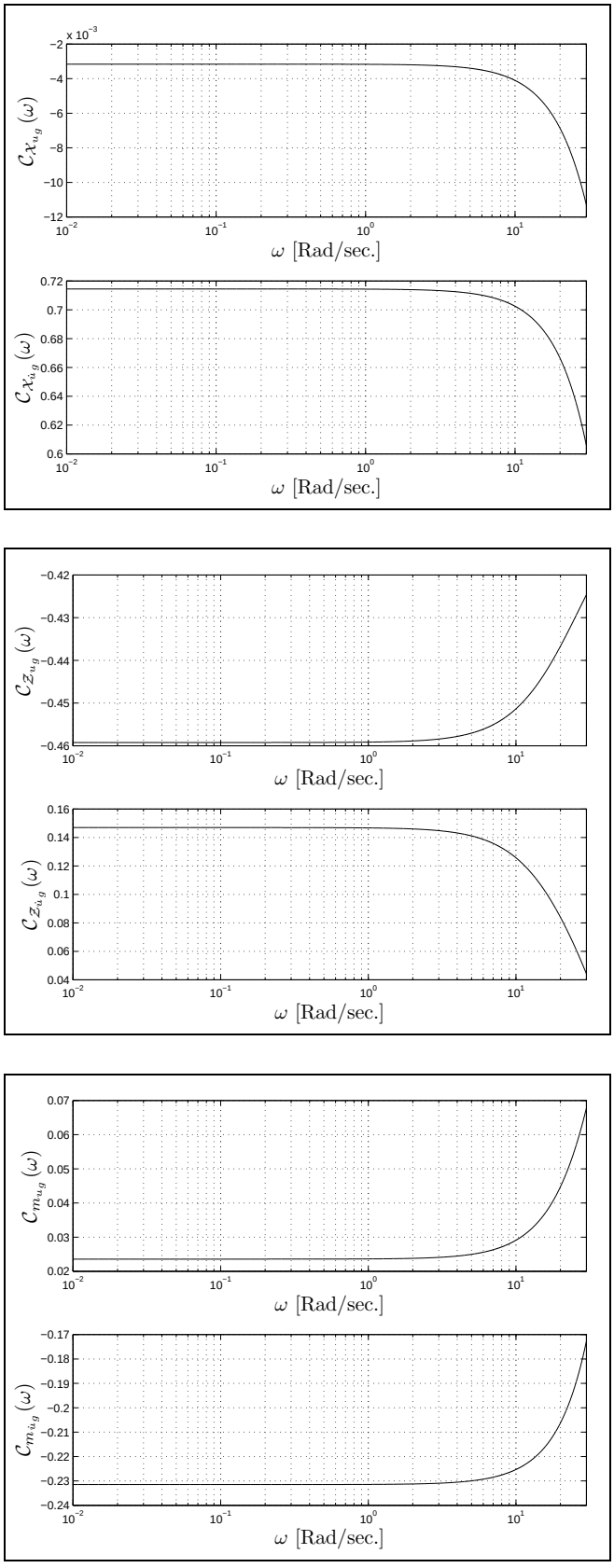


Figure 10.3: The frequency-dependent symmetrical gust derivatives $\mathcal{C}_{\mathcal{X}_{u_g}}(\omega)$ and $\mathcal{C}_{\mathcal{X}_{\dot{u}_g}}(\omega)$ (top), $\mathcal{C}_{\mathcal{Z}_{u_g}}(\omega)$ and $\mathcal{C}_{\mathcal{Z}_{\dot{u}_g}}(\omega)$ (center), and $\mathcal{C}_{m_{u_g}}(\omega)$ and $\mathcal{C}_{m_{\dot{u}_g}}(\omega)$ (bottom).

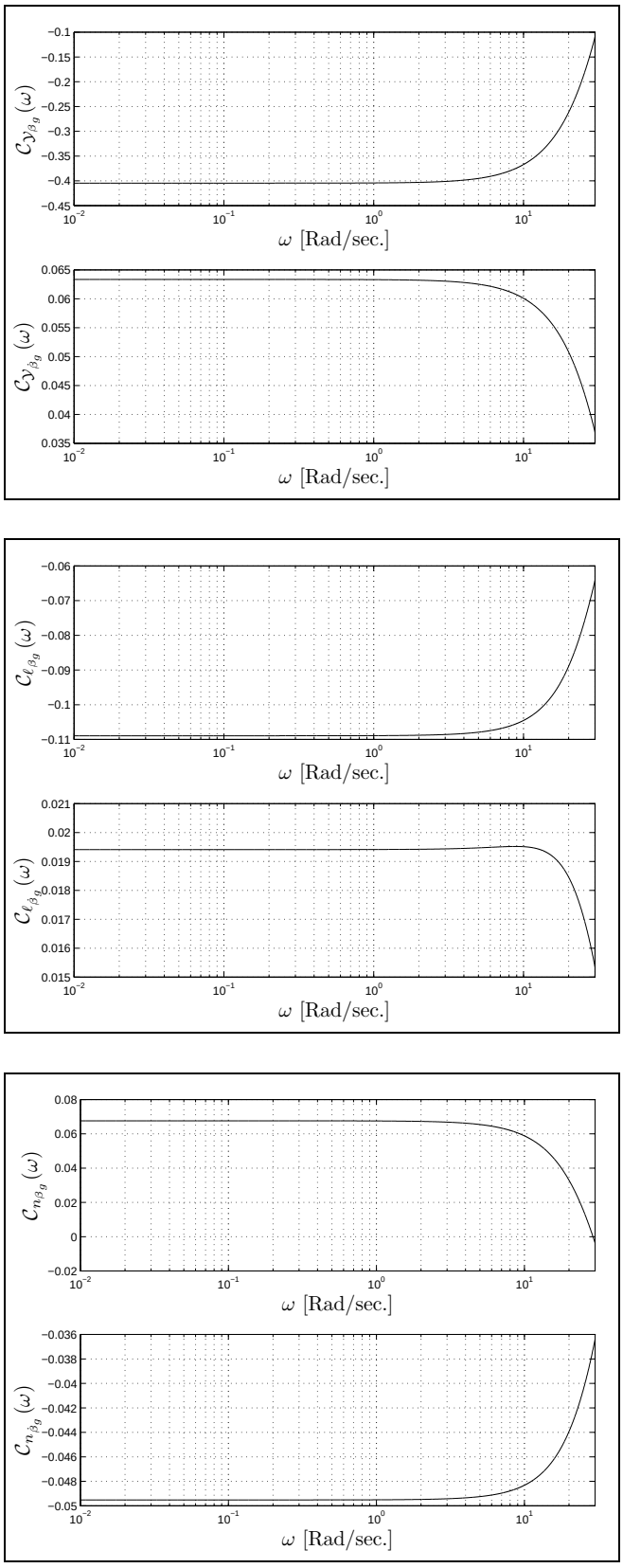


Figure 10.4: The frequency-dependent asymmetrical gust derivatives $\mathcal{C}_{\mathcal{Y}_{\beta_g}}(\omega)$ and $\mathcal{C}_{\mathcal{Y}_{\dot{\beta}_g}}(\omega)$ (top), $\mathcal{C}_{\ell_{\beta_g}}(\omega)$ and $\mathcal{C}_{\ell_{\dot{\beta}_g}}(\omega)$ (center), and $\mathcal{C}_{n_{\beta_g}}(\omega)$ and $\mathcal{C}_{n_{\dot{\beta}_g}}(\omega)$ (bottom).

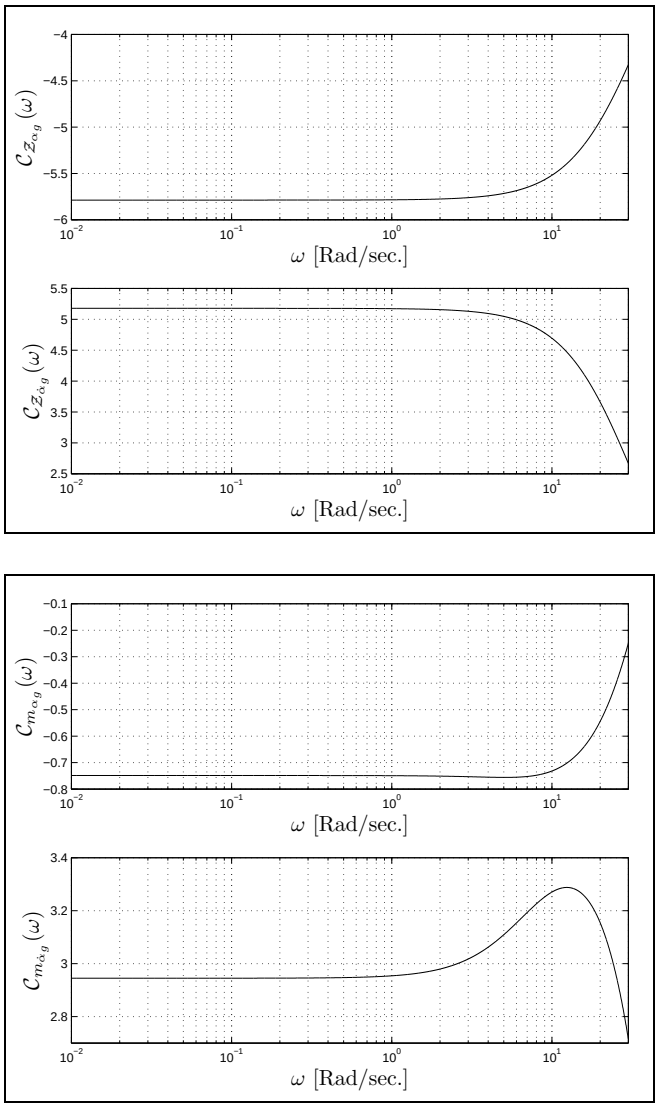


Figure 10.5: The frequency-dependent symmetrical gust derivatives $\mathcal{C}_{\mathcal{Z}_{\alpha_g}}(\omega)$ and $\mathcal{C}_{\mathcal{Z}_{\dot{\alpha}_g}}(\omega)$ (top), and $\mathcal{C}_{m_{\alpha_g}}(\omega)$ and $\mathcal{C}_{m_{\dot{\alpha}_g}}(\omega)$ (bottom).

C_{Y_β}	=	-0.4046	C_{ℓ_β}	=	-0.1090	C_{n_β}	=	0.0676
$C_{Y_{\dot{\beta}}}$	=	-0.1237	$C_{\ell_{\dot{\beta}}}$	=	-0.0078	$C_{n_{\dot{\beta}}}$	=	0.0153
C_{Y_p}	=	-0.0733	C_{ℓ_p}	=	-0.5194	C_{n_p}	=	0.0010
C_{Y_r}	=	0.1193	C_{ℓ_r}	=	0.1039	C_{n_r}	=	-0.1279
$C_{Y_{\beta_g}}$	=	-0.4046	$C_{\ell_{\beta_g}}$	=	-0.1090	$C_{n_{\beta_g}}$	=	0.0676
$C_{Y_{\dot{\beta}_g}}$	=	0.0633	$C_{\ell_{\dot{\beta}_g}}$	=	0.0194	$C_{n_{\dot{\beta}_g}}$	=	-0.0495

Table 10.5: The (constant) asymmetric stability- and 1D gust derivatives for the PCA-model equations of motion in the frame $\mathcal{F}_S$, with the gust scale length $L_g = 300$ [m].

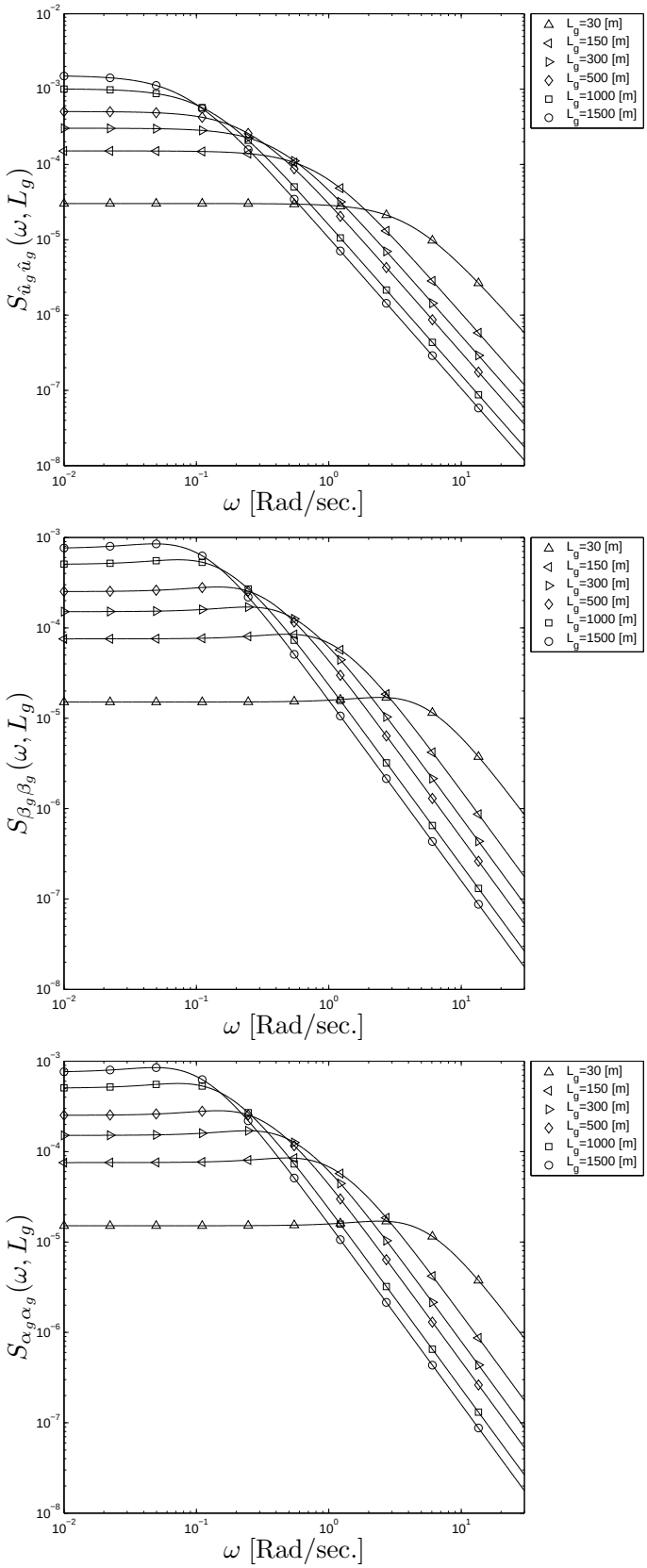


Figure 10.6: The input PSD-functions $S_{\hat{u}_g\hat{u}_g}(\omega)$, $S_{\beta_g\beta_g}(\omega)$ and $S_{\alpha_g\alpha_g}(\omega)$ for a series of atmospheric turbulence gust scale length L_g.

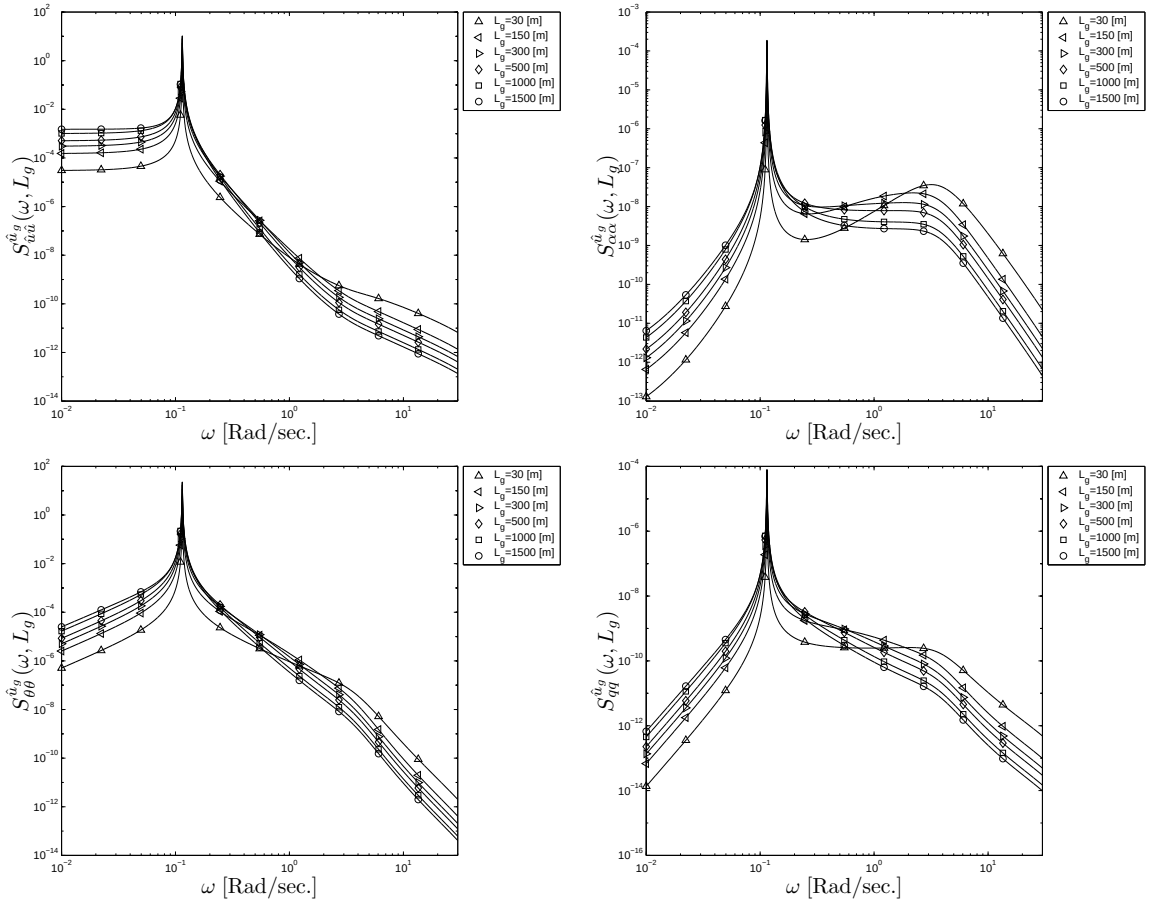


Figure 10.7: The PCA-model output PSD-functions $S^{\hat{u}_g}_{\hat{u}\hat{u}}(\omega)$, $S^{\hat{u}_g}_{\alpha\alpha}(\omega)$, $S^{\hat{u}_g}_{\theta\theta}(\omega)$ and $S^{\hat{u}_g}_{qq}(\omega)$ for a series of atmospheric turbulence gust scale length L_g. The aircraft model makes use of both frequency-dependent stability- and gust derivatives.

10.5 The parametric aircraft model for 2D gust fields

10.5.1 Introduction

In this section the aircraft models for the response to 2D anti-symmetrical atmospheric turbulence gust fields will be presented. The considered atmospheric turbulence velocity components will include the 2D longitudinal anti-symmetrical gust u_g and the 2D vertical anti-symmetrical gust w_g, only. These gust velocity components now vary along the Y_S-axis of the frame $\mathcal{F}_S$.

The parametric aircraft models, presented in this section, are based on the aircraft equations of motion given in references [29, 30, 35], and they are also based on a constant parameter aerodynamic model. The aerodynamic model will make use of the asymmetrical stability derivatives obtained earlier in section 10.4.1, while both the steady and unsteady gust derivatives for both the longitudinal anti-symmetrical - and the vertical anti-symmetrical gust fields will be calculated in this section. Originally, both the steady - and unsteady gust derivatives are given with respect to the non-dimensional gust inputs $\hat{u}_g$ and α_g. Later in this section, these derivatives will be transformed to the so-called

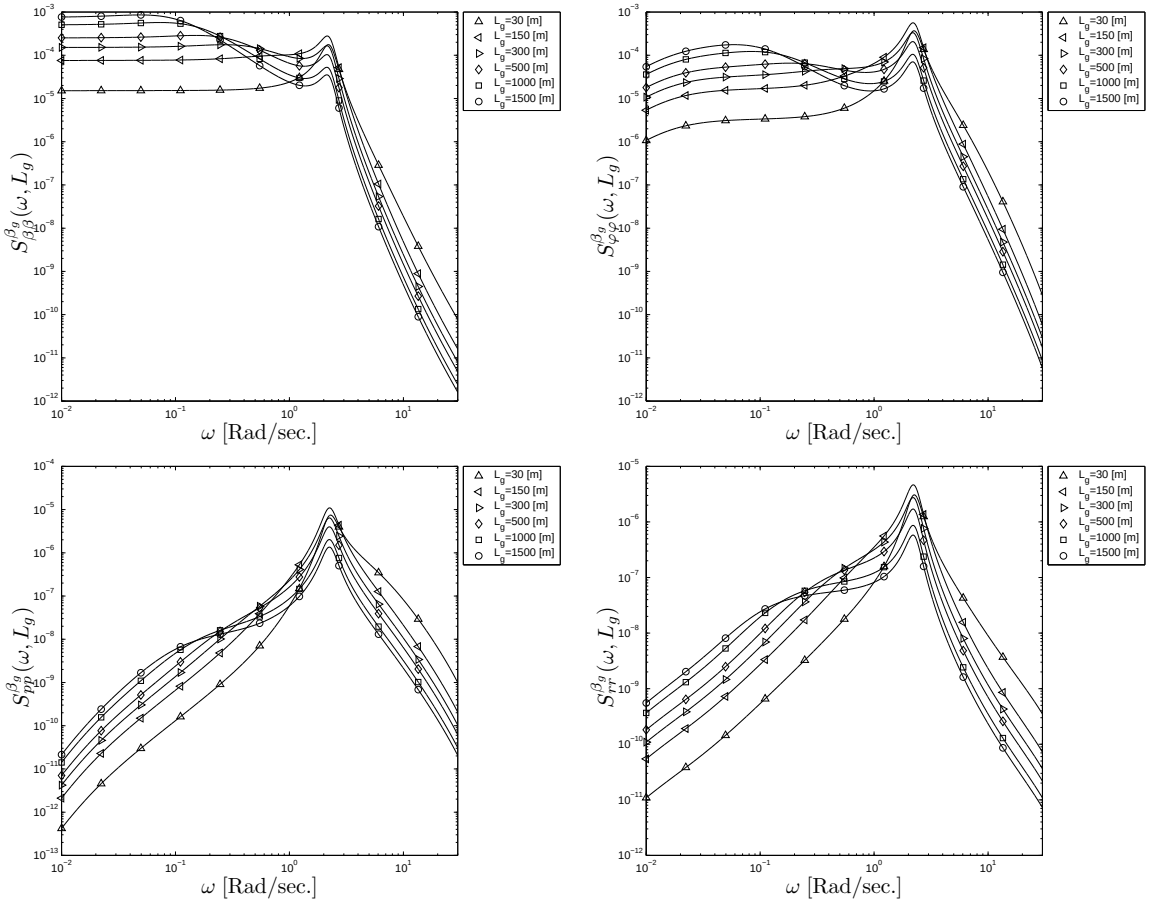


Figure 10.8: The PCA-model output PSD-functions $S^{\beta_g}_{\beta\beta}(\omega)$, $S^{\beta_g}_{\varphi\varphi}(\omega)$, $S^{\beta_g}_{pp}(\omega)$ and $S^{\beta_g}_{rr}(\omega)$ for a series of atmospheric turbulence gust scale length L_g. The aircraft model makes use of both frequency-dependent stability- and gust derivatives.

"yaw-gust" (r_{1_g}) and the so-called "roll-gust" (p_g) derivatives, see also chapter 12 and reference [35]. These new derivatives will allow the calculation of the time-dependent asymmetrical aerodynamic force and moments to 2D spatial-domain gust fields.

10.5.2 The frequency-domain aircraft responses to 2D gust fields

Now consider, for example, the aircraft responses to the 2D anti-symmetrical vertical gust field w_g, or $\alpha_g = \frac{w_g}{Q_\infty}$. Similar to the asymmetrical equations of motion for the 1D lateral gust field, the frequency-domain aircraft equations of motion are written as, see also equation (10.20),

$$P^c_a \; j\omega \; \underline{x} = Q^c_a \; \underline{x} + R^c_a \; \underline{u}$$

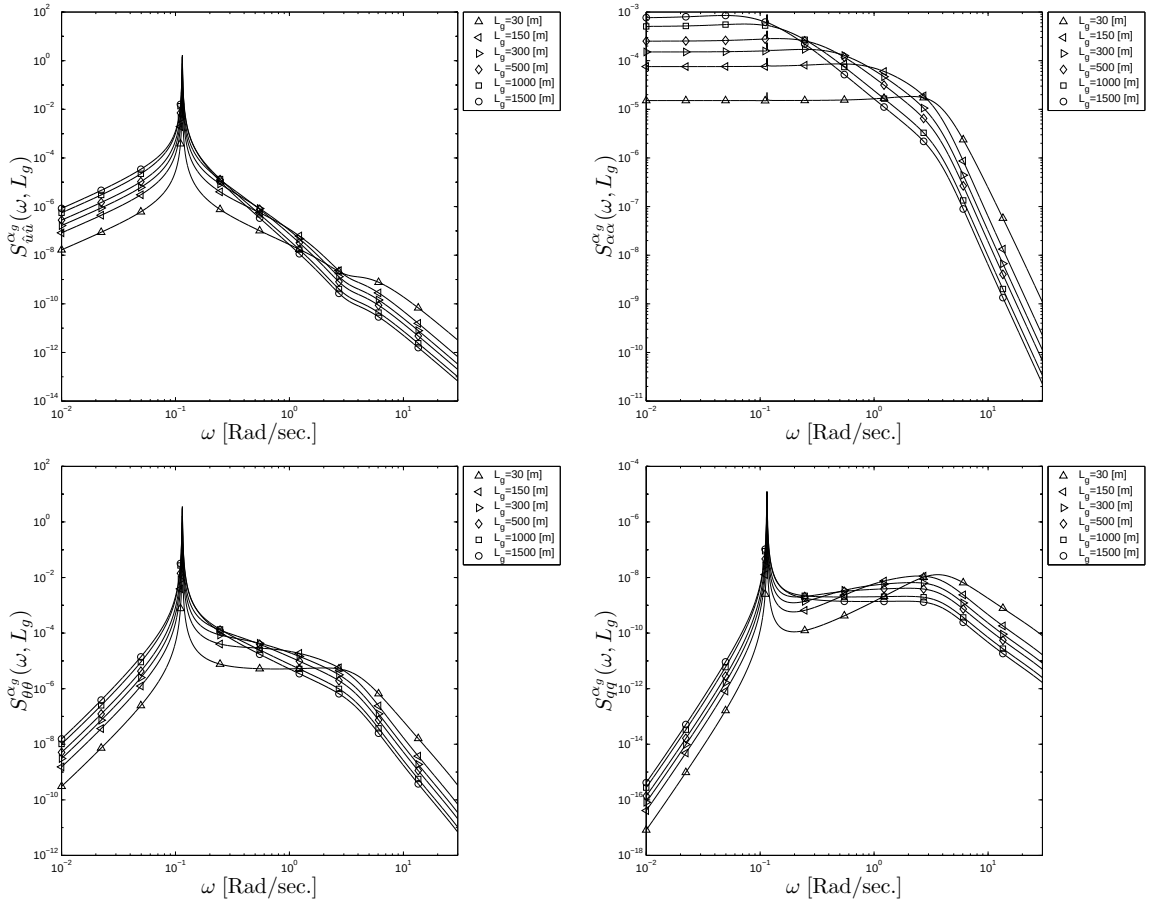


Figure 10.9: The PCA-model output PSD-functions $S^{\alpha_g}_{\hat{u}\hat{u}}(\omega)$, $S^{\alpha_g}_{\alpha\alpha}(\omega)$, $S^{\alpha_g}_{\theta\theta}(\omega)$ and $S^{\alpha_g}_{qq}(\omega)$ for a series of atmospheric turbulence gust scale length L_g. The aircraft model makes use of both frequency-dependent stability- and gust derivatives.

with the aircraft's state $\underline{x} = \left[\beta, \varphi, \frac{pb}{2Q_\infty}, \frac{rb}{2Q_\infty}\right]^T$ and the matrices P_a^c and Q_a^c equal to equations (10.24) and (10.25). The matrix R_a^c is now written as,

$$R_a^c = \begin{bmatrix} -C_{Y_g} \\ 0 \\ -C_{\ell_g} \\ -C_{n_g} \end{bmatrix} \tag{10.27}$$

with the input $\underline{u}$ becoming $\underline{u} = 1$. Equation (10.27) may also be written as,

$$R_a^c = \begin{bmatrix} -1 & 0 & 0 \\ 0 & 0 & 0 \\ 0 & -1 & 0 \\ 0 & 0 & -1 \end{bmatrix} \tag{10.28}$$

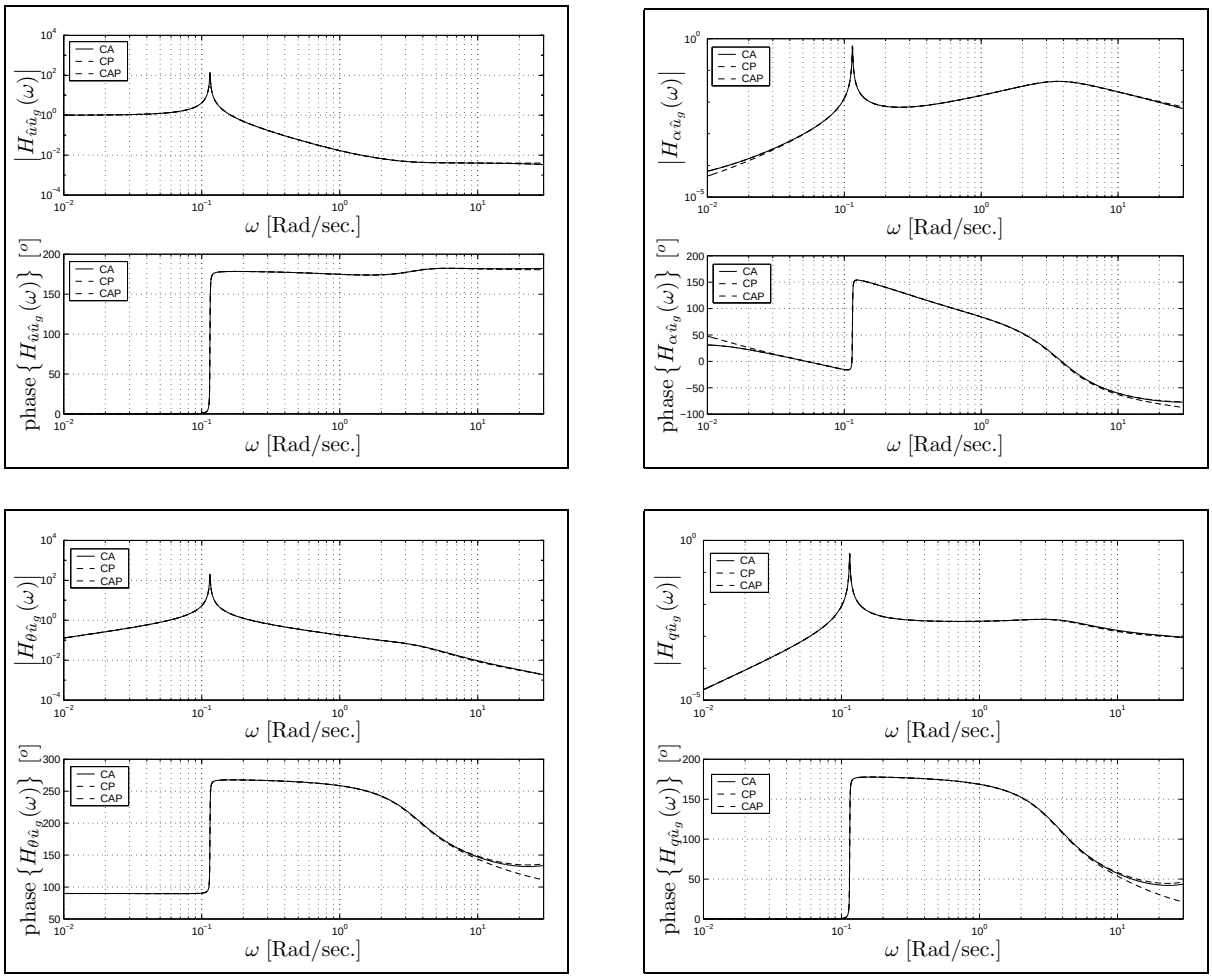


Figure 10.10: The frequency-response functions $H_{\hat{u}\hat{u}_g}(\omega)$, $H_{\alpha\hat{u}_g}(\omega)$, $H_{\theta\hat{u}_g}(\omega)$ and $H_{q\hat{u}_g}(\omega)$ shown as Bode-plots for the 1D symmetrical gust input $\hat{u}_g$. The results are given for the PCA-model using both frequency-dependent stability- and gust derivatives (CA), using constant stability derivatives and frequency-dependent gust derivatives (CAP), and using both constant stability- and gust derivatives (CP).

with the input $\underline{u}$ defined as,

$$\underline{u} = \begin{bmatrix} C_{Y_g} \\ C_{\ell_g} \\ C_{n_g} \end{bmatrix} \tag{10.29}$$

Now, for the example anti-symmetrical vertical gust input case, the aerodynamic force and moment coefficients are given as,

$$\left.\begin{array}{rcl} C_{Y_g}(\omega,\Omega_y) & = & \frac{C_Y}{\alpha_g}(k,\Omega_y)\ \alpha_g(\omega,\Omega_y) \\ C_{\ell_g}(\omega,\Omega_y) & = & \frac{C_\ell}{\alpha_g}(k,\Omega_y)\ \alpha_g(\omega,\Omega_y) \\ C_{n_g}(\omega,\Omega_y) & = & \frac{C_n}{\alpha_g}(k,\Omega_y)\ \alpha_g(\omega,\Omega_y) \end{array}\right\} \tag{10.30}$$

with ω the circular frequency, $k = \frac{\omega\bar{c}}{2Q_\infty}$ the reduced frequency, $\alpha_g(\omega,\Omega_y)$ the 2D non-dimensional vertical gust velocity component and $\frac{C_Y}{\alpha_g}(k,\Omega_y)$, $\frac{C_\ell}{\alpha_g}(k,\Omega_y)$ and $\frac{C_n}{\alpha_g}(k,\Omega_y)$ the

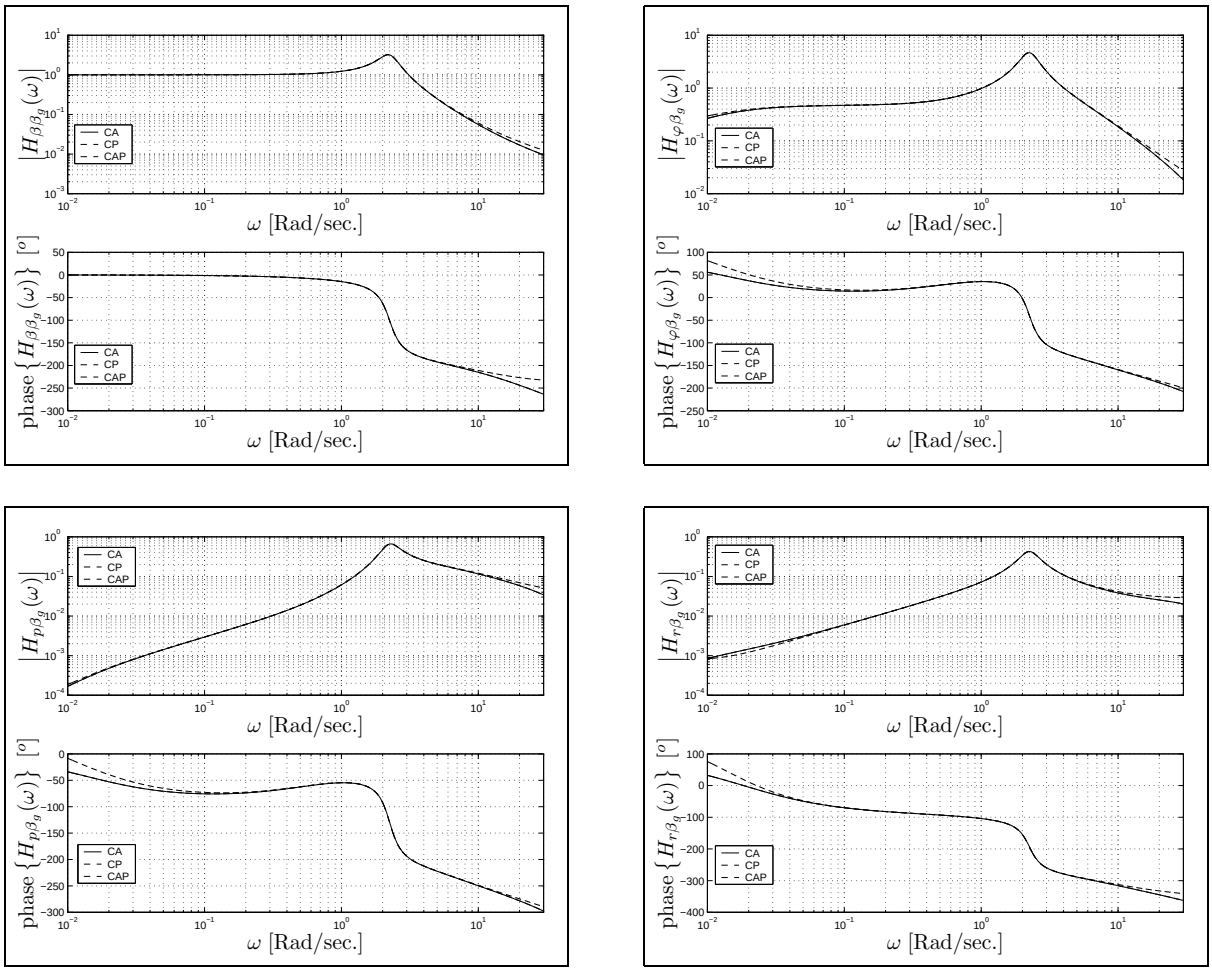


Figure 10.11: The frequency-response functions $H_{\beta\beta_g}(\omega)$, $H_{\varphi\beta_g}(\omega)$, $H_{p\beta_g}(\omega)$ and $H_{r\beta_g}(\omega)$ shown as Bode-plots for the 1D asymmetrical gust input β_g. The results are given for the PCA-model using both frequency-dependent stability- and gust derivatives (CA), using constant stability derivatives and frequency-dependent gust derivatives (CAP), and using both constant stability- and gust derivatives (CP).

frequency-response functions obtained in chapter 8.
Similar to the calculation procedure for the unsteady 1D gust derivatives given in section 10.3, in this section both the steady and unsteady gust derivatives for 2D gust fields are calculated using the resonance frequencies for ω and Ω_y. For both the 2D longitudinal gust field $\hat{u}_g$ and the 2D vertical gust field α_g these frequencies are calculated from a (local) resonance peak search near the dutch-roll resonance frequency ω_{dr} for the 2D yaw-rate PSD-function $S_{rr}(\omega, \Omega_y)$. In order to calculate the aircraft motion 2D output PSD-functions, the input PSD-matrix for equation (10.20) has to be defined. It is given as,

$$S_{\underline{uu}}(\omega, \Omega_y) = S_{\alpha_g \alpha_g}(\omega, \Omega_y) \cdot \tag{10.31}$$

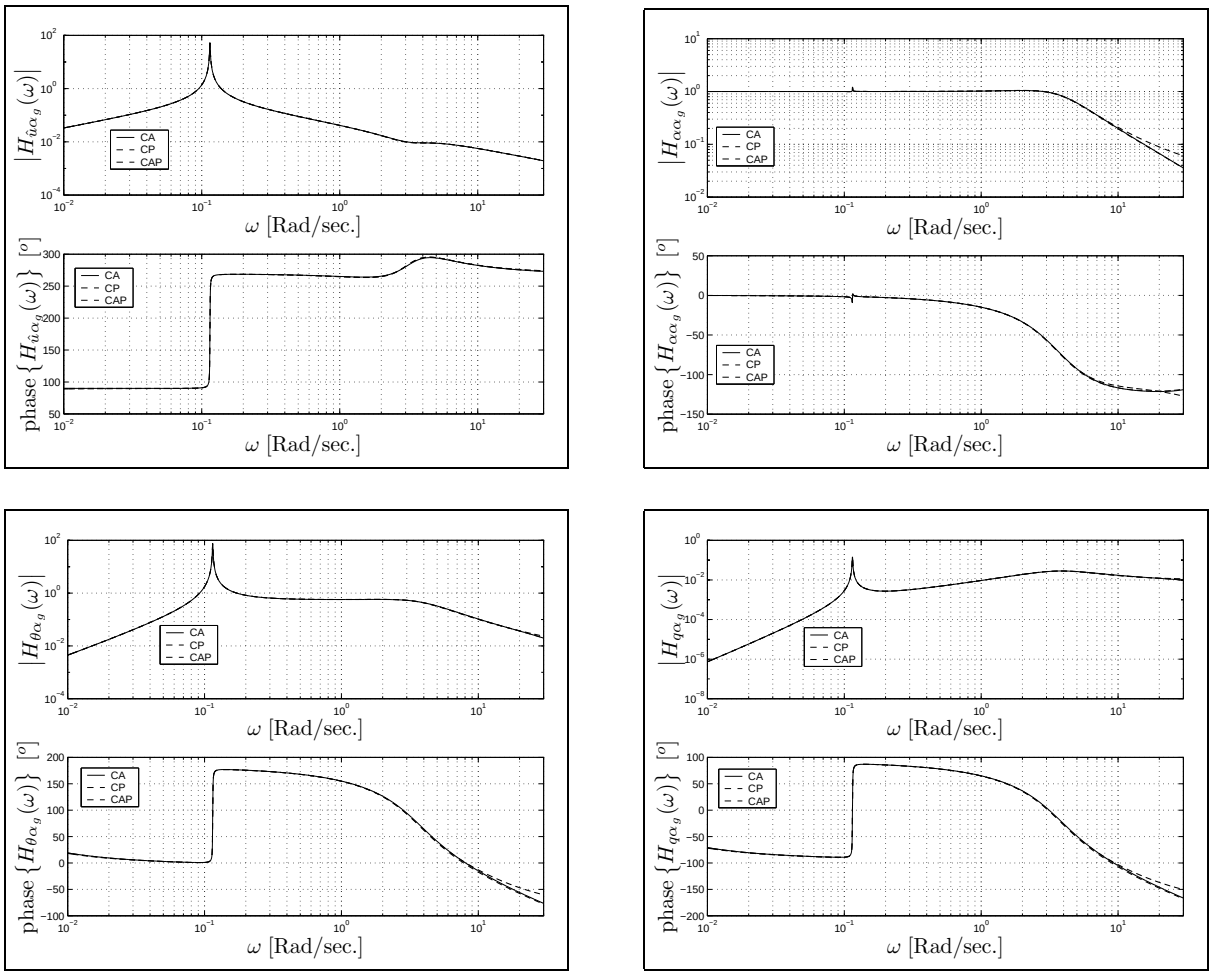


Figure 10.12: The frequency-response functions $H_{\hat{u}\alpha_g}(\omega)$, $H_{\alpha\alpha_g}(\omega)$, $H_{\theta\alpha_g}(\omega)$ and $H_{q\alpha_g}(\omega)$ shown as Bode-plots for the 1D symmetrical gust input α_g. The results are given for the PCA-model using both frequency-dependent stability- and gust derivatives (CA), using constant stability derivatives and frequency-dependent gust derivatives (CAP), and using both constant stability- and gust derivatives (CP).

$$\begin{bmatrix} \left(\frac{C_Y}{\alpha_g}(k,\Omega_y)\right)^* \frac{C_Y}{\alpha_g}(k,\Omega_y) & \left(\frac{C_Y}{\alpha_g}(k,\Omega_y)\right)^* \frac{C_\ell}{\alpha_g}(k,\Omega_y) & \left(\frac{C_Y}{\alpha_g}(k,\Omega_y)\right)^* \frac{C_n}{\alpha_g}(k,\Omega_y) \\ \left(\frac{C_\ell}{\alpha_g}(k,\Omega_y)\right)^* \frac{C_Y}{\alpha_g}(k,\Omega_y) & \left(\frac{C_\ell}{\alpha_g}(k,\Omega_y)\right)^* \frac{C_\ell}{\alpha_g}(k,\Omega_y) & \left(\frac{C_\ell}{\alpha_g}(k,\Omega_y)\right)^* \frac{C_n}{\alpha_g}(k,\Omega_y) \\ \left(\frac{C_n}{\alpha_g}(k,\Omega_y)\right)^* \frac{C_Y}{\alpha_g}(k,\Omega_y) & \left(\frac{C_n}{\alpha_g}(k,\Omega_y)\right)^* \frac{C_\ell}{\alpha_g}(k,\Omega_y) & \left(\frac{C_n}{\alpha_g}(k,\Omega_y)\right)^* \frac{C_n}{\alpha_g}(k,\Omega_y) \end{bmatrix}$$

with $S_{\underline{uu}}(\omega,\Omega_y)$ the equations of motion's input PSD-matrix, * denoting the complex conjungate and $S_{\alpha_g\alpha_g}(\omega,\Omega_y)$ the non-dimensional vertical gust-component 2D atmospheric turbulence PSD-function (see appendix H). Using equation (10.20), with its matrices P_a^c, Q_a^c and R_a^c according to equations (10.24), (10.25) and (10.28), respectively, the 2D aircraft motion frequency-response functions are calculated. Together with equation (10.31), the aircraft state-variables' output PSD-functions are obtained (see also appendix B).

Using the 2D output PSD-function $S_{rr}(\omega,\Omega_y)$, the resonance peak search results in the resonance frequencies ω_{dr} and $\Omega_{y_{dr}}$. From these frequencies both the constant steady and

unsteady gust derivative, for example $C_{Y_{\alpha_g}}$ and $C_{Y_{\dot{\alpha}_g}}$, are calculated according to,

$$\frac{C_Y}{\alpha_g}(\omega_{dr}, \Omega_{y_{dr}}) = C_{Y_{\alpha_g}} + C_{Y_{\dot{\alpha}_g}} j k_{dr} = C_{Y_{\alpha_g}} + \frac{\bar{c}}{2b} C'_{Y_{\dot{\alpha}_g}} j \frac{\omega_{dr} b}{Q_\infty} = C_{Y_{\alpha_g}} + C_{Y_{\dot{\alpha}_g}} j \frac{\omega_{dr} b}{Q_\infty} \quad (10.32)$$

with $\frac{C_Y}{\alpha_g}(\omega_{dr}, \Omega_{y_{dr}})$ the aerodynamic frequency-response for $k = \frac{\omega \bar{c}}{2Q_\infty} = k_{dr}$ and $\Omega_y = \Omega_{y_{dr}}$, both $C_{Y_{\alpha_g}} = Re\left\{\frac{C_Y}{\alpha_g}(k_{dr}, \Omega_{y_{dr}})\right\}$ and $C'_{Y_{\dot{\alpha}_g}} = \frac{1}{k_{dr}} Im\left\{\frac{C_Y}{\alpha_g}(k_{dr}, \Omega_{y_{dr}})\right\}$ the constant steady - and unsteady gust derivative, respectively, as obtained from the aerodynamic frequency-response function at $\omega = \omega_{dr}$ and $\Omega_y = \Omega_{y_{dr}}$ and with the reduced frequency $k_{dr} = \frac{\omega_{dr} \bar{c}}{2Q_\infty}$, $C_{Y_{\dot{\alpha}_g}}$ the unsteady gust derivative with respect to the reduced frequency $\frac{\omega b}{Q_\infty}$ and $\Omega_y = \Omega_{y_{dr}}$, $\bar{c}$ the mean aerodynamic chord, b the aircraft's span, and Q_∞ the airspeed. Similar to equation (10.32), both the 2D steady and the 2D unsteady gust derivatives are obtained for the asymmetrical aerodynamic moments. Also, similar to the α_g derivatives, the 2D gust derivatives with respect to the ant-symmetrical non-dimensional 2D longitudinal gust velocity component $\hat{u}_g$ are obtained using the 2D frequency-response functions $\frac{C_Y}{\hat{u}_g}(k, \Omega_y)$, $\frac{C_\ell}{\hat{u}_g}(k, \Omega_y)$ and $\frac{C_n}{\hat{u}_g}(k, \Omega_y)$. These aerodynamic frequency-response functions are also given in chapter 8.
The definition of the 2D gust derivatives with respect to the anti-symmetrical 2D gust inputs $\hat{u}_g$ and α_g is summarized in table 10.8.

10.5.3 Calculation of the gust derivatives for 2D gust fields

For the numerical calculation of the gust derivatives for the 2D longitudinal and vertical gust fields, the procedure outlined in section 10.4.2 is followed. First, the atmospheric turbulence velocity components' 2D PSD-functions have to be calculated. These analytical functions are given in appendix H, and for a series of the gust scale length parameter L_g they are shown in figures 10.13 and 10.14. Next, the 2D output PSD-function (the 2D yaw-rate PSD-function $S_{rr}(\omega, \Omega_y)$) is calculated. From this 2D PSD-function the resonance frequencies are calculated using a (local) resonance peak search near the dutch-roll's resonance frequency ω_{dr}. In figures 10.15 and 10.16 results of these searches are shown for the non-dimensional 2D longitudinal - ($\hat{u}_g$) and the non-dimensional 2D vertical gust velocity component (α_g), respectively. In figures 10.17 and 10.18 the 2D gust derivatives (both steady and unsteady) with respect to the non-dimensional gust inputs $\hat{u}_g$ and α_g, respectively, are given as a function of the circular frequency ω and the spatial frequency Ω_y. From these results, ánd using the resonance frequencies ω_{dr} and $\Omega_{y_{dr}}$, both the constant steady and constant unsteady gust derivatives $C_{Y_{u_g}}$, $C_{Y_{\dot{u}_g}}$, $C_{\ell_{u_g}}$, $C_{\ell_{\dot{u}_g}}$, $C_{n_{u_g}}$, $C_{n_{\dot{u}_g}}$, $C_{Y_{\alpha_g}}$, $C_{Y_{\dot{\alpha}_g}}$, $C_{\ell_{\alpha_g}}$, $C_{\ell_{\dot{\alpha}_g}}$, $C_{n_{\alpha_g}}$ and $C_{n_{\dot{\alpha}_g}}$, are obtained.
In order to use these derivatives for time-domain simulations using spatial-domain gust fields, both the $\hat{u}_g$- and α_g derivatives are now transformed to "yaw-gust" (r_{1_g}) and "roll-gust" (p_g) derivatives, respectively. For this purpose, use is made of the gust input model definition according to reference [35] (see also chapter 12 and appendices G and H).
Similar to this Four-Point-Aircraft (FPA) model, for both the 2D u_g- and 2D w_g gust fields the atmospheric turbulence velocity components u_g and w_g at $\pm 0.85\frac{b}{2}$ locations on the aircraft wing are required. In the following use is made of these gust inputs at the

positions "1" and "2" of the FPA-model, see also figures G.17 and G.18 for the definition of the FPA-model gust input locations and the definition of the positive directions of the gust inputs, respectively. The dimensional "roll-gust" and "yaw-gust" are defined as,

$$\left.\begin{array}{lcl} p_g & = & \frac{w_{g_1}-w_{g_2}}{b`} \\ r_{1_g} & = & \frac{u_{g_2}-u_{g_1}}{b`} \end{array}\right\} \tag{10.33}$$

respectively, with u_{g_1} the dimensional longitudinal gust velocity component at location "1" (see figure G.17), u_{g_2} the one at location "2", w_{g_1} the dimensional vertical gust velocity component at location "1", w_{g_2} the one at location "2" and $b' = 0.85b$ with b the aircraft's span. For 2D anti-symmetrical harmonic gust fields, equations (10.33) are given as,

$$\left.\begin{array}{lcl} p_g & = & \frac{w_g(\frac{b'}{2})-w_g(\frac{-b'}{2})}{b`} = w_{g_{max}} \frac{sin(\Omega_y \frac{b'}{2})-sin(-\Omega_y \frac{b'}{2})}{b'} \\ r_{1_g} & = & \frac{-u_g(\frac{b'}{2})+u_g(\frac{-b'}{2})}{b`} = -u_{g_{max}} \frac{sin(\Omega_y \frac{b'}{2})-sin(-\Omega_y \frac{b'}{2})}{b'} \end{array}\right\} \tag{10.34}$$

In non-dimensional form, equation (10.34) becomes,

$$\left.\begin{array}{lcl} \frac{p_g b}{2Q_\infty} & = & \frac{w_{g_{max}} b}{2Q_\infty} \cdot \frac{sin(\Omega_y \frac{b'}{2})-sin(-\Omega_y \frac{b'}{2})}{b'} = \alpha_g \frac{b}{2} \cdot \frac{sin(\Omega_y \frac{b'}{2})-sin(-\Omega_y \frac{b'}{2})}{b'} \\ \frac{r_{1_g} b}{2Q_\infty} & = & -\frac{u_{g_{max}} b}{2Q_\infty} \cdot \frac{sin(\Omega_y \frac{b'}{2})-sin(-\Omega_y \frac{b'}{2})}{b'} = -\hat{u}_g \frac{b}{2} \cdot \frac{sin(\Omega_y \frac{b'}{2})-sin(-\Omega_y \frac{b'}{2})}{b'} \end{array}\right\} \tag{10.35}$$

or,

$$\left.\begin{array}{lcl} \frac{p_g b}{2Q_\infty} & = & \alpha_g \frac{b}{2} \cdot K_g \\ \frac{r_{1_g} b}{2Q_\infty} & = & -\hat{u}_g \frac{b}{2} \cdot K_g \end{array}\right\} \tag{10.36}$$

with,

$$K_g = \frac{sin(\Omega_y \frac{b'}{2}) - sin(-\Omega_y \frac{b'}{2})}{b'} \tag{10.37}$$

Using equations (10.35) through (10.37), while also using the resonance frequency $\Omega_y = \Omega_{y_{dr}}$, both the $\hat{u}_g$- and α_g derivatives are transformed into constant yaw-gust - and roll-gust derivatives, respectively. The definition of the new gust derivatives $C_{Y_{r_{1_g}}}$, $C_{Y_{\dot{r}_{1_g}}}$, $C_{\ell_{r_{1_g}}}$, $C_{\ell_{\dot{r}_{1_g}}}$, $C_{n_{r_{1_g}}}$, $C_{n_{\dot{r}_{1_g}}}$, $C_{Y_{p_g}}$, $C_{Y_{\dot{p}_g}}$, $C_{\ell_{p_g}}$, $C_{\ell_{\dot{p}_g}}$, $C_{n_{p_g}}$ and $C_{n_{\dot{p}_g}}$ is summarized in table 10.9. In tables 10.10 and 10.11 the numerical values of these gust derivatives for the PCA-model are shown.

For the gust inputs r_{1_g} and p_g (which now represent the anti-symmetrical gust fields u_g and w_g, respectively) the non-dimensional aerodynamic models in terms of gust derivatives are given as,

$$\left.\begin{array}{lcl} C_{Y_g} & = & C_{Y_{r_{1_g}}} \frac{r_{1_g} b}{2Q\infty} + C_{Y_{\dot{r}_{1_g}}} \frac{b}{Q_\infty} \frac{\dot{r}_{1_g} b}{2Q\infty} \\ C_{\ell_g} & = & C_{\ell_{r_{1_g}}} \frac{r_{1_g} b}{2Q\infty} + C_{\ell_{\dot{r}_{1_g}}} \frac{b}{Q_\infty} \frac{\dot{r}_{1_g} b}{2Q\infty} \\ C_{n_g} & = & C_{n_{r_{1_g}}} \frac{r_{1_g} b}{2Q\infty} + C_{n_{\dot{r}_{1_g}}} \frac{b}{Q_\infty} \frac{\dot{r}_{1_g} b}{2Q\infty} \end{array}\right\} \tag{10.38}$$

and,

$$\left.\begin{array}{rcl} C_{Y_g} & = & C_{Y_{p_g}} \frac{p_g b}{2Q_\infty} + C_{Y_{\dot{p}_g}} \frac{b}{Q_\infty} \frac{\dot{p}_g b}{2Q_\infty} \\ C_{\ell_g} & = & C_{\ell_{p_g}} \frac{p_g b}{2Q_\infty} + C_{\ell_{\dot{p}_g}} \frac{b}{Q_\infty} \frac{\dot{p}_g b}{2Q_\infty} \\ C_{n_g} & = & C_{n_{p_g}} \frac{p_g b}{2Q_\infty} + C_{n_{\dot{p}_g}} \frac{b}{Q_\infty} \frac{\dot{p}_g b}{2Q_\infty} \end{array}\right\} \tag{10.39}$$

respectively, with the definition of the gust derivatives used in equations (10.38) and (10.39) summarized in tables 10.8 and 10.9. In tables 10.10 and 10.11 values for the gust derivatives are given.

10.6 Remarks

In this chapter the Parametric Computational Aerodynamics (PCA) model has been introduced. The model parameters have been calculated using a resonance peak search in aircraft motion output PSD-functions. This identification method resulted in both steady and unsteady gust derivatives. In chapters 11 and 12 the Delft University of Technology (DUT) - and the Four-Point-Aircraft model will be discussed, respectively. In these chapters, the aerodynamic model with respect to atmospheric turbulence is also given in terms of gust derivatives, however, they are now defined as a function of stability derivatives.
In chapter 13 both time- and frequency-domain results for the PCA-model will be compared to the LPF-solutions presented in chapter 9. These results will be given in terms of both aerodynamic model - and aircraft motion responses. The PCA-model results will also be compared to those obtained for the DUT- and FPA-model.

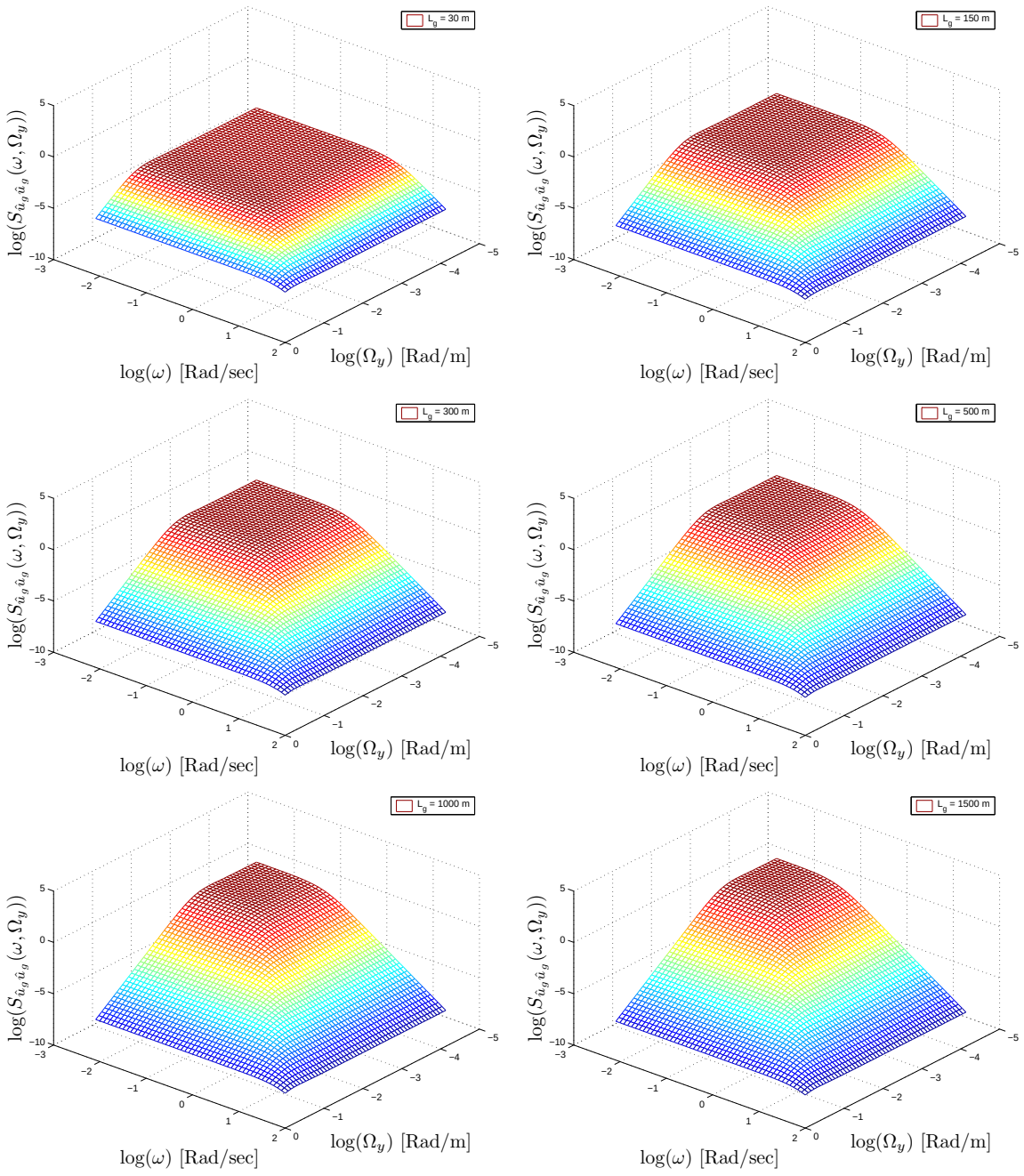


Figure 10.13: The 2D input PSD-function $S_{\hat{u}_g \hat{u}_g}(\omega, \Omega_y)$ for a series of the atmospheric turbulence scale length L_g [m].

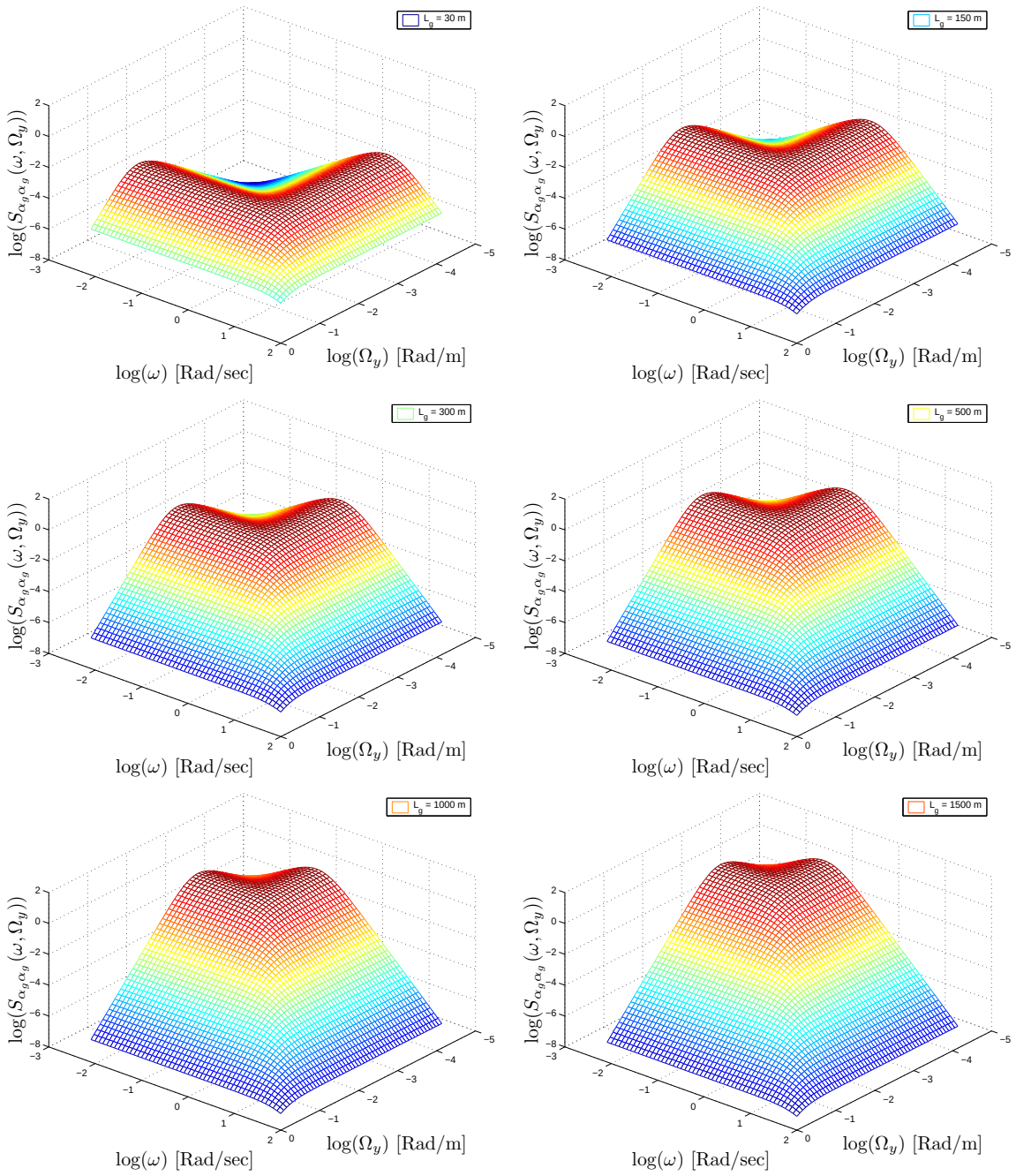


Figure 10.14: The 2D input PSD-function $S_{\alpha_g\alpha_g}(\omega, \Omega_y)$ for a series of the atmospheric turbulence scale length L_g [m].

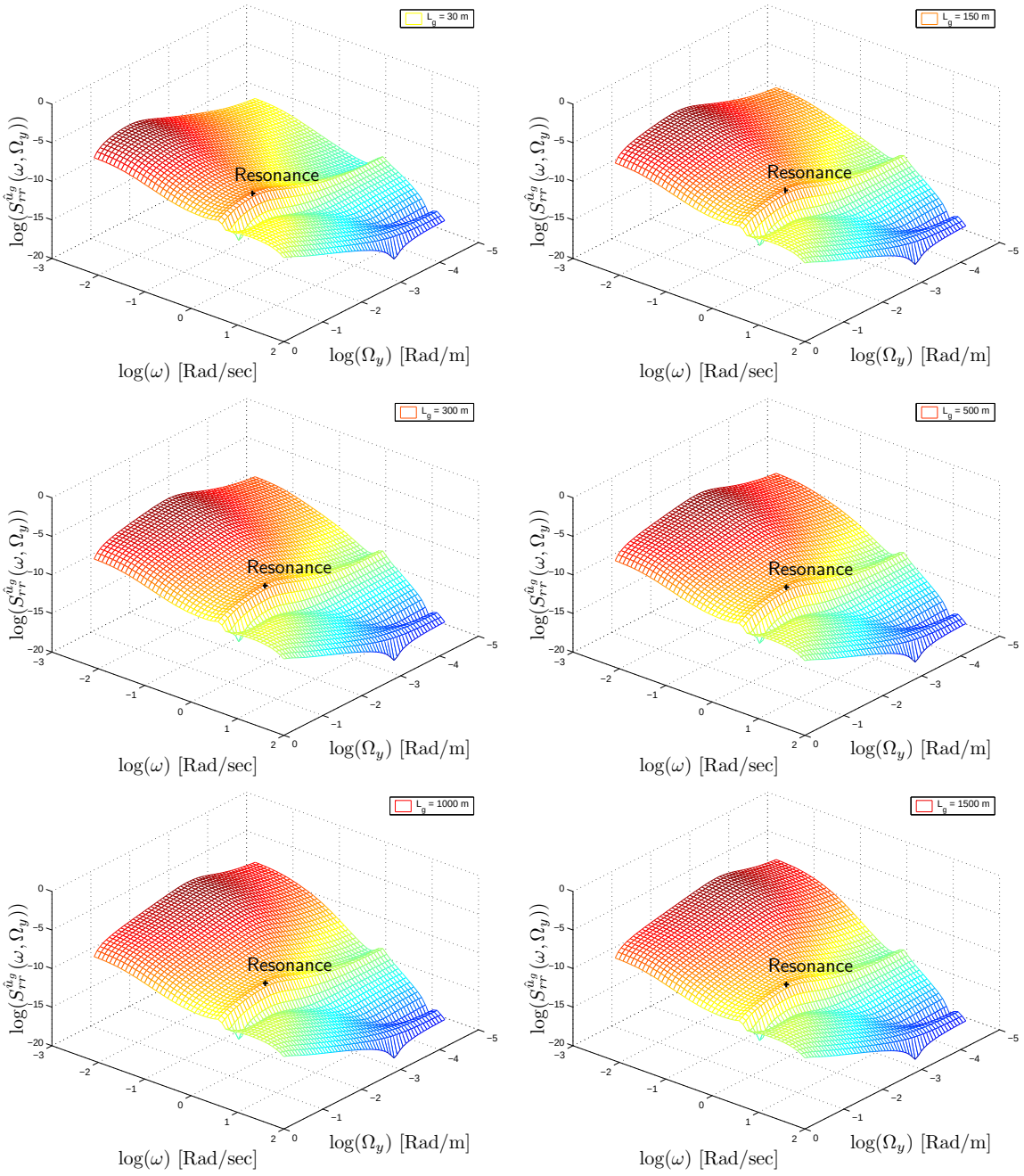


Figure 10.15: The 2D output PSD-function $S_{rr}^{\hat{u}_g}(\omega, \Omega_y)$ for a series of the atmospheric turbulence scale length L_g [m].

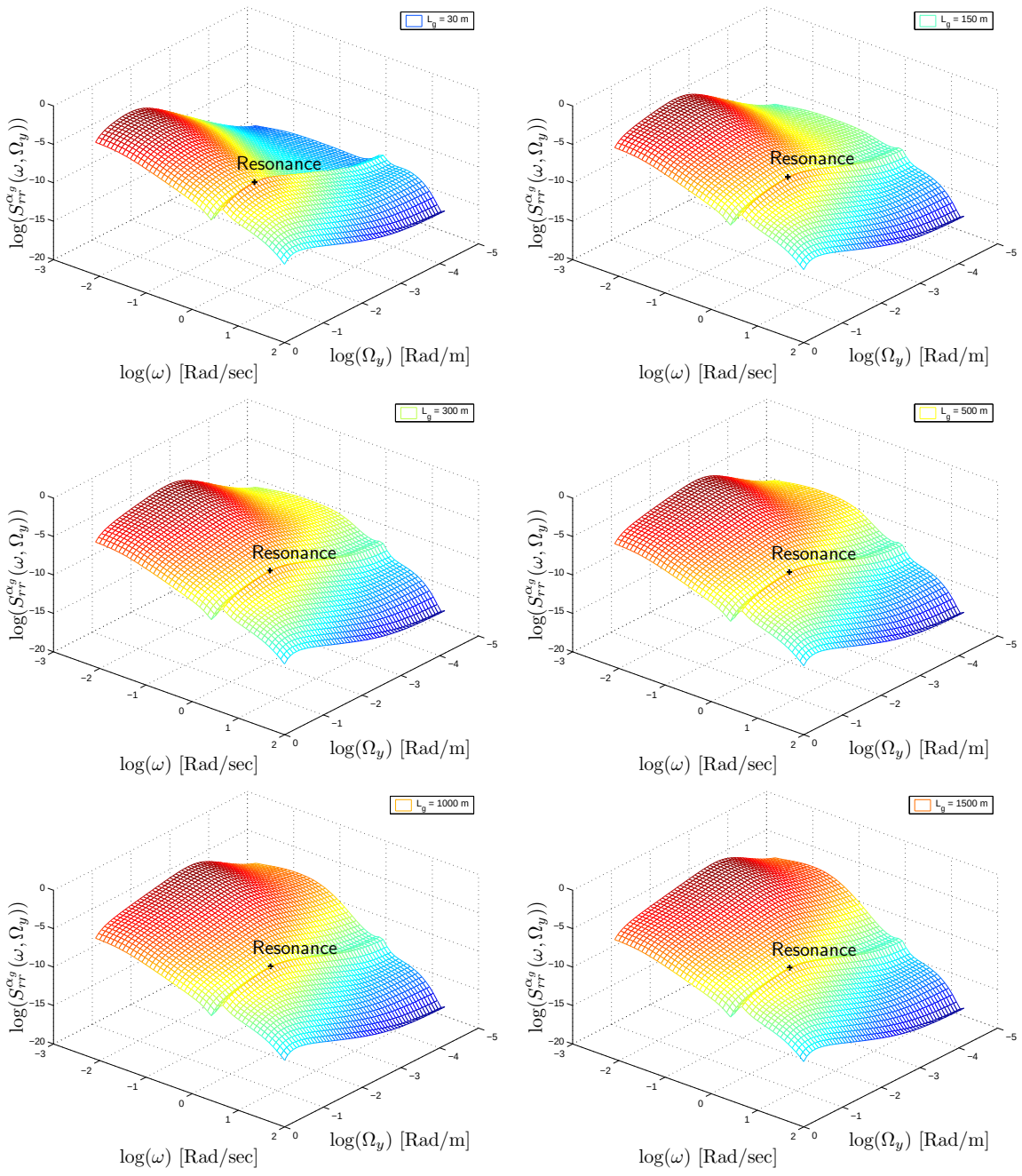


Figure 10.16: The 2D output PSD-function $S_{rr}^{\alpha g}(\omega, \Omega_y)$ for a series of the atmospheric turbulence scale length L_g [m].

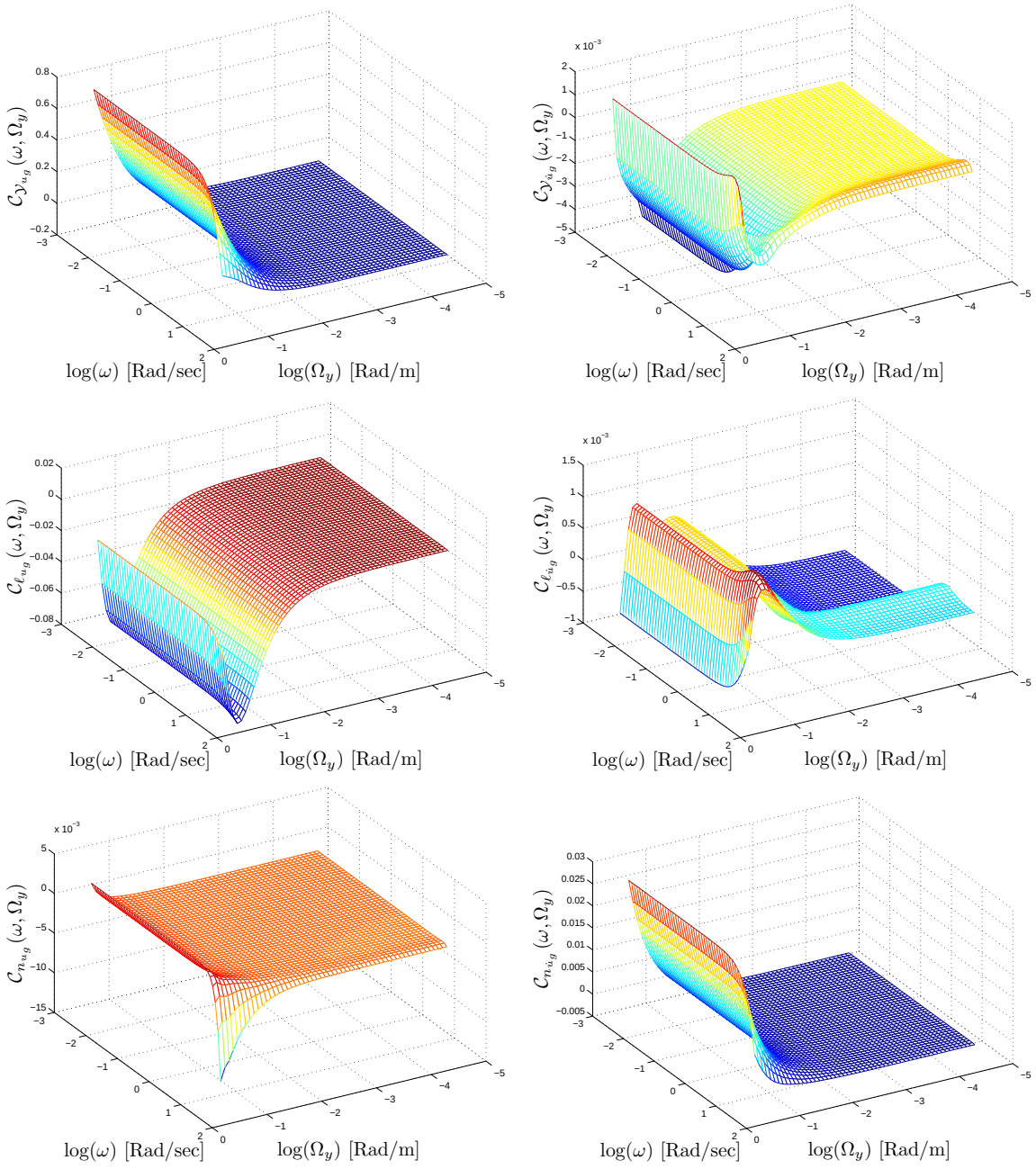


Figure 10.17: The frequency-dependent steady and unsteady gust derivatives $\mathcal{C}_{\mathcal{Y}_{u_g}}(\omega,\Omega_y)$ and $\mathcal{C}_{\mathcal{Y}_{\dot{u}_g}}(\omega,\Omega_y)$ (top), $\mathcal{C}_{\ell_{u_g}}(\omega,\Omega_y)$ and $\mathcal{C}_{\ell_{\dot{u}_g}}(\omega,\Omega_y)$ (center), and $\mathcal{C}_{n_{u_g}}(\omega,\Omega_y)$ and $\mathcal{C}_{n_{\dot{u}_g}}(\omega,\Omega_y)$ (bottom), with respect to the anti-symmetrical gust input $\hat{u}_g$.

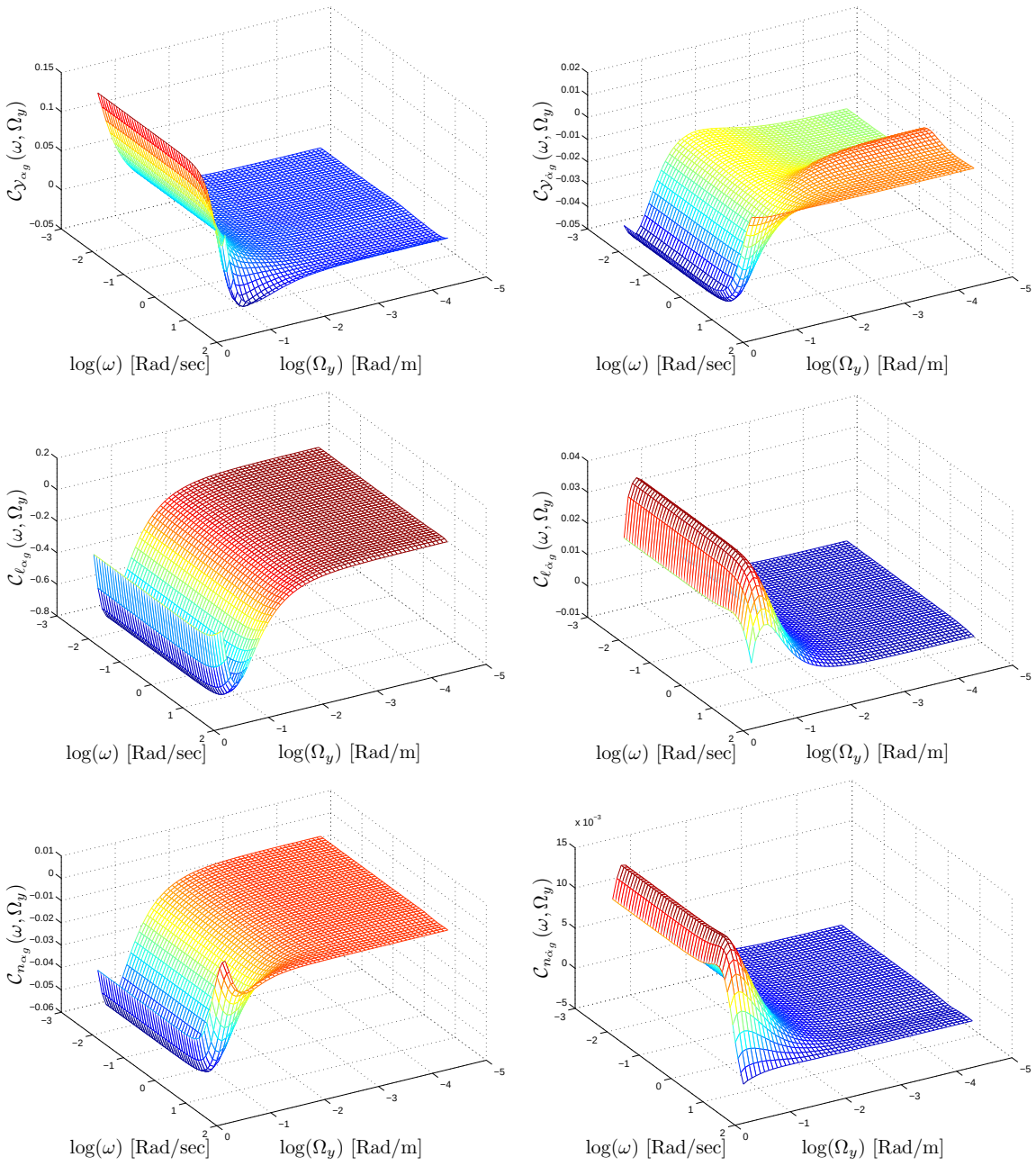


Figure 10.18: The frequency-dependent steady and unsteady gust derivatives $\mathcal{C}_{\mathcal{Y}_{\alpha_g}}(\omega,\Omega_y)$ and $\mathcal{C}_{\mathcal{Y}_{\dot{\alpha}_g}}(\omega,\Omega_y)$ (top), $\mathcal{C}_{\ell_{\alpha_g}}(\omega,\Omega_y)$ and $\mathcal{C}_{\ell_{\dot{\alpha}_g}}(\omega,\Omega_y)$ (center), and $\mathcal{C}_{n_{\alpha_g}}(\omega,\Omega_y)$ and $\mathcal{C}_{n_{\dot{\alpha}_g}}(\omega,\Omega_y)$ (bottom), with respect to the anti-symmetrical gust input α_g.

	Frequency-dependent stability- and 1D gust derivatives		
	C_X	C_Z	C_m
$\hat{u}$	$\mathcal{C}_{\mathcal{X}_u}(k) = Re\left\{\frac{C_X}{\hat{u}}(k)\right\}$	$\mathcal{C}_{\mathcal{Z}_u}(k) = Re\left\{\frac{C_Z}{\hat{u}}(k)\right\}$	$\mathcal{C}_{m_u}(k) = Re\left\{\frac{C_m}{\hat{u}}(k)\right\}$
$\frac{\dot{\hat{u}}\bar{c}}{Q_\infty}$	$\mathcal{C}_{\mathcal{X}_{\dot{u}}}(k) = \frac{1}{2k} Im\left\{\frac{C_X}{\hat{u}}(k)\right\}$	$\mathcal{C}_{\mathcal{Z}_{\dot{u}}}(k) = \frac{1}{2k} Im\left\{\frac{C_Z}{\hat{u}}(k)\right\}$	$\mathcal{C}_{m_{\dot{u}}}(k) = \frac{1}{2k} Im\left\{\frac{C_m}{\hat{u}}(k)\right\}$
α	$\mathcal{C}_{\mathcal{X}_\alpha}(k) = Re\left\{\frac{C_X}{\alpha}(k)\right\}$	$\mathcal{C}_{\mathcal{Z}_\alpha}(k) = Re\left\{\frac{C_Z}{\alpha}(k)\right\}$	$\mathcal{C}_{m_\alpha}(k) = Re\left\{\frac{C_m}{\alpha}(k)\right\}$
$\frac{\dot{\alpha}\bar{c}}{Q_\infty}$	$\mathcal{C}_{\mathcal{X}_{\dot{\alpha}}}(k) = \frac{1}{2k} Im\left\{\frac{C_X}{\alpha}(k)\right\}$	$\mathcal{C}_{\mathcal{Z}_{\dot{\alpha}}}(k) = \frac{1}{2k} Im\left\{\frac{C_Z}{\alpha}(k)\right\}$	$\mathcal{C}_{m_{\dot{\alpha}}}(k) = \frac{1}{2k} Im\left\{\frac{C_m}{\alpha}(k)\right\}$
$\hat{u}_g$	$\mathcal{C}_{\mathcal{X}_{u_g}}(k) = Re\left\{\frac{C_X}{\hat{u}_g}(k)\right\}$	$\mathcal{C}_{\mathcal{Z}_{u_g}}(k) = Re\left\{\frac{C_Z}{\hat{u}_g}(k)\right\}$	$\mathcal{C}_{m_{u_g}}(k) = Re\left\{\frac{C_m}{\hat{u}_g}(k)\right\}$
$\frac{\dot{\hat{u}}_g\bar{c}}{Q_\infty}$	$\mathcal{C}_{\mathcal{X}_{\dot{u}_g}}(k) = \frac{1}{2k} Im\left\{\frac{C_X}{\hat{u}_g}(k)\right\}$	$\mathcal{C}_{\mathcal{Z}_{\dot{u}_g}}(k) = \frac{1}{2k} Im\left\{\frac{C_Z}{\hat{u}_g}(k)\right\}$	$\mathcal{C}_{m_{\dot{u}_g}}(k) = \frac{1}{2k} Im\left\{\frac{C_m}{\hat{u}_g}(k)\right\}$
α_g	$\mathcal{C}_{\mathcal{X}_{\alpha_g}}(k) = Re\left\{\frac{C_X}{\alpha_g}(k)\right\}$	$\mathcal{C}_{\mathcal{Z}_{\alpha_g}}(k) = Re\left\{\frac{C_Z}{\alpha_g}(k)\right\}$	$\mathcal{C}_{m_{\alpha_g}}(k) = Re\left\{\frac{C_m}{\alpha_g}(k)\right\}$
$\frac{\dot{\alpha}_g\bar{c}}{Q_\infty}$	$\mathcal{C}_{\mathcal{X}_{\dot{\alpha}_g}}(k) = \frac{1}{2k} Im\left\{\frac{C_X}{\alpha_g}(k)\right\}$	$\mathcal{C}_{\mathcal{Z}_{\dot{\alpha}_g}}(k) = \frac{1}{2k} Im\left\{\frac{C_Z}{\alpha_g}(k)\right\}$	$\mathcal{C}_{m_{\dot{\alpha}_g}}(k) = \frac{1}{2k} Im\left\{\frac{C_m}{\alpha_g}(k)\right\}$

Table 10.6: Definition of the symmetrical frequency-dependent stability derivatives and the symmetrical frequency-dependent 1D gust derivatives for the frame $\mathcal{F}_S$ given as a function of the reduced frequency $k = \frac{\omega\bar{c}}{2Q_\infty}$, and as used in the aircraft's equations of motion.

	Frequency-dependent stability- and 1D gust derivatives		
	C_Y	C_ℓ	C_n
β	$\mathcal{C}_{y_\beta}(k) = Re\left\{\frac{C_Y}{\beta}(k)\right\}$	$\mathcal{C}_{\ell_\beta}(k) = Re\left\{\frac{C_\ell}{\beta}(k)\right\}$	$\mathcal{C}_{n_\beta}(k) = Re\left\{\frac{C_n}{\beta}(k)\right\}$
$\frac{\dot{\beta}b}{Q_\infty}$	$\mathcal{C}_{y_{\dot{\beta}}}(k) = \frac{\bar{c}}{2bk} Im\left\{\frac{C_Y}{\beta}(k)\right\}$	$\mathcal{C}_{\ell_{\dot{\beta}}}(k) = \frac{\bar{c}}{2bk} Im\left\{\frac{C_\ell}{\beta}(k)\right\}$	$\mathcal{C}_{n_{\dot{\beta}}}(k) = \frac{\bar{c}}{2bk} Im\left\{\frac{C_n}{\beta}(k)\right\}$
β_g	$\mathcal{C}_{y_{\beta_g}}(k) = Re\left\{\frac{C_Y}{\beta_g}(k)\right\}$	$\mathcal{C}_{\ell_{\beta_g}}(k) = Re\left\{\frac{C_\ell}{\beta_g}(k)\right\}$	$\mathcal{C}_{n_{\beta_g}}(k) = Re\left\{\frac{C_n}{\beta_g}(k)\right\}$
$\frac{\dot{\beta}_g b}{Q_\infty}$	$\mathcal{C}_{y_{\dot{\beta}_g}}(k) = \frac{\bar{c}}{2bk} Im\left\{\frac{C_Y}{\beta_g}(k)\right\}$	$\mathcal{C}_{\ell_{\dot{\beta}_g}}(k) = \frac{\bar{c}}{2bk} Im\left\{\frac{C_\ell}{\beta_g}(k)\right\}$	$\mathcal{C}_{n_{\dot{\beta}_g}}(k) = \frac{\bar{c}}{2bk} Im\left\{\frac{C_n}{\beta_g}(k)\right\}$

Table 10.7: Definition of the asymmetrical frequency-dependent stability derivatives and the asymmetrical frequency-dependent 1D gust derivatives for the frame $\mathcal{F}_S$ given as a function of the reduced frequency $k = \frac{\omega \bar{c}}{2Q_\infty}$, and as used in the aircraft's equations of motion.

	Frequency-dependent 2D gust derivatives		
	C_Y	C_ℓ	C_n
$\hat{u}_g$	$\mathcal{C}_{\mathcal{Y}_{u_g}}(k,\Omega_y) = Re\left\{\frac{C_Y}{u_g}(k,\Omega_y)\right\}$	$\mathcal{C}_{\ell_{u_g}}(k,\Omega_y) = Re\left\{\frac{C_\ell}{u_g}(k,\Omega_y)\right\}$	$\mathcal{C}_{n_{u_g}}(k,\Omega_y) = Re\left\{\frac{C_n}{u_g}(k,\Omega_y)\right\}$
$\frac{\dot{\hat{u}}_g b}{Q_\infty}$	$\mathcal{C}_{\mathcal{Y}_{\dot{u}_g}}(k,\Omega_y) = \frac{\bar{c}}{2bk} Im\left\{\frac{C_Y}{u_g}(k,\Omega_y)\right\}$	$\mathcal{C}_{\ell_{\dot{u}_g}}(k,\Omega_y) = \frac{\bar{c}}{2bk} Im\left\{\frac{C_\ell}{u_g}(k,\Omega_y)\right\}$	$\mathcal{C}_{n_{\dot{u}_g}}(k,\Omega_y) = \frac{\bar{c}}{2bk} Im\left\{\frac{C_n}{u_g}(k,\Omega_y)\right\}$
α_g	$\mathcal{C}_{\mathcal{Y}_{\alpha_g}}(k,\Omega_y) = Re\left\{\frac{C_Y}{\alpha_g}(k,\Omega_y)\right\}$	$\mathcal{C}_{\ell_{\alpha_g}}(k,\Omega_y) = Re\left\{\frac{C_\ell}{\alpha_g}(k,\Omega_y)\right\}$	$\mathcal{C}_{n_{\alpha_g}}(k,\Omega_y) = Re\left\{\frac{C_n}{\alpha_g}(k,\Omega_y)\right\}$
$\frac{\dot{\alpha}_g b}{Q_\infty}$	$\mathcal{C}_{\mathcal{Y}_{\dot{\alpha}_g}}(k,\Omega_y) = \frac{\bar{c}}{2bk} Im\left\{\frac{C_Y}{\alpha_g}(k,\Omega_y)\right\}$	$\mathcal{C}_{\ell_{\dot{\alpha}_g}}(k,\Omega_y) = \frac{\bar{c}}{2bk} Im\left\{\frac{C_\ell}{\alpha_g}(k,\Omega_y)\right\}$	$\mathcal{C}_{n_{\dot{\alpha}_g}}(k,\Omega_y) = \frac{\bar{c}}{2bk} Im\left\{\frac{C_n}{\alpha_g}(k,\Omega_y)\right\}$

Table 10.8: Definition of the anti-symmetrical frequency-dependent 2D gust derivatives for the frame $\mathcal{F}_S$ given as a function of the reduced frequency $k = \frac{\omega\bar{c}}{2Q_\infty}$ and the spatial frequency Ω_y, and as used in the aircraft's equations of motion.

	Constant 2D gust derivatives		
	C_Y	C_ℓ	C_n
$\frac{r_{1_g} b}{2Q_\infty}$	$-\mathcal{C}_{\mathcal{Y}_{u_g}}(k_{dr}, \Omega_{y_{dr}}) \cdot \frac{2}{K_g b}$	$-\mathcal{C}_{\ell_{u_g}}(k_{dr}, \Omega_{y_{dr}}) \cdot \frac{2}{K_g b}$	$-\mathcal{C}_{n_{u_g}}(k_{dr}, \Omega_{y_{dr}}) \cdot \frac{2}{K_g b}$
$\frac{\dot{r}_{1_g} b^2}{2Q_\infty^2}$	$-\mathcal{C}_{\mathcal{Y}_{\dot{u}_g}}(k_{dr}, \Omega_{y_{dr}}) \cdot \frac{2}{K_g b}$	$-\mathcal{C}_{\ell_{\dot{u}_g}}(k_{dr}, \Omega_{y_{dr}}) \cdot \frac{2}{K_g b}$	$-\mathcal{C}_{n_{\dot{u}_g}}(k_{dr}, \Omega_{y_{dr}}) \cdot \frac{2}{K_g b}$
$\frac{p_g b}{2Q_\infty}$	$\mathcal{C}_{\mathcal{Y}_{\alpha_g}}(k_{dr}, \Omega_{y_{dr}}) \cdot \frac{2}{K_g b}$	$\mathcal{C}_{\ell_{\alpha_g}}(k_{dr}, \Omega_{y_{dr}}) \cdot \frac{2}{K_g b}$	$\mathcal{C}_{n_{\alpha_g}}(k_{dr}, \Omega_{y_{dr}}) \cdot \frac{2}{K_g b}$
$\frac{\dot{p}_g b^2}{2Q_\infty^2}$	$\mathcal{C}_{\mathcal{Y}_{\dot{\alpha}_g}}(k_{dr}, \Omega_{y_{dr}}) \cdot \frac{2}{K_g b}$	$\mathcal{C}_{\ell_{\dot{\alpha}_g}}(k_{dr}, \Omega_{y_{dr}}) \cdot \frac{2}{K_g b}$	$\mathcal{C}_{n_{\dot{\alpha}_g}}(k_{dr}, \Omega_{y_{dr}}) \cdot \frac{2}{K_g b}$

Table 10.9: Definition of the PCA-model's constant yawing and rolling gust derivatives (with $K_g = \frac{sin(\Omega_{y_{dr}} \frac{b'}{2}) - sin(-\Omega_{y_{dr}} \frac{b'}{2})}{b'}$) for both the 2D longitudinal - and the 2D vertical gust fields, for the frame $\mathcal{F}_S$.

Gust scale length L_g **[m]**	**DR resonance** ω [Rad/sec]	**DR resonance** Ω_y [Rad/m]	$C_{Y_{r_{1_g}}}(L_g)$	$C_{Y_{\dot{r}_{1_g}}}(L_g)$	$C_{\ell_{r_{1_g}}}(L_g)$	$C_{\ell_{\dot{r}_{1_g}}}(L_g)$	$C_{n_{r_{1_g}}}(L_g)$	$C_{n_{\dot{r}_{1_g}}}(L_g)$
3.0000e+001	2.1171e+000	6.5246e-002	-2.4428e-001	3.9671e-003	5.2476e-002	-1.2396e-003	-2.8688e-004	-6.1071e-003
1.5000e+002	2.1171e+000	3.2810e-002	-2.3933e-001	5.0850e-003	5.1907e-002	-1.6953e-003	-2.7896e-004	-5.8549e-003
3.0000e+002	2.1171e+000	3.1120e-002	-2.3917e-001	5.1797e-003	5.1889e-002	-1.7003e-003	-2.7863e-004	-5.8413e-003
5.0000e+002	2.1171e+000	3.0576e-002	-2.3912e-001	5.2117e-003	5.1883e-002	-1.7007e-003	-2.7853e-004	-5.8368e-003
1.0000e+003	2.1171e+000	3.0576e-002	-2.3912e-001	5.2117e-003	5.1883e-002	-1.7007e-003	-2.7853e-004	-5.8368e-003
1.5000e+003	2.1171e+000	3.0576e-002	-2.3912e-001	5.2117e-003	5.1883e-002	-1.7007e-003	-2.7853e-004	-5.8368e-003
Gust scale length L_g **[m]**	**DR resonance** ω [Rad/sec]	**DR resonance** Ω_y [Rad/m]	$C_{Y_{p_g}}(L_g)$	$C_{Y_{\dot{p}_g}}(L_g)$	$C_{\ell_{p_g}}(L_g)$	$C_{\ell_{\dot{p}_g}}(L_g)$	$C_{n_{p_g}}(L_g)$	$C_{n_{\dot{p}_g}}(L_g)$
3.0000e+001	2.3305e+000	6.7587e-002	3.3254e-002	-2.7961e-002	-5.1463e-001	2.4847e-002	-3.3392e-002	9.3084e-003
1.5000e+002	2.2862e+000	2.8495e-002	3.4241e-002	-3.5170e-002	-5.0894e-001	2.5891e-002	-3.2840e-002	9.8944e-003
3.0000e+002	2.2862e+000	2.6555e-002	3.4653e-002	-3.5949e-002	-5.0877e-001	2.6129e-002	-3.2817e-002	9.9288e-003
5.0000e+002	2.2862e+000	2.6091e-002	3.4766e-002	-3.6138e-002	-5.0874e-001	2.6193e-002	-3.2812e-002	9.9371e-003
1.0000e+003	2.2862e+000	2.5635e-002	3.4882e-002	-3.6323e-002	-5.0870e-001	2.6259e-002	-3.2807e-002	9.9451e-003
1.5000e+003	2.2862e+000	2.5635e-002	3.4882e-002	-3.6323e-002	-5.0870e-001	2.6259e-002	-3.2807e-002	9.9451e-003

Table 10.10: The PCA-model's anti-symmetrical gust derivatives obtained from frequency-domain simulations. The derivatives hold for the Dutch-Roll's (DR) resonance frequency.

1D gust fields						**2D gust fields**			
symmetrical				**asymmetrical**		**anti-symmetrical**			
$C_{X_{u_g}}$	$C_{X_{\dot{u}_g}}$	$C_{X_{\alpha_g}}$	$C_{X_{\dot{\alpha}_g}}$	$C_{Y_{\beta_g}}$	$C_{Y_{\dot{\beta}_g}}$	$C_{Y_{r_{1_g}}}$	$C_{Y_{\dot{r}_{1_g}}}$	$C_{Y_{p_g}}$	$C_{Y_{\dot{p}_g}}$
-0.0032	+0.7145	+0.1692	•	-0.4046	+0.0632	-0.2392	+0.0052	+0.0347	-0.0359
$C_{Z_{u_g}}$	$C_{Z_{\dot{u}_g}}$	$C_{Z_{\alpha_g}}$	$C_{Z_{\dot{\alpha}_g}}$	$C_{\ell_{\beta_g}}$	$C_{\ell_{\dot{\beta}_g}}$	$C_{\ell_{r_{1_g}}}$	$C_{\ell_{\dot{r}_{1_g}}}$	$C_{\ell_{p_g}}$	$C_{\ell_{\dot{p}_g}}$
-0.4592	+0.1470	-5.7874	+5.1534	-0.1090	+0.0194	+0.0519	-0.0017	-0.5088	+0.0261
$C_{m_{u_g}}$	$C_{m_{\dot{u}_g}}$	$C_{m_{\alpha_g}}$	$C_{m_{\dot{\alpha}_g}}$	$C_{n_{\beta_g}}$	$C_{n_{\dot{\beta}_g}}$	$C_{n_{r_{1_g}}}$	$C_{n_{\dot{r}_{1_g}}}$	$C_{n_{p_g}}$	$C_{n_{\dot{p}_g}}$
+0.0236	-0.2315	-0.7486	+2.9846	+0.0676	-0.0495	-0.0003	-0.0058	-0.0328	+0.0099

Table 10.11: The calculated gust derivatives for the Parametric Computational Aerodynamics (PCA) model ("•" means not applicable for the model). The results are valid for the frame $\mathcal{F}_S$, with the gust scale length $L_g = 300$ [m].

Chapter 11

The Delft University of Technology model

11.1 Introduction

In the previous chapter the aerodynamic model with respect to one-dimensional (1D) and two-dimensional (2D) gust fields has been identified using results obtained from Linearized Potential Flow (LPF) simulations. These results have been summarized for the so-called Parametric Computational Aerodynamics (PCA) model which relies on constant gust derivatives. For the 1D gust fields the atmospheric turbulence velocity components u_g, v_g and w_g were included only. For these fields the gust derivatives have been obtained from numerical LPF experiments assuming that these gust velocity components do not vary over the aircraft's span. Also, the gust derivatives for 2D gust fields have been obtained. The 2D gust fields included the longitudinal atmospheric turbulence velocity component u_g and the vertical atmospheric turbulence velocity component w_g, only. Obviously, contrary to the 1D case, these gust fields do vary over the aircraft's span.
In this chapter the aerodynamic model for the gust inputs indicated above is given according to the Delft University of Technology (DUT) theory (see references [33, 34]). Also for this model a separation is made in the gust inputs considered, that is 1D gust fields for the longitudinal u_g, lateral v_g and vertical w_g gust velocity components, and 2D gust fields for the longitudinal u_g and vertical w_g gust velocity components.
Similar to the PCA-model results presented earlier, a distinction is made between symmetrical and asymmetrical turbulence inputs. Symmetrical gust velocities will give rise to symmetrical aircraft responses whereas asymmetrical turbulence will cause asymmetrical aircraft responses, thus assuming small disturbance theory and therefore decoupling of symmetric and asymmetric aircraft motions is allowed. Also in this chapter the symmetrical and asymmetrical aircraft responses will be treated separately, thus assuming linear aircraft responses.

11.2 Atmospheric turbulence field definitions

For the DUT-model the 2D stochastic gust fields are considered as a superposition of infinitely many elementary fields of flow, see references [33, 34] and see chapter 5. In each of these elementary fields, the gust velocity varies sinusoidally along the X_E-axis as well as along the Y_E-axis of the Earth-Fixed Frame of Reference $\mathcal{F}_E$ (which is defined in appendix B). The elementary 2D velocity fields are written as,

$$\begin{aligned} u_g(x,y) &= u_{g_{max}} Re\left\{e^{j(\Omega_x x+\Omega_y y)}\right\} \\ v_g(x,y) &= v_{g_{max}} Re\left\{e^{j(\Omega_x x+\Omega_y y)}\right\} \\ w_g(x,y) &= w_{g_{max}} Re\left\{e^{j(\Omega_x x+\Omega_y y)}\right\} \end{aligned} \tag{11.1}$$

with u_g, v_g and w_g the longitudinal, lateral and vertical gust components in $\mathcal{F}_E$, respectively, $u_{g_{max}}$, $v_{g_{max}}$ and $w_{g_{max}}$ the amplitude of the 2D gust fields, Ω_x the spatial frequency along the X_E-axis of $\mathcal{F}_E$, Ω_y the spatial frequency along the Y_E-axis of $\mathcal{F}_E$ and $[x, y, (z = 0)]^T$ the position in $\mathcal{F}_E$.
The 1D gust fields are obtained from the 2D gust fields with Ω_y set to 0. Equation (11.1) is then reduced to,

$$\begin{aligned} u_g(x) &= u_{g_{max}} Re\left\{e^{j(\Omega_x x)}\right\} \\ v_g(x) &= v_{g_{max}} Re\left\{e^{j(\Omega_x x)}\right\} \\ w_g(x) &= w_{g_{max}} Re\left\{e^{j(\Omega_x x)}\right\} \end{aligned} \tag{11.2}$$

Equation (11.2) is used for the calculation of symmetrical gust inputs. In the following, another interpretation is given for the expressions given in equations (11.1). As an example, the expression for u_g in equation (11.1) is therefore written as,

$$\begin{aligned} u_g(x,y) &= u_{g_{max}} Re\left\{e^{j(\Omega_x x+\Omega_y y)}\right\} \\ &= u_{g_{max}} Re\left\{\left(cos\left(\Omega_x x\right) + j\ sin\left(\Omega_x x\right)\right)\left(cos\left(\Omega_y y\right) + j\ sin\left(\Omega_y y\right)\right)\right\} \\ &= u_{g_{max}}\left(cos\left(\Omega_x x\right)\ cos\left(\Omega_y y\right) - sin\left(\Omega_x x\right)\ sin\left(\Omega_y y\right)\right) \\ &= u_{g_1}(x,y) - u_{g_2}(x,y) \end{aligned} \tag{11.3}$$

According to the expressions given in equation (11.3) the elementary 2D gust field can be considered as the superposition of two separate fields in which each of the gust velocity component varies sinusoidally along the X_E- as well as along the Y_E-axis of $\mathcal{F}_E$,

$$\left.\begin{aligned} u_{g_1}(x,y) &= u_{g_{max}}\ cos\left(\Omega_x x\right)\ cos\left(\Omega_y y\right) && \text{(symmetric)} \\ u_{g_2}(x,y) &= u_{g_{max}}\ sin\left(\Omega_x x\right)\ sin\left(\Omega_y y\right) && (\text{anti}-\text{symmetric}) \end{aligned}\right\} \tag{11.4}$$

The characteristic difference between the two fields $u_{g_1}(x,y)$ and $u_{g_2}(x,y)$ is that the first is symmetrical with respect to the vertical $O_E X_E Z_E$-plane in the frame $\mathcal{F}_E$ and the second is anti-symmetrical with respect to this plane. Similarly, the v_g- and w_g-fields can be separated in these symmetrical and anti-symmetrical gust fields,

$$\left.\begin{array}{rcll} v_{g_1}(x,y) & = & v_{g_{max}} cos\,(\Omega_x x)\ cos\,(\Omega_y y) & (\text{anti}-\text{symmetric}) \\ v_{g_2}(x,y) & = & v_{g_{max}} sin\,(\Omega_x x)\ sin\,(\Omega_y y) & (\text{symmetric}) \end{array}\right\} \tag{11.5}$$

$$\left.\begin{array}{rcll} w_{g_1}(x,y) & = & w_{g_{max}} cos\,(\Omega_x x)\ cos\,(\Omega_y y) & (\text{symmetric}) \\ w_{g_2}(x,y) & = & w_{g_{max}} sin\,(\Omega_x x)\ sin\,(\Omega_y y) & (\text{anti}-\text{symmetric}) \end{array}\right\} \tag{11.6}$$

For the aircraft trim condition assumed in this thesis, which is nominally steady straight level flight, the aircraft plane of symmetry coincides with the $O_E X_E Z_E$-plane. As a consequence the symmetric parts $u_{g_1}(x,y)$, $v_{g_2}(x,y)$ and $w_{g_1}(x,y)$ of the elementary fields can only cause symmetric deviations from steady flight. For the symmetrical aircraft motions the spatial frequency Ω_y is set to zero. According to equation (11.5), the $v_{g_2}(x,y)$-field can be omitted when considering symmetrical aircraft responses. Only the u_g and w_g gust fields will be considered for the simulation of symmetrical aircraft motions.
The three anti-symmetric parts $u_{g_2}(x,y)$, $v_{g_1}(x,y)$ and $w_{g_2}(x,y)$ given in equations (11.4), (11.5) and (11.6) of the elementary gust fields will be used for the simulation of asymmetrical aircraft motions.
The DUT-model atmospheric turbulence velocity-component (u_g, v_g and w_g) Power Spectral Density (PSD) functions are summarized in chapter 2 and appendix H. For the gust velocity components considered in this chapter, they are also summarized in section 11.4.

11.3 Aerodynamic models

11.3.1 1D Symmetrical longitudinal gust fields

For the DUT-model 1D symmetrical longitudinal gust velocity component u_g the aerodynamic force and moment coefficients are given as, (see references [33, 34, 30]),

$$C_{X_g} = C_{X_{u_g}} \hat{u}_g \tag{11.7}$$

$$C_{Z_g} = C_{Z_{u_g}} \hat{u}_g \tag{11.8}$$

$$C_{m_g} = C_{m_{u_g}} \hat{u}_g \tag{11.9}$$

with $\hat{u}_g = \frac{u_g}{Q_\infty}$. The steady gust derivatives $C_{X_{u_g}}$, $C_{Z_{u_g}}$ and $C_{m_{u_g}}$ are expressed in terms of stability derivatives, see also reference [30], while the unsteady gust derivatives with respect to $\frac{\dot{\hat{u}}_g \bar{c}}{Q_\infty}$, that is $C_{X_{\dot{u}_g}}$, $C_{Z_{\dot{u}_g}}$ and $C_{m_{\dot{u}_g}}$, are neglected for the DUT-model. The gust derivatives with respect to the non-dimensional gust velocity component $\hat{u}_g$ are defined as,

$$\left.\begin{array}{rcl} C_{X_{u_g}} & = & C_{X_u} \\ C_{Z_{u_g}} & = & C_{Z_u} \\ C_{m_{u_g}} & = & C_{m_u} \end{array}\right\} \tag{11.10}$$

with C_{X_u}, C_{Z_u} and C_{m_u} the aircraft's stability derivatives.

11.3.2 1D Asymmetrical lateral gust fields

For the 1D asymmetrical gust fields, the lateral gust velocity component v_g is considered only. According to the DUT-model, for the linearized aircraft model the aerodynamic force and moments coefficients are given as, see also references [33, 34, 30],

$$C_{Y_g} = C_{Y_{\beta_g}}\beta_g + C_{Y_{\dot{\beta}_g}}\frac{\dot{\beta}_g b}{Q_\infty} \tag{11.11}$$

$$C_{\ell_g} = C_{\ell_{\beta_g}}\beta_g + C_{\ell_{\dot{\beta}_g}}\frac{\dot{\beta}_g b}{Q_\infty} \tag{11.12}$$

$$C_{n_g} = C_{n_{\beta_g}}\beta_g + C_{n_{\dot{\beta}_g}}\frac{\dot{\beta}_g b}{Q_\infty} \tag{11.13}$$

with $\beta_g = \frac{v_g}{Q_\infty}$ and $\dot{\beta}_g = \frac{\dot{v}_g}{Q_\infty}$. The gust derivatives $C_{Y_{\beta_g}}$, $C_{Y_{\dot{\beta}_g}}$, $C_{\ell_{\beta_g}}$, $C_{\ell_{\dot{\beta}_g}}$, $C_{n_{\beta_g}}$ and $C_{n_{\dot{\beta}_g}}$ are expressed in terms of stability derivatives, see also reference [30]. The asymmetrical gust derivative $C_{Y_{\dot{\beta}_g}}$ is written as,

$$C_{Y_{\dot{\beta}_g}} = C_{Y_{\dot{\beta}}} + \frac{1}{2}C_{Y_r} \tag{11.14}$$

with $C_{Y_{\dot{\beta}}}$ and C_{Y_r} the stability derivatives. It should be remarked, that only the contribution of the vertical tailplane to C_{Y_r} is taken into account.
In summary, the DUT-model's 1D lateral gust derivatives are defined as,

$$\left.\begin{array}{rcl} C_{Y_{\beta_g}} & = & C_{Y_\beta} \\ C_{\ell_{\beta_g}} & = & C_{\ell_\beta} \\ C_{n_{\beta_g}} & = & C_{n_\beta} \end{array}\right\} \tag{11.15}$$

with C_{Y_β}, C_{ℓ_β} and C_{n_β} the stability derivatives. The unsteady gust derivatives with respect to the time derivative of the non-dimensional gust velocity component β_g, written as $\frac{\beta_g b}{Q\infty}$, are defined as,

$$\left.\begin{array}{rcl} C_{Y_{\dot{\beta}_g}} & = & C_{Y_{\dot{\beta}}} + \frac{1}{2}C_{Y_{r_v}} \\ C_{\ell_{\dot{\beta}_g}} & = & C_{\ell_{\dot{\beta}}} + \frac{1}{2}C_{\ell_{r_v}} \\ C_{n_{\dot{\beta}_g}} & = & C_{n_{\dot{\beta}}} + \frac{1}{2}C_{n_{r_v}} \end{array}\right\} \tag{11.16}$$

with $C_{Y_{\dot{\beta}}}$, $C_{\ell_{\dot{\beta}}}$, $C_{n_{\dot{\beta}}}$, C_{Y_r}, C_{ℓ_r} and C_{n_r} the aircraft's stability derivatives (with the subscript v denoting the vertical tailplane's contribution to the stability derivative). Since the derivation of these unsteady gust derivatives is not always provided in the literature, it is given in the following definition using a frequency-domain approach.

Definition 11.1 *The definition of the constant unsteady gust derivatives with respect to asymmetrical 1D lateral gusts $\beta_g = \frac{v_g}{Q_\infty}$ according to equation (11.16), holds for wing-fuselage/vertical stabilizer configurations only. These unsteady gust derivatives only depend on vertical-tailplane contributions.*

Derivation

In the following the definition of both the steady and unsteady gust derivatives, $C_{Y_{\beta_g}}$ and $C_{Y_{\dot{\beta}_g}}$, respectively, will be derived. This derivation is representative for the calculation of the steady gust derivatives $C_{\ell_{\beta_g}}$ and $C_{n_{\beta_g}}$, and for the unsteady gust derivatives $C_{\ell_{\dot{\beta}_g}}$ and $C_{n_{\dot{\beta}_g}}$.

For the derivation of the unsteady gust derivatives with respect to asymmetrical 1D lateral gust inputs, the definition of both the steady and unsteady stability derivatives has to be determined first.
For example, consider the aerodynamic force response along the Y_S-axis of the Stability Frame of Reference $\mathcal{F}_S$ of a wing-fuselage-vertical-fin configuration to a steady swaying aircraft motion, see also figure 11.1. In this figure the swaying motion is given in terms of the steady side-slip-angle β, with the wing-fuselage combination inducing a sidewash, given as σ. The vertical tailplane's perceived angle-of-attack (see also reference [29]) is defined as $\alpha_v = -(\beta - \sigma)$. The minus sign in the expression for α_v is due to the sign convention used for the normal force gradient of the vertical tailplane $C_{Y_{\alpha_v}}$. The perceived angle-of-attack α_v is the local angle-of-attack of the vertical tailplane measured in the $X_S O Y_S$-plane and counted positive if the airflow hits the tailplane from the left, see also figure 11.1. For the present analysis, it is assumed that the positions of the aerodynamic center of the wing/fuselage configuration and the center of gravity coincide.

For the derivation of the steady and unsteady stability derivatives, the aerodynamic force along the Y_S-axis of the frame $\mathcal{F}_S$, is written as,

$$Y = C_{Y_{\beta_{w+f}}} \frac{1}{2}\rho Q_\infty^2 S \ \beta + C_{Y_{\alpha_v}} \frac{1}{2}\rho Q_{\infty_v}^2 S_v \ \alpha_v$$

or in non-dimensional form with $C_Y = \frac{Y}{\frac{1}{2}\rho Q_\infty^2 S}$,

$$C_Y = C_{Y_{\beta_{w+f}}} \beta + C_{Y_{\alpha_v}} \left(\frac{Q_{\infty_v}}{Q_\infty}\right)^2 \frac{S_v}{S} \ \alpha_v \tag{11.17}$$

with Y the dimensional aerodynamic force along the Y_S-axis in $\mathcal{F}_S$, ρ air-density, Q_∞ the airspeed, S the aircraft's (reference) wing surface area, S_v the aircraft's vertical fin surface area, $C_{Y_{\beta_{w+f}}}$ the wing/fuselage's aerodynamic stiffness term, $C_{Y_{\alpha_v}}$ the vertical fin's aerodynamic stiffness term taken with respect to S_v, Q_{∞_v} the airspeed at the vertical tailplane's aerodynamic center (taken as $Q_{\infty_v} = Q_\infty$), $\beta = \frac{v}{Q_\infty}$ the side-slip-angle at the aircraft's center of gravity (or, using the assumption indicated above, at the wing/fuselage's aerodynamic center), v the aircraft motion's swaying velocity and α_v the perceived angle-of-attack at the vertical tailplane's aerodynamic center.

Assuming that the sidewash angle σ is solely induced by the wing/fuselage configuration, while also assuming that it reaches its maximum value at the center of gravity, for unsteady swaying motions the perceived angle-of-attack α_v is given by the side-slip-angle β and by the sidewash angle σ reaching the vertical tailplane after $\tau = \frac{l_v}{Q_\infty}$ [secs.], with l_v the vertical tail-length ([m]). In the frequency-domain the perceived angle-of-attack $\alpha_v(\omega)$ is given as,

$$\alpha_v(\omega) = -\left(\beta - \sigma e^{-j\omega\frac{l_v}{Q_\infty}}\right) = -\left(\beta - \frac{\partial\sigma}{\partial\beta}\beta e^{-j\omega\frac{l_v}{Q_\infty}}\right) = -\left(1 - \frac{\partial\sigma}{\partial\beta}e^{-j\omega\frac{l_v}{Q_\infty}}\right)\beta \tag{11.18}$$

assuming that the sidewash σ is solely dependent of the side-slip-angle β. Substituting equation (11.18) into equation (11.17), after some elaboration the aerodynamic Frequency-Response Function

(FRF) $\frac{C_Y}{\beta}(\omega)$ is obtained,

$$\frac{C_Y}{\beta}(\omega) = C_{Y_{\beta_{w+f}}} - C_{Y_{\alpha_v}} \left(\frac{Q_{\infty_v}}{Q_\infty}\right)^2 \frac{S_v}{S} \left(1 - \frac{\partial\sigma}{\partial\beta} e^{-j\omega\frac{l_v}{Q_\infty}}\right) \tag{11.19}$$

Using a first-order Taylor polynomial approximation for the time-delay ($e^{-j\omega\tau} \approx 1 - j\omega\tau$), thus assuming $\omega\tau$ to be small, the aerodynamic FRF given in equation (11.19) becomes,

$$\begin{aligned}
\frac{C_Y}{\beta}(\omega) &= C_{Y_{\beta_{w+f}}} - C_{Y_{\alpha_v}} \left(\frac{Q_{\infty_v}}{Q_\infty}\right)^2 \frac{S_v}{S} \left(1 - \frac{\partial\sigma}{\partial\beta}\left(1 - j\omega\frac{l_v}{Q_\infty}\right)\right) \\
&= \left\{C_{Y_{\beta_{w+f}}} - C_{Y_{\alpha_v}} \left(\frac{Q_{\infty_v}}{Q_\infty}\right)^2 \frac{S_v}{S} \left(1 - \frac{\partial\sigma}{\partial\beta}\right)\right\} - \\
&\quad \left\{C_{Y_{\alpha_v}} \left(\frac{Q_{\infty_v}}{Q_\infty}\right)^2 \frac{S_v}{S}\frac{\partial\sigma}{\partial\beta}\right\} \frac{l_v}{Q_\infty} j\omega \\
&= \left\{C_{Y_{\beta_{w+f}}} - C_{Y_{\alpha_v}} \left(\frac{Q_{\infty_v}}{Q_\infty}\right)^2 \frac{S_v}{S} \left(1 - \frac{\partial\sigma}{\partial\beta}\right)\right\} - \\
&\quad \left\{C_{Y_{\alpha_v}} \left(\frac{Q_{\infty_v}}{Q_\infty}\right)^2 \frac{S_v l_v}{Sb}\frac{\partial\sigma}{\partial\beta}\right\} \frac{b}{Q_\infty} j\omega \\
&= C_{Y_\beta} + C_{Y_{\dot\beta}} \frac{b}{Q_\infty} j\omega
\end{aligned}$$

with b the wingspan, and,

$$C_{Y_\beta} = C_{Y_{\beta_{w+f}}} - C_{Y_{\alpha_v}} \left(\frac{Q_{\infty_v}}{Q_\infty}\right)^2 \frac{S_v}{S} \left(1 - \frac{\partial\sigma}{\partial\beta}\right) \tag{11.20}$$

and,

$$C_{Y_{\dot\beta}} = -C_{Y_{\alpha_v}} \left(\frac{Q_{\infty_v}}{Q_\infty}\right)^2 \frac{S_v l_v}{Sb}\frac{\partial\sigma}{\partial\beta} \tag{11.21}$$

Similar to the expressions for C_{Y_β} and $C_{Y_{\dot\beta}}$ given in equations (11.20) and (11.21), respectively, both the steady and unsteady stability derivatives C_{ℓ_β}, $C_{\ell_{\dot\beta}}$, C_{n_β} and $C_{n_{\dot\beta}}$ are derived.

The following step in obtaining the steady and unsteady gust derivatives, requires the definition of the stability derivatives with respect to the yaw-rate r. These quasi-steady derivatives are obtained using the following expression for the vertical tailplane's perceived angle-of-attack given in terms of the non-dimensional yaw-rate $\frac{rb}{2Q_\infty}$,

$$\alpha_v = \frac{rb}{2Q_\infty} \frac{l_v}{b/2} \tag{11.22}$$

The non-dimensional aerodynamic force coefficient C_Y is now written as,

$$C_Y = C_{Y_{\alpha_v}} \left(\frac{Q_{\infty_v}}{Q_\infty}\right)^2 \frac{S_v}{S}\ \alpha_v = C_{Y_{\alpha_v}} \left(\frac{Q_{\infty_v}}{Q_\infty}\right)^2 \frac{S_v}{S}\ \frac{rb}{2Q_\infty}\ \frac{l_v}{b/2}$$

from which the stability derivative C_{Y_r} is derived,

$$C_{Y_r} = 2\ C_{Y_{\alpha_v}} \left(\frac{Q_{\infty_v}}{Q_\infty} \right)^2 \frac{S_v l_v}{Sb} \tag{11.23}$$

Similar expressions are obtained for the stability derivatives C_{ℓ_r} and C_{n_r}. Note that only vertical tailplane contributions to the stability derivatives C_{Y_r}, C_{ℓ_r} and C_{n_r} were considered.

For the derivation of the steady and unsteady gust derivatives, now consider a discrete 1D lateral gust $\beta_g = \frac{v_g}{Q_\infty}$ coming from the right, see figure 11.2 (see also chapter 5 for the definition of the positive direction of the lateral gust velocity component v_g in the frame $\mathcal{F}_S$). Upon reaching the wing/fuselage configuration's aerodynamic center (with its position assumed to coincide with the aircraft's center of gravity) the lateral gust will induce a sidewash which is also denoted by σ. After an instant in time τ, equalling $\tau = \frac{l_v}{Q_\infty}$ [secs.], the sidewash reaches the vertical tailplane causing a change in the aerodynamic force on it. The lateral gust in itself will reach the vertical tailplane after an equal amount of time. The aerodynamic force along the Y_S-axis of the frame $\mathcal{F}_S$ is now written as Y_g, or,

$$Y_g = C_{Y_{\beta_{w+f}}} \frac{1}{2} \rho Q_\infty^2 S\ \beta_g - C_{Y_{\alpha_v}} \frac{1}{2} \rho Q_{\infty_v}^2 S_v\ \beta_{v_g}$$

while in non-dimensional form the aerodynamic force coefficient along the Y_S-axis of the frame $\mathcal{F}_S$ is written as,

$$C_{Y_g} = C_{Y_{\beta_{w+f}}} \beta_g - C_{Y_{\alpha_v}} \left(\frac{Q_{\infty_v}}{Q_\infty} \right)^2 \frac{S_v}{S}\ \beta_{v_g}$$

with $C_{Y_g} = \frac{Y_g}{\frac{1}{2}\rho Q_\infty^2 S}$ the lateral gust induced non-dimensional aerodynamic force coefficient in $\mathcal{F}_S$, $\beta_g = \frac{v_g}{Q_\infty}$ the lateral gust-induced side-slip-angle at the center of gravity (or, using the assumption indicated above, at the wing/fuselage configuration aerodynamic center) and β_{v_g} the lateral gust-induced side-slip-angle at the vertical tailplane aerodynamic center. For the frequency-domain the latter becomes,

$$\beta_{v_g}(\omega) = \beta_g\ e^{-j\omega\tau} - \frac{\partial \sigma}{\partial \beta} e^{-j\omega\tau} \beta_g = \left(1 - \frac{\partial \sigma}{\partial \beta} \right) e^{-j\omega\tau} \beta_g = \left(1 - \frac{\partial \sigma}{\partial \beta} \right) e^{-j\omega \frac{l_v}{Q_\infty}} \beta_g$$

with ω the circular frequency given in [Rad/sec.].
The aerodynamic force coefficient C_{Y_g} is now written as,

$$C_{Y_g} = C_{Y_{\beta_{w+f}}} \beta_g - C_{Y_{\alpha_v}} \left(\frac{Q_{\infty_v}}{Q_\infty} \right)^2 \frac{S_v}{S} \left(1 - \frac{\partial \sigma}{\partial \beta} \right) e^{-j\omega \frac{l_v}{Q_\infty}} \beta_g$$

The aerodynamic FRF $\frac{C_{Y_g}}{\beta_g}(\omega)$ is defined as,

$$\frac{C_{Y_g}}{\beta_g}(\omega) = C_{Y_{\beta_{w+f}}} - C_{Y_{\alpha_v}} \left(\frac{Q_{\infty_v}}{Q_\infty} \right)^2 \frac{S_v}{S} \left(1 - \frac{\partial \sigma}{\partial \beta} \right) e^{-j\omega \frac{l_v}{Q_\infty}}$$

Similar to the derivation of the stability derivatives, this aerodynamic FRF is now expanded using a first-order Taylor polynomial approximation for the time-delay,

$$\frac{C_{Y_g}}{\beta_g}(\omega) \quad = \quad C_{Y_{\beta_{w+f}}} - C_{Y_{\alpha_v}} \left(\frac{Q_{\infty_v}}{Q_\infty} \right)^2 \frac{S_v}{S} \left(1 - \frac{\partial \sigma}{\partial \beta} \right) \left(1 - j\omega \frac{l_v}{Q_\infty} \right)$$

$$
\begin{aligned}
&= \left\{ C_{Y_{\beta_{w+f}}} - C_{Y_{\alpha_v}} \left(\frac{Q_{\infty_v}}{Q_\infty} \right)^2 \frac{S_v}{S} \left(1 - \frac{\partial \sigma}{\partial \beta} \right) \right\} + \\
&\quad \left\{ C_{Y_{\alpha_v}} \left(\frac{Q_{\infty_v}}{Q_\infty} \right)^2 \frac{S_v}{S} \left(1 - \frac{\partial \sigma}{\partial \beta} \right) \right\} \frac{l_v}{Q_\infty} j\omega \\
&= \left\{ C_{Y_{\beta_{w+f}}} - C_{Y_{\alpha_v}} \left(\frac{Q_{\infty_v}}{Q_\infty} \right)^2 \frac{S_v}{S} \left(1 - \frac{\partial \sigma}{\partial \beta} \right) \right\} + \\
&\quad \left\{ C_{Y_{\alpha_v}} \left(\frac{Q_{\infty_v}}{Q_\infty} \right)^2 \frac{S_v l_v}{S b} \left(1 - \frac{\partial \sigma}{\partial \beta} \right) \right\} \frac{b}{Q_\infty} j\omega \\
&= C_{Y_{\beta_g}} + C_{Y_{\dot{\beta}_g}} \frac{b}{Q_\infty} j\omega
\end{aligned}
$$

with,

$$
C_{Y_{\beta_g}} = C_{Y_\beta} = C_{Y_{\beta_{w+f}}} - C_{Y_{\alpha_v}} \left(\frac{Q_{\infty_v}}{Q_\infty} \right)^2 \frac{S_v}{S} \left(1 - \frac{\partial \sigma}{\partial \beta} \right)
$$

and,

$$
\begin{aligned}
C_{Y_{\dot{\beta}_g}} &= C_{Y_{\alpha_v}} \left(\frac{Q_{\infty_v}}{Q_\infty} \right)^2 \frac{S_v l_v}{S b} \left(1 - \frac{\partial \sigma}{\partial \beta} \right) \\
&= C_{Y_{\alpha_v}} \left(\frac{Q_{\infty_v}}{Q_\infty} \right)^2 \frac{S_v l_v}{S b} - C_{Y_{\alpha_v}} \left(\frac{Q_{\infty_v}}{Q_\infty} \right)^2 \frac{S_v l_v}{S b} \frac{\partial \sigma}{\partial \beta} \\
&= \frac{1}{2} C_{Y_r} + C_{Y_{\dot{\beta}}}
\end{aligned}
$$

with the definitions of the stability derivative $C_{Y_{\dot{\beta}}}$ and C_{Y_r} according to equations (11.21) and (11.23), respectively, which are the theoretical vertical tailplane contributions to the stability derivatives $C_{Y_{\dot{\beta}}}$ and C_{Y_r}, see also reference [29].

Similar expressions for the gust derivatives for the aerodynamic moments along the X_S-axis and Z_S-axis of $\mathcal{F}_S$ are obtained.
In this derivation of the DUT-model's steady and unsteady gust derivatives only a wing-fuselage/vertical tailplane configuration has been considered. Also, all aircraft parts' aerodynamics were considered steady, that is only aerodynamic stiffness terms were used in all derivations. Furthermore, no aerodynamic interference effects have been included in the gust derivatives' derivations.

11.3.3 1D Symmetrical vertical gust fields

The aerodynamic forces and moment coefficients with respect to the vertical gust velocity component w_g are given as (see references [33, 34, 30]),

$$
C_{X_g} = C_{X_{\alpha_g}} \alpha_g + C_{X_{\dot{\alpha}_g}} \frac{\dot{\alpha}_g \bar{c}}{Q_\infty} \tag{11.24}
$$

$$
C_{Z_g} = C_{Z_{\alpha_g}} \alpha_g + C_{Z_{\dot{\alpha}_g}} \frac{\dot{\alpha}_g \bar{c}}{Q_\infty} \tag{11.25}
$$

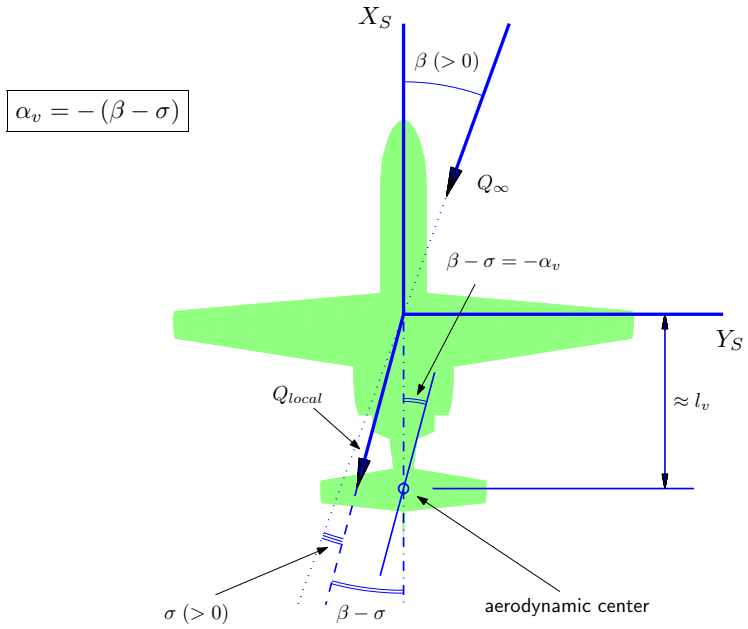


Figure 11.1: Relation between the side-slip-angle β, the sidewash-angle σ and the vertical tailplane angle-of-attack α_v.

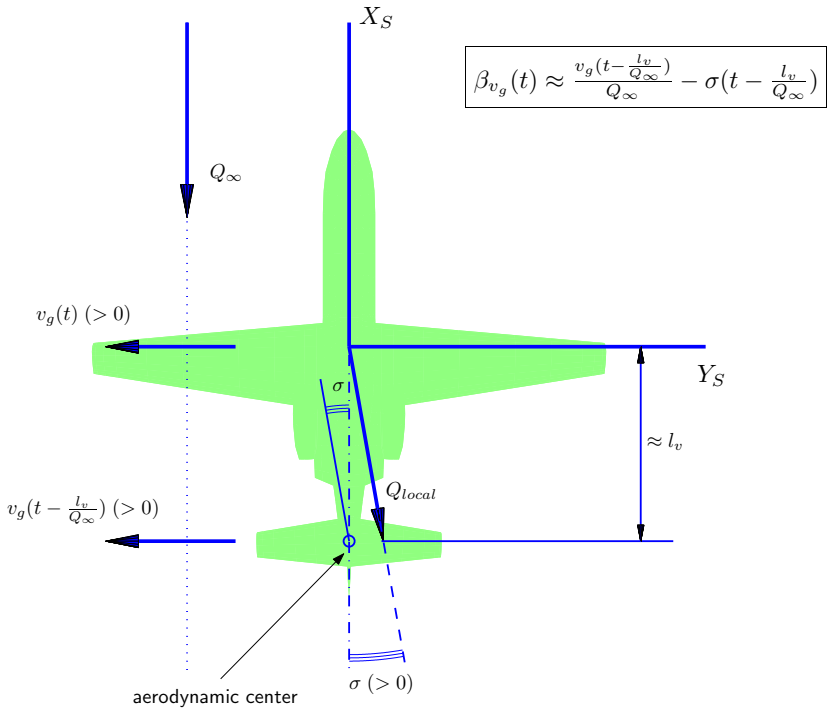


Figure 11.2: Definition of the vertical tailplane side-slip-angle β_{v_g} due to the 1D lateral atmospheric turbulence velocity component v_g.

$$C_{m_g} = C_{m_{\alpha_g}} \alpha_g + C_{m_{\dot{\alpha}_g}} \frac{\dot{\alpha}_g \bar{c}}{Q_\infty} \tag{11.26}$$

with $\alpha_g = \frac{w_g}{Q_\infty}$ and $\dot{\alpha}_g = \frac{\dot{w}_g}{Q_\infty}$. Both the steady and unsteady gust derivatives $C_{X_{\alpha_g}}$, $C_{X_{\dot{\alpha}_g}}$, $C_{Z_{\alpha_g}}$, $C_{Z_{\dot{\alpha}_g}}$, $C_{m_{\alpha_g}}$, $C_{m_{\dot{\alpha}_g}}$, are expressed in terms of stability derivatives, see also reference [30]. For the DUT-model, the gust derivatives with respect to the non-dimensional gust velocity component $\alpha_g = \frac{w_g}{Q_\infty}$ are defined as,

$$\left.\begin{array}{rcl} C_{X_{\alpha_g}} & = & C_{X_\alpha} \\ C_{Z_{\alpha_g}} & = & C_{Z_\alpha} \\ C_{m_{\alpha_g}} & = & C_{m_\alpha} \end{array}\right\} \tag{11.27}$$

with C_{X_α}, C_{Z_α} and C_{m_α} the stability derivatives. The gust derivatives with respect to the time derivative of the non-dimensional gust velocity component α_g, written as $\frac{\dot{\alpha}_g \bar{c}}{Q\infty}$, are defined as,

$$\left.\begin{array}{rcl} C_{X_{\dot{\alpha}_g}} & = & C_{X_{\dot{\alpha}}} - C_{X_q} \\ C_{Z_{\dot{\alpha}_g}} & = & C_{Z_{\dot{\alpha}}} - C_{Z_q} \\ C_{m_{\dot{\alpha}_g}} & = & C_{m_{\dot{\alpha}}} - C_{m_q} \end{array}\right\} \tag{11.28}$$

with $C_{X_{\dot{\alpha}}}$, $C_{Z_{\dot{\alpha}}}$, $C_{m_{\dot{\alpha}}}$, C_{X_q}, C_{Z_q} and C_{m_q} the aircraft's stability derivatives. Although the definition of the unsteady gust derivatives given in equations (11.28) are used for complete aircraft configurations, see reference [30], they actually only hold for wing-stabilizer configurations. Since the derivation of these unsteady derivatives is álso not always provided in the literature, it is given in the following definition using a frequency-domain approach.

Definition 11.2 *The definition of the constant unsteady gust derivatives with respect to symmetrical 1D vertical gusts $\alpha_g = \frac{w_g}{Q_\infty}$ according to equation (11.28), holds for wing-stabilizer configurations only. These unsteady gust derivatives only depend on horizontal tailplane contributions.*

Derivation

In the following the definition of both the steady and unsteady gust derivatives $C_{Z_{\alpha_g}}$ and $C_{Z_{\dot{\alpha}_g}}$, respectively, will be derived. This derivation is representative for the steady gust derivatives $C_{X_{\alpha_g}}$ and $C_{m_{\alpha_g}}$, and for the unsteady gust derivatives $C_{X_{\dot{\alpha}_g}}$ and $C_{m_{\dot{\alpha}_g}}$.

For the derivation of the unsteady gust derivatives with respect to symmetrical 1D vertical gust inputs, the definition of both the steady and unsteady stability derivatives has to be determined first.
Similar to the derivation of the asymmetrical stability derivatives, now, for example, consider the aerodynamic force response along the Z_S-axis of the frame $\mathcal{F}_S$ of a wing-stabilizer configuration to a steady heaving aircraft motion, see also figure 11.3. The heaving motion is given in terms of the steady angle-of-attack α. In this case, the wing induces a downwash, given as ε, at the horizontal tailplane. The horizontal tailplane's perceived angle-of-attack (see also reference [29]) is defined as $\alpha_h = \alpha - \varepsilon + i_h$, with i_h the horizontal stabilizer's inclination (which is set to zero, $i_h = 0\ [^o]$). The tailplane's perceived (or local) angle-of-attack α_h is measured in the $X_S O Z_S$-plane and counted as positive if the airflow hits this tailplane from the bottom, see also figure 11.3. For the present analysis,

it is assumed that the positions of the aerodynamic center of the wing and the center of gravity coincide.

For the derivation of the steady and unsteady stability derivatives, the aerodynamic force along the Z_S-axis of the frame $\mathcal{F}_S$ is written as,

$$Z = C_{Z_{\alpha_w}} \frac{1}{2}\rho Q_\infty^2 S\ \alpha + C_{Z_{\alpha_h}} \frac{1}{2}\rho Q_{\infty_h}^2 S_h\ \alpha_h$$

or in non-dimensional form,

$$C_Z = C_{Z_{\alpha_w}} \alpha + C_{Z_{\alpha_h}} \left(\frac{Q_{\infty_h}}{Q_\infty}\right)^2 \frac{S_h}{S}\ \alpha_h \tag{11.29}$$

with $C_Z = \frac{Z}{\frac{1}{2}\rho Q_\infty^2 S}$, Z the dimensional aerodynamic force in $\mathcal{F}_S$, ρ air-density, Q_∞ the airspeed, S the (reference) wing surface area, S_h the horizontal tailplane surface area, $C_{Z_{\alpha_w}}$ the wing aerodynamic stiffness term, $C_{Z_{\alpha_h}}$ the horizontal stabilizer aerodynamic stiffness term taken with respect to S_h, Q_{∞_h} the airspeed at the horizontal tailplane aerodynamic center (similar to Q_{∞_v}, taken as $Q_{\infty_h} = Q_\infty$), $\alpha = \frac{w}{Q_\infty}$ the angle-of-attack at the aircraft center of gravity (or, using the assumption indicated above, at the wing aerodynamic center), w the aircraft motion heaving velocity and α_h the perceived angle-of-attack at the horizontal tailplane aerodynamic center.

Assuming that the downwash angle ε is solely induced by the wing, while also assuming that it reaches its maximum value at the center of gravity, for unsteady heaving motions the perceived angle-of-attack α_h is given in terms of the angle-of-attack α and the downwash angle ε reaching the horizontal tailplane after $\tau = \frac{l_h}{Q_\infty}$ [secs.], with l_h the horizontal tail-length (given in [m]). In the frequency-domain the perceived angle-of-attack $\alpha_h(\omega)$ is given as,

$$\alpha_h(\omega) = \alpha - \varepsilon e^{-j\omega\frac{l_h}{Q_\infty}} = \alpha - \frac{\partial\varepsilon}{\partial\alpha}\alpha e^{-j\omega\frac{l_h}{Q_\infty}} = \left(1 - \frac{\partial\varepsilon}{\partial\alpha}e^{-j\omega\frac{l_h}{Q_\infty}}\right)\alpha \tag{11.30}$$

assuming that the downwash angle ε is solely dependent of the angle-of-attack α. Substituting equation (11.30) into equation (11.29), yields after some elaboration the aerodynamic Frequency-Response Function (FRF) $\frac{C_Z}{\alpha}(\omega)$ is obtained,

$$\frac{C_Z}{\alpha}(\omega) = C_{Z_{\alpha_w}} + C_{Z_{\alpha_h}} \left(\frac{Q_{\infty_h}}{Q_\infty}\right)^2 \frac{S_h}{S}\left(1 - \frac{\partial\varepsilon}{\partial\alpha}e^{-j\omega\frac{l_h}{Q_\infty}}\right) \tag{11.31}$$

Similar to the derivation of the asymmetrical steady and unsteady stability derivatives with respect to swaying motions, a first-order Taylor polynomial approximation is used for the time-delay ($e^{-j\omega\tau} \approx 1 - j\omega\tau$). The aerodynamic FRF given in equation (11.31) becomes,

$$\begin{aligned}
\frac{C_Z}{\alpha}(\omega) &= C_{Z_{\alpha_w}} + C_{Z_{\alpha_h}} \left(\frac{Q_{\infty_h}}{Q_\infty}\right)^2 \frac{S_h}{S}\left(1 - \frac{\partial\varepsilon}{\partial\alpha}\left(1 - j\omega\frac{l_h}{Q_\infty}\right)\right) \\
&= \left\{C_{Z_{\alpha_w}} + C_{Z_{\alpha_h}} \left(\frac{Q_{\infty_h}}{Q_\infty}\right)^2 \frac{S_h}{S}\left(1 - \frac{\partial\varepsilon}{\partial\alpha}\right)\right\} + \\
&\quad \left\{C_{Z_{\alpha_h}} \left(\frac{Q_{\infty_h}}{Q_\infty}\right)^2 \frac{S_h}{S}\frac{\partial\varepsilon}{\partial\alpha}\right\} \frac{l_h}{Q_\infty} j\omega \\
&= \left\{C_{Z_{\alpha_w}} + C_{Z_{\alpha_h}} \left(\frac{Q_{\infty_h}}{Q_\infty}\right)^2 \frac{S_h}{S}\left(1 - \frac{\partial\varepsilon}{\partial\alpha}\right)\right\} +
\end{aligned}$$

$$\left\{ C_{Z_{\alpha_h}} \left(\frac{Q_{\infty_h}}{Q_\infty} \right)^2 \frac{S_h l_h}{S\bar{c}} \frac{\partial \varepsilon}{\partial \alpha} \right\} \frac{\bar{c}}{Q_\infty} j\omega$$

$$= \quad C_{Z_\alpha} + C_{Z_{\dot{\alpha}}} \frac{\bar{c}}{Q_\infty} j\omega$$

with $\bar{c}$ the mean aerodynamic chord, and,

$$C_{Z_\alpha} = C_{Z_{\alpha_w}} + C_{Z_{\alpha_h}} \left(\frac{Q_{\infty_h}}{Q_\infty} \right)^2 \frac{S_h}{S} \left(1 - \frac{\partial \varepsilon}{\partial \alpha} \right) \tag{11.32}$$

and,

$$C_{Z_{\dot{\alpha}}} = C_{Z_{\alpha_h}} \left(\frac{Q_{\infty_h}}{Q_\infty} \right)^2 \frac{S_h l_h}{S\bar{c}} \frac{\partial \varepsilon}{\partial \alpha} \tag{11.33}$$

Similar to the expressions for C_{Z_α} and $C_{Z_{\dot{\alpha}}}$ given in equations (11.32) and (11.33), respectively, both the steady and unsteady stability derivatives C_{X_α}, $C_{X_{\dot{\alpha}}}$, C_{m_α} and $C_{m_{\dot{\alpha}}}$ are derived.

The following step in obtaining the steady and unsteady gust derivatives is the definition of the stability derivatives with respect to the pitch-rate q. Similar to the yaw derivatives, these quasi-steady derivatives are obtained using the following expression for the horizontal tailplane perceived angle-of-attack given in terms of the non-dimensional pitch-rate $\frac{q\bar{c}}{Q_\infty}$,

$$\alpha_h = \frac{q\bar{c}}{Q_\infty} \; \frac{l_h}{\bar{c}} \tag{11.34}$$

The non-dimensional aerodynamic force coefficient C_Z is now written as,

$$C_Z = C_{Z_{\alpha_h}} \left(\frac{Q_{\infty_h}}{Q_\infty} \right)^2 \frac{S_h}{S} \; \alpha_h = C_{Z_{\alpha_h}} \left(\frac{Q_{\infty_h}}{Q_\infty} \right)^2 \frac{S_h}{S} \; \frac{q\bar{c}}{Q_\infty} \; \frac{l_h}{\bar{c}}$$

from which the stability derivative C_{Z_q} follows,

$$C_{Z_q} = C_{Z_{\alpha_h}} \left(\frac{Q_{\infty_h}}{Q_\infty} \right)^2 \frac{S_h l_h}{S\bar{c}} \tag{11.35}$$

Similar expressions are obtained for the stability derivatives C_{X_q} and C_{m_q}. Note that only horizontal tailplane contributions to the stability derivatives C_{X_q}, C_{Z_q} and C_{m_q} were considered.

For the derivation of the steady and unsteady gust derivatives, now consider a wing-stabilizer configuration with the aerodynamic stiffness terms given as $C_{Z_{\alpha_w}}$ and $C_{Z_{\alpha_h}}$ for the wing and horizontal stabilizer, respectively. Also consider a discrete symmetrical vertical gust $\alpha_g = \frac{w_g}{Q_\infty}$. This gust reaches the wing first resulting in an increase of (for example) the aerodynamic force coefficient C_{Z_g}. Upon reaching the wing, the vertical gust will induce a change in the downwash angle ε. After an instant in time τ, equalling $\tau = \frac{l_h}{Q_\infty}$ [secs.] with l_h the horizontal tail-length and Q_∞ the airspeed, the downwash reaches the horizontal tailplane causing a change in the aerodynamic force on it, see also figure 11.4. The vertical gust in itself will reach the horizontal tailplane after an equal amount of time. Also for this analysis it is assumed that the positions of the aerodynamic center of the wing and the center of gravity coincide. The aerodynamic force along the Z_S-axis of $\mathcal{F}_S$ is written as,

$$Z_g = C_{Z_{\alpha_w}} \; \frac{1}{2}\rho Q_\infty^2 S \; \alpha_g + C_{Z_{\alpha_h}} \; \frac{1}{2}\rho Q_{\infty_h}^2 S_h \; \alpha_{h_g}$$

with Z_g the vertical gust's induced dimensional aerodynamic force in $\mathcal{F}_S$ and α_{h_g} the vertical gust-induced angle-of-attack at the horizontal tailplane's aerodynamic center. For the frequency-domain the latter is written as,

$$\alpha_{h_g}(\omega) = \alpha_g\, e^{-j\omega\tau} - \frac{\partial\varepsilon}{\partial\alpha} e^{-j\omega\tau}\alpha_g = \left(1 - \frac{\partial\varepsilon}{\partial\alpha}\right) e^{-j\omega\tau}\alpha_g = \left(1 - \frac{\partial\varepsilon}{\partial\alpha}\right) e^{-j\omega\frac{l_h}{Q_\infty}}\,\alpha_g$$

with ω the circular frequency given in [Rad/sec.]. The non-dimensional aerodynamic force along the Z_S-axis of the frame $\mathcal{F}_S$ is now written as, with $C_{Z_g} = \frac{Z_g}{\frac{1}{2}\rho Q_\infty^2 S}$,

$$C_{Z_g}(\omega) = C_{Z_{\alpha_w}}\alpha_g + C_{Z_{\alpha_h}}\left(\frac{Q_{\infty_h}}{Q_\infty}\right)^2 \frac{S_h}{S}\left(1 - \frac{\partial\varepsilon}{\partial\alpha}\right) e^{-j\omega\frac{l_h}{Q_\infty}}\,\alpha_g$$

and the aerodynamic FRF $\frac{C_{Z_g}}{\alpha_g}(\omega)$ defined as,

$$\frac{C_{Z_g}}{\alpha_g}(\omega) = C_{Z_{\alpha_w}} + C_{Z_{\alpha_h}}\left(\frac{Q_{\infty_h}}{Q_\infty}\right)^2 \frac{S_h}{S}\left(1 - \frac{\partial\varepsilon}{\partial\alpha}\right) e^{-j\omega\frac{l_h}{Q_\infty}}$$

Similar to the derivation of the steady and unsteady stability derivatives, this aerodynamic FRF is now expanded using a first-order Taylor polynomial approximation for the time-delay ($e^{-j\omega\tau} \approx 1 - j\omega\tau$), that is,

$$\begin{aligned}
\frac{C_{Z_g}}{\alpha_g}(\omega) &= C_{Z_{\alpha_w}} + C_{Z_{\alpha_h}}\left(\frac{Q_{\infty_h}}{Q_\infty}\right)^2 \frac{S_h}{S}\left(1 - \frac{\partial\varepsilon}{\partial\alpha}\right)\left(1 - j\omega\frac{l_h}{Q_\infty}\right) \\
&= C_{Z_{\alpha_w}} + C_{Z_{\alpha_h}}\left(\frac{Q_{\infty_h}}{Q_\infty}\right)^2 \frac{S_h}{S}\left(1 - \frac{\partial\varepsilon}{\partial\alpha}\right) - \\
&\quad C_{Z_{\alpha_h}}\left(\frac{Q_{\infty_h}}{Q_\infty}\right)^2 \frac{S_h}{S}\left(1 - \frac{\partial\varepsilon}{\partial\alpha}\right)\frac{l_h}{Q_\infty} j\omega \\
&= \left\{C_{Z_{\alpha_w}} + C_{Z_{\alpha_h}}\left(\frac{Q_{\infty_h}}{Q_\infty}\right)^2 \frac{S_h}{S}\left(1 - \frac{\partial\varepsilon}{\partial\alpha}\right)\right\} + \\
&\quad \left\{-C_{Z_{\alpha_h}}\left(\frac{Q_{\infty_h}}{Q_\infty}\right)^2 \frac{S_h l_h}{S\bar{c}}\left(1 - \frac{\partial\varepsilon}{\partial\alpha}\right)\right\}\frac{\bar{c}}{Q_\infty} j\omega \\
&= C_{Z_{\alpha_g}} + C_{Z_{\dot{\alpha}_g}}\frac{\bar{c}}{Q_\infty} j\omega
\end{aligned}$$

with $\bar{c}$ the mean aerodynamic chord, and,

$$C_{Z_{\alpha_g}} = C_{Z_\alpha} = C_{Z_{\alpha_w}} + C_{Z_{\alpha_h}}\left(\frac{Q_{\infty_h}}{Q_\infty}\right)^2 \frac{S_h}{S}\left(1 - \frac{\partial\varepsilon}{\partial\alpha}\right)$$

and,

$$\begin{aligned}
C_{Z_{\dot{\alpha}_g}} &= -C_{Z_{\alpha_h}}\left(\frac{Q_{\infty_h}}{Q_\infty}\right)^2 \frac{S_h l_h}{S\bar{c}}\left(1 - \frac{\partial\varepsilon}{\partial\alpha}\right) \\
&= C_{Z_{\alpha_h}}\left(\frac{Q_{\infty_h}}{Q_\infty}\right)^2 \frac{S_h l_h}{S\bar{c}}\frac{\partial\varepsilon}{\partial\alpha} - C_{Z_{\alpha_h}}\left(\frac{Q_{\infty_h}}{Q_\infty}\right)^2 \frac{S_h l_h}{S\bar{c}} \\
&= C_{Z_{\dot{\alpha}}} - C_{Z_q}
\end{aligned}$$

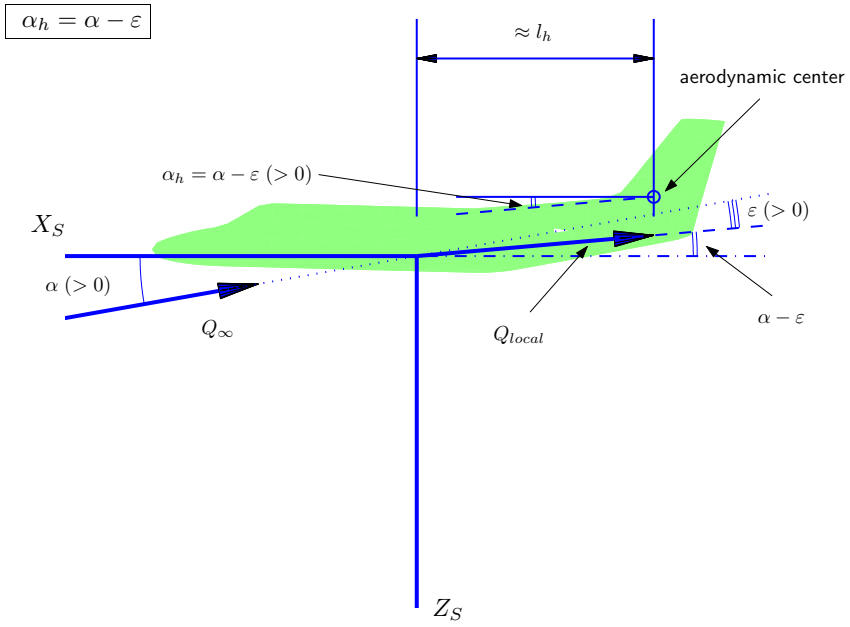


Figure 11.3: Relation between the angle-of-attack α, the downwash angle ε and the horizontal tailplane's angle-of-attack α_h (with the horizontal stabilizer angle of incidence $i_h = 0\ [^o]$).

with the definitions of the stability derivative $C_{Z_{\dot{\alpha}}}$ and C_{Z_q} according to equations (11.33) and (11.35), respectively, which are the theoretical horizontal tailplane contributions to the stability derivatives $C_{Z_{\dot{\alpha}}}$ and C_{Z_q}, see also reference [29].

Similar expressions for the gust derivatives for the aerodynamic force along the X_S-axis and the aerodynamic moment about the Y_S-axis are obtained, see also equation (11.28). In this derivation of the DUT-model's steady and unsteady gust derivatives only a wing-horizontal tailplane configuration has been considered. Also, both the wing and horizontal tailplane's aerodynamics were considered steady, that is only aerodynamic stiffness terms were used in all derivations. Furthermore, no aerodynamic interference effects have been included in the gust derivatives' derivations. Finally, similar to the derivation of the unsteady gust derivatives with respect to 1D lateral gusts, the aerodynamic forces and moment are linearized using a first-order Taylor polynomial approximation for the time-delay.

11.3.4 2D Anti-symmetrical longitudinal gust fields

For the 2D anti-symmetrical gust fields, in this section the 2D anti-symmetrical gust velocity component u_g is considered. The asymmetrical aerodynamic force and moments caused by these gust fields will be discussed here.

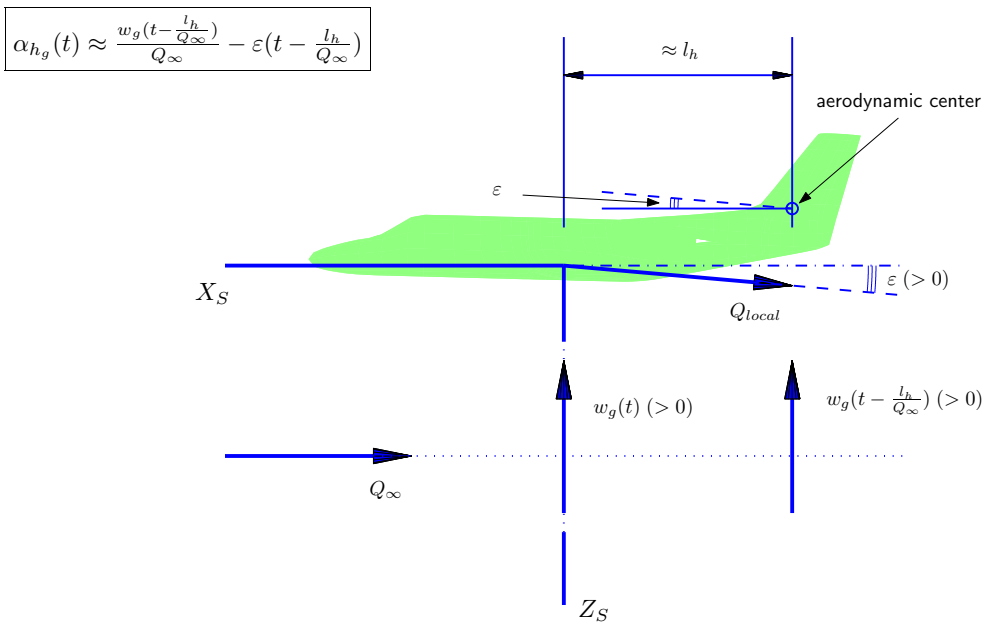


Figure 11.4: Definition of the horizontal tailplane angle-of-attack α_{h_g} due to the 1D vertical atmospheric turbulence velocity component w_g (with the horizontal stabilizer angle of incidence $i_h = 0\ [^o]$).

For the derivation of the asymmetrical aerodynamic force and moments, the longitudinal 2D atmospheric turbulence velocity component $u_{g_2}(x, y)$-field is used according to equation (11.4),

$$u_{g_2}(x, y) = u_{g_{max}}\ sin\,(\Omega_x x)\ \ sin\,(\Omega_y y)$$

In the following the 2D longitudinal gust velocity component in the $O_E X_E Y_E$-plane (Earth-Fixed Frame of Reference $\mathcal{F}_E$) will be referred to as $u_g(x, y)$. Omitting the index 2 of the anti-symmetrical gust field $u_{g_2}(x, y)$, it is written as,

$$u_g(x, y) = u'_g\ \ \sin\,(\Omega_y y) \tag{11.36}$$

with,

$$u'_g = u_{g_{max}}\ \ \sin\,(\Omega_x x)$$

and Ω_x the spatial frequency along the X_E-axis, Ω_y the spatial frequency along the Y_E-axis, x and y the positions in the frame $\mathcal{F}_E$ and $u_{g_{max}}$ the 2D longitudinal gust field amplitude.

Due to variations of $u_g(x, y)$ along the Y_E-axis, both a rolling- and yawing moment will act on the aircraft, see also figure 11.5. For the derivation of the DUT-model's aerodynamic moments, only the wing's contribution to the aerodynamic rolling moment L_g and

the aerodynamic yawing moment N_g along the X_S- and the Z_S-axis of the frame $\mathcal{F}_S$, respectively, will be taken into account. The aerodynamic sideforce Y_g along the Y_S-axis of the frame $\mathcal{F}_S$ due to the atmospheric turbulence velocity component $u_g(x,y)$ is assumed negligible in the current model.
The calculation of, for example, the rolling moment coefficient C_{ℓ_g} is based on the assumption that the additional lift due to the considered atmospheric turbulence velocity component can be determined by means of strip-theory. A wing's chordwise strip of width dy at a distance y from the plane of symmetry contributes to the increment of the rolling moment according to, see also figure 11.5,

$$\begin{aligned} dL_g &= -c_\ell(y)\ \frac{1}{2}\rho\left\{[Q_\infty + u_g(x,y)]^2 - Q_\infty^2\right\}\ c(y)\ y\ dy \\ &= -c_\ell(y)\ \frac{1}{2}\rho\left\{2u_g(x,y)\ Q_\infty + (u_g(x,y))^2\right\}\ c(y)\ y\ dy \end{aligned} \tag{11.37}$$

with $c_\ell(y)$ the aerofoil lift-coefficient, $c(y)$ the aerofoil chord-length, ρ air-density, and y the distance taken from the aircraft plane of symmetry in $\mathcal{F}_S$.
Assuming that $(u_g(x,y))^2$ is sufficiently small (that is $|u_g(x,y)| << |Q_\infty|$), and using equation (11.36), after some elaboration equation (11.37) becomes,

$$dL_g = -c_\ell(y)\ \rho\ Q_\infty\ u_g'\ sin\,(\Omega_y y)\ \ c(y)\ y\ dy$$

The rolling moment L_g due to the 2D gust field $u_g(x,y)$ becomes,

$$L_g = \int_{-\frac{b}{2}}^{\frac{b}{2}} dL_g = 2\int_0^{\frac{b}{2}} dL_g = -2\rho Q_\infty\ u_g' \int_0^{\frac{b}{2}} c_\ell(y)\ c(y)\ sin\,(\Omega_y y)\ \ y\ dy$$

The rolling moment is now given in terms of the non-dimensional coefficient C_{ℓ_g},

$$C_{\ell_g} = \frac{L_g}{\frac{1}{2}\rho Q_\infty^2 Sb} = -\frac{4}{Sb}\frac{u_g'}{Q_\infty}\int_0^{\frac{b}{2}} c_\ell(y)\ c(y)\ sin\,(\Omega_y y)\ \ y\ dy$$

Next, the non-dimensional rolling moment coefficient C_{ℓ_g}, using the gust derivative $C_{\ell_{u_g}}(\Omega_y\ \frac{b}{2})$, is written as,

$$C_{\ell_g} = C_{\ell_{u_g}}(\Omega_y\ \frac{b}{2})\ \hat{u}_g \tag{11.38}$$

with,

$$\hat{u}_g = \frac{u_g'}{Q_\infty}$$

and,

$$C_{\ell_{u_g}}(\Omega_y\ \frac{b}{2}) = -\frac{4}{Sb}\int_0^{\frac{b}{2}} c_\ell(y)\ c(y)\ sin\,(\Omega_y y)\ \ y\ dy \tag{11.39}$$

For sufficiently small values of $\Omega_y \frac{b}{2}$, that is for large spatial wave lengths of $u_g(x,y)$ along the Y_E/Y_S-axes, the gust velocity $u_g(x,y)$ varies approximately linear along the wingspan. For these small values of $\Omega_y \frac{b}{2}$, $u_g(x,y)$ can be approximated by replacing $sin\,(\Omega_y y)$ by $\Omega_y y$,

$$u_g(x,y) = u'_g\ \Omega_y y$$

This gust velocity distribution corresponds to the additional velocity due to a constant yaw-rate r, or,

$$\Delta u = -ry$$

When further elaborating the expression for $C_{\ell_{u_g}}$, use is made of this similarity. The rolling moment acting on the wing due to a constant yaw-rate r can also be calculated by means of strip-theory. Due to a yawing motion, a wing element of width dy located at a distance y from the plane of symmetry contributes to the increment of the rolling moment according to,

$$\begin{aligned} dL &= -c_\ell(y)\ \frac{1}{2}\rho \left\{ [Q_\infty + \Delta u]^2 - Q_\infty^2 \right\}\ c(y)\ y\ dy \\ &= -c_\ell(y)\ \frac{1}{2}\rho \left\{ 2\Delta u\ Q_\infty + (\Delta u)^2 \right\}\ c(y)\ y\ dy \end{aligned} \tag{11.40}$$

or with $\Delta u = -ry$, and assuming $\Delta u << Q_\infty$ resulting in $(\Delta u)^2 \approx 0$ (thus assuming small yaw-rates),

$$dL = c_\ell(y)\ \frac{1}{2}\rho\ 2Q_\infty\ ry\ c(y)\ y\ dy = c_\ell(y)\ \rho\ Q_\infty\ r\ c(y)\ y^2\ dy$$

The total rolling moment acting on the wing due to a yawing motion becomes,

$$L = \int_{-\frac{b}{2}}^{\frac{b}{2}} dL = 2 \int_0^{\frac{b}{2}} dL = 2\rho Q_\infty\ r \int_0^{\frac{b}{2}} c_\ell(y)\ c(y)\ y^2\ dy = C_{\ell_{r_w}}\ \frac{rb}{2Q_\infty} \frac{1}{2}\rho Q_\infty^2 Sb$$

or for the rolling moment coefficient $C_\ell = \frac{L}{\frac{1}{2}\rho Q_\infty^2 Sb}$,

$$C_\ell = \frac{2\rho Q_\infty\ r \int_0^{\frac{b}{2}} c_\ell(y)\ c(y)\ y^2\ dy}{\frac{1}{2}\rho Q_\infty^2 Sb} = C_{\ell_{r_w}}\ \frac{rb}{2Q_\infty}$$

with, after some elaboration, the contribution of the wing to the stability derivative C_{ℓ_r},

$$C_{\ell_{r_w}} = \frac{8}{Sb^2} \int_0^{\frac{b}{2}} c_\ell(y)\ c(y)\ y^2\ dy \tag{11.41}$$

The expression given in equation (11.41) for $C_{\ell_{r_w}}$ is now related to $C_{\ell_{u_g}}$ given in equation (11.39), or,

$$C_{\ell_{u_g}}(\Omega_y \frac{b}{2}) = -C_{\ell_{r_w}} \; \frac{b}{2} \frac{\int_0^{\frac{b}{2}} c_\ell(y) \; c(y) \; sin\,(\Omega_y y) \;\; y \; dy}{\int_0^{\frac{b}{2}} c_\ell(y) \; c(y) \; y^2 \; dy}$$

Introducing the non-dimensional function $h(\Omega_y \frac{b}{2})$ according to,

$$h(\Omega_y \frac{b}{2}) = \frac{b}{2} \frac{\int_0^{\frac{b}{2}} c_\ell(y) \; c(y) \; sin\,(\Omega_y y) \;\; y \; dy}{\int_0^{\frac{b}{2}} c_\ell(y) \; c(y) \; y^2 \; dy} \tag{11.42}$$

the aerodynamic moment coefficient $C_{\ell_{u_g}}$ is written as,

$$C_{\ell_{u_g}}(\Omega_y \frac{b}{2}) = -C_{\ell_{r_w}} \; h(\Omega_y \frac{b}{2}) \tag{11.43}$$

According to reference [30], in an identical manner the aerodynamic moment along the Z_S-axis of the frame $\mathcal{F}_S$ acting on the wing due to the longitudinal gust velocity $u_g(x, y)$ is derived. This moment is written as,

$$N_g = C_{n_g} \; \frac{1}{2} \rho Q_\infty^2 S b$$

with,

$$C_{n_g} = C_{n_{u_g}}(\Omega_y \frac{b}{2}) \; \hat{u}_g$$

and,

$$C_{n_{u_g}}(\Omega_y \frac{b}{2}) = -C_{n_{r_w}} \; h(\Omega_y \frac{b}{2}) \tag{11.44}$$

with $h(\Omega_y \frac{b}{2})$ supposedly according to equation (11.42), and,

$$C_{n_{r_w}} = -\frac{8}{S b^2} \int_0^{\frac{b}{2}} c_d(y) \; c(y) \; y^2 \; dy \tag{11.45}$$

However, when deriving the gust derivative $C_{n_g} = C_{n_{u_g}}(\Omega_y \frac{b}{2})$, while following the same lines of derivation for the gust derivative $C_{\ell_g} = C_{\ell_{u_g}}(\Omega_y \frac{b}{2})$, contary to reference [30] it has to be concluded that the expression for the function $h(\Omega_y \frac{b}{2})$ should equal,

$$h(\Omega_y \frac{b}{2}) = \frac{b}{2} \frac{\int_0^{\frac{b}{2}} c_d(y) \; c(y) \; sin\,(\Omega_y y) \;\; y \; dy}{\int_0^{\frac{b}{2}} c_d(y) \; c(y) \; y^2 \; dy} \tag{11.46}$$

with $c_d(y)$ the aerofoil drag-coefficient (see also figure 11.5). Since the definition of the non-dimensional function $h(\Omega_y \frac{b}{2})$ is inconclusive in reference [30], its definition according to reference [34] will be used throughout this thesis. Following this reference, the approximation of equation (11.42) is written as,

$$h(\Omega_y \frac{b}{2}) = \frac{b}{2} \frac{\int_0^{\frac{b}{2}} sin\,(\Omega_y y)\ \ y\ dy}{\int_0^{\frac{b}{2}} y^2\ dy} \tag{11.47}$$

which in closed form becomes, see reference [34],

$$h(\Omega_y \frac{b}{2}) = 3 \frac{sin\,(\Omega_y \frac{b}{2}) - (\Omega_y \frac{b}{2})\, cos\,(\Omega_y \frac{b}{2})}{(\Omega_y \frac{b}{2})^2} \tag{11.48}$$

According to reference [34] the motivation for using the approximation of $h(\Omega_y \frac{b}{2})$ (as given in equation (11.47)) follows from the assumption that for small Ω_y values the $c_\ell c$-distribution has a neglible effect on it. However, no comments are made on the validity of equation (11.47) with respect to $c_d c$-distributions.
In the following section the gust derivatives with respect to the 2D vertical gust velocity component w_g are given. In this section other definitions of the function $h(\Omega_y \frac{b}{2})$ will be discussed.

11.3.5 2D Anti-symmetrical vertical gust fields

For the 2D anti-symmetrical gust fields, in this section the 2D anti-symmetrical gust velocity component w_g is considered. Similar to section 11.3.4, the asymmetrical aerodynamic force and moments caused by these gust fields will be discussed here.

For the derivation of the asymmetrical aerodynamic force and moments, the vertical 2D atmospheric turbulence velocity component $w_{g_2}(x, y)$-field is used according to equation (11.6), or,

$$w_{g_2}(x, y) = w_{g_{max}}\ sin\,(\Omega_x x)\ \ sin\,(\Omega_y y)$$

Similar to the definition of $u_g(x, y)$, in the following the 2D vertical gust velocity component in the $O_E X_E Y_E$-plane will be referred to as $w_g(x, y)$. Omitting the index 2 of the anti-symmetrical gust field $w_{g_2}(x, y)$, it is written as,

$$w_g(x, y) = w'_g\ \ \sin\,(\Omega_y y) \tag{11.49}$$

with,

$$w'_g = w_{g_{max}}\ \ \sin\,(\Omega_x x)$$

and Ω_x the spatial frequency along the X_E-axis, Ω_y the spatial frequency along the Y_E-axis, x and y the positions in $\mathcal{F}_E$ and $w_{g_{max}}$ the 2D vertical gust field amplitude.

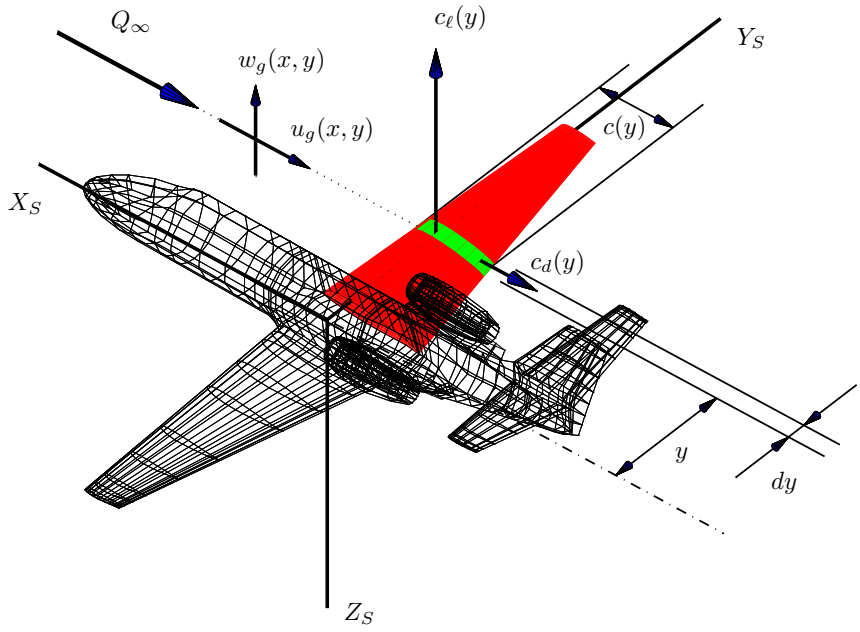


Figure 11.5: The contribution to the rolling- and yawing moment of a right-hand wing chord-wise strip, due to 2D longitudinal ($u_g(x,y)$) and due to 2D vertical ($w_g(x,y)$) gusts.

Due to variations of $w_g(x,y)$ along the Y_E-axis, both a rolling- and yawing moment will act on the aircraft, see also figure 11.5. Although the 2D vertical anti-symmetrical gust is given as $w_g(x,y)$ in figure 11.5, in the following the non-dimensional gust-induced angle-of-attack $\alpha_g(x,y) = \frac{w_g(x,y)}{Q_\infty}$ is used.
Similar to the derivation of the aerodynamic force and moments due to the 2D anti-symmetrical longitudinal gust fields u_g, also in this case the wing's contribution to the aerodynamic rolling moment L_g and the aerodynamic yawing moment N_g along the X_S- and the Z_S-axis of the frame $\mathcal{F}_S$, respectively, will be taken into account only. The aerodynamic sideforce Y_g along the Y_S-axis of the frame $\mathcal{F}_S$ due to the gust-induced angle-of-attack $\alpha_g(x,y)$ is assumed negligible.
Similar to the rolling moment coefficient due to the 2D anti-symmetrical longitudinal gust fields, the calculation of this coefficient due to 2D anti-symmetrical vertical gust fields is based on the assumption that the additional lift due to the vertical gust velocity component can be determined by means of strip-theory. A wing chordwise strip of width dy at a distance y from the plane of symmetry contributes to the increment of the rolling moment according to, see also figure 11.5,

$$\begin{aligned} dL_g &= -\{c_{\ell_\alpha}(y)\ (\alpha_{trim} + \alpha_g(x,y)) + c_{\ell_0}\}\ \frac{1}{2}\rho Q_\infty^2\ c(y)\ y\ dy - \\ &\quad -\{c_{\ell_\alpha}(y)\ \alpha_{trim} + c_{\ell_0}\}\ \frac{1}{2}\rho Q_\infty^2\ c(y)\ y\ dy \\ &= -c_{\ell_\alpha}(y)\ \alpha_g(x,y)\ \frac{1}{2}\rho Q_\infty^2\ c(y)\ y\ dy \end{aligned} \tag{11.50}$$

with $c_{\ell_\alpha}(y)$ the aerofoil lift-curve slope, α_{trim} the angle-of-attack during steady flight, c_{ℓ_0} the aerofoil lift-coefficient for zero angle-of-attack, $c(y)$ the local aerofoil chord-length, ρ air-density, Q_∞ the airspeed and y the distance taken from the aircraft's plane of symmetry in the frame $\mathcal{F}_S$.
Using equation (11.49), after some elaboration equation (11.50) becomes,

$$dL_g = -c_{\ell_\alpha}(y)\ \alpha'_g\ sin\,(\Omega_y y)\ \ \frac{1}{2}\rho Q_\infty^2\ c(y)\ y\ dy$$

with $\alpha'_g = \frac{w_{g_{max}}}{Q_\infty}\ \sin(\Omega_x x)$.
The rolling moment L_g due to the 2D gust field, given as $\alpha_g(x,y)$, becomes,

$$L_g = \int_{-\frac{b}{2}}^{\frac{b}{2}} dL_g = 2\int_0^{\frac{b}{2}} dL_g = -\rho Q_\infty^2\ \alpha'_g \int_0^{\frac{b}{2}} c_{\ell_\alpha}(y)\ c(y)\ sin\,(\Omega_y y)\ \ y\ dy$$

and it is now given in terms of the non-dimensional coefficient C_{ℓ_g},

$$C_{\ell_g} = \frac{L_g}{\frac{1}{2}\rho Q_\infty^2 Sb} = -\frac{2}{Sb}\ \alpha'_g \int_0^{\frac{b}{2}} c_{\ell_\alpha}(y)\ c(y)\ sin\,(\Omega_y y)\ \ y\ dy$$

Next, the non-dimensional rolling moment coefficient C_{ℓ_g}, using the gust derivative $C_{\ell_{\alpha_g}}(\Omega_y\ \frac{b}{2})$, is written as,

$$C_{\ell_g} = C_{\ell_{\alpha_g}}(\Omega_y\ \frac{b}{2})\ \alpha'_g \tag{11.51}$$

with,

$$C_{\ell_{\alpha_g}}(\Omega_y\ \frac{b}{2}) = -\frac{2}{Sb}\int_0^{\frac{b}{2}} c_{\ell_\alpha}(y)\ c(y)\ sin\,(\Omega_y y)\ \ y\ dy \tag{11.52}$$

For sufficiently small values of $\Omega_y \frac{b}{2}$, that is for large spatial wave lengths of $\alpha_g(x,y)$ along the Y_E/Y_S-axes, the gust-induced angle-of-attack $\alpha_g(x,y)$ varies approximately linear along the wingspan. For these small values of $\Omega_y \frac{b}{2}$, $\alpha_g(x,y)$ can be approximated by replacing $sin\,(\Omega_y y)$ by $\Omega_y y$,

$$\alpha_g(x,y) = \alpha'_g\ \Omega_y y$$

This angle-of-attack distribution corresponds to the additional angle-of-attack due to a constant roll-rate p, or,

$$\Delta\alpha = \frac{py}{Q_\infty}$$

When further elaborating the expression for $C_{\ell_{\alpha_g}}$, use is made of this similarity. The rolling moment acting on the wing due to a constant roll-rate p can also be calculated by

means of strip-theory. Due to a rolling motion, a wing element of width dy located at a distance y from the plane of symmetry contributes to the increment of the rolling moment according to,

$$\begin{aligned} dL &= -\{c_{\ell_\alpha}(y)\ (\alpha_{trim}+\Delta\alpha)+c_{\ell_0}\}\ \frac{1}{2}\rho Q_\infty^2\ c(y)\ y\ dy - \\ &\quad -\{c_{\ell_\alpha}(y)\ \alpha_{trim}+c_{\ell_0}\}\ \frac{1}{2}\rho Q_\infty^2\ c(y)\ y\ dy \\ &= -c_{\ell_\alpha}(y)\ \Delta\alpha\ \frac{1}{2}\rho Q_\infty^2\ c(y)\ y\ dy \end{aligned} \tag{11.53}$$

or with $\Delta\alpha = \frac{py}{Q_\infty}$,

$$dL = -c_{\ell_\alpha}(y)\ \frac{1}{2}\rho\ Q_\infty^2\ \frac{py}{Q_\infty}\ c(y)\ y\ dy$$

The total rolling moment acting on the wing due to a rolling motion becomes,

$$L = \int_{-\frac{b}{2}}^{\frac{b}{2}} dL = 2\int_0^{\frac{b}{2}} dL = -2\frac{1}{2}\rho Q_\infty^2\ p\int_0^{\frac{b}{2}} c_{\ell_\alpha}(y)\ c(y)\ y^2\ dy = C_{\ell_{p_w}}\ \frac{pb}{2Q_\infty}\frac{1}{2}\rho Q_\infty^2 Sb$$

or for the rolling moment coefficient $C_\ell = \frac{L}{\frac{1}{2}\rho Q_\infty^2 Sb}$,

$$C_\ell = \frac{-\rho Q_\infty^2\ p\int_0^{\frac{b}{2}} c_{\ell_\alpha}(y)\ c(y)\ y^2\ dy}{\frac{1}{2}\rho Q_\infty^2 Sb} = C_{\ell_{p_w}}\ \frac{pb}{2Q_\infty}$$

with, after some elaboration, the wing's contribution to the stability derivative C_{ℓ_p} becomes,

$$C_{\ell_{p_w}} = -\frac{4}{Sb^2}\int_0^{\frac{b}{2}} c_{\ell_\alpha}(y)\ c(y)\ y^2\ dy \tag{11.54}$$

The expression given in equation (11.54) for $C_{\ell_{p_w}}$ is now related to $C_{\ell_{\alpha_g}}$ given in equation (11.52), or,

$$C_{\ell_{\alpha_g}}(\Omega_y\frac{b}{2}) = C_{\ell_{p_w}}\ \frac{b}{2}\frac{\int_0^{\frac{b}{2}} c_{\ell_\alpha}(y)\ c(y)\ sin\,(\Omega_y y)\ \ y\ dy}{\int_0^{\frac{b}{2}} c_{\ell_\alpha}(y)\ c(y)\ y^2\ dy}$$

With the non-dimensional function $h(\Omega_y\frac{b}{2})$ according to,

$$h(\Omega_y\frac{b}{2}) = \frac{b}{2}\frac{\int_0^{\frac{b}{2}} c_{\ell_\alpha}(y)\ c(y)\ sin\,(\Omega_y y)\ \ y\ dy}{\int_0^{\frac{b}{2}} c_{\ell_\alpha}(y)\ c(y)\ y^2\ dy} \tag{11.55}$$

the aerodynamic moment coefficient $C_{\ell_{\alpha_g}}$ is written as,

$$C_{\ell_{\alpha_g}}(\Omega_y \frac{b}{2}) = C_{\ell_{p_w}}\ h(\Omega_y \frac{b}{2}) \tag{11.56}$$

Similar to the definition of $C_{\ell_{u_g}}$, according to reference [30] in an identical manner the aerodynamic yawing moment along the Z_S-axis of the frame $\mathcal{F}_S$ acting on the wing due to the vertical gust velocity induced angle-of-attack $\alpha_g(x, y)$ is derived. This moment is written as,

$$N_g = C_{n_g}\ \frac{1}{2}\rho Q_\infty^2 S b$$

with,

$$C_{n_g} = C_{n_{\alpha_g}}(\Omega_y \frac{b}{2})\ \alpha_g'$$

and,

$$C_{n_{\alpha_g}}(\Omega_y \frac{b}{2}) = C_{n_{p_w}}\ h(\Omega_y \frac{b}{2}) \tag{11.57}$$

and,

$$C_{n_{p_w}} = \frac{4}{Sb^2} \int_0^{\frac{b}{2}} c_{d_\alpha}(y)\ c(y)\ y^2\ dy \tag{11.58}$$

When deriving the gust derivative $C_{n_g} = C_{n_{\alpha_g}}(\Omega_y \frac{b}{2})$, while following the same lines of derivation for the gust derivative $C_{\ell_g} = C_{\ell_{\alpha_g}}(\Omega_y \frac{b}{2})$, the expression for the function $h(\Omega_y \frac{b}{2})$ now equals,

$$h(\Omega_y \frac{b}{2}) = \frac{b}{2} \frac{\int_0^{\frac{b}{2}} c_{d_\alpha}(y)\ c(y)\ sin\,(\Omega_y y)\ \ y\ dy}{\int_0^{\frac{b}{2}} c_{d_\alpha}(y)\ c(y)\ y^2\ dy} \tag{11.59}$$

with $c_{d_\alpha}(y)$ the aerofoil drag-coefficient (see also figure 11.5).

Since the definition of the non-dimensional function $h(\Omega_y \frac{b}{2})$ in reference [30] is also inconclusive with respect to the derivation of the gust derivatives with respect to 2D anti-symmetrical vertical gusts, its definition according to reference [34] given in equation (11.47) will be used throughout this thesis.

11.4 The atmospheric turbulence PSD-functions

11.4.1 1D gust fields

The PSD-functions for the 1D atmospheric turbulence velocity components u_g, v_g and w_g are given in chapter 2. They are given here as a function of the spatial frequency Ω_x (or in chapter 2 given as Ω_1), see also reference [30].

In appendix H similar PSD-functions are given for use in conjunction with the aircraft equations of motion. These functions now, however, are given for the non-dimensional gust inputs $\hat{u}_g = \frac{u_g}{Q_\infty}$, $\beta_g = \frac{v_g}{Q_\infty}$ and $\alpha_g = \frac{w_g}{Q_\infty}$, while they are also given as a function of the circular frequency $\omega = \Omega_x Q_\infty$ [Rad/sec], with $\Omega_x = \frac{\omega}{Q_\infty}$ the spatial frequency along the X_E-axis of the frame $\mathcal{F}_E$.

As a function of the circular frequency ω, the PSD-functions are summarized as,

$$S_{\hat{u}_g\hat{u}_g}(\omega) = 2\sigma^2 \frac{L_g}{Q_\infty} \frac{1}{1+\left(\frac{\omega L_g}{Q_\infty}\right)^2} \tag{11.60}$$

$$S_{\beta_g\beta_g}(\omega) = \sigma^2 \frac{L_g}{Q_\infty} \frac{1+3\left(\frac{\omega L_g}{Q_\infty}\right)^2}{\left\{1+\left(\frac{\omega L_g}{Q_\infty}\right)^2\right\}^2} \tag{11.61}$$

$$S_{\alpha_g\alpha_g}(\omega) = \sigma^2 \frac{L_g}{Q_\infty} \frac{1+3\left(\frac{\omega L_g}{Q_\infty}\right)^2}{\left\{1+\left(\frac{\omega L_g}{Q_\infty}\right)^2\right\}^2} \tag{11.62}$$

for the non-dimensional gust velocity components $\hat{u}_g = \frac{u_g}{Q_\infty}$, $\beta_g = \frac{v_g}{Q_\infty}$ and $\alpha_g = \frac{w_g}{Q_\infty}$, respectively, with $\sigma^2 = \frac{1}{Q_\infty^2}$.

11.4.2 2D gust fields

Similar to the PSD-functions for the 1D atmospheric turbulence velocity components, for the 2D atmospheric turbulence velocity components u_g, v_g and w_g these functions are also given in chapter 2. They are given as a function of the spatial frequencies Ω_x and Ω_y (or in chapter 2 given as Ω_1 and Ω_2, respectively), see also reference [30]. As a function of the non-dimensional spatial frequencies $\Omega_x L_g$ and $\Omega_y L_g$ the 2D PSD-functions are summarized as,

$$S_{u_g u_g}(\Omega_x L_g, \Omega_y L_g) = \pi\sigma_{u_g}^2 \frac{1+\Omega_x^2 L_g^2 + 4\Omega_y^2 L_g^2}{\left(1+\Omega_x^2 L_g^2 + \Omega_y^2 L_g^2\right)^{5/2}} \tag{11.63}$$

$$S_{v_g v_g}(\Omega_x L_g, \Omega_y L_g) = \pi\sigma_{v_g}^2 \frac{1+4\Omega_x^2 L_g^2 + \Omega_y^2 L_g^2}{\left(1+\Omega_x^2 L_g^2 + \Omega_y^2 L_g^2\right)^{5/2}} \tag{11.64}$$

$$S_{w_g w_g}(\Omega_x L_g, \Omega_y L_g) = 3\pi\sigma_{w_g}^2 \frac{\Omega_x^2 L_g^2 + \Omega_y^2 L_g^2}{\left(1 + \Omega_x^2 L_g^2 + \Omega_y^2 L_g^2\right)^{5/2}} \tag{11.65}$$

for the atmospheric turbulence velocity components u_g, v_g and w_g, respectively, and with $\sigma_{u_g}^2 = \sigma_{v_g}^2 = \sigma_{w_g}^2$ the atmospheric turbulence variance (given in $[m^2/s^2]$) and with L_g the atmospheric turbulence scale length (in [m]).

Also similar to the 1D PSD-functions, in appendix H these functions are given for use in conjunction with the aircraft equations of motion. They are summarized for the non-dimensional gust inputs $\hat{u}_g = \frac{u_g}{Q_\infty}$, $\beta_g = \frac{v_g}{Q_\infty}$ and $\alpha_g = \frac{w_g}{Q_\infty}$, while they are also given as a function of the circular frequency $\omega = \Omega_x Q_\infty$ [Rad/sec] and the spatial frequency Ω_y along the Y_E-axis of the frame $\mathcal{F}_E$. Similar to the 2D PSD-functions given in equations (11.63), (11.64) and (11.65), these functions are shown in equations (H.1), (H.2) and (H.3), respectively. For the sake of completeness, for the non-dimensional gust velocity components $\hat{u}_g = \frac{u_g}{Q_\infty}$, $\beta_g = \frac{v_g}{Q_\infty}$ and $\alpha_g = \frac{w_g}{Q_\infty}$ these PSD-functions are summarized as,

$$S_{\hat{u}_g \hat{u}_g}(\omega, \Omega_y) = \pi\sigma^2 \frac{L_g^2}{Q_\infty} \frac{1 + \left(\frac{\omega L_g}{Q_\infty}\right)^2 + 4\left(\Omega_y L_g\right)^2}{\left\{1 + \left(\frac{\omega L_g}{Q_\infty}\right)^2 + \left(\Omega_y L_g\right)^2\right\}^{5/2}} \tag{11.66}$$

$$S_{\beta_g \beta_g}(\omega, \Omega_y) = \pi\sigma^2 \frac{L_g^2}{Q_\infty} \frac{1 + 4\left(\frac{\omega L_g}{Q_\infty}\right)^2 + \left(\Omega_y L_g\right)^2}{\left\{1 + \left(\frac{\omega L_g}{Q_\infty}\right)^2 + \left(\Omega_y L_g\right)^2\right\}^{5/2}} \tag{11.67}$$

and,

$$S_{\alpha_g \alpha_g}(\omega, \Omega_y) = 3\pi\sigma^2 \frac{L_g^2}{Q_\infty} \frac{\left(\frac{\omega L_g}{Q_\infty}\right)^2 + \left(\Omega_y L_g\right)^2}{\left\{1 + \left(\frac{\omega L_g}{Q_\infty}\right)^2 + \left(\Omega_y L_g\right)^2\right\}^{5/2}} \tag{11.68}$$

respectively, with $\sigma^2 = \frac{1}{Q_\infty^2}$.

For the DUT-model the cross PSD-function according to equation (H.4) is not considered, thus neglecting the correlation between the 2D atmospheric turbulence velocity components u_g and v_g.

11.4.3 Effective 1D PSD-functions for 2D gust fields

In section 11.3 the aerodynamic moment coefficients with respect to the 2D anti-symmetrical gust fields u_g and w_g have been derived. It was shown that the aerodynamic moments C_{ℓ_g} and C_{n_g} are dependent of the spatial frequencies Ω_x and Ω_y.
In the expressions given in section 11.3, only Ω_x can directly be related to time; an aircraft traveling with an airspeed Q_∞ through an elementary field of turbulent flow with

the spatial frequency Ω_x undergoes the changes of u_g, v_g and w_g with a circular frequency ω, that is,

$$\omega = \Omega_x \; Q_\infty$$

The influence of the spatial frequency Ω_y on the aerodynamic coefficients C_{ℓ_g} and C_{n_g} is now given in more detail for both the anti-symmetrical u_g- and w_g gust fields. As an example the aerodynamic rolling moment due to $u_g(x,y)$ is considered here.
In the turbulent atmosphere all values of Ω_y may be considered to occur simultaneously. It is possible, however, to evaluate the mean or effective value of the amplitude of C_{ℓ_g} due to $u_g(x,y)$ as a function of the spatial frequency Ω_x. This mean value of C_{ℓ_g}, caused by the contributions of all values of the spatial frequency Ω_y, is determined with the aid of the 2D PSD-function of the gust velocity at a given Ω_x. Using the aerodynamic moment coefficient according to equation (11.38),

$$C_{\ell_g} = C_{\ell_{u_g}}(\Omega_y \frac{b}{2}) \; \hat{u}_g$$

the PSD-function of the aerodynamic moment coefficient C_{ℓ_g} is defined as,

$$\begin{aligned} S_{C_{\ell_g} C_{\ell_g}}(\Omega_x L_g, \Omega_y L_g, B) &= \left\{ C_{\ell_{u_g}}(\Omega_y \frac{b}{2}) \; \hat{u}_g \right\}^* \left\{ \hat{u}_g \; C_{\ell_{u_g}}(\Omega_y \frac{b}{2}) \right\} \\ &= C^2_{\ell_{u_g}}(\Omega_y \frac{b}{2}) \; S_{\hat{u}_g \hat{u}_g}(\Omega_x L_g, \Omega_y L_g) \end{aligned}$$

with * denoting the complex conjungate, $B = \frac{b}{2L_g}$, $S_{\hat{u}_g \hat{u}_g}(\Omega_x L_g, \Omega_y L_g)$ the PSD-function similar to equation (11.63), however, now with the gust velocity component variance $\sigma^2_{\hat{u}_g} = \frac{\sigma^2_{u_g}}{Q^2_\infty}$. Using equation (11.43) for the coefficient $C_{\ell_{u_g}}(\Omega_y \frac{b}{2})$ and equation (11.63) for $S_{\hat{u}_g \hat{u}_g}(\Omega_x L_g, \Omega_y L_g)$, the PSD-function for $S_{C_{\ell_g} C_{\ell_g}}(\Omega_x L_g, \Omega_y L_g, B)$ is written as,

$$S_{C_{\ell_g} C_{\ell_g}}(\Omega_x L_g, \Omega_y L_g, B) = C^2_{\ell_{r_w}} \; h^2(\Omega_y \frac{b}{2}) \; \pi \; \sigma^2_{\hat{u}_g} \frac{1 + \Omega_x^2 L_g^2 + 4\Omega_y^2 L_g^2}{\left(1 + \Omega_x^2 L_g^2 + \Omega_y^2 L_g^2\right)^{5/2}}$$

with the function $h(\Omega_y \frac{b}{2})$ given in equations (11.47) and (11.48).

The so-called Effective 1D PSD-function is calculated by integration over all non-dimensional spatial frequencies $\Omega_y L_g$,

$$\begin{aligned} S_{C_{\ell_g} C_{\ell_g}}(\Omega_x L_g, B) &= \frac{1}{2\pi} \int_{-\infty}^{\infty} S_{C_{\ell_g} C_{\ell_g}}(\Omega_x L_g, \Omega_y L_g, B) \; d\,(\Omega_y L_g) \\ &= \frac{1}{\pi} \int_{0}^{\infty} S_{C_{\ell_g} C_{\ell_g}}(\Omega_x L_g, \Omega_y L_g, B) \; d\,(\Omega_y L_g) = \end{aligned}$$

or,

$$S_{C_{\ell_g} C_{\ell_g}}(\Omega_x L_g, B) = \sigma^2_{\hat{u}_g} \; C^2_{\ell_{r_w}} \int_0^\infty h^2(\Omega_y \frac{b}{2}) \; \frac{1 + \Omega_x^2 L_g^2 + 4\Omega_y^2 L_g^2}{\left(1 + \Omega_x^2 L_g^2 + \Omega_y^2 L_g^2\right)^{5/2}} \; d(\Omega_y L_g)$$

This 1D PSD-function is a function of the non-dimensional spatial frequency $\Omega_x L_g$ and the non-dimensional parameter $B = \frac{b}{2Lg}$, and it is now written as,

$$S_{C_{\ell_g} C_{\ell_g}}(\Omega_x L_g, B) = C^2_{\ell_{r_w}} \; I_{\hat{u}_g \hat{u}_g}(\Omega_x L_g, B)$$

with,

$$I_{\hat{u}_g \hat{u}_g}(\Omega_x L_g, B) = \sigma^2_{\hat{u}_g} \int_0^\infty h^2(\Omega_y \frac{b}{2}) \; \frac{1 + \Omega_x^2 L_g^2 + 4\Omega_y^2 L_g^2}{\left(1 + \Omega_x^2 L_g^2 + \Omega_y^2 L_g^2\right)^{5/2}} \; d(\Omega_y L_g) \tag{11.69}$$

The term $I_{\hat{u}_g \hat{u}_g}(\Omega_x L_g, B)$ is considered as an Effective 1D PSD-function for the 2D atmospheric turbulence velocity component $\hat{u}_g$.

Similarly, the PSD-function for the yawing moment coefficient due to $\hat{u}_g$ can be written as,

$$S_{C_{n_g} C_{n_g}}(\Omega_x L_g, B) = C^2_{n_{r_w}} \; I_{\hat{u}_g \hat{u}_g}(\Omega_x L_g, B)$$

Similar to the derivation of the aerodynamic moment coefficient PSD-functions $S_{C_{\ell_g} C_{\ell_g}}(\Omega_x L_g, B)$ and $S_{C_{n_g} C_{n_g}}(\Omega_x L_g, B)$ due to the atmospheric turbulence velocity component u_g, the corresponding PSD-functions with respect to the vertical gust (w_g) induced angle-of-attack α_g are derived. They are summarized as,

$$S_{C_{\ell_g} C_{\ell_g}}(\Omega_x L_g, B) = C^2_{\ell_{p_w}} \; I_{\alpha_g \alpha_g}(\Omega_x L_g, B)$$

and,

$$S_{C_{n_g} C_{n_g}}(\Omega_x L_g, B) = C^2_{n_{p_w}} \; I_{\alpha_g \alpha_g}(\Omega_x L_g, B)$$

where the Effective 1D PSD-function $I_{\alpha_g \alpha_g}$ is given as,

$$I_{\alpha_g \alpha_g}(\Omega_x L_g, B) = 3 \; \sigma^2_{\alpha_g} \int_0^\infty h^2(\Omega_y \frac{b}{2}) \; \frac{\Omega_x^2 L_g^2 + \Omega_y^2 L_g^2}{\left(1 + \Omega_x^2 L_g^2 + \Omega_y^2 L_g^2\right)^{5/2}} \; d(\Omega_y L_g) \tag{11.70}$$

The Effective PSD-functions $I_{\hat{u}_g \hat{u}_g}(\Omega_x L_g, B)$ and $I_{\alpha_g \alpha_g}(\Omega_x L_g, B)$ given in equations (11.69) and (11.70), respectively, are approximated by the following general expressions (see reference [34]),

$$I_{\hat{u}_g \hat{u}_g}(\Omega_x L_g, B) = I_{\hat{u}_g \hat{u}_g}(0, B) \; \frac{1 + \tau_3^2 \; \Omega_x^2 L_g^2}{\left(1 + \tau_1^2 \; \Omega_x^2 L_g^2\right) \left(1 + \tau_2^2 \; \Omega_x^2 L_g^2\right)} \tag{11.71}$$

and,

$$I_{\alpha_g \alpha_g}(\Omega_x L_g, B) = I_{\alpha_g \alpha_g}(0, B) \; \frac{1 + \tau_6^2 \; \Omega_x^2 L_g^2}{\left(1 + \tau_4^2 \; \Omega_x^2 L_g^2\right) \left(1 + \tau_5^2 \; \Omega_x^2 L_g^2\right)} \tag{11.72}$$

respectively. As a function of the circular frequency ω, equations (11.71) and (11.72) are given as,

$$I_{\hat{u}_g\hat{u}_g}(\omega, B) = \frac{L_g}{Q_\infty} I_{\hat{u}_g\hat{u}_g}(0, B) \frac{1 + \tau_3^2 \left(\frac{\omega L_g}{Q_\infty}\right)^2}{\left(1 + \tau_1^2 \left(\frac{\omega L_g}{Q_\infty}\right)^2\right)\left(1 + \tau_2^2 \left(\frac{\omega L_g}{Q_\infty}\right)^2\right)} \tag{11.73}$$

$$I_{\alpha_g\alpha_g}(\omega, B) = \frac{L_g}{Q_\infty} I_{\alpha_g\alpha_g}(0, B) \frac{1 + \tau_6^2 \left(\frac{\omega L_g}{Q_\infty}\right)^2}{\left(1 + \tau_4^2 \left(\frac{\omega L_g}{Q_\infty}\right)^2\right)\left(1 + \tau_5^2 \left(\frac{\omega L_g}{Q_\infty}\right)^2\right)} \tag{11.74}$$

The parameters $I_{\hat{u}_g\hat{u}_g}(0, B)$, $I_{\alpha_g\alpha_g}(0, B)$ and τ_1 to τ_6 are obtained using the fit procedure given in appendix E, section E.5. As a function of $B = \frac{b}{2L_g}$, the parameters $I_{\hat{u}_g\hat{u}_g}(0, B)$ and $I_{\alpha_g\alpha_g}(0, B)$ are summarized in table 11.1. Similarly, as a function of B the parameters τ_1, τ_2 and τ_3 are given in table 11.2, while, the parameters τ_4, τ_5 and τ_6 are shown in table 11.3.

11.5 Aircraft modeling

11.5.1 Aircraft equations of motion for 1D gust fields

In this section the DUT-model linearized equations of motion are given (see also appendix I), which make use of the following aerodynamic model for the 1D gust-induced aerodynamic force and moment coefficients,

$$C_{X_g} = C_{X_{u_g}} \hat{u}_g + C_{X_{\alpha_g}} \alpha_g + C_{X_{\dot{\alpha}_g}} \frac{\dot{\alpha}_g \bar{c}}{Q_\infty} \tag{11.75}$$

$$C_{Z_g} = C_{Z_{u_g}} \hat{u}_g + C_{Z_{\alpha_g}} \alpha_g + C_{Z_{\dot{\alpha}_g}} \frac{\dot{\alpha}_g \bar{c}}{Q_\infty} \tag{11.76}$$

$$C_{m_g} = C_{m_{u_g}} \hat{u}_g + C_{m_{\alpha_g}} \alpha_g + C_{m_{\dot{\alpha}_g}} \frac{\dot{\alpha}_g \bar{c}}{Q_\infty} \tag{11.77}$$

and,

$$C_{Y_g} = C_{Y_{\beta_g}} \beta_g + C_{Y_{\dot{\beta}_g}} \frac{\dot{\beta}_g b}{Q_\infty} \tag{11.78}$$

$$C_{\ell_g} = C_{\ell_{\beta_g}} \beta_g + C_{\ell_{\dot{\beta}_g}} \frac{\dot{\beta}_g b}{Q_\infty} \tag{11.79}$$

$$C_{n_g} = C_{n_{\beta_g}} \beta_g + C_{n_{\dot{\beta}_g}} \frac{\dot{\beta}_g b}{Q_\infty} \tag{11.80}$$

for the 1D non-dimensional symmetrical and the 1D non-dimensional asymmetrical gust fields, respectively.

The equations of motion are written similar to equation (10.20),

$$P^c \; j\omega \; \underline{x} = Q^c \; \underline{x} + R^c \; \underline{u} \tag{11.81}$$

with for the symmetrical equations of motion the matrices P^c, Q^c and R^c equal to,

$$P_s^c = \frac{\bar{c}}{Q_\infty}\begin{bmatrix} -2\mu_c & 0 & 0 & 0 \\ 0 & (C_{Z_{\dot\alpha}} - 2\mu_c) & 0 & 0 \\ 0 & 0 & -1 & 0 \\ 0 & C_{m_{\dot\alpha}} & 0 & -2\mu_c K_Y^2 \end{bmatrix} \tag{11.82}$$

$$Q_s^c = \begin{bmatrix} -C_{X_u} & -C_{X_\alpha} & -C_{Z_0} & -C_{X_q} \\ -C_{Z_u} & -C_{Z_\alpha} & C_{X_0} & -\left(C_{Z_q} + 2\mu_c\right) \\ 0 & 0 & 0 & -1 \\ -C_{m_u} & -C_{m_\alpha} & 0 & -C_{m_q} \end{bmatrix} \tag{11.83}$$

and,

$$R_s^c = \begin{bmatrix} -C_{X_{u_g}} & -C_{X_{\alpha_g}} & -C_{X_{\dot\alpha_g}} \\ -C_{Z_{u_g}} & -C_{Z_{\alpha_g}} & -C_{Z_{\dot\alpha_g}} \\ 0 & 0 & 0 \\ -C_{m_{u_g}} & -C_{m_{\alpha_g}} & -C_{m_{\dot\alpha_g}} \end{bmatrix} \tag{11.84}$$

respectively. In equation (11.81), the aircraft's state and the input are $\underline{x} = \left[\hat{u}, \alpha, \theta, \frac{q\bar{c}}{Q_\infty}\right]^T$, and $\underline{u} = \left[\hat{u}_g,\ \alpha_g,\ \frac{\dot\alpha_g \bar{c}}{Q_\infty}\right]^T$, respectively. The definition of all stability- and gust derivatives is given in appendix I, table I.5. The 1D symmetrical gust derivatives are defined as, see also section 11.3, $C_{X_{u_g}} = C_{X_u}$, $C_{Z_{u_g}} = C_{Z_u}$, $C_{m_{u_g}} = C_{m_u}$, $C_{X_{\alpha_g}} = C_{X_\alpha}$, $C_{Z_{\alpha_g}} = C_{Z_\alpha}$, $C_{m_{\alpha_g}} = C_{m_\alpha}$, $C_{X_{\dot\alpha_g}} = C_{X_{\dot\alpha}} - C_{X_q}$, $C_{Z_{\dot\alpha_g}} = C_{Z_{\dot\alpha}} - C_{Z_q}$ and $C_{m_{\dot\alpha_g}} = C_{m_{\dot\alpha}} - C_{m_q}$.

Similar to the symmetrical equations of motion, the asymmetrical equations of motion are written as equation (11.81) with the matrices P^c, Q^c and R^c now according to,

$$P_a^c = \frac{b}{Q_\infty}\begin{bmatrix} \left(C_{Y_{\dot\beta}} - 2\mu_b\right) & 0 & 0 & 0 \\ 0 & -\frac{1}{2} & 0 & 0 \\ C_{\ell_{\dot\beta}} & 0 & -4\mu_b K_X^2 & 4\mu_b K_{XZ} \\ C_{n_{\dot\beta}} & 0 & 4\mu_b K_{XZ} & -4\mu_b K_Z^2 \end{bmatrix} \tag{11.85}$$

$$Q_a^c = \begin{bmatrix} -C_{Y_\beta} & -C_L & -C_{Y_p} & -\left(C_{Y_r} - 4\mu_b\right) \\ 0 & 0 & -1 & 0 \\ -C_{\ell_\beta} & 0 & -C_{\ell_p} & -C_{\ell_r} \\ -C_{n_\beta} & 0 & -C_{n_p} & -C_{n_r} \end{bmatrix} \tag{11.86}$$

and,

$$R_a^c = \begin{bmatrix} -C_{Y_{\beta_g}} & -C_{Y_{\dot\beta_g}} \\ 0 & 0 \\ -C_{\ell_{\beta_g}} & -C_{\ell_{\dot\beta_g}} \\ -C_{n_{\beta_g}} & -C_{n_{\dot\beta_g}} \end{bmatrix} \tag{11.87}$$

respectively, with the aircraft's state $\underline{x} = \left[\beta, \varphi, \frac{pb}{2Q_\infty}, \frac{rb}{2Q_\infty}\right]^T$ and the input $\underline{u} = \left[\beta_g, \frac{j\omega\beta_g b}{Q_\infty}\right]^T$, and the definition of all stability- and gust derivatives given in appendix I, table I.6. The 1D asymmetrical gust derivatives are defined as, see also section 11.3, $C_{Y_{\beta_g}} = C_{Y_\beta}$, $C_{\ell_{\beta_g}} = C_{\ell_\beta}$, $C_{n_{\beta_g}} = C_{n_\beta}$, $C_{Y_{\dot\beta_g}} = C_{Y_{\dot\beta}} + \frac{1}{2}\, C_{Y_{r_v}}$, $C_{\ell_{\dot\beta_g}} = C_{\ell_{\dot\beta}} + \frac{1}{2}\, C_{\ell_{r_v}}$ and $C_{n_{\dot\beta_g}} = C_{n_{\dot\beta}} + \frac{1}{2}\, C_{n_{r_v}}$.

The 1D PSD-functions for the non-dimensional gust velocity components $\hat{u}_g$ and α_g are summarized in equations (11.60) and (11.62), respectively, while for the non-dimensional gust velocity component β_g it is given in equation (11.61).

11.5.2 Aircraft equations of motion for 2D gust fields

In this section the DUT-model asymmetrical linearized equations of motion are given for the 2D anti-symmetrical gust fields $\hat{u}_g$ and α_g. The non-dimensional aerodynamic force and moment coefficients due to these inputs are written as,

$$C_{Y_g} = C_{Y_{u_g}}\hat{u}_g + C_{Y_{\alpha_g}}\alpha_g \tag{11.88}$$

$$C_{\ell_g} = C_{\ell_{u_g}}\hat{u}_g + C_{\ell_{\alpha_g}}\alpha_g \tag{11.89}$$

$$C_{n_g} = C_{n_{u_g}}\hat{u}_g + C_{n_{\alpha_g}}\alpha_g \tag{11.90}$$

For the asymmetrical equations of motion given in equation (11.81), the matrices P^c, Q^c are equal to the ones given in equations (11.85) and (11.86), respectively, with the aircraft state $\underline{x} = \left[\beta, \varphi, \frac{pb}{2Q_\infty}, \frac{rb}{2Q_\infty}\right]^T$. However, the matrix R^c is now defined as,

$$R^c_a = \begin{bmatrix} -C_{Y_{u_g}}(\Omega_y \frac{b}{2}) & -C_{Y_{\alpha_g}}(\Omega_y \frac{b}{2}) \\ 0 & 0 \\ -C_{\ell_{u_g}}(\Omega_y \frac{b}{2}) & -C_{\ell_{\alpha_g}}(\Omega_y \frac{b}{2}) \\ -C_{n_{u_g}}(\Omega_y \frac{b}{2}) & -C_{n_{\alpha_g}}(\Omega_y \frac{b}{2}) \end{bmatrix} \tag{11.91}$$

with the input $\underline{u} = [\hat{u}_g,\ \alpha_g]^T$, and the frequency-dependent gust derivatives $C_{\ell_{u_g}}(\Omega_y \frac{b}{2})$, $C_{n_{u_g}}(\Omega_y \frac{b}{2})$, $C_{\ell_{\alpha_g}}(\Omega_y \frac{b}{2})$ and $C_{n_{\alpha_g}}(\Omega_y \frac{b}{2})$, according to equations (11.43), (11.44), (11.56) and (11.57), respectively (note that the frequency dependent gust derivatives $C_{Y_{u_g}}(\Omega_y \frac{b}{2})$ and $C_{Y_{\alpha_g}}(\Omega_y \frac{b}{2})$ are set to zero). The equations of motion are then used in conjunction with the input PSD-functions given in equations (11.66) and (11.68) for the 2D non-dimensional gust velocity components $\hat{u}_g$ and α_g, respectively.
However, for the response to 2D atmospheric turbulence, the DUT-model, in this thesis, uses constant gust derivatives, see sections 11.3.4 and 11.3.5. For this constant parameter model the matrix R^c is defined as,

$$R^c_a = \begin{bmatrix} 0 & 0 \\ 0 & 0 \\ +C_{\ell_{r_w}} & -C_{\ell_{p_w}} \\ +C_{n_{r_w}} & -C_{n_{p_w}} \end{bmatrix} \tag{11.92}$$

Given the matrices in equations (11.85), (11.86) and (11.92), they are now used for the equations of motion defined in equation (11.81). In conjunction with the Effective 1D

input PSD-functions given in equations (11.73) and (11.74) for the non-dimensional gust velocity components $\hat{u}_g$ and α_g, respectively, the aircraft responses to these 2D gusts are calculated.

11.6 Remarks

In this chapter the DUT-model has been discussed. This model relies on several assumptions which are summarized as, see also references [33, 34, 30],

1. The aircraft initial (or trim) condition is a recti-linear flightpath.
2. A linearized aircraft model is used, thus the deviations from the flightpath defined in assumption 1, remain small, see also appendix I.
3. The symmetrical, asymmetrical and anti-symmetrical gust inputs to the aircraft model are sufficiently small to allow the aircraft model linearization, see also assumption 2.
4. Given the assumptions 1, 2 and 3, the equations of motions are decoupled in the symmetrical and asymmetrical equations of motion, see also appendix I.
5. For the 1D non-dimensional gust input $\hat{u}_g = \frac{u_g}{Q_\infty}$ the aerodynamic effect of its time derivative is neglected.
6. For the 2D non-dimensional gust inputs $\hat{u}_g = \frac{u_g}{Q_\infty}$ and $\alpha_g = \frac{w_g}{Q_\infty}$, aerodynamic stiffness terms are used in the aerodynamic model only, thus neglecting unsteady aerodynamic effects such as lags or transients in the aerodynamic coefficient force - and moment buildup.
7. Only the contribution of the wing to the gust derivatives with respect to 2D longitudinal and 2D vertical gusts, $\hat{u}_g$ and α_g, respectively, are taken into account.
8. The side-force coefficient derivatives with respect to 2D longitudinal and 2D vertical gusts, $\hat{u}_g$ and α_g, respectively, are usually neglected. However, they are retained in this thesis.
9. In the derivation of the gust derivatives with respect to 2D longitudinal and 2D vertical gust fields, the spatial frequency Ω_y is assumed sufficiently small to allow the linearization $sin\,(\Omega_y y) \approx \Omega_y y$.
10. Using assumption 9, the relation between the spatial frequency-dependent 2D gust derivatives and stability derivatives is governed by the non-dimensional function $h(\Omega_y \frac{b}{2})$.
11. The non-dimensional function $h(\Omega_y \frac{b}{2})$ is described by equation (11.47), see reference [34].

In the following chapter the Four-Point-Aircraft (FPA) model will be discussed. Also for this model 1D longitudinal, 1D lateral and 1D vertical gust inputs will be considered, along with both 2D anti-symmetrical longitudinal and 2D vertical gust inputs. The FPA-model will rely on similar assumptions made for the DUT-model.

In chapter 13 both time- and frequency-domain results for the DUT-model will be compared to the LPF-solutions presented in chapter 9. These results will be given in terms of both aerodynamic model and aircraft motion responses. The DUT-model responses will also be compared to those obtained for the PCA- and the FPA-model.

$B = \frac{b}{2L_g}$	$\frac{I_{\hat{u}_g\hat{u}_g}(0,B)}{\sigma^2_{\hat{u}_g}}$	$\frac{I_{\alpha_g\alpha_g}(0,B)}{\sigma^2_{\alpha_g}}$
5.0000e-001	7.8586e-001	5.3816e-001
4.5000e-001	7.0282e-001	4.8444e-001
4.0000e-001	6.1606e-001	4.2741e-001
3.5000e-001	5.2632e-001	3.6753e-001
3.0000e-001	4.3464e-001	3.0550e-001
2.5000e-001	3.4252e-001	2.4234e-001
2.0000e-001	2.5205e-001	1.7953e-001
1.5000e-001	1.6625e-001	1.1924e-001
1.4000e-001	1.5001e-001	1.0774e-001
1.3500e-001	1.4204e-001	1.0209e-001
1.3000e-001	1.3417e-001	9.6507e-002
1.2500e-001	1.2642e-001	9.0997e-002
1.2000e-001	1.1878e-001	8.5565e-002
1.1500e-001	1.1127e-001	8.0217e-002
1.1000e-001	1.0390e-001	7.4958e-002
1.0500e-001	9.6669e-002	6.9794e-002
1.0000e-001	8.9587e-002	6.4730e-002
9.5000e-002	8.2663e-002	5.9775e-002
9.0000e-002	7.5908e-002	5.4933e-002
8.5000e-002	6.9329e-002	5.0213e-002
8.0000e-002	6.2939e-002	4.5622e-002
7.5000e-002	5.6748e-002	4.1169e-002
7.0000e-002	5.0768e-002	3.6862e-002
6.5000e-002	4.5012e-002	3.2711e-002
6.0000e-002	3.9494e-002	2.8727e-002
5.5000e-002	3.4229e-002	2.4920e-002
5.0000e-002	2.9235e-002	2.1304e-002
4.7500e-002	2.6844e-002	1.9571e-002
4.5000e-002	2.4528e-002	1.7892e-002
4.2500e-002	2.2289e-002	1.6267e-002
4.0000e-002	2.0130e-002	1.4699e-002
3.7500e-002	1.8054e-002	1.3190e-002
3.5000e-002	1.6064e-002	1.1742e-002
3.2500e-002	1.4163e-002	1.0359e-002
3.0000e-002	1.2355e-002	9.0416e-003
2.7500e-002	1.0644e-002	7.7943e-003
2.5000e-002	9.0345e-003	6.6198e-003
2.2500e-002	7.5309e-003	5.5218e-003
2.0000e-002	6.1386e-003	4.5040e-003
1.7500e-002	4.8632e-003	3.5709e-003
1.5000e-002	3.7116e-003	2.7275e-003
1.2500e-002	2.6914e-003	1.9795e-003
1.0000e-002	1.8117e-003	1.3338e-003
7.5000e-003	1.0838e-003	7.9880e-004
5.0000e-003	5.2225e-004	3.8543e-004
2.5000e-003	1.4789e-004	1.0936e-004

Table 11.1: Parameters $\frac{I_{\hat{u}_g\hat{u}_g}(0,B)}{\sigma^2_{\hat{u}_g}}$ and $\frac{I_{\alpha_g\alpha_g}(0,B)}{\sigma^2_{\alpha_g}}$ as a function of $B = \frac{b}{2L_g}$.

$B = \frac{b}{2L_g}$	τ_1	τ_2	τ_3
5.0000e-001	6.6336e-001	3.2648e+000	3.2516e+000
4.5000e-001	6.2241e-001	2.0522e+000	2.0274e+000
4.0000e-001	5.7267e-001	1.4896e+000	1.4473e+000
3.5000e-001	5.1319e-001	1.1797e+000	1.1134e+000
3.0000e-001	4.4581e-001	9.9298e-001	8.9838e-001
2.5000e-001	3.7478e-001	8.7001e-001	7.4759e-001
2.0000e-001	3.0406e-001	7.7869e-001	6.3398e-001
1.5000e-001	2.3530e-001	6.9985e-001	5.4168e-001
1.4000e-001	2.2174e-001	6.8424e-001	5.2464e-001
1.3500e-001	2.1496e-001	6.7636e-001	5.1621e-001
1.3000e-001	2.0820e-001	6.6840e-001	5.0784e-001
1.2500e-001	2.0143e-001	6.6035e-001	4.9949e-001
1.2000e-001	1.9466e-001	6.5220e-001	4.9117e-001
1.1500e-001	1.8789e-001	6.4393e-001	4.8287e-001
1.1000e-001	1.8111e-001	6.3552e-001	4.7456e-001
1.0500e-001	1.7433e-001	6.2695e-001	4.6623e-001
1.0000e-001	1.6753e-001	6.1820e-001	4.5788e-001
9.5000e-002	1.6071e-001	6.0926e-001	4.4950e-001
9.0000e-002	1.5387e-001	6.0009e-001	4.4105e-001
8.5000e-002	1.4700e-001	5.9066e-001	4.3251e-001
8.0000e-002	1.4009e-001	5.8093e-001	4.2387e-001
7.5000e-002	1.3314e-001	5.7085e-001	4.1508e-001
7.0000e-002	1.2613e-001	5.6035e-001	4.0608e-001
6.5000e-002	1.1905e-001	5.4937e-001	3.9683e-001
6.0000e-002	1.1189e-001	5.3781e-001	3.8726e-001
5.5000e-002	1.0463e-001	5.2557e-001	3.7729e-001
5.0000e-002	9.7254e-002	5.1254e-001	3.6685e-001
4.7500e-002	9.3519e-002	5.0568e-001	3.6143e-001
4.5000e-002	8.9749e-002	4.9857e-001	3.5585e-001
4.2500e-002	8.5940e-002	4.9119e-001	3.5011e-001
4.0000e-002	8.2090e-002	4.8350e-001	3.4419e-001
3.7500e-002	7.8193e-002	4.7549e-001	3.3806e-001
3.5000e-002	7.4244e-002	4.6709e-001	3.3170e-001
3.2500e-002	7.0237e-002	4.5826e-001	3.2506e-001
3.0000e-002	6.6163e-002	4.4892e-001	3.1809e-001
2.7500e-002	6.2011e-002	4.3899e-001	3.1072e-001
2.5000e-002	5.7772e-002	4.2835e-001	3.0289e-001
2.2500e-002	5.3431e-002	4.1687e-001	2.9449e-001
2.0000e-002	4.8976e-002	4.0441e-001	2.8543e-001
1.7500e-002	4.4386e-002	3.9076e-001	2.7558e-001
1.5000e-002	3.9635e-002	3.7561e-001	2.6471e-001
1.2500e-002	3.4679e-002	3.5844e-001	2.5247e-001
1.0000e-002	2.9455e-002	3.3842e-001	2.3824e-001
7.5000e-003	2.3876e-002	3.1421e-001	2.2113e-001
5.0000e-003	1.7771e-002	2.8301e-001	1.9917e-001
2.5000e-003	1.0733e-002	2.3660e-001	1.6659e-001

Table 11.2: Parameters τ_1, τ_2 and τ_3 in the approximated PSD-function of the horizontal gust velocity, as a function of $B = \frac{b}{2L_g}$.

$B = \frac{b}{2L_g}$	τ_4	τ_5	τ_6
5.0000e-001	5.2763e-001	7.2143e-001	7.9609e-001
4.5000e-001	4.5593e-001	1.5885e+000	1.6130e+000
4.0000e-001	4.2619e-001	3.1844e+000	3.1991e+000
3.5000e-001	3.2906e-001	4.3069e-001	3.6085e-001
3.0000e-001	2.7704e-001	4.4478e-001	3.4771e-001
2.5000e-001	2.3376e-001	4.4479e-001	3.3236e-001
2.0000e-001	1.9420e-001	4.3740e-001	3.1713e-001
1.5000e-001	1.5517e-001	4.2204e-001	2.9958e-001
1.4000e-001	1.4718e-001	4.1764e-001	2.9537e-001
1.3500e-001	1.4316e-001	4.1525e-001	2.9317e-001
1.3000e-001	1.3911e-001	4.1273e-001	2.9090e-001
1.2500e-001	1.3505e-001	4.1007e-001	2.8856e-001
1.2000e-001	1.3095e-001	4.0727e-001	2.8616e-001
1.1500e-001	1.2684e-001	4.0433e-001	2.8369e-001
1.1000e-001	1.2270e-001	4.0124e-001	2.8115e-001
1.0500e-001	1.1853e-001	3.9799e-001	2.7852e-001
1.0000e-001	1.1432e-001	3.9456e-001	2.7581e-001
9.5000e-002	1.1007e-001	3.9094e-001	2.7300e-001
9.0000e-002	1.0578e-001	3.8710e-001	2.7006e-001
8.5000e-002	1.0143e-001	3.8302e-001	2.6698e-001
8.0000e-002	9.7028e-002	3.7865e-001	2.6373e-001
7.5000e-002	9.2555e-002	3.7397e-001	2.6027e-001
7.0000e-002	8.8007e-002	3.6894e-001	2.5659e-001
6.5000e-002	8.3378e-002	3.6351e-001	2.5266e-001
6.0000e-002	7.8661e-002	3.5765e-001	2.4845e-001
5.5000e-002	7.3848e-002	3.5130e-001	2.4394e-001
5.0000e-002	6.8928e-002	3.4439e-001	2.3909e-001
4.7500e-002	6.6423e-002	3.4071e-001	2.3651e-001
4.5000e-002	6.3884e-002	3.3684e-001	2.3382e-001
4.2500e-002	6.1308e-002	3.3277e-001	2.3100e-001
4.0000e-002	5.8691e-002	3.2848e-001	2.2803e-001
3.7500e-002	5.6029e-002	3.2392e-001	2.2489e-001
3.5000e-002	5.3317e-002	3.1908e-001	2.2155e-001
3.2500e-002	5.0550e-002	3.1390e-001	2.1799e-001
3.0000e-002	4.7723e-002	3.0835e-001	2.1417e-001
2.7500e-002	4.4830e-002	3.0237e-001	2.1007e-001
2.5000e-002	4.1865e-002	2.9592e-001	2.0564e-001
2.2500e-002	3.8819e-002	2.8889e-001	2.0084e-001
2.0000e-002	3.5678e-002	2.8119e-001	1.9558e-001
1.7500e-002	3.2424e-002	2.7263e-001	1.8973e-001
1.5000e-002	2.9034e-002	2.6295e-001	1.8312e-001
1.2500e-002	2.5477e-002	2.5182e-001	1.7550e-001
1.0000e-002	2.1715e-002	2.3874e-001	1.6655e-001
7.5000e-003	1.7673e-002	2.2273e-001	1.5558e-001
5.0000e-003	1.3214e-002	2.0166e-001	1.4110e-001
2.5000e-003	8.0286e-003	1.6977e-001	1.1907e-001

Table 11.3: Parameters τ_4, τ_5 and τ_6 in the approximated PSD-function of the horizontal gust velocity, as a function of $B = \frac{b}{2L_g}$.

Chapter 12

The Four Point Aircraft model

12.1 Introduction

In this chapter the Four-Point-Aircraft (FPA) model will be described. It is based on the theory outlined in reference [35]. The model makes use of a discretized aircraft on which four points are specified. The atmospheric turbulence velocity components at these points are used to define the FPA-model gust inputs. Using the gust inputs at the specified points, the FPA-model input correlation functions are defined and, using the Fourier transform, the input Power Spectral Density (PSD) functions are calculated from them.

Similar to chapters 10 and 11, the aircraft responses to atmospheric turbulence inputs are limited to 1D longitudinal - (u_g), lateral - (v_g) and vertical gust inputs (w_g). Also, the aircraft responses to both 2D anti-symmetrical longitudinal - (u_g) and vertical gusts (w_g) will be considered.

12.2 The FPA-model gust inputs

12.2.1 Definition of the gust inputs

With reference to figure 12.1, in the following use is made of the atmospheric turbulence velocity components u_g, v_g and w_g at the FPA-model four-point positions "0", "1", "2", and "3" for the definition of the model's gust inputs. The dimensional translational gust inputs are defined as, see also reference [35],

$$\left.\begin{array}{rcl} u_g &=& u_{g_0} \\ v_g &=& v_{g_0} \\ w_g &=& \frac{1}{3}\left(w_{g_0} + w_{g_1} + w_{g_2}\right) \end{array}\right\} \tag{12.1}$$

while for the dimensional rotational gusts they are defined as,

$$\left.\begin{array}{rcl} p_g & = & \frac{w_{g_1}-w_{g_2}}{b'} \\ q_g & = & \frac{w_{g_3}-w_{g_0}}{l_h} \\ r_{1_g} & = & \frac{u_{g_2}-u_{g_1}}{b'} \\ r_{2_g} & = & \frac{v_{g_0}-v_{g_3}}{l_v} \end{array}\right\} \tag{12.2}$$

with u_{g_0} the longitudinal gust velocity component, v_{g_0} the lateral gust velocity component and w_{g_0} the vertical gust velocity component all at the aircraft center of gravity. Further, u_{g_1} the longitudinal gust velocity component at location "1" (see figure 12.1), u_{g_2} the one at location "2" and v_{g_3} the lateral gust velocity component at location "3". Next, w_{g_1}, w_{g_2} and w_{g_3} the vertical gust velocity components at locations "1", "2" and "3", respectively. Finally, $b' = 0.85b$ with b the wingspan in [m], l_h the horizontal tail-length in [m] and l_v the vertical tail-length in [m] (with l_v taken to be $l_v = l_h$).

For the Stability Frame of Reference $\mathcal{F}_S$ the positive directions of the gust inputs u_g, v_g, w_g, p_g, q_g, r_{1_g} and r_{2_g} are shown in figure 12.2. Besides the gust input w_g, its time derivative is required as well,

$$\dot{w}_g = \frac{dw_g}{dt} \tag{12.3}$$

Similar to the DUT-model, the time derivative of the longitudinal gust u_g is not taken into account. Contrary to the DUT-model, however, the time derivative of the lateral gust v_g is also not taken into account.

12.2.2 Correlation functions

In this section the correlation functions will be presented for each atmospheric turbulence input, both symmetric and asymmetric. The correlation functions are calculated from the four points' gust velocity components at, for example $t = 0$, and their values at $t = \tau$, with t time and τ the separation time, see also figure 12.3. As an example, consider the gust input p_g,

$$p_g = \frac{w_{g_1} - w_{g_2}}{b'}$$

For an arbitrary instant in time, the autocorrelation function $C_{p_g p_g}(\tau)$ only becomes a function of the time-separation τ, and it is defined as,

$$\begin{array}{rcl} C_{p_g p_g}(\tau) & = & E\{p_g(t)\, p_g(t+\tau)\} \\ & = & \frac{1}{b'^2}\, E\{(w_{g_1} - w_{g_2})(w'_{g_1} - w'_{g_2})\} \\ & = & \frac{1}{b'^2}\, \left[E\{w_{g_1} w'_{g_1}\} + E\{w_{g_2} w'_{g_2}\} - E\{w_{g_1} w'_{g_2}\} - E\{w_{g_2} w'_{g_1}\}\right] \end{array} \tag{12.4}$$

with w_{g_1} and w_{g_2} the vertical gust velocity components at locations "1" and "2" for time $t = 0$ and w'_{g_1} and w'_{g_2} the vertical gust velocity components at locations "1" and

"2" for time $t = \tau$. The four points "0", "1", "2" and "3" in figure 12.3 have the coordinates $(x_1, 0, 0)^T$, $(x_1, \frac{b'}{2}, 0)^T$, $(x_1, -\frac{b'}{2}, 0)^T$ and $(x_1 - l_v, 0, 0)^T$, respectively, while the points "0' ", "1' ", "2' " and "3' " in figure 12.3 have the coordinates $(x_1 + Q_\infty\tau, 0, 0)^T$, $(x_1 + Q_\infty\tau, \frac{b'}{2}, 0)^T$, $(x_1 + Q_\infty\tau, -\frac{b'}{2}, 0)^T$ and $(x_1 + Q_\infty\tau - l_v, 0, 0)^T$, respectively. The separation vectors $\underline{\xi}_{ij}$ in figure 12.3 become,

$$\underline{\xi}_{11'} = (Q_\infty\tau, 0, 0)^T$$

$$\underline{\xi}_{12'} = (Q_\infty\tau, -b', 0)^T$$

$$\underline{\xi}_{21'} = (Q_\infty\tau, b', 0)^T$$

$$\underline{\xi}_{22'} = (Q_\infty\tau, 0, 0)^T$$

Recalling the covariance matrix given in equation (2.15),

$$E\{u_i u_j\} = C_{u_i u_j}(\underline{\xi}) = \sigma^2 \left(\frac{f(|\underline{\xi}|) - g(|\underline{\xi}|)}{|\underline{\xi}|^2} \, \xi_i \, \xi_j + g(|\underline{\xi}|) \, \delta_{ij} \right) \tag{12.5}$$

with the indices, $i = 1, 2, 3$ and $j = 1, 2, 3$, δ_{ij} the Kronecker delta, σ^2 the variance of atmospheric turbulence, $|\underline{\xi}| = \xi = \sqrt{\xi_1^2 + \xi_2^2 + \xi_3^2}$ the spatial separation, and f and g the one-dimensional (1D) fundamental longitudinal and lateral correlation function according to Dryden, respectively (see also equations (2.11) and (2.12)), the covariance function $C_{p_g p_g}(\tau)$ is calculated. Also, in equation (12.5) ξ_i is the i-th element of the separation vector $\underline{\xi}$, and given that the vertical gust velocity component w_g is considered only, in the covariance matrix equation $i = j = 3$ with both u_i and u_j becoming u_3 (which corresponds to the vertical gust velocity component w_g). Therefore, the autocovariance function $C_{p_g p_g}(\tau)$ becomes,

$$C_{p_g p_g}(\tau) = \frac{2}{b'^2} \left[C_{33}(Q_\infty\tau, 0, 0) - C_{33}(Q_\infty\tau, b', 0) \right]$$

or using equation (2.12),

$$\frac{(b')^2}{2\sigma^2} \, C_{p_g p_g}(\tau) = g(\xi_1) - g(\xi_3)$$

or,

$$C_{p_g p_g}(\tau) = \frac{2\sigma^2}{(b')^2} \, \{g(\xi_1) - g(\xi_3)\} \tag{12.6}$$

with the non-dimensional seperations (now given as ξ_1 and ξ_3) equal to,

$$\frac{\xi_1}{L_g} = \zeta_1 = \left| \frac{Q_\infty\tau}{L_g} \right|$$

$$\frac{\xi_3}{L_g} = \zeta_3 = \sqrt{\left(\frac{Q_\infty\tau}{L_g} \right)^2 + \left(\frac{b'}{L_g} \right)^2}$$

Similar to equation (12.6), the covariance functions for the other four-point model turbulence inputs are derived. They are summarized as,

$$C_{u_g u_g}(\tau) = \sigma^2 \; f(\xi_1)$$

$$C_{v_g v_g}(\tau) = \sigma^2 \; g(\xi_1)$$

$$C_{w_g w_g}(\tau) = \sigma^2 \left\{ \frac{1}{3} g(\xi_1) + \frac{4}{9} g(\xi_2) + \frac{2}{9} g(\xi_3) \right\}$$

$$C_{q_g q_g}(\tau) = \frac{\sigma^2}{l_h^2} \left\{ 2g(\xi_1) - g(\xi_4) - g(\xi_5) \right\}$$

$$C_{r_{1_g} r_{1_g}}(\tau) = \frac{2\sigma^2}{(b')^2} \left\{ f(\xi_1) - K_1 f(\xi_3) - (1 - K_1)\, g(\xi_3) \right\}$$

$$C_{r_{2_g} r_{2_g}}(\tau) = \frac{\sigma^2}{l_v^2} \left\{ 2g(\xi_1) - g(\xi_6) - g(\xi_7) \right\}$$

$$C_{w_g q_g}(\tau) = \frac{\sigma^2}{3 l_h} \left\{ g(\xi_5) - g(\xi_1) + 2g(\xi_8) - 2g(\xi_2) \right\}$$

$$C_{v_g r_{1_g}}(\tau) = \frac{\sigma^2}{b'} \left\{ 2K_2 \left[g(\xi_2) - f(\xi_2) \right] \right\}$$

$$C_{v_g r_{2_g}}(\tau) = \frac{\sigma^2}{l_v} \left\{ g(\xi_1) - g(\xi_7) \right\}$$

$$C_{r_{1_g} r_{2_g}}(\tau) = \frac{\sigma^2}{b' l_v} \left\{ K_3 \left[g(\xi_9) - f(\xi_9) \right] + K_2 \left[f(\xi_2) - g(\xi_2) \right] \right\}$$

with σ^2 the atmospheric turbulence variance (taken to be $\sigma^2 = 1 \; [\frac{\mathrm{m}^2}{\mathrm{s}^2}]$), l_v [m] the vertical tail-length, l_h [m] the horizontal tail-length, $b' = 0.85b$ [m] with b [m] the wingspan, τ the time-separation [sec.], and,

$$K_1 = \frac{\left(\frac{Q_\infty \tau}{L_g} \right)^2}{\left(\frac{Q_\infty \tau}{L_g} \right)^2 + \left(\frac{b'}{2L_g} \right)^2}$$

$$K_2 = \frac{\left(\frac{Q_\infty \tau}{L_g} \right) \left(\frac{b'}{2L_g} \right)}{\left(\frac{Q_\infty \tau}{L_g} \right)^2 + \left(\frac{b'}{L_g} \right)^2}$$

$$K_3 = \frac{\left(\frac{Q_\infty \tau}{L_g} - \frac{l_v}{L_g} \right) \left(\frac{b'}{2L_g} \right)}{\left(\frac{Q_\infty \tau}{L_g} - \frac{l_v}{L_g} \right)^2 + \left(\frac{b'}{L_g} \right)^2}$$

and the non-dimensional separations according to,

$$\frac{\xi_2}{L_g} = \zeta_2 = \sqrt{\left(\frac{Q_\infty \tau}{L_g}\right)^2 + \left(\frac{b'}{2L_g}\right)^2}$$

$$\frac{\xi_4}{L_g} = \zeta_4 = \left|\frac{Q_\infty \tau}{L_g} + \frac{l_h}{L_g}\right|$$

$$\frac{\xi_5}{L_g} = \zeta_5 = \left|\frac{Q_\infty \tau}{L_g} - \frac{l_h}{L_g}\right|$$

$$\frac{\xi_6}{L_g} = \zeta_6 = \left|\frac{Q_\infty \tau}{L_g} + \frac{l_v}{L_g}\right|$$

$$\frac{\xi_7}{L_g} = \zeta_7 = \left|\frac{Q_\infty \tau}{L_g} - \frac{l_h}{L_g}\right|$$

$$\frac{\xi_8}{L_g} = \zeta_8 = \sqrt{\left(\frac{Q_\infty \tau}{L_g} - \frac{l_h}{L_g}\right)^2 + \left(\frac{b'}{2L_g}\right)^2}$$

$$\frac{\xi_9}{L_g} = \zeta_9 = \sqrt{\left(\frac{Q_\infty \tau}{L_g} - \frac{l_v}{L_g}\right)^2 + \left(\frac{b'}{2L_g}\right)^2}$$

with the f and g functions the Dryden longitudinal and lateral correlation functions, respectively (see also chapter 2),

$$f(\xi) = e^{-\frac{\xi}{L_g}}$$

$$g(\xi) = e^{-\frac{\xi}{L_g}}\left(1 - \frac{\xi}{2L_g}\right)$$

and the dimensional separations ξ [m] either ξ_1 [m] to ξ_9 [m], Q_∞ [m/s] the airspeed and L_g [m] the gust scale length. The dimensional covariance functions are shown in figures 12.4 as a function of the non-dimensional distance traveled $\frac{Q_\infty \tau}{L_g}$ for a series of the gust scale length: $L_g = [30, 150, 300, 500, 1000, 1500]$ [m], and the variance $\sigma^2 = 1$ $[\frac{\mathrm{m}^2}{\mathrm{s}^2}]$. These results have been calculated for the time-separation discretization $\Delta\tau = 1\frac{\bar{c}}{Q_\infty}$ [sec] (with $\bar{c}$ the mean aerodynamic chord in [m]), τ [sec.], equal to $\tau = [-N\ \Delta\tau \cdots N\ \Delta\tau]$ and $N = 60000$.
The kinks in some of the correlation functions are the result of the FPA representation. They occur at that value of $Q_\infty \tau / L_g$ for which the tail arrives at the position occupied $\tau = \frac{l_h}{Q_\infty}$ or $\tau = \frac{l_v}{Q_\infty}$ seconds earlier by the center of gravity (also known as the so-called "gust penetration effect").

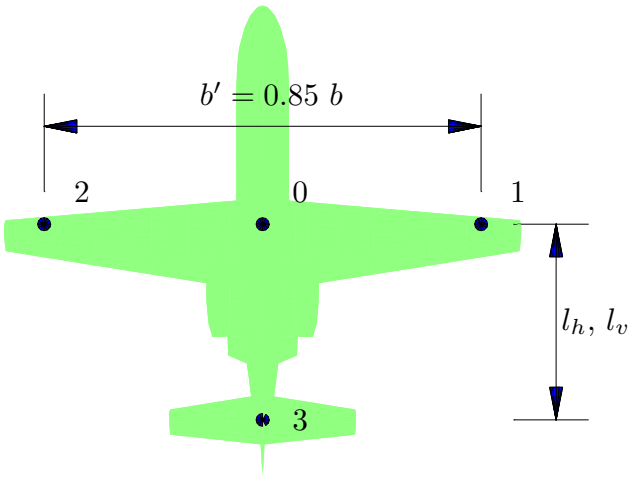


Figure 12.1: The Four-Point-Aircraft model including the definitions of b', l_h and l_v.

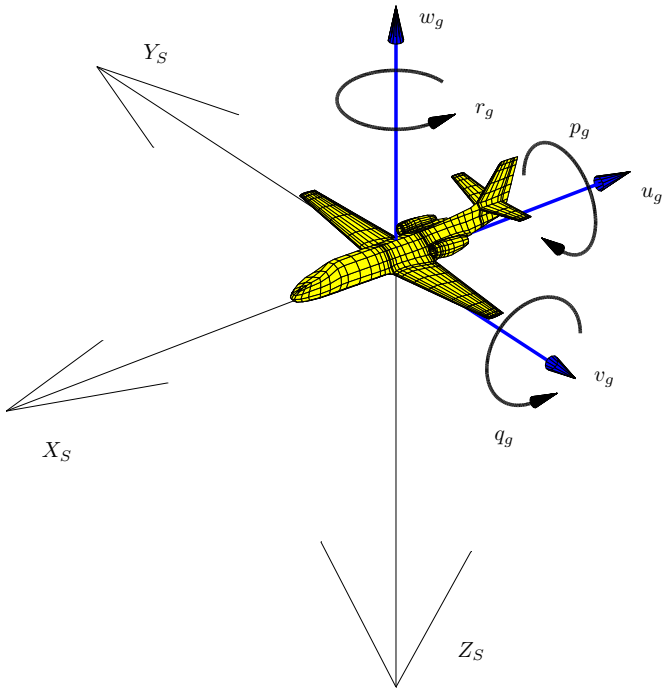


Figure 12.2: The frame $\mathcal{F}_S$, including the definition of the FPA-model atmospheric turbulence velocity component inputs $[u_g, v_g, w_g]^T$ and the rotational inputs $[p_g, q_g, r_g]^T$.

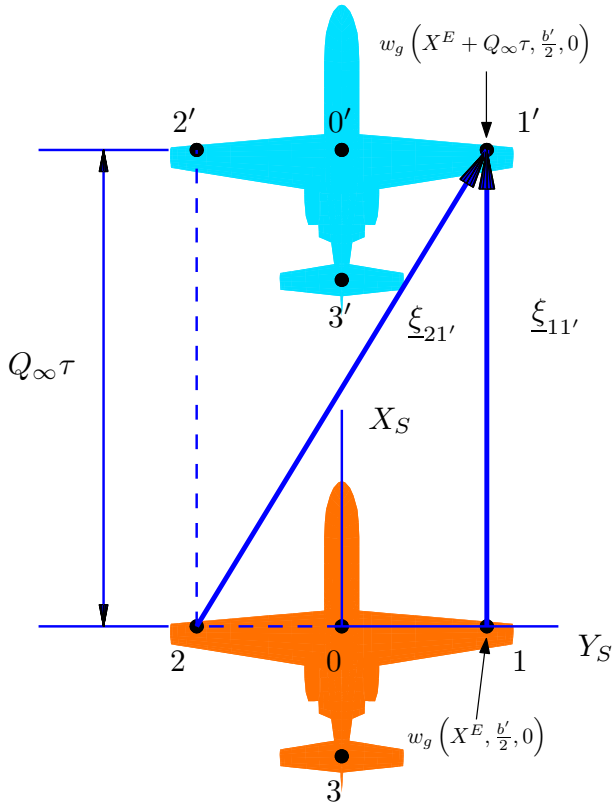


Figure 12.3: Illustration of the seperation vectors $\underline{\xi}_{11'}$ and $\underline{\xi}_{21'}$ as used in the definition of the correlation functions (taken from reference [35]).

12.2.3 PSD-functions

The FPA-model gust input PSD-functions are obtained by Fourier transforming the covariance functions defined in section 12.2.2. The functions are obtained using MATLAB's Fast Fourier Transform (FFT), or,

$$S[k] = \sum_{n=0}^{N-1} C[n]\, e^{-j\frac{2\pi kn}{N}}$$

with $S[k]$ the PSD-function estimate (or "Periodogram"), k the frequency-counter, $C[n]$ the covariance function and n the time-separation counter as in $\tau = n\ \Delta\tau$. As a function of the circular frequency ω [Rad/sec.] the numerically calculated PSD-functions $S_{u_g u_g}(\omega)$, $S_{v_g v_g}(\omega)$, $S_{w_g w_g}(\omega)$, $S_{p_g p_g}(\omega)$, $S_{q_g q_g}(\omega)$, $S_{r_{1_g} r_{1_g}}(\omega)$, $S_{r_{2_g} r_{2_g}}(\omega)$, $S_{w_g q_g}(\omega)$, $S_{v_g r_{1_g}}(\omega)$, $S_{v_g r_{2_g}}(\omega)$ and $S_{r_{1_g} r_{2_g}}(\omega)$ are given in figures 12.5 for a number of the gust scale length: $L_g = [30, 150, 300, 500, 1000, 1500]$ [m], and the variance $\sigma^2 = 1\ [\frac{\mathrm{m}^2}{\mathrm{s}^2}]$, with,

$$\omega_k = \frac{2\pi\ k}{N\ \Delta\tau} \tag{12.7}$$

and $k = 0 \cdots N-1$. Also, $2N+1$ equals the number of samples of the covariance functions (with N taken to be $N = 60000$ for the shown results) and $\Delta\tau$ [sec.] the time-separation

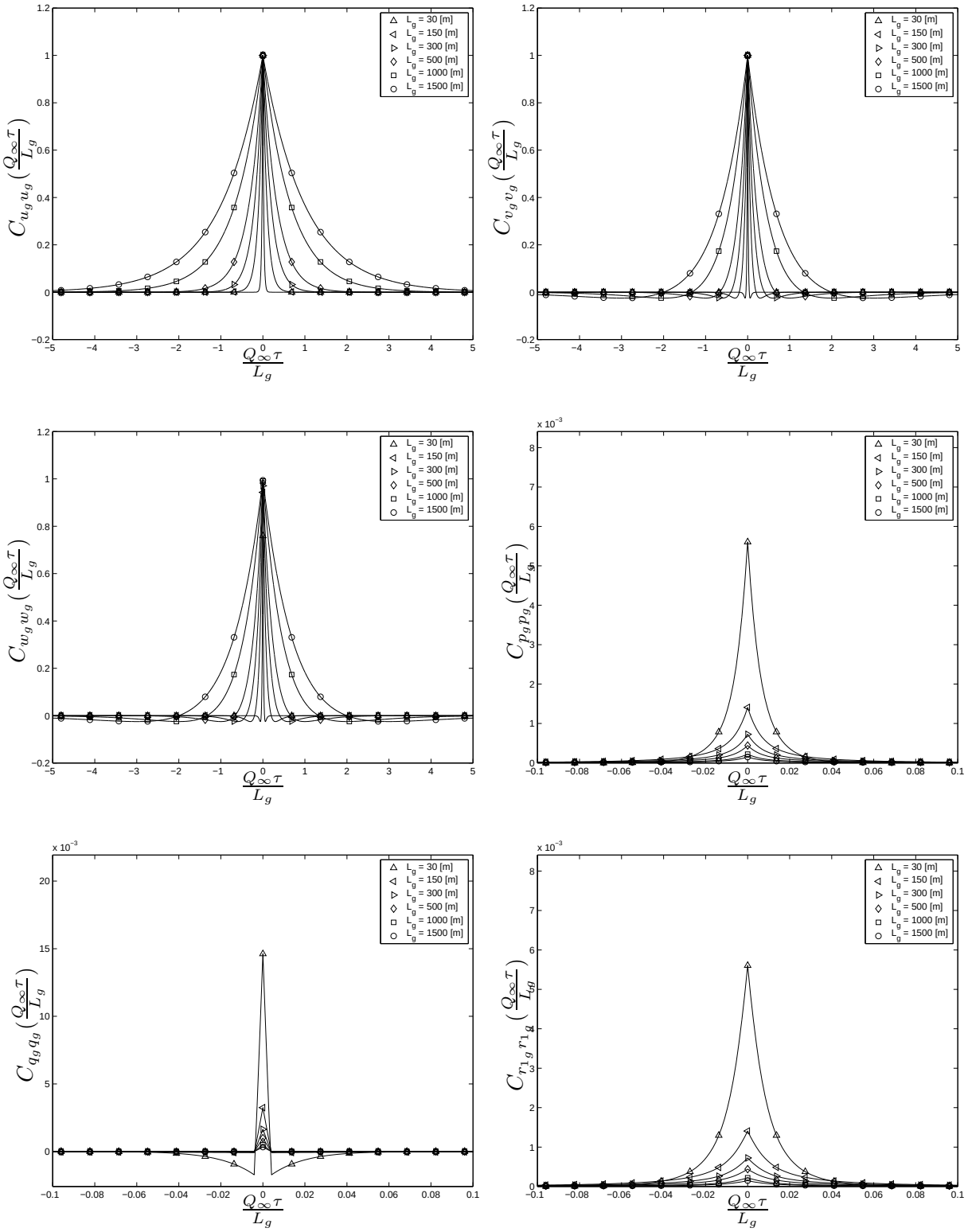


Figure 12.4: The covaraiance functions for dimensional gust inputs, $C_{u_g u_g}(\frac{Q_\infty \tau}{L_g})$, $C_{v_g v_g}(\frac{Q_\infty \tau}{L_g})$, $C_{w_g w_g}(\frac{Q_\infty \tau}{L_g})$, $C_{p_g p_g}(\frac{Q_\infty \tau}{L_g})$, $C_{q_g q_g}(\frac{Q_\infty \tau}{L_g})$ and $C_{r_{1_g} r_{1_g}}(\frac{Q_\infty \tau}{L_g})$, for a series of the gust scale length L_g.

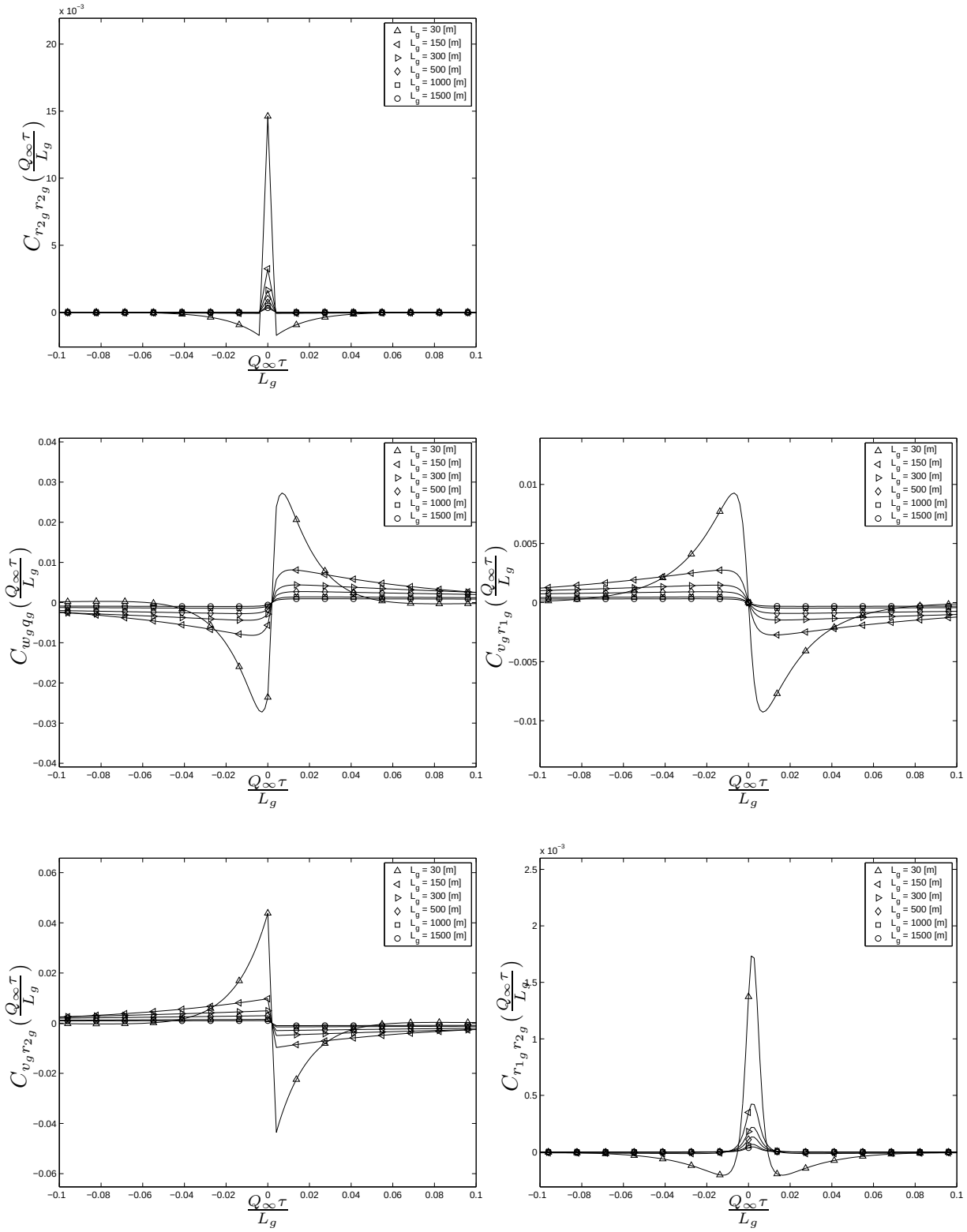


Figure 12.4: (Continued) The correlation functions for dimensional gust inputs, $C_{r_{2_g} r_{2_g}}(\frac{Q_\infty \tau}{L_g})$, $C_{w_g q_g}(\frac{Q_\infty \tau}{L_g})$, $C_{v_g r_{1_g}}(\frac{Q_\infty \tau}{L_g})$, $C_{v_g r_{2_g}}(\frac{Q_\infty \tau}{L_g})$ and $C_{r_{1_g} r_{2_g}}(\frac{Q_\infty \tau}{L_g})$, for a series of the gust scale length L_g.

discretization (taken to be $\Delta\tau = 1\frac{\bar{c}}{Q_\infty}$, with $\bar{c}$ the mean aerodynamic chord in [m]). The motivation for the choice of both N and $\Delta\tau$ is such that the PSD-function frequency-response ranges from at least $\omega_{min} = 0.01$ [Rad/sec.] to at least $\omega_{max} = 100$ [Rad/sec.]. Similar to the covariance functions, these PSD-functions are also given in dimensional form.

For the non-dimensional FPA-model gust inputs $\hat{u}_g = \frac{u_g}{Q_\infty}$, $\beta_g = \frac{v_g}{Q_\infty}$, $\alpha_g = \frac{w_g}{Q_\infty}$, $\frac{p_g b}{2Q_\infty}$, $\frac{q_g \bar{c}}{Q_\infty}$, $\frac{r_{1_g} b}{2Q_\infty}$ and $\frac{r_{2_g} b}{2Q_\infty}$ the non-dimensional PSD-functions become,

$$\left.\begin{array}{lcl}
S_{\hat{u}_g \hat{u}_g}(\omega) & = & \frac{1}{Q_\infty^2} S_{u_g u_g}(\omega) \\
S_{\beta_g \beta_g}(\omega) & = & \frac{1}{Q_\infty^2} S_{v_g v_g}(\omega) \\
S_{\alpha_g \alpha_g}(\omega) & = & \frac{1}{Q_\infty^2} S_{w_g w_g}(\omega) \\
 & & \\
S_{\frac{p_g b}{2Q_\infty} \frac{p_g b}{2Q_\infty}}(\omega) & = & \left(\frac{b}{2Q_\infty}\right)^2 S_{p_g p_g}(\omega) \\
S_{\frac{q_g \bar{c}}{Q_\infty} \frac{q_g \bar{c}}{Q_\infty}}(\omega) & = & \left(\frac{\bar{c}}{Q_\infty}\right)^2 S_{q_g q_g}(\omega) \\
S_{\frac{r_{1_g} b}{2Q_\infty} \frac{r_{1_g} b}{2Q_\infty}}(\omega) & = & \left(\frac{b}{2Q_\infty}\right)^2 S_{r_{1_g} r_{1_g}}(\omega) \\
S_{\frac{r_{2_g} b}{2Q_\infty} \frac{r_{2_g} b}{2Q_\infty}}(\omega) & = & \left(\frac{b}{2Q_\infty}\right)^2 S_{r_{2_g} r_{2_g}}(\omega) \\
 & & \\
S_{\alpha_g \frac{q_g \bar{c}}{Q_\infty}}(\omega) & = & \frac{\bar{c}}{Q_\infty^2} S_{w_g q_g}(\omega) \\
S_{\beta_g \frac{r_{1_g} b}{2Q_\infty}}(\omega) & = & \frac{b}{2Q_\infty^2} S_{v_g r_{1_g}}(\omega) \\
S_{\beta_g \frac{r_{2_g} b}{2Q_\infty}}(\omega) & = & \frac{b}{2Q_\infty^2} S_{v_g r_{2_g}}(\omega) \\
S_{\frac{r_{1_g} b}{2Q_\infty} \frac{r_{2_g} b}{2Q_\infty}}(\omega) & = & \left(\frac{b}{2Q_\infty}\right)^2 S_{r_{1_g} r_{2_g}}(\omega)
\end{array}\right\} \quad (12.8)$$

12.3 Aerodynamic models

12.3.1 1D Symmetrical longitudinal gust fields

Similar to the DUT-model, for the FPA-model's 1D symmetrical longitudinal gust velocity component u_g the aerodynamic forces and moment coefficients are given as, (see also reference [35]),

$$C_{X_g} = C_{X_u} \hat{u}_g \quad (12.9)$$

$$C_{Z_g} = C_{Z_u} \hat{u}_g \quad (12.10)$$

$$C_{m_g} = C_{m_u} \hat{u}_g \quad (12.11)$$

with $\hat{u}_g = \frac{u_g}{Q_\infty}$, and C_{X_u}, C_{Z_u} and C_{m_u} the aircraft stability derivatives.

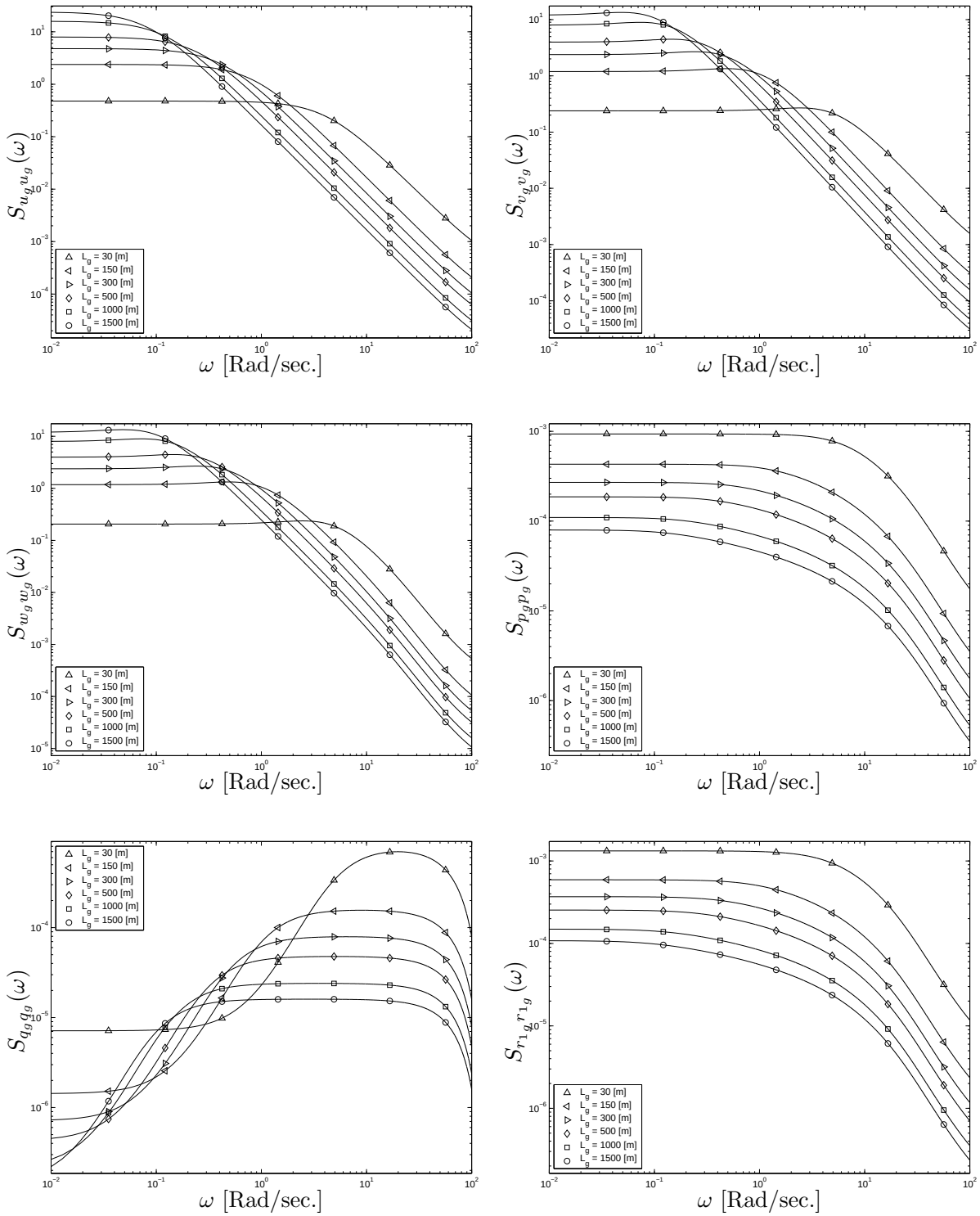


Figure 12.5: The PSD-functions for dimensional gust inputs, $S_{u_g u_g}(\omega)$, $S_{v_g v_g}(\omega)$, $S_{w_g w_g}(\omega)$, $S_{p_g p_g}(\omega)$, $S_{q_g q_g}(\omega)$ and $S_{r_{1_g} r_{1_g}}(\omega)$, for a series of the gust scale length L_g.

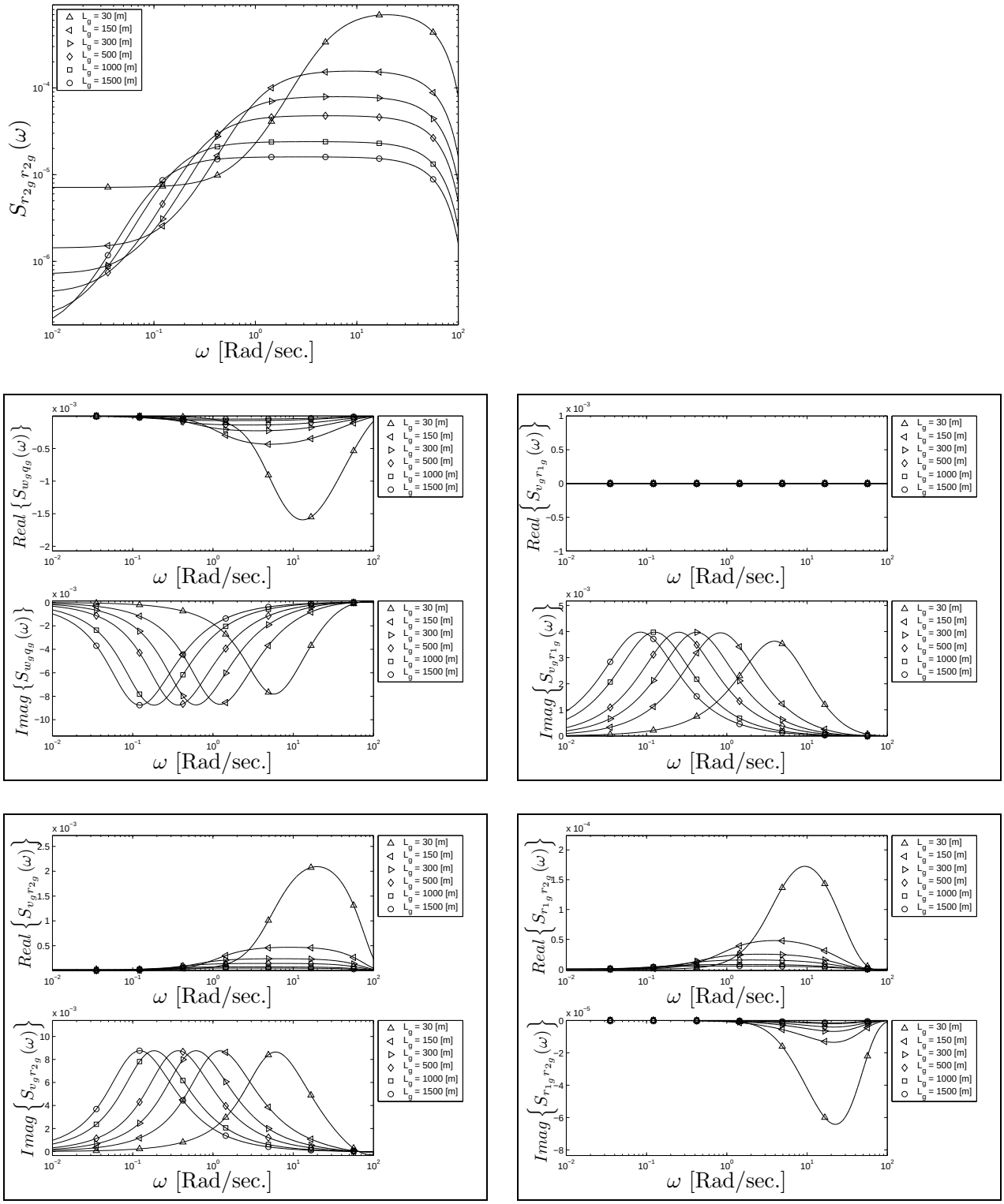


Figure 12.5: (Continued) The PSD-functions for dimensional gust inputs, $S_{r_{2_g} r_{2_g}}(\omega)$, $S_{w_g q_g}(\omega)$, $S_{v_g r_{1_g}}(\omega)$, $S_{v_g r_{2_g}}(\omega)$ and $S_{r_{1_g} r_{2_g}}(\omega)$, for a series of the gust scale length L_g.

12.3.2 1D Asymmetrical lateral gust fields

For the 1D asymmetrical gust fields, the lateral gust velocity component v_g is considered only. According to the FPA-model, for the linearized aircraft model the aerodynamic force and moments coefficients are given as, see also reference [35],

$$C_{Y_g} = C_{Y_\beta}\beta_g + C_{Y_{r_{2_g}}}\frac{r_{2_g}b}{2Q_\infty} \tag{12.12}$$

$$C_{\ell_g} = C_{\ell_\beta}\beta_g + C_{\ell_{r_{2_g}}}\frac{r_{2_g}b}{2Q_\infty} \tag{12.13}$$

$$C_{n_g} = C_{n_\beta}\beta_g + C_{n_{r_{2_g}}}\frac{r_{2_g}b}{2Q_\infty} \tag{12.14}$$

with $\beta_g = \frac{v_g}{Q_\infty}$, and C_{Y_β}, C_{ℓ_β} and C_{n_β} the stability derivatives. Also, $r_{2_g} = \frac{v_{g_0} - v_{g_3}}{l_v}$ with v_{g_0} the lateral gust velocity component at the center of gravity, v_{g_3} the lateral gust velocity component at location "3" of the FPA-model (see figure 12.1) and l_v the vertical tail-length in [m]. The gust derivatives $C_{Y_{r_{2_g}}}$, $C_{\ell_{r_{2_g}}}$ and $C_{n_{r_{2_g}}}$ are equal to the vertical tailplane's contribution to the stability derivatives C_{Y_r}, C_{ℓ_r} and C_{n_r}, respectively (see also table 6.11).

12.3.3 1D Symmetrical vertical gust fields

The aerodynamic forces and moment coefficients with respect to the vertical gust velocity component w_g, are given as (see also reference [35]),

$$C_{X_g} = C_{X_\alpha}\alpha_g + C_{X_q}\frac{q_g\bar{c}}{Q_\infty} + C_{X_{\dot{\alpha}}}\frac{\dot{\alpha}_g\bar{c}}{Q_\infty} \tag{12.15}$$

$$C_{Z_g} = C_{Z_\alpha}\alpha_g + C_{Z_q}\frac{q_g\bar{c}}{Q_\infty} + C_{Z_{\dot{\alpha}}}\frac{\dot{\alpha}_g\bar{c}}{Q_\infty} \tag{12.16}$$

$$C_{m_g} = C_{m_\alpha}\alpha_g + C_{m_q}\frac{q_g\bar{c}}{Q_\infty} + C_{m_{\dot{\alpha}}}\frac{\dot{\alpha}_g\bar{c}}{Q_\infty} \tag{12.17}$$

with $\alpha_g = \frac{w_g}{Q_\infty}$ and $\dot{\alpha}_g = \frac{\dot{w}_g}{Q_\infty}$ and C_{X_α}, $C_{X_{\dot{\alpha}}}$, C_{Z_α}, $C_{Z_{\dot{\alpha}}}$, C_{m_α}, $C_{m_{\dot{\alpha}}}$, C_{X_q}, C_{Z_q} and C_{m_q} the aircraft stability derivatives. The stability derivative $C_{X_{\dot{\alpha}}}$ is set to zero for this model.

12.3.4 2D Anti-symmetrical longitudinal gust fields

For the 2D anti-symmetrical longitudinal gust fields, the longitudinal gust velocity component u_g is considered only. The gust input is given as a yawing gust input, that is r_{1_g}. For the linearized aircraft model the aerodynamic force and moments coefficients are given as, see also reference [35],

$$C_{Y_g} = C_{Y_{r_{1_g}}}\frac{r_{1_g}b}{2Q_\infty} \tag{12.18}$$

$$C_{\ell_g} = C_{\ell_{r_{1_g}}} \frac{r_{1_g} b}{2Q_\infty} \tag{12.19}$$

$$C_{n_g} = C_{n_{r_{1_g}}} \frac{r_{1_g} b}{2Q_\infty} \tag{12.20}$$

with $r_{1_g} = \frac{u_{g_2} - u_{g_1}}{b'}$, u_{g_1} the longitudinal gust velocity component at location "1" (see figure 12.1), u_{g_2} the one at location "2" and $b' = 0.85b$ with b the aircraft's span in [m]. The gust derivatives $C_{Y_{r_{1_g}}}$, $C_{\ell_{r_{1_g}}}$ and $C_{n_{r_{1_g}}}$ are equal to the wing's contribution to the stability derivatives C_{Y_r}, C_{ℓ_r} and C_{n_r}, respectively (see also table 6.11).

12.3.5 2D Anti-symmetrical vertical gust fields

For the 2D anti-symmetrical vertical gust fields, the vertical gust velocity component w_g is considered only. The gust input is now given as a rolling gust input, that is p_g. For the linearized aircraft model the aerodynamic force and moments coefficients are given as, see also reference [35],

$$C_{Y_g} = C_{Y_{p_g}} \frac{p_g b}{2Q_\infty} \tag{12.21}$$

$$C_{\ell_g} = C_{\ell_{p_g}} \frac{p_g b}{2Q_\infty} \tag{12.22}$$

$$C_{n_g} = C_{n_{p_g}} \frac{p_g b}{2Q_\infty} \tag{12.23}$$

with $p_g = \frac{w_{g_1} - w_{g_2}}{b'}$, w_{g_1} the vertical gust velocity component at location "1" (see figure 12.1), w_{g_2} the one at location "2" and $b' = 0.85b$ with b the aircraft's span in [m]. The gust derivatives $C_{Y_{p_g}}$, $C_{\ell_{p_g}}$ and $C_{n_{p_g}}$ are equal to the wing's contribution to the stability derivatives C_{Y_p}, C_{ℓ_p} and C_{n_p}, respectively (see also table 6.11).

12.4 Aircraft modeling

12.4.1 Aircraft equations of motion for 1D gust fields

Similar to section 11.5.1, in this section the FPA-model's linearized equations of motion are given (see also appendix I). The FPA-model's aircraft equations of motion make use of the following aerodynamic model for the 1D gust-induced aerodynamic force and moment coefficients,

$$C_{X_g} = C_{X_u} \hat{u}_g + C_{X_\alpha} \alpha_g + C_{X_q} \frac{q_g \bar{c}}{Q_\infty} \tag{12.24}$$

$$C_{Z_g} = C_{Z_u} \hat{u}_g + C_{Z_\alpha} \alpha_g + C_{Z_{\dot{\alpha}}} \frac{\dot{\alpha}_g \bar{c}}{Q_\infty} + C_{Z_q} \frac{q_g \bar{c}}{Q_\infty} \tag{12.25}$$

$$C_{m_g} = C_{m_u} \hat{u}_g + C_{m_\alpha} \alpha_g + C_{m_{\dot{\alpha}}} \frac{\dot{\alpha}_g \bar{c}}{Q_\infty} + C_{m_q} \frac{q_g \bar{c}}{Q_\infty} \tag{12.26}$$

and,

$$C_{Y_g} = C_{Y_{\beta_g}}\beta_g + C_{Y_{r_{2_g}}}\frac{r_{2_g}b}{2Q_\infty} \tag{12.27}$$

$$C_{\ell_g} = C_{\ell_{\beta_g}}\beta_g + C_{\ell_{r_{2_g}}}\frac{r_{2_g}b}{2Q_\infty} \tag{12.28}$$

$$C_{n_g} = C_{n_{\beta_g}}\beta_g + C_{n_{r_{2_g}}}\frac{r_{2_g}b}{2Q_\infty} \tag{12.29}$$

for the 1D non-dimensional symmetrical and 1D non-dimensional asymmetrical gust fields, respectively. Similar to reference [35], the contribution of $\dot{\beta}_g$ in equations (12.27), (12.28) and (12.29) is left out of consideration.

The equations of motion are written similar to equations (10.20) and (11.81),

$$P^c\ j\omega\ \underline{x} = Q^c\ \underline{x} + R^c\ \underline{u} \tag{12.30}$$

with for the symmetrical equations of motion the matrices P^c, Q^c and R^c equal to,

$$P_s^c = \frac{\bar{c}}{Q_\infty}\begin{bmatrix} -2\mu_c & 0 & 0 & 0 \\ 0 & (C_{Z_{\dot{\alpha}}} - 2\mu_c) & 0 & 0 \\ 0 & 0 & -1 & 0 \\ 0 & C_{m_{\dot{\alpha}}} & 0 & -2\mu_c K_Y^2 \end{bmatrix} \tag{12.31}$$

$$Q_s^c = \begin{bmatrix} -C_{X_u} & -C_{X_\alpha} & -C_{Z_0} & -C_{X_q} \\ -C_{Z_u} & -C_{Z_\alpha} & C_{X_0} & -\left(C_{Z_q} + 2\mu_c\right) \\ 0 & 0 & 0 & -1 \\ -C_{m_u} & -C_{m_\alpha} & 0 & -C_{m_q} \end{bmatrix} \tag{12.32}$$

and,

$$R_s^c = \begin{bmatrix} -C_{X_u} & -C_{X_\alpha} & 0 & -C_{X_q} \\ -C_{Z_u} & -C_{Z_\alpha} & -C_{Z_{\dot{\alpha}}} & -C_{Z_q} \\ 0 & 0 & 0 & 0 \\ -C_{m_u} & -C_{m_\alpha} & -C_{m_{\dot{\alpha}}} & -C_{m_q} \end{bmatrix} \tag{12.33}$$

respectively. In equation (12.30) the aircraft state and the input are defined as $\underline{x} = \left[\hat{u}, \alpha, \theta, \frac{q\bar{c}}{Q_\infty}\right]^T$, and $\underline{u} = \left[\hat{u}_g,\ \alpha_g,\ \frac{\dot{\alpha}_g\bar{c}}{Q_\infty},\ \frac{q_g\bar{c}}{Q_\infty}\right]^T$, respectively. The definition of the stability derivatives is given in appendix I, table I.5.

Similar to the symmetrical equations of motion, the asymmetrical equations of motion are also written as equation (12.30) with the matrices P^c, Q^c and R^c now according to,

$$P_a^c = \frac{b}{Q_\infty}\begin{bmatrix} \left(C_{Y_{\dot{\beta}}} - 2\mu_b\right) & 0 & 0 & 0 \\ 0 & -\frac{1}{2} & 0 & 0 \\ C_{\ell_{\dot{\beta}}} & 0 & -4\mu_b K_X^2 & 4\mu_b K_{XZ} \\ C_{n_{\dot{\beta}}} & 0 & 4\mu_b K_{XZ} & -4\mu_b K_Z^2 \end{bmatrix} \tag{12.34}$$

$$Q_a^c = \begin{bmatrix} -C_{Y_\beta} & -C_L & -C_{Y_p} & -(C_{Y_r} - 4\mu_b) \\ 0 & 0 & -1 & 0 \\ -C_{\ell_\beta} & 0 & -C_{\ell_p} & -C_{\ell_r} \\ -C_{n_\beta} & 0 & -C_{n_p} & -C_{n_r} \end{bmatrix} \tag{12.35}$$

and,

$$R_a^c = \begin{bmatrix} -C_{Y_\beta} & -C_{Y_{r_{2_g}}} \\ 0 & 0 \\ -C_{\ell_\beta} & -C_{\ell_{r_{2_g}}} \\ -C_{n_\beta} & -C_{n_{r_{2_g}}} \end{bmatrix} \tag{12.36}$$

respectively, with the aircraft state $\underline{x} = \left[\beta, \varphi, \frac{pb}{2Q_\infty}, \frac{rb}{2Q_\infty}\right]^T$ and the input $\underline{u} = \left[\beta_g, \ \frac{r_{2_g} b}{2Q_\infty}\right]^T$. The definition of the stability derivatives is given in appendix I, table I.6.

The 1D PSD-functions for the non-dimensional gust velocity components $\hat{u}_g$, α_g, $\frac{q_g \bar{c}}{Q_\infty}$, β_g and $\frac{r_{2_g} b}{2Q_\infty}$ are summarized in equation (12.8).

12.4.2 Aircraft equations of motion for 2D gust fields

In this section the FPA-model asymmetrical linearized equations of motion are given for the 2D anti-symmetrical gust fields $\hat{u}_g$ and α_g. The non-dimensional aerodynamic force and moment coefficients due to these fields are written as,

$$C_{Y_g} = C_{Y_{r_{1_g}}} \frac{r_{1_g} b}{2Q_\infty} + C_{Y_{p_g}} \frac{p_g b}{2Q_\infty} \tag{12.37}$$

$$C_{\ell_g} = C_{\ell_{r_{1_g}}} \frac{r_{1_g} b}{2Q_\infty} + C_{\ell_{p_g}} \frac{p_g b}{2Q_\infty} \tag{12.38}$$

$$C_{n_g} = C_{n_{r_{1_g}}} \frac{r_{1_g} b}{2Q_\infty} + C_{n_{p_g}} \frac{p_g b}{2Q_\infty} \tag{12.39}$$

For the asymmetrical equations of motion given in equation (12.30), the matrices P^c, Q^c are equal to ones given in equations (12.34) and (12.35), respectively, with the aircraft state $\underline{x} = \left[\beta, \varphi, \frac{pb}{2Q_\infty}, \frac{rb}{2Q_\infty}\right]^T$. The matrix R^c is defined as,

$$R_a^c = \begin{bmatrix} -C_{Y_{r_{1_g}}} & -C_{Y_{p_g}} \\ 0 & 0 \\ -C_{\ell_{r_{1_g}}} & -C_{\ell_{p_g}} \\ -C_{n_{r_{1_g}}} & -C_{n_{p_g}} \end{bmatrix} \tag{12.40}$$

with the input $\underline{u} = \left[\frac{r_{1_g} b}{2Q_\infty}, \ \frac{p_g b}{2Q_\infty}\right]^T$, and the gust derivatives $C_{Y_{r_{1_g}}} = C_{Y_{r_w}}$, $C_{\ell_{r_{1_g}}} = C_{\ell_{r_w}}$, $C_{n_{r_{1_g}}} = C_{n_{r_w}}$, $C_{Y_{p_g}} = C_{Y_{p_w}}$, $C_{\ell_{p_g}} = C_{\ell_{p_w}}$ and $C_{n_{p_g}} = C_{n_{p_w}}$.

The PSD-functions for the non-dimensional gust inputs $\frac{r_{1_g} b}{2Q_\infty}$ and $\frac{p_g b}{2Q_\infty}$ are summarized in equation (12.8).

12.5 Remarks

The assumptions made in the derivation of the FPA-model equations of motion are similar to those presented in chapter 11.
In chapter 13 both time- and frequency-domain results for the FPA-model will be compared to the LPF-solutions presented in chapter 9. These results will be given in terms of both aerodynamic model and aircraft motion responses. The FPA-model results will also be compared to those obtained for the PCA- and the DUT-model.

Part V

Comparison of Gust Response Calculations

Chapter 13

Comparison of results and discussion

13.1 Introduction

This chapter discusses the aircraft responses of the Linearized Potential Flow (LPF) solution for recti-linear flightpaths, the Parametric Computational Aerodynamics (PCA), the Delft University of Technology (DUT) and the Four-Point-Aircraft (FPA) models. Comparisons will be made in terms of both time- and frequency-domain results of the aerodynamic force and moment coefficients. Furthermore, comparisons will be made in terms of aircraft motion results. Also these responses will be given for both the time- and frequency-domain. The LPF-EOM-solution results for stochastic flightpaths will be discussed as well, however, they are given for time-domain aircraft motion responses only. These results are assumed to be the benchmark, that is they resemble reality the closest. In section 13.2 an overview of the models is given, while in section 13.3 the aerodynamic responses are discussed for the recti-linear flightpath LPF-solution and the PCA-, DUT- and FPA-models. Next, in section 13.4, the models' aircraft motion responses are given. Section 13.5 is dedicated to the LPF-EOM-model. Here, its time-domain aircraft responses are compared to the ones obtained for the recti-linear flightpath LPF-solution and the PCA-, DUT- and FPA-models.
For all models, the responses to symmetrical longitudinal - (u_g), asymmetrical lateral - (v_g), symmetrical vertical - (w_g), anti-symmetrical longitudinal - (u_g) and anti-symmetrical vertical gust velocity component (w_g) will be shown and discussed. The presented results hold for the gust scale length $L_g = 300$ [m] only.

13.2 Overview of models

13.2.1 Introduction

Apart from the LPF-(EOM-) solutions, the PCA-, DUT- and FPA-methods make use of parametric aerodynamic models in terms of constant stability- and gust derivatives. The calculation of the steady stability derivatives has been performed in chapter 6, while the calculation of the unsteady stability derivatives is given in chapter 10. These derivatives will be used for all models (except the LPF-solution). As the steady and unsteady gust derivatives are concerned, they are calculated (or defined) in chapters 10, 11 and 12 for the PCA-, DUT- and FPA-model, respectively, while the gust input definitions are summarized in appendix G for all models.
With respect to the mathematical aircraft models, they are decoupled resulting in two sets of equations of motion: that is the symmetrical and asymmetrical linearized equations of motion, see also appendix I. In the frequency-domain both the symmetrical and asymmetrical equations of motion were written as, see also chapters 10 through 12,

$$P\ j\omega\ \underline{x} = Q\ \underline{x} + R\ \underline{u} \tag{13.1}$$

or, since the matrix elements in equation (13.1) are constant, the time-domain equations of motion are written as,

$$P\ \frac{d\underline{x}}{dt} = Q\ \underline{x} + R\ \underline{u} \tag{13.2}$$

For the symmetrical equations of motion the matrices P and Q in equation (13.2) are given as,

$$P_s = \frac{\bar{c}}{Q_\infty} \begin{bmatrix} -2\mu_c & 0 & 0 & 0 \\ 0 & (C_{Z_{\dot{\alpha}}} - 2\mu_c) & 0 & 0 \\ 0 & 0 & -1 & 0 \\ 0 & C_{m_{\dot{\alpha}}} & 0 & -2\mu_c K_Y^2 \end{bmatrix} \tag{13.3}$$

$$Q_s = \begin{bmatrix} -C_{X_u} & -C_{X_\alpha} & -C_{Z_0} & -C_{X_q} \\ -C_{Z_u} & -C_{Z_\alpha} & C_{X_0} & -\left(C_{Z_q} + 2\mu_c\right) \\ 0 & 0 & 0 & -1 \\ -C_{m_u} & -C_{m_\alpha} & 0 & -C_{m_q} \end{bmatrix} \tag{13.4}$$

respectively. For these equations the aircraft state equals $\underline{x} = \left[\hat{u}, \alpha, \theta, \frac{q\bar{c}}{Q_\infty}\right]^T$, while (for now) the matrix P in equations (13.1) and (13.2) is given as,

$$R_s = -\begin{bmatrix} C_{X_g} \\ C_{Z_g} \\ 0 \\ C_{m_g} \end{bmatrix} \tag{13.5}$$

with as input vector the scalar $\underline{u} = 1$.

Similar to the symmetrical equations of motion, for the asymmetrical ones the matrices P, Q and R in equation (13.2) are given as,

$$P_a = \frac{b}{Q_\infty}\begin{bmatrix} \left(C_{Y_{\dot\beta}} - 2\mu_b\right) & 0 & 0 & 0 \\ 0 & -\frac{1}{2} & 0 & 0 \\ C_{\ell_{\dot\beta}} & 0 & -4\mu_b K_X^2 & 4\mu_b K_{XZ} \\ C_{n_{\dot\beta}} & 0 & 4\mu_b K_{XZ} & -4\mu_b K_Z^2 \end{bmatrix} \tag{13.6}$$

$$Q_a = \begin{bmatrix} -C_{Y_\beta} & -C_L & -C_{Y_p} & -\left(C_{Y_r} - 4\mu_b\right) \\ 0 & 0 & -1 & 0 \\ -C_{\ell_\beta} & 0 & -C_{\ell_p} & -C_{\ell_r} \\ -C_{n_\beta} & 0 & -C_{n_p} & -C_{n_r} \end{bmatrix} \tag{13.7}$$

and,

$$R_a = -\begin{bmatrix} C_{Y_g} \\ 0 \\ C_{\ell_g} \\ C_{n_g} \end{bmatrix} \tag{13.8}$$

respectively. For the asymmetrical equations of motion the aircraft's state equals $\underline{x} = \left[\beta, \varphi, \frac{pb}{2Q_\infty}, \frac{rb}{2Q_\infty}\right]^T$, while, similar to the symmetrical equations of motion, the input-vector also becomes the scalar $\underline{u} = 1$.

The aerodynamic coefficients C_{X_g}, C_{Z_g} and C_{m_g} in equation (13.5), and their asymmetrical counterparts C_{Y_g}, C_{ℓ_g} and C_{n_g} in equation (13.8) will be discussed in the following sections. First the LPF-solution aerodynamic coefficients will be briefly discussed. Next, for the PCA-, the DUT- and the FPA-model these coefficients will be given as parametric aerodynamic models in terms of constant gust derivatives and gust inputs.

13.2.2 The LPF solution

In chapters 3, 4 and 9 the LPF theory has been discussed for recti-linear flightpaths (no aircraft motions are considered). Application of the theory has eventually resulted in the time-domain aerodynamic response of the aircraft grid defined in chapter 6. The results were given in terms of the time-domain response of the aerodynamic coefficients $C_{X_g}(t)$, $C_{Y_g}(t)$, $C_{Z_g}(t)$, $C_{\ell_g}(t)$, $C_{m_g}(t)$ and $C_{n_g}(t)$ for both symmetrical and anti-symmetrical gust fields. These fields are generated in appendix G and are based on the theory provided in chapter 2. In section 13.3 the LPF-model time-domain response will be compared to the parametric aerodynamic model results obtained for the PCA-, the DUT- and the FPA-model.

13.2.3 The LPF-EOM-solution

Similar to the recti-linear flightpath LPF simulations, in chapters 3, 4 and 9 the LPF-EOM theory has been discussed. The LPF-solution, which is now coupled to the equations

of motion, also makes use of the aircraft grid defined in chapter 6 and the gust fields generated in appendix G. In section 13.5 the LPF-EOM-model time-domain aircraft motion responses will be compared to the ones obtained for the recti-linear flightpath LPF-solution. Aircraft motion results will be compared to the ones obtained for the PCA-, DUT- and FPA-model.

13.2.4 The PCA-model

For the PCA-model, the symmetrical gust inputs (u_g and w_g), the asymmetrical gust input (v_g) and the anti-symmetrical gust inputs (u_g and w_g) will be considered only. For these inputs the aerodynamic model is written as (using non-dimensional gust inputs for the symmetrical gust inputs u_g and w_g),

$$\left.\begin{array}{rcl} C_{X_g} &=& C_{X_{u_g}}\ \hat{u}_g + C_{X_{\dot{u}_g}}\ \frac{\dot{\hat{u}}_g \bar{c}}{Q_\infty} \\ C_{Z_g} &=& C_{Z_{u_g}}\ \hat{u}_g + C_{Z_{\dot{u}_g}}\ \frac{\dot{\hat{u}}_g \bar{c}}{Q_\infty} \\ C_{m_g} &=& C_{m_{u_g}}\ \hat{u}_g + C_{m_{\dot{u}_g}}\ \frac{\dot{\hat{u}}_g \bar{c}}{Q_\infty} \end{array}\right\} \tag{13.9}$$

with $\hat{u}_g = \frac{u_g}{Q_\infty}$, $\bar{c}$ the mean aerodynamic chord and Q_∞ the airspeed. For the aerodynamic model with respect to the vertical gust input, it becomes,

$$\left.\begin{array}{rcl} C_{X_g} &=& C_{X_{\alpha_g}}\ \alpha_g + C_{X_{\dot{\alpha}_g}}\ \frac{\dot{\alpha}_g \bar{c}}{Q_\infty} \\ C_{Z_g} &=& C_{Z_{\alpha_g}}\ \alpha_g + C_{Z_{\dot{\alpha}_g}}\ \frac{\dot{\alpha}_g \bar{c}}{Q_\infty} \\ C_{m_g} &=& C_{m_{\alpha_g}}\ \alpha_g + C_{m_{\dot{\alpha}_g}}\ \frac{\dot{\alpha}_g \bar{c}}{Q_\infty} \end{array}\right\} \tag{13.10}$$

with $\alpha_g = \frac{w_g}{Q_\infty}$ and the gust derivatives shown in equations (13.9) and (13.10) summarized in tables 13.1 and 13.2.

Similarly, the aerodynamic model with respect to the asymmetrical gust input (v_g) written in non-dimensional form is given as,

$$\left.\begin{array}{rcl} C_{Y_g} &=& C_{Y_{\beta_g}}\ \beta_g + C_{Y_{\dot{\beta}_g}}\ \frac{\dot{\beta}_g b}{Q_\infty} \\ C_{\ell_g} &=& C_{\ell_{\beta_g}}\ \beta_g + C_{\ell_{\dot{\beta}_g}}\ \frac{\dot{\beta}_g b}{Q_\infty} \\ C_{n_g} &=& C_{n_{\beta_g}}\ \beta_g + C_{n_{\dot{\beta}_g}}\ \frac{\dot{\beta}_g b}{Q_\infty} \end{array}\right\} \tag{13.11}$$

with $\beta_g = \frac{v_g}{Q_\infty}$ and b the wingspan.

For the anti-symmetrical gust fields u_g and w_g, use is made of the gust inputs r_{1_g} and p_g, respectively (see also chapter 12 and appendices G and H). For these fields the non-dimensional aerodynamic models are written as,

$$\left.\begin{array}{rcl} C_{Y_g} &=& C_{Y_{r_{1_g}}}\ \frac{r_{1_g} b}{2Q\infty} + C_{Y_{\dot{r}_{1_g}}}\ \frac{b}{Q_\infty}\frac{\dot{r}_{1_g} b}{2Q\infty} \\ C_{\ell_g} &=& C_{\ell_{r_{1_g}}}\ \frac{r_{1_g} b}{2Q\infty} + C_{\ell_{\dot{r}_{1_g}}}\ \frac{b}{Q_\infty}\frac{\dot{r}_{1_g} b}{2Q\infty} \\ C_{n_g} &=& C_{n_{r_{1_g}}}\ \frac{r_{1_g} b}{2Q\infty} + C_{n_{\dot{r}_{1_g}}}\ \frac{b}{Q_\infty}\frac{\dot{r}_{1_g} b}{2Q\infty} \end{array}\right\} \tag{13.12}$$

and,

$$\left.\begin{array}{rcl} C_{Y_g} & = & C_{Y_{p_g}} \frac{p_g b}{2Q_\infty} + C_{Y_{\dot{p}_g}} \frac{b}{Q_\infty} \frac{\dot{p}_g b}{2Q_\infty} \\ C_{\ell_g} & = & C_{\ell_{p_g}} \frac{p_g b}{2Q_\infty} + C_{\ell_{\dot{p}_g}} \frac{b}{Q_\infty} \frac{\dot{p}_g b}{2Q_\infty} \\ C_{n_g} & = & C_{n_{p_g}} \frac{p_g b}{2Q_\infty} + C_{n_{\dot{p}_g}} \frac{b}{Q_\infty} \frac{\dot{p}_g b}{2Q_\infty} \end{array}\right\} \tag{13.13}$$

respectively, with the gust derivatives given in equations (13.11), (13.12) and (13.13) summarized in tables 13.1 and 13.2. The PCA-model gust derivatives were calculated in chapter 10 from resonance frequencies in aircraft motion output Power Spectral Density (PSD) functions.
The aerodynamic model definition given above is used in equations (13.5) and (13.8), and it will allow the calculation of both time- ánd frequency-domain aircraft motion responses. For the time-domain aircraft motion simulations use is made of the 2D spatial-domain gust fields calculated in appendix G. For the frequency-domain aircraft motion responses (which are given in terms of the aircraft state PSD-functions), the input PSD-functions are summarized in appendix H. For the one-dimensional (1D) non-dimensional gust inputs $\hat{u}_g$, β_g and α_g, the PCA-model makes use of the 1D PSD-functions given in equations (H.7), (H.8) and (H.9), respectively. For the two-dimensional (2D) non-dimensional gust inputs $\frac{r_{1_g} b}{2Q_\infty}$ and $\frac{p_g b}{2Q_\infty}$, the PCA-model makes use of the PSD-functions summarized in equation (H.12).

13.2.5 The DUT-model

Similar to the PCA-model, for the DUT-model the 1D symmetrical gust inputs (u_g and w_g), the 1D asymmetrical gust input (v_g) and the 2D anti-symmetrical gust inputs (u_g and w_g) will be considered only.
For the 1D gust inputs the aerodynamic model is written as (using non-dimensional gust inputs),

$$\left.\begin{array}{rcl} C_{X_g} & = & C_{X_{u_g}} \hat{u}_g \\ C_{Z_g} & = & C_{Z_{u_g}} \hat{u}_g \\ C_{m_g} & = & C_{m_{u_g}} \hat{u}_g \end{array}\right\} \tag{13.14}$$

with $\hat{u}_g = \frac{u_g}{Q_\infty}$ and Q_∞ the airspeed. Note that no unsteady gust derivatives are used with respect to the u_g gust field.
The aerodynamic model with respect to the vertical gust input becomes,

$$\left.\begin{array}{rcl} C_{X_g} & = & C_{X_{\alpha_g}} \alpha_g + C_{X_{\dot{\alpha}_g}} \frac{\dot{\alpha}_g \bar{c}}{Q_\infty} \\ C_{Z_g} & = & C_{Z_{\alpha_g}} \alpha_g + C_{Z_{\dot{\alpha}_g}} \frac{\dot{\alpha}_g \bar{c}}{Q_\infty} \\ C_{m_g} & = & C_{m_{\alpha_g}} \alpha_g + C_{m_{\dot{\alpha}_g}} \frac{\dot{\alpha}_g \bar{c}}{Q_\infty} \end{array}\right\} \tag{13.15}$$

with $\alpha_g = \frac{w_g}{Q_\infty}$ and the definition of the gust derivatives used in equations (13.14) and (13.15) summarized in tables 13.1 and 13.2. These gust derivatives are now given in terms of stability derivatives.

Similarly, the aerodynamic model with respect to the 1D asymmetrical gust input (v_g) written in non-dimensional form is given as,

$$\left.\begin{array}{rcl} C_{Y_g} &=& C_{Y_{\beta_g}}\ \beta_g + C_{Y_{\dot{\beta}_g}}\ \frac{\dot{\beta}_g b}{Q_\infty} \\ C_{\ell_g} &=& C_{\ell_{\beta_g}}\ \beta_g + C_{\ell_{\dot{\beta}_g}}\ \frac{\dot{\beta}_g b}{Q_\infty} \\ C_{n_g} &=& C_{n_{\beta_g}}\ \beta_g + C_{n_{\dot{\beta}_g}}\ \frac{\dot{\beta}_g b}{Q_\infty} \end{array}\right\} \tag{13.16}$$

with $\beta_g = \frac{v_g}{Q_\infty}$ and b the wingspan.
For the anti-symmetrical gust fields u_g and w_g, the non-dimensional aerodynamic models are written as,

$$\left.\begin{array}{rcl} C_{Y_g} &=& C_{Y_{u_g}}\ \hat{u}_g \\ C_{\ell_g} &=& C_{\ell_{u_g}}\ \hat{u}_g \\ C_{n_g} &=& C_{n_{u_g}}\ \hat{u}_g \end{array}\right\} \tag{13.17}$$

and,

$$\left.\begin{array}{rcl} C_{Y_g} &=& C_{Y_{\alpha_g}}\ \alpha_g \\ C_{\ell_g} &=& C_{\ell_{\alpha_g}}\ \alpha_g \\ C_{n_g} &=& C_{n_{\alpha_g}}\ \alpha_g \end{array}\right\} \tag{13.18}$$

respectively, with the gust derivatives given in equations (13.16), (13.17) and (13.18) also summarized in tables 13.1 and 13.2.

The definition of the aerodynamic models presented in this section are also used in equations (13.5) and (13.8) to calculate both time- and frequency-domain aircraft responses. Similar to the PCA-model, for the time-domain aircraft motion responses use is made of the 2D spatial-domain gust fields calculated in appendix G. Also, for the frequency-domain aircraft motion responses (which are given in terms of the aircraft state PSD-functions), the input PSD-functions are summarized in appendix H. For the 1D non-dimensional gust inputs $\hat{u}_g$, β_g and α_g, the DUT-model also makes use of the 1D PSD-functions given in equations (H.7), (H.8) and (H.9), respectively. For the 2D non-dimensional gust inputs $\hat{u}_g$ and α_g, the DUT-model makes use of the Effective 1D PSD-functions defined in chapter 11, see equations (11.73) and (11.74), respectively.

13.2.6 The FPA-model

Also for the FPA-model, the 1D symmetrical gust inputs (u_g and w_g), the 1D asymmetrical gust input (v_g) and the 2D anti-symmetrical gust inputs (u_g and w_g) will be considered only. For the 1D longitudinal gust input the aerodynamic model is equal to the one given in equation (13.14). The aerodynamic model with respect to the symmetrical vertical gust input (w_g) becomes,

$$\left.\begin{array}{rcl} C_{X_g} &=& C_{X_{\alpha_g}}\ \alpha_g + C_{X_{\dot{\alpha}_g}}\ \frac{\dot{\alpha}_g \bar{c}}{Q_\infty} + C_{X_{q_g}}\ \frac{q_g \bar{c}}{Q_\infty} \\ C_{Z_g} &=& C_{Z_{\alpha_g}}\ \alpha_g + C_{Z_{\dot{\alpha}_g}}\ \frac{\dot{\alpha}_g \bar{c}}{Q_\infty} + C_{Z_{q_g}}\ \frac{q_g \bar{c}}{Q_\infty} \\ C_{m_g} &=& C_{m_{\alpha_g}}\ \alpha_g + C_{m_{\dot{\alpha}_g}}\ \frac{\dot{\alpha}_g \bar{c}}{Q_\infty} + C_{m_{q_g}}\ \frac{q_g \bar{c}}{Q_\infty} \end{array}\right\} \tag{13.19}$$

with the gust inputs defined in chapter 12 and summarized in appendix G. The definition of the gust derivatives used in equation (13.19) is summarized in tables 13.1 and 13.2. Similar to the DUT-model gust derivatives, the FPA-model gust derivatives are also given in terms of stability derivatives.
The aerodynamic model with respect to the 1D asymmetrical gust input (v_g) written in non-dimensional form is given as,

$$\left.\begin{array}{rcl} C_{Y_g} &=& C_{Y_{\beta_g}}\ \beta_g + C_{Y_{r_{2_g}}}\ \frac{r_{2_g} b}{2Q_\infty} \\ C_{\ell_g} &=& C_{\ell_{\beta_g}}\ \beta_g + C_{\ell_{r_{2_g}}}\ \frac{r_{2_g} b}{2Q_\infty} \\ C_{n_g} &=& C_{n_{\beta_g}}\ \beta_g + C_{n_{r_{2_g}}}\ \frac{r_{2_g} b}{2Q_\infty} \end{array}\right\} \qquad (13.20)$$

with the gust inputs defined in chapter 12 and summarized in appendix G.
For the anti-symmetrical gust fields u_g and w_g, use is made of the gust inputs r_{1_g} and p_g, respectively (see also chapter 12 and appendices G and H). For these fields the non-dimensional aerodynamic models are written as,

$$\left.\begin{array}{rcl} C_{Y_g} &=& C_{Y_{r_{1_g}}}\ \frac{r_{1_g} b}{2Q_\infty} \\ C_{\ell_g} &=& C_{\ell_{r_{1_g}}}\ \frac{r_{1_g} b}{2Q_\infty} \\ C_{n_g} &=& C_{n_{r_{1_g}}}\ \frac{r_{1_g} b}{2Q_\infty} \end{array}\right\} \qquad (13.21)$$

and,

$$\left.\begin{array}{rcl} C_{Y_g} &=& C_{Y_{p_g}}\ \frac{p_g b}{2Q_\infty} \\ C_{\ell_g} &=& C_{\ell_{p_g}}\ \frac{p_g b}{2Q_\infty} \\ C_{n_g} &=& C_{n_{p_g}}\ \frac{p_g b}{2Q_\infty} \end{array}\right\} \qquad (13.22)$$

with the gust derivatives given in equations (13.20), (13.21) and (13.22) summarized in tables 13.1 and 13.2.

The definition of the aerodynamic models presented in this section are also used in equations (13.5) and (13.8) to calculate both the time- and frequency-domain aircraft motion responses. Also for the FPA-model the time-domain aircraft motion responses are calculated using the 2D spatial-domain gust fields given in appendix G. For the frequency-domain aircraft motion responses (which are given in terms of the aircraft state PSD-functions), the gust input PSD-functions are summarized in appendix H. All FPA-model non-dimensional input PSD-functions are summarized in equation (H.12).

13.3 Aerodynamic model responses

13.3.1 Introduction

In this section the time-domain aerodynamic-model responses are given to both the symmetrical and anti-symmetrical gust fields defined in appendix G. The aircraft's aerodynamic response will be given in terms of the non-dimensional force- and moment-coefficients due to isolated gust fields, i.e. $C_{X_g}(t)$, $C_{Y_g}(t)$, $C_{Z_g}(t)$, $C_{\ell_g}(t)$, $C_{m_g}(t)$ and

Model	1D gust fields								2D gust fields			
	symmetrical					asymmetrical			anti-symmetrical			
	$C_{X_{u_g}}$	$C_{X_{\dot{u}_g}}$	$C_{X_{\alpha_g}}$	$C_{X_{\dot{\alpha}_g}}$	$C_{X_{q_g}}$	$C_{Y_{\beta_g}}$	$C_{Y_{\dot{\beta}_g}}$	$C_{Y_{r_{2_g}}}$	$C_{Y_{r_{1_g}}}$ / $C_{Y_{u_g}}$	$C_{Y_{\dot{r}_{1_g}}}$	$C_{Y_{p_g}}$ / $C_{Y_{\alpha_g}}$	$C_{Y_{\dot{p}_g}}$
PCA	-0.0032	+0.7145	+0.1692	•	•	-0.4046	+0.0632	•	-0.2392	+0.0052	+0.0347	-0.0359
DUT	C_{X_u}	0	C_{X_α}	$C_{X_{\dot{\alpha}}} - C_{X_q}$	•	C_{Y_β}	$C_{Y_{\dot{\beta}}} + \frac{1}{2}C_{Y_{r_v}}$	•	$C_{Y_{r_w}}$	•	$C_{Y_{p_w}}$	•
FPA	C_{X_u}	0	C_{X_α}	$C_{X_{\dot{\alpha}}}$	C_{X_q}	C_{Y_β}	•	$C_{Y_{r_v}}$	$C_{Y_{r_w}}$	•	$C_{Y_{p_w}}$	•
	$C_{Z_{u_g}}$	$C_{Z_{\dot{u}_g}}$	$C_{Z_{\alpha_g}}$	$C_{Z_{\dot{\alpha}_g}}$	$C_{Z_{q_g}}$	$C_{\ell_{\beta_g}}$	$C_{\ell_{\dot{\beta}_g}}$	$C_{\ell_{r_{2_g}}}$	$C_{\ell_{r_{1_g}}}$ / $C_{\ell_{u_g}}$	$C_{\ell_{\dot{r}_{1_g}}}$	$C_{\ell_{p_g}}$ / $C_{\ell_{\alpha_g}}$	$C_{\ell_{\dot{p}_g}}$
PCA	-0.4592	+0.1470	-5.7874	+5.1534	•	-0.1090	+0.0194	•	+0.0519	-0.0017	-0.5088	+0.0261
DUT	C_{Z_u}	0	C_{Z_α}	$C_{Z_{\dot{\alpha}}} - C_{Z_q}$	•	C_{ℓ_β}	$C_{\ell_{\dot{\beta}}} + \frac{1}{2}C_{\ell_{r_v}}$	•	$C_{\ell_{r_w}}$	•	$C_{\ell_{p_w}}$	•
FPA	C_{Z_u}	0	C_{Z_α}	$C_{Z_{\dot{\alpha}}}$	C_{Z_q}	C_{ℓ_β}	•	$C_{\ell_{r_v}}$	$C_{\ell_{r_w}}$	•	$C_{\ell_{p_w}}$	•
	$C_{m_{u_g}}$	$C_{m_{\dot{u}_g}}$	$C_{m_{\alpha_g}}$	$C_{m_{\dot{\alpha}_g}}$	$C_{m_{q_g}}$	$C_{n_{\beta_g}}$	$C_{n_{\dot{\beta}_g}}$	$C_{n_{r_{2_g}}}$	$C_{n_{r_{1_g}}}$ / $C_{n_{u_g}}$	$C_{n_{\dot{r}_{1_g}}}$	$C_{n_{p_g}}$ / $C_{n_{\alpha_g}}$	$C_{n_{\dot{p}_g}}$
PCA	+0.0236	-0.2315	-0.7486	+2.9846	•	+0.0676	-0.0495	•	-0.0003	-0.0058	-0.0328	+ 0.0099
DUT	C_{m_u}	0	C_{m_α}	$C_{m_{\dot{\alpha}}} - C_{m_q}$	•	C_{n_β}	$C_{n_{\dot{\beta}}} + \frac{1}{2}C_{n_{r_v}}$	•	$C_{n_{r_w}}$	•	$C_{n_{p_w}}$	•
FPA	C_{m_u}	0	C_{m_α}	$C_{m_{\dot{\alpha}}}$	C_{m_q}	C_{n_β}	•	$C_{n_{r_v}}$	$C_{n_{r_w}}$	•	$C_{n_{p_w}}$	•

Table 13.1: The calculated gust derivatives for the Parametric Computational Aerodynamics (PCA) model and the definition of them for both the Delft University of Technology (DUT) and the Four-Point-Aircraft (FPA) model ("•" means not applicable for the model). The results are valid for the Stability Frame of Reference $\mathcal{F}_S$ and for the gust scale length $L_g = 300$ [m].

	1D gust fields								2D gust fields			
Model	**symmetrical**					**asymmetrical**			**anti-symmetrical**			
	$C_{X_{u_g}}$	$C_{X_{\dot{u}_g}}$	$C_{X_{\alpha_g}}$	$C_{X_{\dot{\alpha}_g}}$	$C_{X_{q_g}}$	$C_{Y_{\beta_g}}$	$C_{Y_{\dot{\beta}_g}}$	$C_{Y_{r_{2_g}}}$	$C_{Y_{r_{1_g}}}$ / $C_{Y_{u_g}}$	$C_{Y_{\dot{r}_{1_g}}}$	$C_{Y_{p_g}}$ / $C_{Y_{\alpha_g}}$	$C_{Y_{\dot{p}_g}}$
PCA	-0.0032	+0.7145	+0.1692	•	•	-0.4046	+0.0632	•	-0.2392	+0.0052	+0.0347	-0.0359
DUT	-0.0032	0	+0.1692	+0.0450	•	-0.4046	-0.0043	•	-0.0398	•	-0.0912	•
FPA	-0.0032	0	+0.1692	0	-0.0450	-0.4046	•	+0.2387	-0.0398	•	-0.0912	•
	$C_{Z_{u_g}}$	$C_{Z_{\dot{u}_g}}$	$C_{Z_{\alpha_g}}$	$C_{Z_{\dot{\alpha}_g}}$	$C_{Z_{q_g}}$	$C_{\ell_{\beta_g}}$	$C_{\ell_{\dot{\beta}_g}}$	$C_{\ell_{r_{2_g}}}$	$C_{\ell_{r_{1_g}}}$ / $C_{\ell_{u_g}}$	$C_{\ell_{\dot{r}_{1_g}}}$	$C_{\ell_{p_g}}$ / $C_{\ell_{\alpha_g}}$	$C_{\ell_{\dot{p}_g}}$
PCA	-0.4592	+0.1470	-5.7874	+5.1534	•	-0.1090	+0.0194	•	+0.0519	-0.0017	-0.5088	+0.0261
DUT	-0.4592	0	-5.7874	+4.1519	•	-0.1090	+0.0107	•	+0.0616	•	-0.5093	•
FPA	-0.4592	0	-5.7874	-0.3980	-4.5499	-0.1090	•	+0.0370	+0.0616	•	-0.5093	•
	$C_{m_{u_g}}$	$C_{m_{\dot{u}_g}}$	$C_{m_{\alpha_g}}$	$C_{m_{\dot{\alpha}_g}}$	$C_{m_{q_g}}$	$C_{n_{\beta_g}}$	$C_{n_{\dot{\beta}_g}}$	$C_{n_{r_{2_g}}}$	$C_{n_{r_{1_g}}}$ / $C_{n_{u_g}}$	$C_{n_{\dot{r}_{1_g}}}$	$C_{n_{p_g}}$ / $C_{n_{\alpha_g}}$	$C_{n_{\dot{p}_g}}$
PCA	+0.0236	-0.2315	-0.7486	+2.9846	•	+0.0676	-0.0495	•	-0.0003	-0.0058	-0.0328	+ 0.0099
DUT	+0.0236	0	-0.7486	+3.2392	•	+0.0676	-0.0317	•	-0.0010	•	-0.0172	•
FPA	+0.0236	0	-0.7486	-4.2255	-7.4647	+0.0676	•	-0.0940	-0.0010	•	-0.0172	•

Table 13.2: The calculated gust derivatives for the Parametric Computational Aerodynamics (PCA) model and their numerical values for both the Delft University of Technology (DUT) and the Four-Point-Aircraft (FPA) model ("•" means not applicable for the model). The results are valid for the Stability Frame of Reference $\mathcal{F}_S$ and for the gust scale length $L_g = 300$ [m].

$C_{n_g}(t)$. For these simulations, the aircraft travels along the negative X_E-axis of the Earth-Fixed Frame of Reference $\mathcal{F}_E$, see also figures 9.1 and 9.2, while no aircraft motions are considered.

For the symmetrical aerodynamic responses, the 2D symmetrical gust fields with respect to the atmospheric turbulence velocity components u_g and w_g are considered only. These aerodynamic responses are considered to be representative for 1D gust fields, that is both the longitudinal and vertical turbulence velocity components are assumed to be constant over the aircraft wingspan.
Similarly, for the asymmetrical aerodynamic responses, the 2D asymmetrical gust field with respect to the lateral atmospheric turbulence velocity component v_g is considered. The aerodynamic response to this input is also considered to be representative for a 1D lateral gust field v_g (the gust velocity component is constant over the aircraft wingspan).
Finally, the asymmetrical aerodynamic response to both the 2D anti-symmetrical gust fields u_g and w_g will be given. In this case both the u_g- and w_g-fields vary over the aircraft wingspan.
The PCA-, DUT- and FPA-model's aerodynamic responses will be compared to the LPF-solution, with the LPF-solution considered to be the benchmark, or the results that match reality the closest.

13.3.2 Time-domain results

In appendix G the definition of the gust inputs is summarized for all models. From both the spatial-domain gust fields, also defined in appendix G, ánd the definition of the gust inputs, the time-history of them is calculated. The non-dimensional translational gust inputs $\hat{u}_g(t) = \frac{u_g(t)}{Q_\infty}$, $\beta_g(t) = \frac{v_g(t)}{Q_\infty}$, $\alpha_g(t) = \frac{w_g(t)}{Q_\infty}$ are shown in figure 13.1, while in figure 13.2 their time derivatives are given. Furthermore, in figure 13.3 the non-dimensional rotational gust inputs $\frac{p_g b}{2Q_\infty}(t)$, $\frac{q_g \bar{c}}{Q_\infty}(t)$, $\frac{r_{1_g} b}{2Q_\infty}(t)$ and $\frac{r_{2_g} b}{2Q_\infty}(t)$ are shown, while in figure 13.4 the gust inputs $\frac{\dot{p}_g b}{2Q_\infty}(t)$ and $\frac{\dot{r}_{1_g} b}{2Q_\infty}(t)$ are given for the PCA-model only.
The gust inputs shown in figures 13.1 through 13.4 are used to calculate the gust-induced time-domain aerodynamic force and moment coefficients $C_{X_g}(t)$, $C_{Y_g}(t)$, $C_{Z_g}(t)$, $C_{\ell_g}(t)$, $C_{m_g}(t)$ and $C_{n_g}(t)$ presented in section 13.2.

In figures 13.5 through 13.7 the aerodynamic model response in terms of the coefficients C_{X_g}, C_{Z_g} and C_{m_g} with respect to the symmetrical longitudinal gust field u_g is shown. The PCA-model response for $C_{X_g}(\hat{u}_g(t))$ accurately follows the LPF-solution, while the DUT- and FPA-model responses do not. This is a consequence of the use of the unsteady gust derivative $C_{X_{\dot{u}_g}}$ in the PCA-model (both the DUT- and the FPA-model do not include unsteady gust derivatives for the u_g-fields).
For all models' $C_{Z_g}(\hat{u}_g(t))$ responses it follows that they almost coincide with the LPF-solution. Apparantly, the unsteady gust derivative as used in the PCA-model, that is $C_{Z_{\dot{u}_g}}$, does not improve accuracy.

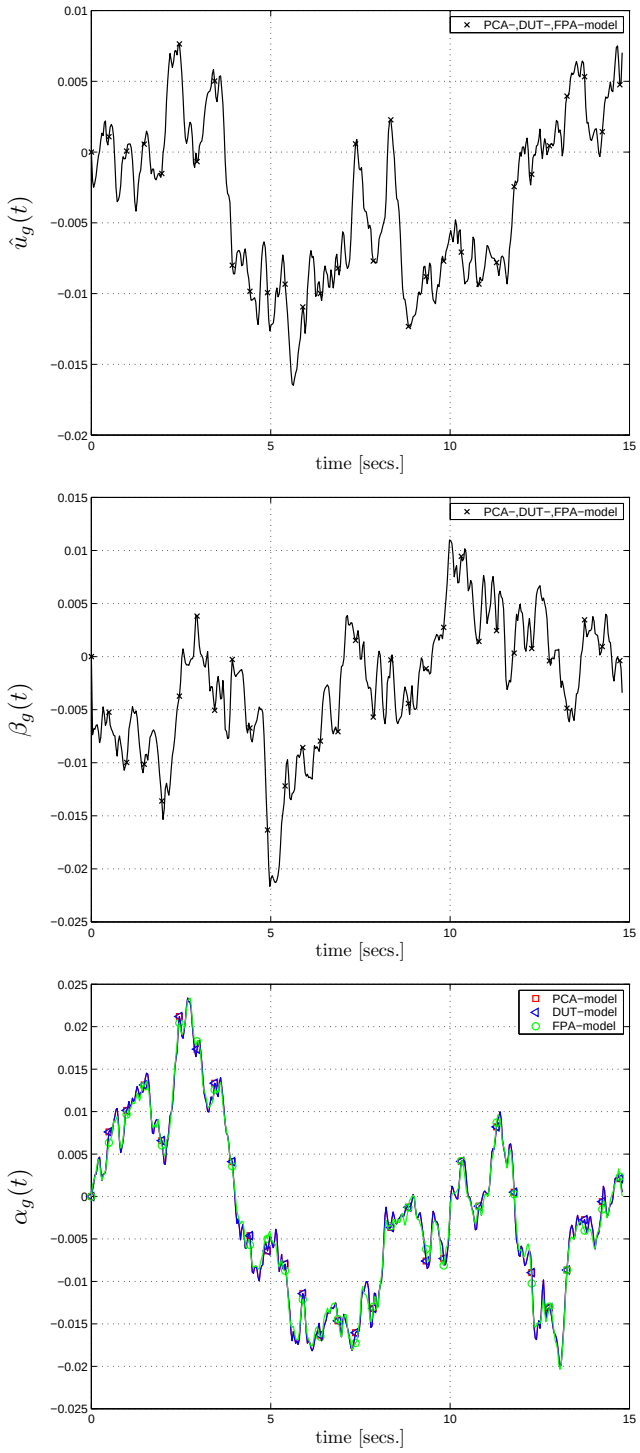


Figure 13.1: The non-dimensional translational gust inputs, $\hat{u}_g(t)$, $\beta_g(t)$ and $\alpha_g(t)$, for the parametric aerodynamic models.

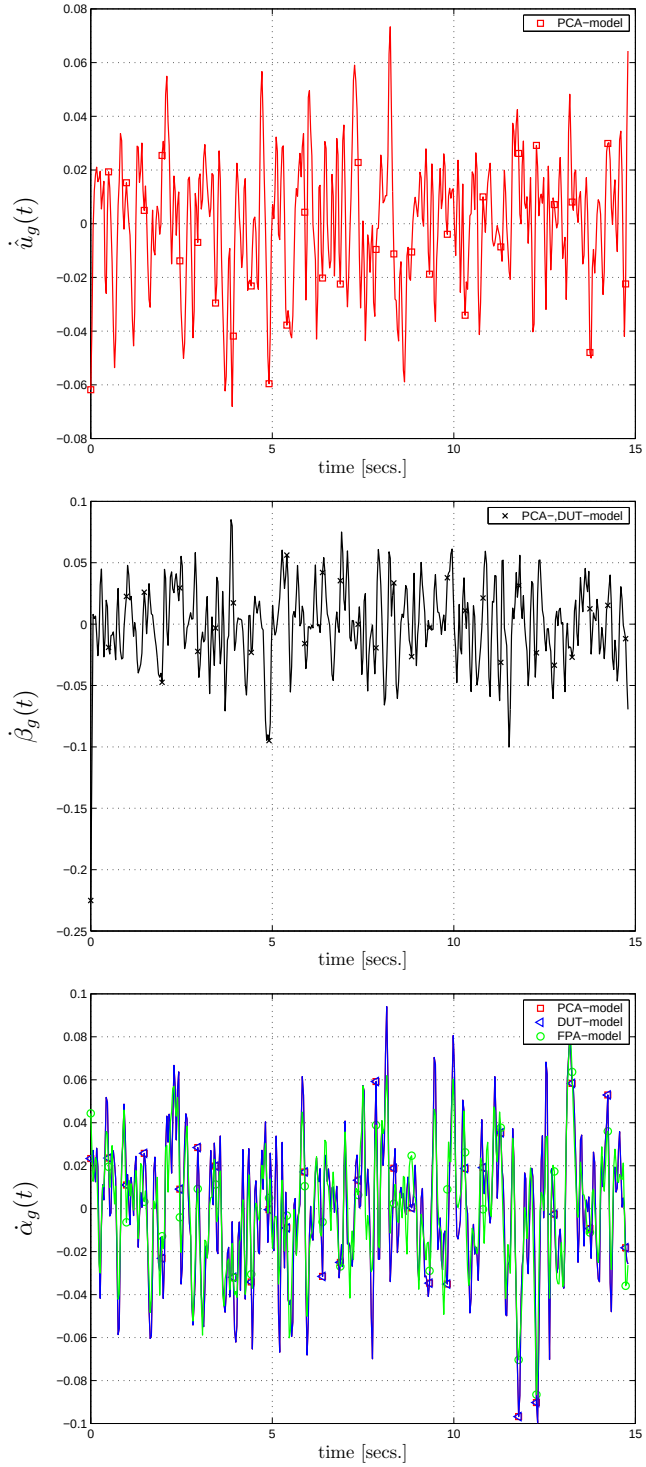


Figure 13.2: The time derivative of the non-dimensional translational gust inputs, $\dot{\hat{u}}_g(t)$, $\dot{\beta}_g(t)$ and $\dot{\alpha}_g(t)$, for the parametric aerodynamic models.

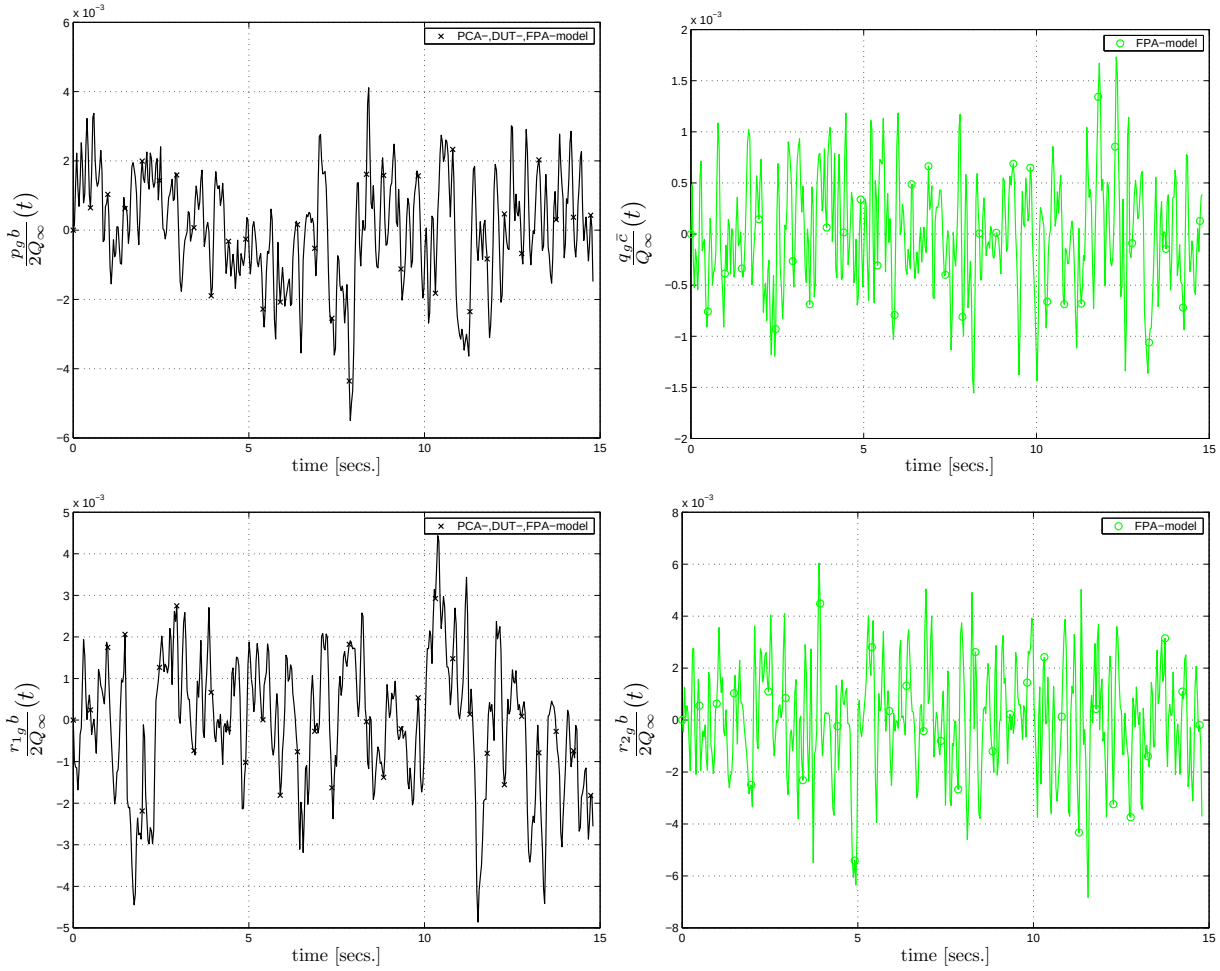


Figure 13.3: The non-dimensional rotational gust inputs, $\frac{p_g b}{2Q_\infty}(t)$, $\frac{q_g \bar{c}}{Q_\infty}(t)$, $\frac{r_{1_g} b}{2Q_\infty}(t)$ and $\frac{r_{2_g} b}{2Q_\infty}(t)$, for the parametric aerodynamic models.

Similar to the discussion with respect to the $C_{X_g}(\hat{u}_g(t))$ responses, for the $C_{m_g}(\hat{u}_g(t))$ responses it follows that the use of the unsteady gust derivative $C_{m_{\dot{u}_g}}$ does improve the response compared to the LPF-solution. It follows from figure 13.7 that the PCA-model response is more high-frequent as compared to the ones obtained for the DUT- and FPA-model. This is a consequence of the usage of the unsteady gust derivative $C_{m_{\dot{u}_g}}$.

In figures 13.8 through 13.10 the aerodynamic model response in terms of the aerodynamic coefficients C_{Y_g}, C_{ℓ_g} and C_{n_g} with respect to the asymmetrical lateral gust field v_g is given. It is shown that all model responses show very good agreement with those obtained for the LPF-solution.

In figures 13.11 through 13.13 the aerodynamic model response in terms of the aerodynamic coefficients C_{X_g}, C_{Z_g} and C_{m_g} with respect to the symmetrical vertical gust field w_g is shown. For the $C_{X_g}(\alpha_g(t))$ results all model responses are almost equal, however they all show bad agreement with the LPF-solution. This is attributed to the non-linear

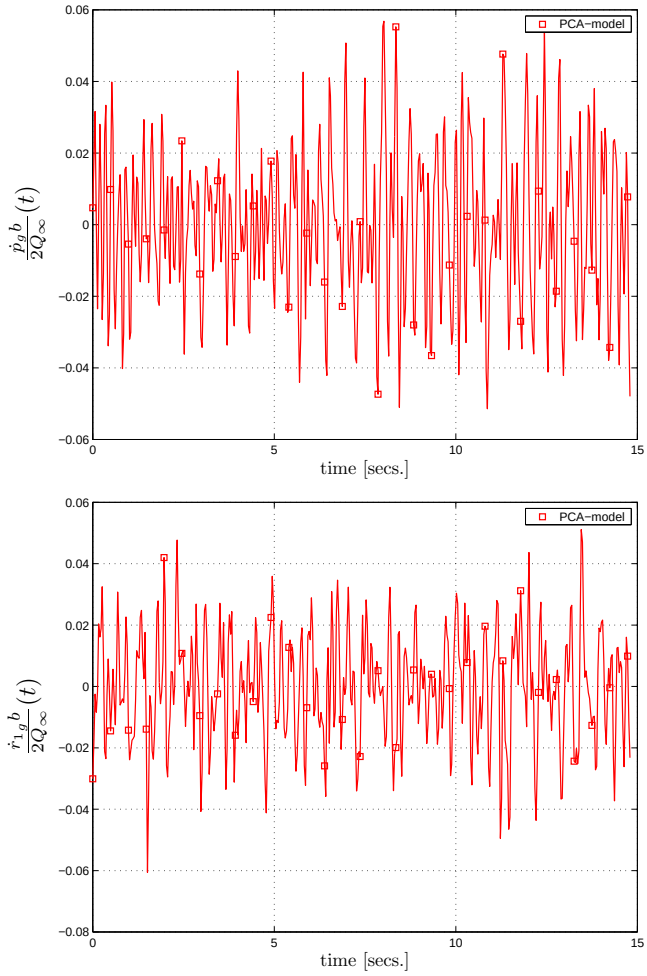


Figure 13.4: The time derivative of the non-dimensional rotational gust inputs, $\frac{\dot{p}_g b}{2Q_\infty}(t)$ and $\frac{\dot{r}_{1_g} b}{2Q_\infty}(t)$, for the PCA-model.

behaviour of the coefficient C_X with respect to angle-of-attack perturbations, see also figure 6.12. Furthermore, it is also attributed to the omission of the unsteady gust derivative $C_{X_{\dot{\alpha}_g}}$ for the PCA-model and setting the stability derivative $C_{X_{\dot{\alpha}}}$ to zero for the gust derivatives belonging to the DUT- and FPA-model.
Both the $C_{Z_g}(\alpha_g(t))$ and $C_{m_g}(\alpha_g(t))$ results are almost equal for all models and show excellent agreement with those obtained for the LPF-solution, which is attributed to the usage of unsteady gust derivatives. For all models these derivatives show good agreement, see also table 13.2.

Next, the PCA-, DUT- and FPA-model results are compared to the ones obtained for the LPF-solution. The results are shown for the 2D longitudinal gust field u_g. The FPA-model responses are representative for those of the DUT-model and the latter are therefore omitted in the figures. In figures 13.14 through 13.16 the aerodynamic model response in terms of the aerodynamic coefficients C_{Y_g}, C_{ℓ_g} and C_{n_g} with respect to the anti-symmetrical longitudinal gust field u_g is shown. For the $C_{Y_g}(\hat{u}_g(t))$ results, the PCA-model shows the

best agreement with the LPF-solution. This is attributed to the use of the unsteady gust derivative in the PCA-model leading to a more high frequent model-response. Also, it appears that the aerodynamic stiffness term $C_{Y_{u_g}}/C_{Y_{r_{1_g}}}$ is underestimated for both the DUT- and FPA-model. It should be noted, however, that the aerodynamic force response to 2D anti-symmetrical turbulence $C_{Y_g}(\hat{u}_g(t))$ is usually neglected in the DUT- and FPA-model, see references [30, 34, 35]. However, they áre retained in this thesis.
For the $C_{\ell_g}(\hat{u}_g(t))$ results, all models show excellent agreement with those obtained for the LPF-solution. This is attributed to the aerodynamic stiffness term $C_{\ell_{u_g}}/C_{\ell_{r_{1_g}}}$, which is of similar magnitude for all parametric models.
Similar to the $C_{Y_g}(\hat{u}_g(t))$ results, for the $C_{n_g}(\hat{u}_g(t))$ responses the PCA-model shows the best agreement with the LPF-solution. This is attributed to the use of the unsteady gust derivative in the PCA-model leading to a more high frequent model-response.

Finally, the PCA-, DUT- and FPA-model results are compared to the LPF-solution for the 2D vertical gust field w_g. Also now the FPA-model responses are representative for those of the DUT-model and the latter are therefore again omitted in the figures. In figures 13.17 through 13.19 the aerodynamic model response in terms of the aerodynamic coefficients C_{Y_g}, C_{ℓ_g} and C_{n_g} with respect to the anti-symmetrical vertical gust field w_g is shown. For the $C_{Y_g}(\alpha_g(t))$ results, the PCA-model shows the best agreement with the LPF-solution. This is attributed to an apparently correct sign of the PCA-model gust derivative $C_{Y_{p_g}}$, and the use of the unsteady gust derivative $C_{Y_{\dot{p}_g}}$ leading to a more high frequent model-response. Also here it should be noted, however, that the aerodynamic force response to 2D anti-symmetrical turbulence $C_{Y_g}(\alpha_g(t))$ is usually neglected in the DUT- and FPA-model, see references [30, 34, 35]. However, similar to aerodynamic force $C_{Y_g}(\hat{u}_g(t))$, they are again retained in this thesis.
For the $C_{\ell_g}(\alpha_g(t))$ results, all models show excellent agreement with the responses obtained for the LPF-solution. This is attributed to the aerodynamic stiffness term $C_{\ell_{p_g}}$, which is of similar magnitude for all parametric models.
For the $C_{n_g}(\alpha_g(t))$ results the PCA-model shows the best agreement with those obtained for the LPF-solution. This is attributed to a more accurate estimation of the gust derivative $C_{n_{p_g}}$ ánd the use of the unsteady gust derivative $C_{n_{\dot{p}_g}}$ in the PCA-model, leading to a more high frequent model-response. The DUT- and the FPA-model gust derivative, or aerodynamic stiffness term, $C_{n_{p_g}}$ is underestimated.

As a concluding remark, it follows that the PCA-model gust derivatives were calculated for the complete aircraft configuration. The DUT- and FPA-model gust derivatives, however, are defined as a function of stability derivatives using the contribution of specific aircraft parts (such as wing, vertical fin, etcetera) to them.

13.3.3 Frequency-domain results

The time-domain results presented in the previous section can easily be transformed into the frequency-domain by means of the Fast Fourier Transform. In this section the analytical PSD-functions of the aerodynamic coefficients will be compared to their numerically

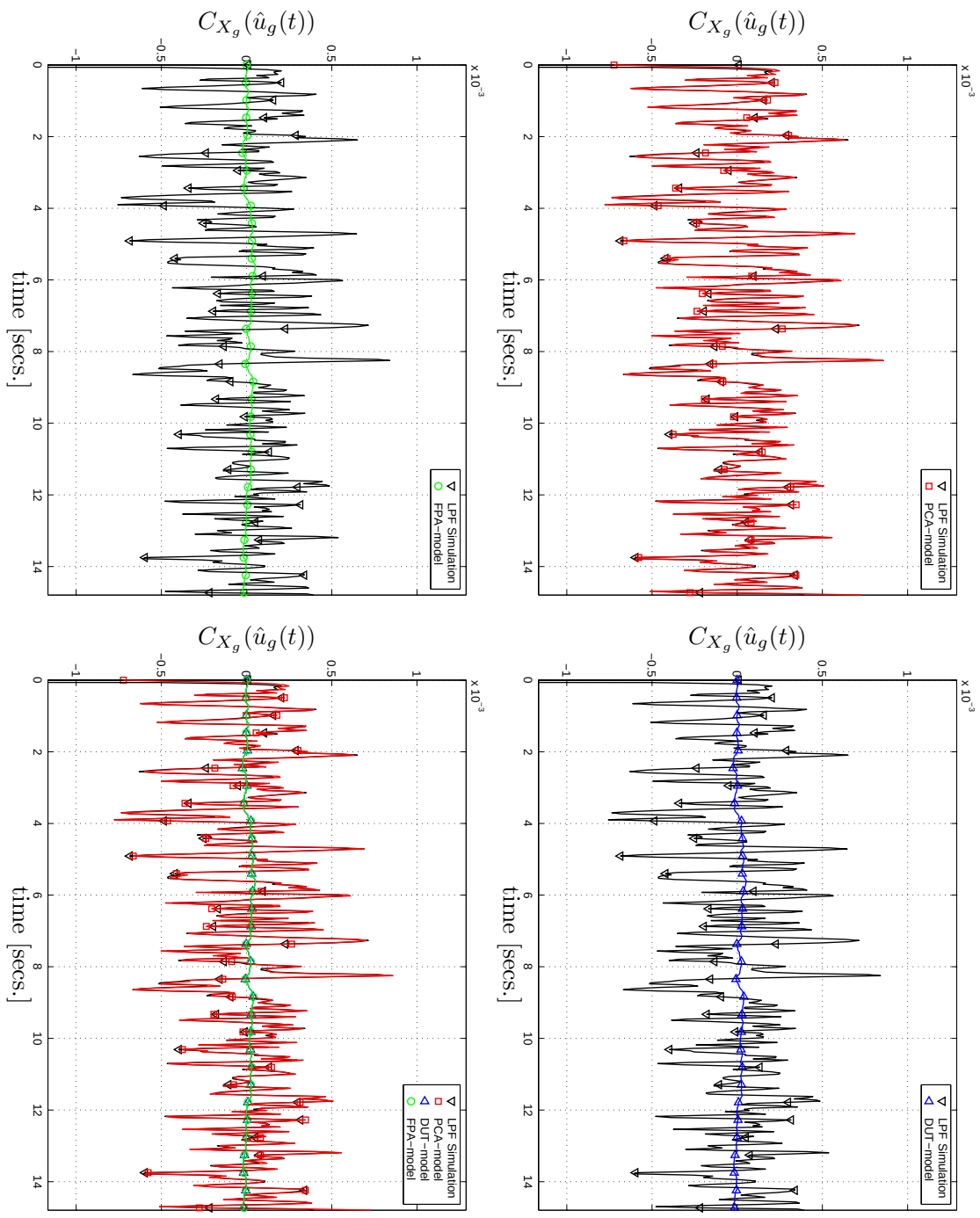


Figure 13.5: The simulated symmetrical aerodynamic force coefficient $C_{X_g}(t)$ in $\mathcal{F}_S$ for the PCA- (left top), the DUT- (right top) and the FPA-model (left bottom), ánd all model-responses summarized (right bottom) due to the symmetrical gust input $\hat{u}_g(t)$, for the Cessna Ce550 Citation II complete aircraft configuration, $\alpha_0 = 1.5^o$.

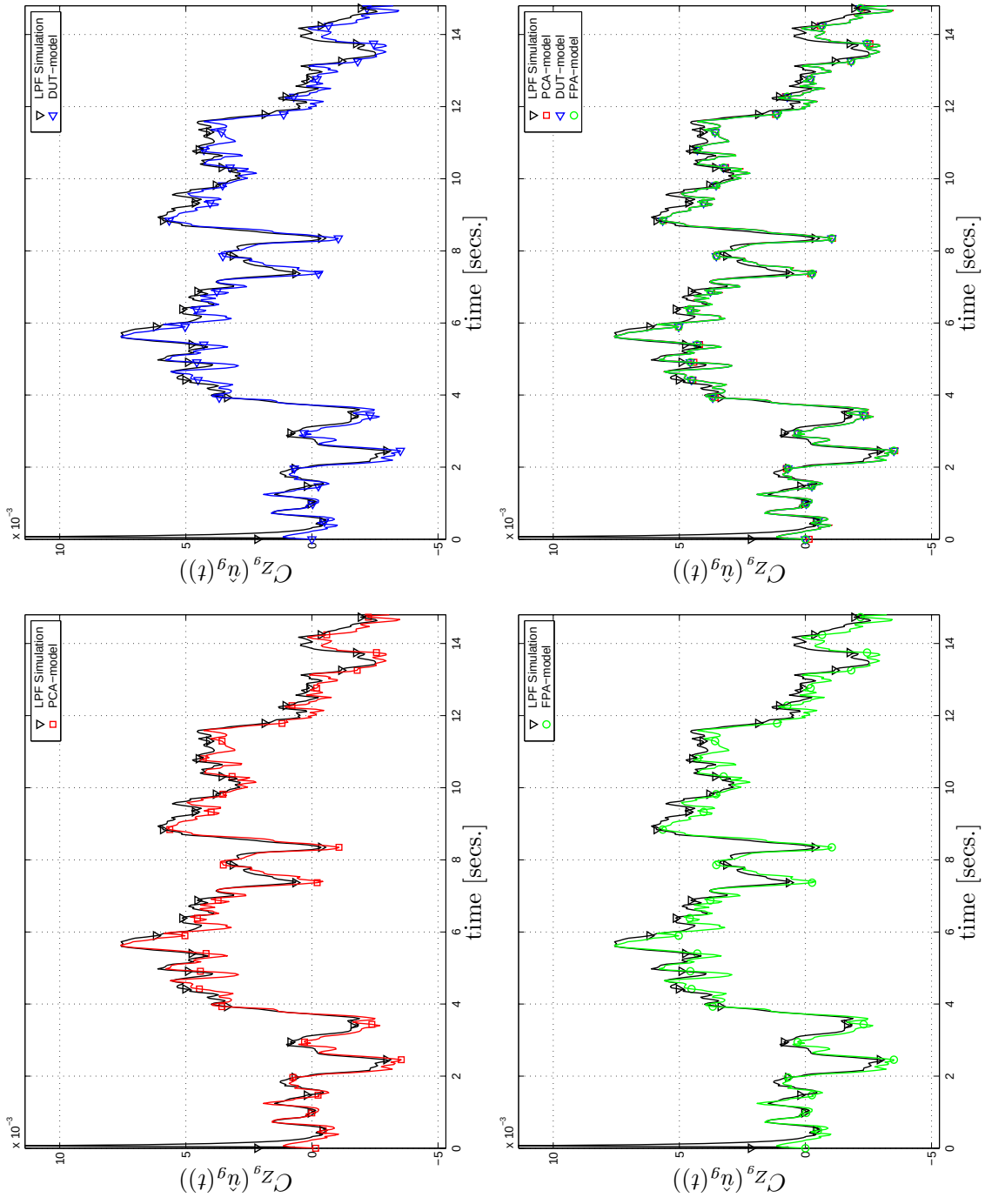


Figure 13.6: The simulated symmetrical aerodynamic force coefficient $C_{Z_g}(t)$ in $\mathcal{F}_S$ for the PCA- (left top), the DUT- (right top) and the FPA-model (left bottom), ánd all model-responses summarized (right bottom) due to the symmetrical gust input $\hat{u}_g(t)$, for the Cessna Ce550 Citation II complete aircraft configuration, $\alpha_0 = 1.5^o$.

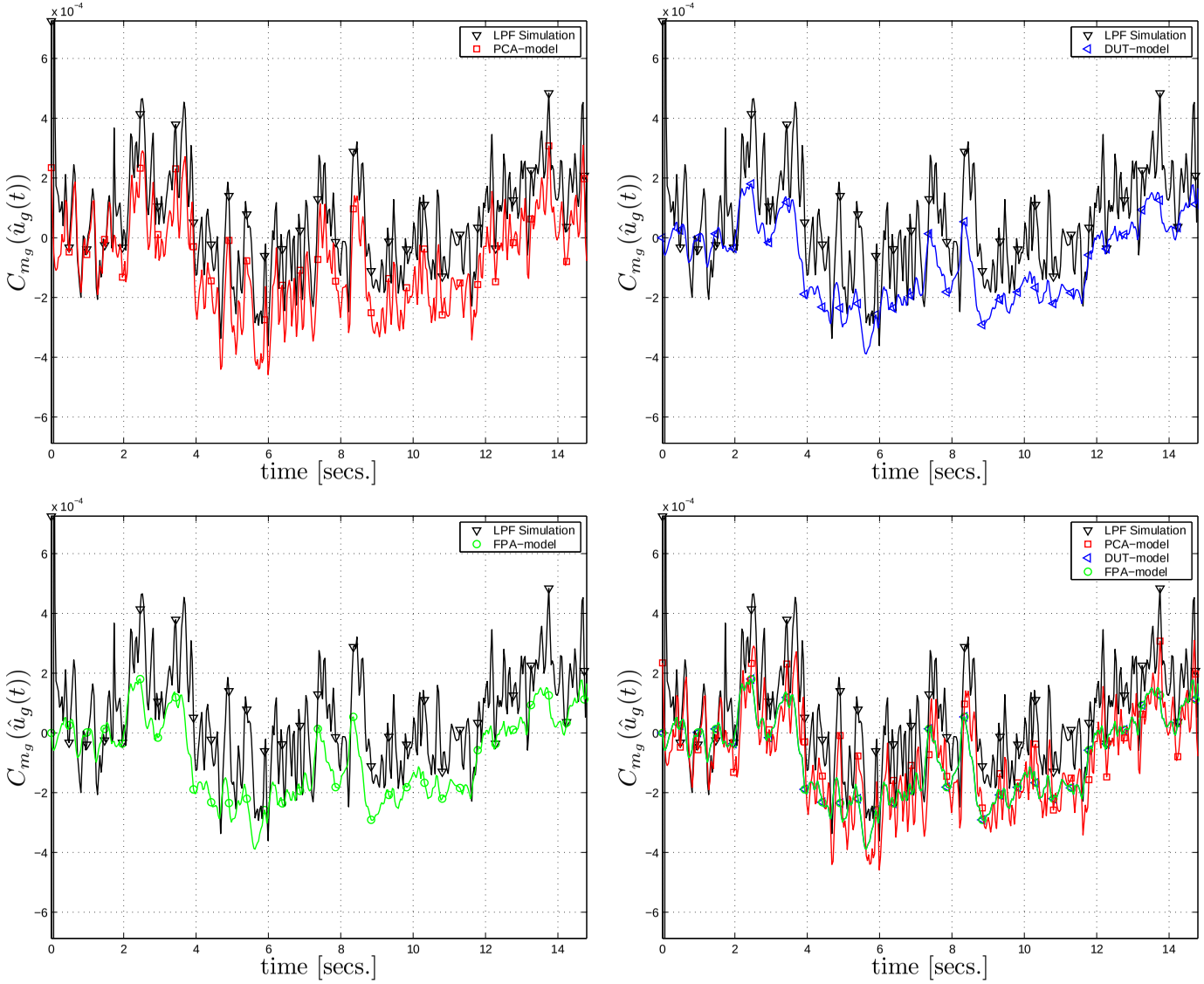


Figure 13.7: The simulated symmetrical aerodynamic moment coefficient $C_{m_g}(t)$ in $\mathcal{F}_S$ for the PCA- (left top), the DUT- (right top) and the FPA-model (left bottom), ánd all model-responses summarized (right bottom) due to the symmetrical gust input $\hat{u}_g(t)$, for the Cessna Ce550 Citation II complete aircraft configuration, $\alpha_0 = 1.5^o$.

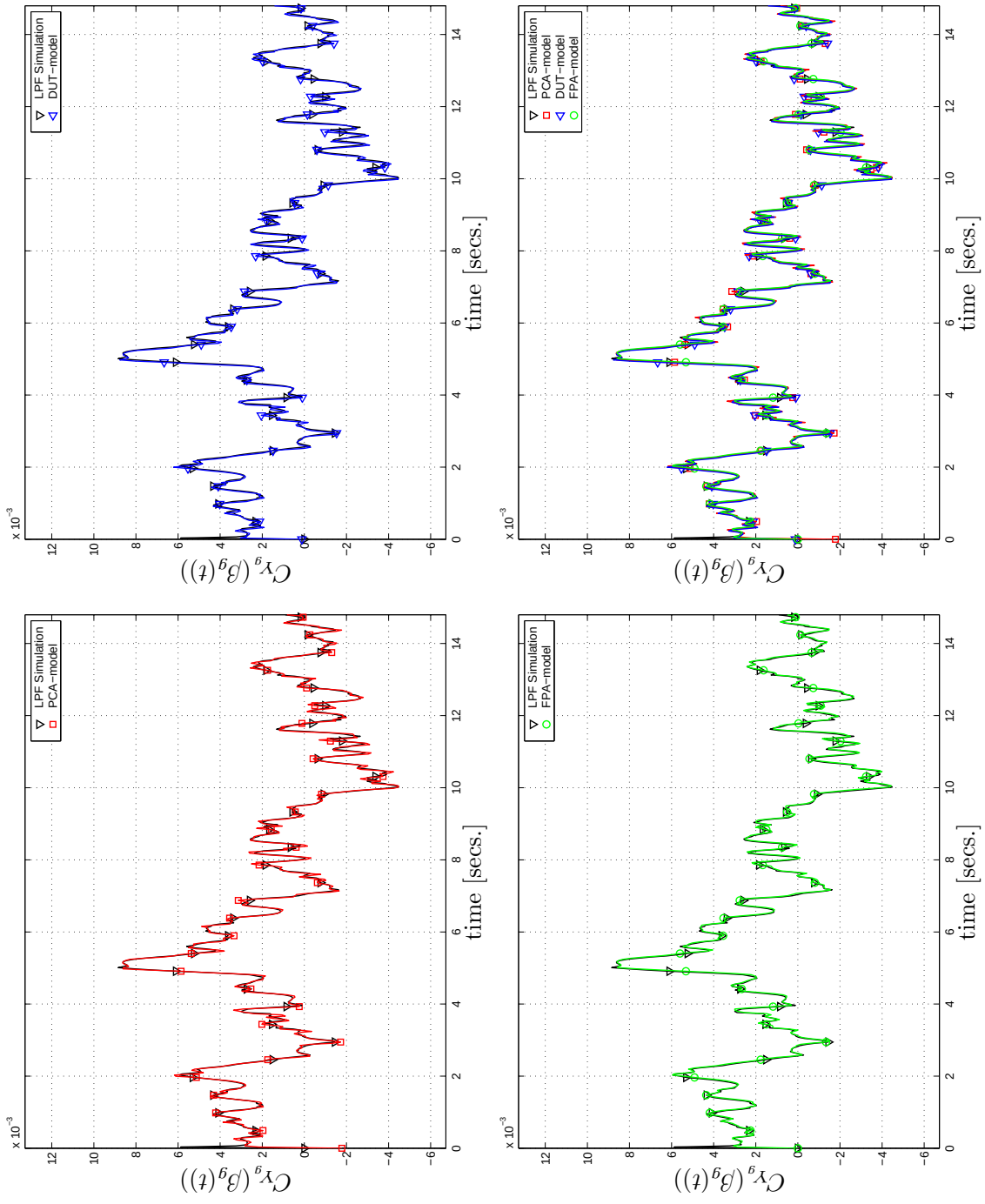


Figure 13.8: The simulated asymmetrical aerodynamic force coefficient $C_{Y_g}(t)$ in $\mathcal{F}_S$ for the PCA- (left top), the DUT- (right top) and the FPA-model (left bottom), ánd all model-responses summarized (right bottom) due to the asymmetrical gust input $\beta_g(t)$, for the Cessna Ce550 Citation II complete aircraft configuration, $\alpha_0 = 1.5^o$.

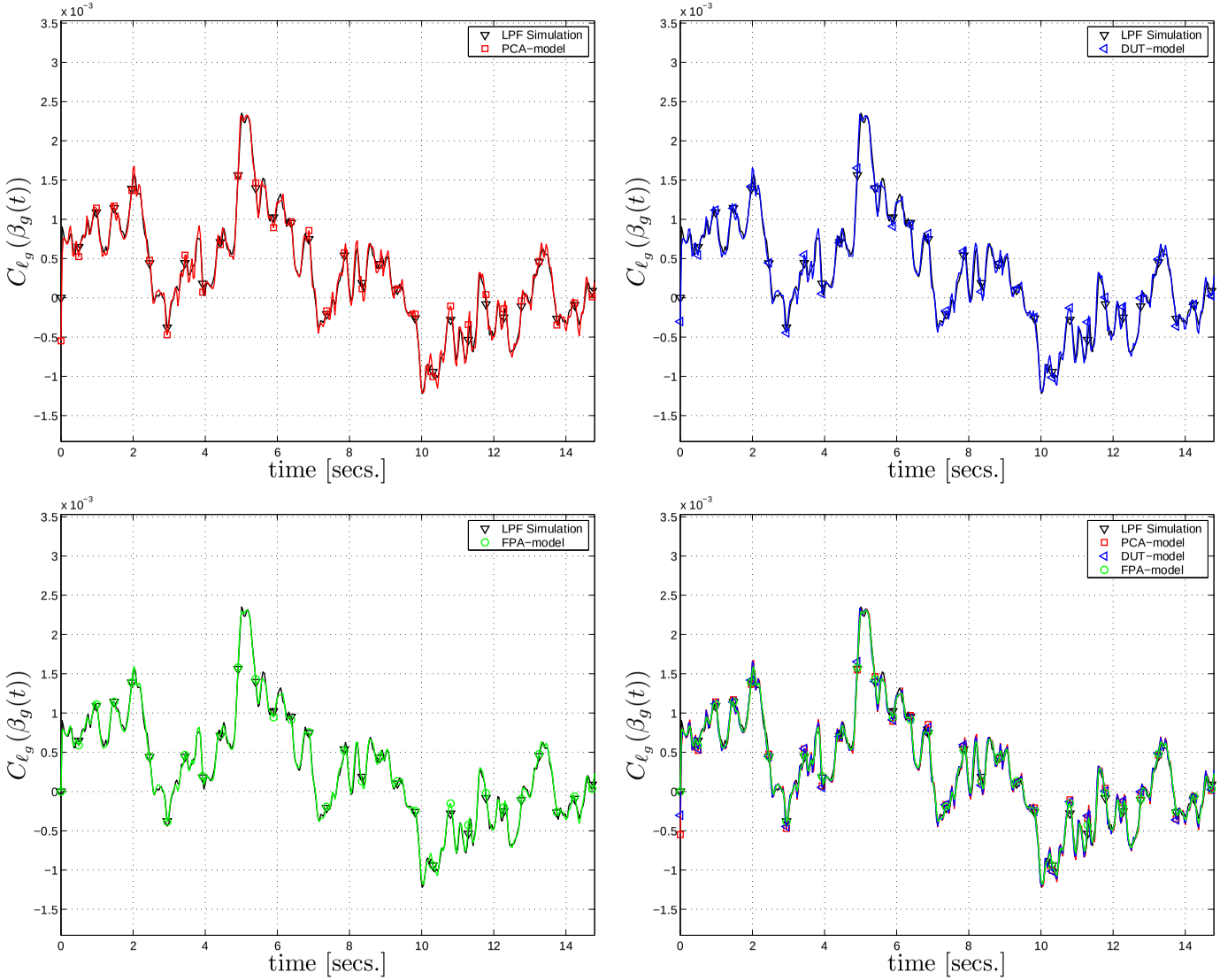


Figure 13.9: The simulated asymmetrical aerodynamic moment coefficient $C_{\ell_g}(t)$ in $\mathcal{F}_S$ for the PCA- (left top), DUT- (right top) and the FPA-model (left bottom), ánd all model-responses summarized (right bottom) due to the asymmetrical gust input $\beta_g(t)$, for the Cessna Ce550 Citation II complete aircraft configuration, $\alpha_0 = 1.5^o$.

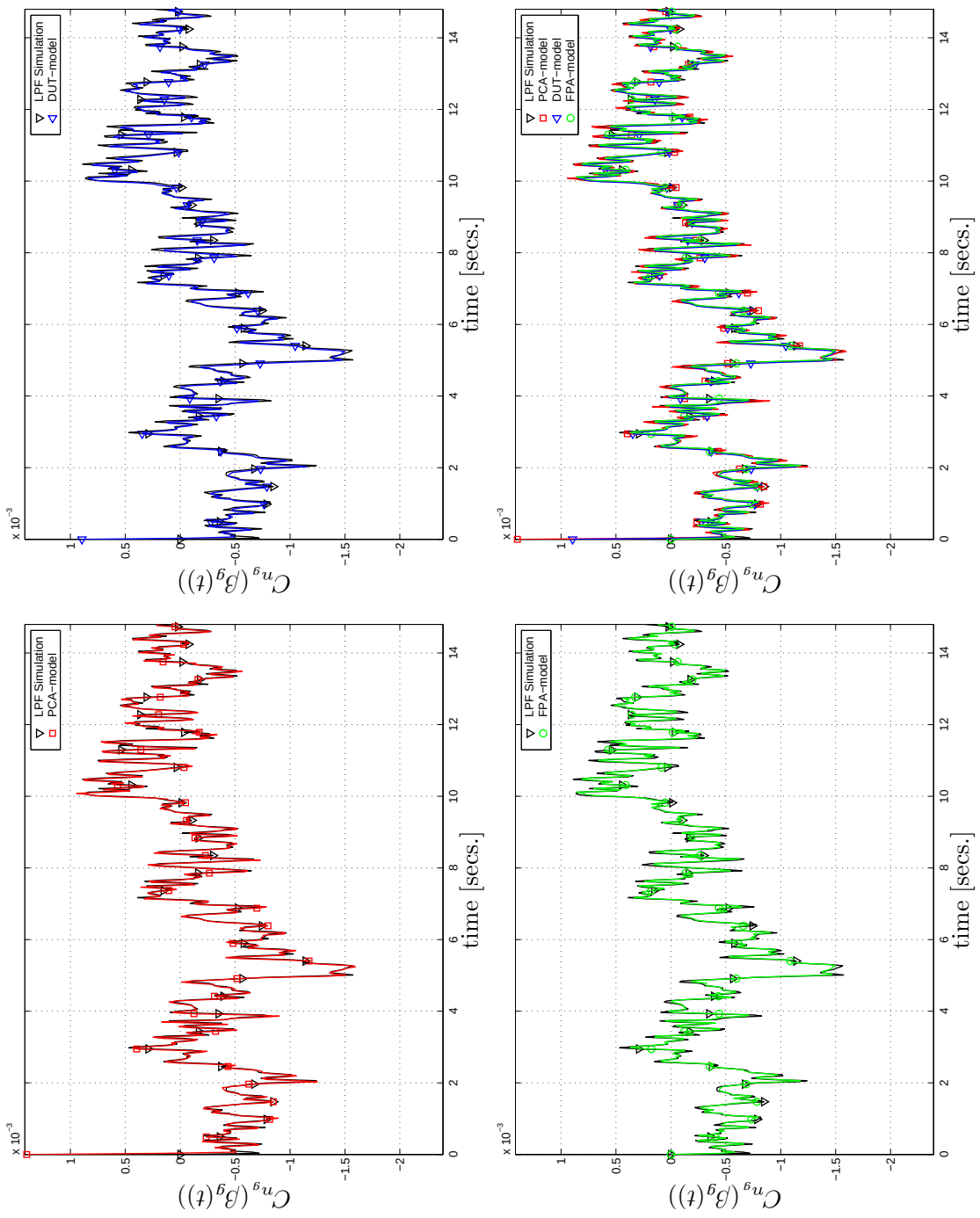


Figure 13.10: The simulated asymmetrical aerodynamic moment coefficient $C_{ng}(t)$ in $\mathcal{F}_S$ for the PCA- (left top), the DUT- (right top) and the FPA-model (left bottom), ánd all model-responses summarized (right bottom) due to the asymmetrical gust input $\beta_g(t)$, for the Cessna Ce550 Citation II complete aircraft configuration, $\alpha_0 = 1.5^o$.

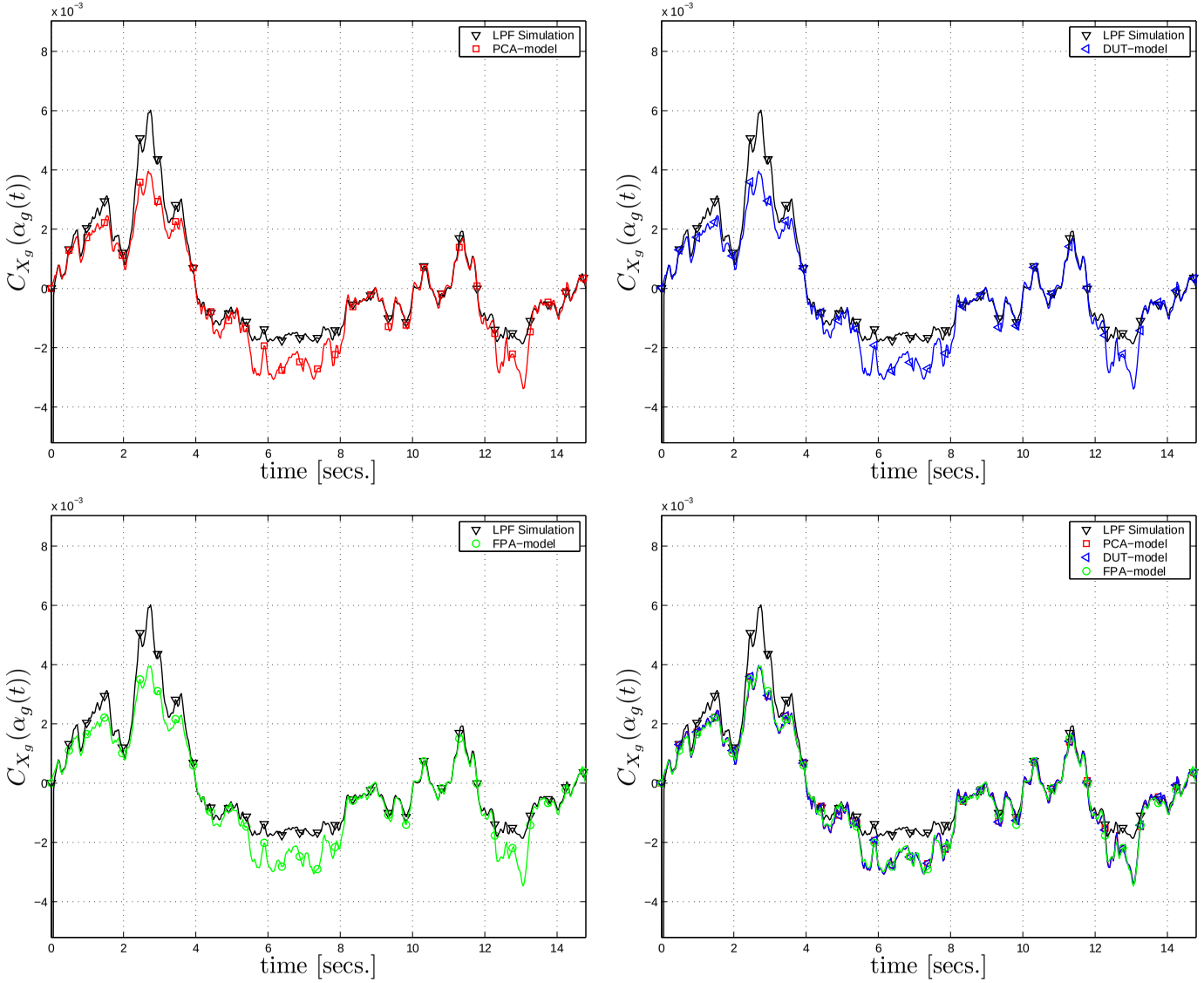


Figure 13.11: The simulated symmetrical aerodynamic force coefficient $C_{X_g}(t)$ in $\mathcal{F}_S$ for the PCA- (left top), the DUT- (right top) and the FPA-model (left bottom), ánd all model-responses summarized (right bottom) due to the symmetrical gust input $\alpha_g(t)$, for the Cessna Ce550 Citation II complete aircraft configuration, $\alpha_0 = 1.5^o$.

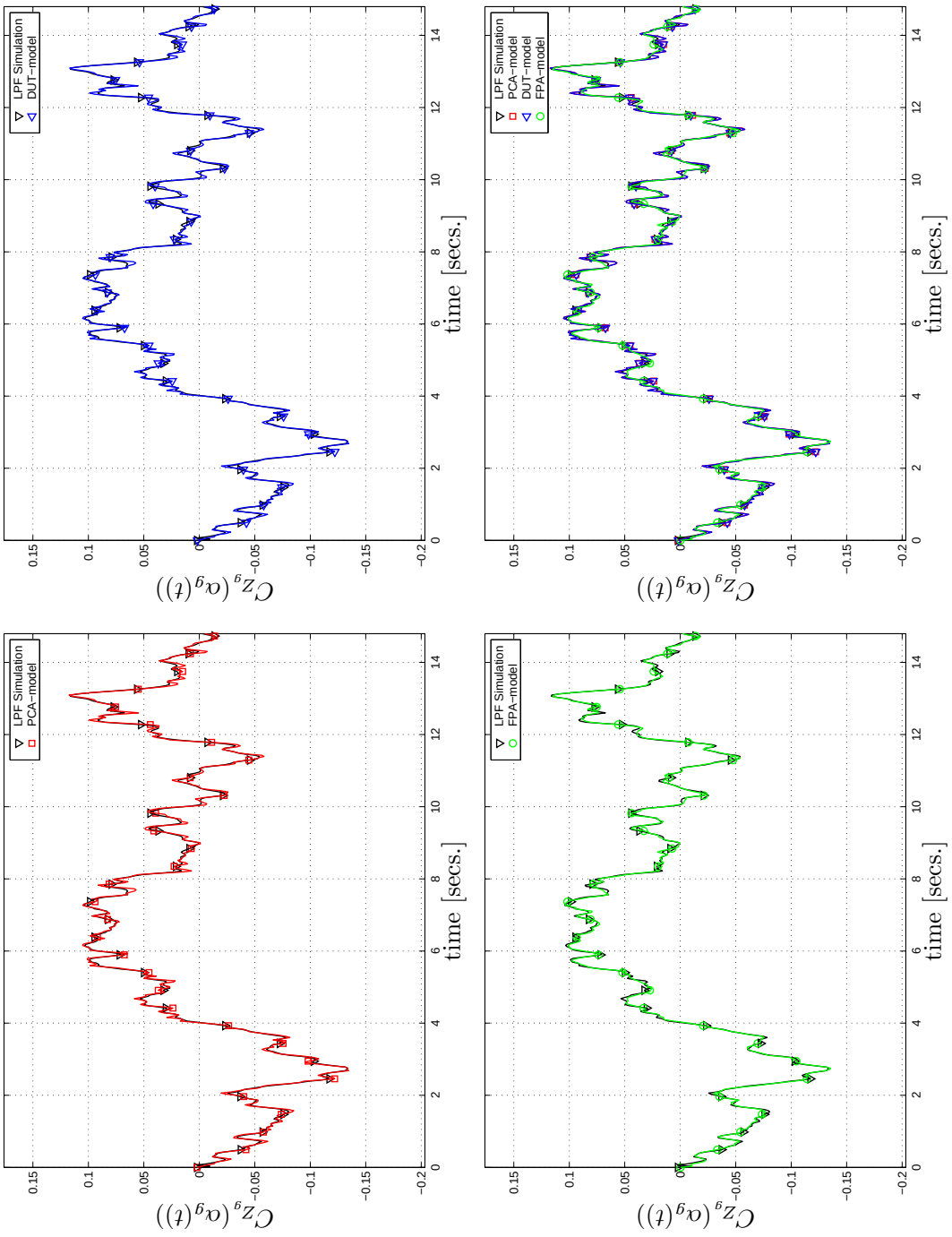


Figure 13.12: The simulated symmetrical aerodynamic force coefficient $C_{Z_g}(t)$ in $\mathcal{F}_S$ for the PCA- (left top), the DUT- (right top) and the FPA-model (left bottom), ánd all model-responses summarized (right bottom) due to the symmetrical gust input $\alpha_g(t)$, for the Cessna Ce550 Citation II complete aircraft configuration, $\alpha_0 = 1.5^o$.

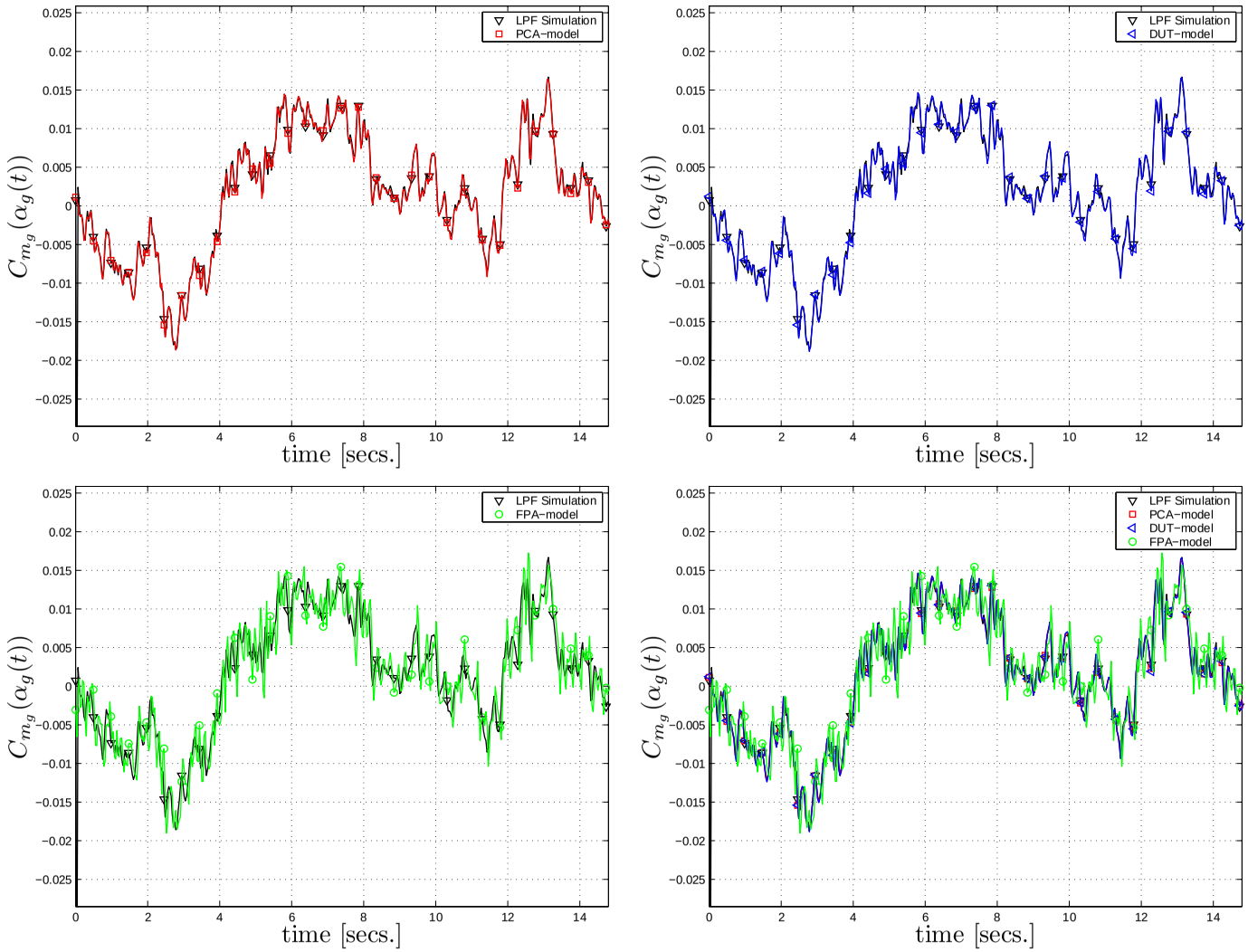


Figure 13.13: The simulated symmetrical aerodynamic moment coefficient $C_{m_g}(t)$ in $\mathcal{F}_S$ for the PCA- (left top), the DUT- (right top) and the FPA-model (left bottom), ánd all model-responses summarized (right bottom) due to the symmetrical gust input $\alpha_g(t)$, for the Cessna Ce550 Citation II complete aircraft configuration, $\alpha_0 = 1.5^o$.

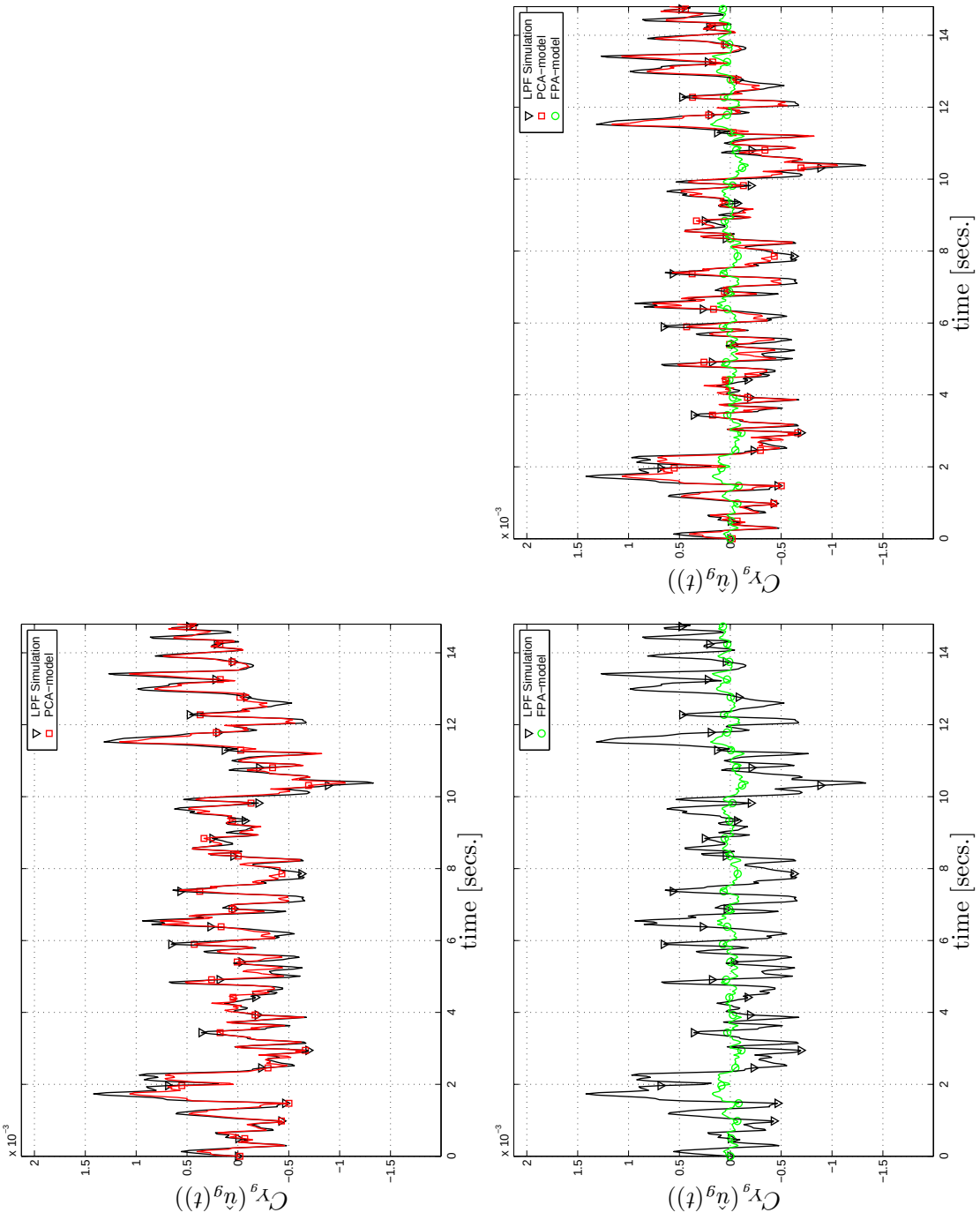


Figure 13.14: The simulated asymmetrical aerodynamic force coefficient $C_{Y_g}(t)$ in $\mathcal{F}_S$ for the PCA-model (left top), the FPA-model (left bottom) and all model-responses summarized (right bottom) due to the anti-symmetrical gust input $\hat{u}_g(t)$, for the Cessna Ce550 Citation II complete aircraft configuration, $\alpha_0 = 1.5^o$.

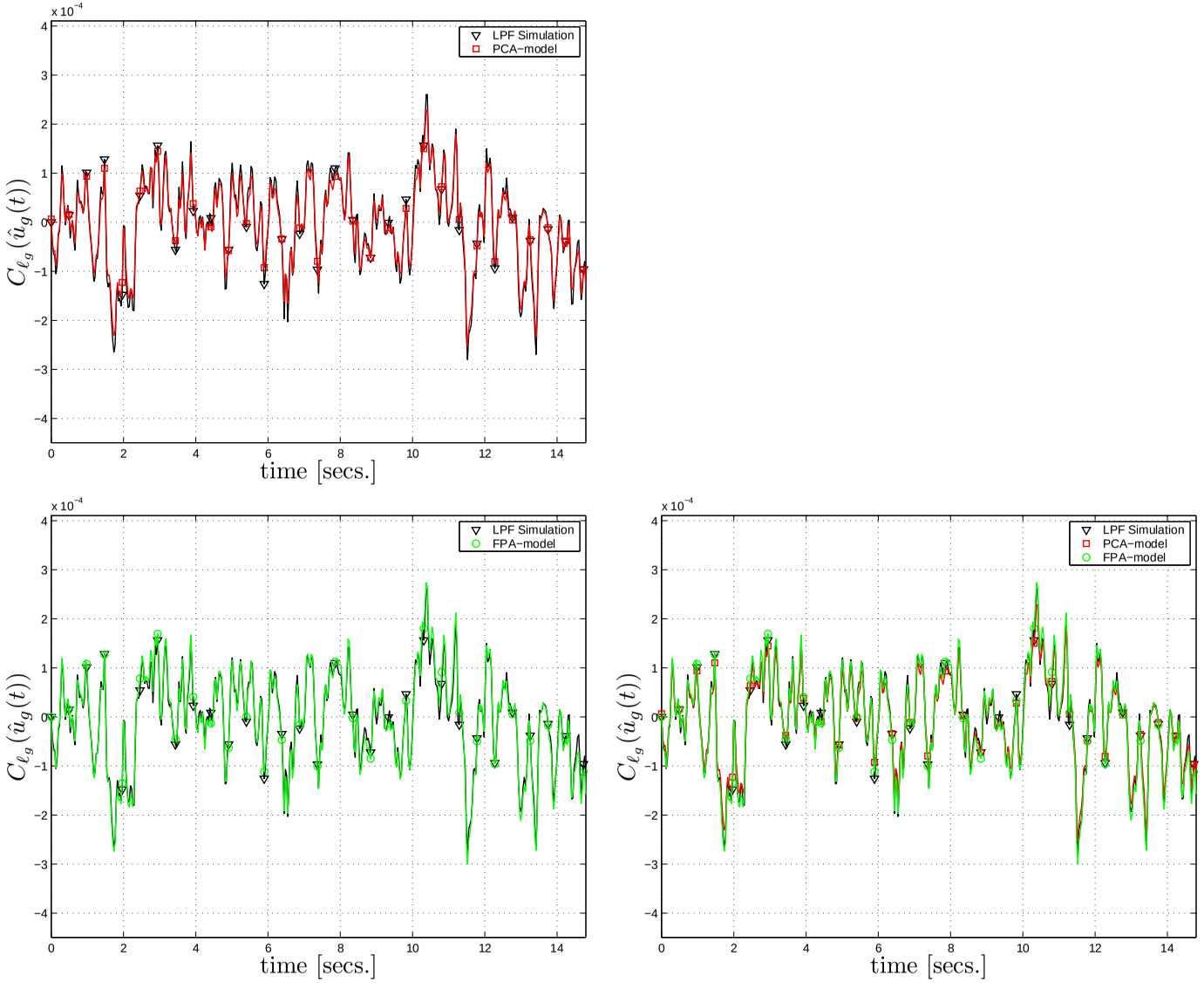


Figure 13.15: The simulated asymmetrical aerodynamic moment coefficient $C_{\ell_g}(t)$ in $\mathcal{F}_S$ for the PCA-model (left top), the FPA-model (left bottom) and all model-responses summarized (right bottom) due to the anti-symmetrical gust input $\hat{u}_g(t)$, for the Cessna Ce550 Citation II complete aircraft configuration, $\alpha_0 = 1.5^o$.

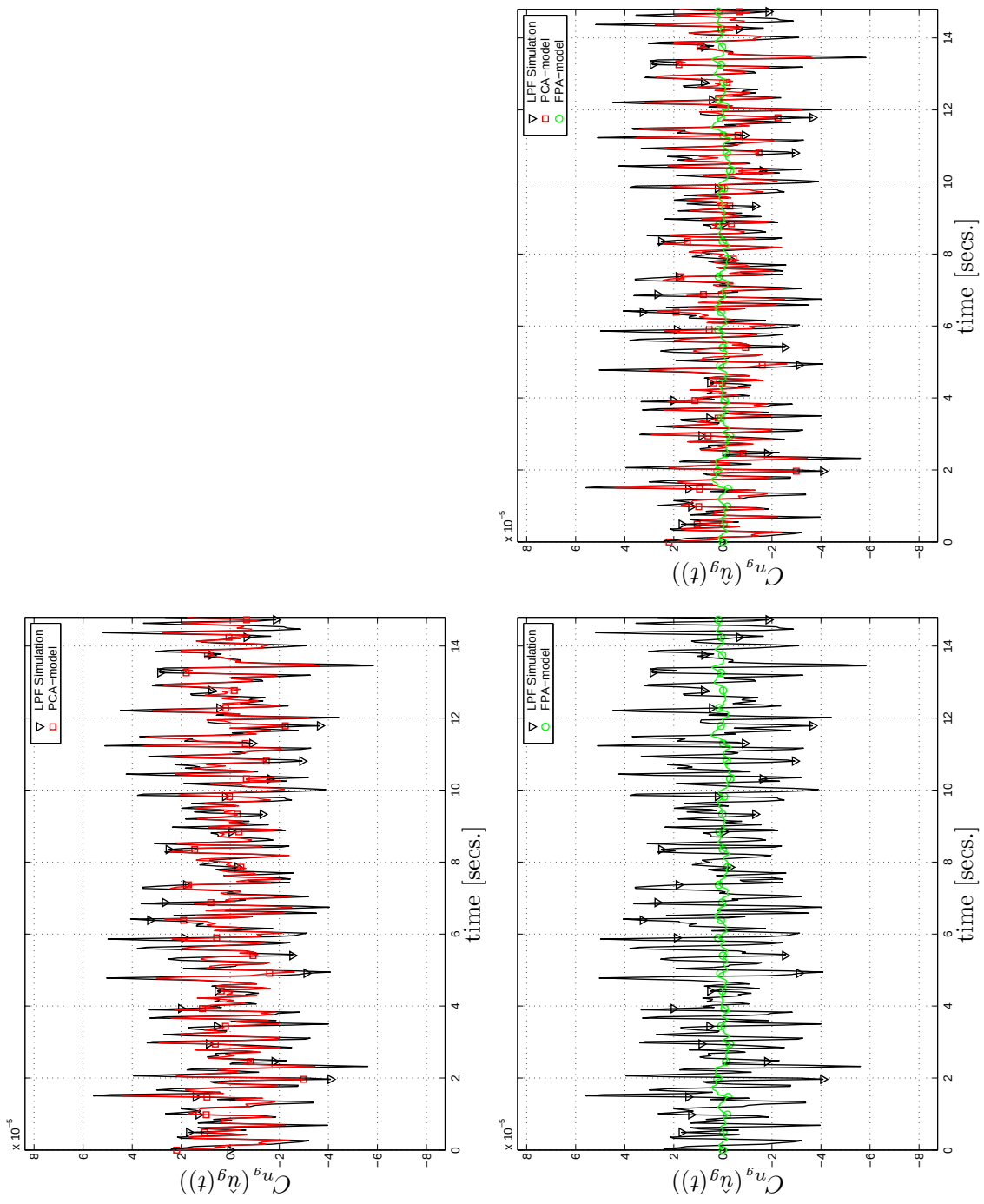


Figure 13.16: The simulated asymmetrical aerodynamic moment coefficient $C_{n_g}(t)$ in $\mathcal{F}_S$ for the PCA-model (left top), the FPA-model (left bottom) and all model-responses summarized (right bottom) due to the anti-symmetrical gust input $\hat{u}_g(t)$, for the Cessna Ce550 Citation II complete aircraft configuration, $\alpha_0 = 1.5^o$.

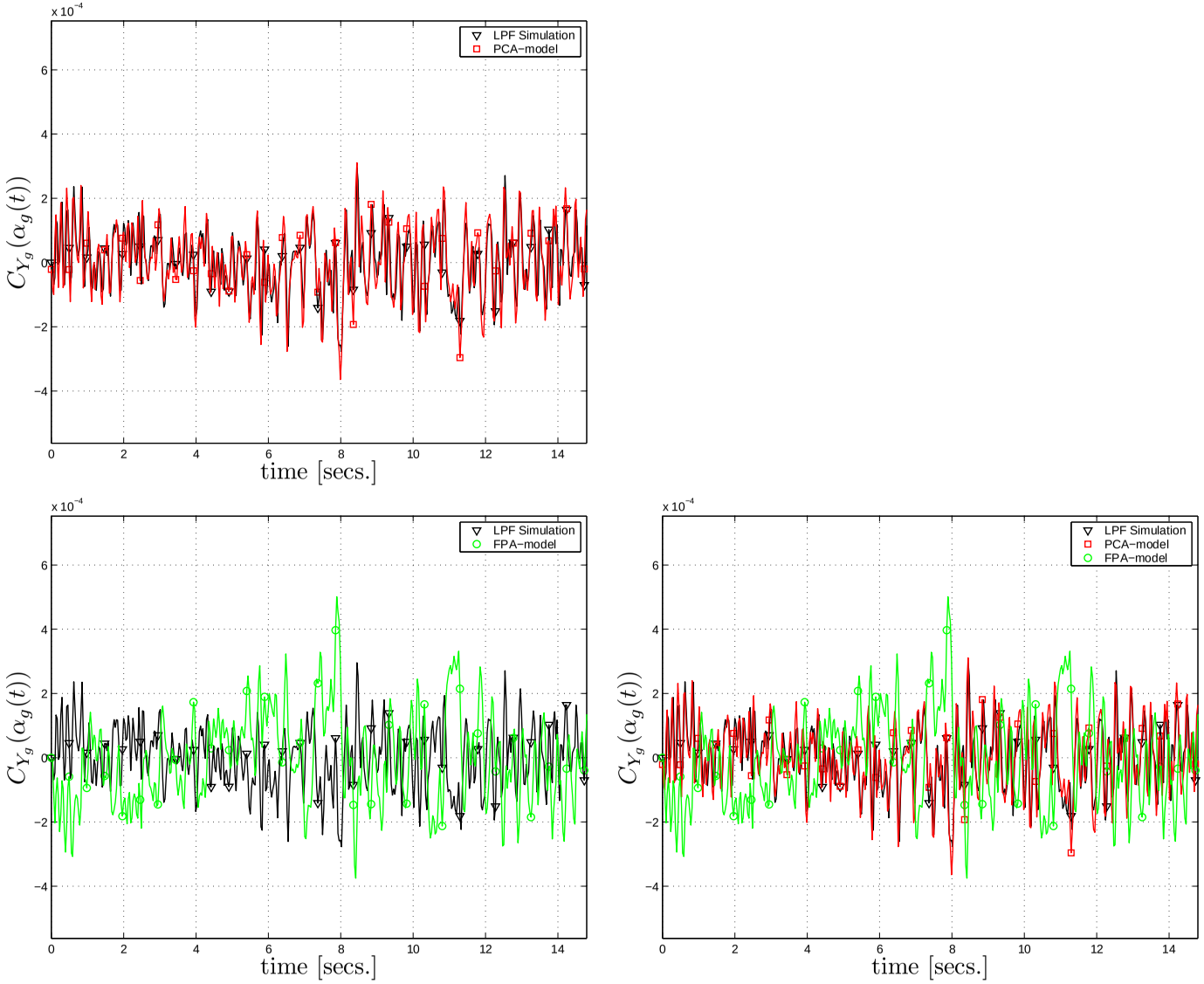


Figure 13.17: The simulated asymmetrical aerodynamic force coefficient $C_{Y_g}(t)$ in $\mathcal{F}_S$ for the PCA-model (left top), the FPA-model (left bottom) and all model-responses summarized (right bottom) due to the anti-symmetrical gust input $\alpha_g(t)$, for the Cessna Ce550 Citation II complete aircraft configuration, $\alpha_0 = 1.5^o$.

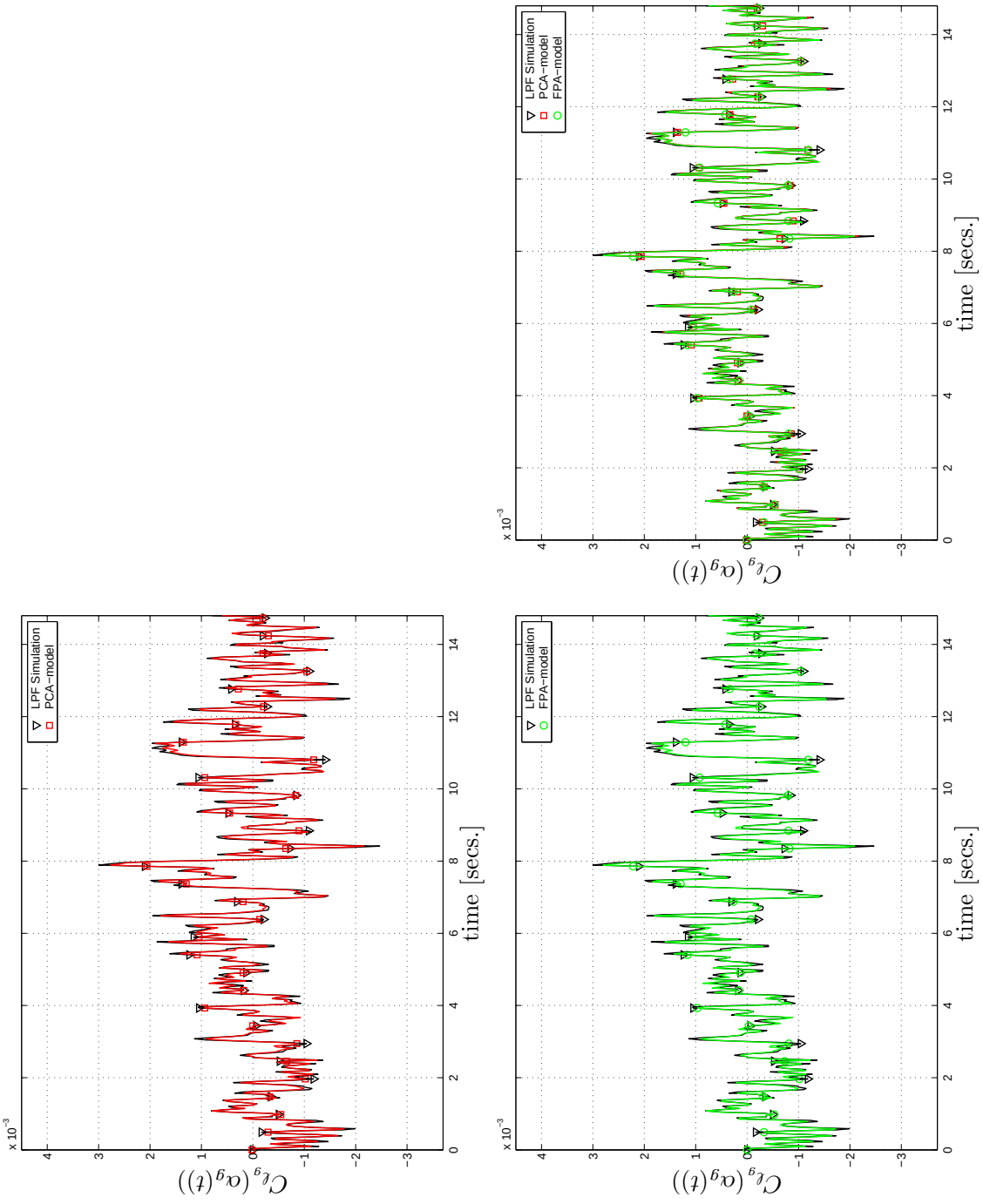


Figure 13.18: The simulated asymmetrical aerodynamic moment coefficient $C_{\ell_g}(t)$ in $\mathcal{F}_S$ for the PCA-model (left top), the FPA-model (left bottom) and all model-responses summarized (right bottom) due to the anti-symmetrical gust input $\alpha_g(t)$, for the Cessna Ce550 Citation II complete aircraft configuration, $\alpha_0 = 1.5^o$.

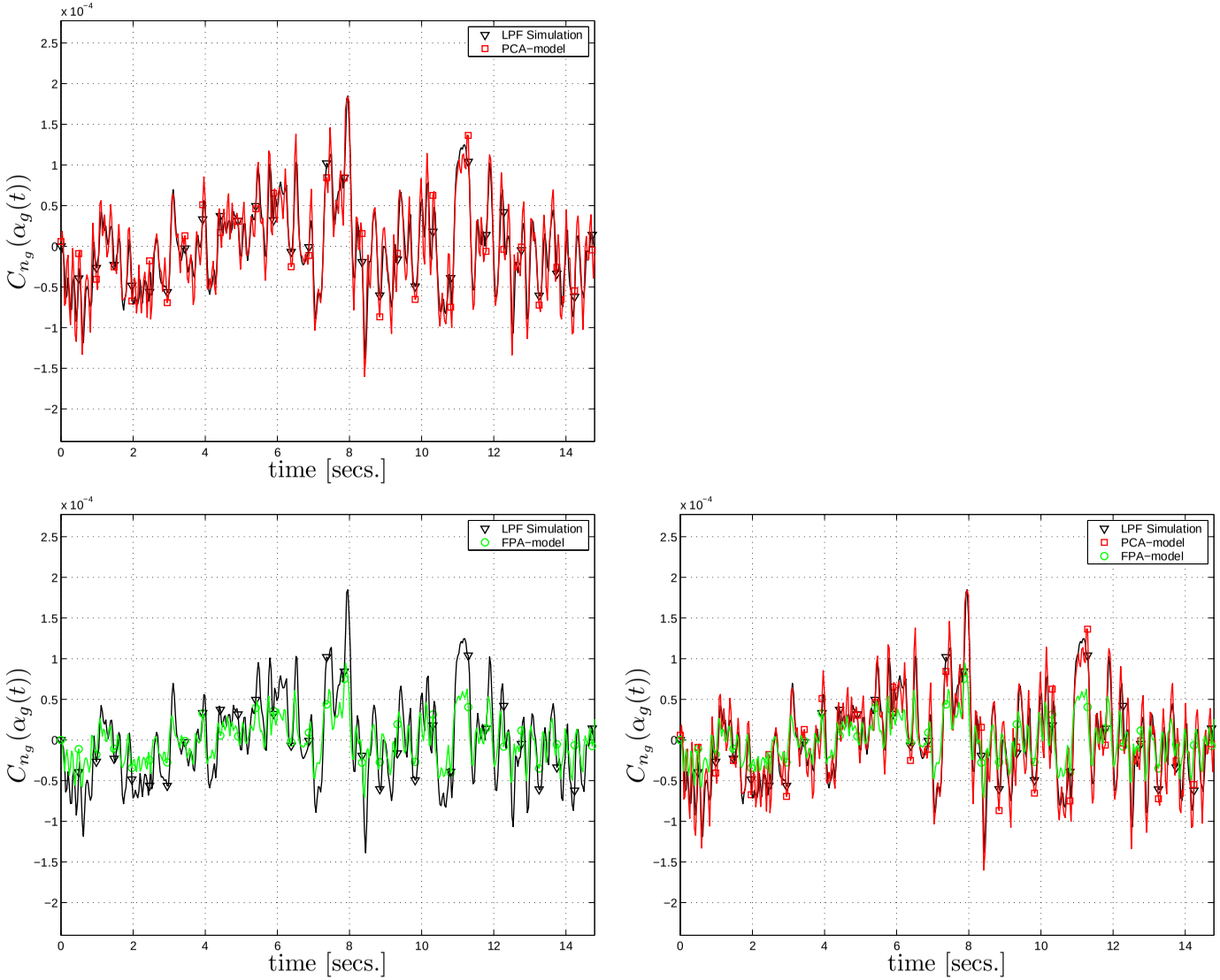


Figure 13.19: The simulated asymmetrical aerodynamic moment coefficient $C_{n_g}(t)$ in $\mathcal{F}_S$ for the PCA-model (left top), the FPA-model (left bottom) and all model-responses summarized (right bottom) due to the anti-symmetrical gust input $\alpha_g(t)$, for the Cessna Ce550 Citation II complete aircraft configuration, $\alpha_0 = 1.5^o$.

obtained PSD-function counterparts (or Periodograms) obtained from time-domain data. The Periodograms are calculated by, see also reference [30],

$$S_{yy}[k] = Y^*[k] \cdot Y[k]/N \tag{13.23}$$

with $Y[k]$ the discrete Fast Fourier Transform of the time-domain array $y[n]$, * denoting the complex conjungate of $Y[k]$, $S_{yy}[k]$ the numerical PSD-function (or Periodogram) of $y[n]$, k the frequency counter (with $k = [0, 1, 2 \cdots N-1]$, N the number of samples in the time-domain array and n the time-domain counter ($t_n = n\Delta t$, with Δt the discretization time and $n = [0, 1, 2 \cdots N-1]$). The discrete Fourier transform is defined as,

$$Y[k] = \sum_{n=0}^{N-1} y[n]\ e^{-j\frac{2\pi kn}{N}} \tag{13.24}$$

with ω_k the discrete circular frequency in [Rad/sec.],

$$\omega_k = \frac{2\pi k}{N\Delta t} \tag{13.25}$$

and $k = 0, 1, 2, \cdots, \frac{N}{2} - 1$.

In figures 13.20 through 13.24 the analytical PSD-functions of the aerodynamic force and moment coefficients are compared to the numerically obtained Periodograms. The analytical PSD-functions are calculated according to, taking for example the FPA-model's PSD-function of the aerodynamic force coefficient C_{Z_g} due to the non-dimensional symmetrical vertical gust velocity component $\alpha_g = \frac{w_g}{Q_\infty}$,

$$S^{\alpha_g}_{C_{Z_g}C_{Z_g}}(\omega) = \left(C_{Z_g}(\omega)\right)^* \cdot C_{Z_g}(\omega) \tag{13.26}$$

with the output C_{Z_g} similar to the coefficient given in equation (13.19). For the frequency-domain this becomes,

$$C_{Z_g}(\omega) = C_{Z_{\alpha_g}}\ \alpha_g(\omega) + C_{Z_{\dot{\alpha}_g}}\ \frac{j\omega\alpha_g\bar{c}}{Q_\infty}(\omega) + C_{Z_{q_g}}\ \frac{q_g\bar{c}}{Q_\infty}(\omega) \tag{13.27}$$

Elaborating equation (13.26), while making use of equation (13.27), results in the analytical PSD-function $S^{\alpha_g}_{C_{Z_g}C_{Z_g}}(\omega)$. It becomes a function of the auto input PSD-functions $S_{\alpha_g\alpha_g}(\omega) = \alpha_g^*(\omega) \cdot \alpha_g(\omega)$ and $S_{\frac{q_g\bar{c}}{Q_\infty}\frac{q_g\bar{c}}{Q_\infty}}(\omega) = \left(\frac{q_g\bar{c}}{Q_\infty}(\omega)\right)^* \cdot \frac{q_g\bar{c}}{Q_\infty}(\omega)$, and the cross PSD-functions $S_{\alpha_g\frac{q_g\bar{c}}{Q_\infty}}(\omega) = \alpha_g^*(\omega) \cdot \frac{q_g\bar{c}}{Q_\infty}(\omega)$ and $S_{\frac{q_g\bar{c}}{Q_\infty}\alpha_g}(\omega) = \left(\frac{q_g\bar{c}}{Q_\infty}(\omega)\right)^* \cdot \alpha_g(\omega)$. Input PSD-functions with respect to $\frac{j\omega\alpha_g\bar{c}}{Q_\infty}$ will also appear in the expression for $S^{\alpha_g}_{C_{Z_g}C_{Z_g}}(\omega)$, for example $S_{\frac{q_g\bar{c}}{Q_\infty}\frac{\dot{\alpha}_g\bar{c}}{Q_\infty}}(\omega) = \left(\frac{q_g\bar{c}}{Q_\infty}(\omega)\right)^* \cdot \frac{j\omega\bar{c}}{Q_\infty}\alpha_g(\omega)$, see also appendix B. Similar PSD-function expressions for other aerodynamic coefficients can be derived. For all aerodynamic models, the analytical PSD-functions are calculated making use of the analytical aerodynamic force and moment definitions given in section 13.2.

From figure 13.20 it follows that the analytical PSD-functions $S^{\hat{u}_g}_{C_{X_g}C_{X_g}}(\omega)$, $S^{\hat{u}_g}_{C_{Z_g}C_{Z_g}}(\omega)$ and $S^{\hat{u}_g}_{C_{m_g}C_{m_g}}(\omega)$ due to 1D longitudinal gusts almost coincide for the DUT- and FPA-model. The PCA-model analytical PSD-functions, however, are considerably different than the ones for the DUT- and FPA-model. The major differences occur for the PSD-functions $S^{\hat{u}_g}_{C_{X_g}C_{X_g}}(\omega)$ and $S^{\hat{u}_g}_{C_{m_g}C_{m_g}}(\omega)$. Similar to the time-domain aerodynamic coefficient discussion, the difference in the frequency-domain PCA-model responses is explained by the use of the unsteady gust derivatives. Also shown in figure 13.20, it follows that the Periodograms for the LPF-solution follow the PCA-model responses best.

In figure 13.21 the PSD-functions and Periodograms $S^{\beta_g}_{C_{Y_g}C_{Y_g}}(\omega)$, $S^{\beta_g}_{C_{\ell_g}C_{\ell_g}}(\omega)$ and $S^{\beta_g}_{C_{n_g}C_{n_g}}(\omega)$ due to 1D lateral gusts are given. Similar to the time-domain discussion, it follows that uptill a fairly high frequency ($\omega = 10$ [Rad/sec.]) all model responses almost coincide. Similar obeservations are made for the PSD-functions and Periodograms $S^{\alpha_g}_{C_{X_g}C_{X_g}}(\omega)$, $S^{\alpha_g}_{C_{Z_g}C_{Z_g}}(\omega)$ and $S^{\alpha_g}_{C_{m_g}C_{m_g}}(\omega)$ due to 1D vertical gusts shown in figure 13.22.

In figures 13.23 the PSD-functions and Periodograms $S^{\hat{u}_g}_{C_{Y_g}C_{Y_g}}(\omega)$, $S^{\hat{u}_g}_{C_{\ell_g}C_{\ell_g}}(\omega)$ and $S^{\hat{u}_g}_{C_{n_g}C_{n_g}}(\omega)$ due to 2D longitudinal gusts are shown. Similar to the time-domain observations, it follows that the DUT- and FPA-model results coincide. Major differences occur, however, with respect to the PCA-model. It is shown that the PSD-functions for the DUT- and FPA-model are underestimated for both $S^{\hat{u}_g}_{C_{Y_g}C_{Y_g}}(\omega)$ and $S^{\hat{u}_g}_{C_{n_g}C_{n_g}}(\omega)$. With respect to the PSD-function $S^{\hat{u}_g}_{C_{\ell_g}C_{\ell_g}}(\omega)$, the frequency-domain PCA-model responses show good agreement with those obtained for both the DUT- and FPA-model (as can be expected looking at figure 13.15). Also as expected, the LPF-solution's Periodograms show good agreement with all the PCA-model responses.

Finally, in figures 13.24 the PSD-functions and Periodograms $S^{\alpha_g}_{C_{Y_g}C_{Y_g}}(\omega)$, $S^{\alpha_g}_{C_{\ell_g}C_{\ell_g}}(\omega)$ and $S^{\alpha_g}_{C_{n_g}C_{n_g}}(\omega)$ are shown. Similar to the time-domain observations, it follows that the DUT- and FPA-model results coincide. Major differences occur again, however, with respect to the PCA-model. It is shown that the PSD-functions for the DUT- and FPA-model are overestimated for $S^{\hat{u}_g}_{C_{Y_g}C_{Y_g}}(\omega)$ and that they are underestimated for $S^{\hat{u}_g}_{C_{n_g}C_{n_g}}(\omega)$. The PCA-model responses show excellent agreement with the DUT- and FPA-model for the PSD-function $S^{\hat{u}_g}_{C_{\ell_g}C_{\ell_g}}(\omega)$ (as can be expected looking at figure 13.18). Also as expected, the LPF-solution Periodograms show good agreement with the PCA-model responses.

13.4 Aircraft motion responses

13.4.1 Introduction

In this section the aircraft motion responses will be given for both the time- and frequency-domain. For the time-domain responses use is made of the gust inputs calculated from the spatial-domain gust-fields given in appendix G. Assuming a recti-linear flightpath, the calculated aerodynamic coefficient responses given in section 13.3 are used to simulate the

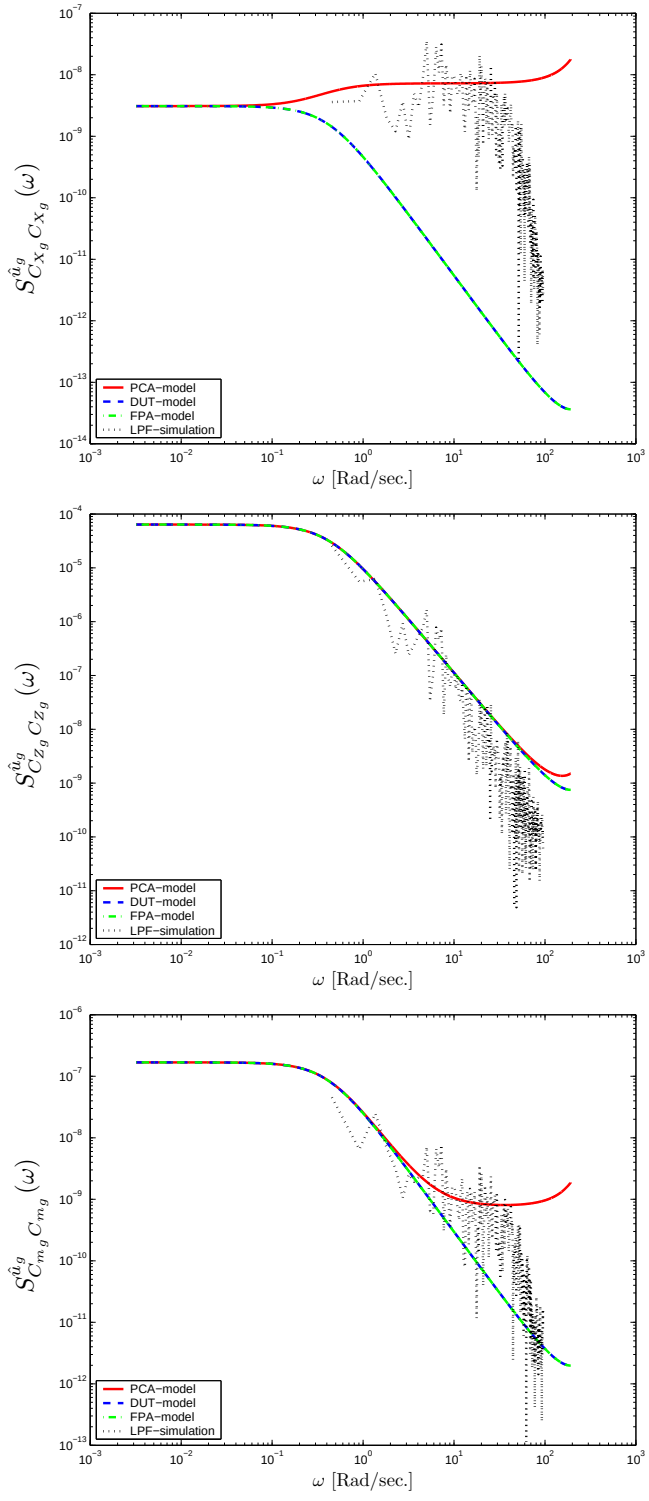


Figure 13.20: The aerodynamic coefficient C_{X_g}, C_{Z_g} and C_{m_g} PSD-functions for the 1D symmetrical longitudinal gust input $\hat{u}_g$ given for the gust scale length $L_g = 300$ [m]. Results are given for the LPF-solution, as well as for the PCA-, DUT- and FPA-model.

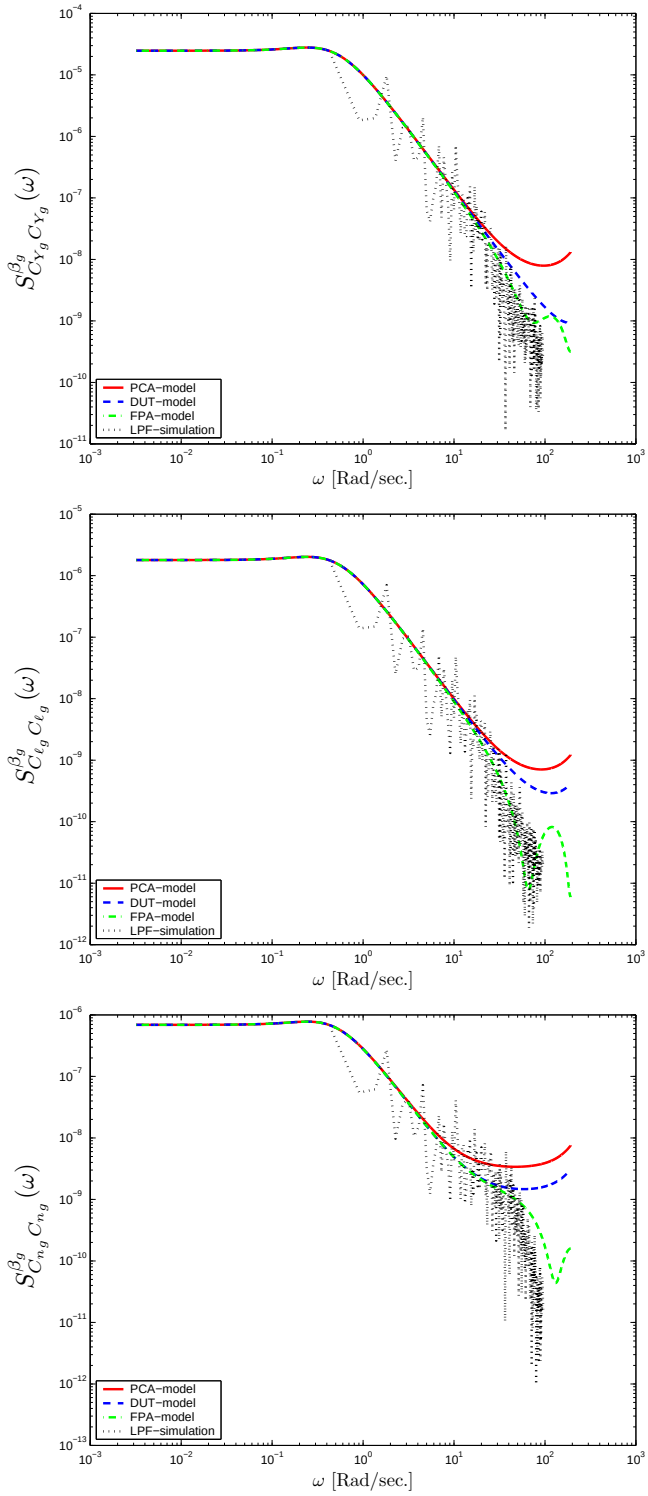


Figure 13.21: The aerodynamic coefficient C_{Y_g}, C_{ℓ_g} and C_{n_g} PSD-functions for the 1D asymmetrical lateral gust input β_g given for the gust scale length $L_g = 300$ [m]. Results are given for the LPF-solution, as well as for the PCA-, DUT- and FPA-model.

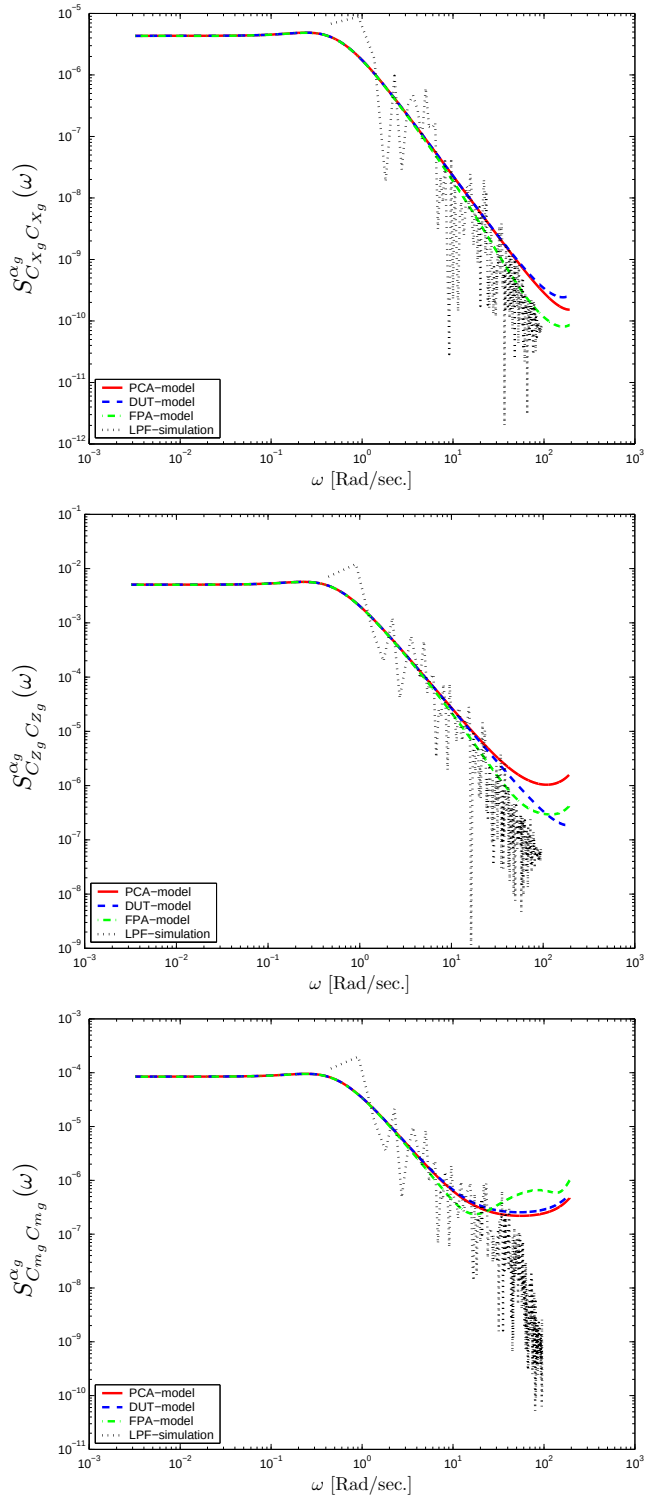


Figure 13.22: The aerodynamic coefficient C_{X_g}, C_{Z_g} and C_{m_g} PSD-functions for the 1D symmetrical vertical gust input α_g given for the gust scale length $L_g = 300$ [m]. Results are given for the LPF-solution, as well as for the PCA-, DUT- and FPA-model.

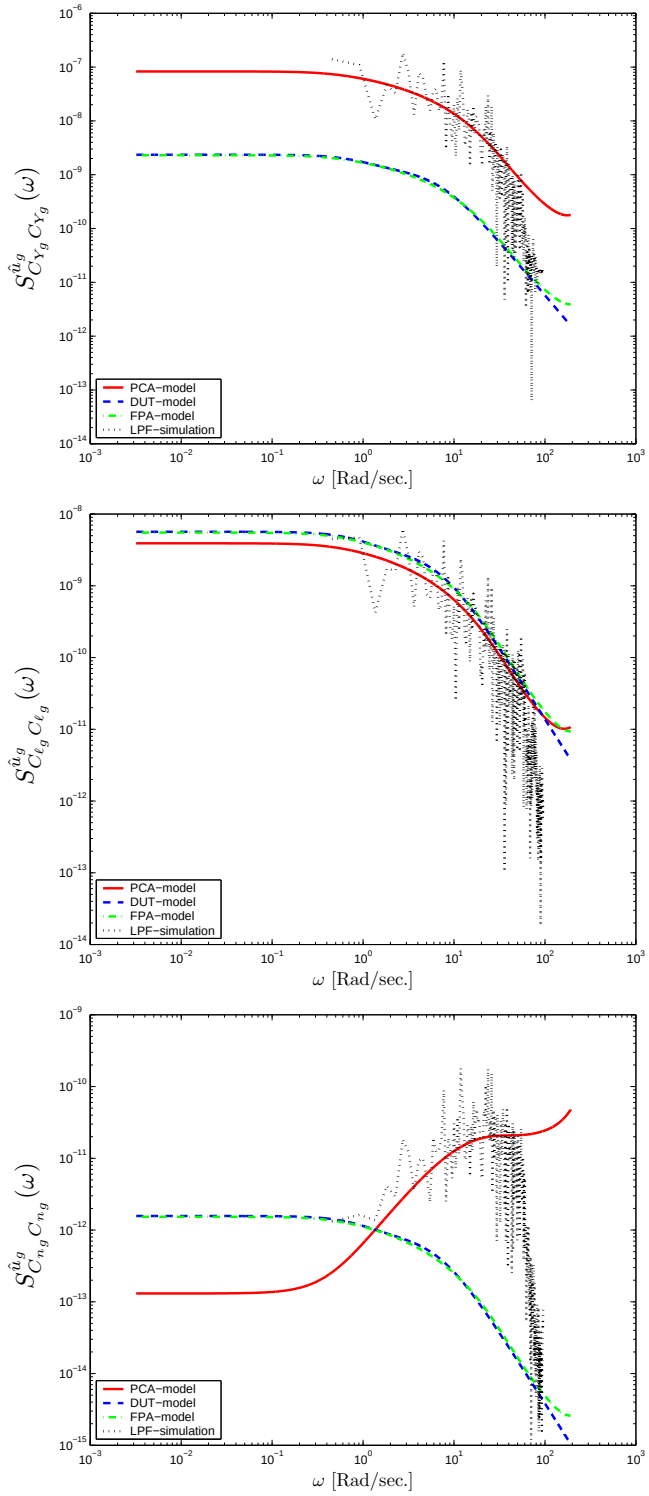


Figure 13.23: The aerodynamic coefficient C_{Y_g}, C_{ℓ_g} and C_{n_g} PSD-functions for the 2D anti-symmetrical longitudinal gust input $\hat{u}_g$ given for the gust scale length $L_g = 300$ [m]. Results are given for the LPF-solution, as well as for the PCA-, DUT- and FPA-model.

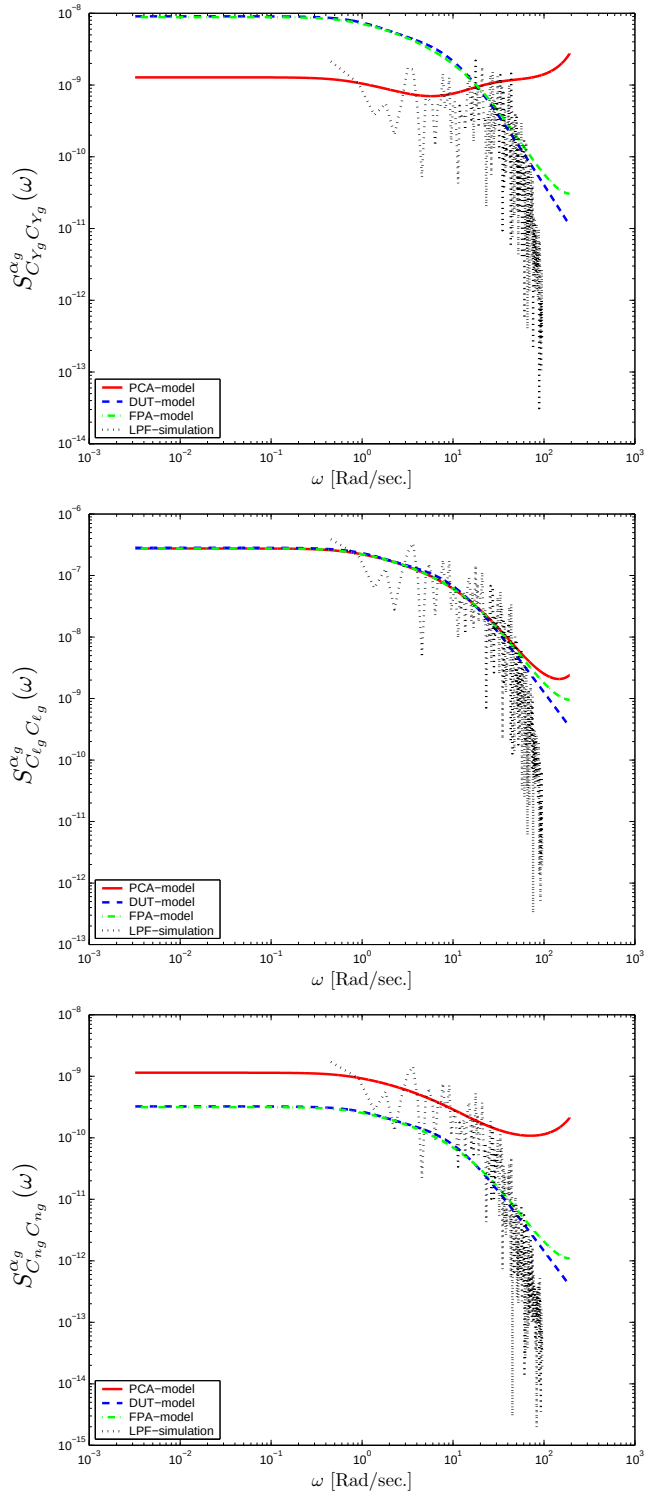


Figure 13.24: The aerodynamic coefficient C_{Y_g}, C_{ℓ_g} and C_{n_g} PSD-functions for the 2D anti-symmetrical vertical gust input α_g given for the gust scale length $L_g = 300$ [m]. Results are given for the LPF-solution, as well as for the PCA-, DUT- and FPA-model.

aircraft motion responses. The results will be given in terms of aircraft state time-histories with respect to the encountered gust fields. For the frequency-domain, the aircraft motion responses are given in terms of the aircraft motion state variable PSD-functions ánd their variances.

For the calculation of these responses, use is made of the equations of motion written in state-space form. Previously, see equation (13.2), the time-domain equations of motion have been written as,

$$P\ \frac{d\underline{x}}{dt} = Q\ \underline{x} + R\ \underline{u}$$

which are transformed into the state-space form,

$$\frac{d\underline{x}}{dt} = A\ \underline{x} + B\ \underline{u}$$

with $A = P^{-1}Q$ the system-matrix, $B = P^{-1}R$ the input-matrix, $\underline{x}$ the aircraft state and $\underline{u}$ the gust input vector. The additional equation required to calculate the state-space system's response is the output equation,

$$\underline{y} = C\ \underline{x} + D\ \underline{u}$$

with C the output-matrix and D the direct-matrix. In the following, the response of the aircraft-state is considered only. Therefore, the C matrix becomes the identity matrix of order 4 (four states are present in both the symmetrical and asymmetrical aircraft equations of motion) while the D-matrix is the zero-matrix of order $4 \times m$ with m the number of gust inputs.

For the calculation of time-domain aircraft motion responses use is made of gust inputs obtained from the spatial-domain gust-fields given in appendix G. For the calculation of the analytical frequency-domain aircraft motion responses the input PSD-functions summarized in section 13.2 are used. The definition of the gust inputs is also summarized in appendix G.

13.4.2 Time-domain results

In figures 13.25 the aircraft motion responses due to the longitudinal gust velocity component u_g are given. It is shown that the responses of the DUT-, FPA- and PCA-model are well correlated with the LPF-solution responses. The offset in the aircraft motion responses is also due to the value of the aerodynamic coefficients at $t = 0$, see the responses of $C_{X_g}(u_g(t))$, $C_{Z_g}(u_g(t))$ and $C_{m_g}(u_g(t))$ in figures 13.5 through 13.7, respectively.

Next, in figures 13.26 the aircraft motion responses due to the lateral gust velocity component v_g are given. It is shown that the responses of all models correlate very well in both phase and magnitude, as can be expected since the aerodynamic coefficients $C_{Y_g}(\beta_g(t))$,

$C_{\ell_g}(\beta_g(t))$ and $C_{n_g}(\beta_g(t))$ shown in figures 13.8 through 13.10, respectively, showed excellent agreement for all models.
Also, in figures 13.27 the aircraft motion responses due to the vertical gust velocity component w_g are given. Except for the speed-response $\hat{u}(t)$, it is shown that all model responses correlate very well in both phase and magnitude. The bad correlation of the speed-response is attributed to the omission of the gust derivative $C_{X_{\dot{\alpha}_g}}$ for the PCA-model, and the omission of $C_{X_{\dot{\alpha}}}$ in the DUT- and FPA-model.
For the asymmetrical equations of motion, the aircraft motion responses due to 2D longitudinal anti-symmetrical gust fields are given in figure 13.28. The PCA-model results show excellent agreement with the LPF-solution results, whereas the agreement of the FPA-model results is bad, see also figures 13.14 through 13.16 where the aerodynamic coefficients $C_{Y_g}(\hat{u}_g(t))$, $C_{\ell_g}(\hat{u}_g(t))$ and $C_{n_g}(\hat{u}_g(t))$ are shown, respectively.
Finally, in figure 13.29 the aircraft motion responses due to the 2D anti-symmetrical vertical gust velocity component w_g are given. Also here the PCA-model responses show excellent agreement with the LPF-solution results. The FPA-model responses show less good agreement, especially for the side-slip-angle and yaw-rate.

13.4.3 Analytical frequency-domain results

In this section the frequency-domain aircraft motion responses are given in terms of PSD-functions and calculated variances. To obtain these functions, first the aircraft motion Frequency-Response Functions (FRF's) are calculated using standard routines in MATLAB (such as `mv2fr.m`). Next, the output PSD-functions are calculated using the theory provided in appendix B, section B.2. From these PSD-functions the variance is calculated using the following equation,

$$\sigma_y^2 = \frac{1}{2\pi}\int_{-\infty}^{+\infty} S_{yy}(\omega)\, d\omega = \frac{1}{\pi}\int_{0}^{+\infty} S_{yy}(\omega)\, d\omega \tag{13.28}$$

with σ_y^2 the variance, $S_{yy}(\omega)$ the PSD-function and ω the circular frequency in [Rad/sec.]. The variances are calculated uptill the frequency $\omega_{end} = \frac{Q_\infty}{\bar{c}} \approx 61.1$ [Rad/sec.].

In figure 13.30 the input PSD-function $S_{\hat{u}_g\hat{u}_g}(\omega)$ and the output PSD-functions of the PCA-, the DUT- and the FPA-model with respect to the 1D gust input $\hat{u}_g$, $S^{\hat{u}_g}_{\hat{u}\hat{u}}(\omega)$, $S^{\hat{u}_g}_{\alpha\alpha}(\omega)$, $S^{\hat{u}_g}_{\theta\theta}(\omega)$ and $S^{\hat{u}_g}_{\frac{q\bar{c}}{Q_\infty}\frac{q\bar{c}}{Q_\infty}}(\omega)$ for the gust scale length $L_g = 300$ [m] are given. While the model input PSD-functions are almost equal, compared to the other models for high frequencies the PCA-model output PSD-functions differ considerably. This is attributed to the use of the unsteady gust derivatives $C_{X_{\dot{u}_g}}$, $C_{Z_{\dot{u}_g}}$ and $C_{m_{\dot{u}_g}}$. In table 13.3 the calculated variances of the input $\hat{u}_g$ and the outputs $\hat{u}$, α, θ and $\frac{q\bar{c}}{Q_\infty}$ are summarized for all models. The variances of all models show excellent agreement, except for σ_α^2. Apparently, the effect of the use of the PCA-model unsteady gust derivatives $C_{X_{\dot{u}_g}}$, $C_{Z_{\dot{u}_g}}$ and $C_{m_{\dot{u}_g}}$ is small.

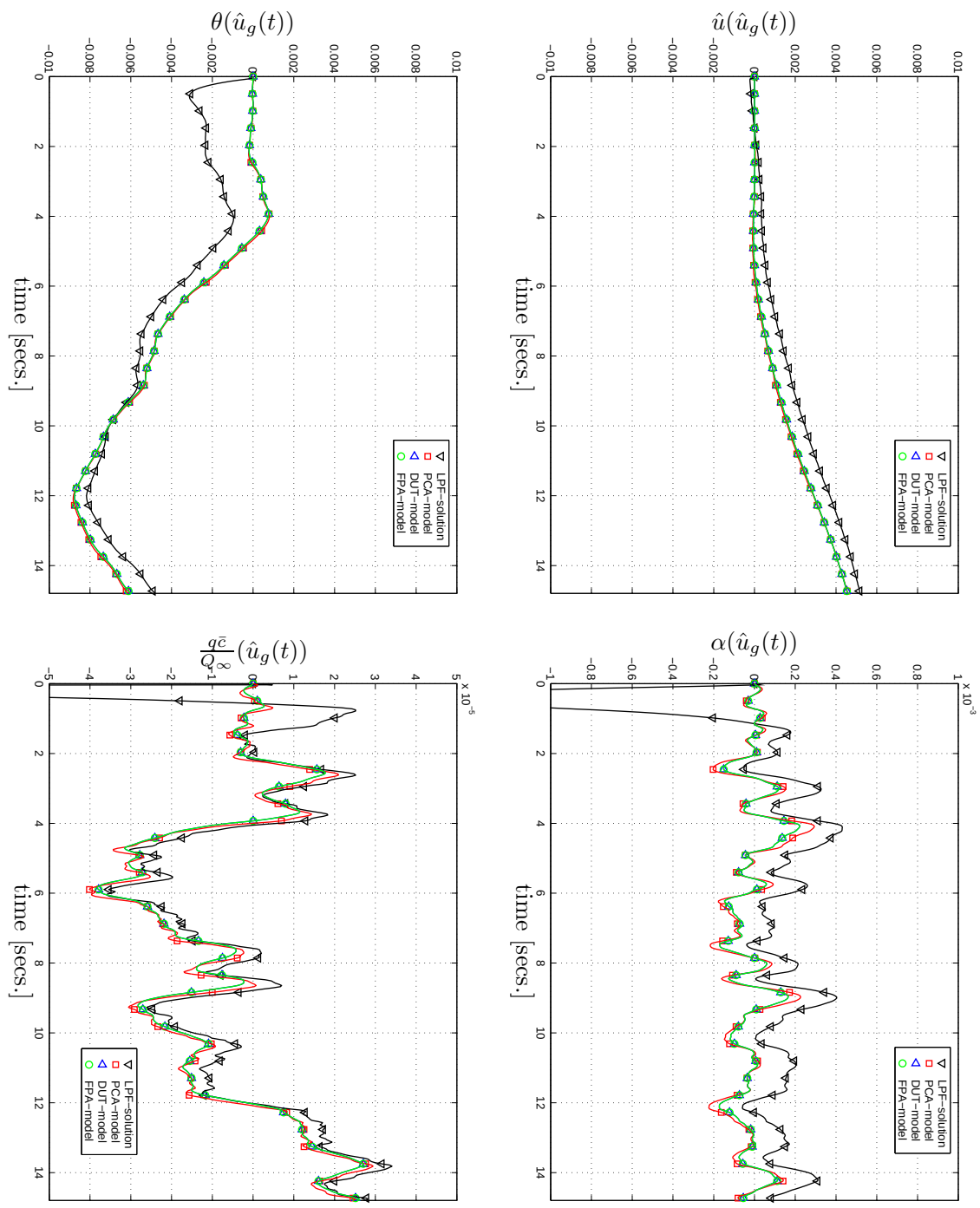


Figure 13.25: The symmetrical aircraft motion responses $\hat{u}$, α, θ and $\frac{q\bar{c}}{Q_\infty}$ due to the symmetrical longitudinal gust-field u_g, for the gust scale length $L_g = 300$ [m].

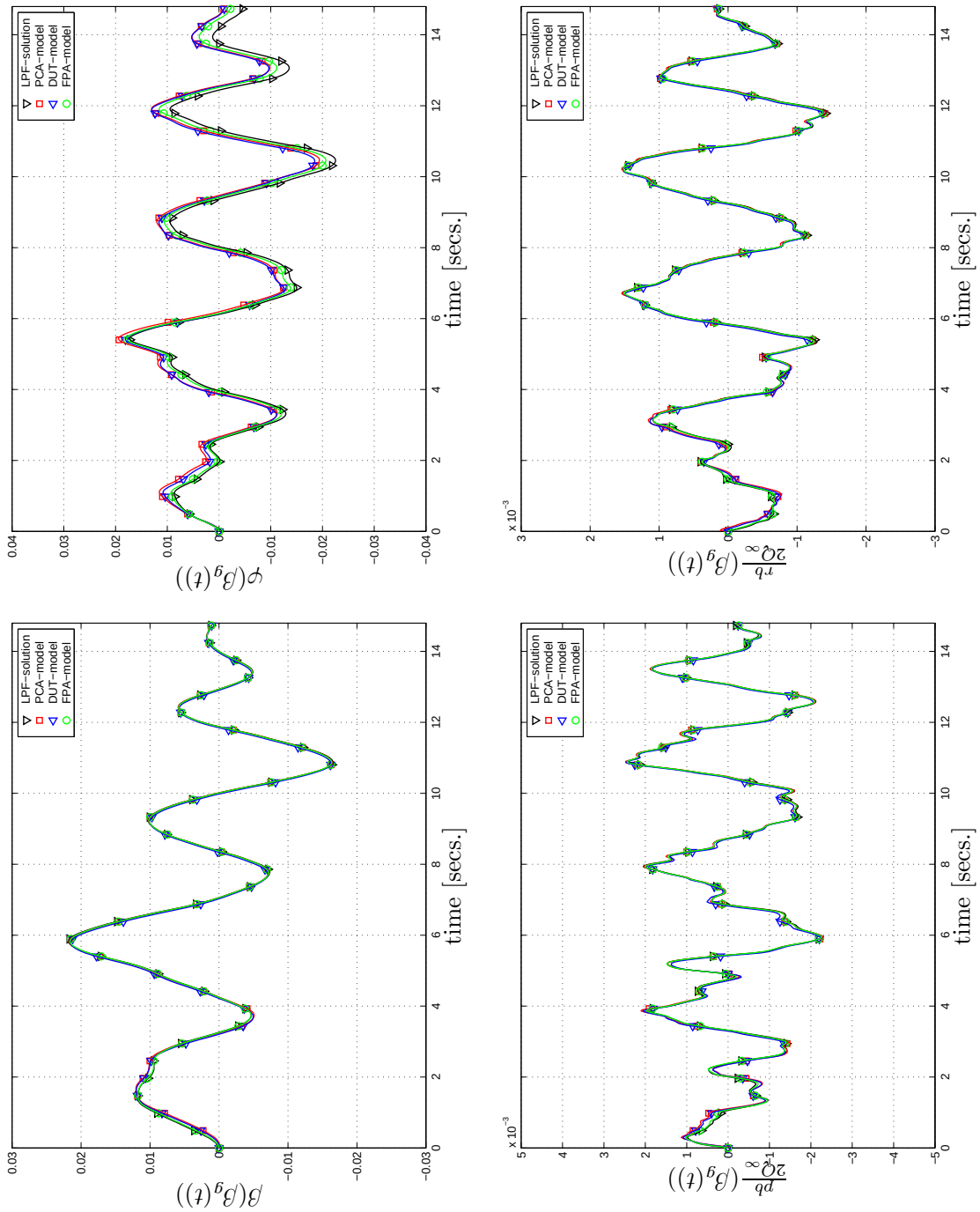


Figure 13.26: The asymmetrical aircraft motion responses β, φ, $\frac{pb}{2Q_\infty}$ and $\frac{rb}{2Q_\infty}$ due to the asymmetrical lateral gust-field v_g, for the gust scale length $L_g = 300$ [m].

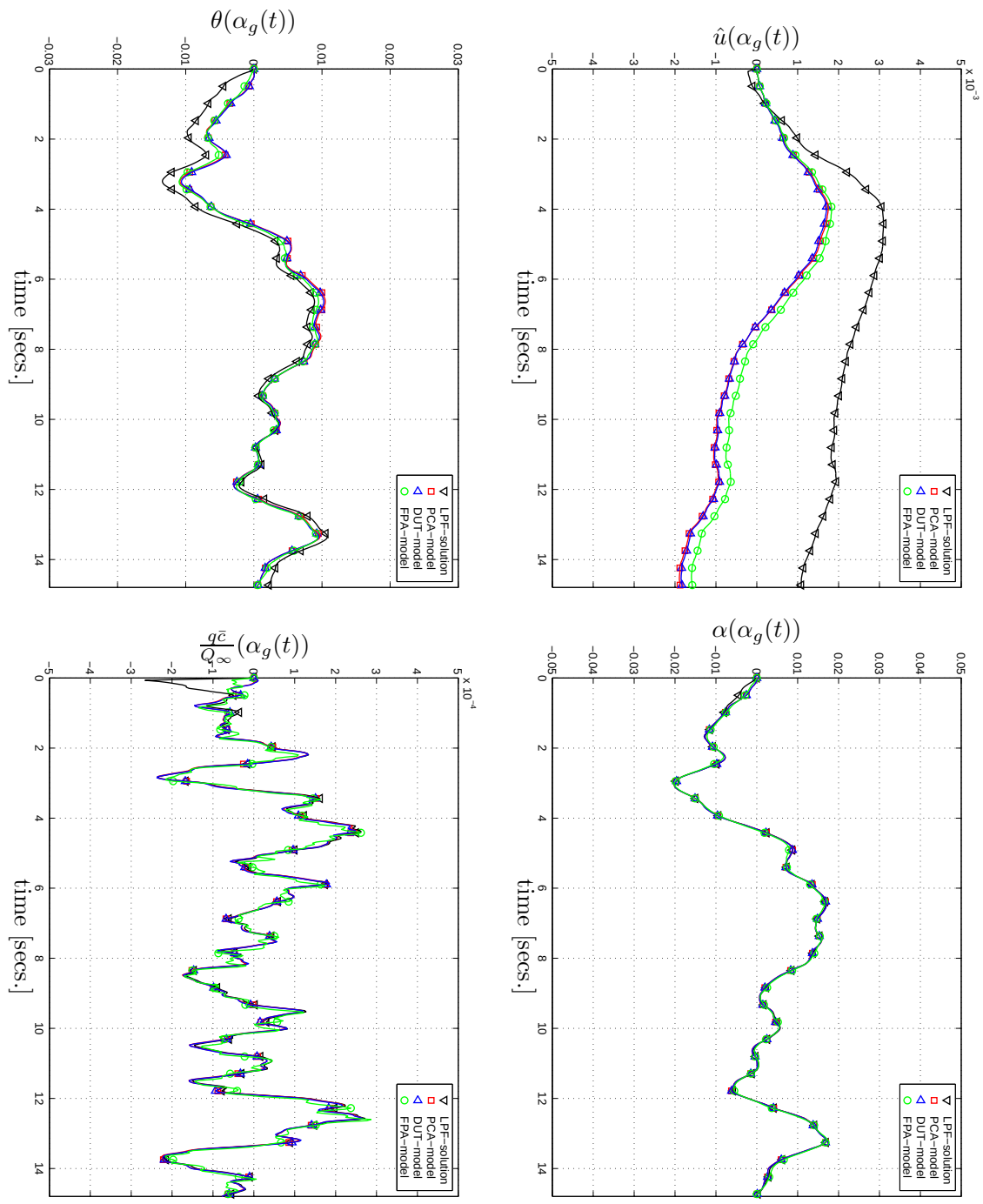


Figure 13.27: The symmetrical aircraft motion responses $\hat{u}$, α, θ and $\frac{q\bar{c}}{Q_\infty}$ due to the symmetrical vertical gust-field w_g, for the gust scale length $L_g = 300$ [m].

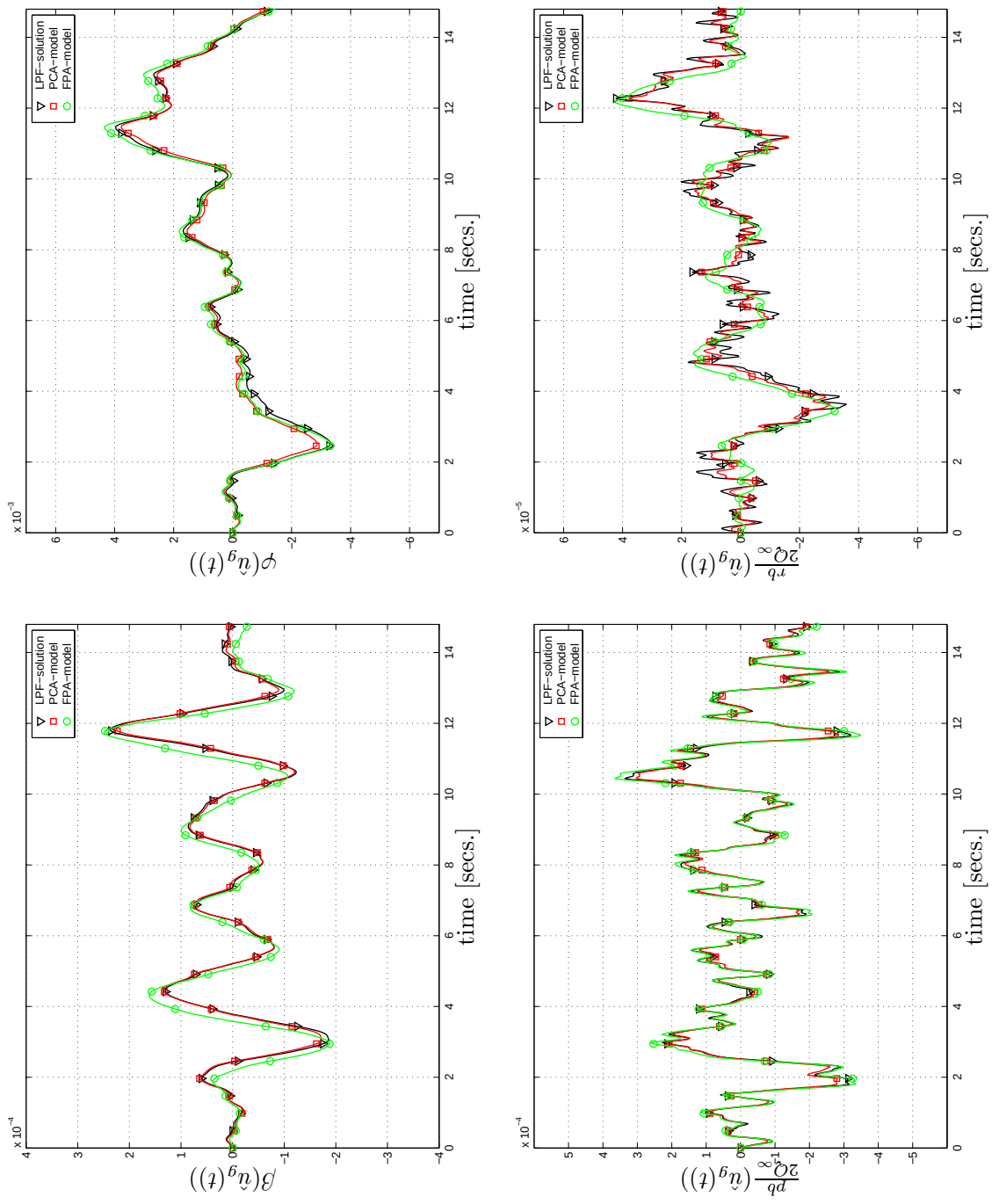


Figure 13.28: The asymmetrical aircraft motion responses β, φ, $\frac{pb}{2Q_\infty}$ and $\frac{rb}{2Q_\infty}$ due to the anti-symmetrical longitudinal gust-field u_g, for the gust scale length $L_g = 300$ [m].

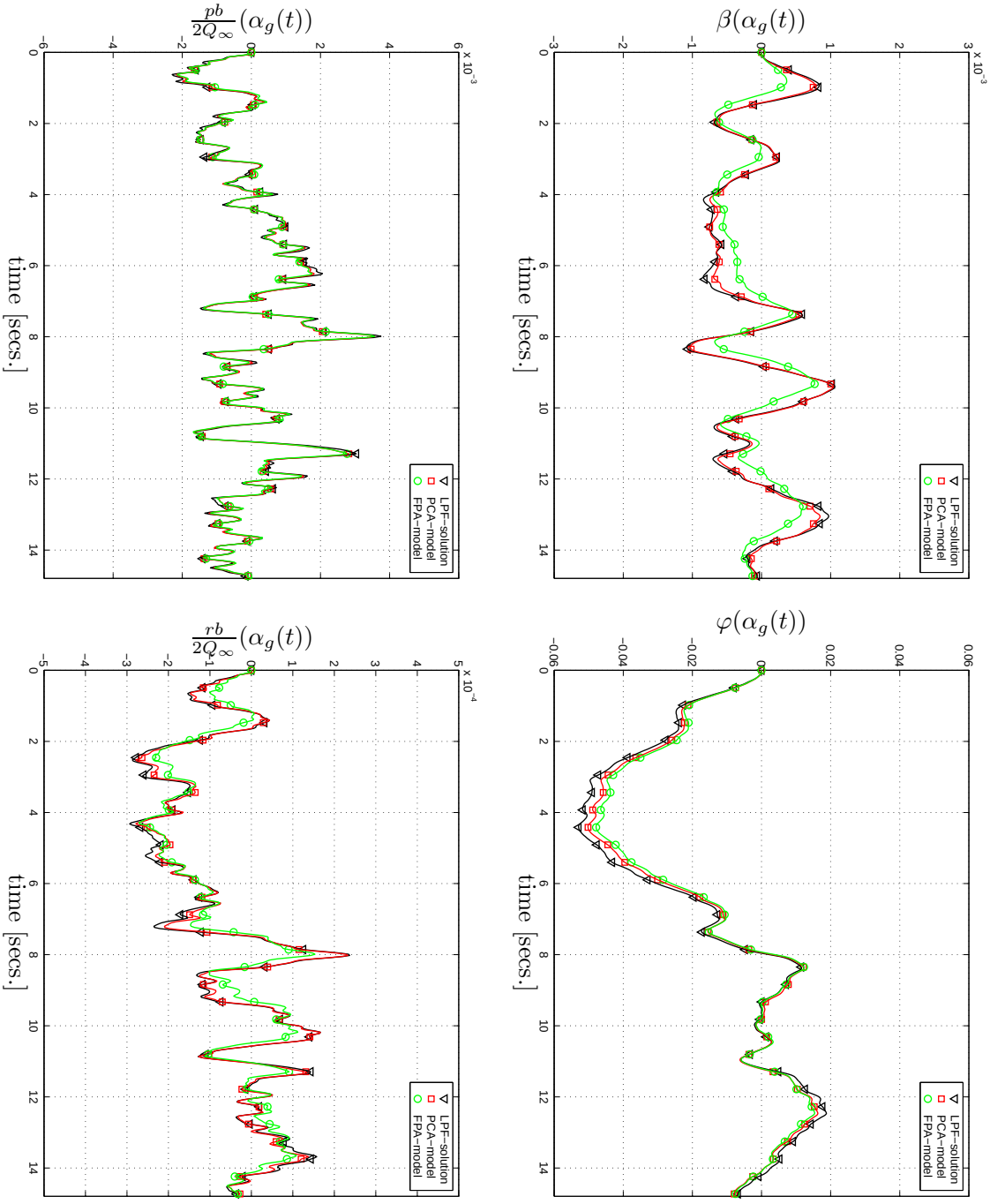


Figure 13.29: The asymmetrical aircraft motion responses β, φ, $\frac{pb}{2Q_\infty}$ and $\frac{rb}{2Q_\infty}$ due to the anti-symmetrical vertical gust-field w_g, for the gust scale length $L_g = 300$ [m].

Next, in figure 13.31 the input PSD-function $S_{\beta_g\beta_g}(\omega)$ and the output PSD-functions of the PCA-, the DUT- and the FPA-model with respect to the 1D gust input β_g, $S^{\beta_g}_{\beta\beta}(\omega)$, $S^{\beta_g}_{\varphi\varphi}(\omega)$, $S^{\beta_g}_{\frac{pb}{2Q_\infty}\frac{pb}{2Q_\infty}}(\omega)$ and $S^{\beta_g}_{\frac{rb}{2Q_\infty}\frac{rb}{2Q_\infty}}(\omega)$ for the gust scale length $L_g = 300$ [m] are given. Both the models' input - and output PSD-functions coincide over a wide frequency range, as can be expected since the model time-domain responses showed excellent agreement. In table 13.4 the calculated variances of the input β_g and the outputs β, φ, $\frac{pb}{2Q_\infty}$ and $\frac{rb}{2Q_\infty}$ are summarized for all models. The variances of all models show excellent agreement as was already expected from the time-domain aircraft motion results.

Also, in figure 13.32 the input PSD-function $S_{\alpha_g\alpha_g}(\omega)$ and the output PSD-functions of the PCA-, the DUT- and the FPA-model with respect to the 1D gust input α_g, $S^{\alpha_g}_{\hat{u}\hat{u}}(\omega)$, $S^{\alpha_g}_{\alpha\alpha}(\omega)$, $S^{\alpha_g}_{\theta\theta}(\omega)$ and $S^{\alpha_g}_{\frac{q\bar{c}}{Q_\infty}\frac{q\bar{c}}{Q_\infty}}(\omega)$ for the gust scale length $L_g = 300$ [m] are given. Both the models' input - and output PSD-functions are almost equal, as was also already expected from the time-domain aircraft-responses. In table 13.3 the calculated variances of the input $\hat{u}_g$ and the outputs $\hat{u}$, α, θ and $\frac{q\bar{c}}{Q_\infty}$ are summarized for all models. Similar to the PSD-functions, the variances of all models show excellent agreement.

For the asymmetrical equations of motion, the frequency-domain aircraft motion responses due to 2D longitudinal anti-symmetrical gust fields are given in figure 13.33. Here, the input PSD-functions $S_{\frac{r_{1_g}b}{2Q_\infty}\frac{r_{1_g}b}{2Q_\infty}}(\omega)$ ánd the Effective input PSD-function $I_{\hat{u}_g}(\omega)$, and the output PSD-functions of the PCA-, the DUT- and the FPA-model with respect to the 2D gust input $\hat{r}_{1_g} = \frac{r_{1_g}b}{2Q_\infty}$ (PCA- and FPA-model) and the 2D gust input $\hat{u}_g$ (DUT-model), $S^{\hat{r}_{1_g},\hat{u}_g}_{\beta\beta}(\omega)$, $S^{\hat{r}_{1_g},\hat{u}_g}_{\varphi\varphi}(\omega)$, $S^{\hat{r}_{1_g},\hat{u}_g}_{\frac{pb}{2Q_\infty}\frac{pb}{2Q_\infty}}(\omega)$ and $S^{\hat{r}_{1_g},\hat{u}_g}_{\frac{rb}{2Q_\infty}\frac{rb}{2Q_\infty}}(\omega)$ for the gust scale length $L_g = 300$ [m] are shown. Except for the side-slip-angle - and the yaw-rate response, all model responses show good agreement. It is shown that the side-slip response is overestimated for the FPA-model (compared to the PCA-model results), while the yaw-rate response is too low-frequent in nature for the FPA-model, see also figure 13.28. In table 13.4 the calculated variances of the inputs $\frac{r_{1_g}b}{2Q_\infty}$ and $\hat{u}_g$ and the outputs β, φ, $\frac{pb}{2Q_\infty}$ and $\frac{rb}{2Q_\infty}$ are summarized for all models. The variances of the DUT- and FPA-model show excellent agreement. They both differ considerably, however, with respect to the PCA-model variances as was already expected from the frequency-domain aircraft motion results.

Finally, in figure 13.34 the input PSD-functions $S_{\frac{p_gb}{2Q_\infty}\frac{p_gb}{2Q_\infty}}(\omega)$ ánd the effective input PSD-function $I_{\alpha_g}(\omega)$, and the output PSD-functions of the PCA-, the DUT- and the FPA-model with respect to the 2D gust input $\hat{p}_g = \frac{p_gb}{2Q_\infty}$ (PCA- and FPA-model) and the 2D gust input α_g (DUT-model), $S^{\hat{p}_g,\alpha_g}_{\beta\beta}(\omega)$, $S^{\hat{p}_g,\alpha_g}_{\varphi\varphi}(\omega)$, $S^{\hat{p}_g,\alpha_g}_{\frac{pb}{2Q_\infty}\frac{pb}{2Q_\infty}}(\omega)$ and $S^{\hat{p}_g,\alpha_g}_{\frac{rb}{2Q_\infty}\frac{rb}{2Q_\infty}}(\omega)$ for the gust scale length $L_g = 300$ [m] are given. Similar to aircraft motion results with respect to the longitudinal anti-symmetrical gust field, all model responses show good agreement except for the side-slip-angle - and the yaw-rate response. It is shown that the side-slip response is now underestimated for the FPA-model (compared to the PCA-model results), while the yaw-rate response is over-estimated, see also figure 13.29. In table 13.4 the calculated

variances of the inputs $\frac{p_g b}{2Q_\infty}$ and α_g and the outputs β, φ, $\frac{pb}{2Q_\infty}$ and $\frac{rb}{2Q_\infty}$ are summarized for all models. The variances of the DUT- and FPA-model show good agreement. They differ, however, with respect to the PCA-model variances as can already be from the frequency-domain aircraft motion results.

13.5 LPF-EOM-model simulations

13.5.1 Introduction

In this section the aircraft responses for the LPF-EOM-model are given. For this model, the potential flow solution is now coupled to the aircraft equations of motion. Although the responses are calculated for both symmetrical and anti-symmetrical gust fields used earlier, the aircraft grid is now allowed to travel along stochastic flightpaths.

Results are given for the non-dimensional aerodynamic force and moment coefficients acting on the aircraft, that is C_X, C_Y, C_Z, C_ℓ, C_m and C_n. These results will only be given for the LPF-solution (for recti-linear flightpaths) and the LPF-EOM-solution (for stochastic flight-paths). For the symmetrical aircraft motions, as an example the LPF-solution coeffients due to the symmetrical vertical gust field are treated first. They are written as,

$$\begin{aligned}
C_X^{LPF}(t)\Big|_{\alpha_g} &= C_{X_u}\hat{u}(t) + C_{X_\alpha}\alpha(t) + C_{X_q}\tfrac{q\bar{c}}{Q_\infty}(t) + C_{X_g}^{LPF}(t)\Big|_{\alpha_g} \\
C_Z^{LPF}(t)\Big|_{\alpha_g} &= C_{Z_u}\hat{u}(t) + C_{Z_\alpha}\alpha(t) + C_{Z_{\dot{\alpha}}}\dot{\alpha}(t)\tfrac{\bar{c}}{Q_\infty} + C_{Z_q}\tfrac{q\bar{c}}{Q_\infty}(t) + C_{Z_g}^{LPF}(t)\Big|_{\alpha_g} \qquad (13.29) \\
C_m^{LPF}(t)\Big|_{\alpha_g} &= C_{m_u}\hat{u}(t) + C_{m_\alpha}\alpha(t) + C_{m_{\dot{\alpha}}}\dot{\alpha}(t)\tfrac{\bar{c}}{Q_\infty} + C_{m_q}\tfrac{q\bar{c}}{Q_\infty}(t) + C_{m_g}^{LPF}(t)\Big|_{\alpha_g}
\end{aligned}$$

with the steady - and unsteady stability derivatives determined in chapters 5 and 10, the LPF-solution gust induced aerodynamic force and moment coefficients $C_{X_g}^{LPF}(t)\Big|_{\alpha_g}$, $C_{Z_g}^{LPF}(t)\Big|_{\alpha_g}$ and $C_{m_g}^{LPF}(t)\Big|_{\alpha_g}$ shown in figures 13.11, 13.12 and 13.13, respectively, and the LPF-solution aircraft motion responses $\hat{u}(t)$, $\alpha(t)$, $\theta(t)$ and $\frac{q\bar{c}}{Q_\infty}(t)$ shown in figures 13.27. The coefficient definitions for symmetrical longitudinal gust fields are similar to the ones given in equation (13.29).

For the asymmetrical aircraft motions, as an example the LPF-solution coeffients due to the anti-symmetrical vertical gust field is written as,

$$\begin{aligned}
C_Y^{LPF}(t)\Big|_{\alpha_g} &= C_{Y_\beta}\beta(t) + C_{Y_{\dot{\beta}}}\dot{\beta}(t)\tfrac{b}{Q_\infty} + C_{Y_p}\tfrac{pb}{2Q_\infty}(t) + C_{Y_r}\tfrac{rb}{2Q_\infty}(t) + C_{Y_g}^{LPF}(t)\Big|_{\alpha_g} \\
C_\ell^{LPF}(t)\Big|_{\alpha_g} &= C_{\ell_\beta}\beta(t) + C_{\ell_{\dot{\beta}}}\dot{\beta}(t)\tfrac{b}{Q_\infty} + C_{\ell_p}\tfrac{pb}{2Q_\infty}(t) + C_{\ell_r}\tfrac{rb}{2Q_\infty}(t) + C_{\ell_g}^{LPF}(t)\Big|_{\alpha_g} \qquad (13.30) \\
C_n^{LPF}(t)\Big|_{\alpha_g} &= C_{n_\beta}\beta(t) + C_{n_{\dot{\beta}}}\dot{\beta}(t)\tfrac{b}{Q_\infty} + C_{n_p}\tfrac{pb}{2Q_\infty}(t) + C_{n_r}\tfrac{rb}{2Q_\infty}(t) + C_{n_g}^{LPF}(t)\Big|_{\alpha_g}
\end{aligned}$$

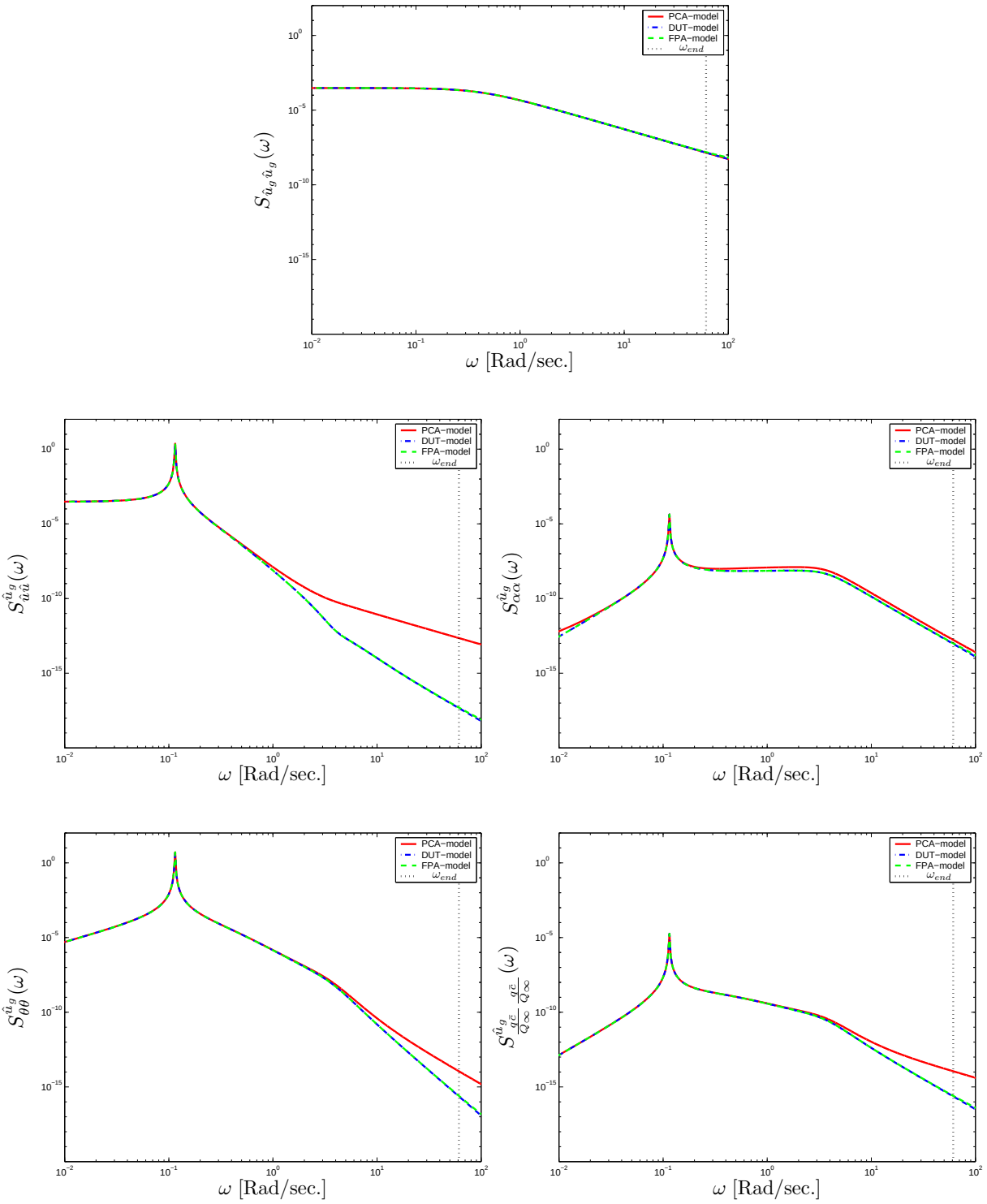


Figure 13.30: Both the 1D input PSD-function $S_{\hat{u}_g\hat{u}_g}(\omega)$ and the output PSD-functions of the PCA-, the DUT- and the FPA-model with respect to the 1D gust input $\hat{u}_g$, $S^{\hat{u}_g}_{\hat{u}\hat{u}}(\omega)$, $S^{\hat{u}_g}_{\alpha\alpha}(\omega)$, $S^{\hat{u}_g}_{\theta\theta}(\omega)$ and $S^{\hat{u}_g}_{\frac{q\bar{c}}{Q_\infty}\frac{q\bar{c}}{Q_\infty}}(\omega)$ for the gust scale length $L_g = 300$ [m].

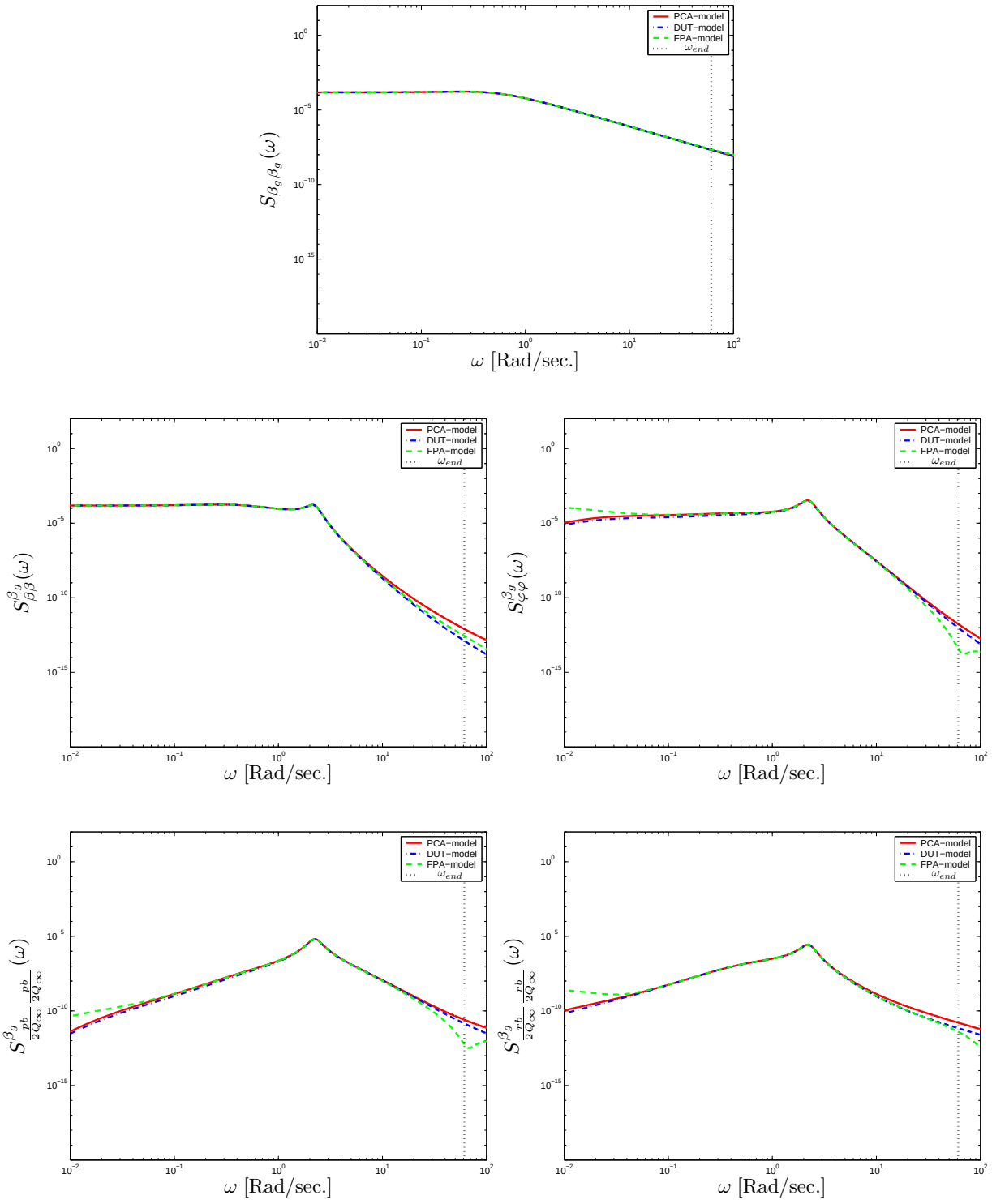


Figure 13.31: Both the 1D input PSD-function $S_{\beta_g\beta_g}(\omega)$ and the output PSD-functions of the PCA-, the DUT- and the FPA-model with respect to the 1D gust input β_g, $S^{\beta_g}_{\beta\beta}(\omega)$, $S^{\beta_g}_{\varphi\varphi}(\omega)$, $S^{\beta_g}_{\frac{pb}{2Q_\infty}\frac{pb}{2Q_\infty}}(\omega)$ and $S^{\beta_g}_{\frac{rb}{2Q_\infty}\frac{rb}{2Q_\infty}}(\omega)$ for the gust scale length $L_g = 300$ [m].

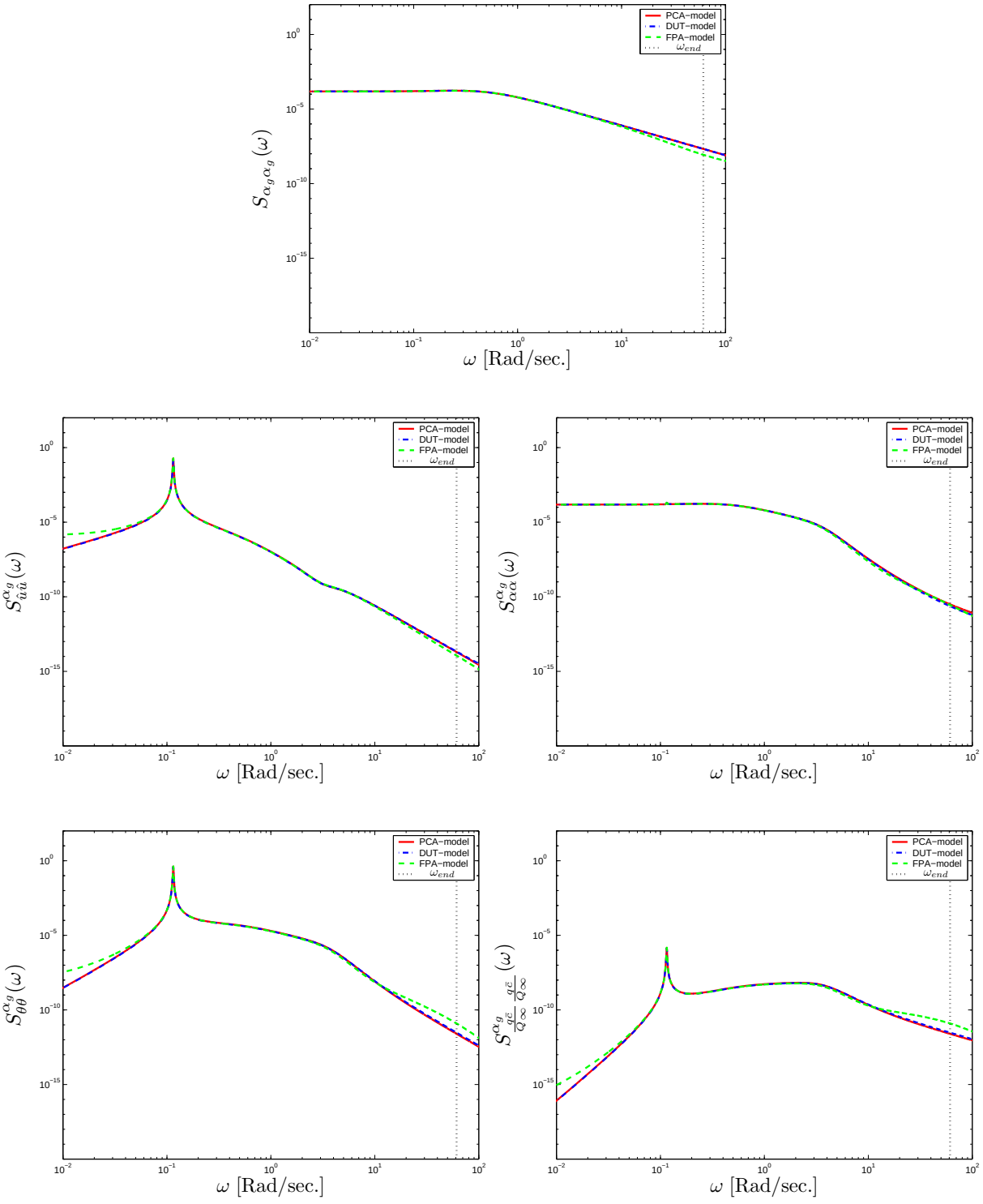


Figure 13.32: Both the 1D input PSD-function $S_{\alpha_g\alpha_g}(\omega)$ and the output PSD-functions of the PCA-, the DUT- and the FPA-model with respect to the 1D gust input α_g, $S^{\alpha_g}_{\hat{u}\hat{u}}(\omega)$, $S^{\alpha_g}_{\alpha\alpha}(\omega)$, $S^{\alpha_g}_{\theta\theta}(\omega)$ and $S^{\alpha_g}_{\frac{q\bar{c}}{Q_\infty}\frac{q\bar{c}}{Q_\infty}}(\omega)$ for the gust scale length $L_g = 300$ [m].

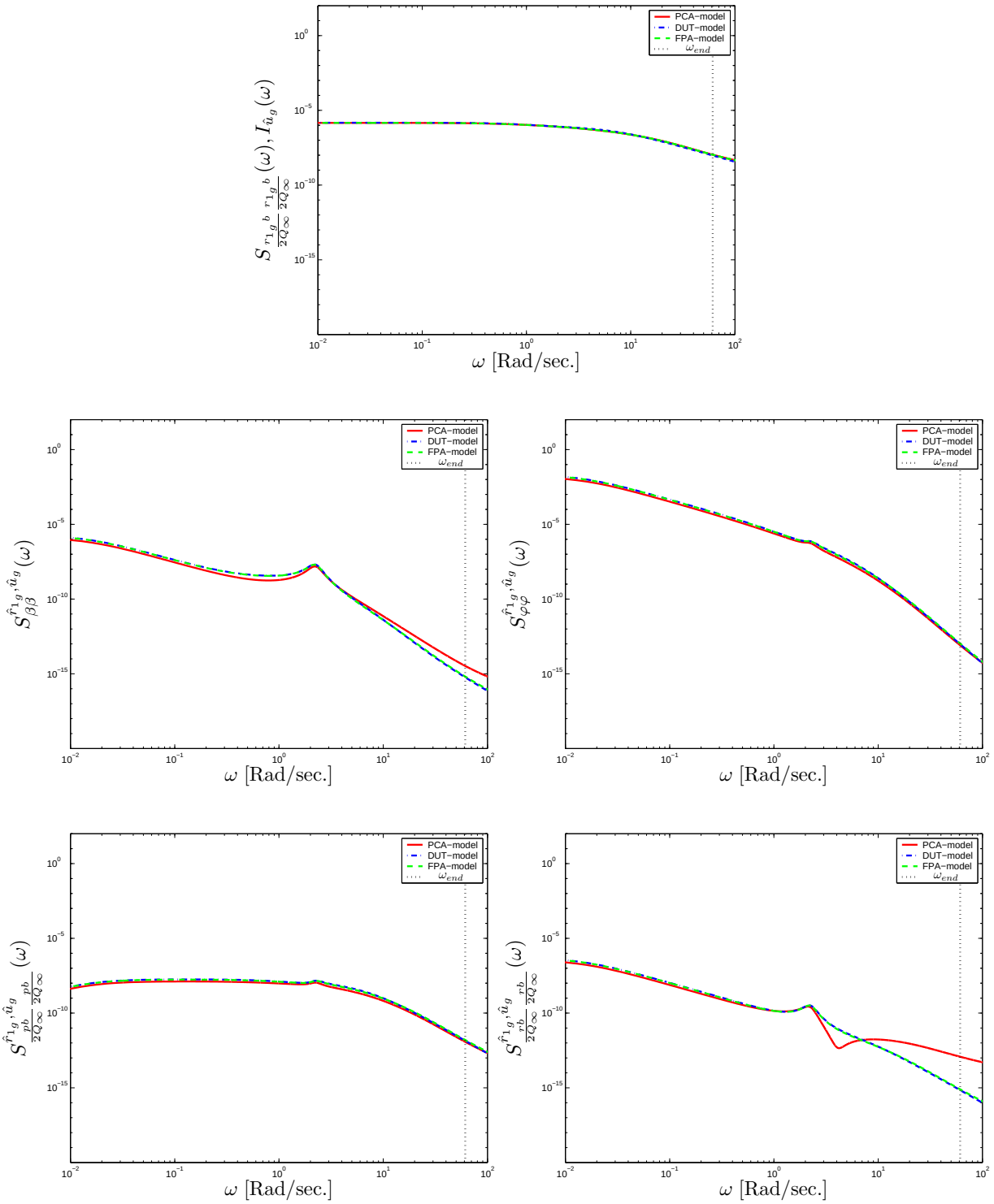


Figure 13.33: The input PSD-functions $S_{\frac{r_{1_g}b}{2Q_\infty}\frac{r_{1_g}b}{2Q_\infty}}(\omega)$ and the effective input PSD-function $I_{\hat{u}_g}(\omega)$, and the output PSD-functions of the PCA-, the DUT- and the FPA-model with respect to the 2D gust input $\hat{r}_{1_g} = \frac{r_{1_g}b}{2Q_\infty}$ (PCA- and FPA-model) and the 2D gust input $\hat{u}_g$ (DUT-model), $S^{\hat{r}_{1_g},\hat{u}_g}_{\beta\beta}(\omega)$, $S^{\hat{r}_{1_g},\hat{u}_g}_{\varphi\varphi}(\omega)$, $S^{\hat{r}_{1_g},\hat{u}_g}_{\frac{pb}{2Q_\infty}\frac{pb}{2Q_\infty}}(\omega)$ and $S^{\hat{r}_{1_g},\hat{u}_g}_{\frac{rb}{2Q_\infty}\frac{rb}{2Q_\infty}}(\omega)$ for the gust scale length $L_g = 300$ [m].

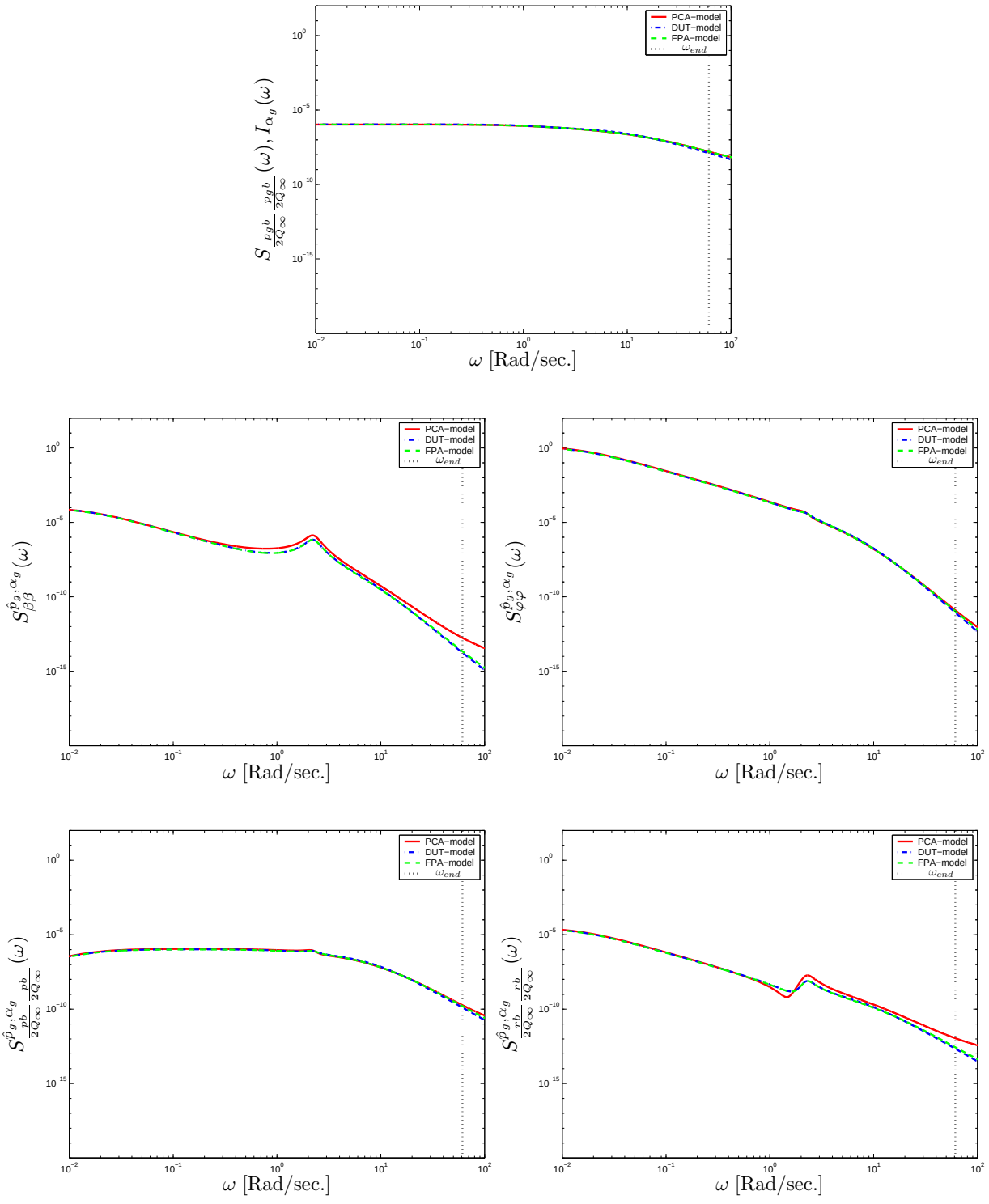


Figure 13.34: The input PSD-functions $S_{\frac{pgb}{2Q_\infty}\frac{pgb}{2Q_\infty}}(\omega)$ and the effective input PSD-function $I_{\alpha_g}(\omega)$, and the output PSD-functions of the PCA-, the DUT- and the FPA-model with respect to the 2D gust input $\hat{p}_g = \frac{pgb}{2Q_\infty}$ (PCA- and FPA-model) and the 2D gust input α_g (DUT-model), $S^{\hat{p}_g,\alpha_g}_{\beta\beta}(\omega)$, $S^{\hat{p}_g,\alpha_g}_{\varphi\varphi}(\omega)$, $S^{\hat{p}_g,\alpha_g}_{\frac{pb}{2Q_\infty}\frac{pb}{2Q_\infty}}(\omega)$ and $S^{\hat{p}_g,\alpha_g}_{\frac{rb}{2Q_\infty}\frac{rb}{2Q_\infty}}(\omega)$ for the gust scale length $L_g = 300$ [m].

with the asymmetrical steady - and unsteady stability derivatives also determined in chapters 5 and 10, the LPF-solution gust induced aerodynamic force and moment coefficients $C_{Y_g}^{LPF}(t)\Big|_{\alpha_g}$, $C_{\ell_g}^{LPF}(t)\Big|_{\alpha_g}$ and $C_{n_g}^{LPF}(t)\Big|_{\alpha_g}$ shown in figures 13.17, 13.18 and 13.19, respectively, and the LPF-solution aircraft motion responses $\beta(t)$, $\frac{pb}{2Q_\infty}(t)$ and $\frac{rb}{2Q_\infty}(t)$ shown in figures 13.29. The coefficient definitions to asymmetrical lateral gust fields and to anti-symmetrical longitudinal gust fields are similar to the ones given in equation (13.30).

The LPF-EOM-model aerodynamic coefficients are determined using the theory given in chapter 9. For comparison with the LPF-solution coefficients, they are corrected for their values calculated for the trim condition.

In this section the LPF-EOM-model aircraft motion responses will be compared to the ones obtained for the LPF-solution as well. For the sake of completeness, the PCA-, DUT- and FPA-model aircraft motion responses will be given as well, however they will not be discussed (for their discussion, see section 13.4). For the discussion of both the LPF-solution - and LPF-EOM-model responses, it should be borne in mind that,

1. Contrary to the LPF-solution's planar wake, the LPF-EOM-model's wake becomes three dimensional since it is created along the stochastic flightpath.

2. Since the LPF-EOM-model's flightpath is stochastic, for the asymmetrical aircraft motions the encountered gust fields will differ from those encountered during recti-linear flightpaths. Since deviations from the recti-linear flightpaths remained small during simulations, the difference in encountered gust fields remained small as well (for the gust scale length $L_g = 300$ [m]).

3. The encountered gust fields (which are given in the frame $\mathcal{F}_E$) are transformed to the frame $\mathcal{F}_S$ for the LPF-EOM-model simulations. Since the Euler angles $[\Psi, \theta, \varphi]^T$ remained small during simulations ($[\Psi, \theta, \varphi]^T << [1, 1, 1]^T$), the gust field of interest in $\mathcal{F}_E$ always remained dominant, even when it was decomposed in the frame $\mathcal{F}_S$.

13.5.2 LPF-EOM model responses

Responses to symmetrical longitudinal gust fields

In figure 13.35 the response of the aerodynamic coefficients C_X, C_Z and C_m to the symmetrical longitudinal gust field u_g is shown for both the LPF-solution and the LPF-EOM-model. The model responses show good correlation, both in phase and magnitude. However, for initial time-steps the LPF-solution responses show bad agreement with the LPF-EOM-model responses. This is attributed to the unrestrained simulation used for the LPF-EOM-model. Whereas the LPF-solution is constrained to a rectilinear flightpath, the LPF-EOM-model responses are free, resulting in an offset by the aircraft motions of the aerodynamic forces and moments. Once the LPF-solution's transient has expired, both the LPF-solution and the LPF-EOM-model responses show good agreement. From these re-

sponses it may be concluded that the parametric aerodynamic model, as given in equation (13.29), is accurate.
Next, in figure 13.36 the aircraft motion responses to the symmetrical longitudinal gust field u_g are shown. As expected, the LPF-solution's transient response of the gust induced coefficients C_X, C_Z and C_m result in aircraft motions dissimilar to the ones obtained for the LPF-EOM-model. It should be noted, however, that the PCA-model responses show good correlation with the ones for the LPF-EOM-model, especially for the non-dimensional speed perturbation - $(\hat{u})$, the pitch-angle - (θ) and the non-dimensional pitch-rate $(\frac{q\bar{c}}{Q_\infty})$ responses.

Responses to asymmetrical lateral gust fields

In figure 13.37 the response of the aerodynamic coefficients C_Y, C_ℓ and C_n to the asymmetrical lateral gust field v_g is shown for both the LPF-solution and the LPF-EOM-model. Here, the model responses show good correlation, both in phase and magnitude, and it may be concluded that the parametric aerodynamic model, as given in equation (13.30), is accurate.
Next, in figure 13.38 the aircraft motion responses to the asymmetrical lateral gust field v_g are shown. From the aerodynamic coefficient responses shown in figure 13.37, it is expected that the aircraft motion responses for both the LPF-solution and the LPF-EOM-model show good correlation. Especially for the side-slip-angle (β), the non-dimensional roll-rate $(\frac{pb}{2Q_\infty})$ and the non-dimensional yaw-rate $(\frac{rb}{2Q_\infty})$ the results show good agreement. Apparantly, the (sometimes) larger amplitude of the LPF-EOM-model rolling moment coefficient C_ℓ leads to considerable differences in the roll-angle (φ) as time progresses. Here, it may also be concluded that the PCA-, DUT- and FPA-model accurately simulate the aircraft motion responses to asymmetrical lateral gust fields.

Responses to symmetrical vertical gust fields

In figure 13.39 the response of the aerodynamic coefficients C_X, C_Z and C_m to the symmetrical vertical gust field w_g is shown for both the LPF-solution and the LPF-EOM-model. The model responses show good correlation, both in phase and magnitude. Similar to the coefficient responses to the symmetrical longitudinal gust field, also here the LPF-solution contains transient responses: for initial time-steps the LPF-solution responses show less agreement with the LPF-EOM-model responses. Also here this is attributed to the free simulation of the LPF-EOM-model. Once the LPF-solution's transient has expired, both the LPF-solution and the LPF-EOM-model responses show good agreement. From these responses it may be concluded that the parametric aerodynamic model, as given in equation (13.29), is inaccurate for the aerodynamic force coefficient C_X (the model may be enhanced including a contribution according to $C_{X_{\dot{\alpha}}}\dot{\alpha}(t)\frac{\bar{c}}{Q_\infty}$). For both the aerodynamic force coefficient C_Z and the aerodynamic moment coefficient C_m the parametric aerodynamic is accurate.
Next, in figure 13.40 the aircraft motion responses to the symmetrical vertical gust field w_g are shown. Similar to the aircraft motion responses to the symmetrical longitudinal gust

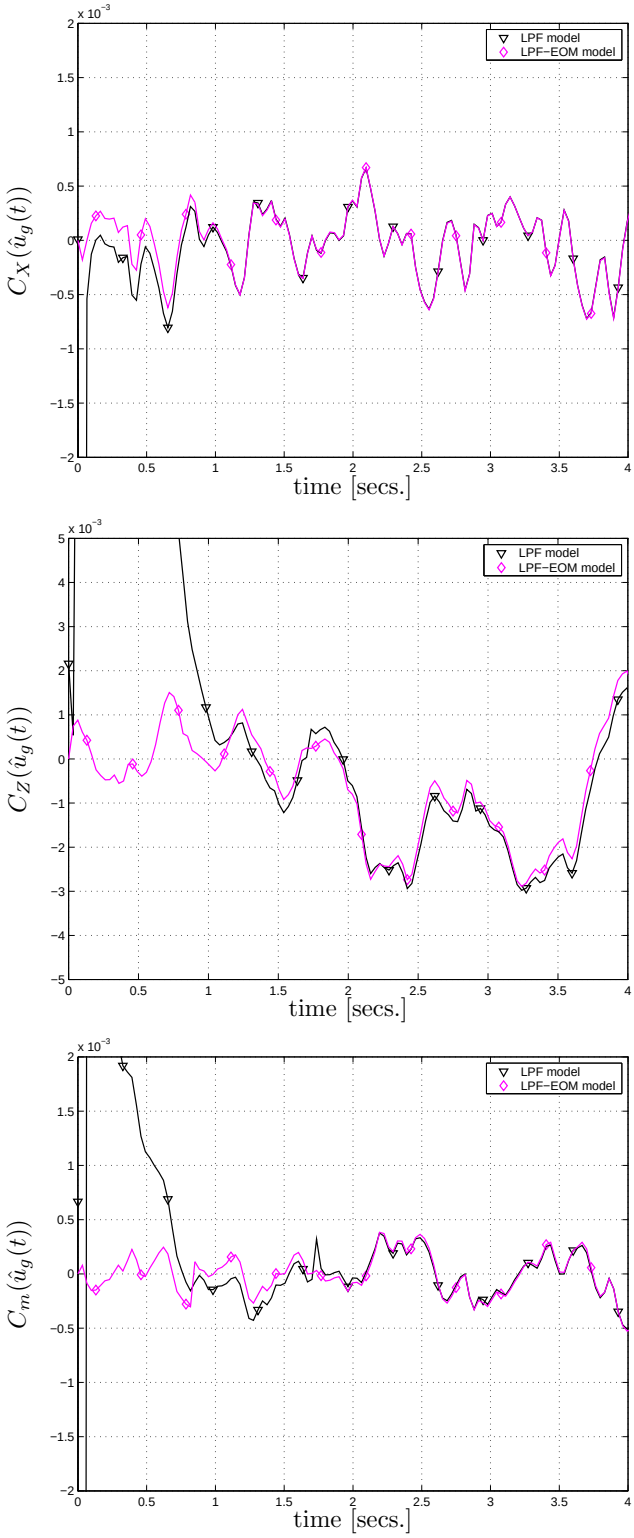


Figure 13.35: The time-domain aerodynamic coefficient responses C_X, C_Z and C_m for the symmetrical longitudinal gust field u_g given for the gust scale length $L_g = 300$ [m]. Results are given for both the LPF- and LPF-EOM-solution.

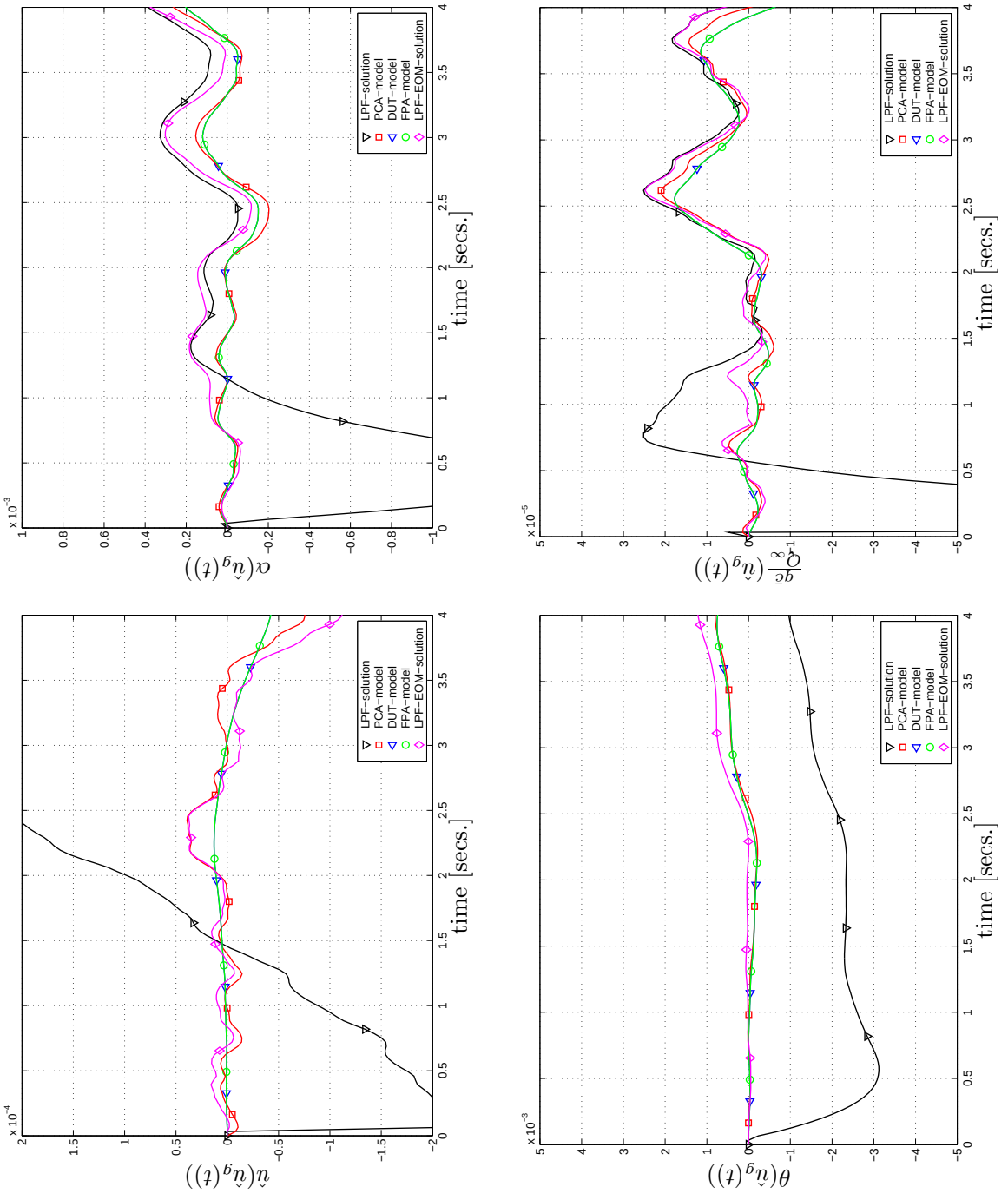


Figure 13.36: The LPF-, PCA-, DUT-, FPA- and LPF-EOM-model symmetrical aircraft motion responses $\hat{u}$, α, θ and $\frac{q\bar{c}}{Q_\infty}$ due to the symmetrical longitudinal gust-field u_g, for the gust scale length $L_g = 300$ [m].

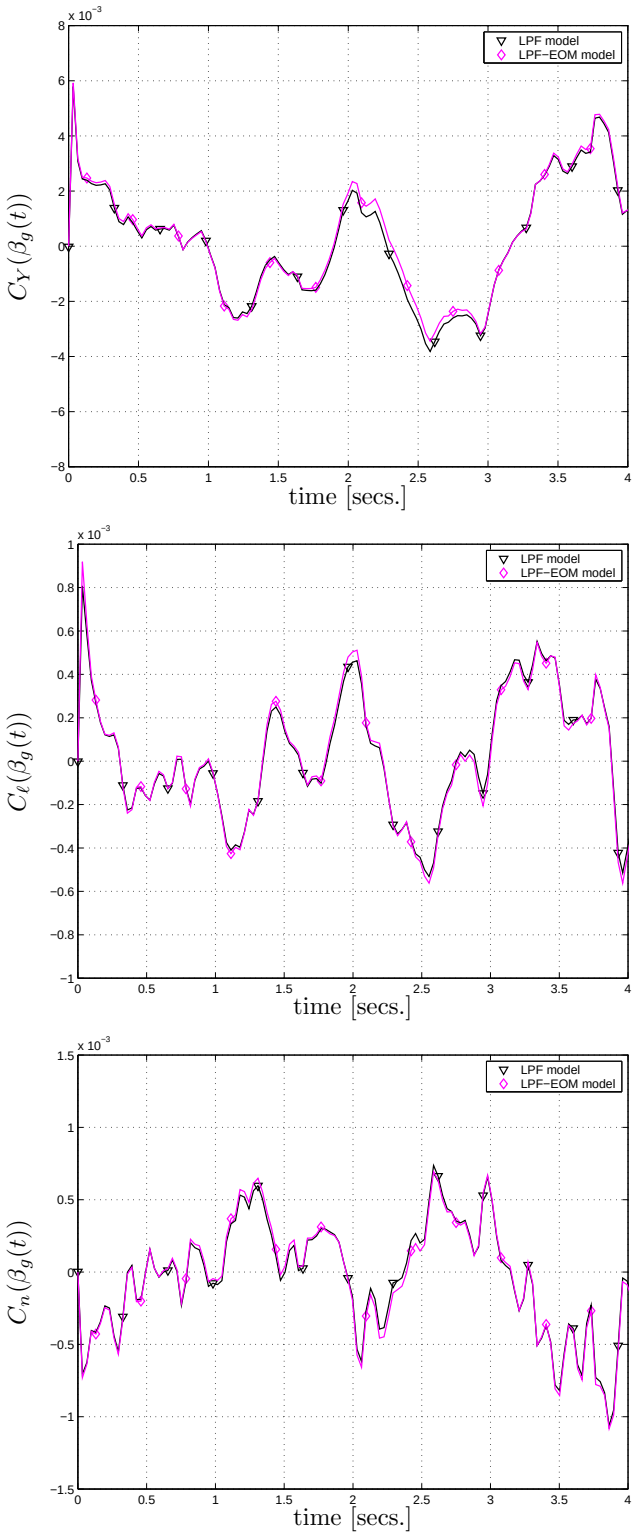


Figure 13.37: The time-domain aerodynamic coefficient responses C_Y, C_ℓ and C_n for the asymmetrical lateral gust field v_g given for the gust scale length $L_g = 300$ [m]. Results are given for both the LPF- and LPF-EOM-solution.

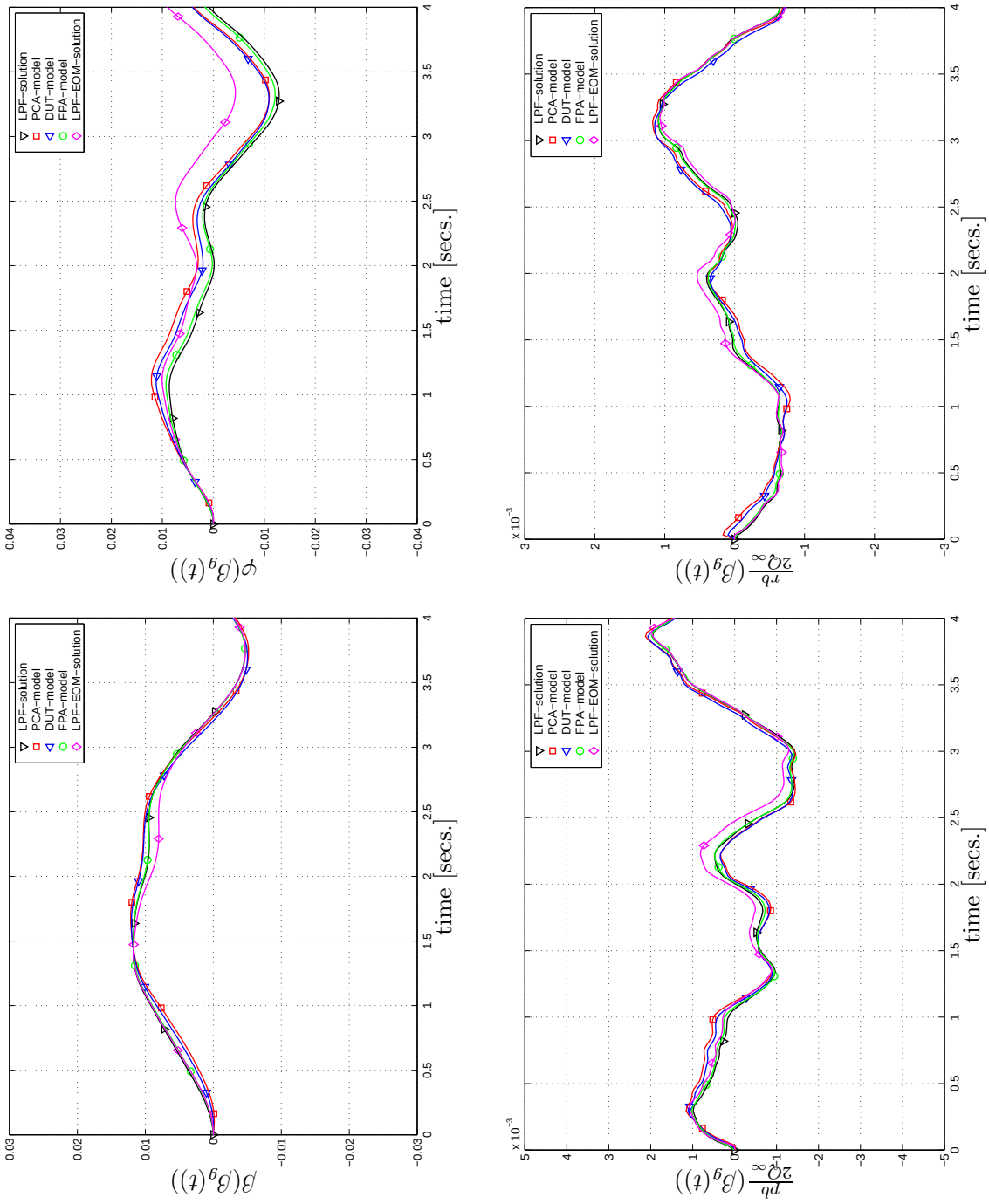


Figure 13.38: The LPF-, PCA-, DUT-, FPA- and LPF-EOM-model asymmetrical aircraft motion responses β, φ, $\frac{pb}{2Q_\infty}$ and $\frac{rb}{2Q_\infty}$ due to the asymmetrical lateral gust-field v_g, for the gust scale length $L_g = 300$ [m].

field u_g, as expected, the LPF-solution's transient response of the gust induced coefficients C_X and C_m result in aircraft motions dissimilar to the ones obtained for the LPF-EOM-model. Especially the non-dimensional speed perturbation ($\hat{u}$) - and the pitch-angle (θ) responses show less agreement with the LPF-EOM model responses. It should be noted, however, that the PCA-, DUT- and FPA-model responses show good correlation with the ones for the LPF-EOM-model, especially for the angle-of-attack - (α) and the pitch-angle (θ) responses.

Responses to anti-symmetrical longitudinal gust fields

In figure 13.41 the response of the aerodynamic coefficients C_Y, C_ℓ and C_n to the anti-symmetrical longitudinal gust field u_g is shown for both the LPF-solution and the LPF-EOM-model. Here, the model responses show excellent correlation, both in phase and magnitude, and it may be concluded that the parametric aerodynamic model, as given in equation (13.30), is extremely accurate.
Next, in figure 13.42 the aircraft motion responses to the anti-symmetrical longitudinal gust field u_g are shown. From the aerodynamic coefficient responses shown in figure 13.41, it is also here expected that the aircraft motion responses for both the LPF-solution and the LPF-EOM-model show good correlation. For all aircraft motion variables, the side-slip-angle (β), the roll-angle (φ), the non-dimensional roll-rate ($\frac{pb}{2Q_\infty}$) and the non-dimensional yaw-rate ($\frac{rb}{2Q_\infty}$) the results show good agreement. Here, it may also be concluded that the PCA-model accurately simulates the aircraft motion responses to anti-symmetrical longitudinal gust fields. The FPA/DUT-model responses show less agreement with the LPF-EOM-model responses, especially for the side-slip-angle - (β) and the non-dimensional yaw-rate ($\frac{rb}{2Q_\infty}$) responses.

Responses to anti-symmetrical vertical gust fields

In figure 13.43 the response of the aerodynamic coefficients C_Y, C_ℓ and C_n to the anti-symmetrical vertical gust field w_g is shown for both the LPF-solution and the LPF-EOM-model. For the rolling moment coefficient C_ℓ the model responses show excellent agreement, both in phase and magnitude. Both the aerodynamic force coefficient C_Y and the yawing moment coefficient C_n show excellent agreement in phase, however, they show less agreement in terms of magnitude. This difference in magnitude cannot be explained by contributions of the arising lateral gust velocity component (LPF-EOM-model) to the aerodynamic force and moment coefficients. Since the vertical gust field is anti-symmetrical, the, for example, arising lateral gust velocity component at the left wingtip cancels the one at the right wingtip. Therefor, it may be concluded that the parametric aerodynamic model, as given in equation (13.30), is less accurate for the aerodynamic coefficients C_Y and C_n. The inclusion of stability derivatives with respect to the time-derivative of the non-dimensional roll- and yaw-rate, that is for example $C_{Y_{\dot{p}}}$, $C_{Y_{\dot{r}}}$, etc., may result in a more accurate parametric aerodynamic model.
Next, in figure 13.44 the aircraft motion responses to the anti-symmetrical vertical gust field w_g are shown. From the aerodynamic coefficient responses shown in figure 13.43, it

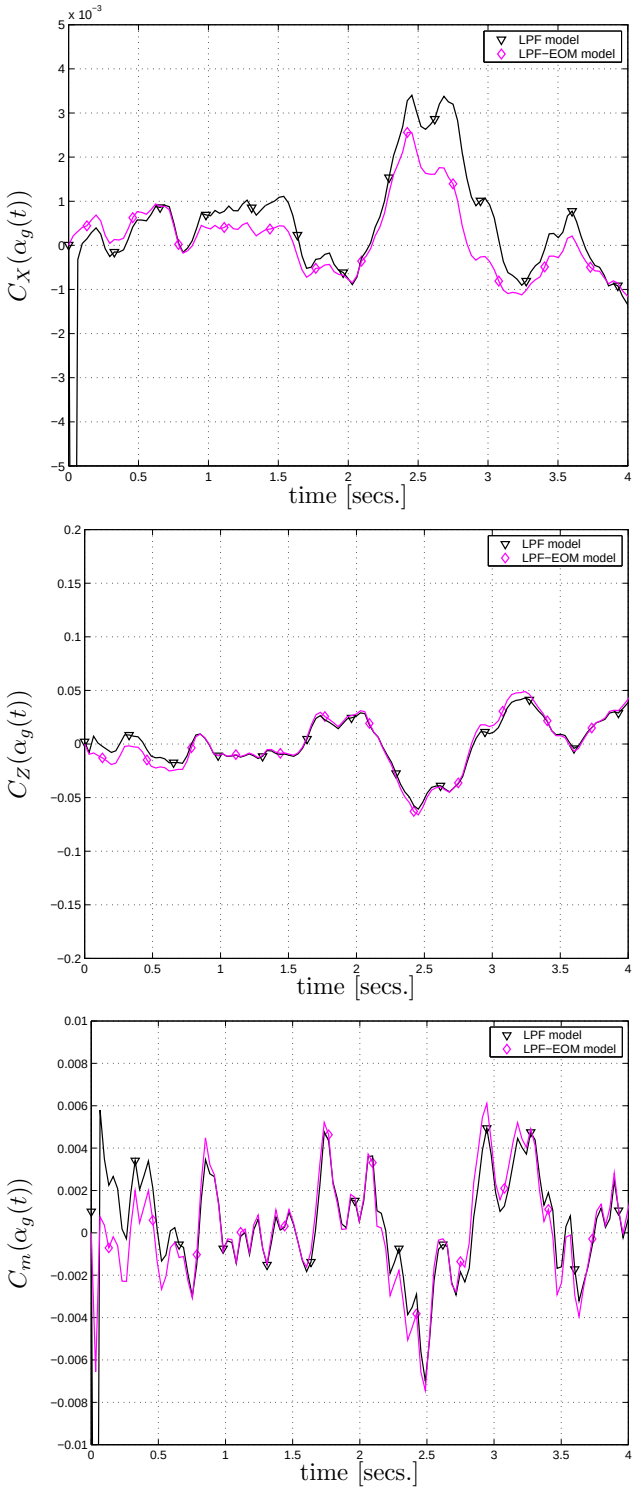


Figure 13.39: The time-domain aerodynamic coefficient responses C_X, C_Z and C_m for the symmetrical vertical gust field w_g given for the gust scale length $L_g = 300$ [m]. Results are given for both the LPF- and LPF-EOM-solution.

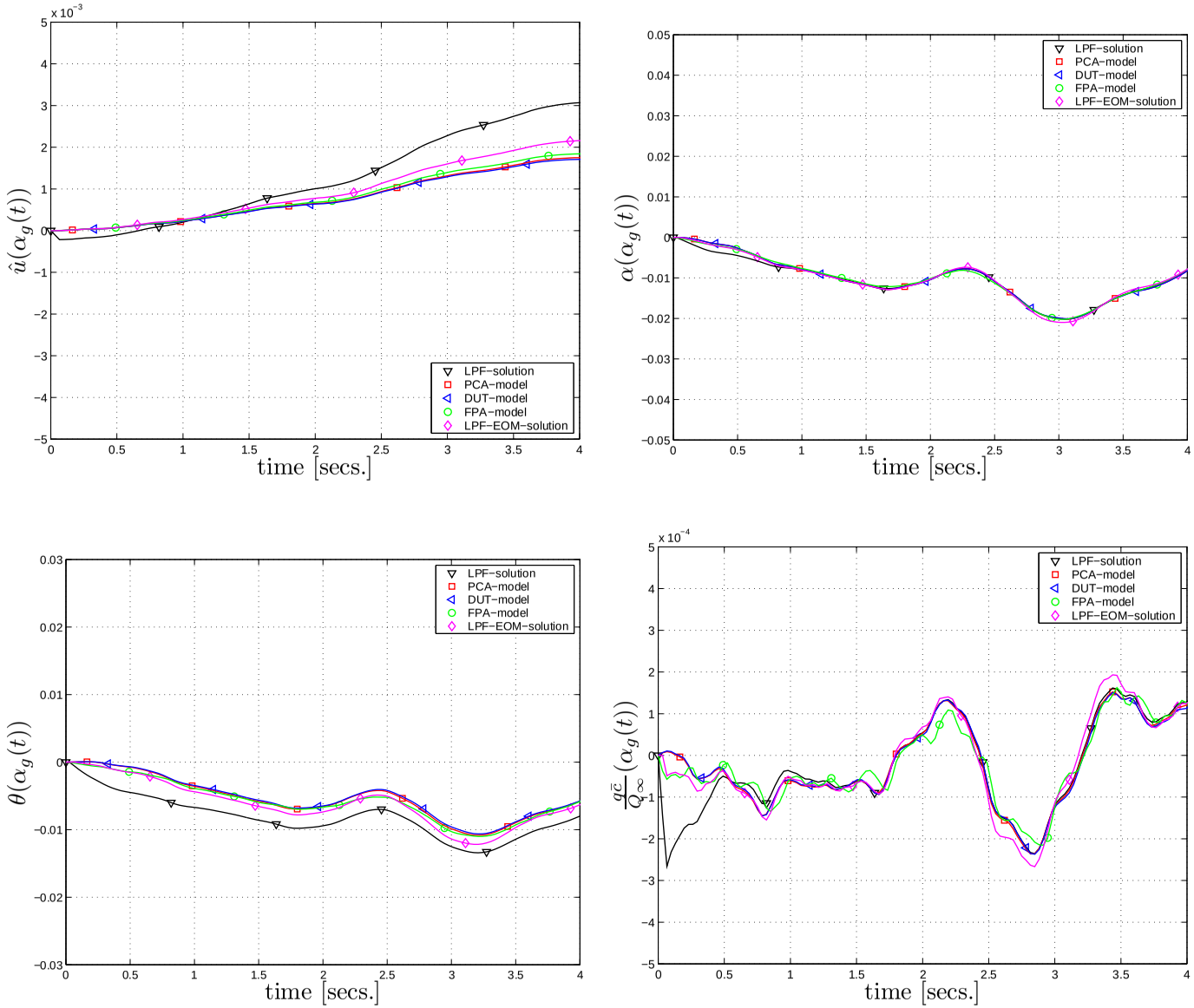


Figure 13.40: The LPF-, PCA-, DUT-, FPA- and LPF-EOM-model symmetrical aircraft motion responses $\hat{u}$, α, θ and $\frac{q\bar{c}}{Q_\infty}$ due to the symmetrical vertical gust-field w_g, for the gust scale length $L_g = 300$ [m].

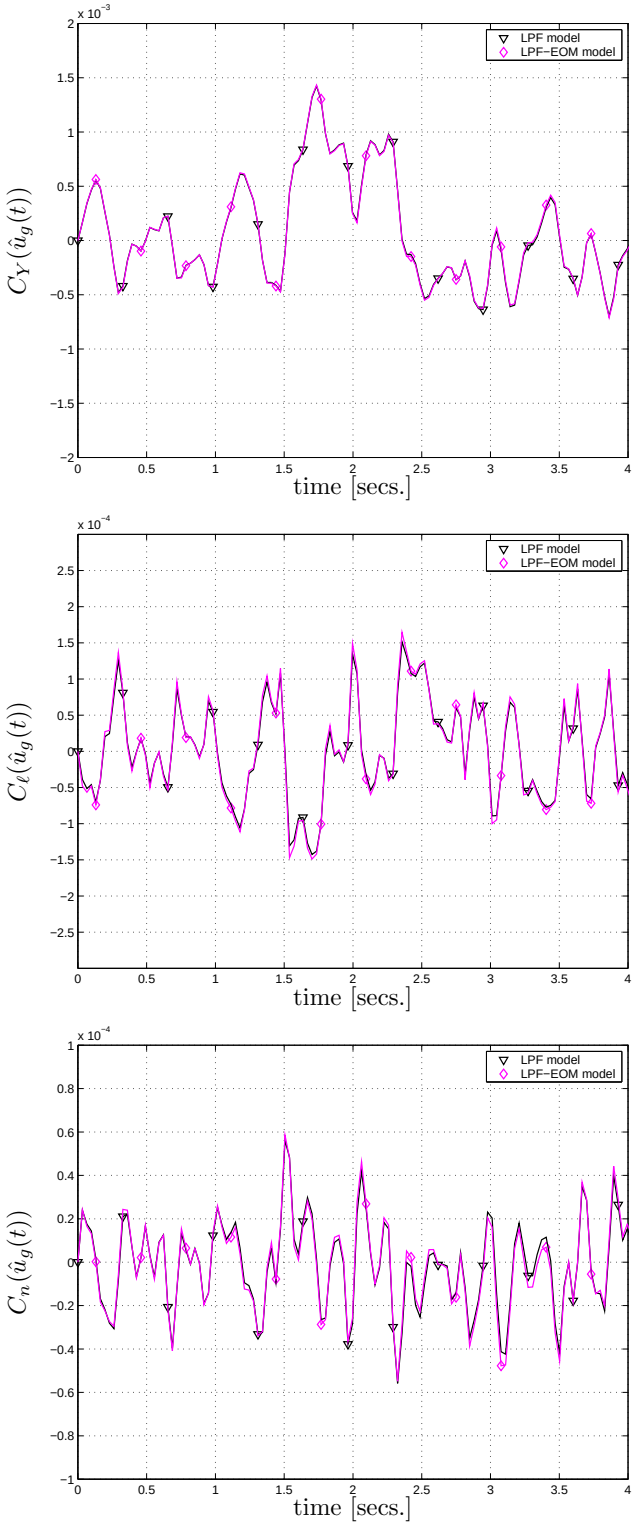


Figure 13.41: The time-domain aerodynamic coefficient responses C_Y, C_ℓ and C_n for the 2D anti-symmetrical longitudinal gust field u_g given for the gust scale length $L_g = 300$ [m]. Results are given for both the LPF- and LPF-EOM-solution.

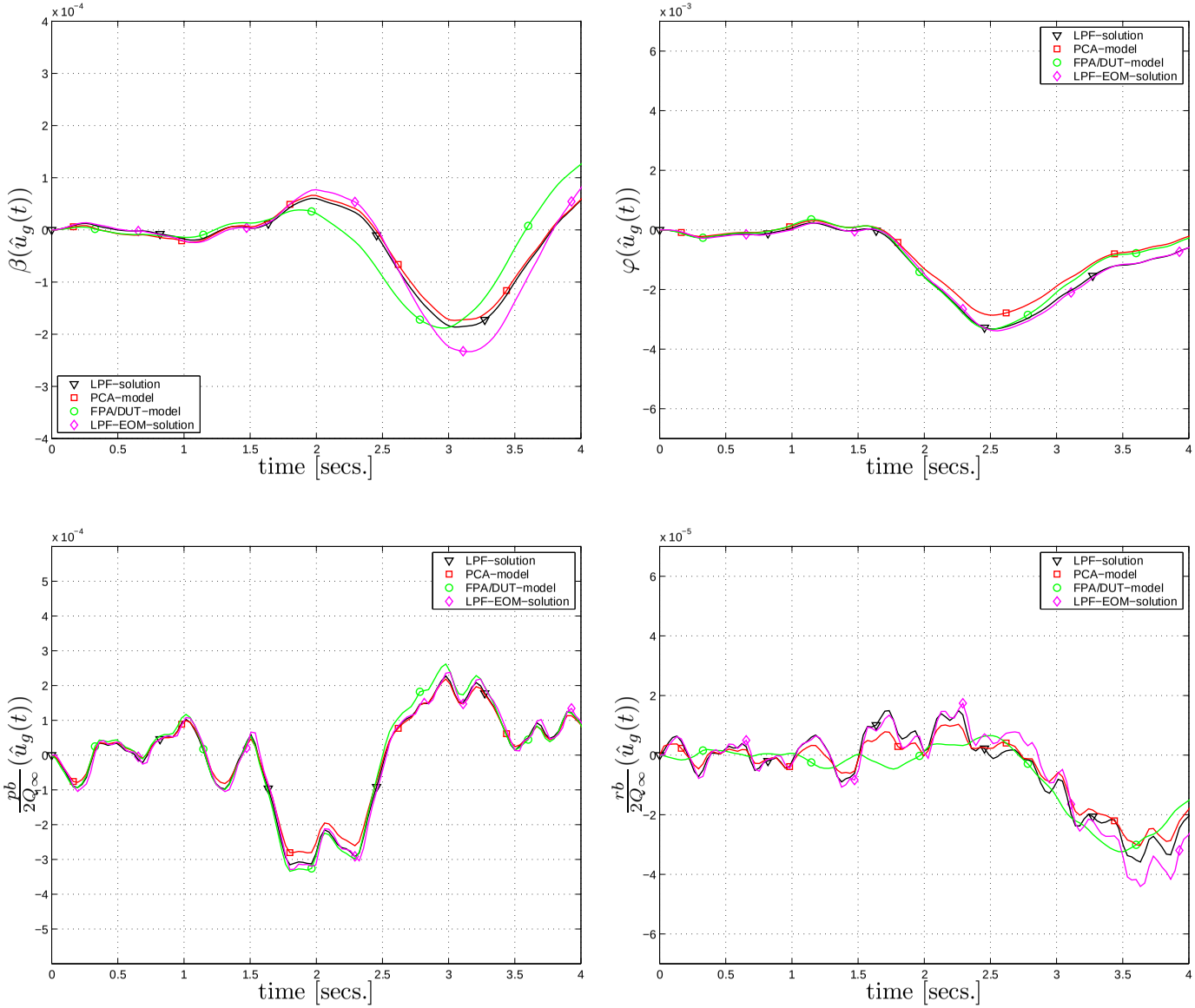


Figure 13.42: The LPF-, PCA-, DUT-, FPA- and LPF-EOM-model asymmetrical aircraft motion responses β, φ, $\frac{pb}{2Q_\infty}$ and $\frac{rb}{2Q_\infty}$ due to the 2D anti-symmetrical longitudinal gust-field u_g, for the gust scale length $L_g = 300$ [m].

is also here expected that the aircraft motion responses for both the LPF-solution and the LPF-EOM-model show good correlation in phase. For all aircraft motion variables, the side-slip-angle (β), the roll-angle (φ), the non-dimensional roll-rate ($\frac{pb}{2Q_\infty}$) and the non-dimensional yaw-rate ($\frac{rb}{2Q_\infty}$) the results show good agreement in phase indeed. As expected, the roll-rate responses ($\frac{pb}{2Q_\infty}$) show excellent agreement. Here, it may also be concluded that the PCA-model accurately simulates the aircraft motion responses to anti-symmetrical vertical gust fields. The FPA/DUT-model responses show less agreement with the LPF-EOM-model responses, especially for the side-slip-angle - (β) and the non-dimensional yaw-rate ($\frac{rb}{2Q_\infty}$) responses.

13.6 Conclusions

From the results presented in this chapter, it is shown that the here introduced PCA-model is the most accurate for all considered gust fields; compared to the LPF-(EOM)-solution, the new parametric model shows more accuracy over the other models (the DUT- and the FPA-model), especially for aircraft responses to anti-symmetrical gust fields. Furthermore, it showes more accuracy for symmetrical longitudinal gust fields as well.
Also, it may be concluded that the parametric aerodynamic models given in equations (13.29) and (13.30) are adequate. However, they may be enhanced by adding the stability derivative $C_{X_{\dot{\alpha}}}$, and stability derivatives with respect to both $\frac{\dot{p}b^2}{2Q_\infty^2}$ and $\frac{\dot{r}b^2}{2Q_\infty^2}$.
Although the introduced PCA-model produces the most accurate results, it requires considerably more effort to compute the steady and unsteady gust derivatives (as compared to the DUT- and the FPA-model). However, once the PCA-model gust derivatives have been obtained, they are easy to implement into the equations of motion as these are not fundamentally different for all aircraft models considered here.

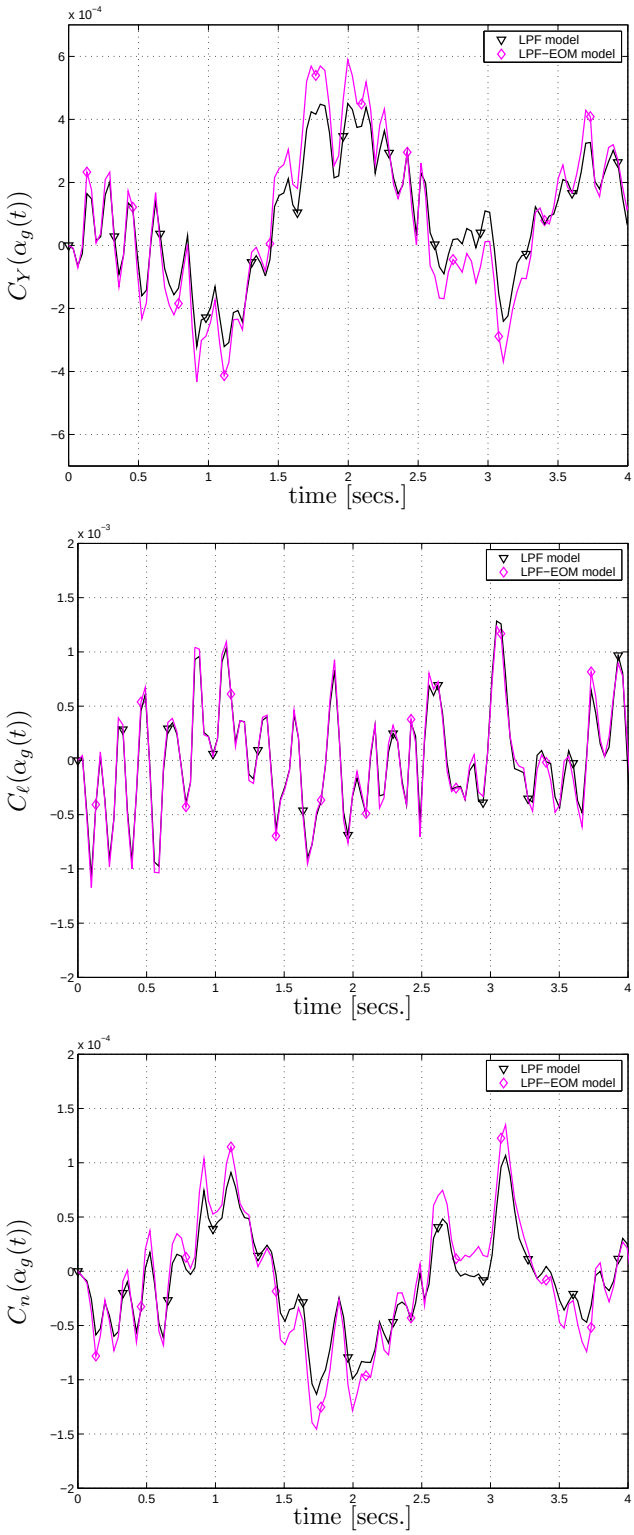


Figure 13.43: The time-domain aerodynamic coefficient responses C_Y, C_ℓ and C_n for the 2D anti-symmetrical vertical gust field w_g given for the gust scale length $L_g = 300$ [m]. Results are given for both the LPF- and LPF-EOM-solution.

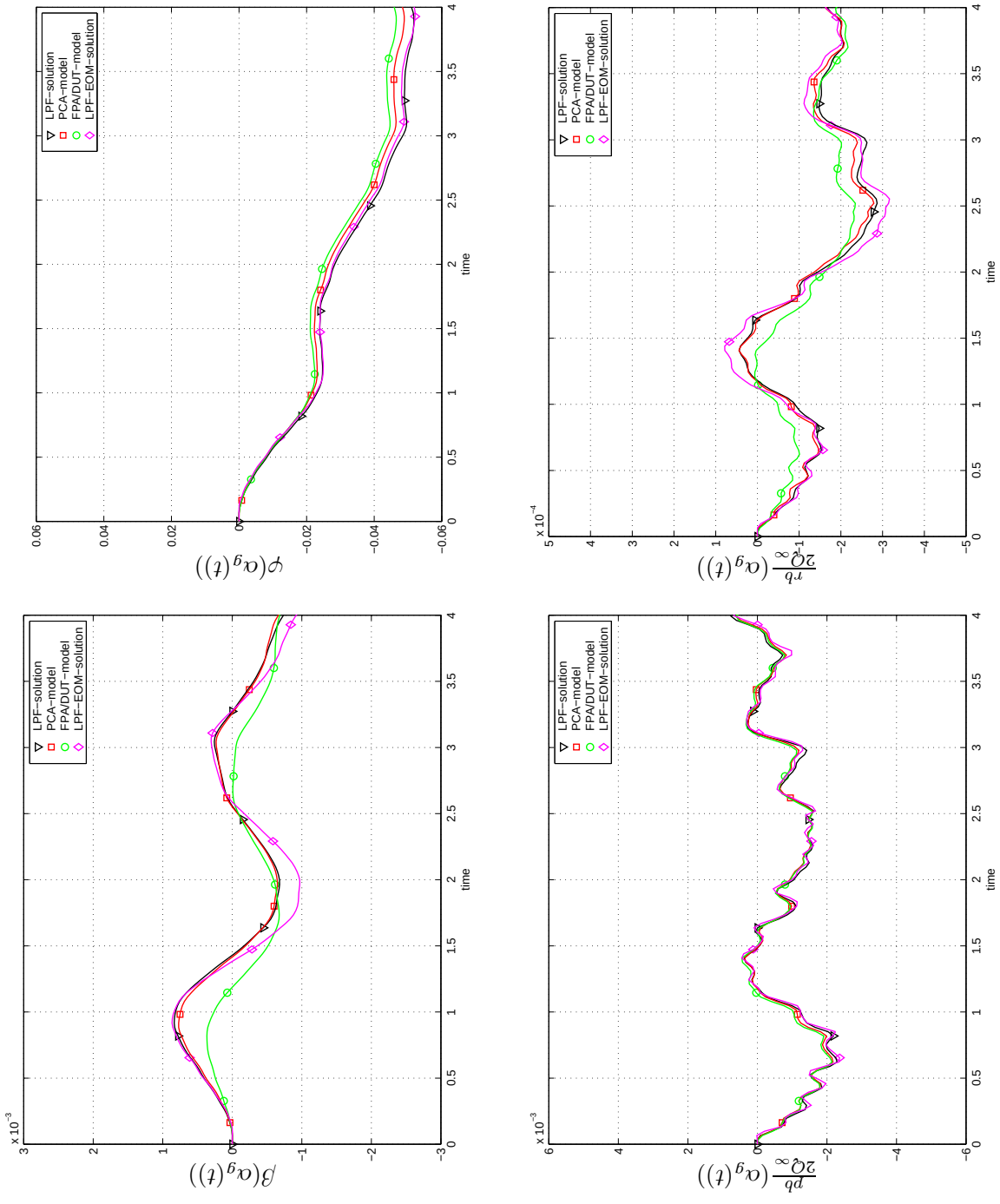


Figure 13.44: The LPF-, PCA-, DUT-, FPA- and LPF-EOM-model asymmetrical aircraft motion responses β, φ, $\frac{pb}{2Q_\infty}$ and $\frac{rb}{2Q_\infty}$ due to the 2D anti-symmetrical vertical gust-field w_g, for the gust scale length $L_g = 300$ [m].

1D symmetrical gust input $\hat{u}_g$			
	PCA-model	**DUT-model**	**FPA-model**
$\sigma^2_{\hat{u}_g}$	6.3192e-005	6.3192e-005	6.3215e-005
$\sigma^2_{\hat{u}}$	2.7181e-003	2.6968e-003	2.6968e-003
σ^2_{α}	6.6179e-008	5.8893e-008	5.8897e-008
σ^2_{θ}	5.9054e-003	5.8594e-003	5.8594e-003
$\sigma^2_{\frac{q\bar{c}}{Q_\infty}}$	2.1409e-008	2.1223e-008	2.1223e-008
1D symmetrical gust input α_g			
	PCA-model	**DUT-model**	**FPA-model**
$\sigma^2_{\alpha_g}$	6.2977e-005	6.2977e-005	6.1417e-005
$\sigma^2_{\hat{u}}$	2.2078e-004	2.1073e-004	2.2237e-004
σ^2_{α}	5.9303e-005	5.9157e-005	5.8040e-005
σ^2_{θ}	4.9864e-004	4.7602e-004	5.0083e-004
$\sigma^2_{\frac{q\bar{c}}{Q_\infty}}$	1.0646e-008	1.0389e-008	9.4762e-009

Table 13.3: The PCA-, DUT- and FPA-model calculated symmetrical gust input variances $\sigma^2_{\hat{u}_g}$ and $\sigma^2_{\alpha_g}$ and the calculated symmetrical aircraft motion variables' variances $\sigma^2_{\hat{u}}$, σ^2_{α}, σ^2_{θ} and $\sigma^2_{\frac{q\bar{c}}{Q_\infty}}$, for the gust scale length parameter $L_g = 300$ [m].

2D anti-symmetrical gust input $\hat{u}_g$			
	PCA-model	**DUT-model**	**FPA-model**
$\sigma^2_{\hat{u}_g}$, $\sigma^2_{\frac{r_{1_g}b}{2Q_\infty}}$	2.6748e-006	2.7323e-006	2.6748e-006
σ^2_β	1.5323e-008	2.1948e-008	2.1319e-008
σ^2_φ	1.2354e-004	1.6981e-004	1.6536e-004
$\sigma^2_{\frac{pb}{2Q_\infty}}$	1.5039e-008	2.1633e-008	2.0577e-008
$\sigma^2_{\frac{rb}{2Q_\infty}}$	2.9408e-009	4.0689e-009	3.9613e-009
1D asymmetrical gust input β_g			
	PCA-model	**DUT-model**	**FPA-model**
$\sigma^2_{\beta_g}$	6.2977e-005	6.2977e-005	6.3012e-005
σ^2_β	1.0530e-004	1.0391e-004	1.0437e-004
σ^2_φ	1.1955e-004	1.1063e-004	1.1797e-004
$\sigma^2_{\frac{pb}{2Q_\infty}}$	2.0894e-006	1.9787e-006	2.0390e-006
$\sigma^2_{\frac{rb}{2Q_\infty}}$	8.9401e-007	8.6999e-007	8.7611e-007
2D anti-symmetrical gust input α_g			
	PCA-model	**DUT-model**	**FPA-model**
$\sigma^2_{\alpha_g}$, $\sigma^2_{\frac{p_g b}{2Q_\infty}}$	2.5875e-006	2.6346e-006	2.5875e-006
σ^2_β	1.2599e-006	1.0191e-006	9.9345e-007
σ^2_φ	1.0601e-002	9.9418e-003	9.6863e-003
$\sigma^2_{\frac{pb}{2Q_\infty}}$	1.3261e-006	1.3295e-006	1.2719e-006
$\sigma^2_{\frac{rb}{2Q_\infty}}$	2.5303e-007	2.3501e-007	2.2893e-007

Table 13.4: The PCA-, DUT- and FPA-model calculated anti- and asymmetrical gust input variances $\sigma^2_{\hat{u}_g}$ or $\sigma^2_{\frac{r_{1_g}b}{2Q_\infty}}$, $\sigma^2_{\beta_g}$, and $\sigma^2_{\alpha_g}$ or $\sigma^2_{\frac{p_g b}{2Q_\infty}}$, given along with the calculated asymmetrical aircraft motion variables' variances σ^2_β, σ^2_φ, $\sigma^2_{\frac{pb}{2Q_\infty}}$ and $\sigma^2_{\frac{rb}{2Q_\infty}}$ to the 2D anti-symmetrical gust input $\hat{u}_g$, the 1D asymmetrical gust input β_g and the 2D anti-symmetrical gust input α_g, for the gust scale length parameter $L_g = 300$ [m].

Part VI

Conclusions and Recommendations

Chapter 14

Conclusions and recommendations

14.1 Introduction

The response of aircraft to atmospheric turbulence plays an important role in aircraft design (load calculations), Flight Control System design and flight simulation (Handling Qualities research and pilot training). To simulate these aircraft responses, an accurate mathematical aircraft model is required.

Since it remains extremely difficult to obtain (experimental) data of aircraft responses to atmospheric turbulence, while also considering that this input to the aircraft is almost unknown, the validation of mathematical aircraft models is arduous. Therefore, in this thesis a virtual flighttest facility was developed to simulate the aircraft responses to known stochastic two-dimensional (2D) gust fields. Results of these virtual flighttests, i.e. the LPF-solution for recti-linear flightpaths and the LPF-EOM-solution for stochastic flightpaths, were compared to those obtained for the parametric models discussed in this thesis. For this verification, the LPF-EOM-model results were considered to be the benchmark. That is they resemble reality the closest.
For the two classical parametric aircraft models discussed in this thesis, i.e. the Delft University of Technology (DUT) - and the Four Point Aircraft (FPA) model, their aircraft responses correlated with the ones obtained for the LPF- and LPF-EOM-solutions. However, the classical models showed substantial deficiencies when the aircraft responses to anti-symmetrical gust fields were considered. The novel Parametric Computational Aerodynamics (PCA) model introduced in this thesis, however, produced more accurate results to these gust fields.

In section 14.2 the conclusions of this thesis are summarized, with reference to the chapters. See figure 1.1 for a thesis overview. Next, in section 14.3, recommendations for future research are given.

14.2 Conclusions

- From the results presented in this thesis (which are summarized in chapter 13), it is concluded that the introduced PCA-model is the most accurate for all considered gust fields. Compared to the LPF-EOM-solution, for both the aerodynamic - and aircraft motion responses to two-dimensional (2D) gust fields, this new parametric aircraft model showed higher accuracy over the other parametric models (that is the classical DUT- and FPA-model). Furthermore, in its aerodynamic response, the new model showed more accuracy for one-dimensional (1D) longitudinal gust fields.

- The unsteady Linearized Potential Flow (LPF) method (or unsteady panel-method) used in chapter 4, reproduced the classical analytical solutions obtained by Horlock, Sears and Theodorsen. These functions describe the 2D aerofoil frequency-domain dynamics of the aerodynamic lift due to harmonically varying longitudinal gusts, vertical gusts and heaving motions, respectively. Furthermore, the method reproduced the time-domain Jones solution for an aerofoil's step-wise change in angle-of-attack.

- Horlock's function can be used to account for the dynamics of an aerofoil's lift due to longitudinal gusts. This function only holds for aerofoils with the origin located at the semi-chord point of it. If the origin is chosen to differ from the semi-chord point, Horlock's function should be multiplied by $e^{jk\frac{2x_0}{c}}$, resulting in the Modified Horlock function $T_{mod}(k) = T(k)\, e^{jk\frac{2x_0}{c}}$, with x_0 the origin's location positive downstream. For the origin located at the aerofoil leading-edge, x_0 becomes $x_0 = -\frac{\bar{c}}{2}$ and the Modified Horlock function is written as $T_{mod}(k) = T(k)\, e^{-jk}$. See also chapter 4.

- For complete aircraft configurations, the (un)steady LPF method described in chapters 3 and 4 required a considerable wake modeling effort.

- The steady stability derivatives C_{Z_α}, C_{m_α} and C_{m_q} obtained from LPF simulations showed excellent agreement with those obtained from flighttest data analysis. See chapter 6.

- The in chapter 8 and appendix E introduced procedure for the fitting of the 2D aerodynamic frequency-response data $\frac{C_Y}{\hat{u}_g}(k,\Omega_y)$, $\frac{C_\ell}{\hat{u}_g}(k,\Omega_y)$, $\frac{C_n}{\hat{u}_g}(k,\Omega_y)$, $\frac{C_Y}{\alpha_g}(k,\Omega_y)$, $\frac{C_\ell}{\alpha_g}(k,\Omega_y)$ and $\frac{C_n}{\alpha_g}(k,\Omega_y)$ produced excellent results. For both more dense circular - and spatial frequency arrays, the obtained function fit parameters resulted in accurate representations of the frequency-response data.

- For 1D vertical gusts $\alpha_g = \frac{w_g}{Q_\infty}$ care should be taken when using the DUT-model definition of the constant symmetrical unsteady gust derivatives, see reference [30]. Usually these derivatives are given in terms of stability derivatives, that is $C_{Z_{\dot{\alpha}_g}} = C_{Z_{\dot{\alpha}}} - C_{Z_q}$ and $C_{m_{\dot{\alpha}_g}} = C_{m_{\dot{\alpha}}} - C_{m_q}$. For wing-stabilizer configurations, the definition of these gust derivatives is correct. However, for complete aircraft configurations (that is including the fuselage, nacelles, pylons, et cetera), this definition of the unsteady gust derivatives does not hold. See also chapter 11.

- Similarly, for the 1D lateral gust $\beta_g = \frac{v_g}{Q_\infty}$ care should be taken when using the DUT-model definition of the constant asymmetrical unsteady gust derivatives, see reference [30]. These unsteady derivatives are usually given in terms of stability derivatives as well, that is $C_{Y_{\dot{\beta}_g}} = C_{Y_{\dot{\beta}}} + \frac{1}{2}C_{Y_r}$, $C_{\ell_{\dot{\beta}_g}} = C_{\ell_{\dot{\beta}}} + \frac{1}{2}C_{\ell_r}$ and $C_{n_{\dot{\beta}_g}} = C_{n_{\dot{\beta}}} + \frac{1}{2}C_{n_r}$. For wing-fuselage-fin configurations the definition of these gust derivatives is correct, however, for complete aircraft configurations (that is including the nacelles, pylons, et cetera) this definition of the unsteady gust derivatives does not hold. See also chapter 11.

- For the PCA-model, the constant unsteady gust derivatives with respect to both 1D and 2D gusts, i.e. $\hat{u}_g = \frac{u_g}{Q_\infty}$, $\beta_g = \frac{v_g}{Q_\infty}$ and $\alpha_g = \frac{w_g}{Q_\infty}$, were obtained using resonance peaks in the output Power Spectral Density (PSD) functions of aircraft motion variables. A consequence of this identification method is that these unsteady derivatives now become a function of the gust scale length L_g and the aircraft mass properties. This pitfall of the PCA-model identification method can be overcome by the use of aerodynamic frequency-response functions which are independent of the atmospheric turbulence scale length L_g and the aircraft mass properties. See also chapter 10.

- The aerodynamic frequency-response data for aircraft motions and 1D gust inputs can be accurately represented by the function approximation $H(k) = A_0 + A_1(jk) + A_2(jk)^2 + \sum_{i=1}^{i=N} B_i \frac{jk}{jk+\beta_i}$, with $H(k)$ the aerodynamic frequency-response function, A_0, A_1, A_2 the aerodynamic stiffness, damping and inertia parameters, respectively, k the reduced frequency, $j = \sqrt{-1}$, B_i the gains of the lag-terms, β_i the poles of the lag-terms and N the number of lag-terms. For PCA-model identification purposes it is recommended to use this function for the estimation of the constant unsteady stability- and gust derivatives. See also chapter 7.

- The use of the function $h(\Omega_y \frac{b}{2})$ according to equation (11.47) for the determination of the Effective 1D input PSD-functions $I_{\hat{u}_g\hat{u}_g}(\omega, B)$ and $I_{\alpha_g\alpha_g}(\omega, B)$, see equations (11.73) and (11.74), respectively, produced excellent agreement with the FPA-model input PSD-functions $S_{\frac{r_{1_g}b}{2Q_\infty}\frac{r_{1_g}b}{2Q_\infty}}(\omega)$ and $S_{\frac{p_g b}{2Q_\infty}\frac{p_g b}{2Q_\infty}}(\omega)$ (see equation (12.8)). See also chapter 13.

- Contrary to the recommendation given in references [35, 30], the unsteady derivatives with respect to the longitudinal gust u_g, i.e. $C_{X_{\dot{u}_g}}$, $C_{Z_{\dot{u}_g}}$ and $C_{m_{\dot{u}_g}}$, should always be used in the equations of motion. Omitting these gust derivatives will lead to an underestimation of the symmetrical aerodynamic force and moment. See also chapter 13.

- Although the PCA-model produced more accurate results, the calculation of its gust derivatives required considerably more effort as compared to the calculation of them for the DUT- and FPA-model. However, once the PCA-model gust derivatives had been obtained, they were easy to implement into the equations of motion (since for all models these equations are not fundamentally different). See also chapter 13.

14.3 Recommendations for future research

- It is recommended to extend the used atmospheric turbulence model to three-dimensional (3D) correlated atmospheric turbulence (including Ω_z). For large aircraft including a T-tail this may be of importance since the correlation between, for example, the vertical gust velocity component at the wing's aerodynamic center with it at the position of the horizontal tailplane's aerodynamic center becomes less. Therefore, the application of solely time-delays (as were used in the derivation of the DUT-model unsteady gust derivatives) may not be applicable at all, and, as a consequence, the definition of this model's derivatives cannot be used. Using CFD or Computational Aerodynamics methods, and the introduced model-identification procedure (the PCA-model), all frequency-dependent gust derivatives can be determined. However, they will now become a function of the spatial-frequency Ω_z as well.

- The aircraft configuration used in this thesis is not representative for larger series of civil aircraft. Therefore, it is recommended to perform a similar study for aircraft with wing-mounted engines (such as the Airbus A3**- and the Boeing B7*7-series).

- In this thesis the engines of the example aircraft were modeled as ring-wings and the effect of jets was not modeled. It is recommended to investigate the effect of jet-plumes on the aerodynamic response of aircraft subjected to atmospheric turbulence. Especially for the example aircraft considered in this thesis, the effect of jets may result in a straightening of the airflow at the horizontal tailplane position resulting in a reduced dependency of the downwash with respect to angle-of-attack perturbations. Thus, for high engine throttle settings, the stabilizing effect of the horizontal tailplane may be reduced despite of the increased dynamic pressure (that is an increase of Q_{∞_h}).

- Since for higher Mach-numbers aerodynamic lags will increase, it is recommended to extend the LPF method for compressible flow. For the transonic speed range it is recommended to use Full Potential, Euler or Navier-Stokes methods.

- In this thesis the atmospheric turbulence fields were assumed to be frozen. It is suggested that for large aircraft non-stationary atmospheric turbulence is used. The motivation is twofold. First, because of the size of the aircraft, the gust velocity components reaching the horizontal or vertical tailplane may be quite different than the ones that reached the main wing some time earlier. Second, an increase in aircraft size usually leads to an increased wing size as well, which, in its turn, may result in smoothed gust velocity components reaching the tailplanes.

- It is recommended to extend the PCA-model for elastic aircraft. Since it has been shown that for large circular frequencies both the frequency-dependent steady - and unsteady gust derivatives become increasingly dependent of it, the additional structural modes could interact with the (rigid) aircraft motions resulting in shifted

resonance frequencies. Furthermore, it has been shown that for large circular frequencies the energy content of the gust induced aerodynamic forces and moments (see figures 13.20 through 13.24) is higher than it is for the DUT- and FPA-model. Therefore, the extended PCA-model will show increased elastic mode responses as compared to those obtained for the (extended) DUT- and FPA-models.

- The major drawback of the introduced PCA-model is that the gust derivatives have become dependent of the gust scale length L_g and the aircraft mass properties. This dependency may be overcome by the use of aerodynamic transfer functions. To implement these functions, they should be transformed to state-space realizations first, and then be added to the equations of motion. Also, it is then recommended to fit the aerodynamic frequency-response data by the function $H(k) = A_0 + \sum_{i=1}^{i=N} B_i \frac{jk}{jk+\beta_i}$ (thus eliminating the aerodynamic damping and mass terms).

- In order to decrease CPU-time, the (exploration phase) panel-method codes should be translated in a faster programming language.

- A code, similar to the one used for the LPF-EOM-model, should be developed for a real-time flight simulation application. The parametric mathematical aircraft model could then be replaced by a Computational Aerodynamics module.

- It is recommended to collect experimental data to validate the simulation models presented in this thesis.

Appendix A

Abbreviations and symbols

Abbreviations

1D	One-dimensional
2D	Two-dimensional
3D	Three-dimensional
CA	Computational Aerodynamics
CAD	Computer Aided Design
CAT	Clear Air Turbulence
CFD	Computational Fluid Dynamics
c.o.g.	center of gravity
DATCOM	DATa COMpendium
D(N)BC	Dirichlet (Neumann) Boundary Condition
DUT	Delft University of Technology
EOM	Equations of Motion
FCS	Flight Control System
FPA	Four Point Aircraft
FRF	Frequency-Response Function
LCO	Limit Cycle Oscillation
LPF(-EOM)	Linearized Potential Flow (coupled with the Equations Of Motion)
LTI	Linear Time Invariant
mac	mean aerodynamic chord
N.A.	Not Available, Not Applicable
NASA	National Aeronautics and Space Administration
NASTRAN	NAsa STRuctural ANalysis
NLR	Nationaal Lucht- en Ruimtevaartlaboratorium (National Aerospace Laboratory, The Netherlands)
PCA	Parametric Computational Aerodynamics
PSD	Power Spectral Density
UAV	Uninhabited Aerial Vehicle

Symbols

a	speed of sound
$a.c.$	aerodynamic center
A	$= \frac{b^2}{S}$ wing aspect ratio
b	wing span
$\underline{B}$	moment of momentum, angular momentum
C_p	pressure coefficient $\frac{\Delta p}{\frac{1}{2}\rho Q_\infty^2}$
c	local wing chord
$\bar{c}$	mean aerodynamic chord
C_D	$= \frac{D}{\frac{1}{2}\rho Q_\infty^2 S}$ 3D drag-coefficient
c_d	$= \frac{d}{\frac{1}{2}\rho Q_\infty^2 c}$ 2D drag-coefficient
$c.g.$	center of gravity
c_ℓ	$= \frac{\ell}{\frac{1}{2}\rho Q_\infty^2 \bar{c}}$, sectional 2D lift-coefficient
C_ℓ	$= \frac{L}{\frac{1}{2}\rho Q_\infty^2 Sb}$, rolling moment coefficient
C_L	$= \frac{L}{\frac{1}{2}\rho Q_\infty^2 S}$, lift-coefficient
C_l	$= \frac{L}{\frac{1}{2}\rho Q_\infty^2 \bar{c}}$, 2D lift-coefficient
c_{ℓ_α}	$= \frac{dc_\ell}{d\alpha}$ 2D lift-coefficient slope
C_{L_α}	$= \frac{dC_L}{d\alpha}$ 3D lift-coefficient slope
C_{ℓ_p}	$= \frac{\partial C_\ell}{\partial \frac{pb}{2Q_\infty}}$
C_{ℓ_r}	$= \frac{\partial C_\ell}{\partial \frac{rb}{2Q_\infty}}$
C_{ℓ_β}	$= \frac{\partial C_\ell}{\partial \beta}$
c_m	$= \frac{m}{\frac{1}{2}\rho Q_\infty^2 c^2}$, 2D moment-coefficient
C_m	$= \frac{M}{\frac{1}{2}\rho Q_\infty^2 S\bar{c}}$, 3D moment-coefficient
$c_{m_{a.c.}}$	moment-coefficient about the aerodynamic center, 2D flow
$C_{m_{a.c.}}$	moment-coefficient about the aerodynamic center, 3D flow
C_{m_f}	contribution of the fuselage to C_m
C_{m_h}	contribution of the horizontal tailplane to C_m
$C_{m_{nac}}$	contribution of the nacelles to C_m
C_{m_p}	contribution of the pylons to C_m
C_{m_q}	$= \frac{\partial C_m}{\partial \frac{q\bar{c}}{Q_\infty}}$
C_{m_u}	$= \frac{1}{\frac{1}{2}\rho Q_\infty S\bar{c}} \frac{\partial M}{\partial u}$
C_{m_v}	contribution of the vertical tail to C_m
C_{m_w}	contribution of the wing to C_m
C_{m_0}	C_m in steady flight
C_{m_α}	$= \frac{\partial C_m}{\partial \alpha}$
$C_{m_{\dot{\alpha}}}$	$= \frac{\partial C_m}{\partial \frac{\dot{\alpha}\bar{c}}{Q_\infty}}$
c_n	$= \frac{n}{\frac{1}{2}\rho Q_\infty^2 c}$

C_n $= \frac{N}{\frac{1}{2}\rho Q_\infty^2 Sb}$, yawing moment coefficient

C_{n_p} $= \frac{\partial C_n}{\partial \frac{pb}{2Q_\infty}}$

C_{n_r} $= \frac{\partial C_n}{\partial \frac{rb}{2Q_\infty}}$

C_{n_β} $= \frac{\partial C_n}{\partial \beta}$

C_X $= \frac{X}{\frac{1}{2}\rho Q_\infty^2 S}$

C_{X_q} $= \frac{\partial C_X}{\partial \frac{q\bar{c}}{Q_\infty}}$

C_{X_u} $= \frac{1}{\frac{1}{2}\rho Q_\infty S}\frac{\partial X}{\partial u}$

C_{X_0} C_X in steady flight

C_{X_α} $= \frac{\partial C_X}{\partial \alpha}$

C_{Y_0} C_Y in steady flight

C_Y $= \frac{Y}{\frac{1}{2}\rho Q_\infty^2 S}$

C_{Y_p} $= \frac{\partial C_Y}{\partial \frac{pb}{2Q_\infty}}$

C_{Y_r} $= \frac{\partial C_Y}{\partial \frac{rb}{2Q_\infty}}$

C_{Y_β} $= \frac{\partial C_Y}{\partial \beta}$

C_Z $= \frac{Z}{\frac{1}{2}\rho Q_\infty^2 S}$

C_{Z_q} $= \frac{\partial C_Z}{\partial \frac{q\bar{c}}{Q_\infty}}$

C_{Z_u} $= \frac{1}{\frac{1}{2}\rho Q_\infty S}\frac{\partial Z}{\partial u}$

C_{Z_0} C_Z in steady flight

C_{Z_α} $= \frac{\partial C_Z}{\partial \alpha}$

$C_{Z_{\dot{\alpha}}}$ $= \frac{\partial C_Z}{\partial \frac{\dot{\alpha}\bar{c}}{Q_\infty}}$

d $= c_d\ \frac{1}{2}\rho Q_\infty^2 \bar{c}$ drag 2D flow

D $= C_D\ \frac{1}{2}\rho Q_\infty^2 S$ drag 3D flow

D_b $= \frac{d}{ds_b} = \frac{b}{Q_\infty}\frac{d}{dt}$

D_c $= \frac{d}{ds_c} = \frac{\bar{c}}{Q_\infty}\frac{d}{dt}$

g Earth gravitational acceleration

h altitude

$\underline{i}$ unit vector along the X-axis

$i_{h,p}$ angle of incidence of the horizontal tail or engine(s)

I_x $= \int \left(y^2 + z^2\right) dm$

I_{xy} $= \int xy\ dm$

I_{xz} $= \int xz\ dm$

I_y $= \int \left(x^2 + z^2\right) dm$

I_z $= \int \left(x^2 + y^2\right) dm$

$\underline{j}$ unit vector along the Y-axis

J_{xy} $= \int xy\ dm$

J_{xz} $= \int xz\ dm$

J_{yz} $= \int yz\ dm$

$\underline{k}$ unit vector along the Z-axis

k reduced frequency

k frequency-counter

k_x $= \sqrt{\frac{I_x}{m}}$
k_y $= \sqrt{\frac{I_y}{m}}$
k_z $= \sqrt{\frac{I_x}{m}}$
k_{xz} $= \frac{J_{xz}}{m}$
K_X $= \frac{k_x}{b}$
K_Y $= \frac{k_y}{b}$
K_Z $= \frac{k_z}{b}$
K_{XZ} $= \frac{k_{xz}}{b^2}$
ℓ $= c_\ell \, \frac{1}{2}\rho Q_\infty^2 c$, 2D flow
l_f fuselage length
l_h $= x_h - x_w$ horizontal tail-length
l_v $= x_v - x_w$ vertical tail-length
L $= C_\ell \, \frac{1}{2}\rho Q_\infty^2 Sb$, rolling moment
L $= C_L \, \frac{1}{2}\rho Q_\infty^2 S$, lift
m $= c_m \, \frac{1}{2}\rho Q_\infty^2 c^2$
m mass
m meters
M $= C_m \, \frac{1}{2}\rho Q_\infty^2 S\bar{c}$, pitching moment
M $= \frac{a}{Q_\infty}$, Mach number
$\underline{\mathcal{M}}$ moment-vector
n time-counter
n $= c_n \, \frac{1}{2}\rho Q_\infty^2 c$
N $= C_N \, \frac{1}{2}\rho Q_\infty^2 S$, normal force coefficient
N $= C_n \, \frac{1}{2}\rho Q_\infty^2 Sb$, yawing moment
O origin of reference frames
p static pressure
p angular velocity about the X_B- or X_S-axis
Q_∞ magnitude of the airspeed vector $\underline{Q}_\infty$
$\underline{Q}_\infty$ the airspeed vector $[U_\infty, V_\infty, W_\infty]^T$
q $= \frac{1}{2}\rho Q_\infty^2$, dynamic pressure
q angular velocity about the Y_B- or Y_S-axis
r angular velocity about the Z_B- or Z_S-axis
Re Reynolds number
s semi-chord travelled $s = \frac{2Q_\infty t_n}{\bar{c}}$
s Laplace variable $s = j\omega$ for harmonic motions
S wing area
t time
$\hat{u}$ $= \frac{du}{Q_\infty}$
U_∞ component of $\underline{Q}_\infty$ along the X-axis
u change in the component of Q_∞ along the X-axis
u_g longitudinal gust velocity component
u_i induced velocity vector component along the X-axis

V_∞	component of $\underline{Q}_\infty$ along the Y-axis
v	change in the component of Q_∞ along the Y-axis
v_g	lateral gust velocity component
v_i	induced velocity vector component along the Y-axis
W_∞	component of $\underline{Q}_\infty$ along the Z-axis
w	change in the component of Q_∞ along the Z-axis
w_g	vertical gust velocity component
w_i	induced velocity vector component along the Z-axis
W	aircraft weight
x	x-coordinate
$x_{a.c.}$	x-coordinate of the a.c. of the wing
$x_{c.g.}$	x-coordinate of the c.g.
x_h	x-coordinate the a.c. of the horizontal tailplane
x_v	x-coordinate the a.c. of the vertical tailplane
x_w	x-coordinate the a.c. of the wing with fuselage and nacelles
X	$= C_X \, \frac{1}{2}\rho Q_\infty^2 S$
X_A	X-axis of $\mathcal{F}_A$
X_{aero}	X-axis of $\mathcal{F}_{aero}$
X_B	X-axis of $\mathcal{F}_B$
X_E	X-axis of $\mathcal{F}_E$
X_I	X-axis of $\mathcal{F}_I$
X_P	X-axis of $\mathcal{F}_P$
X_{rig}	X-axis of $\mathcal{F}_{rig}$
X_S	X-axis of $\mathcal{F}_S$
y	y-coordinate
$y_{a.c.}$	y-coordinate of the a.c. of the wing
$y_{c.g.}$	y-coordinate of the c.g.
y_h	y-coordinate the a.c. of the horizontal tailplane
y_v	y-coordinate the a.c. of the vertical tailplane
y_w	y-coordinate the a.c. of the wing with fuselage and nacelles
Y	$= C_Y \, \frac{1}{2}\rho Q_\infty^2 S$
Y_A	Y-axis of $\mathcal{F}_A$
Y_{aero}	Y-axis of $\mathcal{F}_{aero}$
Y_B	Y-axis of $\mathcal{F}_B$
Y_E	Y-axis of $\mathcal{F}_E$
Y_I	Y-axis of $\mathcal{F}_I$
Y_P	Y-axis of $\mathcal{F}_P$
Y_{rig}	Y-axis of $\mathcal{F}_{rig}$
Y_S	Y-axis of $\mathcal{F}_S$
z	z-coordinate
$z_{a.c.}$	z-coordinate of the a.c. of the wing
$z_{c.g.}$	z-coordinate of the c.g.
z_h	z-coordinate the a.c. of the horizontal tailplane

z_v	z-coordinate the a.c. of the vertical tailplane
z_w	z-coordinate the a.c. of the wing with fuselage and nacelles
Z	$= C_Z \ \frac{1}{2}\rho Q_\infty^2 S$
Z_A	Z-axis of $\mathcal{F}_A$
Z_{aero}	Z-axis of $\mathcal{F}_{aero}$
Z_B	Z-axis of $\mathcal{F}_B$
Z_E	Z-axis of $\mathcal{F}_E$
Z_I	Z-axis of $\mathcal{F}_I$
Z_P	Z-axis of $\mathcal{F}_P$
Z_{rig}	Z-axis of $\mathcal{F}_{rig}$
Z_S	Z-axis of $\mathcal{F}_S$

Greek symbols

α	angle-of-attack
α_0	angle-of-attack in steady flight
$\alpha_{h,v,w}$	angle-of-attack of the horizontal, the vertical tailplane or the wing
β	angle-of-sideslip
γ	flightpath angle
γ_0	flightpath angle in steady flight
Γ_e	effective dihedral
ε	downwash angle
ζ	damping ratio of an oscillation
θ	angle of pitch, angle between the X_r-axis and the horizontal plane
θ_0	angle of pitch in steady flight
λ	eigenvalue
μ_b	$= \frac{m}{\rho S b}$
μ_c	$= \frac{m}{\rho S \bar{c}}$
ρ	air density
σ	sidewash angle
σ	standard deviation (with the variance equal to σ^2)
τ	time-constant or time-delay
φ	angle of roll
Φ	velocity potential
χ	track angle
ψ	angle of yaw
ω	circular frequency
$\underline{\Omega}$	total angular velocity about the center of gravity

Reference frames

$\mathcal{F}_A$	Atmosphere-Fixed Frame of Reference $\mathcal{F}_A$ (O_A, X_A, Y_A, Z_A)
$\mathcal{F}_{aero}$	Aerodynamic Frame of Reference $\mathcal{F}_{aero}$ $(O_{aero}, X_{aero}, Y_{aero}, Z_{aero})$
$\mathcal{F}_B$	Body-Fixed Frame of Reference $\mathcal{F}_B$ (O_B, X_B, Y_B, Z_B)
$\mathcal{F}_E$	Earth-Fixed Frame of Reference $\mathcal{F}_E$ (O_E, X_E, Y_E, Z_E)
$\mathcal{F}_I$	Inertial Frame of Reference $\mathcal{F}_I$ (O_I, X_I, Y_I, Z_I)
$\mathcal{F}_P$	Panel Frame of Reference $\mathcal{F}_P$ (O_P, X_P, Y_P, Z_P)
$\mathcal{F}_{rig}$	Rig Frame of Reference $\mathcal{F}_{rig}$ $(O_{rig}, X_{rig}, Y_{rig}, Z_{rig})$
$\mathcal{F}_S$	Stability Frame of Reference $\mathcal{F}_S$ (O_S, X_S, Y_S, Z_S)

Subscripts

0	initial value, steady flight condition
A	atmosphere reference frame
$aero$	aerodynamic reference frame
a	aerodynamic
$a.c.$	aerodynamic center
B	body reference frame
$c.g.$	center of gravity
E	earth reference frame
f	fuselage
h	horizontal tailplane
I	inertial reference frame
i	initial, interference
ind	induced
n	nacelle
P	panel reference frame
p	pylon
rig	aircraft (rig) reference frame
S	stability reference frame
v	vertical tailplane
w	wing
x	along the X-axis
y	along the Y-axis
z	along the Z-axis

Superscripts

*	complex conjungate
^{DUT}	Delft University of Technology model

FPA	Four Point Aircraft model
LPF	Linearized Potential Flow model
PCA	Parametric Computational Aerodynamics model
T	transpose of a vector or matrix
-1	inverse of a matrix

Other symbols

$\hat{}$	estimated
$\dot{}$	first time derivative
∂	partial derivative

Appendix B

Reference frames and definitions

B.1 Reference frames

B.1.1 The Atmosphere-Fixed Frame of Reference $\mathcal{F}_A$

The Atmosphere-Fixed Frame of Reference $\mathcal{F}_A$ ($O_A X_A Y_A Z_A$) is a right-handed frame of reference which is convected with the (uniform) mean wind while keeping its predefined axes orientations. The X_A-axis is pointing, for example, to the North, the Y_A-axis is pointing to the East perpendicular to the X_A-axis, and the Z_A-axis is pointed towards the center of the Earth or aligned with the gravity vector $\underline{g}$, see also reference [1]. The Z_A-axis is oriented perpendicular to the $O_A X_A Y_A$-plane.

B.1.2 The Aerodynamic Frame of Reference $\mathcal{F}_{aero}$

In Computational Aerodynamics (CA) the right-handed orthogonal Aerodynamic Frame of Reference $\mathcal{F}_{aero}$ ($O_{aero} X_{aero} Y_{aero} Z_{aero}$) is used. It is depicted in figure B.1 with the X_{aero}-axis pointing aft (downstream) in the configuration plane of symmetry, the Y_{aero}-axis pointing to the right perpendicular to the plane of symmetry, and the Z_{aero}-axis pointing upwards. The origin of $\mathcal{F}_{aero}$ is located at the center of gravity. In unsteady motion the frame $\mathcal{F}_{aero}$ remains connected to the airframe and does not change its position relative to the aircraft. Considering a symmetrical steady-state initial condition, in this thesis the X_{aero}-axis is chosen to be parallel to the airflow at infinity $\underline{Q}_\infty = [U_\infty, V_\infty, W_\infty]^T$ with $V_\infty = W_\infty = 0$.

The frame $\mathcal{F}_{aero}$ is closely correlated with the Stability Frame of Reference $\mathcal{F}_S$; both the Y_{aero}-axis ánd the Y_S-axis always coincide, while both the X_{aero}-axis and the X_S-axis have an opposite orientation, similar to the Z_{aero}-axis and the Z_S-axis. Also, both the origins of $\mathcal{F}_{aero}$ and $\mathcal{F}_S$ are located at the aircraft center of gravity.

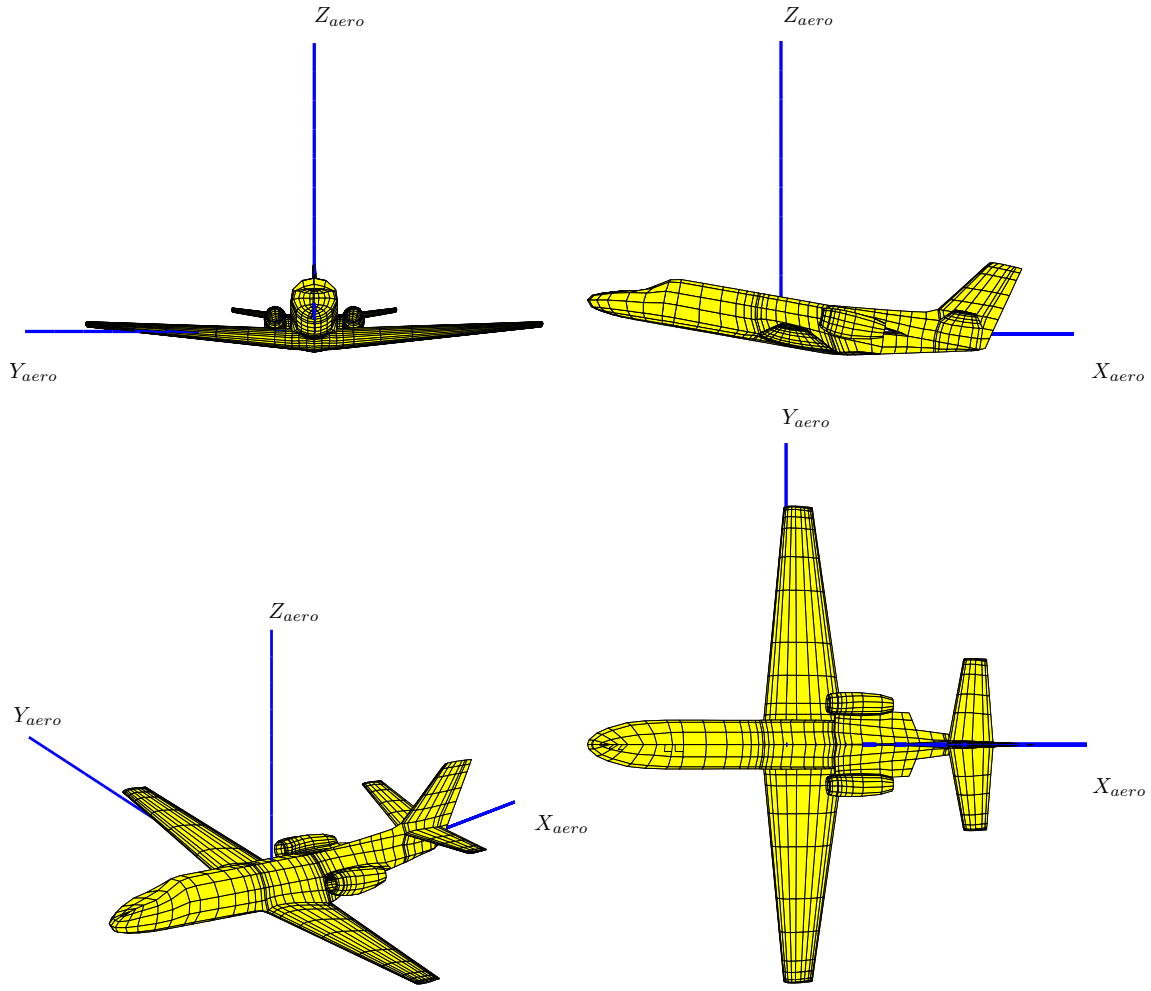


Figure B.1: An aircraft geometry in the Aerodynamic Frame of Reference $\mathcal{F}_{aero}$, angle-of-attack $\alpha = 10.0^o$.

B.1.3 The Body-Fixed Frame of Reference $\mathcal{F}_B$

The Body-Fixed Frame of Reference $\mathcal{F}_B$ $O_B X_B Y_B Z_B$ is a right-handed orthogonal axis-system with the origin located at the aircraft center of gravity. The frame $\mathcal{F}_B$ remains fixed to the aircraft, also in perturbed motion. The choice of the direction of the axes is arbitrary, the most commonly used axes-system is depicted in figure B.2. The X_B-axis is located in the plane of symmetry, in a direction fixed relative to the aircraft, and points forward. The Y_B-axis is directed perpendicular to the plane of symmetry $O_B X_B Z_B$, and is taken positive to the right. The Z_B-axis is perpendicular to the $O_B X_B Y_B$-plane, and therefor, the positive Z_B-axis points downwards in normal, upright, flight.

B.1.4 The Earth-Fixed Frame of Reference $\mathcal{F}_E$

The orthogonal Earth-Fixed Frame of Reference, $\mathcal{F}_E$ (O_E, X_E, Y_E, Z_E), is a right-handed orthogonal frame of reference. It is fixed with respect to Earth with its origin, O_E, at a prescribed location. The X_E-axis points, for example, to the North, the Y_E-axis points

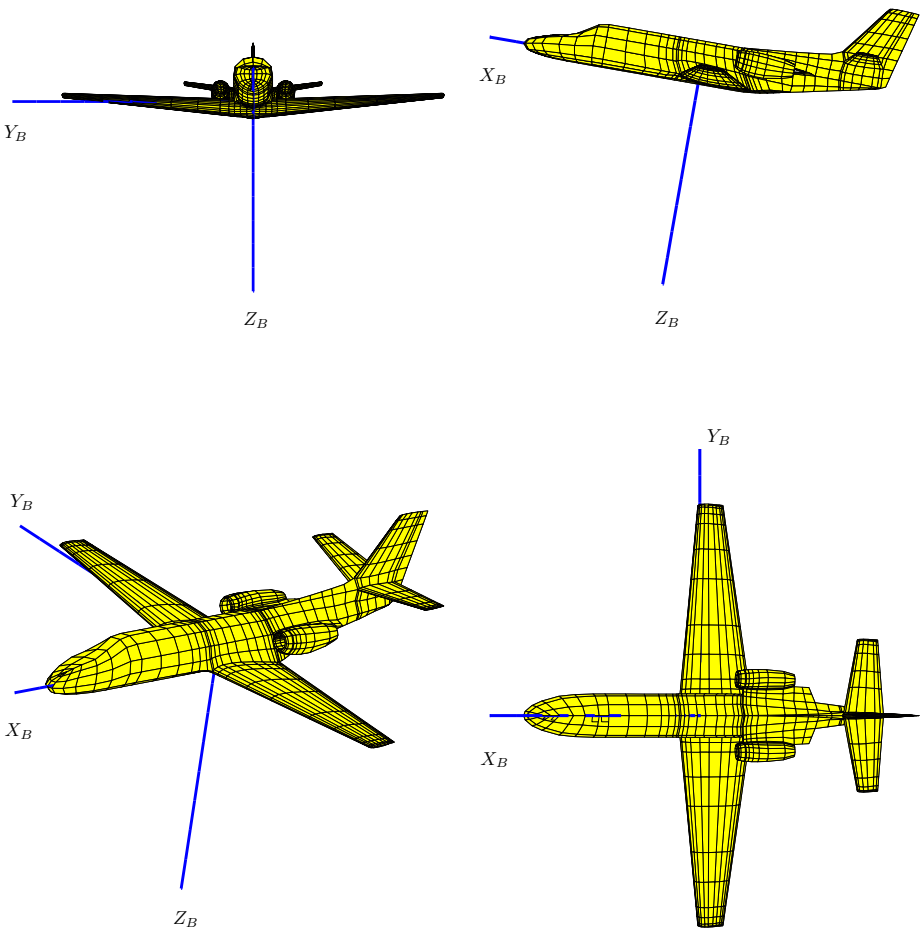


Figure B.2: An aircraft geometry in the Body-Fixed Frame of Reference $\mathcal{F}_B$, angle-of-attack $\alpha = 10.0^o$.

East (perpendicular to the X_E-axis) while the Z_E-axis is pointed perpendicular to the $O_E X_E Y_E$-plane. The Z_E-axis is always pointed downwards to the Earth center. The $O_E X_E Y_E$-plane is a plane tangential to the Earth surface, see also figure B.3.

B.1.5 The Inertial Frame of Reference $\mathcal{F}_I$

The Inertial Frame of Reference $\mathcal{F}_I$ $(O_I X_I Y_I Z_I)$ is a right-handed orthogonal frame of reference. It is used for unsteady Computational Aerodynamic simulations. At the start of an unsteady simulation this frame of reference coincides with the frame $\mathcal{F}_{aero}$. For a rectilinear flightpath, the origin of the frame $\mathcal{F}_{aero}$, O_{aero}, travels along the negative X_I-axis during unsteady simulations. During these simulations, the Inertial Frame of Reference $\mathcal{F}_I$ $(O_I X_I Y_I Z_I)$ remains fixed with respect to Earth. Both the frames $\mathcal{F}_I$ and $\mathcal{F}_{aero}$ are

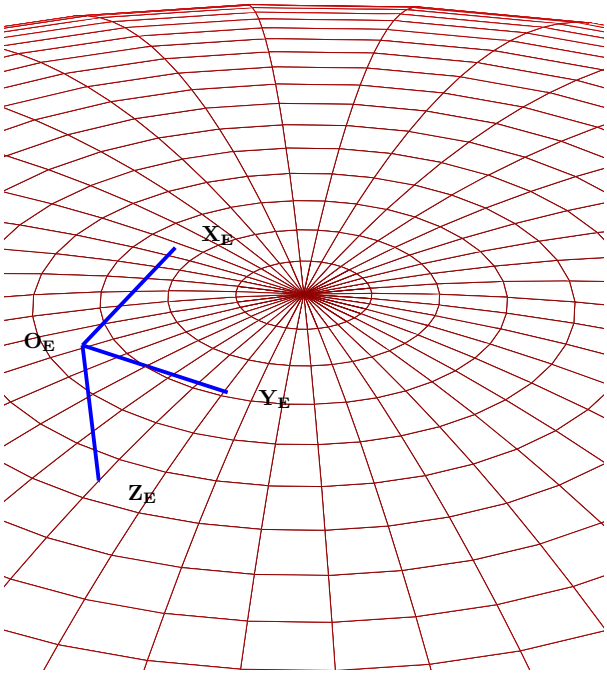


Figure B.3: The Earth-Fixed Frame of Reference $\mathcal{F}_E$.

depicted in figure B.4.

B.1.6 The Panel Frame of Reference $\mathcal{F}_P$

For Computational Aerodynamics the Panel Frame of Reference $\mathcal{F}_P$ is often used. The frame $\mathcal{F}_P$ $(O_P X_P Y_P Z_P)$ is a right-handed orthogonal frame of reference with its origin located at the panel centroid (or collocation point), see figure B.5. All four corner points of a panel are located in the $(O_P X_P Y_P)$-plane. See also appendix C where this frame of reference is used to define the influence of both a quadri-lateral source and a quadri-lateral doublet panel at an arbitrary point in $\mathcal{F}_P$ is given.

B.1.7 The Rig Frame of Reference $\mathcal{F}_{rig}$

For the description of an aircraft configuration's outer (or wetted) surface, the right-handed orthogonal aircraft manufacturer Rig-Frame of Reference $\mathcal{F}_{rig}$ $(O_{rig} X_{rig} Y_{rig} Z_{rig})$ is used. The X_{rig}-axis points aft in the plane of symmetry, $(O_{rig} X_{rig} Z_{rig})$, the Y_{rig}-axis is pointed to the right perpendicular to the $(O_{rig} X_{rig} Z_{rig})$-plane, while the Z_{rig}-axis is pointed upwards, see figure B.6. The origin O_{rig} is situated at some prescribed point (dependent of the manufacturer) in the $O_{rig} X_{rig} Z_{rig}$ plane of symmetry and is, in this thesis, located outside the actual airframe.

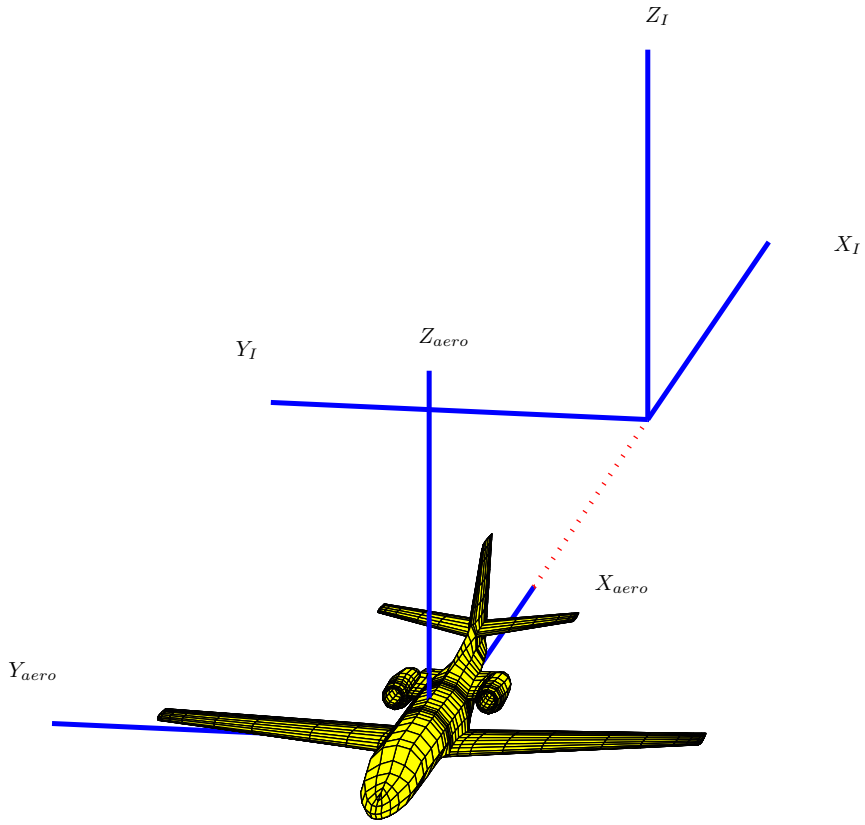


Figure B.4: The Aerodynamic Frame of Reference $\mathcal{F}_{aero}$ and the Inertial Frame of Reference $\mathcal{F}_I$.

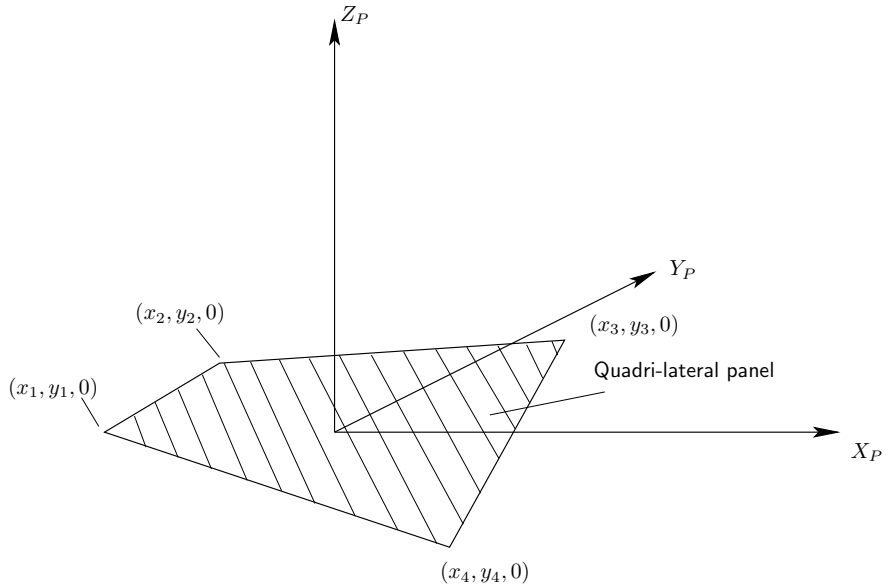


Figure B.5: A Quadri-lateral element in the Panel Frame of Reference $\mathcal{F}_P$.

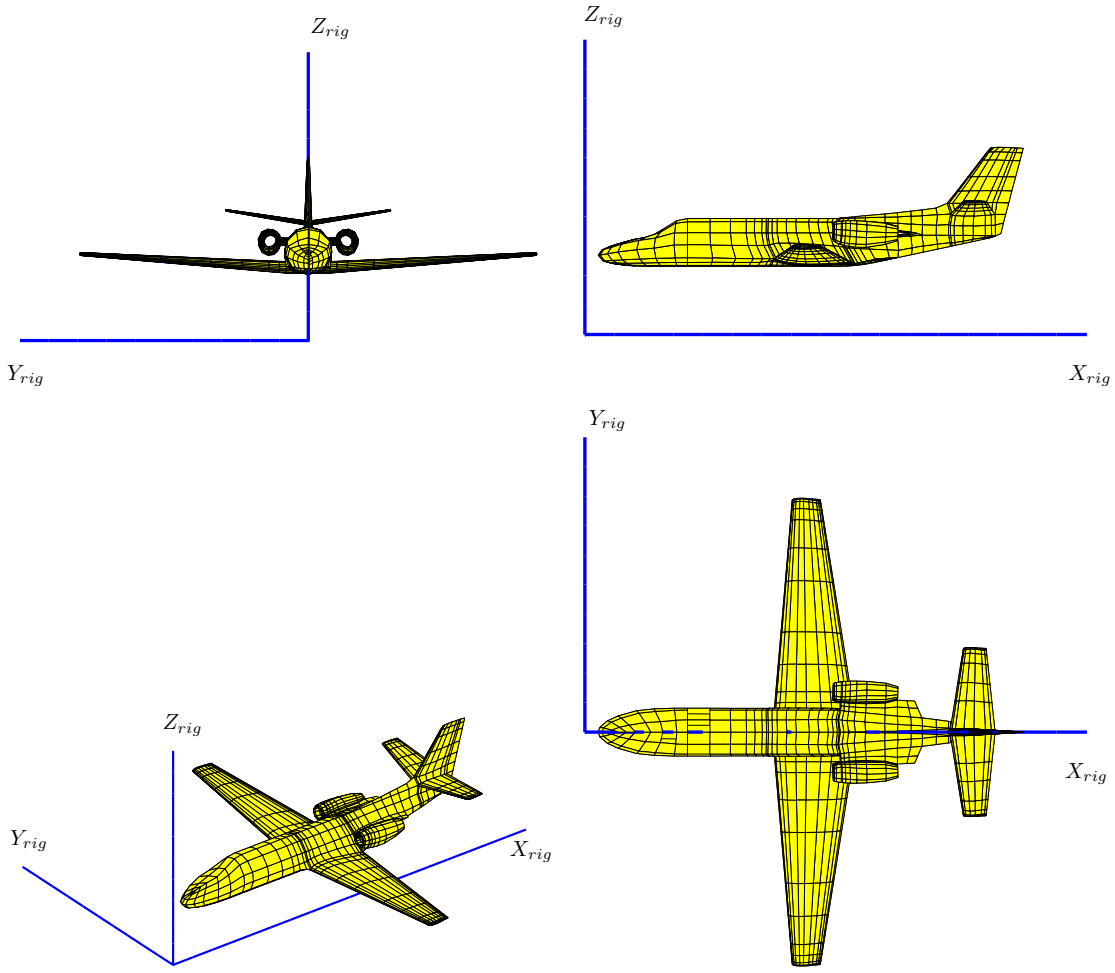


Figure B.6: An aircraft geometry in the rig-frame $\mathcal{F}_{rig}$.

B.1.8 The Stability Frame of Reference $\mathcal{F}_S$

The Stability Frame of Reference $\mathcal{F}_S$ $(O_S X_S Y_S Z_S)$ is a right-handed orthogonal axis-system with the origin located at the aircraft center of gravity. The reference frame is fixed to the aircraft, also in perturbed motion. By definition the frame $\mathcal{F}_S$ is also a body-fixed frame of reference $\mathcal{F}_B$, but the X_S-axis now has a prescribed direction. This aerodynamic frame of reference is given in figure B.7 with the X_S-axis pointing forward, parallel to the airflow at infinity, the Y_S-axis pointing to the right and, perpendicular to the $O_S X_S Y_S$-plane, the Z_S-axis is pointing downwards.
In this thesis the frame $\mathcal{F}_S$ is closely correlated with the Aerodynamic Frame of Reference $\mathcal{F}_{aero}$; both the Y_S-axis and the Y_{aero}-axis always coincide, while both the X_S-axis ánd the X_{aero}-axis have an opposite orientation, similar to the Z_S-axis and the Z_{aero}-axis. Also, both the origins of the frames $\mathcal{F}_S$ and $\mathcal{F}_{aero}$ are located at the center of gravity.

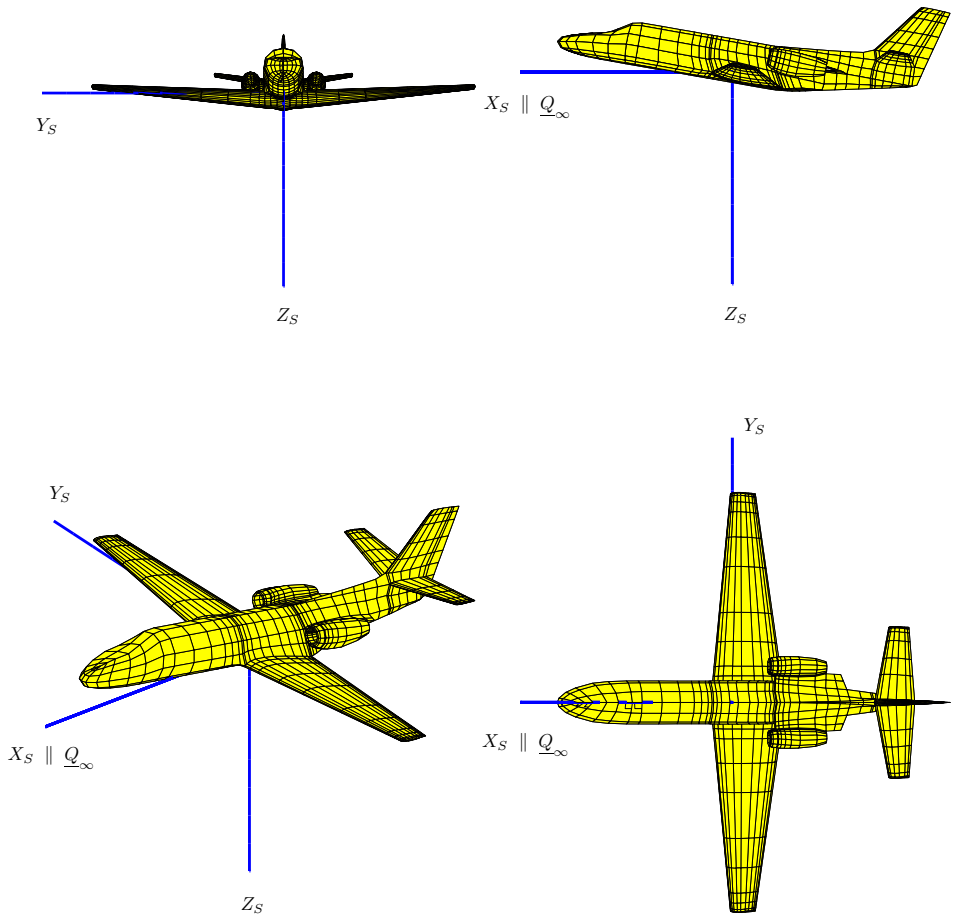


Figure B.7: An aircraft geometry in the Stability Frame of Reference $\mathcal{F}_S$, angle-of-attack $\alpha = 10.0^o$.

B.2 Definitions

B.2.1 The Fourier-transform

In this thesis the Fourier-transform is widely used. Throughout this thesis, the one-dimensional (1D) Fourier-transform, $X(\Omega) = \mathcal{F}\{x(\xi)\}$ is used, and is defined as,

$$\mathcal{F}\{x(\xi)\} = X(\Omega) = \int_{-\infty}^{+\infty} x(\xi) e^{-j\Omega\xi} d\xi$$

where $x(\xi)$ a (random) signal in, for example, the time-domain, $X(\Omega)$ the Fourier-transform of $x(\xi)$, ξ, for example, time and Ω the circular frequency.

The inverse Fourier-transform, $x(\xi) = \mathcal{F}^{-1}\{X(\Omega)\}$, is defined as,

$$\mathcal{F}^{-1}\{X(\Omega)\} = x(\xi) = \frac{1}{2\pi}\int_{-\infty}^{+\infty} X(\Omega)e^{+j\Omega\xi}d\Omega$$

The n$^{\text{th}}$-dimensional Fourier-transform of $x(\underline{\xi})$, $X(\underline{\Omega}) = \mathcal{F}^n\left\{x(\underline{\xi})\right\}$, with $\underline{\xi} = [\xi_1, \xi_2, \xi_3, \cdots, \xi_n]^T$ and $\underline{\Omega} = [\Omega_1, \Omega_2, \Omega_3, \cdots, \Omega_n]^T$, is defined as,

$$\begin{aligned}
\mathcal{F}^n\left\{x(\underline{\xi})\right\} &= X(\underline{\Omega}) \\
&= \int_{-\infty}^{+\infty}\int_{-\infty}^{+\infty}\int_{-\infty}^{+\infty}\cdots\int_{-\infty}^{+\infty} x(\underline{\xi})e^{-j\underline{\Omega}\cdot\underline{\xi}}d\underline{\xi} \\
&= \int_{-\infty}^{+\infty}\int_{-\infty}^{+\infty}\int_{-\infty}^{+\infty}\cdots\int_{-\infty}^{+\infty} x(\xi_1, \xi_2, \xi_3, \cdots, \xi_n)\cdot \\
&\qquad e^{-j(\Omega_1\xi_1+\Omega_2\xi_2+\Omega_3\xi_3+\cdots+\Omega_n\xi_n)}d\xi_1\, d\xi_2\, d\xi_3\cdots d\xi_n
\end{aligned}$$

The n$^{\text{th}}$-dimensional inverse Fourier-transform is defined as,

$$\begin{aligned}
\mathcal{F}^{-n}\{X(\underline{\Omega})\} &= x(\underline{\xi}) \\
&= \frac{1}{(2\pi)^n}\int_{-\infty}^{+\infty}\int_{-\infty}^{+\infty}\int_{-\infty}^{+\infty}\cdots\int_{-\infty}^{+\infty} X(\underline{\Omega})e^{+j\underline{\Omega}\cdot\underline{\xi}}d\underline{\Omega} \\
&= \frac{1}{(2\pi)^n}\int_{-\infty}^{+\infty}\int_{-\infty}^{+\infty}\int_{-\infty}^{+\infty}\cdots\int_{-\infty}^{+\infty} X(\Omega_1, \Omega_2, \Omega_3, \cdots, \Omega_n)\cdot \\
&\qquad e^{+j(\Omega_1\xi_1+\Omega_2\xi_2+\Omega_3\xi_3+\cdots+\Omega_n\xi_n)}d\Omega_1\, d\Omega_2\, d\Omega_3\cdots d\Omega_n
\end{aligned}$$

B.2.2 The calculation of frequency-response functions from the state-space representation

In this thesis both the symmetrical and asymmetrical equations of motion are given as,

$$P(\omega)\ j\omega\ \underline{x} = Q(\omega)\ \underline{x} + R(\omega)\ \underline{u} \tag{B.1}$$

with $P(\omega)$, $Q(\omega)$ and $R(\omega)$ frequency-dependent system matrices, $\underline{x}$ the system state and $\underline{u}$ the system inputs. If the matrix-elements in equation (B.1) are independent of frequency, the time-domain equations of motion are given as,

$$P\frac{d\underline{x}}{dt} = Q\ \underline{x} + R\ \underline{u} \tag{B.2}$$

or,

$$\frac{d\underline{x}}{dt} = A\ \underline{x} + B\ \underline{u} \tag{B.3}$$

with $A = P^{-1}Q$ the system-matrix and $B = P^{-1}R$ the input-matrix. The additional equation required to calculate the state-space system frequency-response is the output equation,

$$\underline{y} = C\ \underline{x} + D\ \underline{u}$$

with C the output-matrix and D the direct-matrix. In this section the output PSD-functions are assumed to be equal to the ones for the aircraft state; therefore, the output-matrix C becomes the identity-matrix of order 4 (four states are present in both the symmetrical and asymmetrical aircraft equations of motion) while the direct-matrix D is the zero-matrix of order $4 \times m$ with m the number of inputs.

The output frequency-response functions are calculated using standard routines in MATLAB (such as `mv2fr.m`), according to,

$$H_{\underline{y}\underline{u}}(\omega) = C\ \left(j\omega I - A\right)^{-1} B + D \tag{B.4}$$

with ω the circular frequency [Rad/sec.] and I the identity-matrix. Using equation (B.4), the output PSD-functions are calculated from the theory given in section B.2.3.

Note that if the matrix-elements of the system matrices A and B are frequency-dependent, that is $A = A(\omega)$ and $B = B(\omega)$, respectively, the output frequency-response functions are also calculated using MATLAB routines (using the script-file `mv2fr.m` as well). The output frequency-response functions now become,

$$H_{\underline{y}\underline{u}}(\omega) = C\ \left(j\omega I - A(\omega)\right)^{-1} B(\omega) + D \tag{B.5}$$

with $A(\omega) = P(\omega)^{-1}Q(\omega)$ the frequency-dependent system-matrix, $B(\omega) = P(\omega)^{-1}R(\omega)$ the frequency-dependent input-matrix and ω the circular frequency [Rad/sec.].

B.2.3 The output Power Spectral Density function matrix

Consider a Multi-Input Multi-Output (MIMO) system in terms of the frequency-response matrix $H_{\underline{y}\underline{u}}(\omega)$ (see equation (B.4)) according to,

$$H_{\underline{y}\underline{u}}(\omega) = \frac{Y_i(\omega)}{U_j(\omega)} = \begin{bmatrix} H_{y_1u_1}(\omega) & H_{y_1u_2}(\omega) & \cdots & H_{y_1u_n}(\omega) \\ H_{y_2u_1}(\omega) & H_{y_2u_2}(\omega) & \cdots & H_{y_2u_n}(\omega) \\ \vdots & \vdots & \vdots & \vdots \\ H_{y_mu_1}(\omega) & H_{y_mu_2}(\omega) & \cdots & H_{y_mu_n}(\omega) \end{bmatrix} \tag{B.6}$$

with ω the circular frequency in [Rad/sec.], $i = 1 \cdots m$ and m the number of outputs, $j = 1 \cdots n$ and n the number of inputs, and $Y_i(\omega)$ and $U_j(\omega)$ the Fourier-transforms of the i^{th} output and the j^{th} input, respectively.

The MIMO system frequency-response to correlated stationary random inputs in terms of the output Power Spectral Density (PSD) function matrix $S_{\underline{yy}}(\omega)$ is given by (see also references [5, 30]),

$$S_{\underline{yy}}(\omega) = \underline{Y}(\omega)^* \, \underline{Y}(\omega)^T = H_{\underline{yu}}(\omega)^* \, S_{\underline{uu}}(\omega) \, H_{\underline{yu}}(\omega)^T \tag{B.7}$$

with $H_{\underline{yu}}(\omega)^*$ and $H_{\underline{yu}}(\omega)^T$ denoting the complex-conjungate and the transpose of the frequency-response matrix $H_{\underline{yu}}(\omega)$, respectively, $\underline{Y}(\omega) = [Y_1(\omega), Y_2(\omega), \cdots, Y_m(\omega)]^T$, the input PSD-function matrix $S_{\underline{uu}}(\omega)$ according to,

$$S_{\underline{uu}}(\omega) = \underline{U}(\omega)^* \, \underline{U}(\omega)^T = \begin{bmatrix} S_{u_1u_1}(\omega) & S_{u_1u_2}(\omega) & \cdots & S_{u_1u_n}(\omega) \\ S_{u_2u_1}(\omega) & S_{u_2u_2}(\omega) & \cdots & S_{u_2u_n}(\omega) \\ \vdots & \vdots & \ddots & \vdots \\ S_{u_nu_1}(\omega) & S_{u_nu_2}(\omega) & \cdots & S_{u_nu_n}(\omega) \end{bmatrix} \tag{B.8}$$

with $\underline{U}(\omega) = [U_1(\omega), U_2(\omega), \cdots, U_n(\omega)]^T$, and the output PSD-function matrix $S_{\underline{yy}}(\omega)$ according to,

$$S_{\underline{yy}}(\omega) = \underline{Y}(\omega)^* \, \underline{Y}(\omega)^T = \begin{bmatrix} S_{y_1y_1}(\omega) & S_{y_1y_2}(\omega) & \cdots & S_{y_1y_m}(\omega) \\ S_{y_2y_1}(\omega) & S_{y_2y_2}(\omega) & \cdots & S_{y_2y_m}(\omega) \\ \vdots & \vdots & \ddots & \vdots \\ S_{y_my_1}(\omega) & S_{y_my_2}(\omega) & \cdots & S_{y_my_m}(\omega) \end{bmatrix} \tag{B.9}$$

The cross PSD-function matrices $S_{\underline{uy}}(\omega)$ and $S_{\underline{yu}}(\omega)$ are defined as (see also references [5, 30]),

$$S_{\underline{uy}}(\omega) = \underline{U}(\omega)^* \, \underline{Y}(\omega)^T = \left[H_{\underline{yu}}(\omega) S_{\underline{uu}}(\omega) \right]^T \tag{B.10}$$

and,

$$S_{\underline{yu}}(\omega) = \underline{Y}(\omega)^* \, \underline{U}(\omega)^T = H_{\underline{yu}}(\omega)^* S_{\underline{uu}}(\omega) \tag{B.11}$$

respectively.

Appendix C

Quadrilateral source - and doublet elements

C.1 Introduction

In this thesis Linearized Potential Flow theory is used to obtain the (time-dependent) aerodynamic forces and moments acting on aircraft configurations. For this purpose, the calculation of the Aerodynamic Influence Coefficient (AIC) matrix elements is required. In this appendix the applied formulae for calculating these AIC matrix elements are provided. These formulae define both the influence of a quadri-lateral source panel and a quadri-lateral doublet panel at an arbitrary point in the Panel Frame of Reference $\mathcal{F}_P$. Details of this reference frame can be found in appendix B. Although the formulae presented in this appendix have been taken from references [11, 12], the applied formula for the doublet influence has been adjusted for this thesis.

C.2 Quadri-lateral source elements

The quadri-lateral source panel with its straight line boundaries is depicted in figure C.1. The induced potential $\Phi(x, y, z)$ at location $(x, y, z)^T$ of such a quadri-lateral source panel with constant strength source σ and with the panel elements' corner points designated as $(x_1, y_1, 0)$, $(x_2, y_2, 0)$, $(x_3, y_3, 0)$ and $(x_4, y_4, 0)$ in the frame $\mathcal{F}_P$, is written as, see reference [11, 12],

$$\begin{aligned}\Phi(x,y,z) &= -\frac{\sigma}{4\pi}\left\{\left[\frac{(x-x_1)(y_2-y_1)-(y-y_1)(x_2-x_1)}{d_{12}} ln\left(\frac{r_1+r_2+d_{12}}{r_1+r_2-d_{12}}\right)\right.\right. \\ &\quad + \frac{(x-x_2)(y_3-y_2)-(y-y_2)(x_3-x_2)}{d_{23}} ln\left(\frac{r_2+r_3+d_{23}}{r_2+r_3-d_{23}}\right) \\ &\quad \left.\left. + \frac{(x-x_3)(y_4-y_3)-(y-y_3)(x_4-x_3)}{d_{34}} ln\left(\frac{r_3+r_4+d_{34}}{r_3+r_4-d_{34}}\right)\right.\right.\end{aligned}$$

$$
\begin{aligned}
&+ \frac{(x-x_4)(y_1-y_4)-(y-y_4)(x_1-x_4)}{d_{41}} ln\left(\frac{r_4+r_1+d_{41}}{r_4+r_1-d_{41}}\right)\Bigg] \\
&- |z| \left[tan^{-1}\left(\frac{m_{12}e_1-h_1}{z\, r_1}\right) - tan^{-1}\left(\frac{m_{12}e_2-h_2}{z\, r_2}\right) \right. \\
&+ tan^{-1}\left(\frac{m_{23}e_2-h_2}{z\, r_2}\right) - tan^{-1}\left(\frac{m_{23}e_3-h_3}{z\, r_3}\right) + \\
&+ tan^{-1}\left(\frac{m_{34}e_3-h_3}{z\, r_3}\right) - tan^{-1}\left(\frac{m_{34}e_4-h_4}{z\, r_4}\right) + \\
&\left. + \; tan^{-1}\left(\frac{m_{41}e_4-h_4}{z\, r_4}\right) - tan^{-1}\left(\frac{m_{41}e_1-h_1}{z\, r_1}\right)\right]\Bigg\} \qquad \text{(C.1)}
\end{aligned}
$$

with,

$$d_{12} = \sqrt{(x_2-x_1)^2+(y_2-y_1)^2} \qquad \text{(C.2)}$$

$$d_{23} = \sqrt{(x_3-x_2)^2+(y_3-y_2)^2} \qquad \text{(C.3)}$$

$$d_{34} = \sqrt{(x_4-x_3)^2+(y_4-y_3)^2} \qquad \text{(C.4)}$$

$$d_{41} = \sqrt{(x_1-x_4)^2+(y_1-y_4)^2} \qquad \text{(C.5)}$$

and,

$$m_{12} = \frac{y_2-y_1}{x_2-x_1} \qquad \text{(C.6)}$$

$$m_{23} = \frac{y_3-y_2}{x_3-x_2} \qquad \text{(C.7)}$$

$$m_{34} = \frac{y_4-y_3}{x_4-x_3} \qquad \text{(C.8)}$$

$$m_{41} = \frac{y_1-y_4}{x_1-x_4} \qquad \text{(C.9)}$$

and,

$$r_k = \sqrt{(x-x_k)^2+(y-y_k)^2+z^2} \qquad \text{(C.10)}$$

$$e_k = (x-x_k)^2+z^2 \qquad \text{(C.11)}$$

$$h_k = (x-x_k)\,(y-y_k) \qquad \text{(C.12)}$$

with $k = 1, 2, 3, 4$, and $[x, y, z]^T$ an arbitrary point in the frame $\mathcal{F}_P$.

The induced velocity components (u, v, w) are obtained by differentiating the velocity potential Φ,

$$(u, v, w) = \left(\frac{\partial\Phi}{\partial x},\ \frac{\partial\Phi}{\partial y},\ \frac{\partial\Phi}{\partial z}\right) \qquad \text{(C.13)}$$

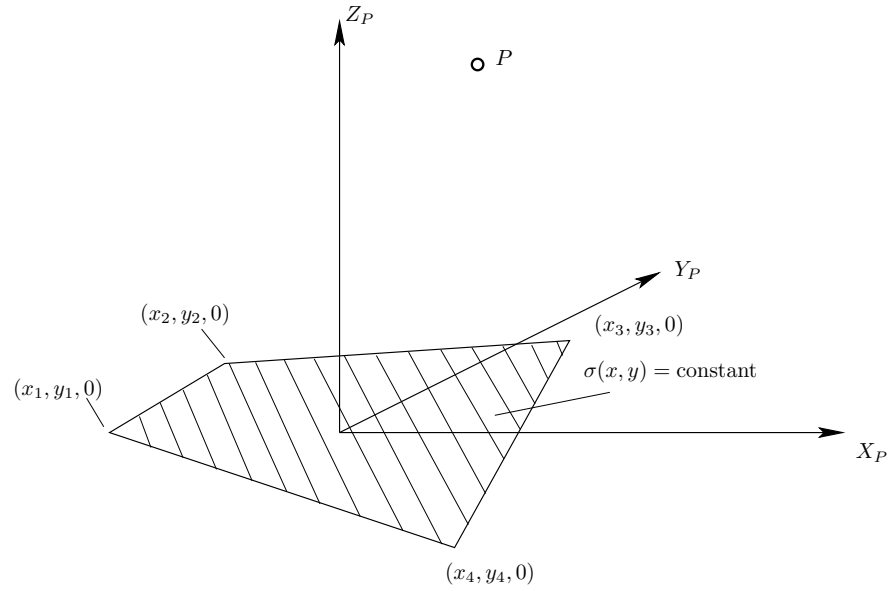


Figure C.1: Quadri-lateral constant strength source element in the Panel Frame of Reference $\mathcal{F}_P$.

which are, see reference [11, 12],

$$u = \frac{\sigma}{4\pi}\left[\frac{y_2-y_1}{d_{12}}ln\left(\frac{r_1+r_2-d_{12}}{r_1+r_2+d_{12}}\right)+\frac{y_3-y_2}{d_{23}}ln\left(\frac{r_2+r_3-d_{23}}{r_2+r_3+d_{23}}\right)+\right.$$
$$\left.+\frac{y_4-y_3}{d_{34}}ln\left(\frac{r_3+r_4-d_{34}}{r_3+r_4+d_{34}}\right)+\frac{y_1-y_4}{d_{41}}ln\left(\frac{r_4+r_1-d_{41}}{r_4+r_1+d_{41}}\right)\right] \quad \text{(C.14)}$$

$$v = \frac{\sigma}{4\pi}\left[\frac{x_1-x_2}{d_{12}}ln\left(\frac{r_1+r_2-d_{12}}{r_1+r_2+d_{12}}\right)+\frac{x_2-x_3}{d_{23}}ln\left(\frac{r_2+r_3-d_{23}}{r_2+r_3+d_{23}}\right)+\right.$$
$$\left.+\frac{x_3-x_4}{d_{34}}ln\left(\frac{r_3+r_4-d_{34}}{r_3+r_4+d_{34}}\right)+\frac{x_4-x_1}{d_{41}}ln\left(\frac{r_4+r_1-d_{41}}{r_4+r_1+d_{41}}\right)\right] \quad \text{(C.15)}$$

$$w = \frac{\sigma}{4\pi}\left[tan^{-1}\left(\frac{m_{12}e_1-h_1}{z\,r_1}\right)-tan^{-1}\left(\frac{m_{12}e_2-h_2}{z\,r_2}\right)\right.$$
$$+tan^{-1}\left(\frac{m_{23}e_2-h_2}{z\,r_2}\right)-tan^{-1}\left(\frac{m_{23}e_3-h_3}{z\,r_3}\right)+$$
$$+tan^{-1}\left(\frac{m_{34}e_3-h_3}{z\,r_3}\right)-tan^{-1}\left(\frac{m_{34}e_4-h_4}{z\,r_4}\right)+$$
$$\left.+\,tan^{-1}\left(\frac{m_{41}e_4-h_4}{z\,r_4}\right)-tan^{-1}\left(\frac{m_{41}e_1-h_1}{z\,r_1}\right)\right] \quad \text{(C.16)}$$

C.3 Quadri-lateral doublet elements

Similar to the quadri-lateral source panel, the quadri-lateral doublet panel with its straight line boundaries is depicted in figure C.2. The induced potential Φ of such a quadri-lateral doublet panel with constant strength doublet μ and with the panel elements' corner points designated as $(x_1, y_1, 0)$, $(x_2, y_2, 0)$, $(x_3, y_3, 0)$ and $(x_4, y_4, 0)$ in the frame $\mathcal{F}_P$ is written as, see reference [11, 12],

$$\begin{aligned}\Phi(x,y,z) \;=\; & -\frac{\mu}{4\pi}\left[tan^{-1}\left(\frac{m_{12}e_1-h_1}{z\,r_1}\right)-tan^{-1}\left(\frac{m_{12}e_2-h_2}{z\,r_2}\right)\right.\\ & +tan^{-1}\left(\frac{m_{23}e_2-h_2}{z\,r_2}\right)-tan^{-1}\left(\frac{m_{23}e_3-h_3}{z\,r_3}\right)+\\ & +tan^{-1}\left(\frac{m_{34}e_3-h_3}{z\,r_3}\right)-tan^{-1}\left(\frac{m_{34}e_4-h_4}{z\,r_4}\right)+\\ & \left.+\,tan^{-1}\left(\frac{m_{41}e_4-h_4}{z\,r_4}\right)-tan^{-1}\left(\frac{m_{41}e_1-h_1}{z\,r_1}\right)\right]\end{aligned} \tag{C.17}$$

with m_{12}, m_{23}, m_{34} and m_{41} as given in equations (C.6) to (C.9); $e_k,\ k = 1,2,3,4$ as given in equation (C.11); $h_k,\ k = 1,2,3,4$ as given in equation (C.12) and $r_k,\ k = 1,2,3,4$ as given in equation (C.10).

Contrary to references [11, 12], the factor $\frac{-\mu}{4\pi}$ is used in equation (C.17), instead of the factor $+\frac{\mu}{4\pi}$.

Again, the induced velocity components (u, v, w) are obtained by differentiating the velocity potential Φ, see equation (C.13),

$$(u,v,w) = \left(\frac{\partial\Phi}{\partial x},\ \frac{\partial\Phi}{\partial y},\ \frac{\partial\Phi}{\partial z}\right)$$

which are, see reference [11, 12],

$$\begin{aligned}u \;=\; & \frac{\mu}{4\pi}\left[\frac{z\,(y_1-y_2)\,(r_1+r_2)}{r_1r_2\,\{r_1r_2-[(x-x_1)\,(x-x_2)+(y-y_1)\,(y-y_2)+z^2]\}}+\right.\\ & +\frac{z\,(y_2-y_3)\,(r_2+r_3)}{r_2r_3\,\{r_2r_3-[(x-x_2)\,(x-x_3)+(y-y_2)\,(y-y_3)+z^2]\}}+\\ & +\frac{z\,(y_3-y_4)\,(r_3+r_4)}{r_3r_4\,\{r_3r_4-[(x-x_3)\,(x-x_4)+(y-y_3)\,(y-y_4)+z^2]\}}+\\ & \left.+\,\frac{z\,(y_4-y_1)\,(r_4+r_1)}{r_4r_1\,\{r_4r_1-[(x-x_4)\,(x-x_1)+(y-y_4)\,(y-y_1)+z^2]\}}\right]\end{aligned} \tag{C.18}$$

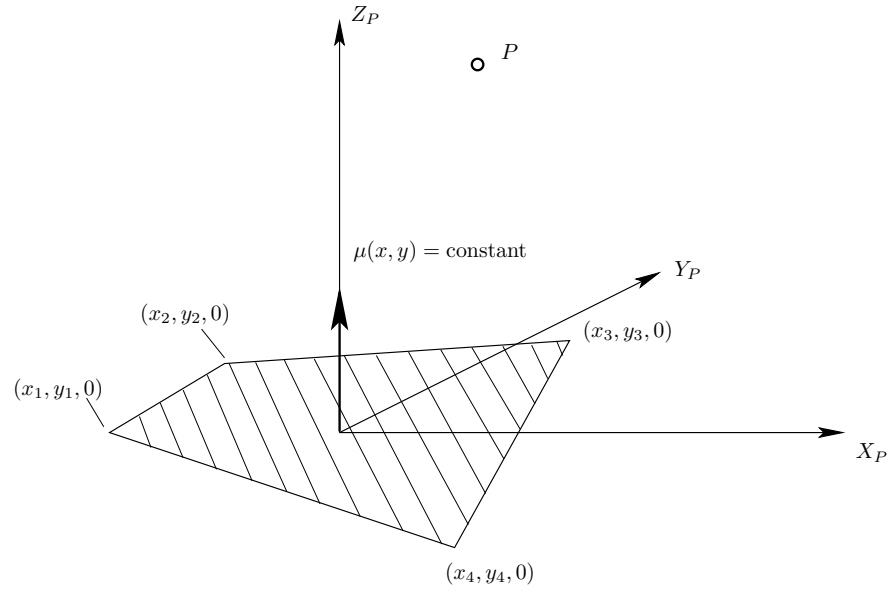


Figure C.2: Quadri-lateral constant strength doublet element in the Panel Frame of Reference $\mathcal{F}_P$.

$$
\begin{aligned}
v \;=\; & \frac{\mu}{4\pi}\left[\frac{z\,(x_2-x_1)\,(r_1+r_2)}{r_1 r_2\,\{r_1 r_2-[(x-x_1)\,(x-x_2)+(y-y_1)\,(y-y_2)+z^2]\}}+\right.\\
& +\frac{z\,(x_3-x_2)\,(r_2+r_3)}{r_2 r_3\,\{r_2 r_3-[(x-x_2)\,(x-x_3)+(y-y_2)\,(y-y_3)+z^2]\}}+\\
& +\frac{z\,(x_4-x_3)\,(r_3+r_4)}{r_3 r_4\,\{r_3 r_4-[(x-x_3)\,(x-x_4)+(y-y_3)\,(y-y_4)+z^2]\}}+\\
& \left.+\,\frac{z\,(x_1-x_4)\,(r_4+r_1)}{r_4 r_1\,\{r_4 r_1-[(x-x_4)\,(x-x_1)+(y-y_4)\,(y-y_1)+z^2]\}}\right]
\end{aligned}
\tag{C.19}
$$

$$
\begin{aligned}
w \;=\; & \frac{\mu}{4\pi}\left[\frac{[(x-x_2)\,(y-y_1)-(x-x_1)\,(y-y_2)]\,(r_1+r_2)}{r_1 r_2\,\{r_1 r_2-[(x-x_1)\,(x-x_2)+(y-y_1)\,(y-y_2)+z^2]\}}+\right.\\
& +\frac{[(x-x_3)\,(y-y_2)-(x-x_2)\,(y-y_3)]\,(r_2+r_3)}{r_2 r_3\,\{r_2 r_3-[(x-x_2)\,(x-x_3)+(y-y_2)\,(y-y_3)+z^2]\}}+\\
& +\frac{[(x-x_4)\,(y-y_3)-(x-x_3)\,(y-y_4)]\,(r_3+r_4)}{r_3 r_4\,\{r_3 r_4-[(x-x_3)\,(x-x_4)+(y-y_3)\,(y-y_4)+z^2]\}}+\\
& \left.+\,\frac{[(x-x_1)\,(y-y_4)-(x-x_4)\,(y-y_1)]\,(r_4+r_1)}{r_4 r_1\,\{r_4 r_1-[(x-x_4)\,(x-x_1)+(y-y_4)\,(y-y_1)+z^2]\}}\right]
\end{aligned}
\tag{C.20}
$$

with $r_k,\ k=1,2,3,4$, as given in equation (C.10).

Appendix D

Stability - and gust derivative definitions

This appendix contains the definitions of the stability- and gust derivatives given in chapter 5. These derivatives are valid for the Stability Frame of Reference $\mathcal{F}_S$.

In tables D.1 to D.10, the definition of the stability- and gust derivatives are given in terms of transformations from the Aerodynamic Frame of Reference $\mathcal{F}_{aero}$ to the frame $\mathcal{F}_S$.
In tables D.11 to D.20 the definition of the stability- and gust derivatives is given in terms of partial derivatives.

Details of the frames $\mathcal{F}_S$ and $\mathcal{F}_{aero}$ can be found in appendix B.

	C_X	C_Z	C_m
$\hat{u}$	$C_{X_u} = -C^a_{X_u}$	$C_{Z_u} = -C^a_{Z_u}$	$C_{m_u} = +C^a_{m_u}$
α	$C_{X_\alpha} = -C^a_{X_\alpha}$	$C_{Z_\alpha} = -C^a_{Z_\alpha}$	$C_{m_\alpha} = +C^a_{m_\alpha}$
$\frac{\dot{\alpha}\bar{c}}{2Q_\infty}$	$C_{X_{\dot{\alpha}}} = -C^a_{X_{\dot{\alpha}}}$	$C_{Z_{\dot{\alpha}}} = -C^a_{Z_{\dot{\alpha}}}$	$C_{m_{\dot{\alpha}}} = +C^a_{m_{\dot{\alpha}}}$
$\frac{q\bar{c}}{2Q_\infty}$	$C_{X_q} = -C^a_{X_q}$	$C_{Z_q} = -C^a_{Z_q}$	$C_{m_q} = +C^a_{m_q}$

Table D.1: Definition of the symmetrical stability derivatives for $\mathcal{F}_S$ in terms of the calculated symmetrical aerodynamic derivatives for $\mathcal{F}_{aero}$.

	C_Y	C_ℓ	C_n
β	$C_{Y_\beta} = -C^a_{Y_\beta}$	$C_{\ell_\beta} = +C^a_{\ell_\beta}$	$C_{n_\beta} = +C^a_{n_\beta}$
$\frac{\dot{\beta}b}{2Q_\infty}$	$C_{Y_{\dot{\beta}}} = -C^a_{Y_{\dot{\beta}}}$	$C_{\ell_{\dot{\beta}}} = +C^a_{\ell_{\dot{\beta}}}$	$C_{n_{\dot{\beta}}} = +C^a_{n_{\dot{\beta}}}$
$\frac{pb}{2Q_\infty}$	$C_{Y_p} = -C^a_{Y_p}$	$C_{\ell_p} = +C^a_{\ell_p}$	$C_{n_p} = +C^a_{n_p}$
$\frac{rb}{2Q_\infty}$	$C_{Y_r} = -C^a_{Y_r}$	$C_{\ell_r} = +C^a_{\ell_r}$	$C_{n_r} = +C^a_{n_r}$

Table D.2: Definition of the asymmetrical stability derivatives for $\mathcal{F}_S$ in terms of the calculated asymmetrical aerodynamic derivatives for $\mathcal{F}_{aero}$.

	C_X	C_Z	C_m
$\hat{u}_g$	$C_{X_{u_g}} = -C^a_{X_{u_g}}$	$C_{Z_{u_g}} = -C^a_{Z_{u_g}}$	$C_{m_{u_g}} = +C^a_{m_{u_g}}$
$\frac{\dot{\hat{u}}_g \bar{c}}{2Q_\infty}$	$C_{X_{\dot{u}_g}} = -C^a_{X_{\dot{u}_g}}$	$C_{Z_{\dot{u}_g}} = -C^a_{Z_{\dot{u}_g}}$	$C_{m_{\dot{u}_g}} = +C^a_{m_{\dot{u}_g}}$
α_g	$C_{X_{\alpha_g}} = -C^a_{X_{\alpha_g}}$	$C_{Z_{\alpha_g}} = -C^a_{Z_{\alpha_g}}$	$C_{m_{\alpha_g}} = +C^a_{m_{\alpha_g}}$
$\frac{\dot{\alpha}_g \bar{c}}{2Q_\infty}$	$C_{X_{\dot{\alpha}_g}} = -C^a_{X_{\dot{\alpha}_g}}$	$C_{Z_{\dot{\alpha}_g}} = -C^a_{Z_{\dot{\alpha}_g}}$	$C_{m_{\dot{\alpha}_g}} = +C^a_{m_{\dot{\alpha}_g}}$

Table D.3: Definition of the symmetrical gust derivatives for $\mathcal{F}_S$ in terms of the calculated symmetrical aerodynamic derivatives for $\mathcal{F}_{aero}$.

	C_Y	C_ℓ	C_n
β_g	$C_{Y_{\beta_g}} = -C^a_{Y_{\beta_g}}$	$C_{\ell_{\beta_g}} = +C^a_{\ell_{\beta_g}}$	$C_{n_{\beta_g}} = +C^a_{n_{\beta_g}}$
$\frac{\dot{\beta}_g b}{2Q_\infty}$	$C_{Y_{\dot{\beta}_g}} = -C^a_{Y_{\dot{\beta}_g}}$	$C_{\ell_{\dot{\beta}_g}} = +C^a_{\ell_{\dot{\beta}_g}}$	$C_{n_{\dot{\beta}_g}} = +C^a_{n_{\dot{\beta}_g}}$

Table D.4: Definition of the asymmetrical gust derivatives for $\mathcal{F}_S$ in terms of the calculated asymmetrical aerodynamic derivatives for $\mathcal{F}_{aero}$.

	C_X	C_Z	C_m
$\hat{u}$	$\mathcal{C}_{\mathcal{X}_u} = -\mathcal{C}^a_{\mathcal{X}_u}$	$\mathcal{C}_{\mathcal{Z}_u} = -\mathcal{C}^a_{\mathcal{Z}_u}$	$\mathcal{C}_{m_u} = +\mathcal{C}^a_{m_u}$
	$\mathcal{C}_{\mathcal{X}_{\dot{u}}} = -\mathcal{C}^a_{\mathcal{X}_{\dot{u}}}$	$\mathcal{C}_{\mathcal{Z}_{\dot{u}}} = -\mathcal{C}^a_{\mathcal{Z}_{\dot{u}}}$	$\mathcal{C}_{m_{\dot{u}}} = +\mathcal{C}^a_{m_{\dot{u}}}$
α	$\mathcal{C}_{\mathcal{X}_\alpha} = -\mathcal{C}^a_{\mathcal{X}_\alpha}$	$\mathcal{C}_{\mathcal{Z}_\alpha} = -\mathcal{C}^a_{\mathcal{Z}_\alpha}$	$\mathcal{C}_{m_\alpha} = +\mathcal{C}^a_{m_\alpha}$
	$\mathcal{C}_{\mathcal{X}_{\dot{\alpha}}} = -\mathcal{C}^a_{\mathcal{X}_{\dot{\alpha}}}$	$\mathcal{C}_{\mathcal{Z}_{\dot{\alpha}}} = -\mathcal{C}^a_{\mathcal{Z}_{\dot{\alpha}}}$	$\mathcal{C}_{m_{\dot{\alpha}}} = +\mathcal{C}^a_{m_{\dot{\alpha}}}$

Table D.5: Definition of the frequency-dependent symmetrical stability derivatives for $\mathcal{F}_S$ in terms of the calculated frequency-dependent symmetrical aerodynamic derivatives for $\mathcal{F}_{aero}$.

	C_Y	C_ℓ	C_n
β	$\mathcal{C}_{\mathcal{Y}_\beta} = -\mathcal{C}^a_{\mathcal{Y}_\beta}$	$\mathcal{C}_{\ell_\beta} = +\mathcal{C}^a_{\ell_\beta}$	$\mathcal{C}_{n_\beta} = +\mathcal{C}^a_{n_\beta}$
	$\mathcal{C}_{\mathcal{Y}_{\dot\beta}} = -\mathcal{C}^a_{\mathcal{Y}_{\dot\beta}}$	$\mathcal{C}_{\ell_{\dot\beta}} = +\mathcal{C}^a_{\ell_{\dot\beta}}$	$\mathcal{C}_{n_{\dot\beta}} = +\mathcal{C}^a_{n_{\dot\beta}}$

Table D.6: Definition of the frequency-dependent asymmetrical stability derivatives for $\mathcal{F}_S$ in terms of the calculated frequency-dependent asymmetrical aerodynamic derivatives for $\mathcal{F}_{aero}$.

	C_X	C_Z	C_m
$\hat{u}_g$	$\mathcal{C}_{\mathcal{X}_{u_g}} = -\mathcal{C}^a_{\mathcal{X}_{u_g}}$	$\mathcal{C}_{\mathcal{Z}_{u_g}} = -\mathcal{C}^a_{\mathcal{Z}_{u_g}}$	$\mathcal{C}_{m_{u_g}} = +\mathcal{C}^a_{m_{u_g}}$
	$\mathcal{C}_{\mathcal{X}_{\dot u_g}} = -\mathcal{C}^a_{\mathcal{X}_{\dot u_g}}$	$\mathcal{C}_{\mathcal{Z}_{\dot u_g}} = -\mathcal{C}^a_{\mathcal{Z}_{\dot u_g}}$	$\mathcal{C}_{m_{\dot u_g}} = +\mathcal{C}^a_{m_{\dot u_g}}$
α_g	$\mathcal{C}_{\mathcal{X}_{\alpha_g}} = -\mathcal{C}^a_{\mathcal{X}_{\alpha_g}}$	$\mathcal{C}_{\mathcal{Z}_{\alpha_g}} = -\mathcal{C}^a_{\mathcal{Z}_{\alpha_g}}$	$\mathcal{C}_{m_{\alpha_g}} = +\mathcal{C}^a_{m_{\alpha_g}}$
	$\mathcal{C}_{\mathcal{X}_{\dot\alpha_g}} = -\mathcal{C}^a_{\mathcal{X}_{\dot\alpha_g}}$	$\mathcal{C}_{\mathcal{Z}_{\dot\alpha_g}} = -\mathcal{C}^a_{\mathcal{Z}_{\dot\alpha_g}}$	$\mathcal{C}_{m_{\dot\alpha_g}} = +\mathcal{C}^a_{m_{\dot\alpha_g}}$

Table D.7: Definition of the frequency-dependent symmetrical gust derivatives for $\mathcal{F}_S$ in terms of the calculated frequency-dependent symmetrical aerodynamic gust derivatives for $\mathcal{F}_{aero}$, for 1D gust fields.

	C_Y	C_ℓ	C_n
β_g	$\mathcal{C}_{\mathcal{Y}_{\beta_g}} = -\mathcal{C}^a_{\mathcal{Y}_{\beta_g}}$	$\mathcal{C}_{\ell_{\beta_g}} = +\mathcal{C}^a_{\ell_{\beta_g}}$	$\mathcal{C}_{n_{\beta_g}} = +\mathcal{C}^a_{n_{\beta_g}}$
	$\mathcal{C}_{\mathcal{Y}_{\dot\beta_g}} = -\mathcal{C}^a_{\mathcal{Y}_{\dot\beta_g}}$	$\mathcal{C}_{\ell_{\dot\beta_g}} = +\mathcal{C}^a_{\ell_{\dot\beta_g}}$	$\mathcal{C}_{n_{\dot\beta_g}} = +\mathcal{C}^a_{n_{\dot\beta_g}}$

Table D.8: Definition of the frequency-dependent asymmetrical gust derivatives for $\mathcal{F}_S$ in terms of the calculated frequency-dependent asymmetrical aerodynamic gust derivatives for $\mathcal{F}_{aero}$, for 1D gust fields.

	C_X	C_Z	C_m
$\hat{u}_g$	$\mathcal{C}_{\mathcal{X}_{u_g}}(\Omega_y) = -\mathcal{C}^a_{\mathcal{X}_{u_g}}(\Omega_y)$	$\mathcal{C}_{\mathcal{Z}_{u_g}}(\Omega_y) = -\mathcal{C}^a_{\mathcal{Z}_{u_g}}(\Omega_y)$	$\mathcal{C}_{m_{u_g}}(\Omega_y) = +\mathcal{C}^a_{m_{u_g}}(\Omega_y)$
	$\mathcal{C}_{\mathcal{X}_{\dot{u}_g}}(\Omega_y) = -\mathcal{C}^a_{\mathcal{X}_{\dot{u}_g}}(\Omega_y)$	$\mathcal{C}_{\mathcal{Z}_{\dot{u}_g}}(\Omega_y) = -\mathcal{C}^a_{\mathcal{Z}_{\dot{u}_g}}(\Omega_y)$	$\mathcal{C}_{m_{\dot{u}_g}}(\Omega_y) = +\mathcal{C}^a_{m_{\dot{u}_g}}(\Omega_y)$
β_g	$\mathcal{C}_{\mathcal{X}_{\beta_g}}(\Omega_y) = +\mathcal{C}^a_{\mathcal{X}_{\beta_g}}(\Omega_y)$	$\mathcal{C}_{\mathcal{Z}_{\beta_g}}(\Omega_y) = +\mathcal{C}^a_{\mathcal{Z}_{\beta_g}}(\Omega_y)$	$\mathcal{C}_{m_{\beta_g}}(\Omega_y) = -\mathcal{C}^a_{m_{\beta_g}}(\Omega_y)$
	$\mathcal{C}_{\mathcal{X}_{\dot{\beta}_g}}(\Omega_y) = +\mathcal{C}^a_{\mathcal{X}_{\dot{\beta}_g}}(\Omega_y)$	$\mathcal{C}_{\mathcal{Z}_{\dot{\beta}_g}}(\Omega_y) = +\mathcal{C}^a_{\mathcal{Z}_{\dot{\beta}_g}}(\Omega_y)$	$\mathcal{C}_{m_{\dot{\beta}_g}}(\Omega_y) = -\mathcal{C}^a_{m_{\dot{\beta}_g}}(\Omega_y)$
α_g	$\mathcal{C}_{\mathcal{X}_{\alpha_g}}(\Omega_y) = -\mathcal{C}^a_{\mathcal{X}_{\alpha_g}}(\Omega_y)$	$\mathcal{C}_{\mathcal{Z}_{\alpha_g}}(\Omega_y) = -\mathcal{C}^a_{\mathcal{Z}_{\alpha_g}}(\Omega_y)$	$\mathcal{C}_{m_{\alpha_g}}(\Omega_y) = +\mathcal{C}^a_{m_{\alpha_g}}(\Omega_y)$
	$\mathcal{C}_{\mathcal{X}_{\dot{\alpha}_g}}(\Omega_y) = -\mathcal{C}^a_{\mathcal{X}_{\dot{\alpha}_g}}(\Omega_y)$	$\mathcal{C}_{\mathcal{Z}_{\dot{\alpha}_g}}(\Omega_y) = -\mathcal{C}^a_{\mathcal{Z}_{\dot{\alpha}_g}}(\Omega_y)$	$\mathcal{C}_{m_{\dot{\alpha}_g}}(\Omega_y) = +\mathcal{C}^a_{m_{\dot{\alpha}_g}}(\Omega_y)$

Table D.9: Definition of the frequency-dependent symmetrical gust derivatives for $\mathcal{F}_S$ in terms of the calculated frequency-dependent symmetrical aerodynamic gust derivatives for $\mathcal{F}_{aero}$, for 2D gust fields.

	C_Y	C_ℓ	C_n
$\hat{u}_g$	$\mathcal{C}_{\mathcal{Y}_{u_g}}(\Omega_y) = +\mathcal{C}^a_{\mathcal{Y}_{u_g}}(\Omega_y)$	$\mathcal{C}_{\ell_{u_g}}(\Omega_y) = -\mathcal{C}^a_{\ell_{u_g}}(\Omega_y)$	$\mathcal{C}_{n_{u_g}}(\Omega_y) = -\mathcal{C}^a_{n_{u_g}}(\Omega_y)$
	$\mathcal{C}_{\mathcal{Y}_{\dot{u}_g}}(\Omega_y) = +\mathcal{C}^a_{\mathcal{Y}_{\dot{u}_g}}(\Omega_y)$	$\mathcal{C}_{\ell_{\dot{u}_g}}(\Omega_y) = -\mathcal{C}^a_{\ell_{\dot{u}_g}}(\Omega_y)$	$\mathcal{C}_{n_{\dot{u}_g}}(\Omega_y) = -\mathcal{C}^a_{n_{\dot{u}_g}}(\Omega_y)$
β_g	$\mathcal{C}_{\mathcal{Y}_{\beta_g}}(\Omega_y) = -\mathcal{C}^a_{\mathcal{Y}_{\beta_g}}(\Omega_y)$	$\mathcal{C}_{\ell_{\beta_g}}(\Omega_y) = +\mathcal{C}^a_{\ell_{\beta_g}}(\Omega_y)$	$\mathcal{C}_{n_{\beta_g}}(\Omega_y) = +\mathcal{C}^a_{n_{\beta_g}}(\Omega_y)$
	$\mathcal{C}_{\mathcal{Y}_{\dot{\beta}_g}}(\Omega_y) = -\mathcal{C}^a_{\mathcal{Y}_{\dot{\beta}_g}}(\Omega_y)$	$\mathcal{C}_{\ell_{\dot{\beta}_g}}(\Omega_y) = +\mathcal{C}^a_{\ell_{\dot{\beta}_g}}(\Omega_y)$	$\mathcal{C}_{n_{\dot{\beta}_g}}(\Omega_y) = +\mathcal{C}^a_{n_{\dot{\beta}_g}}(\Omega_y)$
α_g	$\mathcal{C}_{\mathcal{Y}_{\alpha_g}}(\Omega_y) = +\mathcal{C}^a_{\mathcal{Y}_{\alpha_g}}(\Omega_y)$	$\mathcal{C}_{\ell_{\alpha_g}}(\Omega_y) = -\mathcal{C}^a_{\ell_{\alpha_g}}(\Omega_y)$	$\mathcal{C}_{n_{\alpha_g}}(\Omega_y) = -\mathcal{C}^a_{n_{\alpha_g}}(\Omega_y)$
	$\mathcal{C}_{\mathcal{Y}_{\dot{\alpha}_g}}(\Omega_y) = +\mathcal{C}^a_{\mathcal{Y}_{\dot{\alpha}_g}}(\Omega_y)$	$\mathcal{C}_{\ell_{\dot{\alpha}_g}}(\Omega_y) = -\mathcal{C}^a_{\ell_{\dot{\alpha}_g}}(\Omega_y)$	$\mathcal{C}_{n_{\dot{\alpha}_g}}(\Omega_y) = -\mathcal{C}^a_{n_{\dot{\alpha}_g}}(\Omega_y)$

Table D.10: Definition of the frequency-dependent asymmetrical gust derivatives for $\mathcal{F}_S$ in terms of the calculated frequency-dependent asymmetrical aerodynamic gust derivatives for $\mathcal{F}_{aero}$, for 2D gust fields.

	C_X	C_Z	C_m
$\hat{u}$	$C_{X_u} = \frac{\partial C_X}{\partial \hat{u}}$	$C_{Z_u} = \frac{\partial C_Z}{\partial \hat{u}}$	$C_{m_u} = \frac{\partial C_m}{\partial \hat{u}}$
α	$C_{X_\alpha} = \frac{\partial C_X}{\partial \alpha}$	$C_{Z_\alpha} = \frac{\partial C_Z}{\partial \alpha}$	$C_{m_\alpha} = \frac{\partial C_m}{\partial \alpha}$
$\frac{\dot{\alpha}\bar{c}}{2Q_\infty}$	$C_{X_{\dot{\alpha}}} = \frac{\partial C_X}{\partial \frac{\dot{\alpha}\bar{c}}{2Q_\infty}}$	$C_{Z_{\dot{\alpha}}} = \frac{\partial C_Z}{\partial \frac{\dot{\alpha}\bar{c}}{2Q_\infty}}$	$C_{m_{\dot{\alpha}}} = \frac{\partial C_m}{\partial \frac{\dot{\alpha}\bar{c}}{2Q_\infty}}$
$\frac{q\bar{c}}{2Q_\infty}$	$C_{X_q} = \frac{\partial C_X}{\partial \frac{q\bar{c}}{2Q_\infty}}$	$C_{Z_q} = \frac{\partial C_Z}{\partial \frac{q\bar{c}}{2Q_\infty}}$	$C_{m_q} = \frac{\partial C_m}{\partial \frac{q\bar{c}}{2Q_\infty}}$

Table D.11: Definition of the constant symmetrical stability derivatives for $\mathcal{F}_S$.

	C_Y	C_ℓ	C_n
β	$C_{Y_\beta} = \frac{\partial C_Y}{\partial \beta}$	$C_{\ell_\beta} = \frac{\partial C_\ell}{\partial \beta}$	$C_{n_\beta} = \frac{\partial C_n}{\partial \beta}$
$\frac{\dot{\beta}b}{2Q_\infty}$	$C_{Y_{\dot{\beta}}} = \frac{\partial C_Y}{\partial \frac{\dot{\beta}b}{2Q_\infty}}$	$C_{\ell_{\dot{\beta}}} = \frac{\partial C_\ell}{\partial \frac{\dot{\beta}b}{2Q_\infty}}$	$C_{n_{\dot{\beta}}} = \frac{\partial C_n}{\partial \frac{\dot{\beta}b}{2Q_\infty}}$
$\frac{pb}{2Q_\infty}$	$C_{Y_p} = \frac{\partial C_Y}{\partial \frac{pb}{2Q_\infty}}$	$C_{\ell_p} = \frac{\partial C_\ell}{\partial \frac{pb}{2Q_\infty}}$	$C_{n_p} = \frac{\partial C_n}{\partial \frac{pb}{2Q_\infty}}$
$\frac{rb}{2Q_\infty}$	$C_{Y_r} = \frac{\partial C_Y}{\partial \frac{rb}{2Q_\infty}}$	$C_{\ell_r} = \frac{\partial C_\ell}{\partial \frac{rb}{2Q_\infty}}$	$C_{n_r} = \frac{\partial C_n}{\partial \frac{rb}{2Q_\infty}}$

Table D.12: Definition of the constant asymmetrical stability derivatives for $\mathcal{F}_S$.

	C_X	C_Z	C_m
$\hat{u}_g$	$C_{X_{u_g}} = \frac{\partial C_X}{\partial \hat{u}_g}$	$C_{Z_{u_g}} = \frac{\partial C_Z}{\partial \hat{u}_g}$	$C_{m_{u_g}} = \frac{\partial C_m}{\partial \hat{u}_g}$
$\frac{\dot{\hat{u}}_g\bar{c}}{2Q_\infty}$	$C_{X_{\dot{\hat{u}}_g}} = \frac{\partial C_X}{\partial \frac{\dot{\hat{u}}_g\bar{c}}{2Q_\infty}}$	$C_{Z_{\dot{\hat{u}}_g}} = \frac{\partial C_Z}{\partial \frac{\dot{\hat{u}}_g\bar{c}}{2Q_\infty}}$	$C_{m_{\dot{\hat{u}}_g}} = \frac{\partial C_m}{\partial \frac{\dot{\hat{u}}_g\bar{c}}{2Q_\infty}}$
α_g	$C_{X_{\alpha_g}} = \frac{\partial C_X}{\partial \alpha_g}$	$C_{Z_{\alpha_g}} = \frac{\partial C_Z}{\partial \alpha_g}$	$C_{m_{\alpha_g}} = \frac{\partial C_m}{\partial \alpha_g}$
$\frac{\dot{\alpha}_g\bar{c}}{2Q_\infty}$	$C_{X_{\dot{\alpha}_g}} = \frac{\partial C_X}{\partial \frac{\dot{\alpha}_g\bar{c}}{2Q_\infty}}$	$C_{Z_{\dot{\alpha}_g}} = \frac{\partial C_Z}{\partial \frac{\dot{\alpha}_g\bar{c}}{2Q_\infty}}$	$C_{m_{\dot{\alpha}_g}} = \frac{\partial C_m}{\partial \frac{\dot{\alpha}_g\bar{c}}{2Q_\infty}}$

Table D.13: Definition of the constant symmetrical gust derivatives for $\mathcal{F}_S$.

	C_Y	C_ℓ	C_n
β_g	$C_{Y_{\beta_g}} = \frac{\partial C_Y}{\partial \beta_g}$	$C_{\ell_{\beta_g}} = \frac{\partial C_\ell}{\partial \beta_g}$	$C_{n_{\beta_g}} = \frac{\partial C_n}{\partial \beta_g}$
$\frac{\dot{\beta}_g b}{2Q_\infty}$	$C_{Y_{\dot{\beta}_g}} = \frac{\partial C_Y}{\partial \frac{\beta_g b}{2Q_\infty}}$	$C_{\ell_{\dot{\beta}_g}} = \frac{\partial C_\ell}{\partial \frac{\beta_g b}{2Q_\infty}}$	$C_{n_{\dot{\beta}_g}} = \frac{\partial C_n}{\partial \frac{\beta_g b}{2Q_\infty}}$

Table D.14: Definition of the constant asymmetrical gust derivatives for $\mathcal{F}_S$.

	C_X	C_Z	C_m
$\hat{u}$	$\mathcal{C}_{\mathcal{X}_u} = \frac{\partial C_X}{\partial \hat{u}}$	$\mathcal{C}_{\mathcal{Z}_u} = \frac{\partial C_Z}{\partial \hat{u}}$	$\mathcal{C}_{m_u} = \frac{\partial C_m}{\partial \hat{u}}$
	$\mathcal{C}_{\mathcal{X}_{\dot{u}}} = \frac{\partial C_X}{\partial \frac{\dot{u}\bar{c}}{2Q_\infty}}$	$\mathcal{C}_{\mathcal{Z}_{\dot{u}}} = \frac{\partial C_Z}{\partial \frac{\dot{u}\bar{c}}{2Q_\infty}}$	$\mathcal{C}_{m_{\dot{u}}} = \frac{\partial C_m}{\partial \frac{\dot{u}\bar{c}}{2Q_\infty}}$
α	$\mathcal{C}_{\mathcal{X}_\alpha} = \frac{\partial C_X}{\partial \alpha}$	$\mathcal{C}_{\mathcal{Z}_\alpha} = \frac{\partial C_Z}{\partial \alpha}$	$\mathcal{C}_{m_\alpha} = \frac{\partial C_m}{\partial \alpha}$
	$\mathcal{C}_{\mathcal{X}_{\dot{\alpha}}} = \frac{\partial C_X}{\partial \frac{\dot{\alpha}\bar{c}}{2Q_\infty}}$	$\mathcal{C}_{\mathcal{Z}_{\dot{\alpha}}} = \frac{\partial C_Z}{\partial \frac{\dot{\alpha}\bar{c}}{2Q_\infty}}$	$\mathcal{C}_{m_{\dot{\alpha}}} = \frac{\partial C_m}{\partial \frac{\dot{\alpha}\bar{c}}{2Q_\infty}}$

Table D.15: Definition of the frequency-dependent symmetrical stability derivatives for $\mathcal{F}_S$.

	C_Y	C_ℓ	C_n
β	$\mathcal{C}_{\mathcal{Y}_\beta} = \frac{\partial C_Y}{\partial \beta}$	$\mathcal{C}_{\ell_\beta} = \frac{\partial C_\ell}{\partial \beta}$	$\mathcal{C}_{n_\beta} = \frac{\partial C_n}{\partial \beta}$
	$\mathcal{C}_{\mathcal{Y}_{\dot{\beta}}} = \frac{\partial C_Y}{\partial \frac{\dot{\beta}\bar{c}}{2Q_\infty}}$	$\mathcal{C}_{\ell_{\dot{\beta}}} = \frac{\partial C_\ell}{\partial \frac{\dot{\beta}\bar{c}}{2Q_\infty}}$	$\mathcal{C}_{n_{\dot{\beta}}} = \frac{\partial C_n}{\partial \frac{\dot{\beta}\bar{c}}{2Q_\infty}}$

Table D.16: Definition of the frequency-dependent asymmetrical stability derivatives for $\mathcal{F}_S$.

	C_X	C_Z	C_m
$\hat{u}_g$	$\mathcal{C}_{\mathcal{X}_{u_g}} = \frac{\partial C_X}{\partial \hat{u}_g}$	$\mathcal{C}_{\mathcal{Z}_{u_g}} = \frac{\partial C_Z}{\partial \hat{u}_g}$	$\mathcal{C}_{m_{u_g}} = \frac{\partial C_m}{\partial \hat{u}_g}$
	$\mathcal{C}_{\mathcal{X}_{\dot{u}_g}} = \frac{\partial C_X}{\partial \frac{\dot{\hat{u}}_g \bar{c}}{2Q_\infty}}$	$\mathcal{C}_{\mathcal{Z}_{\dot{u}_g}} = \frac{\partial C_Z}{\partial \frac{\dot{\hat{u}}_g \bar{c}}{2Q_\infty}}$	$\mathcal{C}_{m_{\dot{u}_g}} = \frac{\partial C_m}{\partial \frac{\dot{\hat{u}}_g \bar{c}}{2Q_\infty}}$
β_g	$\mathcal{C}_{\mathcal{X}_{\beta_g}} = \frac{\partial C_X}{\partial \beta_g}$	$\mathcal{C}_{\mathcal{Z}_{\beta_g}} = \frac{\partial C_Z}{\partial \beta_g}$	$\mathcal{C}_{m_{\beta_g}} = \frac{\partial C_m}{\partial \beta_g}$
	$\mathcal{C}_{\mathcal{X}_{\dot{\beta}_g}} = \frac{\partial C_X}{\partial \frac{\dot{\beta}_g \bar{c}}{2Q_\infty}}$	$\mathcal{C}_{\mathcal{Z}_{\dot{\beta}_g}} = \frac{\partial C_Z}{\partial \frac{\dot{\beta}_g \bar{c}}{2Q_\infty}}$	$\mathcal{C}_{m_{\dot{\beta}_g}} = \frac{\partial C_m}{\partial \frac{\dot{\beta}_g \bar{c}}{2Q_\infty}}$
α_g	$\mathcal{C}_{\mathcal{X}_{\alpha_g}} = \frac{\partial C_X}{\partial \alpha_g}$	$\mathcal{C}_{\mathcal{Z}_{\alpha_g}} = \frac{\partial C_Z}{\partial \alpha_g}$	$\mathcal{C}_{m_{\alpha_g}} = \frac{\partial C_m}{\partial \alpha_g}$
	$\mathcal{C}_{\mathcal{X}_{\dot{\alpha}_g}} = \frac{\partial C_X}{\partial \frac{\dot{\alpha}_g \bar{c}}{2Q_\infty}}$	$\mathcal{C}_{\mathcal{Z}_{\dot{\alpha}_g}} = \frac{\partial C_Z}{\partial \frac{\dot{\alpha}_g \bar{c}}{2Q_\infty}}$	$\mathcal{C}_{m_{\dot{\alpha}_g}} = \frac{\partial C_m}{\partial \frac{\dot{\alpha}_g \bar{c}}{2Q_\infty}}$

Table D.17: Definition of the frequency-dependent symmetrical gust derivatives for $\mathcal{F}_S$, for 1D gust fields.

	C_Y	C_ℓ	C_n
$\hat{u}_g$	$\mathcal{C}_{\mathcal{Y}_{u_g}} = \frac{\partial C_Y}{\partial \hat{u}_g}$	$\mathcal{C}_{\ell_{u_g}} = \frac{\partial C_\ell}{\partial \hat{u}_g}$	$\mathcal{C}_{n_{u_g}} = \frac{\partial C_n}{\partial \hat{u}_g}$
	$\mathcal{C}_{\mathcal{Y}_{\dot{u}_g}} = \frac{\partial C_Y}{\partial \frac{\dot{\hat{u}}_g b}{2Q_\infty}}$	$\mathcal{C}_{\ell_{\dot{u}_g}} = \frac{\partial C_\ell}{\partial \frac{\dot{\hat{u}}_g b}{2Q_\infty}}$	$\mathcal{C}_{n_{\dot{u}_g}} = \frac{\partial C_n}{\partial \frac{\dot{\hat{u}}_g b}{2Q_\infty}}$
β_g	$\mathcal{C}_{\mathcal{Y}_{\beta_g}} = \frac{\partial C_Y}{\partial \beta_g}$	$\mathcal{C}_{\ell_{\beta_g}} = \frac{\partial C_\ell}{\partial \beta_g}$	$\mathcal{C}_{n_{\beta_g}} = \frac{\partial C_n}{\partial \beta_g}$
	$\mathcal{C}_{\mathcal{Y}_{\dot{\beta}_g}} = \frac{\partial C_Y}{\partial \frac{\dot{\beta}_g b}{2Q_\infty}}$	$\mathcal{C}_{\ell_{\dot{\beta}_g}} = \frac{\partial C_\ell}{\partial \frac{\dot{\beta}_g b}{2Q_\infty}}$	$\mathcal{C}_{n_{\dot{\beta}_g}} = \frac{\partial C_n}{\partial \frac{\dot{\beta}_g b}{2Q_\infty}}$
α_g	$\mathcal{C}_{\mathcal{Y}_{\alpha_g}} = \frac{\partial C_Y}{\partial \alpha_g}$	$\mathcal{C}_{\ell_{\alpha_g}} = \frac{\partial C_\ell}{\partial \alpha_g}$	$\mathcal{C}_{n_{\alpha_g}} = \frac{\partial C_n}{\partial \alpha_g}$
	$\mathcal{C}_{\mathcal{Y}_{\dot{\alpha}_g}} = \frac{\partial C_Y}{\partial \frac{\dot{\alpha}_g b}{2Q_\infty}}$	$\mathcal{C}_{\ell_{\dot{\alpha}_g}} = \frac{\partial C_\ell}{\partial \frac{\dot{\alpha}_g b}{2Q_\infty}}$	$\mathcal{C}_{n_{\dot{\alpha}_g}} = \frac{\partial C_n}{\partial \frac{\dot{\alpha}_g b}{2Q_\infty}}$

Table D.18: Definition of the frequency-dependent asymmetrical gust derivatives for $\mathcal{F}_S$, for 1D gust fields.

	C_X	C_Z	C_m
$\hat{u}_g$	$\mathcal{C}_{\mathcal{X}_{u_g}}(\Omega_y) = \frac{\partial C_X}{\partial \hat{u}_g}(\Omega_y)$	$\mathcal{C}_{\mathcal{Z}_{u_g}}(\Omega_y) = \frac{\partial C_Z}{\partial \hat{u}_g}(\Omega_y)$	$\mathcal{C}_{m_{u_g}}(\Omega_y) = \frac{\partial C_m}{\partial \hat{u}_g}(\Omega_y)$
	$\mathcal{C}_{\mathcal{X}_{\dot{u}_g}}(\Omega_y) = \frac{\partial C_X}{\partial \frac{\dot{\hat{u}}_g \bar{c}}{2Q_\infty}}(\Omega_y)$	$\mathcal{C}_{\mathcal{Z}_{\dot{u}_g}}(\Omega_y) = \frac{\partial C_Z}{\partial \frac{\dot{\hat{u}}_g \bar{c}}{2Q_\infty}}(\Omega_y)$	$\mathcal{C}_{m_{\dot{u}_g}}(\Omega_y) = \frac{\partial C_m}{\partial \frac{\dot{\hat{u}}_g \bar{c}}{2Q_\infty}}(\Omega_y)$
β_g	$\mathcal{C}_{\mathcal{X}_{\beta_g}}(\Omega_y) = \frac{\partial C_X}{\partial \beta_g}(\Omega_y)$	$\mathcal{C}_{\mathcal{Z}_{\beta_g}}(\Omega_y) = \frac{\partial C_Z}{\partial \beta_g}(\Omega_y)$	$\mathcal{C}_{m_{\beta_g}}(\Omega_y) = \frac{\partial C_m}{\partial \beta_g}(\Omega_y)$
	$\mathcal{C}_{\mathcal{X}_{\dot{\beta}_g}}(\Omega_y) = \frac{\partial C_X}{\partial \frac{\dot{\beta}_g \bar{c}}{2Q_\infty}}(\Omega_y)$	$\mathcal{C}_{\mathcal{Z}_{\dot{\beta}_g}}(\Omega_y) = \frac{\partial C_Z}{\partial \frac{\dot{\beta}_g \bar{c}}{2Q_\infty}}(\Omega_y)$	$\mathcal{C}_{m_{\dot{\beta}_g}}(\Omega_y) = \frac{\partial C_m}{\partial \frac{\dot{\beta}_g \bar{c}}{2Q_\infty}}(\Omega_y)$
α_g	$\mathcal{C}_{\mathcal{X}_{\alpha_g}}(\Omega_y) = \frac{\partial C_X}{\partial \alpha_g}(\Omega_y)$	$\mathcal{C}_{\mathcal{Z}_{\alpha_g}}(\Omega_y) = \frac{\partial C_Z}{\partial \alpha_g}(\Omega_y)$	$\mathcal{C}_{m_{\alpha_g}}(\Omega_y) = \frac{\partial C_m}{\partial \alpha_g}(\Omega_y)$
	$\mathcal{C}_{\mathcal{X}_{\dot{\alpha}_g}}(\Omega_y) = \frac{\partial C_X}{\partial \frac{\dot{\alpha}_g \bar{c}}{2Q_\infty}}(\Omega_y)$	$\mathcal{C}_{\mathcal{Z}_{\dot{\alpha}_g}}(\Omega_y) = \frac{\partial C_Z}{\partial \frac{\dot{\alpha}_g \bar{c}}{2Q_\infty}}(\Omega_y)$	$\mathcal{C}_{m_{\dot{\alpha}_g}}(\Omega_y) = \frac{\partial C_m}{\partial \frac{\dot{\alpha}_g \bar{c}}{2Q_\infty}}(\Omega_y)$

Table D.19: Definition of the frequency-dependent symmetrical gust derivatives for $\mathcal{F}_S$, for 2D gust fields.

	C_Y	C_ℓ	C_n
$\hat{u}_g$	$\mathcal{C}_{\mathcal{Y}_{u_g}}(\Omega_y) = \frac{\partial C_Y}{\partial \hat{u}_g}(\Omega_y)$	$\mathcal{C}_{\ell_{u_g}}(\Omega_y) = \frac{\partial C_\ell}{\partial \hat{u}_g}(\Omega_y)$	$\mathcal{C}_{n_{u_g}}(\Omega_y) = \frac{\partial C_n}{\partial \hat{u}_g}(\Omega_y)$
	$\mathcal{C}_{\mathcal{Y}_{\dot{u}_g}}(\Omega_y) = \frac{\partial C_Y}{\partial \frac{\dot{\hat{u}}_g b}{2Q_\infty}}(\Omega_y)$	$\mathcal{C}_{\ell_{\dot{u}_g}}(\Omega_y) = \frac{\partial C_\ell}{\partial \frac{\dot{\hat{u}}_g b}{2Q_\infty}}(\Omega_y)$	$\mathcal{C}_{n_{\dot{u}_g}}(\Omega_y) = \frac{\partial C_n}{\partial \frac{\dot{\hat{u}}_g b}{2Q_\infty}}(\Omega_y)$
β_g	$\mathcal{C}_{\mathcal{Y}_{\beta_g}}(\Omega_y) = \frac{\partial C_Y}{\partial \beta_g}(\Omega_y)$	$\mathcal{C}_{\ell_{\beta_g}}(\Omega_y) = \frac{\partial C_\ell}{\partial \beta_g}(\Omega_y)$	$\mathcal{C}_{n_{\beta_g}}(\Omega_y) = \frac{\partial C_n}{\partial \beta_g}(\Omega_y)$
	$\mathcal{C}_{\mathcal{Y}_{\dot{\beta}_g}}(\Omega_y) = \frac{\partial C_Y}{\partial \frac{\dot{\beta}_g b}{2Q_\infty}}(\Omega_y)$	$\mathcal{C}_{\ell_{\dot{\beta}_g}}(\Omega_y) = \frac{\partial C_\ell}{\partial \frac{\dot{\beta}_g b}{2Q_\infty}}(\Omega_y)$	$\mathcal{C}_{n_{\dot{\beta}_g}}(\Omega_y) = \frac{\partial C_n}{\partial \frac{\dot{\beta}_g b}{2Q_\infty}}(\Omega_y)$
α_g	$\mathcal{C}_{\mathcal{Y}_{\alpha_g}}(\Omega_y) = \frac{\partial C_Y}{\partial \alpha_g}(\Omega_y)$	$\mathcal{C}_{\ell_{\alpha_g}}(\Omega_y) = \frac{\partial C_\ell}{\partial \alpha_g}(\Omega_y)$	$\mathcal{C}_{n_{\alpha_g}}(\Omega_y) = \frac{\partial C_n}{\partial \alpha_g}(\Omega_y)$
	$\mathcal{C}_{\mathcal{Y}_{\dot{\alpha}_g}}(\Omega_y) = \frac{\partial C_Y}{\partial \frac{\dot{\alpha}_g b}{2Q_\infty}}(\Omega_y)$	$\mathcal{C}_{\ell_{\dot{\alpha}_g}}(\Omega_y) = \frac{\partial C_\ell}{\partial \frac{\dot{\alpha}_g b}{2Q_\infty}}(\Omega_y)$	$\mathcal{C}_{n_{\dot{\alpha}_g}}(\Omega_y) = \frac{\partial C_n}{\partial \frac{\dot{\alpha}_g b}{2Q_\infty}}(\Omega_y)$

Table D.20: Definition of the frequency-dependent asymmetrical gust derivatives for $\mathcal{F}_S$, for 2D gust fields.

Appendix E

Aerodynamic fitting procedures

E.1 Introduction

In this appendix the aerodynamic fitting-routines used for transforming time-domain results to simulated aerodynamic frequency-response data (or the so-called "frequency-response") is given. Also, the fitting-routines for the analytical expressions of the frequency-response data are given. The results are the analytical aerodynamic frequency-response functions, or the so-called "frequency-response functions" (FRFs), for short.

Aerodynamic frequency-response functions were obtained as a function of the reduced frequency $k = \frac{\omega \bar{c}}{2Q_\infty}$, see chapters 4, 5, 6, 7 and 8. To this end, the aerodynamic response in terms of both aerodynamic forces and moments (outputs) due to harmonically varying inputs were simulated using (Unsteady) Linearized Potential Flow in the time-domain. The inputs considered are aircraft motion perturbations and one- (1D) and two-dimensional (2D) atmospheric turbulence inputs.
For a number of reduced frequencies, $k = [k_1, \cdots, k_M]^T$, aerodynamic frequency-response data is calculated from both the harmonic input ánd the harmonic output. Since the time-domain simulations are extremely time-consuming, the number of reduced input-frequencies was limited. By using the aerodynamic frequency-response data, next the aerodynamic frequency-response function is estimated. This analytical function is also known as a "fit" of the aerodynamic frequency-response data, and the procedure for obtaining this fit will be referred to as "analytical continuation of frequency-response data".

Also, in this appendix the fit-procedure is given for Power Spectral Density (PSD) functions. This approximation (or fit) of PSD-functions is given in a form such that it allows the PSD-function to be transformed to the product of a frequency-response function multiplied by its complex-conjungate.

E.2 Frequency-response data extraction from time-domain simulations

For frequency-domain system identification purposes, the time-domain response of an output to a time-domain harmonically varying input is considered. Writing the input as $u(t)$ and the output as $y(t)$ a frequency-domain representation in terms of attenuation and phase-shift is obtained. The attenuation and phase-shift can be represented as a complex number which, in this thesis, is designated as the aerodynamic frequency-response dataset. In the following, the procedure for estimating the aerodynamic frequency-response data for the aerodynamic lift due to angle-of-attack perturbations $\frac{C_L}{\alpha}(k)$ is given as an example.

Consider the output of an unknown system such as the response of an aerofoil lift-coefficient $C_L(t)$ due to harmonically varying angle-of-attack perturbations
$\alpha(t) = \alpha_{max} sin(\omega\ t)$, for arbitrary circular frequencies ω. In this thesis, however, all aerodynamic responses are given as a function of the reduced frequency $k = \frac{\omega \bar{c}}{2Q_\infty}$, thus making,

$$\alpha(t) = \alpha_{max}\ sin\left(\frac{\omega \bar{c}}{2Q_\infty}\frac{2Q_\infty t}{\bar{c}}\right) = \alpha_{max}\ sin\left(k\frac{2Q_\infty t}{\bar{c}}\right)$$

with Q_∞ the magnitude of the airflow at infinity, α_{max} the amplitude of the angle-of-attack perturbation, and $\bar{c}$ the mean aerodynamic chord. The frequency-response of the unknown system is computed using both the harmonically varying input $\alpha(t)$ ánd the output corrected for its trim condition value, $\bar{C}_L(t) = C_L(t) - C_{L_{trim}}$. Knowing as a function of time both the input, $\alpha(t)$, ánd the output, $\bar{C}_L(t)$ (as obtained from Unsteady LPF simulations), in this thesis a mathematical model for the time-domain lift-coefficient is assumed as, (with the estimated lift-coefficient written as $\hat{C}_L(t)$),

$$\hat{C}_L(t) = \mathcal{C}_{\mathcal{L}_\alpha}(k)\ \alpha(t) + \mathcal{C}_{\mathcal{L}_{\dot{\alpha}}}(k)\ \frac{\dot{\alpha}(t)\bar{c}}{2Q_\infty} \tag{E.1}$$

with $\hat{C}_L(t)$ the model response, $\dot{\alpha}(t)$ the time derivative of the input $\alpha(t)$, and both $\mathcal{C}_{\mathcal{L}_\alpha}(k)$ and $\mathcal{C}_{\mathcal{L}_{\dot{\alpha}}}(k)$ the frequency-dependent steady and unsteady aerodynamic parameters, respectively. Note that in the case of this example for reduced frequency $k = 0$, the frequency-dependent aerodynamic parameter $\mathcal{C}_{\mathcal{L}_\alpha}$ equals C_{L_α} which is the lift-curve slope. The parameter C_{L_α} may be obtained from either windtunnel-experiments or flight tests.

Both the aerodynamic parameters $\mathcal{C}_{\mathcal{L}_\alpha}$ and $\mathcal{C}_{\mathcal{L}_{\dot{\alpha}}}$ are a function of the reduced frequency, k and they follow from a least-squares fit using equation (E.1). As mentioned before, the estimation of these unknown model parameters first requires a modification of the simulated time-domain response of $C_L(t)$ by correcting it for its mean value $C_{L_{trim}}$, or $\bar{C}_L(t) = C_L(t) - C_{L_{trim}}$. Next, the error between the simulated data and the model data is defined as,

$$\varepsilon(t) = \bar{C}_L(t) - \hat{C}_L(t) \tag{E.2}$$

or, using equation (E.1),

$$\varepsilon(t) = \bar{C}_L(t) - \mathcal{C}_{\mathcal{L}_\alpha}(k)\ \alpha(t) - \mathcal{C}_{\mathcal{L}_{\dot{\alpha}}}(k)\ \frac{\dot{\alpha}(t)\bar{c}}{2Q_\infty} \tag{E.3}$$

Estimation of the unknown parameters $\mathcal{C}_{\mathcal{L}_\alpha}(k)$ and $\mathcal{C}_{\mathcal{L}_{\dot{\alpha}}}(k)$, requires a definition of a cost-function designated as J,

$$J = \int_0^T \{\varepsilon(t)\}^2\ dt = \int_0^T \left\{\bar{C}_L(t) - \mathcal{C}_{\mathcal{L}_\alpha}(k)\ \alpha(t) - \mathcal{C}_{\mathcal{L}_{\dot{\alpha}}}(k)\ \frac{\dot{\alpha}(t)\bar{c}}{2Q_\infty}\right\}\ dt \tag{E.4}$$

with T the total simulation time. In this thesis the time-dependent harmonic response is calculated over a number of periods. Once a stationary harmonic response has been obtained, the last cycle of this response is used for the estimation of the frequency-dependent parameters. With T_{cycle} the period of the harmonic simulations, the integral in equation (E.4) should extend from $T - T_{cycle}$ to T, or,

$$J = \int_{T-T_{cycle}}^T \left\{\bar{C}_L(t) - \mathcal{C}_{\mathcal{L}_\alpha}(k)\ \alpha(t) - \mathcal{C}_{\mathcal{L}_{\dot{\alpha}}}(k)\ \frac{\dot{\alpha}(t)\bar{c}}{2Q_\infty}\right\}\ dt \tag{E.5}$$

Now, taking the partial derivatives of equation (E.4) with respect to the unknown model parameters $\mathcal{C}_{\mathcal{L}_\alpha}$ and $\mathcal{C}_{\mathcal{L}_{\dot{\alpha}}}$, $\frac{\partial J}{\partial \mathcal{C}_{\mathcal{L}_\alpha}}$ and $\frac{\partial J}{\partial \mathcal{C}_{\mathcal{L}_{\dot{\alpha}}}}$, respectively. Setting these partial derivatives to zero, the following equations are obtained,

$$\begin{aligned}
\frac{\partial J}{\partial \mathcal{C}_{\mathcal{L}_\alpha}} &= -2 \int_{T-T_{cycle}}^T \left\{\bar{C}_L(t) - \mathcal{C}_{\mathcal{L}_\alpha}(k)\ \alpha(t) - \mathcal{C}_{\mathcal{L}_{\dot{\alpha}}}(k)\ \frac{\dot{\alpha}(t)\bar{c}}{2Q_\infty}\right\}\ \alpha(t)\ dt = 0 \\
\frac{\partial J}{\partial \mathcal{C}_{\mathcal{L}_{\dot{\alpha}}}} &= -2 \int_{T-T_{cycle}}^T \left\{\bar{C}_L(t) - \mathcal{C}_{\mathcal{L}_\alpha}(k)\ \alpha(t) - \mathcal{C}_{\mathcal{L}_{\dot{\alpha}}}(k)\ \frac{\dot{\alpha}(t)\bar{c}}{2Q_\infty}\right\}\ \frac{\dot{\alpha}(t)\bar{c}}{2Q_\infty}\ dt = 0
\end{aligned}$$

or, in matrix notation,

$$\begin{bmatrix} \int_{T-T_{cycle}}^T \alpha(t)^2 dt & \int_{T-T_{cycle}}^T \alpha(t)\frac{\dot{\alpha}(t)\bar{c}}{2Q_\infty} dt \\ \int_{T-T_{cycle}}^T \alpha(t)\frac{\dot{\alpha}(t)\bar{c}}{2Q_\infty} dt & \int_{T-T_{cycle}}^T \left(\frac{\dot{\alpha}(t)\bar{c}}{2Q_\infty}\right)^2 dt \end{bmatrix} \begin{bmatrix} \mathcal{C}_{\mathcal{L}_\alpha}(k) \\ \mathcal{C}_{\mathcal{L}_{\dot{\alpha}}}(k) \end{bmatrix} = \begin{bmatrix} \int_{T-T_{cycle}}^T \bar{C}_L(t)\ \alpha(t) dt \\ \int_{T-T_{cycle}}^T \bar{C}_L(t)\ \frac{\dot{\alpha}(t)\bar{c}}{2Q_\infty} dt \end{bmatrix} \tag{E.6}$$

From equation (E.6) for all reduced frequencies, k, the unknown parameters $\mathcal{C}_{\mathcal{L}_\alpha}(k)$ and $\mathcal{C}_{\mathcal{L}_{\dot{\alpha}}}(k)$ are calculated by matrix-inversion. Using these results, the equivalent of equation (E.1) is now written as,

$$\hat{C_L} = \mathcal{C}_{\mathcal{L}_\alpha}(k)\ \alpha + \mathcal{C}_{\mathcal{L}_{\dot{\alpha}}}(k)\frac{\dot{\alpha}\bar{c}}{2Q_\infty} \tag{E.7}$$

or writing for $\frac{\dot{\alpha}\bar{c}}{2Q_\infty}$ its frequency-domain equivalent $\frac{j\omega\alpha\bar{c}}{2Q_\infty} = jk\,\alpha$, the sought aerodynamic frequency-response data $\frac{C_L}{\alpha}(k)$ is written as,

$$\frac{C_L}{\alpha}(k) = \mathcal{C}_{\mathcal{L}_\alpha}(k) + jk\,\mathcal{C}_{\mathcal{L}_{\dot{\alpha}}}(k) \tag{E.8}$$

Since the number of reduced frequencies is limited, the aerodynamic frequency-response data $\frac{C_L}{\alpha}(k)$ are approximated by an analytical function. The theory of this analytical continuation of frequency-response data is given in section E.3.

Also, it should be noted that all simulations are performed in discrete-time, resulting in a discrete-time equivalent form for equation (E.6),

$$\begin{bmatrix} \sum_{i=1}^{N_t} \alpha[i]^2 & \sum_{i=1}^{N_t} \alpha[i]\frac{\dot{\alpha}[i]\bar{c}}{2Q_\infty} \\ \sum_{i=1}^{N_t} \alpha[i]\frac{\dot{\alpha}[i]\bar{c}}{2Q_\infty} & \sum_{i=1}^{N_t} \left(\frac{\dot{\alpha}[i]\bar{c}}{2Q_\infty}\right)^2 \end{bmatrix} \begin{bmatrix} \mathcal{C}_{\mathcal{L}_\alpha}(k) \\ \mathcal{C}_{\mathcal{L}_{\dot{\alpha}}}(k) \end{bmatrix} = \begin{bmatrix} \sum_{i=1}^{N_t} \bar{C}_L[i]\;\alpha[i] \\ \sum_{i=1}^{N_t} \bar{C}_L[i]\;\frac{\dot{\alpha}[i]\bar{c}}{2Q_\infty} \end{bmatrix} \tag{E.9}$$

with $\alpha[i]$ the discrete-time angle-of-attack, $\frac{\dot{\alpha}[i]\bar{c}}{2Q_\infty}$ the discrete-time non-dimensional time derivative of the angle-of-attack, $C_L[i]$ the discrete-time lift coefficient, $i = 1 \cdots N_t$ the time-counter for the last harmonic cycle of the discrete-time simulation, and N_t the number of samples in the last cycle. Using matrix-inversion, the unknown model parameters are known.

The above procedure holds for the determination of all aerodynamic frequency-response data considered in this thesis.

E.3 1D Analytical continuation of frequency-response data

Since the aerodynamic frequency-response data are only given for a limited number of reduced frequencies, $k = [k_1, \cdots, k_M]^T$, an analytical frequency-response function is fitted through the available data using the frequency-response function,

$$\hat{H}(k) = A_0 + A_1\,jk + A_2\,\left(jk\right)^2 + \sum_{i=1}^{i=N} B_i \frac{jk}{jk + \beta_i} \tag{E.10}$$

with $\hat{H}(k)$ the estimated analytical frequency-response function, and A_0, A_1, A_2 the so-called "aerodynamic stiffness", "aerodynamic damping" and "aerodynamic inertia" parameters, respectively. The parameters $B_i,\ i = 1 \cdots N$, are the gains of the so-called "aerodynamic lag-functions" $\frac{jk}{jk+\beta_i}$, with $\beta_i,\ i = 1 \cdots N$, the poles of the lag-functions,

and N the number of lag-functions, see also reference [36]. The error between the simulated aerodynamic frequency-response data, $H(k)$, and the response of the estimated analytical frequency-response function, $\hat{H}(k)$, is defined as,

$$E(k) = \hat{H}(k) - H(k) \tag{E.11}$$

The error, equation (E.11), is minimized using the cost-function J, which is defined as,

$$J = \sum_{k=k_1}^{k=k_M} \left(Re\left\{\hat{H}(k) - H(k)\right\} + Im\left\{\hat{H}(k) - H(k)\right\}\right)^2 \tag{E.12}$$

with the reduced frequency-vector $k = [k_1, \cdots, k_M]^T$, and M the number of reduced frequencies. Additional weighing of the frequency-response data leads to the cost-function J_1,

$$J_1 = \sum_{k=k_1}^{k=k_M} W \left(Re\left\{\hat{H}(k) - H(k)\right\} + Im\left\{\hat{H}(k) - H(k)\right\}\right)^2 \tag{E.13}$$

with W the vector of weighing parameters, $W = [W_1, \cdots W_M,]^T$, and M the number of reduced frequencies.

The parameter vector $P = [A_0, A_1, A_2, B_1, B_2, B_3, \beta_1, \beta_2, \beta_3]^T$ is obtained by minimizing J_1 (see equation (E.13)) using MATLAB optimization function `fmins.m`.

As a final note for this section, the aerodynamic frequency-response data may also be approximated by a function omitting the aerodynamic damping-term, A_1, and the aerodynamic inertia-term, A_2, resulting in the function,

$$\hat{H}(k) = A_0 + \sum_{i=1}^{i=N} B_i \frac{jk}{jk + \beta_i} \tag{E.14}$$

For the estimation of the aerodynamic stiffness-term A_0, the parameters $B_i,\ i = 1 \cdots N$, and the poles $\beta_i,\ i = 1 \cdots N$, a similar procedure is followed as given in the above.

E.4 2D Analytical continuation of frequency-response data

In this thesis the aerodynamic frequency-response of aerodynamic forces and moments due to 2D atmospheric turbulence is also considered.

For example, consider the aerodynamic frequency-response of the non-dimensional rolling moment coefficient C_ℓ in $\mathcal{F}_S$ due to (non-dimensional) anti-symmetrical vertical 2D atmospheric turbulence $\alpha_g(k, \Omega_y) = \frac{w_g(k,\Omega_y)}{Q_\infty}$, given as $\frac{C_\ell}{\alpha_g}(k, \Omega_y)$. For all configuration col-

location points, the turbulence-input $\alpha_g(k,\Omega_y) = \frac{w_g(k,\Omega_y)}{Q_\infty}$ is written as (see also equation (5.27)),

$$\alpha_{g_{asym_i}}(t_n,\Omega_y) = \alpha_{g_{max}}\ sin\left(k\frac{2X_{col_i}(t_n)}{\bar{c}}\right)\ sin\left(\Omega_y\ Y_{col_i}(t_n)\right)$$

with $t_n = n\Delta t$ discrete-time, $k = \frac{\omega\bar{c}}{2Q_\infty} = \frac{\Omega_x\bar{c}}{2}$ the reduced frequency, $\Omega_x = \frac{2\pi}{\lambda_x}$ the spatial frequency along the X_I-axis, $\Omega_y = \frac{2\pi}{\lambda_y}$ the spatial frequency along the Y_I-axis, both $X_{col_i}(t_n)$ and $Y_{col_i}(t_n)$ the time-dependent x and y components of the position of all collocation points in the Inertial Frame of Reference $\mathcal{F}_I$, $i = 1\cdots N_B$ with N_B the number of configuration panels, and $\alpha_{g_{max}}$ the amplitude of the atmospheric turbulence component $\alpha_{g_{asym}}(t_n,\Omega_y)$.

For each reduced frequency k and each spatial frequency Ω_y, the aerodynamic frequency-response $\frac{C_\ell}{\alpha_g}(k,\Omega_y)$ is calculated using the procedure given in section E.2. For all spatial frequencies Ω_y the frequency-response data are now calculated using the reference-input for the center of gravity,

$$\alpha_{g_{c.g.}}(t_n) = \alpha_{g_{max}}\ sin\left(k\frac{2X_0(t_n)}{\bar{c}}\right)$$

with $X_0(t_n)$ the time-dependent position of the origin of $\mathcal{F}_{aero}$, O_{aero}, in the frame $\mathcal{F}_I$.

For arbitrary frequency-response data $H(k,\Omega_y)$, the aerodynamic frequency-response function $\hat{H}(k,\Omega_y)$ is approximated by,

$$\hat{H}(k,\Omega_y) = A_0(\Omega_y) + A_1(\Omega_y)(jk) + A_2(\Omega_y)(jk)^2 + \sum_{i=1}^{i=N} B_i(\Omega_y)\frac{jk}{jk+\beta_i(\Omega_y)} \tag{E.15}$$

with N the number of lag-terms, and parameters $A_0(\Omega_y)$, $A_1(\Omega_y)$ and $A_2(\Omega_y)$ given by,

$$\begin{aligned}
A_0(\Omega_y) &= A_{00} + A_{01}(\Omega_y) + A_{02}(\Omega_y)^2 + A_{03}(\Omega_y)^3 + A_{04}(\Omega_y)^4\\
A_1(\Omega_y) &= A_{10} + A_{11}(\Omega_y) + A_{12}(\Omega_y)^2 + A_{13}(\Omega_y)^3 + A_{14}(\Omega_y)^4\\
A_2(\Omega_y) &= A_{20} + A_{21}(\Omega_y) + A_{22}(\Omega_y)^2 + A_{23}(\Omega_y)^3 + A_{24}(\Omega_y)^4
\end{aligned}$$

and parameters $B_i(\Omega_y)$ and $\beta_i(\Omega_y)$ given by,

$$B_i(\Omega_y) = B_{i0} + B_{i1}(\Omega_y) + B_{i2}(\Omega_y)^2 + B_{i3}(\Omega_y)^3 + B_{i4}(\Omega_y)^4$$

and,

$$\beta_i(\Omega_y) = \beta_{i0} + \beta_{i1}(\Omega_y) + \beta_{i2}(\Omega_y)^2 + \beta_{i3}(\Omega_y)^3 + \beta_{i4}(\Omega_y)^4$$

respectively.

The parameter-matrix P is defined as the matrix of unknown parameters in equation (E.15),

$$P = \left[\begin{array}{ccccc} A_{00} & A_{01} & A_{02} & A_{03} & A_{04} \\ A_{10} & A_{11} & A_{12} & A_{13} & A_{14} \\ A_{20} & A_{21} & A_{22} & A_{23} & A_{24} \\ \hline B_{10} & B_{11} & B_{12} & B_{13} & B_{14} \\ \vdots & \vdots & \vdots & \vdots & \vdots \\ B_{i0} & B_{i1} & B_{i2} & B_{i3} & B_{i4} \\ \vdots & \vdots & \vdots & \vdots & \vdots \\ B_{N0} & B_{N1} & B_{N2} & B_{N3} & B_{N4} \\ \hline \beta_{10} & \beta_{11} & \beta_{12} & \beta_{13} & \beta_{14} \\ \vdots & \vdots & \vdots & \vdots & \vdots \\ \beta_{i0} & \beta_{i1} & \beta_{i2} & \beta_{i3} & \beta_{i4} \\ \vdots & \vdots & \vdots & \vdots & \vdots \\ \beta_{N0} & \beta_{N1} & \beta_{N2} & \beta_{N3} & \beta_{N4} \end{array}\right] \tag{E.16}$$

This matrix is estimated using a cost-function J_2, similar to equation (E.13), although both the frequency-response data and the frequency-response function now become a function of Ω_y as well,

$$J_2 = \sum_{k=k_1}^{k=k_M} \sum_{\Omega_y=\Omega_{y_1}}^{\Omega_y=\Omega_{y_L}} W \left(Re\left\{\hat{H}(k,\Omega_y) - H(k,\Omega_y)\right\} + Im\left\{\hat{H}(k,\Omega_y) - H(k,\Omega_y)\right\}\right)^2 \tag{E.17}$$

with $\hat{H}(k,\Omega_y)$ the analytical frequency-response function, $H(k,\Omega_y)$ the frequency-response data, the reduced frequency-vector $k = [k_1, \cdots, k_M]^T$, the spatial frequency-vector $\Omega_y = [\Omega_{y_1}, \cdots, \Omega_{y_L}]^T$, M the number of reduced frequencies, L the number of spatial frequencies, and W the matrix of weighing parameters, $W = [W_{ij}, i = 1 \cdots M, j = 1 \cdots L]^T$. The parameter-matrix P is obtained by minimizing J_2 using MATLAB optimization function `fmins.m`.

E.5 PSD-function fits

In this thesis the approximation (or fit) of PSD-functions is given in a form such that it allows the PSD-function to be transformed to the product of a frequency-response function multiplied by its complex-conjungate. Given as a function of the circular frequency ω ([Rad/sec]), the PSD-function data $S_{yy}(\omega)$ are approximated by the analytical PSD-function fit $\hat{S}_{yy}(\omega)$. For example, consider the scalar output y PSD-function approximation due to the scalar input u, $\hat{S}_{yy}(\omega)$. The Single-Input-Single-Output (SISO) system output PSD-function fit is written as, see also appendix B,

$$\hat{S}_{yy}(\omega) = \hat{H}^*_{yu}(\omega)\, \hat{H}_{yu}(\omega)\, S_{uu}(\omega) = \hat{H}_{yu}(-\omega)\, \hat{H}_{yu}(\omega)\, S_{uu}(\omega) = \left|\hat{H}_{yu}(\omega)\right|^2 S_{uu}(\omega)$$

with $\hat{S}_{yy}(\omega)$ the output PSD-function fit, $\hat{H}_{yu}(\omega)$ the estimated frequency-response function, $\hat{H}^*_{yu}(\omega)$ the complex-conjungate of the estimated frequency-response function, and $S_{uu}(\omega)$ the input PSD-function. For known input PSD-functions such as white noise ($S_{uu}(\omega) = S_{ww}(\omega) = 1$) the estimated output PSD-function is written as,

$$\hat{S}'_{yy}(\omega) = \hat{H}^*_{yu}(\omega)\ \hat{H}_{yu}(\omega) = \hat{H}_{yu}(-\omega)\ \hat{H}_{yu}(\omega) \tag{E.18}$$

with $\hat{S}'_{yy}(\omega)$ the estimated output PSD-function corrected for the input PSD-function. In this thesis the corrected estimated output PSD-function is approximated by the ratio of products of elementary functions,

$$\hat{S}'_{yy}(\omega) = \hat{S}'_{yy}(0)\ \frac{\prod_{k=1}^{n} \left\{1 + \tau^2_{num_k}\ \omega^2\right\}}{\prod_{l=1}^{m} \left\{1 + \tau^2_{den_l}\ \omega^2\right\}} \tag{E.19}$$

with $\hat{S}'_{yy}(0)$ the estimated output PSD-function value for $\omega = 0$, both $\tau^2_{num_k}$ and $\tau^2_{den_l}$ numerator and denominator parameters, respectively, and n and m the number of elementary functions used for the numerator and denominator polynomials, respectively. Using both equations (E.18) and (E.19), the frequency-response function given in equation (E.18) is written as,

$$\hat{H}_{yu}(\omega) = \sqrt{\hat{S}'_{yy}(0)}\ \frac{\prod_{k=1}^{n} \{1 + \tau_{num_k}\ j\omega\}}{\prod_{l=1}^{m} \{1 + \tau_{den_l}\ j\omega\}} \tag{E.20}$$

with $j = \sqrt{-1}$. For each PSD-function fit the parameters $\tau^2_{num_k}$, with $k = 1 \cdots n$, and $\tau^2_{den_l}$, with $l = 1 \cdots m$, are required to be positive. With this constraint, the rational filter given in equation (E.20) is both real in its parameters ánd stable. This analytical frequency-response function will be used for time-domain simulations presented in this thesis.

The PSD-function parameters $\tau^2_{num_k}$ and $\tau^2_{den_l}$ in equation (E.19) are estimated defining an error function,

$$E(\omega) = \hat{S}'_{yy}(\omega) - S'_{yy}(\omega) \tag{E.21}$$

with $\hat{S}'_{yy}(\omega)$ the estimated PSD-function and $S'_{yy}(\omega)$ the known PSD-function data (corrected for the input PSD-function). Using a cost-function J, similar to equation (E.13),

$$J = \sum_{\omega=\omega_1}^{\omega=\omega_M} \left(E(\omega)\right)^2 = \sum_{\omega=\omega_1}^{\omega=\omega_M} \left(\hat{S}'_{yy}(\omega) - S'_{yy}(\omega)\right)^2$$

with M the number of circular frequency-points, the unknown filter coefficients $\tau^2_{num_k}$ and $\tau^2_{den_l}$ are obtained using MATLAB optimization function `fmins.m`.

Appendix F

Aerodynamic fit parameters for 2D atmospheric turbulence inputs

F.1 Introduction

In this appendix the numerical values of the parameters of the two-dimensional (2D) function-fits with respect to 2D anti-symmetrical atmospheric turbulence are given. They will include the parameters for the aerodynamic frequency-response functions $\frac{C_Y}{\hat{u}_g}(k,\Omega_y)$, $\frac{C_\ell}{\hat{u}_g}(k,\Omega_y)$, $\frac{C_n}{\hat{u}_g}(k,\Omega_y)$, $\frac{C_Y}{\alpha_g}(k,\Omega_y)$, $\frac{C_\ell}{\alpha_g}(k,\Omega_y)$and $\frac{C_n}{\alpha_g}(k,\Omega_y)$. The parameters of all fits only hold for the trim condition defined in chapter 6.

The analytical function-fits have been discussed in appendix E, and the general approximating frequency-response function is given as, see also equation (E.15),

$$\hat{H}(k,\Omega_y) = A_0(\Omega_y) + A_1(\Omega_y)(jk) + A_2(\Omega_y)(jk)^2 + \sum_{i=1}^{i=N} B_i(\Omega_y)\frac{jk}{jk+\beta_i(\Omega_y)}$$

with $N=3$ the number of lag-terms, and parameters $A_0(\Omega_y)$, $A_1(\Omega_y)$ and $A_2(\Omega_y)$ given by,

$$\begin{aligned} A_0(\Omega_y) &= A_{00} + A_{01}(\Omega_y) + A_{02}(\Omega_y)^2 + A_{03}(\Omega_y)^3 + A_{04}(\Omega_y)^4 \\ A_1(\Omega_y) &= A_{10} + A_{11}(\Omega_y) + A_{12}(\Omega_y)^2 + A_{13}(\Omega_y)^3 + A_{14}(\Omega_y)^4 \\ A_2(\Omega_y) &= A_{20} + A_{21}(\Omega_y) + A_{22}(\Omega_y)^2 + A_{23}(\Omega_y)^3 + A_{24}(\Omega_y)^4 \end{aligned}$$

and coefficients $B_i(\Omega_y)$ and $\beta_i(\Omega_y)$ with $i = 1\cdots3$, given by,

$$B_i(\Omega_y) = B_{i0} + B_{i1}(\Omega_y) + B_{i2}(\Omega_y)^2 + B_{i3}(\Omega_y)^3 + B_{i4}(\Omega_y)^4$$

Aerodynamic function-fit coefficients					
	A_{00}	A_{01}	A_{02}	A_{03}	A_{04}
$\frac{C_Y}{\hat{u}_g}(k,\Omega_y)$	3.7152e-005	1.8720e+000	9.6985e-002	-3.1327e+000	3.0923e+000
$\frac{C_\ell}{\hat{u}_g}(k,\Omega_y)$	-4.0504e-005	-4.0579e-001	-1.0086e-001	2.9920e+000	-2.7981e+000
$\frac{C_n}{\hat{u}_g}(k,\Omega_y)$	-4.3174e-008	2.1435e-003	2.6176e-004	-3.3836e-003	2.6923e-002
$\frac{C_Y}{\alpha_g}(k,\Omega_y)$	-5.1333e-006	2.5735e-001	-1.6254e-002	3.8472e-001	-6.3045e-001
$\frac{C_\ell}{\alpha_g}(k,\Omega_y)$	-3.1649e-004	-3.9759e+000	-8.4058e-001	2.7304e+001	-2.6072e+001
$\frac{C_n}{\alpha_g}(k,\Omega_y)$	-1.9262e-005	-2.5849e-001	-4.8798e-002	1.5101e+000	-1.3944e+000
	A_{10}	A_{11}	A_{12}	A_{13}	A_{14}
$\frac{C_Y}{\hat{u}_g}(k,\Omega_y)$	-1.1411e-001	-2.0241e-001	-7.0084e-001	-7.3376e-001	5.1534e+000
$\frac{C_\ell}{\hat{u}_g}(k,\Omega_y)$	-2.9822e-004	-2.6963e-003	-2.7507e-001	6.8418e-001	-1.8069e-001
$\frac{C_n}{\hat{u}_g}(k,\Omega_y)$	-1.9511e-002	-5.1642e-001	-1.2406e+000	6.6871e-001	5.2422e-001
$\frac{C_Y}{\alpha_g}(k,\Omega_y)$	4.8930e-003	8.8408e-001	-1.0434e+000	3.3686e-001	-1.8774e+000
$\frac{C_\ell}{\alpha_g}(k,\Omega_y)$	4.7923e-001	-1.0185e+000	8.5750e+000	-1.2214e+000	1.4741e+001
$\frac{C_n}{\alpha_g}(k,\Omega_y)$	-8.9859e-004	-2.2392e-001	8.4731e-002	1.3529e-001	1.5273e-001
	A_{20}	A_{21}	A_{22}	A_{23}	A_{24}
$\frac{C_Y}{\hat{u}_g}(k,\Omega_y)$	-1.7900e-001	1.1252e+000	-2.0654e+000	5.4169e+000	-1.2216e+001
$\frac{C_\ell}{\hat{u}_g}(k,\Omega_y)$	7.3920e-004	-1.2903e-001	6.5948e-001	-9.9159e-001	4.4843e-002
$\frac{C_n}{\hat{u}_g}(k,\Omega_y)$	2.8035e-002	-9.0963e-002	7.1509e-001	-9.3869e-001	1.0637e+000
$\frac{C_Y}{\alpha_g}(k,\Omega_y)$	-3.7277e-002	6.2522e-002	-5.7261e+000	5.5062e-001	1.0400e+001
$\frac{C_\ell}{\alpha_g}(k,\Omega_y)$	8.3538e-001	8.8978e-001	5.5153e-001	6.9167e+000	-7.2679e+000
$\frac{C_n}{\alpha_g}(k,\Omega_y)$	6.5638e-004	2.2701e-001	-3.0168e-001	1.2109e-001	-3.2110e-001

Table F.1: Calculated coefficients for the aerodynamic function-fits with respect to anti-symmetrical 2D atmospheric turbulence, $\frac{C_Y}{\hat{u}_g}(k,\Omega_y)$, $\frac{C_\ell}{\hat{u}_g}(k,\Omega_y)$, $\frac{C_n}{\hat{u}_g}(k,\Omega_y)$, $\frac{C_Y}{\alpha_g}(k,\Omega_y)$, $\frac{C_\ell}{\alpha_g}(k,\Omega_y)$and $\frac{C_n}{\alpha_g}(k,\Omega_y)$, as given in equation (E.15).

and poles,

$$\beta_i(\Omega_y) = \beta_{i0} + \beta_{i1}(\Omega_y) + \beta_{i2}(\Omega_y)^2 + \beta_{i3}(\Omega_y)^3 + \beta_{i4}(\Omega_y)^4$$

respectively.

F.2 Parameter tables

In the following the parameter values for all aerodynamic frequency-response functions with respect to 2D anti-symmetrical atmospheric turbulence fields are summarized in tables.

Aerodynamic function-fit coefficients					
	B_{10}	B_{11}	B_{12}	B_{13}	B_{14}
$\frac{C_Y}{\hat{u}_g}(k,\Omega_y)$	-3.0313e-002	-1.1737e+000	1.3596e+000	-1.0421e+000	-2.7345e+000
$\frac{C_\ell}{\hat{u}_g}(k,\Omega_y)$	2.4008e-002	-5.6848e-004	-4.0470e-002	1.2034e-002	-1.6769e-001
$\frac{C_n}{\hat{u}_g}(k,\Omega_y)$	-5.7761e-003	1.7976e-001	2.5743e-001	1.2767e+000	-4.8594e-001
$\frac{C_Y}{\alpha_g}(k,\Omega_y)$	-3.7678e-003	-1.9132e-001	-7.0485e-002	1.0917e-001	-2.2891e+000
$\frac{C_\ell}{\alpha_g}(k,\Omega_y)$	1.4955e+000	6.8332e+000	1.2670e+001	3.9993e+001	7.2258e+000
$\frac{C_n}{\alpha_g}(k,\Omega_y)$	1.5988e-002	2.4204e-001	7.6877e-003	-1.5557e-001	3.8032e-001
	B_{20}	B_{21}	B_{22}	B_{23}	B_{24}
$\frac{C_Y}{\hat{u}_g}(k,\Omega_y)$	-1.9697e-001	-8.4394e-001	-7.4701e-001	-1.0472e+000	-1.4216e+000
$\frac{C_\ell}{\hat{u}_g}(k,\Omega_y)$	-2.3897e-002	-8.2244e-003	8.9490e-002	9.9361e-002	-6.3074e-001
$\frac{C_n}{\hat{u}_g}(k,\Omega_y)$	3.3575e-002	2.6892e-002	2.6409e-001	-1.2168e-001	7.4817e-001
$\frac{C_Y}{\alpha_g}(k,\Omega_y)$	2.5256e-003	2.8252e-001	4.3688e-001	-4.1756e+000	4.6520e+000
$\frac{C_\ell}{\alpha_g}(k,\Omega_y)$	-9.9278e-002	2.6429e+000	-2.7820e+000	-5.3637e+000	3.5003e+000
$\frac{C_n}{\alpha_g}(k,\Omega_y)$	-1.1781e-001	6.9875e-002	-2.2094e-001	3.8694e-001	-4.9666e-001
	B_{30}	B_{31}	B_{32}	B_{33}	B_{34}
$\frac{C_Y}{\hat{u}_g}(k,\Omega_y)$	2.3173e-002	-2.5485e-001	2.4924e-001	4.7421e+000	-1.5676e+001
$\frac{C_\ell}{\hat{u}_g}(k,\Omega_y)$	2.0316e-004	-2.7689e-001	4.6052e-001	2.8101e-001	-7.6655e-001
$\frac{C_n}{\hat{u}_g}(k,\Omega_y)$	4.7515e-003	-4.9359e-001	-2.4842e-001	-1.3054e+000	2.6388e+000
$\frac{C_Y}{\alpha_g}(k,\Omega_y)$	-6.1338e-003	-8.5915e-001	4.5056e-001	-1.6411e+000	3.6413e+000
$\frac{C_\ell}{\alpha_g}(k,\Omega_y)$	4.4526e-001	4.6611e+000	-2.1274e+000	-8.0935e+000	2.3806e+000
$\frac{C_n}{\alpha_g}(k,\Omega_y)$	1.0183e-001	4.0390e-002	-2.2763e-001	-3.5457e-002	-2.5102e-001

Table F.2: Calculated lag term coefficients for the aerodynamic function-fits with respect to anti-symmetrical 2D atmospheric turbulence, $\frac{C_Y}{\hat{u}_g}(k,\Omega_y)$, $\frac{C_\ell}{\hat{u}_g}(k,\Omega_y)$, $\frac{C_n}{\hat{u}_g}(k,\Omega_y)$, $\frac{C_Y}{\alpha_g}(k,\Omega_y)$, $\frac{C_\ell}{\alpha_g}(k,\Omega_y)$and $\frac{C_n}{\alpha_g}(k,\Omega_y)$, as given in equation (E.15).

Aerodynamic function-fit coefficients					
	β_{10}	β_{11}	β_{12}	β_{13}	β_{14}
$\frac{C_Y}{\hat{u}_g}(k,\Omega_y)$	6.0118e-001	-2.6689e-001	-8.3662e-002	1.5039e+000	-8.3364e-001
$\frac{C_\ell}{\hat{u}_g}(k,\Omega_y)$	4.4298e-002	1.7206e-001	1.4478e+000	-7.8679e-001	2.1165e-001
$\frac{C_n}{\hat{u}_g}(k,\Omega_y)$	4.5627e-001	3.6885e-001	-1.8137e-001	2.7475e-001	6.6800e-001
$\frac{C_Y}{\alpha_g}(k,\Omega_y)$	-2.2495e-002	-4.4450e-001	-2.1966e+000	-7.6975e-001	-3.8563e-001
$\frac{C_\ell}{\alpha_g}(k,\Omega_y)$	-1.6924e+000	-4.3145e+000	8.5159e-003	5.0297e+000	-3.2872e+000
$\frac{C_n}{\alpha_g}(k,\Omega_y)$	1.1981e-001	2.2258e-001	2.8597e-002	-6.1494e-001	2.2625e-002
	β_{20}	β_{21}	β_{22}	β_{23}	β_{24}
$\frac{C_Y}{\hat{u}_g}(k,\Omega_y)$	-9.1623e-001	1.4164e+000	-2.5701e+000	-2.8658e-001	2.5327e+000
$\frac{C_\ell}{\hat{u}_g}(k,\Omega_y)$	4.3484e-002	2.3956e-001	7.6863e-001	5.8756e-002	2.4994e+000
$\frac{C_n}{\hat{u}_g}(k,\Omega_y)$	8.7284e-001	-1.9588e+000	4.6070e+000	6.5116e+000	3.2866e+000
$\frac{C_Y}{\alpha_g}(k,\Omega_y)$	-6.6314e-003	-1.0487e+000	1.0646e+000	2.9802e-002	1.4324e+000
$\frac{C_\ell}{\alpha_g}(k,\Omega_y)$	6.9021e+000	-2.2395e+000	2.3387e+001	-8.1407e+001	1.7826e-002
$\frac{C_n}{\alpha_g}(k,\Omega_y)$	1.5364e-001	-1.4999e-001	4.5420e-001	-2.3866e-001	-4.2164e-001
	β_{30}	β_{31}	β_{32}	β_{33}	β_{34}
$\frac{C_Y}{\hat{u}_g}(k,\Omega_y)$	-4.1847e-001	1.6882e+000	1.0543e+001	-1.2482e+001	2.8930e+000
$\frac{C_\ell}{\hat{u}_g}(k,\Omega_y)$	-1.7626e+000	1.8964e+000	2.9387e-003	-3.9593e+000	6.6853e+000
$\frac{C_n}{\hat{u}_g}(k,\Omega_y)$	-6.8509e-001	6.7211e-002	-1.3079e+000	1.1371e+000	1.2064e+000
$\frac{C_Y}{\alpha_g}(k,\Omega_y)$	2.8428e-001	-5.0467e-001	2.1801e+000	-2.1744e+000	3.0339e-001
$\frac{C_\ell}{\alpha_g}(k,\Omega_y)$	1.0261e+000	-7.6505e-001	2.2602e+000	-6.9922e-001	-2.7531e+000
$\frac{C_n}{\alpha_g}(k,\Omega_y)$	1.6054e-001	5.2404e-002	-5.2520e-002	-7.3141e-001	1.6805e+000

Table F.3: Calculated poles for the aerodynamic function-fits with respect to anti-symmetrical 2D atmospheric turbulence, $\frac{C_Y}{\hat{u}_g}(k,\Omega_y)$, $\frac{C_\ell}{\hat{u}_g}(k,\Omega_y)$, $\frac{C_n}{\hat{u}_g}(k,\Omega_y)$, $\frac{C_Y}{\alpha_g}(k,\Omega_y)$, $\frac{C_\ell}{\alpha_g}(k,\Omega_y)$and $\frac{C_n}{\alpha_g}(k,\Omega_y)$, as given in equation (E.15).

Appendix G

Spatial-domain gust fields, the flightpath definition and aerodynamic model gust inputs

G.1 Introduction

In this appendix the theory for generating spatial-domain two-dimensional (2D) gust fields will be discussed first. Starting from the theory for the simulation of the three-dimensional (3D) correlated gust velocity components (see also chapter 2), these 2D gust fields are derived for the longitudinal gust u_g, the lateral gust v_g and the vertical gust w_g. These fields are given as a function of the position in the Earth-Fixed Frame of Reference $\mathcal{F}_E$, that is $u_g(X^E, Y^E)$, $v_g(X^E, Y^E)$ and $w_g(X^E, Y^E)$, with X^E and Y^E the position along the X_E- and Y_E-axis of $\mathcal{F}_E$, respectively (note that these gust velocity components are constant along the Z_E-axis of $\mathcal{F}_E$). The theory for generating these gust fields relies on the assumptions made in chapter 2. Results for both uncorrelated - and correlated gust fields will be given in this appendix. Also, the 2D gust fields will be verified by comparing the calculated gust velocity components' covariance functions to the theoretical ones according to Dryden as given in chapter 2.
Next in this appendix the definition of the flightpath for the aircraft flying through the 2D gust fields is given, along with the definition of both the symmetric and anti-symmetric 2D gust fields. These fields are decompositions of the true gust fields encountered along the flightpath and they are used as inputs for the time-domain aerodynamic models presented in this thesis.
Finally, in this appendix the definition of the aerodynamic model gust inputs is given.

G.2 The generation of spatial-domain gust fields

G.2.1 3D Correlated gust fields

For the generation of gust fields in the spatial-domain, use is made of the theory given in chapter 2. For the frame $\mathcal{F}_E$ the atmospheric turbulence PSD-matrix for correlated gust velocity components u_g, v_g and w_g is given in equation (2.24), and it is now written as,

$$S_{\underline{uu}}(\underline{\Omega} L_g) = \begin{bmatrix} S_{u_g u_g}(\underline{\Omega} L_g) & S_{u_g v_g}(\underline{\Omega} L_g) & S_{u_g w_g}(\underline{\Omega} L_g) \\ S_{v_g u_g}(\underline{\Omega} L_g) & S_{v_g v_g}(\underline{\Omega} L_g) & S_{v_g w_g}(\underline{\Omega} L_g) \\ S_{w_g u_g}(\underline{\Omega} L_g) & S_{w_g v_g}(\underline{\Omega} L_g) & S_{w_g w_g}(\underline{\Omega} L_g) \end{bmatrix} \tag{G.1}$$

with $\underline{u} = [u_g, v_g, w_g]^T$, $\underline{\Omega} L_g = [\Omega_x L_g, \Omega_y L_g, \Omega_z L_g]$, with $\Omega_x L_g$ the non-dimensional spatial frequency along the X_E-axis of the frame $\mathcal{F}_E$, $\Omega_y L_g$ the non-dimensional spatial frequency along the Y_E-axis of $\mathcal{F}_E$, $\Omega_z L_g$ the non-dimensional spatial frequency along the Z_E-axis of $\mathcal{F}_E$ and L_g the gust scale length in [m]. It should be noted that the atmospheric turbulence PSD-matrix for the correlated gust velocity components given in equation (G.1) is real in both the auto- and cross-spectra.

For the simulation of the spatial-domain atmospheric turbulence velocity components, use is made of three independent noise sources (here produced using MATLAB's noise generator `randn.m`). The noise sources are the input for the system of which the frequency-response matrix $\underline{H}(\underline{\Omega} L_g)$ is defined according to,

$$S_{\underline{uu}}(\underline{\Omega} L_g) = \underline{H}^*(\underline{\Omega} L_g)\; S_{\underline{ww}}(\underline{\Omega} L_g)\; \underline{H}^T(\underline{\Omega} L_g) = \underline{H}^*(\underline{\Omega} L_g)\; \underline{H}^T(\underline{\Omega} L_g) \tag{G.2}$$

with $\underline{H}^*(\underline{\Omega} L_g)$ the complex conjungate of $\underline{H}(\underline{\Omega} L_g)$, $\underline{H}^T(\underline{\Omega} L_g)$ the transpose of $\underline{H}(\underline{\Omega} L_g)$ and $S_{\underline{ww}}(\underline{\Omega} L_g)$ the constant (white-) noise input PSD-matrix of intensity one (I) with I the identity matrix. The frequency-response matrix $\underline{H}(\underline{\Omega} L_g)$ is given as (see also reference [1]),

$$\underline{H}(\underline{\Omega} L_g) = \begin{bmatrix} H_{11}(\underline{\Omega} L_g) & 0 & 0 \\ H_{21}(\underline{\Omega} L_g) & H_{22}(\underline{\Omega} L_g) & 0 \\ H_{31}(\underline{\Omega} L_g) & H_{32}(\underline{\Omega} L_g) & H_{33}(\underline{\Omega} L_g) \end{bmatrix} \tag{G.3}$$

or when used for equation (G.2),

$$\begin{bmatrix} H^*_{11}(\underline{\Omega} L_g) & 0 & 0 \\ H^*_{21}(\underline{\Omega} L_g) & H^*_{22}(\underline{\Omega} L_g) & 0 \\ H^*_{31}(\underline{\Omega} L_g) & H^*_{32}(\underline{\Omega} L_g) & H^*_{33}(\underline{\Omega} L_g) \end{bmatrix} \begin{bmatrix} H_{11}(\underline{\Omega} L_g) & H_{21}(\underline{\Omega} L_g) & H_{31}(\underline{\Omega} L_g) \\ 0 & H_{22}(\underline{\Omega} L_g) & H_{32}(\underline{\Omega} L_g) \\ 0 & 0 & H_{33}(\underline{\Omega} L_g) \end{bmatrix} =$$

$$= \begin{bmatrix} S_{u_g u_g}(\underline{\Omega} L_g) & S_{u_g v_g}(\underline{\Omega} L_g) & S_{u_g w_g}(\underline{\Omega} L_g) \\ S_{v_g u_g}(\underline{\Omega} L_g) & S_{v_g v_g}(\underline{\Omega} L_g) & S_{v_g w_g}(\underline{\Omega} L_g) \\ S_{w_g u_g}(\underline{\Omega} L_g) & S_{w_g v_g}(\underline{\Omega} L_g) & S_{w_g w_g}(\underline{\Omega} L_g) \end{bmatrix} \tag{G.4}$$

with,

$$\begin{aligned} H_{11}(\underline{\Omega}L_g) &= \sqrt{S_{u_g u_g}(\underline{\Omega}L_g)} \\ H_{21}(\underline{\Omega}L_g) &= \frac{S_{u_g v_g}(\underline{\Omega}L_g)}{\sqrt{S_{u_g u_g}(\underline{\Omega}L_g)}} \\ H_{31}(\underline{\Omega}L_g) &= \frac{S_{u_g w_g}(\underline{\Omega}L_g)}{\sqrt{S_{u_g u_g}(\underline{\Omega}L_g)}} \end{aligned} \tag{G.5}$$

$$\begin{aligned} H_{22}(\underline{\Omega}L_g) &= \sqrt{S_{v_g v_g}(\underline{\Omega}L_g) - \frac{S^2_{u_g v_g}(\underline{\Omega}L_g)}{S_{u_g u_g}(\underline{\Omega}L_g)}} \\ H_{32}(\underline{\Omega}L_g) &= \frac{S_{w_g v_g}(\underline{\Omega}L_g) - \frac{S_{u_g v_g}(\underline{\Omega}L_g)\ S_{u_g w_g}(\underline{\Omega}L_g)}{S_{u_g u_g}(\underline{\Omega}L_g)}}{H_{22}(\underline{\Omega}L_g)} \\ H_{33}(\underline{\Omega}L_g) &= \sqrt{S_{w_g w_g}(\underline{\Omega}L_g) - H^2_{31}(\underline{\Omega}L_g) - H^2_{32}(\underline{\Omega}L_g)} \end{aligned}$$

For the frequency-domain, the gust velocity components $U_g(\underline{\Omega}L_g)$, $V_g(\underline{\Omega}L_g)$ and $W_g(\underline{\Omega}L_g)$ are calculated from,

$$\begin{bmatrix} U_g(\underline{\Omega}L_g) \\ V_g(\underline{\Omega}L_g) \\ W_g(\underline{\Omega}L_g) \end{bmatrix} = \begin{bmatrix} H_{11}(\underline{\Omega}L_g) & 0 & 0 \\ H_{21}(\underline{\Omega}L_g) & H_{22}(\underline{\Omega}L_g) & 0 \\ H_{31}(\underline{\Omega}L_g) & H_{32}(\underline{\Omega}L_g) & H_{33}(\underline{\Omega}L_g) \end{bmatrix} \begin{bmatrix} W_{n_{u_g}}(\underline{\Omega}L_g) \\ W_{n_{v_g}}(\underline{\Omega}L_g) \\ W_{n_{w_g}}(\underline{\Omega}L_g) \end{bmatrix} \tag{G.6}$$

or,

$$U_g(\underline{\Omega}L_g) = H_{11}(\underline{\Omega}L_g)\ W_{n_{u_g}}(\underline{\Omega}L_g) \tag{G.7}$$

$$V_g(\underline{\Omega}L_g) = H_{21}(\underline{\Omega}L_g)\ W_{n_{u_g}}(\underline{\Omega}L_g) + H_{22}(\underline{\Omega}L_g)\ W_{n_{v_g}}(\underline{\Omega}L_g) \tag{G.8}$$

$$W_g(\underline{\Omega}L_g) = H_{31}(\underline{\Omega}L_g)\ W_{n_{u_g}}(\underline{\Omega}L_g) + H_{32}(\underline{\Omega}L_g)\ W_{n_{v_g}}(\underline{\Omega}L_g) + H_{33}(\underline{\Omega}L_g)\ W_{n_{w_g}}(\underline{\Omega}L_g) \tag{G.9}$$

with in equations (G.6), (G.7), (G.8), (G.9), $W_{n_{u_g}}(\underline{\Omega}L_g)$, $W_{n_{v_g}}(\underline{\Omega}L_g)$ and $W_{n_{w_g}}(\underline{\Omega}L_g)$ the independent frequency-domain noise-matrices. Although 3D gusts (as a function of the non-dimensional spatial frequencies $\underline{\Omega}L_g = [\Omega_x L_g, \Omega_y L_g, \Omega_z L_g]$) are not considered in this thesis, these noise-matrices can be obtained using a 3D Fourier-transform of the spatial-domain "white-noise" matrices $w_{n_{u_g}}\left(\frac{X^E}{L_g}, \frac{Y^E}{L_g}, \frac{Z^E}{L_g}\right)$, $w_{n_{v_g}}\left(\frac{X^E}{L_g}, \frac{Y^E}{L_g}, \frac{Z^E}{L_g}\right)$ and $w_{n_{w_g}}\left(\frac{X^E}{L_g}, \frac{Y^E}{L_g}, \frac{Z^E}{L_g}\right)$. See appendix B for details with respect to the 3D Fourier-transform.

The frequency-domain gust velocity components $U_g(\underline{\Omega}L_g)$, $V_g(\underline{\Omega}L_g)$ and $W_g(\underline{\Omega}L_g)$ are transformed into the spatial-domain using the inverse 3D Fourier-transform, resulting in the correlated spatial-domain gust velocity components $u_g\left(\frac{X^E}{L_g}, \frac{Y^E}{L_g}, \frac{Z^E}{L_g}\right)$, $v_g\left(\frac{X^E}{L_g}, \frac{Y^E}{L_g}, \frac{Z^E}{L_g}\right)$

and $w_g\left(\frac{X^E}{L_g}, \frac{Y^E}{L_g}, \frac{Z^E}{L_g}\right)$, with $\frac{X^E}{L_g}$, $\frac{Y^E}{L_g}$ and $\frac{Z^E}{L_g}$ the non-dimensional positions along the X_E-, Y_E- and Z_E-axis of the frame $\mathcal{F}_E$, respectively.

In sections G.2.2 and G.2.3 examples of 2D uncorrelated - and correlated gust fields will be given, respectively. In section G.2.4 numerical simulation results for both 2D uncorrelated and correlated gust fields will be given.

G.2.2 2D Uncorrelated gust fields

For the generation of uncorrelated 2D gust fields use is made of the theory given in chapter 2 and section G.2.1. Now, the gust velocity components u_g, v_g and w_g are only allowed to vary along the X_E- and Y_E-axis of the frame $\mathcal{F}_E$, and for each position in the $O_E X_E Y_E$-plane they are assumed constant along the Z_E-axis of $\mathcal{F}_E$. For the frame $\mathcal{F}_E$ equation (2.33) is now written as,

$$S_{\underline{u}\underline{u}}(\Omega_x L_g, \Omega_y L_g) = \tag{G.10}$$

$$= \frac{\pi\sigma^2}{\left(1+\Omega_x^2 L_g^2 + \Omega_y^2 L_g^2\right)^{5/2}} \begin{bmatrix} 1+\Omega_x^2 L_g^2 + 4\Omega_y^2 L_g^2 & 0 & 0 \\ 0 & 1+4\Omega_x^2 L_g^2 + \Omega_y^2 L_g^2 & 0 \\ 0 & 0 & 3\left(\Omega_x^2 L_g^2 + \Omega_y^2 L_g^2\right) \end{bmatrix}$$

with $\underline{u} = [u_g, v_g, w_g]^T$ and u_g, v_g and w_g the longitudinal, lateral and vertical atmospheric turbulence velocity components, respectively, $\Omega_x L_g$ the non-dimensional spatial frequency along the X_E-axis of the frame $\mathcal{F}_E$, $\Omega_y L_g$ the non-dimensional spatial frequency along the Y_E-axis of $\mathcal{F}_E$, L_g the gust scale length in [m] and σ^2 the variance of the atmospheric turbulence velocity components in $[\frac{\mathrm{m}^2}{\mathrm{s}^2}]$.
For the gust velocity components u_g, v_g and w_g, the Power Spectral Density (PSD) functions become, respectively,

$$S_{u_g u_g}(\Omega_x L_g, \Omega_y L_g) = \pi\sigma^2 \frac{1+\Omega_x^2 L_g^2 + 4\Omega_y^2 L_g^2}{\left(1+\Omega_x^2 L_g^2 + \Omega_y^2 L_g^2\right)^{5/2}} \tag{G.11}$$

$$S_{v_g v_g}(\Omega_x L_g, \Omega_y L_g) = \pi\sigma^2 \frac{1+4\Omega_x^2 L_g^2 + \Omega_y^2 L_g^2}{\left(1+\Omega_x^2 L_g^2 + \Omega_y^2 L_g^2\right)^{5/2}} \tag{G.12}$$

and,

$$S_{w_g w_g}(\Omega_x L_g, \Omega_y L_g) = 3\pi\sigma^2 \frac{\Omega_x^2 L_g^2 + \Omega_y^2 L_g^2}{\left(1+\Omega_x^2 L_g^2 + \Omega_y^2 L_g^2\right)^{5/2}} \tag{G.13}$$

with $S_{u_g u_g}(\Omega_x L_g, \Omega_y L_g)$ the 2D PSD-function for the longitudinal gust u_g, $S_{v_g v_g}(\Omega_x L_g, \Omega_y L_g)$ the 2D PSD-function for the lateral gust v_g, and $S_{w_g w_g}(\Omega_x L_g, \Omega_y L_g)$ the 2D PSD-function for the vertical gust w_g.

Use is made of equations (G.11), (G.12) and (G.13) for the generation of the spatial-domain 2D gust fields u_g, v_g and w_g. Following the procedure given in reference [1], these gust fields are obtained using 2D "white-noise" matrices (see also section G.2.1) $w_n\left(\frac{X^E}{L_g}, \frac{Y^E}{L_g}\right)$ with $\frac{X^E}{L_g}$ the non-dimensional position along the X_E-axis of the frame $\mathcal{F}_E$ and $\frac{Y^E}{L_g}$ the non-dimensional position along the Y_E-axis of $\mathcal{F}_E$. The noise-matrices $w_n\left(\frac{X^E}{L_g}, \frac{Y^E}{L_g}\right)$ are generated for each (isolated) atmospheric turbulence velocity component $u_g\left(\frac{X^E}{L_g}, \frac{Y^E}{L_g}\right)$, $v_g\left(\frac{X^E}{L_g}, \frac{Y^E}{L_g}\right)$ and $w_g\left(\frac{X^E}{L_g}, \frac{Y^E}{L_g}\right)$ and they are designated as $w_{n_{u_g}}\left(\frac{X^E}{L_g}, \frac{Y^E}{L_g}\right)$, $w_{n_{v_g}}\left(\frac{X^E}{L_g}, \frac{Y^E}{L_g}\right)$ and $w_{n_{w_g}}\left(\frac{X^E}{L_g}, \frac{Y^E}{L_g}\right)$, respectively.
In generating the 2D gust fields, the 2D noise-matrices are
Fourier-transformed resulting in the frequency-domain matrices $W_{n_{u_g}}(\Omega_x L_g, \Omega_y L_g)$, $W_{n_{v_g}}(\Omega_x L_g, \Omega_y L_g)$ and $W_{n_{w_g}}(\Omega_x L_g, \Omega_y L_g)$ (see appendix B for details with respect to the 2D Fourier-transform). Next, the frequency-domain noise-matrices are multiplied by the square-root of the atmospheric turbulence velocity component spectra, or (see also equations (G.7), (G.8) and (G.9)),

$$U_g(\Omega_x L_g, \Omega_y L_g) = \sqrt{S_{u_g u_g}(\Omega_x L_g, \Omega_y L_g)}\, W_{n_{u_g}}(\Omega_x L_g, \Omega_y L_g) \tag{G.14}$$

$$V_g(\Omega_x L_g, \Omega_y L_g) = \sqrt{S_{v_g v_g}(\Omega_x L_g, \Omega_y L_g)}\, W_{n_{v_g}}(\Omega_x L_g, \Omega_y L_g) \tag{G.15}$$

and,

$$W_g(\Omega_x L_g, \Omega_y L_g) = \sqrt{S_{w_g w_g}(\Omega_x L_g, \Omega_y L_g)}\, W_{n_{w_g}}(\Omega_x L_g, \Omega_y L_g) \tag{G.16}$$

with $U_g(\Omega_x L_g, \Omega_y L_g)$, $V_g(\Omega_x L_g, \Omega_y L_g)$ and $W_g(\Omega_x L_g, \Omega_y L_g)$ the 2D frequency-domain transformations of the longitudinal, lateral and vertical atmospheric turbulence velocity components $u_g\left(\frac{X^E}{L_g}, \frac{Y^E}{L_g}\right)$, $v_g\left(\frac{X^E}{L_g}, \frac{Y^E}{L_g}\right)$ and $w_g\left(\frac{X^E}{L_g}, \frac{Y^E}{L_g}\right)$, respectively.

The sought spatial-domain 2D gust fields $u_g\left(\frac{X^E}{L_g}, \frac{Y^E}{L_g}\right)$, $v_g\left(\frac{X^E}{L_g}, \frac{Y^E}{L_g}\right)$ and $w_g\left(\frac{X^E}{L_g}, \frac{Y^E}{L_g}\right)$ are obtained from the 2D inverse Fourier-transform of equations (G.14), (G.15) and (G.16), respectively, or,

$$u_g\left(\frac{X^E}{L_g}, \frac{Y^E}{L_g}\right) = \mathcal{F}^{-2}\left\{U_g(\Omega_x L_g, \Omega_y L_g)\right\} \tag{G.17}$$

$$v_g\left(\frac{X^E}{L_g}, \frac{Y^E}{L_g}\right) = \mathcal{F}^{-2}\left\{V_g(\Omega_x L_g, \Omega_y L_g)\right\} \tag{G.18}$$

and,

$$w_g\left(\frac{X^E}{L_g}, \frac{Y^E}{L_g}\right) = \mathcal{F}^{-2}\left\{W_g(\Omega_x L_g, \Omega_y L_g)\right\} \tag{G.19}$$

G.2.3 2D Correlated gust fields

Similar to section G.2.2, the 2D spatial-domain gust fields for correlated atmospheric turbulence velocity components are calculated in this section. The 2D gust fields defined here are similar to the ones defined in the previous section, however, it is now assumed that the longitudinal gust u_g and the lateral gust v_g are correlated.
For 2D correlated gust velocity components, the input PSD-matrix is now given as,

$$S_{\underline{uu}}(\Omega_x L_g, \Omega_y L_g) = \tag{G.20}$$

$$= \frac{\pi\sigma^2}{\left(1+\Omega_x^2 L_g^2 + \Omega_y^2 L_g^2\right)^{5/2}} \begin{bmatrix} 1+\Omega_x^2 L_g^2 + 4\Omega_y^2 L_g^2 & -3\Omega_x\Omega_y L_g^2 & 0 \\ -3\Omega_y\Omega_x L_g^2 & 1+4\Omega_x^2 L_g^2 + \Omega_y^2 L_g^2 & 0 \\ 0 & 0 & 3\left(\Omega_x^2 L_g^2 + \Omega_y^2 L_g^2\right) \end{bmatrix}$$

For the (spatial) frequency-domain, the gust velocity components $U_g(\Omega_x L_g, \Omega_y L_g)$, $V_g(\Omega_x L_g, \Omega_y L_g)$ and $W_g(\Omega_x L_g, \Omega_y L_g)$ are now calculated from equations similar to equations (G.7), (G.8) and (G.9), or,

$$U_g(\Omega_x L_g, \Omega_y L_g) = H_{11}(\Omega_x L_g, \Omega_y L_g)\, W_{n_{u_g}}(\Omega_x L_g, \Omega_y L_g) \tag{G.21}$$

$$V_g(\Omega_x L_g, \Omega_y L_g) = H_{21}(\Omega_x L_g, \Omega_y L_g)\, W_{n_{u_g}}(\Omega_x L_g, \Omega_y L_g) + H_{22}(\Omega_x L_g, \Omega_y L_g)\, W_{n_{v_g}}(\Omega_x L_g, \Omega_y L_g) \tag{G.22}$$

$$W_g(\Omega_x L_g, \Omega_y L_g) = H_{33}(\Omega_x L_g, \Omega_y L_g)\, W_{n_{w_g}}(\Omega_x L_g, \Omega_y L_g) \tag{G.23}$$

with $W_{n_{u_g}}(\Omega_x L_g, \Omega_y L_g)$, $W_{n_{v_g}}(\Omega_x L_g, \Omega_y L_g)$ and $W_{n_{w_g}}(\Omega_x L_g, \Omega_y L_g)$ the independent frequency-domain noise-matrices. These noise-matrices are obtained using a two-dimensional Fourier-transform of the spatial-domain "white-noise" matrices $w_{n_{u_g}}\left(\frac{X^E}{L_g}, \frac{Y^E}{L_g}\right)$, $w_{n_{v_g}}\left(\frac{X^E}{L_g}, \frac{Y^E}{L_g}\right)$ and $w_{n_{w_g}}\left(\frac{X^E}{L_g}, \frac{Y^E}{L_g}\right)$. In equations (G.21), (G.22) and (G.23), the definition of the transfer-functions $H_{11}(\Omega_x L_g, \Omega_y L_g)$, $H_{21}(\Omega_x L_g, \Omega_y L_g)$, $H_{22}(\Omega_x L_g, \Omega_y L_g)$ and $H_{33}(\Omega_x L_g, \Omega_y L_g)$ now becomes,

$$H_{11}(\Omega_x L_g, \Omega_y L_g) = \sqrt{S_{u_g u_g}(\Omega_x L_g, \Omega_y L_g)}$$

$$H_{21}(\Omega_x L_g, \Omega_y L_g) = \frac{S_{u_g v_g}(\Omega_x L_g, \Omega_y L_g)}{\sqrt{S_{u_g u_g}(\Omega_x L_g, \Omega_y L_g)}}$$

$$H_{22}(\Omega_x L_g, \Omega_y L_g) = \sqrt{S_{v_g v_g}(\Omega_x L_g, \Omega_y L_g) - \frac{S^2_{u_g v_g}(\Omega_x L_g, \Omega_y L_g)}{S_{u_g u_g}(\Omega_x L_g, \Omega_y L_g)}}$$

$$H_{33}(\Omega_x L_g, \Omega_y L_g) = \sqrt{S_{w_g w_g}(\Omega_x L_g, \Omega_y L_g)}$$

Similar to section G.2.2, the sought spatial-domain 2D gust fields $u_g\left(\frac{X^E}{L_g}, \frac{Y^E}{L_g}\right)$, $v_g\left(\frac{X^E}{L_g}, \frac{Y^E}{L_g}\right)$ and $w_g\left(\frac{X^E}{L_g}, \frac{Y^E}{L_g}\right)$ are obtained from the 2D inverse Fourier-transform of equations (G.21), (G.22) and (G.23), respectively.

G.2.4 The numerical simulation of 2D gust fields

For the numerical simulation of the atmospheric turbulence fields, the atmospheric turbulence parameter values were chosen as $L_g = 300$ [m] and $\sigma^2 = 1$ $[\frac{\text{m}^2}{\text{s}^2}]$. For the generation of these gust fields the non-dimensional spatial sampling was chosen as $\frac{\Delta X^E}{L_g} = \frac{\Delta Y^E}{L_g} = 0.02$, while for the non-dimensional spatial dimensions they were chosen as $\frac{X^E}{L_g} = \left[0, \frac{\Delta X^E}{L_g}, \cdots, 25\right]^T$ and $\frac{Y^E}{L_g} = \left[0, \frac{\Delta Y^E}{L_g}, \cdots, 25\right]^T$. The spatial sampling and the spatial dimensions were determined such to allow the simulation of both the low-frequent and high-frequent components for all turbulence velocities.
The non-dimensional spatial frequencies $\Omega_x L_g$ and $\Omega_y L_g$ are calculated from both the non-dimensional spatial sampling and the number of elements in the spatial dimensions, or,

$$\begin{aligned} \Omega_x L_g &= \frac{2\pi[0:(N_x-1)/2]}{N_x \frac{\Delta X^E}{L_g}} \\ \Omega_y L_g &= \frac{2\pi[0:(N_y-1)/2]}{N_y \frac{\Delta Y^E}{L_g}} \end{aligned}$$

with N_x the number of samples along the X^E-axis and N_y the number of samples along the Y^E-axis. Using the non-dimensional spatial frequencies, for the uncorrelated gust fields the PSD-function matrix according to equation (G.10) is calculated, while for the correlated gust fields it is calculated using equation (G.20).

In this thesis the "white-noise" matrices are generated using MATLAB's noise-generator (`randn`) which provides normally distributed random-number matrices (with intensity equal to one), and they are given as $w_{n_{u_g}}\left(\frac{X^E}{L_g}, \frac{Y^E}{L_g}\right)$, $w_{n_{v_g}}\left(\frac{X^E}{L_g}, \frac{Y^E}{L_g}\right)$ and $w_{n_{w_g}}\left(\frac{X^E}{L_g}, \frac{Y^E}{L_g}\right)$. However, for the numerical simulations they are now divided by the square-root of the non-dimensional spatial samplings, $\sqrt{\frac{\Delta X^E}{L_g}}$ and $\sqrt{\frac{\Delta Y^E}{L_g}}$. The noise-input matrices become,

$$\begin{aligned} \hat{w}_{n_{u_g}}\left(\frac{X^E}{L_g}, \frac{Y^E}{L_g}\right) &= \frac{w_{n_{u_g}}\left(\frac{X^E}{L_g}, \frac{Y^E}{L_g}\right)}{\sqrt{\frac{\Delta X^E}{L_g}}\sqrt{\frac{\Delta Y^E}{L_g}}} \\ \hat{w}_{n_{v_g}}\left(\frac{X^E}{L_g}, \frac{Y^E}{L_g}\right) &= \frac{w_{n_{v_g}}\left(\frac{X^E}{L_g}, \frac{Y^E}{L_g}\right)}{\sqrt{\frac{\Delta X^E}{L_g}}\sqrt{\frac{\Delta Y^E}{L_g}}} \\ \hat{w}_{n_{w_g}}\left(\frac{X^E}{L_g}, \frac{Y^E}{L_g}\right) &= \frac{w_{n_{w_g}}\left(\frac{X^E}{L_g}, \frac{Y^E}{L_g}\right)}{\sqrt{\frac{\Delta X^E}{L_g}}\sqrt{\frac{\Delta Y^E}{L_g}}} \end{aligned}$$

with their Fourier-transform equivalents becoming,

$$\hat{W}_{n_{u_g}}(\Omega_x L_g, \Omega_y L_g) = \frac{W_{n_{u_g}}(\Omega_x L_g, \Omega_y L_g)}{\sqrt{\frac{\Delta X^E}{L_g}}\sqrt{\frac{\Delta Y^E}{L_g}}}$$

$$\hat{W}_{n_{v_g}}(\Omega_x L_g, \Omega_y L_g) = \frac{W_{n_{v_g}}(\Omega_x L_g, \Omega_y L_g)}{\sqrt{\frac{\Delta X^E}{L_g}}\sqrt{\frac{\Delta Y^E}{L_g}}}$$

$$\hat{W}_{n_{w_g}}(\Omega_x L_g, \Omega_y L_g) = \frac{W_{n_{w_g}}(\Omega_x L_g, \Omega_y L_g)}{\sqrt{\frac{\Delta X^E}{L_g}}\sqrt{\frac{\Delta Y^E}{L_g}}}$$

Using these noise-inputs, the 2D frequency-domain transformations of the uncorrelated longitudinal, lateral and vertical atmospheric turbulence velocity components are calculated according to equations (G.14), (G.15) and (G.16), respectively. For the 2D frequency-domain transformations of the correlated longitudinal, lateral and vertical atmospheric turbulence velocity components use is made of equations (G.21), (G.22) and (G.23), respectively. Finally, for the numerical simulations of the spatial-domain 2D gust fields $u_g\left(\frac{X^E}{L_g}, \frac{Y^E}{L_g}\right)$, $v_g\left(\frac{X^E}{L_g}, \frac{Y^E}{L_g}\right)$ and $w_g\left(\frac{X^E}{L_g}, \frac{Y^E}{L_g}\right)$, use is made of equations (G.17), (G.18) and (G.19).

For the non-dimensional spatial sampling $\frac{\Delta X^E}{L_g} = 0.02$ (or $\Delta X^E = 6$ [m]) and the non-dimensional spatial sampling $\frac{\Delta Y^E}{L_g} = 0.02$ (or $\Delta Y^E = 6$ [m]) results of the flight path corridor's numerically obtained u_g, v_g (uncorrelated with u_g), v_g (now correlated with u_g) and w_g gust fields are shown in figures G.1, G.2, G.3 and G.4, respectively. These corridor results are slices of data obtained for rectangular computational grids. These original results were determined for dimensional positions in $\mathcal{F}_E$, resulting in a grid spanning 7500 meters by 7500 meters (or $(25\ L_g) \times (25\ L_g)$ [m^2]) along the X_E- and Y_E-axis of $\mathcal{F}_E$. The number of grid-points along both the X_E- and Y_E-axis were chosen to be $N_X = N_Y = N = 1251$. The presented results hold for the atmospheric-turbulence model-parameters values $L_g = 300$ [m] and $\sigma^2 = 1$ [$\frac{\text{m}^2}{\text{s}^2}$].

Note that for the 2D numerical Fourier transform (and its inverse) MATLAB's Fast Fourier Transform (`fft2.m` and `ifft2.m`) were used.

G.2.5 Verification of the 2D gust fields

The verification of the (both correlated and uncorrelated) spatial-domain 2D gust fields $u_g\left(\frac{X^E}{L_g}, \frac{Y^E}{L_g}\right)$, $v_g\left(\frac{X^E}{L_g}, \frac{Y^E}{L_g}\right)$ and $w_g\left(\frac{X^E}{L_g}, \frac{Y^E}{L_g}\right)$ is performed by calculating the covariance-functions $C_{u_g u_g}(\frac{\xi^E}{L_g})$, $C_{v_g v_g}(\frac{\xi^E}{L_g})$ and $C_{w_g w_g}(\frac{\xi^E}{L_g})$ of the simulated gust fields, with ξ^E the one-dimensional (1D) spatial separation. In the following they will be compared to the analytical covariance-functions presented in chapter 2.
From each atmospheric turbulence velocity component matrix (for example, see equations (G.17), (G.18) and (G.19)), these functions are calculated as a function of the spatial

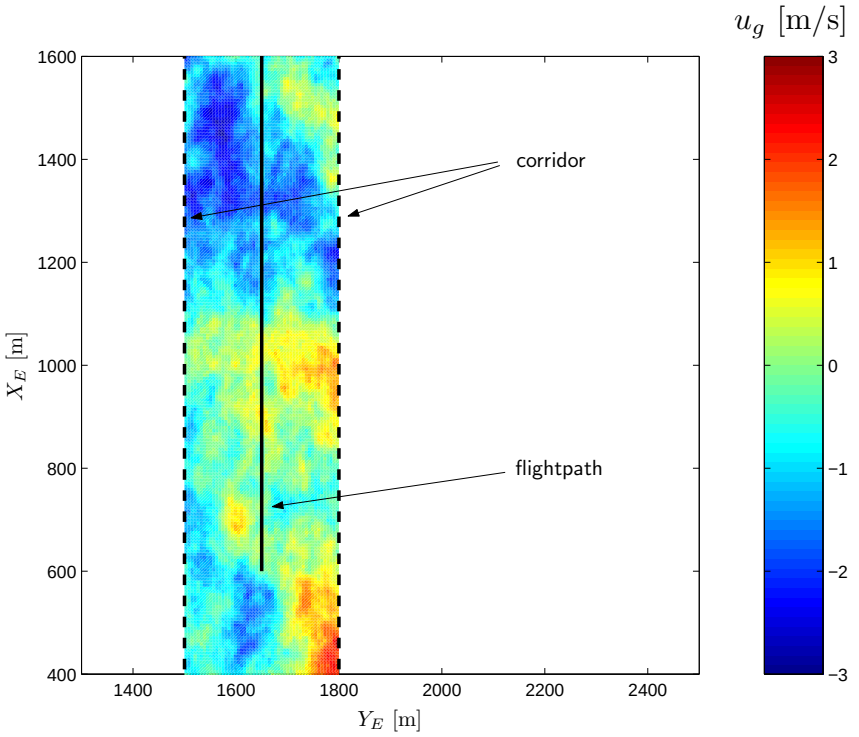


Figure G.1: The simulated 2D gust field $u_g(X^E, Y^E)$ [m/s] for the flightpath-corridor, $L_g = 300$ [m] and $\sigma^2 = 1$ $[\frac{\text{m}^2}{\text{s}^2}]$.

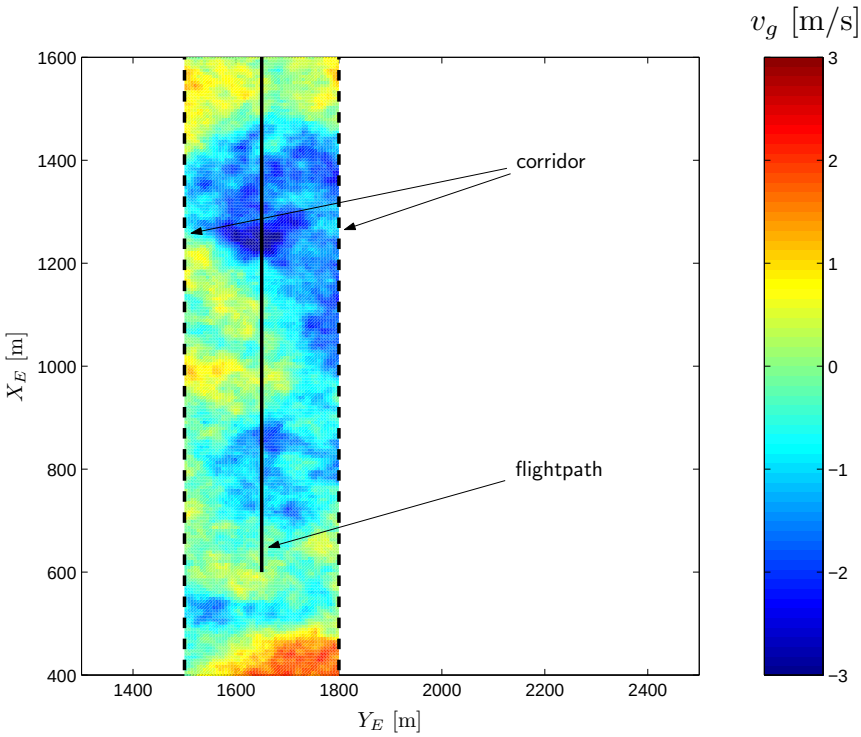


Figure G.2: The simulated (uncorrelated) 2D gust field $v_g(X^E, Y^E)$ [m/s] for the flightpath-corridor, $L_g = 300$ [m] and $\sigma^2 = 1$ $[\frac{\text{m}^2}{\text{s}^2}]$.

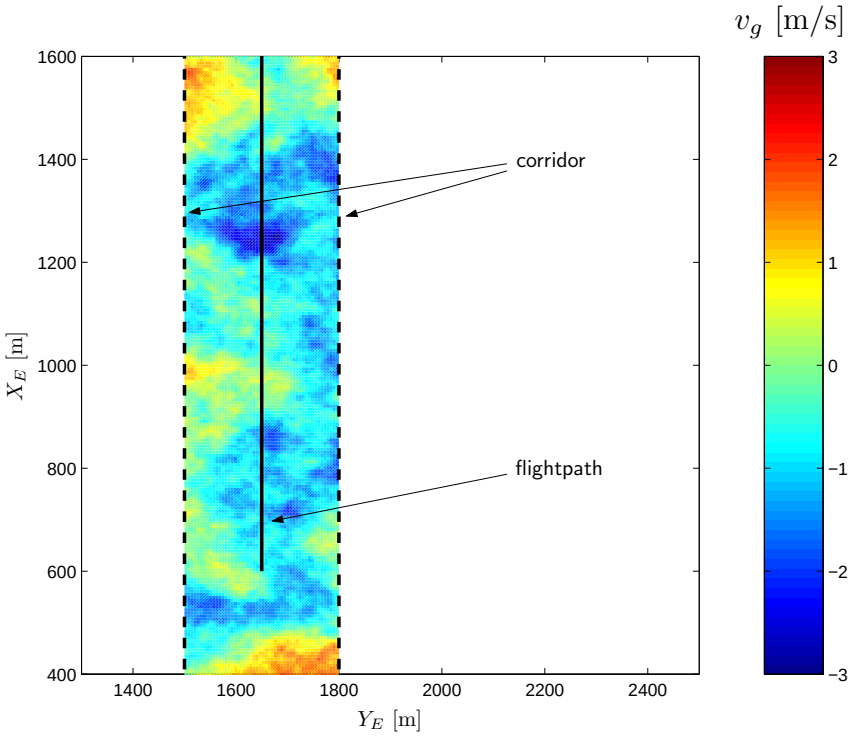


Figure G.3: The simulated (correlated with u_g) 2D gust field $v_g(X^E, Y^E)$ [m/s] for the flightpath-corridor, $L_g = 300$ [m] and $\sigma^2 = 1$ $[\frac{\text{m}^2}{\text{s}^2}]$.

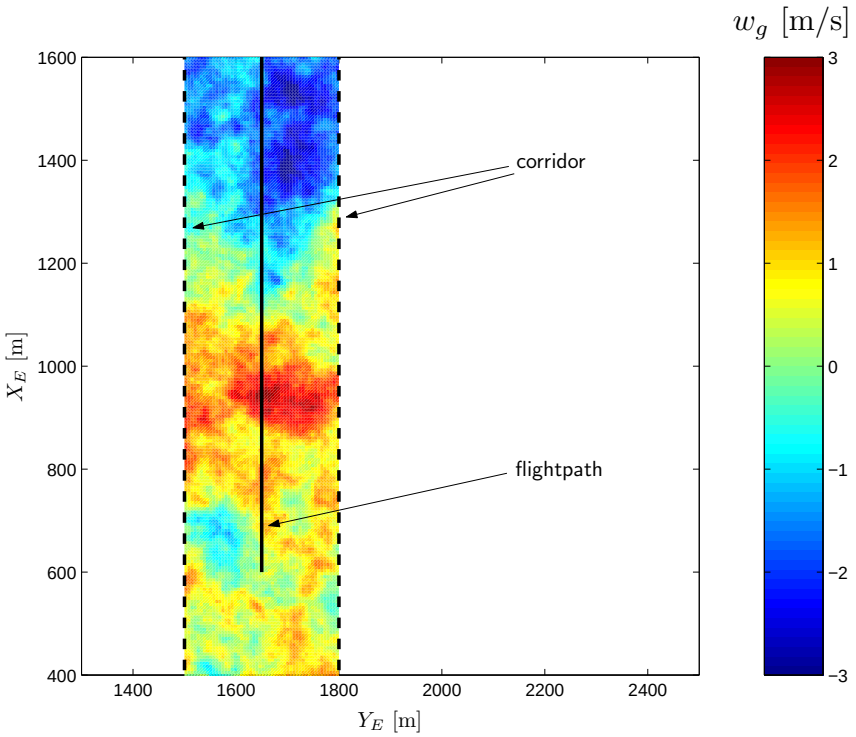


Figure G.4: The simulated 2D gust field $w_g(X^E, Y^E)$ [m/s] for the flightpath-corridor, $L_g = 300$ [m] and $\sigma^2 = 1$ $[\frac{\text{m}^2}{\text{s}^2}]$.

separation along the X_E-axis of the frame $\mathcal{F}_E$, and the spatial separation along the Y_E-axis of $\mathcal{F}_E$.

For the calculation of the discrete covariance-functions, the following equation is used,

$$C_{ab}\left(\frac{\xi^E}{L_g}\right) = \frac{1}{N-1}\sum_{n=1}^{n=N} a[n]\ b[n+m], \qquad m = 0 \cdots N-1 \tag{G.24}$$

with $C_{ab}\left(\frac{\xi^E}{L_g}\right)$ the discrete covariance-function, a and b either the atmospheric turbulence velocity component u_g, v_g or w_g, $\frac{\xi^E}{L_g}$ the non-dimensional spatial separation $\frac{\xi_x^E}{L_g} = m\ \frac{\Delta X^E}{L_g}$ or $\frac{\xi_y^E}{L_g} = m\ \frac{\Delta Y^E}{L_g}$ with ΔX^E and ΔY^E the spatial discretizations, the counters $n = 1 \cdots N$, $m = 0 \cdots N-1$, and N the number of samples in the time-arrays a and b. For the spatial discretizations and the number of samples the following numerical values were used: $\Delta X^E = 6$ [m], $\Delta Y^E = 6$ [m], and $N = 1251$.

Now consider for example the auto-covariance-function $C_{u_g u_g}\left(\frac{\xi_x^E}{L_g}\right)$. For each position along the Y_E-axis of $\mathcal{F}_E$, the covariance-function $C_{u_g u_g}\left(\frac{\xi_x^E}{L_g}\right)$ is calculated for spatial separations along the X_E-axis of $\mathcal{F}_E$, resulting in an ensemble of covariance-functions as a function of $\frac{Y^E}{L_g}$. Similarly, the auto-covariance-function $C_{u_g u_g}\left(\frac{\xi_y^E}{L_g}\right)$ is calculated for spatial separations along the Y_E-axis of $\mathcal{F}_E$, resulting in an ensemble of covariance-functions as a function of $\frac{X^E}{L_g}$.

For the uncorrelated gust velocity components u_g, v_g and w_g (see section G.2.2), the numerically obtained (cross-) covariance-functions are compared to the analytical functions given in chapter 2. In figure G.5 the ensemble-average of $C_{u_g u_g}\left(\frac{\xi_x^E}{L_g}\right)$ is given, together with the standard-deviation of the covariance-function, while also the ensemble-average of $C_{u_g u_g}\left(\frac{\xi_y^E}{L_g}\right)$ is given, also together with its standard-deviation. Both covariance functions $C_{u_g u_g}\left(\frac{\xi_x^E}{L_g}\right)$ and $C_{u_g u_g}\left(\frac{\xi_y^E}{L_g}\right)$ show good agreement with the analytical longitudinal and lateral Dryden correlation functions f and g given in chapter 2 (note that since it was assumed that the variance of all gust-speeds equals $\sigma^2 = 1\ [\frac{\mathrm{m}^2}{\mathrm{s}^2}]$, the covariance-functions and correlation-functions are interchangeable assuming zero-mean atmospheric turbulence velocity components).
Similar to figure G.5, for the uncorrelated gust velocity components v_g and w_g in figures G.6 and G.7 the auto-covariance-functions $C_{v_g v_g}\left(\frac{\xi_x^E}{L_g}\right)$ and $C_{v_g v_g}\left(\frac{\xi_y^E}{L_g}\right)$, and the auto-covariance-functions $C_{w_g w_g}\left(\frac{\xi_x^E}{L_g}\right)$ and $C_{w_g w_g}\left(\frac{\xi_y^E}{L_g}\right)$ are given, respectively. Also here these functions show good agreement with the analytical longitudinal and lateral Dryden correlation functions f and g given in chapter 2. Figures G.8 and G.9 show the cross-covariance-

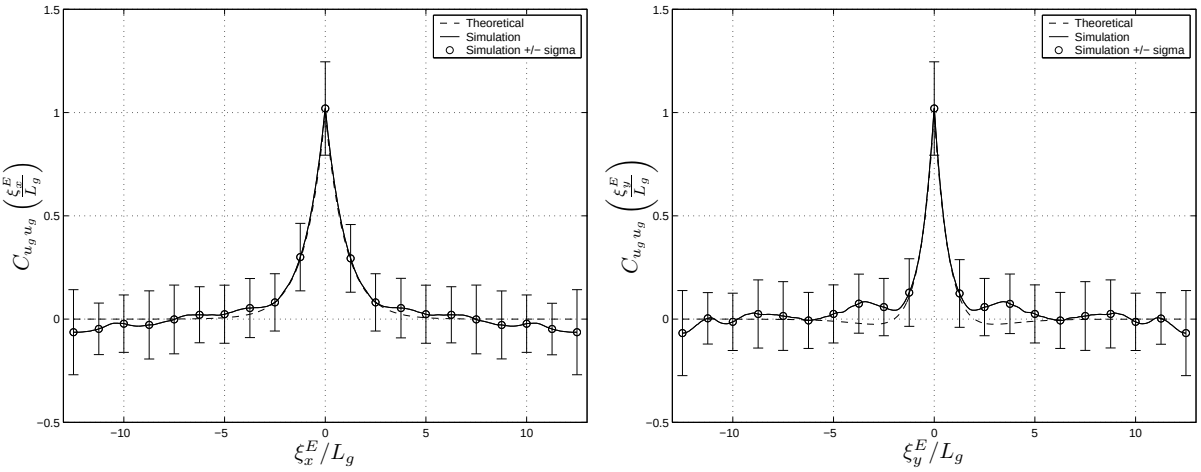


Figure G.5: The simulated correlation functions $C_{u_g u_g}\left(\frac{\xi_x^E}{L_g}\right)$ (for the longitudinal separation, left) and $C_{u_g u_g}\left(\frac{\xi_y^E}{L_g}\right)$ (for the lateral separation, right). The atmospheric turbulence velocity-component u_g is uncorrelated with the gust velocity-components v_g and w_g. Results were obtained from the 2D $L_g = 300$ [m] and $\sigma^2 = 1$ $[\frac{\mathrm{m}^2}{\mathrm{s}^2}]$ gust fields.

functions $C_{u_g v_g}\left(\frac{\xi_x^E}{L_g}\right)$ and $C_{u_g v_g}\left(\frac{\xi_y^E}{L_g}\right)$, and $C_{v_g u_g}\left(\frac{\xi_x^E}{L_g}\right)$ and $C_{v_g u_g}\left(\frac{\xi_y^E}{L_g}\right)$, respectively. Also here the results show good agreement with the analytical cross-covariance-functions, which are in fact zero for all 1D spatial-separations since no correlation between the longitudinal atmospheric turbulence velocity component u_g and the lateral atmospheric turbulence velocity component v_g is considered.

For the correlated gust velocity component v_g (which is now correlated to u_g), the numerically obtained (cross-) covariance-functions are also compared to the analytical functions given in chapter 2.
Similar to figure G.6, for the correlated gust velocity component v_g in figure G.10 the auto-covariance-functions $C_{v_g v_g}\left(\frac{\xi_x^E}{L_g}\right)$ and $C_{v_g v_g}\left(\frac{\xi_y^E}{L_g}\right)$ are given. Also these covariance-functions show good agreement with the analytical longitudinal and lateral Dryden correlation functions f and g given in chapter 2. Figures G.11 and G.12 show the cross-covariance-functions $C_{u_g v_g}\left(\frac{\xi_x^E}{L_g}\right)$ and $C_{u_g v_g}\left(\frac{\xi_y^E}{L_g}\right)$, and $C_{v_g u_g}\left(\frac{\xi_x^E}{L_g}\right)$ and $C_{v_g u_g}\left(\frac{\xi_y^E}{L_g}\right)$, respectively. Also here the results coincide with the analytical cross-covariance-functions (which are also zero for all 1D spatial-separations since for the presented 1D results no correlation between the longitudinal atmospheric turbulence velocity component u_g and the lateral atmospheric turbulence velocity component v_g is considered).

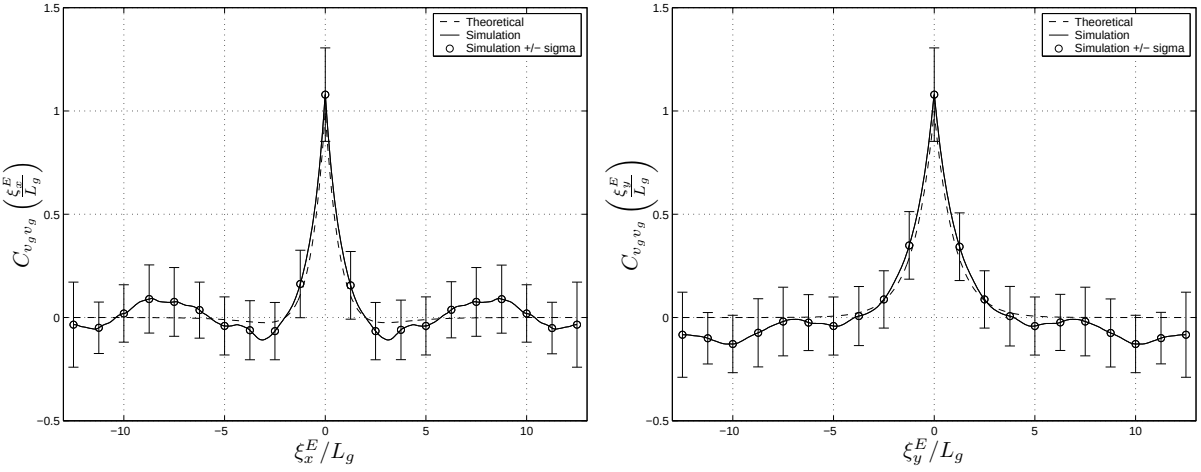


Figure G.6: The simulated correlation functions $C_{v_g v_g}\left(\frac{\xi_x^E}{L_g}\right)$ (for the longitudinal separation, left) and $C_{v_g v_g}\left(\frac{\xi_y^E}{L_g}\right)$ (for the lateral separation, right). The atmospheric turbulence velocity-component v_g is uncorrelated with the gust velocity-components u_g and w_g. Results were obtained from the 2D $L_g = 300$ [m] and $\sigma^2 = 1$ $[\frac{\mathrm{m}^2}{\mathrm{s}^2}]$ gust fields.

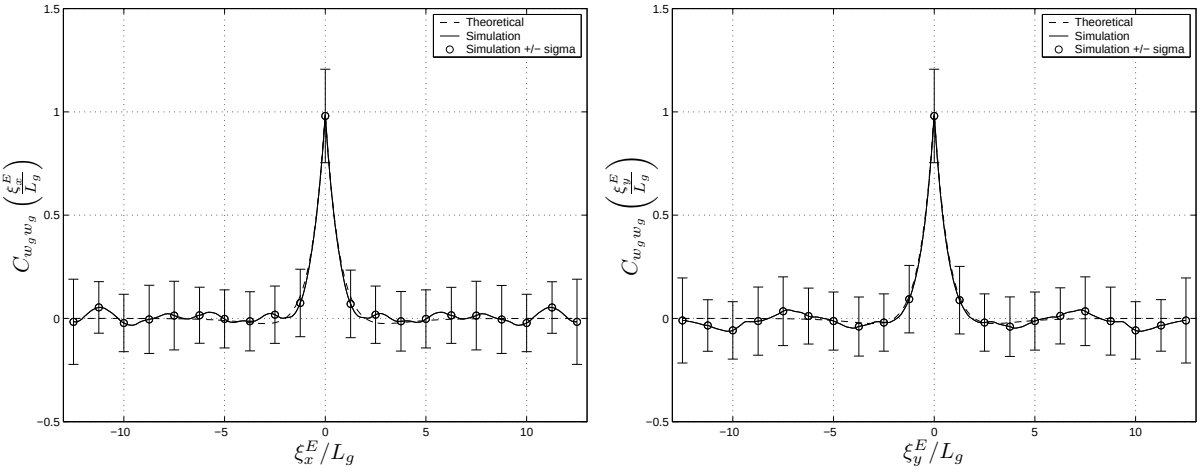


Figure G.7: The simulated correlation functions $C_{w_g w_g}\left(\frac{\xi_x^E}{L_g}\right)$ (for the longitudinal separation, left) and $C_{w_g w_g}\left(\frac{\xi_y^E}{L_g}\right)$ (for the lateral separation, right). The atmospheric turbulence velocity-component w_g is uncorrelated with the gust velocity-components u_g and v_g. Results were obtained from the 2D $L_g = 300$ [m] and $\sigma^2 = 1$ $[\frac{\mathrm{m}^2}{\mathrm{s}^2}]$ gust fields.

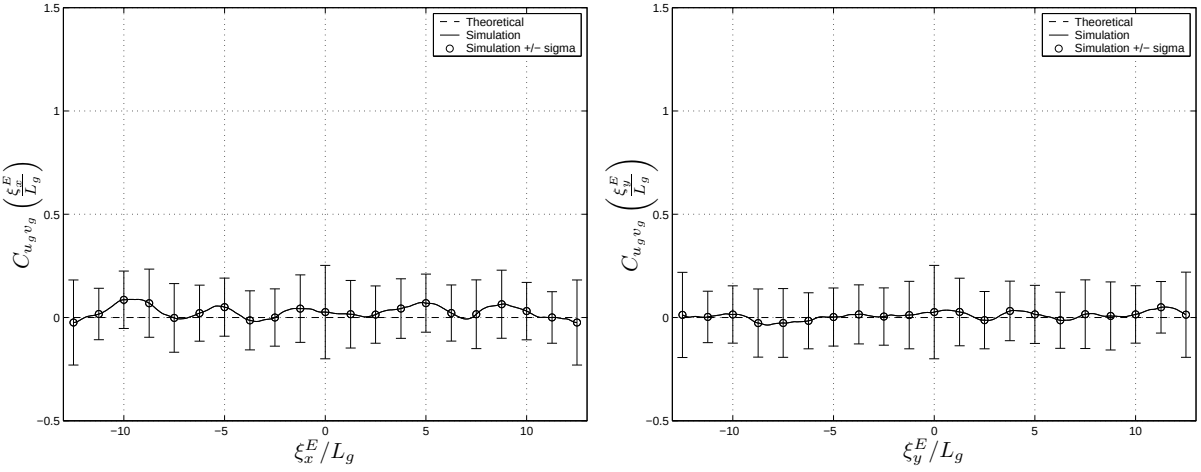


Figure G.8: The simulated correlation functions $C_{u_g v_g}\left(\frac{\xi_x^E}{L_g}\right)$ (for the longitudinal separation, left) and $C_{u_g v_g}\left(\frac{\xi_y^E}{L_g}\right)$ (for the lateral separation, right). The atmospheric turbulence velocity-component u_g is uncorrelated with the gust velocity-components v_g and w_g. Results were obtained from the 2D $L_g = 300$ [m] and $\sigma^2 = 1$ $[\frac{\mathrm{m}^2}{\mathrm{s}^2}]$ gust fields.

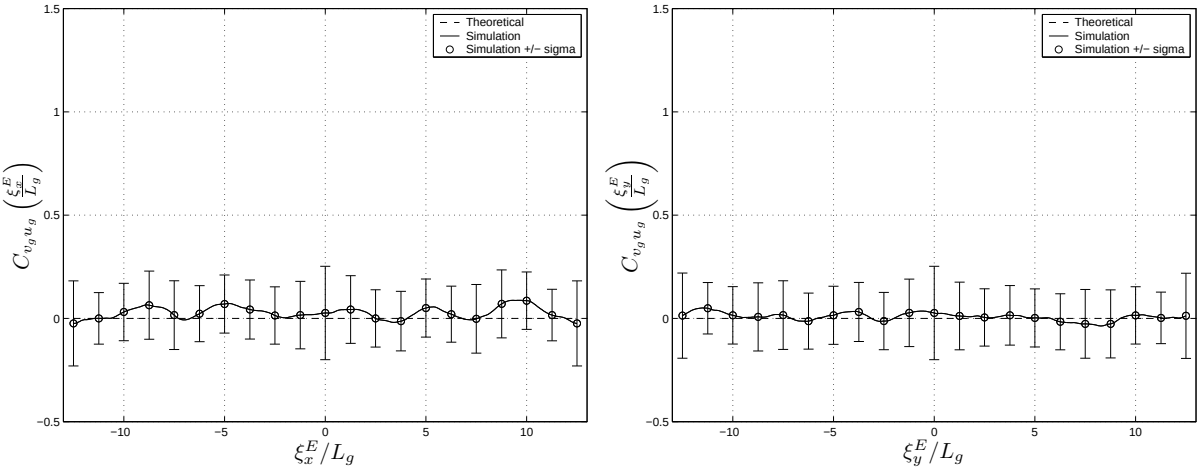


Figure G.9: The simulated correlation functions $C_{v_g u_g}\left(\frac{\xi_x^E}{L_g}\right)$ (for the longitudinal separation, left) and $C_{v_g u_g}\left(\frac{\xi_y^E}{L_g}\right)$ (for the lateral separation, right). The atmospheric turbulence velocity-component v_g is uncorrelated with the gust velocity-components u_g and w_g. Results were obtained from the 2D $L_g = 300$ [m] and $\sigma^2 = 1$ $[\frac{\mathrm{m}^2}{\mathrm{s}^2}]$ gust fields.

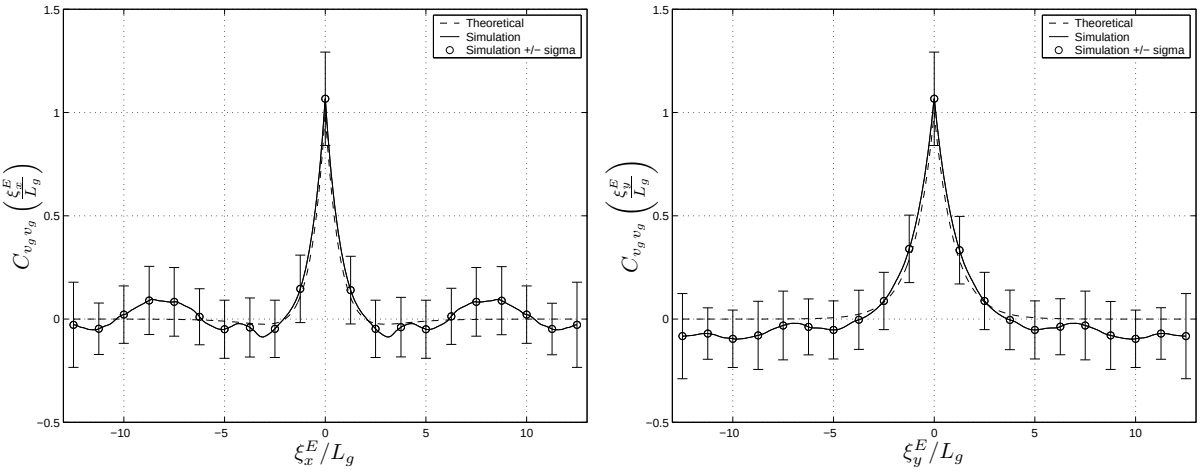


Figure G.10: The simulated correlation functions $C_{v_g v_g}\left(\frac{\xi_x^E}{L_g}\right)$ (for the longitudinal separation, left) and $C_{v_g v_g}\left(\frac{\xi_y^E}{L_g}\right)$ (for the lateral separation, right). The atmospheric turbulence velocity-component v_g is now correlated to the atmospheric turbulence velocity-component u_g. Results were obtained from the 2D $L_g = 300$ [m] and $\sigma^2 = 1$ $[\frac{\mathrm{m}^2}{\mathrm{s}^2}]$ gust fields.

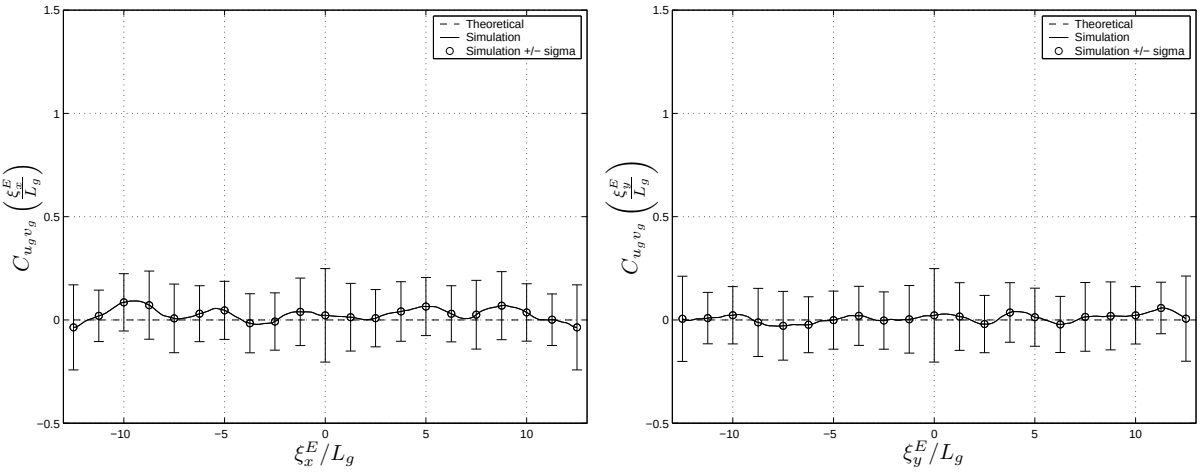


Figure G.11: The simulated correlation functions $C_{u_g v_g}\left(\frac{\xi_x^E}{L_g}\right)$ (for the longitudinal separation, left) and $C_{u_g v_g}\left(\frac{\xi_y^E}{L_g}\right)$ (for the lateral separation, right). The atmospheric turbulence velocity-component v_g is now correlated to the atmospheric turbulence velocity-component u_g. Results were obtained from the 2D $L_g = 300$ [m] and $\sigma^2 = 1$ $[\frac{\mathrm{m}^2}{\mathrm{s}^2}]$ gust fields.

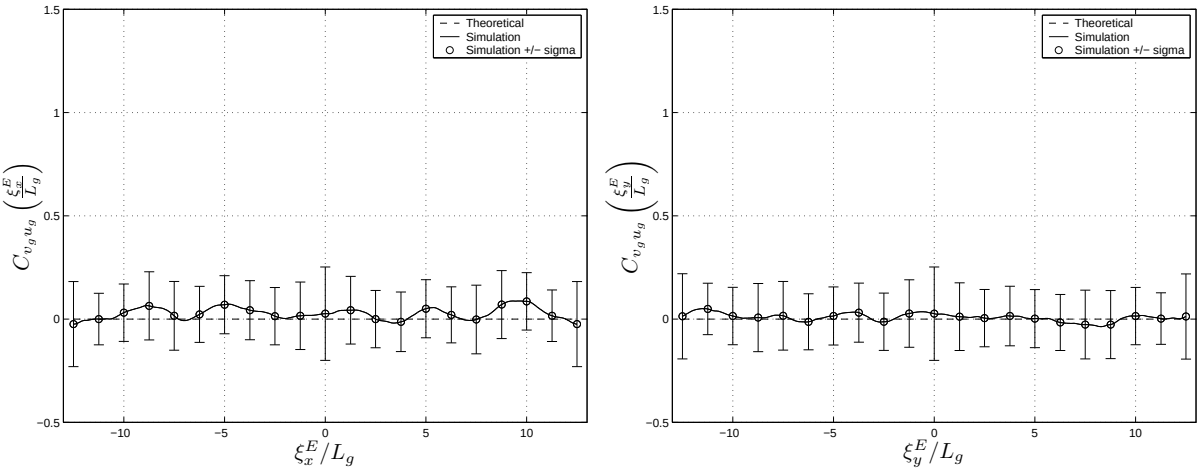


Figure G.12: The simulated correlation functions $C_{v_g u_g}\left(\frac{\xi_x^E}{L_g}\right)$ (longitudinal separation, left) and $C_{v_g u_g}\left(\frac{\xi_y^E}{L_g}\right)$ (lateral separation, right). The atmospheric turbulence velocity-component v_g is now correlated to the atmospheric turbulence velocity-component u_g. Results were obtained from the 2D $L_g = 300$ [m] and $\sigma^2 = 1$ $[\frac{\mathrm{m}^2}{\mathrm{s}^2}]$ gust fields.

G.3 Definition of the flightpath and the encountered gust fields

G.3.1 Definition of the flightpath

The 2D gust fields described in sections G.2.2 and G.2.3 are given for the frame $\mathcal{F}_E$. For the aircraft's responses to these gust fields the time-domain simulations require a flightpath definition. Therefore, for these simulations a corridor in the $O_E X_E Y_E$-plane was selected, with the flightpath defined in the middle of it. It was chosen such that all time-domain simulations start at the position $\left[X_0^E, Y_0^E, Z_0^E\right]^T = [600, 1650, 0]^T$ [m] in $\mathcal{F}_E$. The 300 meter wide flightpath corridor is also given in figures G.1, G.3 and G.4. The corridor (or slice of the 2D gust fields) will be used to simulate the time-domain aircraft's aerodynamic forces- and moments-coefficients' response. It is assumed that the aircraft travels along the recti-linear flightpath (in the direction of the positive X_E-axis of $\mathcal{F}_E$) and no aircraft motions are considered.

G.3.2 Definition of the encountered gust fields

The slices of the 2D gust fields generated in section G.2.3 are used to simulate the time-domain aircraft's aerodynamic forces- and moments-coefficients' response. With respect to the previously defined flightpath, see section G.3.1, the gust fields in $\mathcal{F}_E$ are decomposed into symmetrical- and anti-symmetrical parts. For the calculation of these parts, both the definition of the flightpath and the definition of the corridor (or "'slice") is used.
Now, the gust fields are separated into sections positioned to the left and right of the flightpath. For example, consider the vertical ($w_g(X^E, Y^E)$) gust field given in the bottom

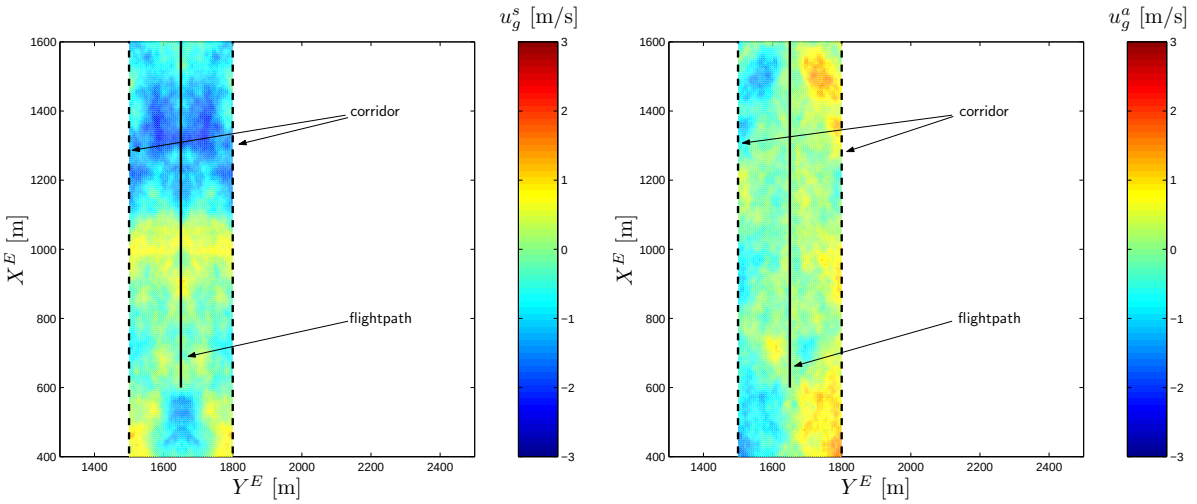


Figure G.13: Decomposition of the 2D gust field $u_g(X^E, Y^E)$ [m/s] into the symmetrical part $u_g^s(X^E, Y^E)$ (left), and the anti-symmetrical part $u_g^a(X^E, Y^E)$ (right), including the definition of the flightpath-corridor, $L_g = 300$ [m] and $\sigma^2 = 1$ $[\frac{\text{m}^2}{\text{s}^2}]$ gust fields.

figure of figure G.4. Using the gust field sections located to the left and right of the flightpath, both the symmetrical and the anti-symmetrical gust fields are calculated by,

$$w_g^s(X^E, Y^E) = \frac{1}{2}\left(w_g^l(X^E, Y^E) + w_g^r(X^E, Y^E)\right)$$
$$w_g^a(X^E, Y^E) = \frac{1}{2}\left(w_g^l(X^E, Y^E) - w_g^r(X^E, Y^E)\right)$$

with $w_g^s(X^E, Y^E)$ the symmetrical gust field, $w_g^a(X^E, Y^E)$ the anti-symmetrical gust field, $w_g^l(X^E, Y^E)$ the left-hand-side gust field of the corridor with respect to the flightpath and $w_g^r(X^E, Y^E)$ the right-hand-side gust field of the corridor with respect to the flightpath. For the longitudinal $(u_g(X^E, Y^E))$, lateral $(v_g(X^E, Y^E))$ and vertical $(w_g(X^E, Y^E))$ gust fields the results of this decomposition are given in figures G.13, G.15 and G.16, respectively. For the sake of completeness, the uncorrelated v_g gust field is given in figure G.14.

It should be noted that the sum of the gust fields' symmetrical and anti-symmetrical parts results in the (corridor) gust fields given in figures G.1, G.2 G.3 and G.4.

The symmetrical and anti-symmetrical gust fields given in figures G.13, G.15 and G.16 will be used as inputs for the LPF-model. Note that next to the aircraft's response to longitudinal (u_g) and vertical (w_g) gusts, the response to correlated lateral gusts v_g will be calculated.

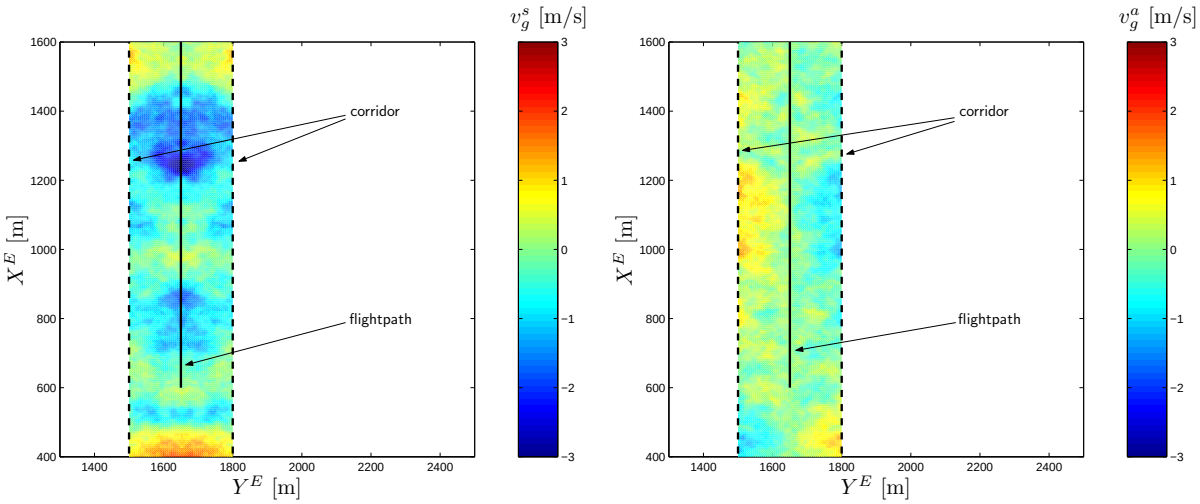


Figure G.14: Decomposition of the 2D (uncorrelated) gust field $v_g(X^E, Y^E)$ [m/s] into the symmetrical part $v_g^s(X^E, Y^E)$ (left), and the anti-symmetrical part $v_g^a(X^E, Y^E)$ (right), including the definition of the flightpath-corridor, $L_g = 300$ [m] and $\sigma^2 = 1$ $[\frac{\text{m}^2}{\text{s}^2}]$ gust fields.

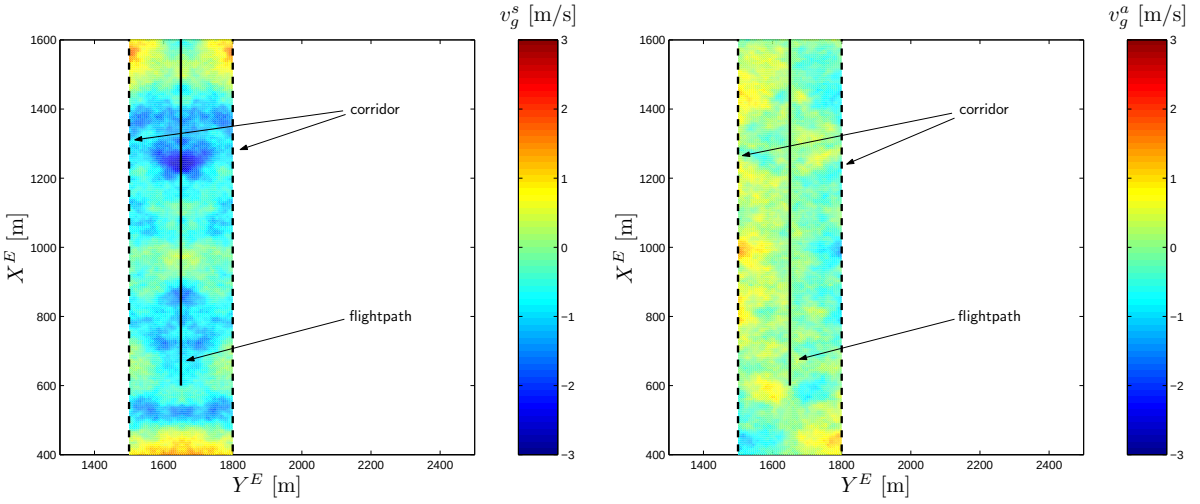


Figure G.15: Decomposition of the 2D (correlated) gust field $v_g(X^E, Y^E)$ [m/s] into the symmetrical part $v_g^s(X^E, Y^E)$ (left), and the anti-symmetrical part $v_g^a(X^E, Y^E)$ (right), including the definition of the flightpath-corridor, $L_g = 300$ [m] and $\sigma^2 = 1$ $[\frac{\text{m}^2}{\text{s}^2}]$ gust fields.

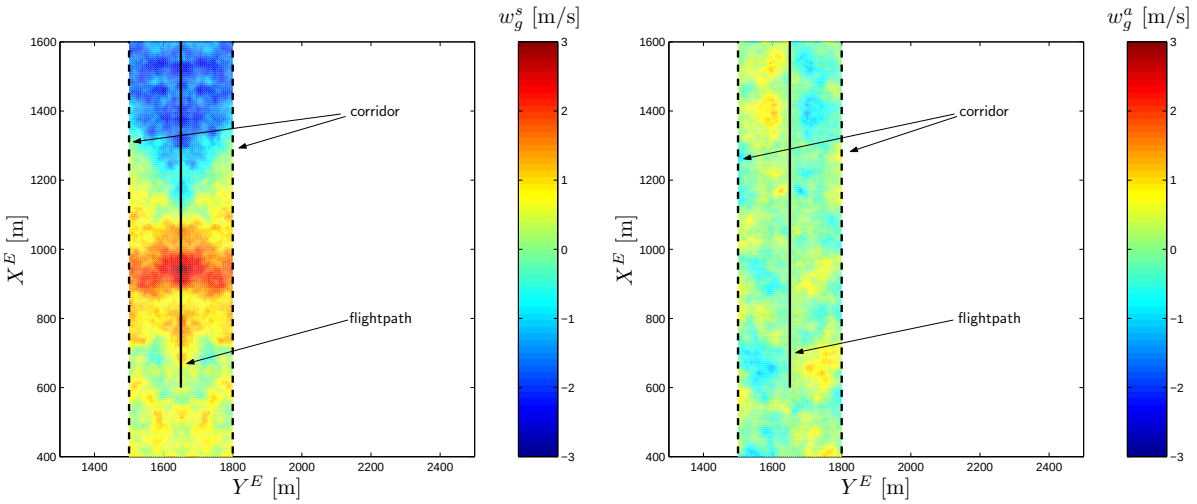


Figure G.16: Decomposition of the 2D gust field $w_g(X^E, Y^E)$ [m/s] into the symmetrical part $w_g^s(X^E, Y^E)$ (left), and the anti-symmetrical part $w_g^a(X^E, Y^E)$ (right), including the definition of the flightpath-corridor, $L_g = 300$ [m] and $\sigma^2 = 1$ $[\frac{\text{m}^2}{\text{s}^2}]$ gust fields.

G.4 Summary of the definition of the aerodynamic model gust inputs

For the calculation of the Parametric Computational Aerodynamics (PCA-), the Delft University of Technology (DUT-) and the Four Point Aircraft (FPA-) model time-domain gust-responses, the gust inputs to these models are summarized here. The inputs for all aerodynamic models are defined for the Stability Frame of Reference $\mathcal{F}_S$ (see also chapter 5).

In the following use is made of the atmospheric turbulence velocity components u_g, v_g and w_g at the positions "0", "1", "2", and "3" of the FPA-model, see also figures G.17 and G.18 for the definition of the FPA-model's gust input locations and the definition of the positive directions of the gust inputs, respectively. The gust field's velocity components at the points "0", "1", "2", and "3" are obtained from the interpolation procedure given in chapter 9.

Starting with the FPA-model, the translational gust inputs are defined as,

$$\left.\begin{array}{rcl} u_g^{FPA} & = & u_{g_0} \\ v_g^{FPA} & = & v_{g_0} \\ w_g^{FPA} & = & \frac{1}{3}\left(w_{g_0} + w_{g_1} + w_{g_2}\right) \end{array}\right\} \tag{G.25}$$

while for the rotational gusts they are defined as,

$$\left.\begin{array}{rcl} p_g^{FPA} & = & \frac{w_{g_1} - w_{g_2}}{b`} \\ q_g^{FPA} & = & \frac{w_{g_3} - w_{g_0}}{l_h} \\ r_{1_g}^{FPA} & = & \frac{u_{g_2} - u_{g_1}}{b`} \\ r_{2_g}^{FPA} & = & \frac{v_{g_0} - v_{g_3}}{l_v} \end{array}\right\} \tag{G.26}$$

with u_{g_0} the longitudinal gust velocity component, v_{g_0} the lateral gust velocity component and w_{g_0} the vertical gust velocity component all at the center of gravity. Further, u_{g_1} the longitudinal gust velocity component at location "1" (see figure G.17), u_{g_2} the one at location "2" and v_{g_3} the lateral gust velocity component at location "3". Next, w_{g_1}, w_{g_2} and w_{g_3} the vertical gust velocity components at locations "1", "2" and "3", respectively. Finally, $b' = 0.85b$ with b the aircraft's span, l_h the horizontal tail-length in [m] and l_v the vertical tail-length in [m] (note that $l_h = l_v$). The positive directions of the gust inputs u_g^{FPA}, v_g^{FPA}, w_g^{FPA}, p_g^{FPA}, q_g^{FPA}, $r_{1_g}^{FPA}$ and $r_{2_g}^{FPA}$ are given in figure G.18. Besides the gust input w_g^{FPA}, the time-derivative of it is required, or,

$$\dot{w}_g^{FPA} = \frac{dw_{g_0}}{dt} \tag{G.27}$$

Next, the PCA-model gust input definition is similar to the one for the FPA-model, however, the vertical-gust input w_g^{PCA} is defined as,

$$w_g^{PCA} = w_{g_0}$$

and the PCA-model gust input definition is summarized as,

$$\left.\begin{array}{rcl} u_g^{PCA} &=& u_{g_0} \\ v_g^{PCA} &=& v_{g_0} \\ w_g^{PCA} &=& w_{g_0} \\ \\ p_g^{PCA} &=& \frac{w_{g_1} - w_{g_2}}{b`} \\ r_{1_g}^{PCA} &=& \frac{u_{g_2} - u_{g_1}}{b`} \\ \\ \dot{u}_g^{PCA} &=& \frac{du_{g_0}}{dt} \\ \dot{v}_g^{PCA} &=& \frac{dv_{g_0}}{dt} \\ \dot{w}_g^{PCA} &=& \frac{dw_{g_0}}{dt} \\ \\ \dot{p}_g^{PCA} &=& \frac{dp_g}{dt} \\ \dot{r}_{1_g}^{PCA} &=& \frac{dr_{1_g}}{dt} \end{array}\right\} \tag{G.28}$$

Finally, the DUT-model gust input definition is similar to the one for the PCA-model, and it is summarized as,

$$\left.\begin{array}{rcl} u_g^{DUT} &=& u_{g_0} \\ v_g^{DUT} &=& v_{g_0} \\ w_g^{DUT} &=& w_{g_0} \\ \\ p_g^{DUT} &=& \frac{w_{g_1} - w_{g_2}}{b`} \\ r_{1_g}^{DUT} &=& \frac{u_{g_2} - u_{g_1}}{b`} \\ \\ \dot{v}_g^{DUT} &=& \frac{dv_{g_0}}{dt} \\ \dot{w}_g^{DUT} &=& \frac{dw_{g_0}}{dt} \end{array}\right\} \tag{G.29}$$

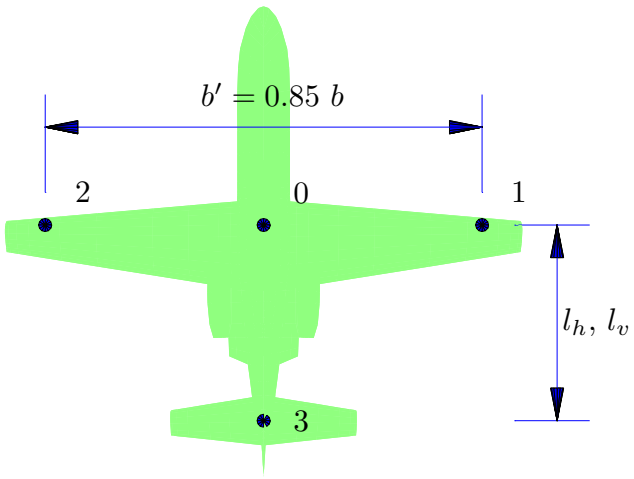


Figure G.17: The Four Point Aircraft model including the definitions of b', l_h and l_v.

From the definition of the flightpath (given in section G.3.1) and the definition of the 2D atmospheric gust fields (given in section G.3.2), the aerodynamic models' gust inputs are calculated. For the calculation of the numerical time-derivative of the gust inputs, use is made of a second order function which is fitted locally through the input-data first (with time being the independent variable). Secondly, using this function, its first order derivative with respect to the independent variable (time) produces the sought time-derivative.
For the FPA-model, in figure G.19 the gust inputs u_g^{FPA}, v_g^{FPA}, w_g^{FPA}, $\dot{u}_g^{FPA}$, $\dot{v}_g^{FPA}$, $\dot{w}_g^{FPA}$, p_g^{FPA}, q_g^{FPA}, $r_{1_g}^{FPA}$ and $r_{2_g}^{FPA}$, are given for the defined flightpath and for the gust fields provided in figures G.1, G.3 and G.4. For comparison, in figure G.20 the gust inputs w_g^{FPA} and w_g^{DUT} for the FPA- and the DUT-model, respectively, are shown.

G.5 Remarks

The spatial-domain simulations of the 2D longitudinal, lateral and vertical gust fields were calculated in the Earth-Fixed Frame of Reference $\mathcal{F}_E$. For the aircraft responses to these gust fields use is made of the Inertial Frame of Reference $\mathcal{F}_I$ and the Aerodynamic Frame of Reference $\mathcal{F}_{aero}$.
Comparing these reference frames it should be noted that the X_E- and X_I-axes point in opposite direction, which also holds for the Z_E- and Z_I-axes. Although these axes point in opposite directions, it should be noted that the encountered gust fields generated in $\mathcal{F}_E$ are not transformed to $\mathcal{F}_I$ in terms of the sign of the gust fields (for example, the positive vertical gust velocity component in $\mathcal{F}_E$ points towards the Earth's surface, while this gust velocity component in $\mathcal{F}_I$ becomes negative).

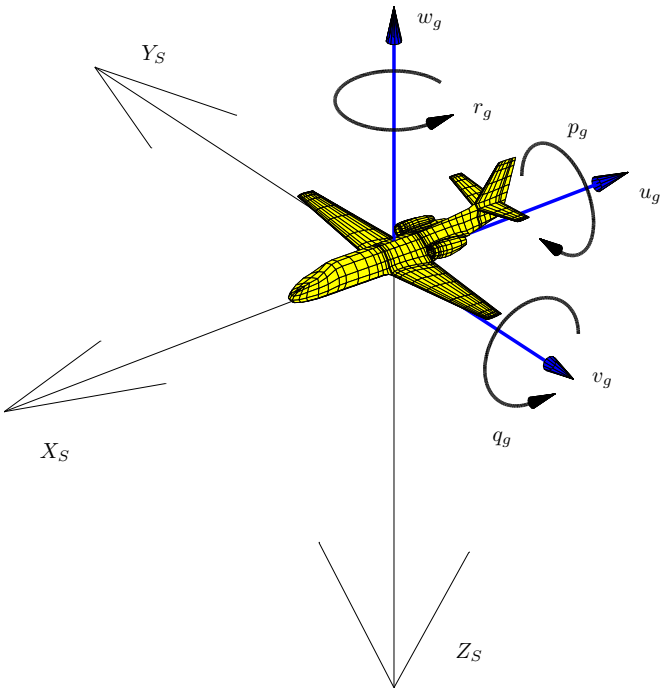


Figure G.18: The Stability Frame of Reference $\mathcal{F}_S$, including the definition of both the FPA-model's atmospheric turbulence velocity component inputs $[u_g, v_g, w_g]^T$ and the rotational inputs $[p_g, q_g, r_g]^T$.

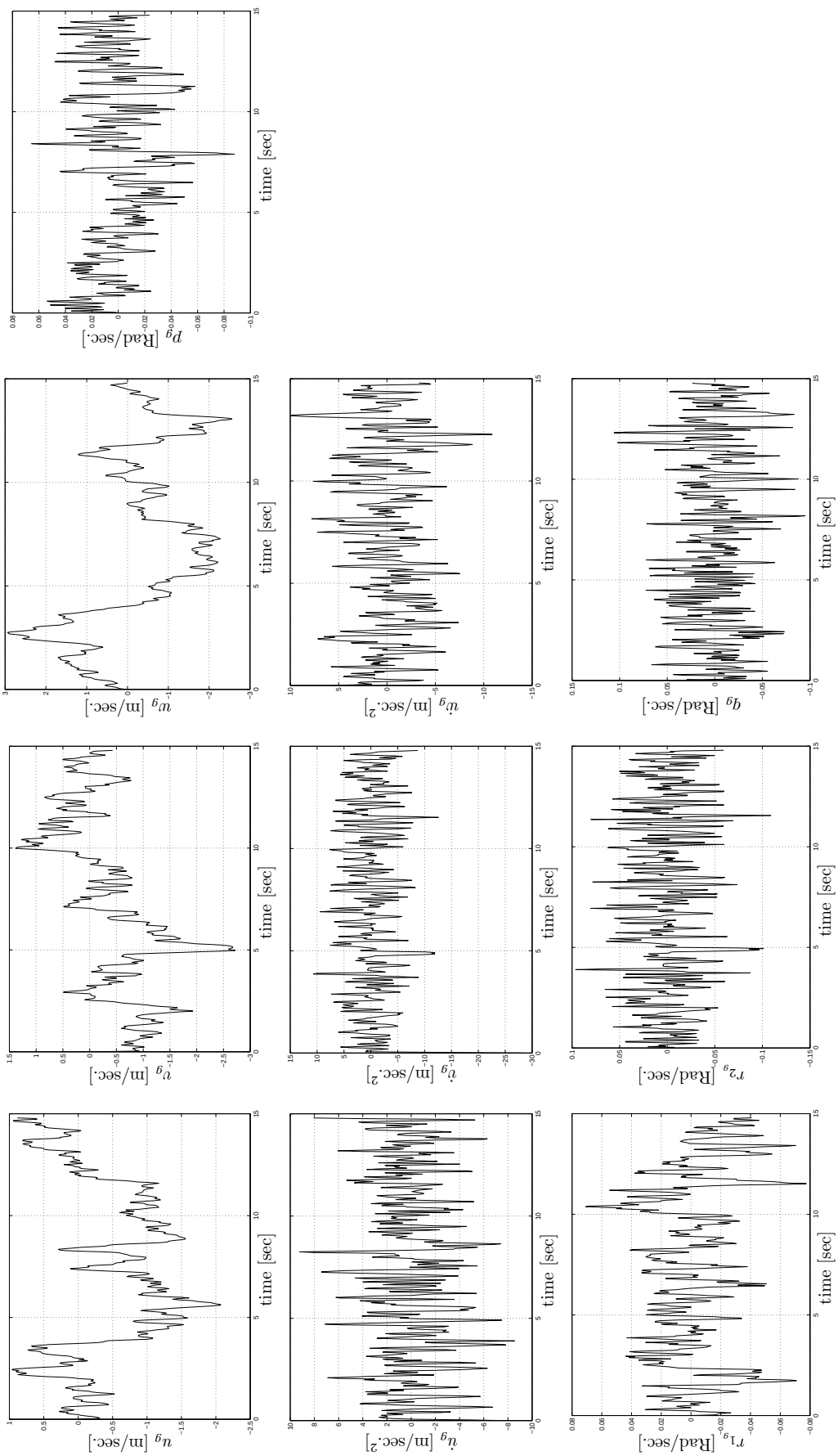


Figure G.19: The FPA-model's gust inputs for the Stability Frame of Reference $\mathcal{F}_S$: u_g^{FPA}, v_g^{FPA}, w_g^{FPA}, $\dot{u}_g^{FPA}$, $\dot{v}_g^{FPA}$, $\dot{w}_g^{FPA}$, p_g^{FPA}, q_g^{FPA}, $r1_g^{FPA}$ and $r2_g^{FPA}$, for the defined flightpath and for the gust fields given in figures G.1, G.3 and G.4.

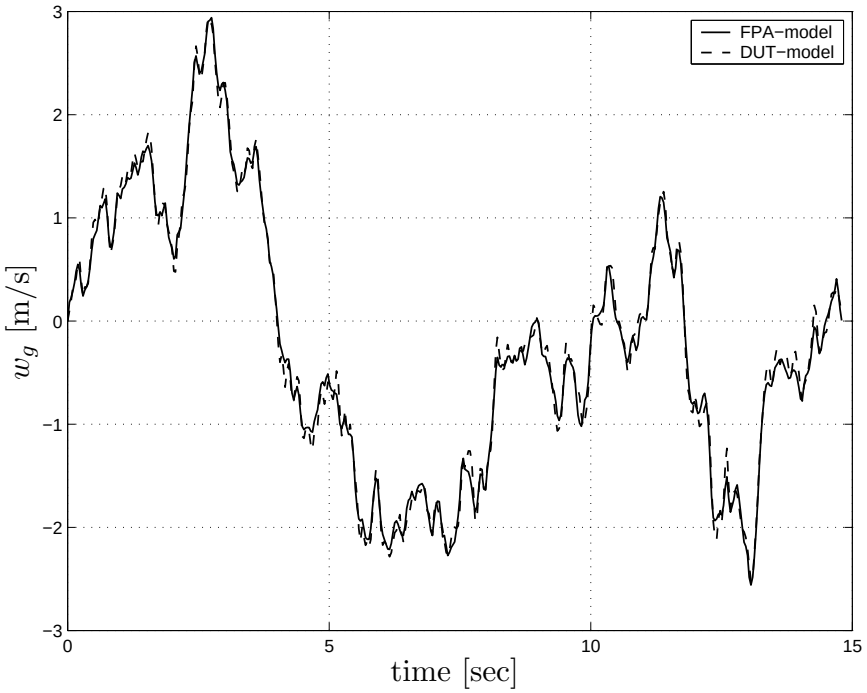


Figure G.20: Both the FPA- and DUT-model's gust inputs w_g^{FPA} and w_g^{DUT}, respectively, for the defined flightpath and for the gust field given in figure G.4.

Appendix H

The atmospheric turbulence PSD-functions for the equations of motion

H.1 Introduction

In chapter 2 the definition of the Power Spectral Density (PSD) functions for the two-dimensional (2D) atmospheric turbulence velocity components is given. For the longitudinal velocity component u_g, the lateral velocity component v_g and the vertical velocity component w_g, the PSD-functions were given as a function of the non-dimensional spatial frequencies $\Omega_1 L_g$ and $\Omega_2 L_g$ (with $\Omega_1 L_g$ and $\Omega_2 L_g$ the non-dimensional spatial frequencies along the X_E- and Y_E-axis of the Earth-Fixed Frame of Reference $\mathcal{F}_E$, respectively, see also equation (2.33)). Similarly, the PSD-functions for the 1D gust-components u_g, v_g and w_g as a function of the non-dimensional spatial frequency $\Omega_1 L_g$ were provided as well (see also equation (2.35)).

For the calculation of the aircraft's response to atmospheric turbulence, the PSD-functions are given in this appendix for the non-dimensional atmospheric turbulence velocity components $\hat{u}_g = \frac{u_g}{Q_\infty}$, $\beta_g = \frac{v_g}{Q_\infty}$ and $\alpha_g = \frac{w_g}{Q_\infty}$. Also, they are now given as a function of the circular frequency $\omega = \Omega_x Q_\infty$ [Rad/sec] and the spatial frequency Ω_y [Rad/m], with $\Omega_x = \frac{\omega}{Q_\infty}$ the spatial frequency along the X_E-axis of the frame $\mathcal{F}_E$, and Ω_y the spatial frequency along the Y_E-axis of $\mathcal{F}_E$. The gust-components' PSD-functions hold for the flightpath corridor defined in appendix G.

In sections H.2 and H.3 the 2D atmospheric turbulence PSD-functions and the one-dimensional (1D) atmospheric turbulence PSD-functions are summarized, respectively. In section H.4 the FPA-model's gust input PSD-functions are summarized. Details of the FPA-model can be found in chapter 12.

H.2 2D PSD-functions

Similar to equation (2.33), the 2D PSD-function for the non-dimensional longitudinal gust velocity component $\hat{u}_g$ is defined as,

$$S_{\hat{u}_g\hat{u}_g}(\omega,\Omega_y) = \pi\sigma^2\frac{L_g^2}{Q_\infty}\,\frac{1+\left(\frac{\omega L_g}{Q_\infty}\right)^2+4\left(\Omega_y L_g\right)^2}{\left\{1+\left(\frac{\omega L_g}{Q_\infty}\right)^2+\left(\Omega_y L_g\right)^2\right\}^{5/2}} \tag{H.1}$$

while for the 2D PSD-function with respect to the non-dimensional lateral gust velocity β_g, it is given as,

$$S_{\beta_g\beta_g}(\omega,\Omega_y) = \pi\sigma^2\frac{L_g^2}{Q_\infty}\,\frac{1+4\left(\frac{\omega L_g}{Q_\infty}\right)^2+\left(\Omega_y L_g\right)^2}{\left\{1+\left(\frac{\omega L_g}{Q_\infty}\right)^2+\left(\Omega_y L_g\right)^2\right\}^{5/2}} \tag{H.2}$$

and, finally, for the 2D PSD-function with respect to the non-dimensional vertical gust velocity component α_g, the following holds,

$$S_{\alpha_g\alpha_g}(\omega,\Omega_y) = 3\pi\sigma^2\frac{L_g^2}{Q_\infty}\,\frac{\left(\frac{\omega L_g}{Q_\infty}\right)^2+\left(\Omega_y L_g\right)^2}{\left\{1+\left(\frac{\omega L_g}{Q_\infty}\right)^2+\left(\Omega_y L_g\right)^2\right\}^{5/2}} \tag{H.3}$$

For the 2D cross PSD-function with respect to $\hat{u}_g$ and β_g, it is then,

$$S_{\hat{u}_g\beta_g}(\omega,\Omega_y) = -3\pi\sigma^2\frac{L_g^2}{Q_\infty}\,\frac{\left(\frac{\omega L_g}{Q_\infty}\right)\left(\Omega_y L_g\right)}{\left\{1+\left(\frac{\omega L_g}{Q_\infty}\right)^2+\left(\Omega_y L_g\right)^2\right\}^{5/2}} \tag{H.4}$$

It should be noted that the integral of equations (H.1), (H.2) and (H.3) over the circular frequency ω and the spatial frequency Ω_y results in the variance σ^2. Taking, for example, equation (H.3) we find,

$$\sigma^2 = \frac{1}{(2\pi)^2}\int_{-\infty}^{+\infty}\int_{-\infty}^{+\infty} S_{\alpha_g\alpha_g}(\omega,\Omega_y)\;d\Omega_y\;d\omega \tag{H.5}$$

with σ^2 the variance of all gust-components according to $\sigma^2 = \frac{1}{Q_\infty^2}$.

The auto PSD-functions given in equations (H.1), (H.2), (H.3), and the cross PSD-function given in equation (H.4), are shown in figures H.1. These (one-sided) PSD-functions are given as a function of both the circular frequency ω (ranging from $\omega = 0$ to $\omega = \frac{Q_\infty}{\bar{c}}$ [Rad/sec], with $\bar{c}$ the mean aerodynamic chord) and the spatial frequency Ω_y (ranging from $\Omega_y = 0$ to $\Omega_y = \frac{2\pi}{0.75b}$ [Rad/m], with b the aircraft's span). The number of logarithmically scaled discretization points for ω and Ω_y are $N_\omega = 500$ and $N_{\Omega_y} = 550$, respectively.

H.3 1D PSD-functions

The 1D gust-component's PSD-function is calculated from the 2D gust-component's PSD-function (see equations (H.1), (H.2) and (H.3)), according to,

$$S_{yy}(\omega) = \frac{1}{2\pi} \int_{-\infty}^{+\infty} S_{yy}(\omega, \Omega_y)\ d\Omega_y \tag{H.6}$$

with y either $\hat{u}_g$, β_g or α_g. For the non-dimensional longitudinal gust-component $\hat{u}_g$, the integration of equation (H.1) over all Ω_y results in the 1D PSD-function,

$$S_{\hat{u}_g\hat{u}_g}(\omega) = 2\sigma^2 \frac{L_g}{Q_\infty} \frac{1}{1 + \left(\frac{\omega L_g}{Q_\infty}\right)^2} \tag{H.7}$$

while for the non-dimensional lateral gust-component β_g, the integration of equation (H.2) over all Ω_y results in the 1D PSD-function,

$$S_{\beta_g\beta_g}(\omega) = \sigma^2 \frac{L_g}{Q_\infty} \frac{1 + 3\left(\frac{\omega L_g}{Q_\infty}\right)^2}{\left\{1 + \left(\frac{\omega L_g}{Q_\infty}\right)^2\right\}^2} \tag{H.8}$$

Finally, for the non-dimensional vertical gust-component α_g, the integration of equation (H.3) over all Ω_y yields in the 1D PSD-function,

$$S_{\alpha_g\alpha_g}(\omega) = \sigma^2 \frac{L_g}{Q_\infty} \frac{1 + 3\left(\frac{\omega L_g}{Q_\infty}\right)^2}{\left\{1 + \left(\frac{\omega L_g}{Q_\infty}\right)^2\right\}^2} \tag{H.9}$$

For the cross PSD-function given in equation (H.4), the integral in equation (H.6) results in,

$$S_{\hat{u}_g\beta_g}(\omega) = 0 \tag{H.10}$$

The analytical one-sided PSD-functions according to equations (H.7), (H.8), (H.9) and (H.10), are given in figures H.2. In these figures the one-sided numerically obtained 1D PSD-functions calculated from the integral over all Ω_y (see equation (H.6)) of the 2D PSD-functions given in equations (H.1), (H.2), (H.3) and (H.4) are provided as well. The numerical 1D PSD-functions were calculated using both the range of the circular frequency ω ánd the range of the spatial frequency Ω_y given in section H.2.

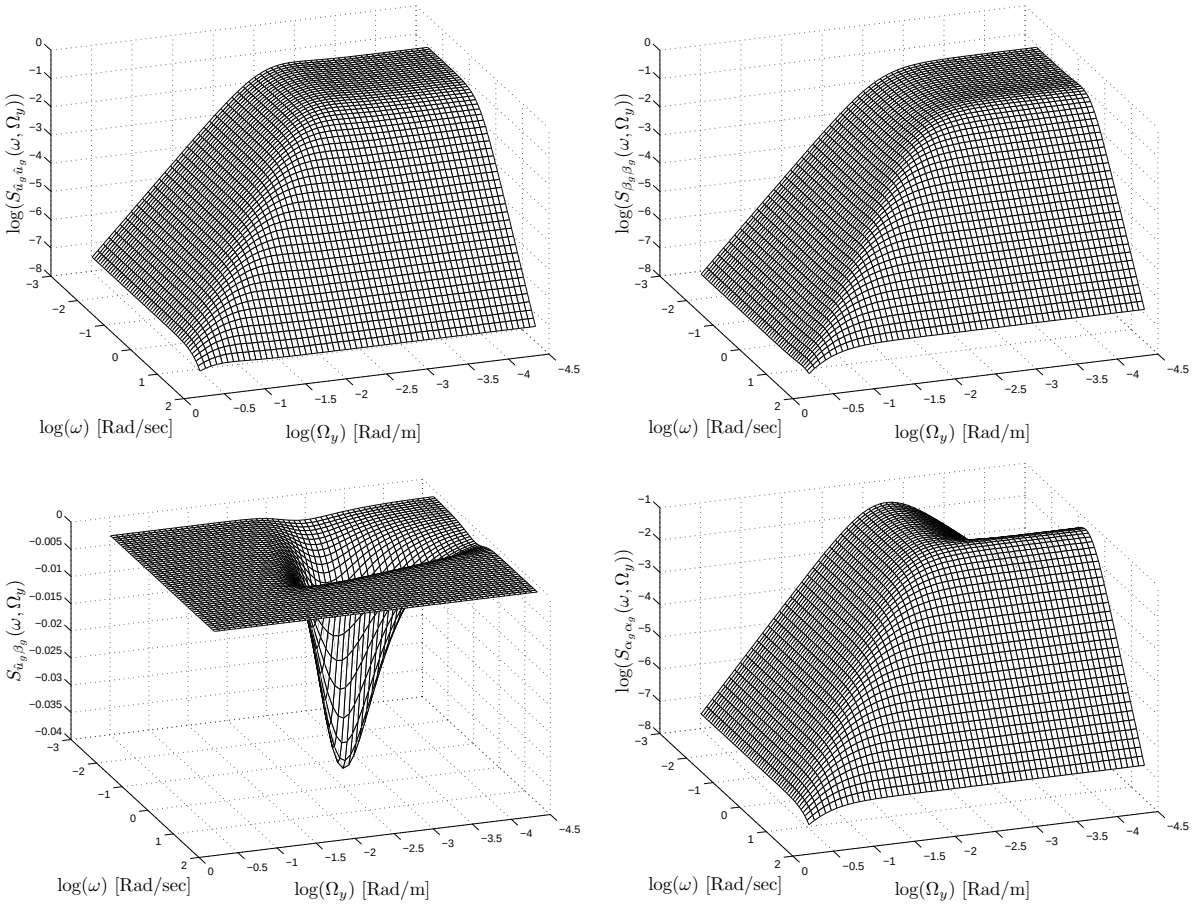


Figure H.1: Starting from the left top figure in clockwise direction, the 2D atmospheric turbulence-component PSD-functions $S_{\hat{u}_g\hat{u}_g}(\omega,\Omega_y)$, $S_{\beta_g\beta_g}(\omega,\Omega_y)$, $S_{\alpha_g\alpha_g}(\omega,\Omega_y)$ and the cross PSD-function $S_{\hat{u}_g\beta_g}(\omega,\Omega_y)$, for the atmospheric turbulence scale length $L_g = 300$ m, and variance $\sigma^2 = \frac{1}{Q_\infty^2}$.

H.4 FPA-model PSD-functions

The FPA-model's input PSD-functions are calculated from the model's gust input covariance functions given in chapter 12. These functions are summarized here as,

$$C_{u_g u_g}(\tau) = \sigma^2 \; f(\xi_1)$$

$$C_{v_g v_g}(\tau) = \sigma^2 \; g(\xi_1)$$

$$C_{w_g w_g}(\tau) = \sigma^2 \left\{ \frac{1}{3} g(\xi_1) + \frac{4}{9} g(\xi_2) + \frac{2}{9} g(\xi_3) \right\}$$

$$C_{p_g p_g}(\tau) = \frac{2\sigma^2}{(b')^2} \left\{ g(\xi_1) - g(\xi_3) \right\}$$

$$C_{q_g q_g}(\tau) = \frac{\sigma^2}{l_h^2} \left\{ 2g(\xi_1) - g(\xi_4) - g(\xi_5) \right\}$$

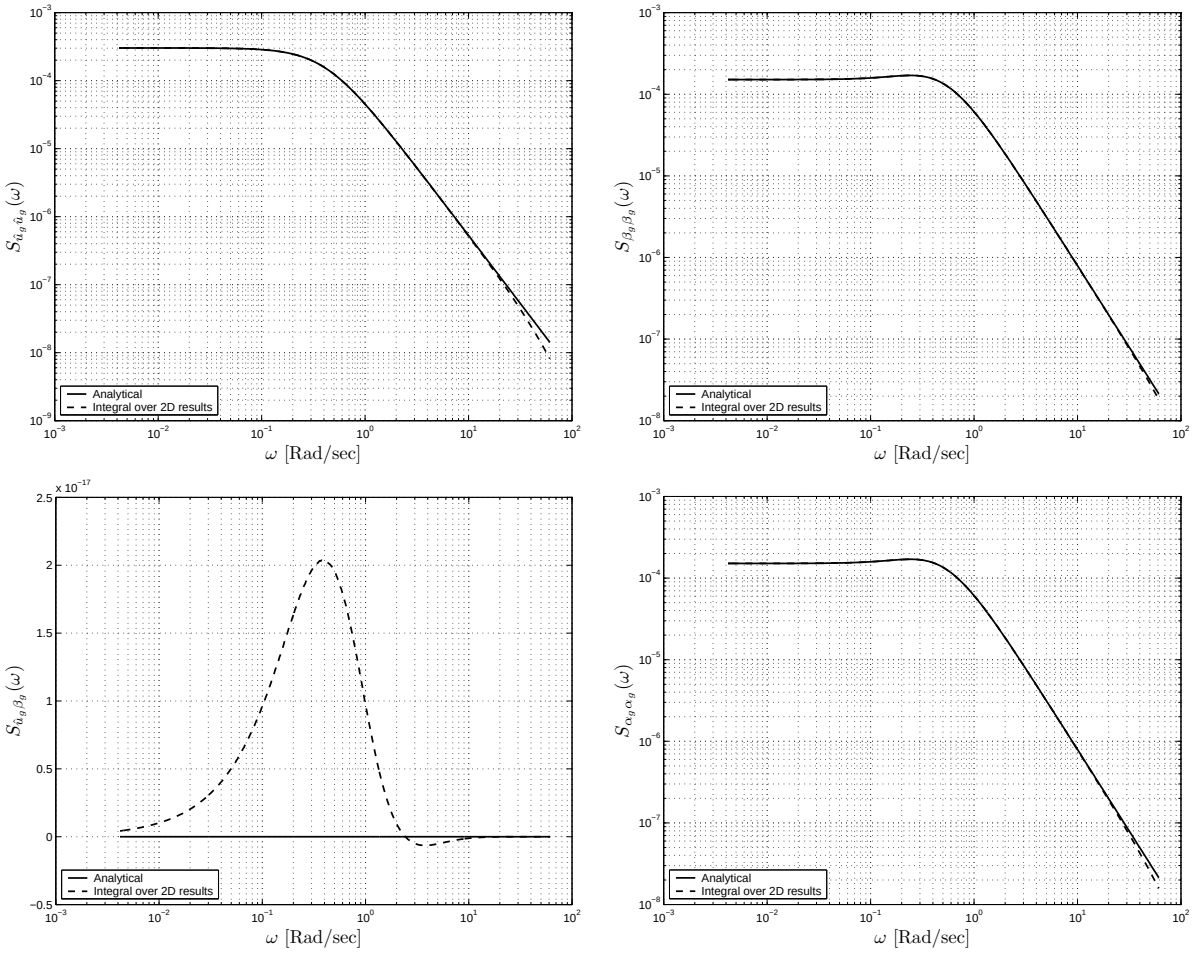


Figure H.2: Starting from the left top figure in clockwise direction, the 1D atmospheric turbulence-component PSD-functions $S_{\hat{u}_g\hat{u}_g}(\omega)$, $S_{\beta_g\beta_g}(\omega)$, $S_{\alpha_g\alpha_g}(\omega)$, and the cross PSD-function $S_{\hat{u}_g\beta_g}(\omega)$, for the atmospheric turbulence scale length $L_g = 300$ m, and variance $\sigma^2 = \frac{1}{Q_\infty^2}$.

$$C_{r_{1_g}r_{1_g}}(\tau) = \frac{2\sigma^2}{(b')^2}\left\{f(\xi_1) - K_1 f(\xi_3) - (1-K_1)\,g(\xi_3)\right\}$$

$$C_{r_{2_g}r_{2_g}}(\tau) = \frac{\sigma^2}{l_v^2}\left\{2g(\xi_1) - g(\xi_6) - g(\xi_7)\right\}$$

$$C_{w_g q_g}(\tau) = \frac{\sigma^2}{3l_h}\left\{g(\xi_5) - g(\xi_1) + 2g(\xi_8) - 2g(\xi_2)\right\}$$

$$C_{v_g r_{1_g}}(\tau) = \frac{\sigma^2}{b'}\left\{2K_2\left[g(\xi_2) - f(\xi_2)\right]\right\}$$

$$C_{v_g r_{2_g}}(\tau) = \frac{\sigma^2}{l_v}\left\{g(\xi_1) - g(\xi_7)\right\}$$

$$C_{r_{1_g}r_{2_g}}(\tau) = \frac{\sigma^2}{b' l_v}\left\{K_3\left[g(\xi_9) - f(\xi_9)\right] + K_2\left[f(\xi_2) - g(\xi_2)\right]\right\}$$

with σ^2 the atmospheric turbulence's variance (taken to be $\sigma^2 = 1$ $[\frac{\mathrm{m}^2}{\mathrm{s}^2}]$), l_v [m] the vertical tail-length, l_h [m] the horizontal tail-length, $b' = 0.85b$ [m] with b [m] the aircraft's span, τ the time-separation [sec.], and,

$$K_1 = \frac{\left(\frac{Q_\infty \tau}{L_g}\right)^2}{\left(\frac{Q_\infty \tau}{L_g}\right)^2 + \left(\frac{b'}{2L_g}\right)^2}$$

$$K_2 = \frac{\left(\frac{Q_\infty \tau}{L_g}\right)\left(\frac{b'}{2L_g}\right)}{\left(\frac{Q_\infty \tau}{L_g}\right)^2 + \left(\frac{b'}{L_g}\right)^2}$$

$$K_3 = \frac{\left(\frac{Q_\infty \tau}{L_g} - \frac{l_v}{L_g}\right)\left(\frac{b'}{2L_g}\right)}{\left(\frac{Q_\infty \tau}{L_g} - \frac{l_v}{L_g}\right)^2 + \left(\frac{b'}{L_g}\right)^2}$$

and the non-dimensional separations according to,

$$\frac{\xi_1}{L_g} = \zeta_1 = \left|\frac{Q_\infty \tau}{L_g}\right|$$

$$\frac{\xi_2}{L_g} = \zeta_2 = \sqrt{\left(\frac{Q_\infty \tau}{L_g}\right)^2 + \left(\frac{b'}{2L_g}\right)^2}$$

$$\frac{\xi_3}{L_g} = \zeta_3 = \sqrt{\left(\frac{Q_\infty \tau}{L_g}\right)^2 + \left(\frac{b'}{L_g}\right)^2}$$

$$\frac{\xi_4}{L_g} = \zeta_4 = \left|\frac{Q_\infty \tau}{L_g} + \frac{l_h}{L_g}\right|$$

$$\frac{\xi_5}{L_g} = \zeta_5 = \left|\frac{Q_\infty \tau}{L_g} - \frac{l_h}{L_g}\right|$$

$$\frac{\xi_6}{L_g} = \zeta_6 = \left|\frac{Q_\infty \tau}{L_g} + \frac{l_v}{L_g}\right|$$

$$\frac{\xi_7}{L_g} = \zeta_7 = \left|\frac{Q_\infty \tau}{L_g} - \frac{l_h}{L_g}\right|$$

$$\frac{\xi_8}{L_g} = \zeta_8 = \sqrt{\left(\frac{Q_\infty \tau}{L_g} - \frac{l_h}{L_g}\right)^2 + \left(\frac{b'}{2L_g}\right)^2}$$

$$\frac{\xi_9}{L_g} = \zeta_9 = \sqrt{\left(\frac{Q_\infty \tau}{L_g} - \frac{l_v}{L_g}\right)^2 + \left(\frac{b'}{2L_g}\right)^2}$$

with the f and g functions the Dryden longitudinal and lateral correlation functions, respectively (see also chapter 2),

$$f(\xi) = e^{-\frac{\xi}{L_g}}$$

$$g(\xi) = e^{-\frac{\xi}{L_g}} \left(1 - \frac{\xi}{2L_g}\right)$$

with the dimensional separation ξ [m] either ξ_1 [m] to ξ_9 [m], Q_∞ [m/s] the airspeed and L_g [m] the gust scale length. The covariance functions are shown in figures H.3 as a function of the non-dimensional distance traveled $\frac{Q_\infty \tau}{L_g}$ for the gust scale length $L_g = 300$ [m] and the variance $\sigma^2 = 1$ $[\frac{\text{m}^2}{\text{s}^2}]$. These results have been calculated for the time-separation's discretization $\Delta\tau = 1\frac{\bar{c}}{Q_\infty}$ [sec] (with $\bar{c}$ the mean aerodynamic chord in [m]) with the time-separation, τ [sec.], equal to $\tau = [-N\ \Delta\tau \cdots N\ \Delta\tau]$ and $N = 60000$.

The FPA-model's gust input PSD-functions are obtained by Fourier transforming the covariance functions using MATLAB's Fast Fourier Transform (FFT), or,

$$S[k] = \sum_{n=0}^{N-1} C[n]\ e^{-j\frac{2\pi kn}{N}}$$

with $S[k]$ the PSD-function's estimate ("periodogram"), k the frequency-counter, $C[n]$ the covariance function and n the time-separation counter as in $\tau = n\ \Delta\tau$. As a function of the circular frequency ω [Rad/sec.] the numerically calculated PSD-functions $S_{u_g u_g}(\omega)$, $S_{v_g v_g}(\omega)$, $S_{w_g w_g}(\omega)$, $S_{p_g p_g}(\omega)$, $S_{q_g q_g}(\omega)$, $S_{r_{1_g} r_{1_g}}(\omega)$, $S_{r_{2_g} r_{2_g}}(\omega)$, $S_{w_g q_g}(\omega)$, $S_{v_g r_{1_g}}(\omega)$, $S_{v_g r_{2_g}}(\omega)$ and $S_{r_{1_g} r_{2_g}}(\omega)$ are given in figures H.4, with,

$$\omega_k = \frac{2\pi\ k}{N\ \Delta\tau} \tag{H.11}$$

with $k = 0 \cdots N-1$, $2N+1$ the number of samples of the covariance functions (with N taken to be $N = 60000$) and $\Delta\tau$ [sec.] the time-separation's discretization (taken to be $\Delta\tau = 1\frac{\bar{c}}{Q_\infty}$, with $\bar{c}$ the mean aerodynamic chord in [m]). The motivation for the choice of both N and $\Delta\tau$ is such that the PSD-functions' frequency-response ranges from at least $\omega_{min} = 0.01$ [Rad/sec.] to at least $\omega_{max} = 100$ [Rad/sec.]. Similar to the covariance functions, the PSD-functions are also given in dimensional form.

For the non-dimensional FPA-model gust inputs $\hat{u}_g = \frac{u_g}{Q_\infty}$, $\beta_g = \frac{v_g}{Q_\infty}$, $\alpha_g = \frac{w_g}{Q_\infty}$, $\frac{p_g b}{2Q_\infty}$, $\frac{q_g \bar{c}}{Q_\infty}$, $\frac{r_{1_g} b}{2Q_\infty}$ and $\frac{r_{2_g} b}{2Q_\infty}$ the non-dimensional PSD-functions are according to,

$$\left.\begin{array}{lcl}
S_{\hat{u}_g \hat{u}_g}(\omega) & = & \frac{1}{Q_\infty^2} S_{u_g u_g}(\omega) \\
S_{\beta_g \beta_g}(\omega) & = & \frac{1}{Q_\infty^2} S_{v_g v_g}(\omega) \\
S_{\alpha_g \alpha_g}(\omega) & = & \frac{1}{Q_\infty^2} S_{w_g w_g}(\omega) \\
 & & \\
S_{\frac{p_g b}{2Q_\infty} \frac{p_g b}{2Q_\infty}}(\omega) & = & \left(\frac{b}{2Q_\infty}\right)^2 S_{p_g p_g}(\omega) \\
S_{\frac{q_g \bar{c}}{Q_\infty} \frac{q_g \bar{c}}{Q_\infty}}(\omega) & = & \left(\frac{\bar{c}}{Q_\infty}\right)^2 S_{q_g q_g}(\omega) \\
S_{\frac{r_{1_g} b}{2Q_\infty} \frac{r_{1_g} b}{2Q_\infty}}(\omega) & = & \left(\frac{b}{2Q_\infty}\right)^2 S_{r_{1_g} r_{1_g}}(\omega) \\
S_{\frac{r_{2_g} b}{2Q_\infty} \frac{r_{2_g} b}{2Q_\infty}}(\omega) & = & \left(\frac{b}{2Q_\infty}\right)^2 S_{r_{2_g} r_{2_g}}(\omega) \\
 & & \\
S_{\alpha_g \frac{q_g \bar{c}}{Q_\infty}}(\omega) & = & \frac{\bar{c}}{Q_\infty^2} S_{w_g q_g}(\omega) \\
S_{\beta_g \frac{r_{1_g} b}{2Q_\infty}}(\omega) & = & \frac{b}{2Q_\infty^2} S_{v_g r_{1_g}}(\omega) \\
S_{\beta_g \frac{r_{2_g} b}{2Q_\infty}}(\omega) & = & \frac{b}{2Q_\infty^2} S_{v_g r_{2_g}}(\omega) \\
S_{\frac{r_{1_g} b}{2Q_\infty} \frac{r_{2_g} b}{2Q_\infty}}(\omega) & = & \left(\frac{b}{2Q_\infty}\right)^2 S_{r_{1_g} r_{2_g}}(\omega)
\end{array}\right\} \qquad \text{(H.12)}$$

Details of the FPA-model can be found in chapter 12.

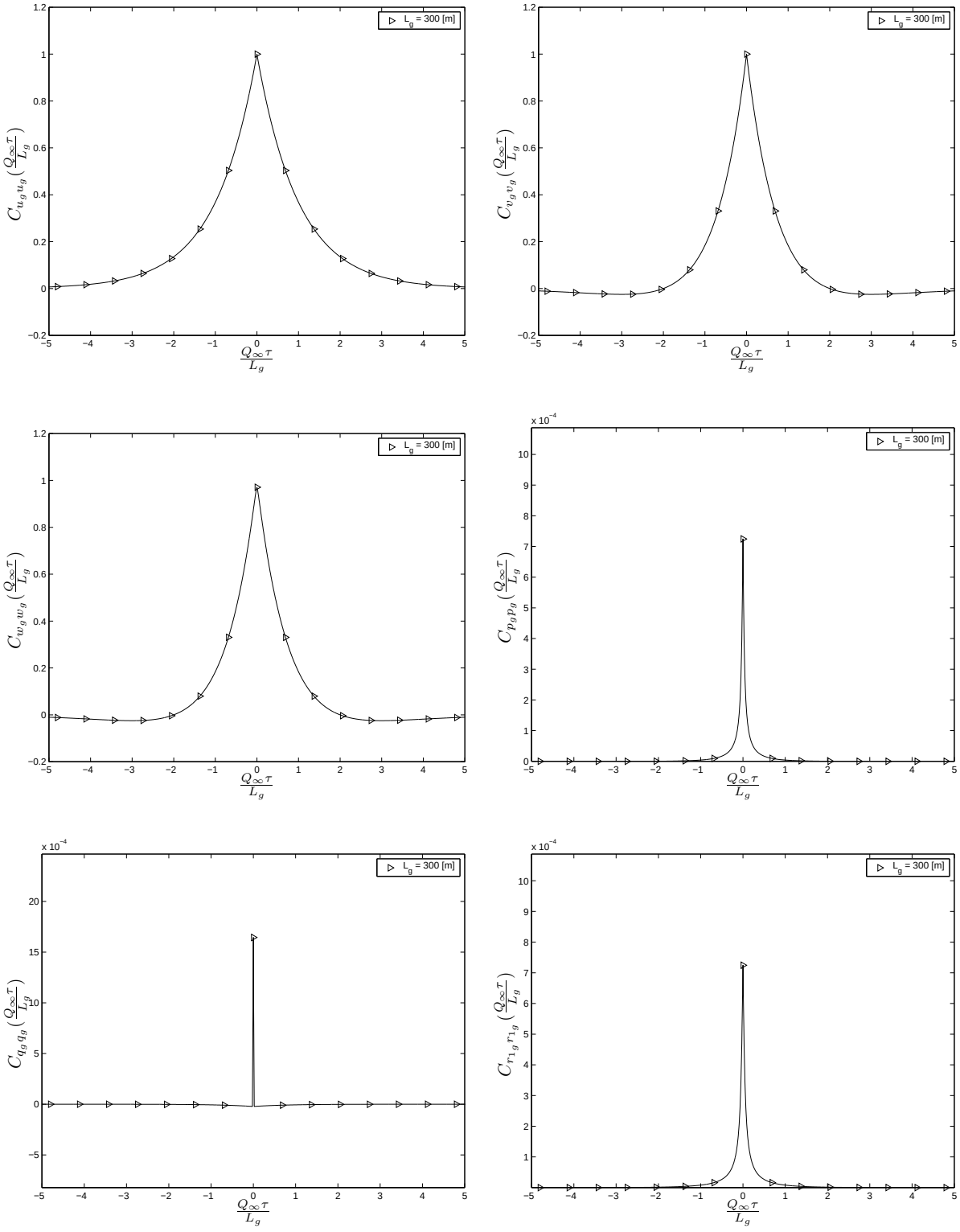


Figure H.3: The covariance functions for dimensional gust inputs, $C_{u_g u_g}(\frac{Q_\infty \tau}{L_g})$, $C_{v_g v_g}(\frac{Q_\infty \tau}{L_g})$, $C_{w_g w_g}(\frac{Q_\infty \tau}{L_g})$, $C_{p_g p_g}(\frac{Q_\infty \tau}{L_g})$, $C_{q_g q_g}(\frac{Q_\infty \tau}{L_g})$ and $C_{r_{1_g} r_{1_g}}(\frac{Q_\infty \tau}{L_g})$, for the gust scale length $L_g = 300$ [m] and the variance $\sigma^2 = 1$ $[\frac{\mathrm{m}^2}{\mathrm{s}^2}]$.

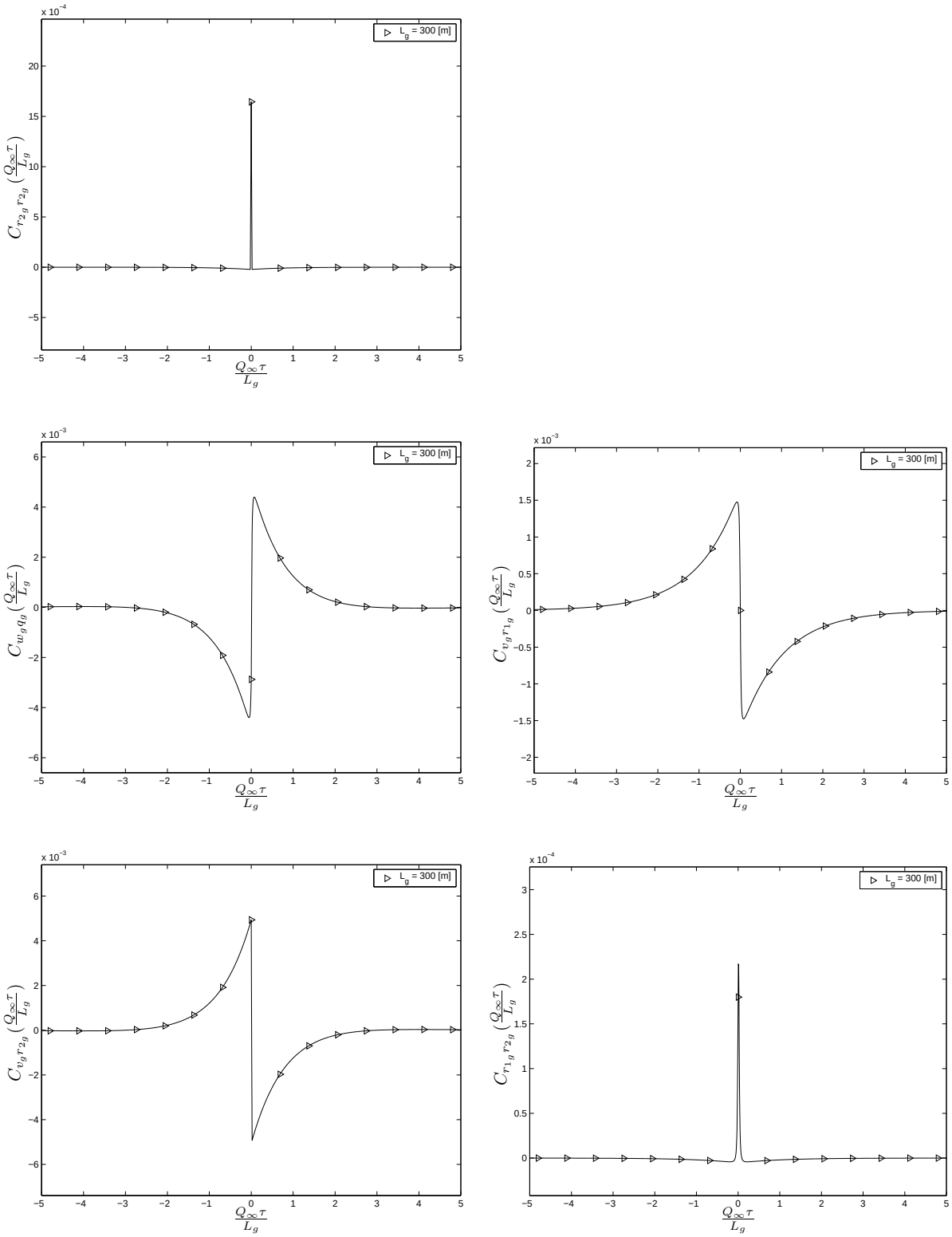


Figure H.3: (Continued) The covariance functions for dimensional gust inputs, $C_{r_{2_g} r_{2_g}}(\frac{Q_\infty \tau}{L_g})$, $C_{w_g q_g}(\frac{Q_\infty \tau}{L_g})$, $C_{v_g r_{1_g}}(\frac{Q_\infty \tau}{L_g})$, $C_{v_g r_{2_g}}(\frac{Q_\infty \tau}{L_g})$ and $C_{r_{1_g} r_{2_g}}(\frac{Q_\infty \tau}{L_g})$, for the gust scale length $L_g = 300$ [m] and the variance $\sigma^2 = 1\ [\frac{\mathrm{m}^2}{\mathrm{s}^2}]$.

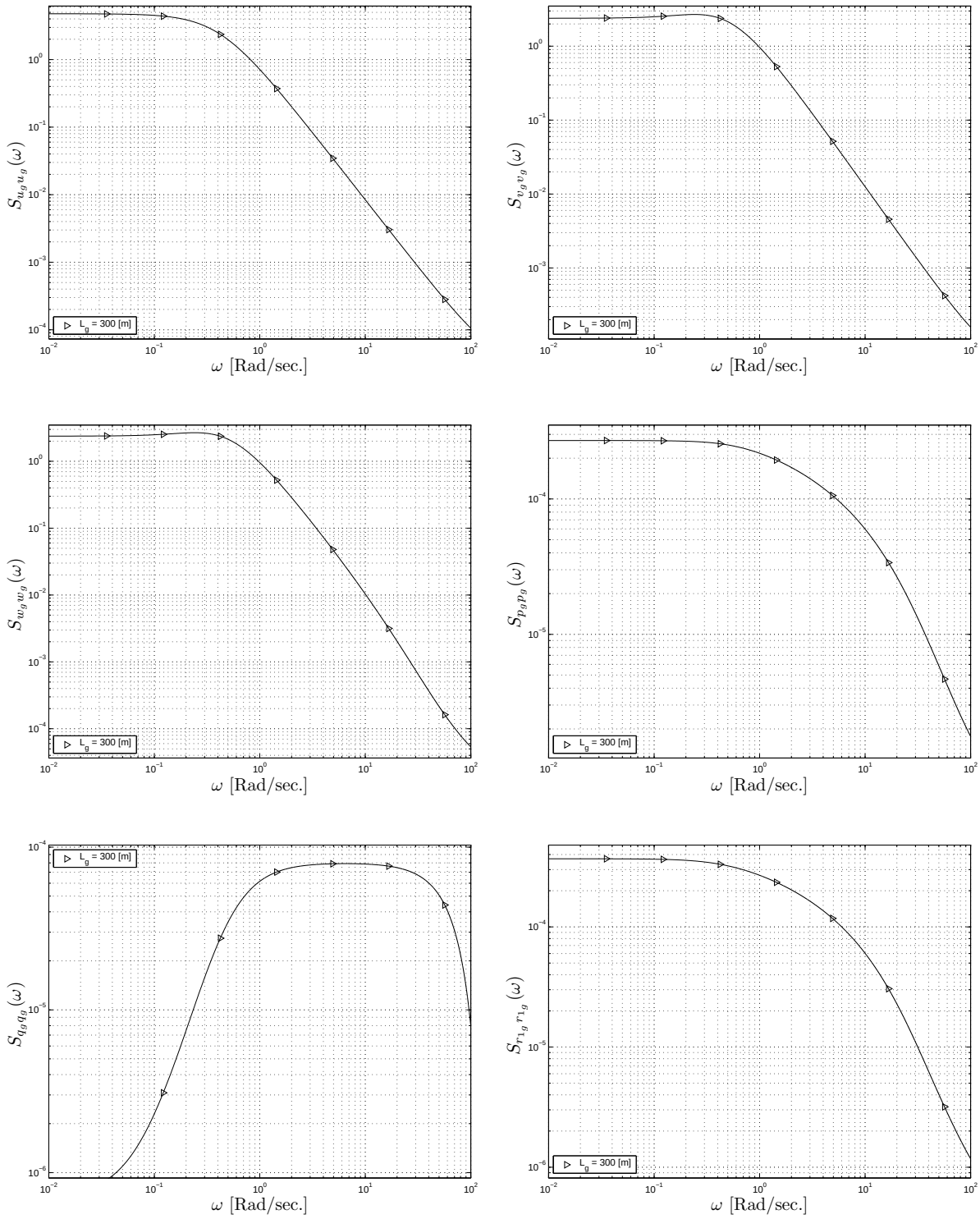


Figure H.4: The PSD-functions for dimensional gust inputs, $S_{u_g u_g}(\omega)$, $S_{v_g v_g}(\omega)$, $S_{w_g w_g}(\omega)$, $S_{p_g p_g}(\omega)$, $S_{q_g q_g}(\omega)$ and $S_{r_{1_g} r_{1_g}}(\omega)$, for the gust scale length $L_g = 300$ [m] and the variance $\sigma^2 = 1$ $[\frac{\mathrm{m}^2}{\mathrm{s}^2}]$.

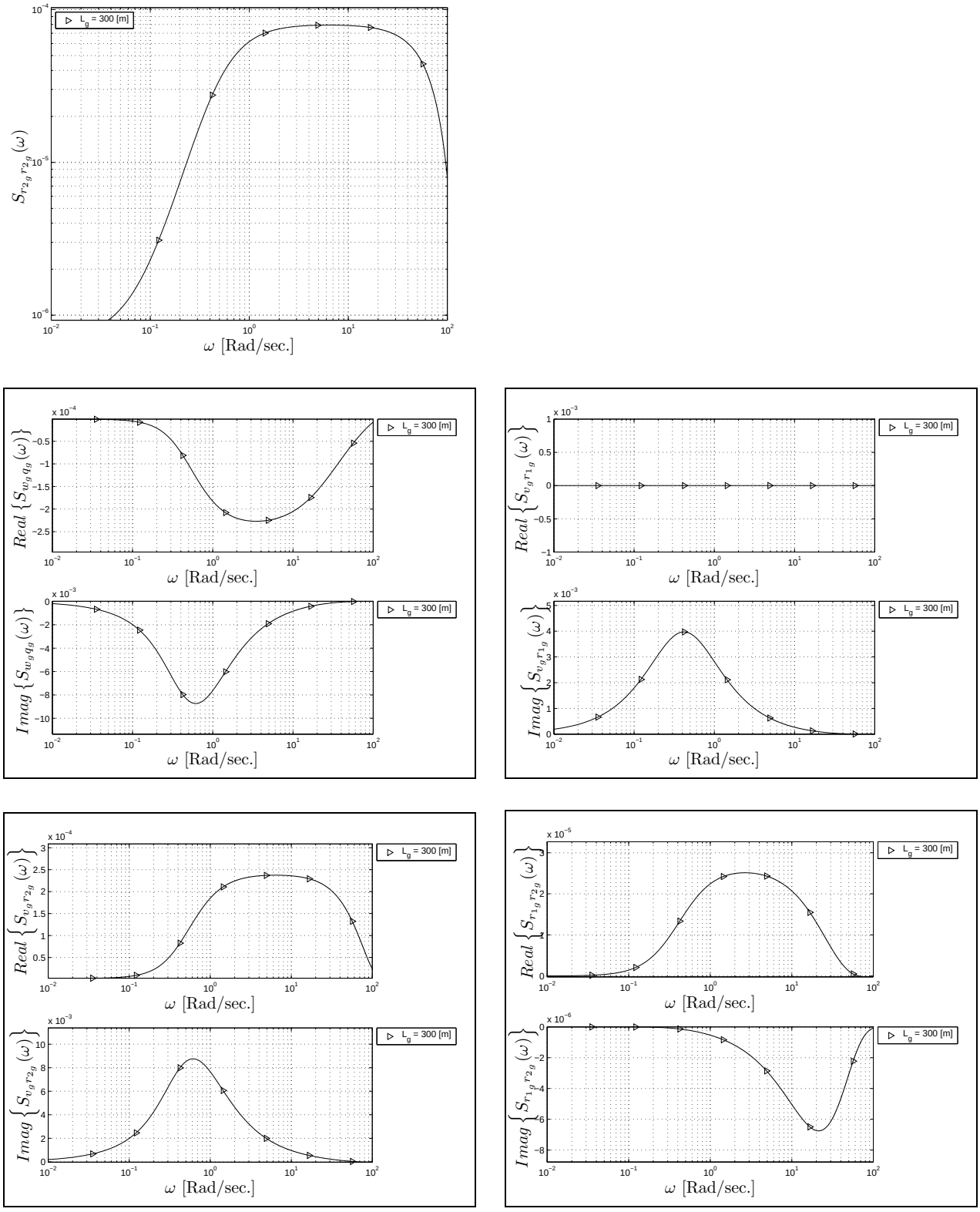


Figure H.4: (Continued) The PSD-functions for dimensional gust inputs, $S_{r_{2_g} r_{2_g}}(\omega)$, $S_{w_g q_g}(\omega)$, $S_{v_g r_{1_g}}(\omega)$, $S_{v_g r_{2_g}}(\omega)$ and $S_{r_{1_g} r_{2_g}}(\omega)$, for the gust scale length $L_g = 300$ [m] and the variance $\sigma^2 = 1$ $[\frac{\mathrm{m}^2}{\mathrm{s}^2}]$.

Appendix I

The aircraft equations of motion

I.1 Introduction

Throughout this thesis the linearized equations of aircraft motion are used according to reference [29]. These equations are summarized in this appendix.

First, the non-linear equations of motion will be given for the Body-Fixed Frame of Reference $\mathcal{F}_B$ ($O_B X_B Y_B Z_B$).

Next, using some simplifying assumptions, from the non-linear equations of motion the linearized equations of motion are derived for both the frame $\mathcal{F}_B$ and the Stability Frame of Reference $\mathcal{F}_S$ ($O_S X_S Y_S Z_S$). These assumptions are, see also reference [29],

1. The steady-state flight-condition is assumed to be steady, straight, symmetric flight (in this thesis also given as the "initial" or "trim condition").
2. Only small perturbations from the steady-state flight-condition are allowed.
3. The aircraft mass is constant in the time interval during which the aircraft motion is studied.
4. The aircraft is a rigid body in the motion under consideration. Elastic aircraft are not considered in this thesis.
5. The mass-distribution of the aircraft is symmetric relative to the $X_B O Z_B$-plane.
6. The rotation of the Earth in space, as well as the curvature of the Earth surface, is neglected.

The linearized equations of motion will eventually result in two independent sets of equations, i.e. the symmetric linear aircraft model and the asymmetric linear aircraft model.

The symmetric linear aircraft model describes the behaviour of the aircraft in the aircraft plane of symmetry, i.e. longitudinal, vertical and rotational (with the rotation vector perpendicular to the plane of symmetry) aircraft motions are considered only. The symmetrical inputs include symmetrical longitudinal gusts (u_g) and symmetrical vertical gusts (w_g).
The asymmetric linear aircraft model describes the behaviour of the aircraft perpendicular to the aircraft plane of symmetry, i.e. lateral and rotational (with the rotation vector located in the plane of symmetry) aircraft motions are considered only. The asymmetrical inputs include anti-symmetrical longitudinal gusts (u_g), symmetrical lateral gusts (v_g) and anti-symmetrical vertical gusts (w_g).
See chapter 5 for the definition of the gust inputs u_g, v_g and w_g.

Finally, the frequency-domain equations of motion are given for both the symmetric and the asymmetric linear aircraft model. These frequency-domain aircraft models are similar to the Linear Time-Invariant (LTI) aircraft models given in reference deriv[29]. However, these models will now incorporate the frequency-dependent stability derivatives obtained from aerodynamic frequency-response functions as derived in chapters 7 and 8.

I.2 The non-linear equations of motion

The general form of the non-linear equations of motion for rigid aircraft are given in the frame $\mathcal{F}_B$ $O_B X_B Y_B Z_B$, with its origin located in the center of gravity, and they are given in the form, see reference [29],

$$\left.\begin{array}{rclrcl} F_x &=& -W\,sin\,\theta & +X &=& m\,(\dot{u} + qw - rv) \\ F_y &=& +W\,cos\,\theta\,sin\,\varphi & +Y &=& m\,(\dot{v} + ru - pw) \\ F_z &=& +W\,cos\,\theta\,cos\,\varphi & +Z &=& m\,(\dot{w} + pv - qu) \\ & & & & & \\ \mathcal{M}_x &=& & L &=& I_x\,\dot{p} + (I_z - I_y)\,qr - J_{xz}\,(\dot{r} + pq) \\ \mathcal{M}_y &=& & M &=& I_y\,\dot{q} + (I_x - I_z)\,rp + J_{xz}\left(p^2 - r^2\right) \\ \mathcal{M}_z &=& & N &=& I_z\,\dot{r} + (I_y - I_x)\,pq - J_{xz}\,(\dot{p} - rq) \end{array}\right\} \quad \text{(I.1)}$$

with $[u, v, w]^T$ the aircraft center of gravity translational velocity components along the X_B-, Y_B- and Z_B-axis, respectively, $[p, q, r]^T$ the rotational velocity components along the X_B-, Y_B- and Z_B-axis, respectively, $[F_x, F_y, F_z]^T$ the force components along the X_B-, Y_B- and Z_B-axis, respectively, $[\mathcal{M}_x, \mathcal{M}_y, \mathcal{M}_z]^T$ the moment components along the X_B-, Y_B- and Z_B-axis, respectively, $[X, Y, Z]^T$ the aerodynamic force components along the X_B-, Y_B- and Z_B-axis, respectively, $[L, M, N]^T$ the aerodynamic moment components along the X_B-, Y_B- and Z_B-axis, respectively, W the aircraft weight, m the aircraft mass and θ, φ the aircraft attitude angles. For the frame $\mathcal{F}_B$ ($O_B X_B Y_B Z_B$), the moments and product

of inertia, I_x, I_y, I_z, J_{xz}, are given as,

$$\left.\begin{array}{rcl} I_x &=& \int\limits_m \left(y^2+z^2\right)\, dm \\ I_y &=& \int\limits_m \left(x^2+z^2\right)\, dm \\ I_z &=& \int\limits_m \left(x^2+y^2\right)\, dm \\ J_{xz} &=& \int\limits_m xz\, dm \end{array}\right\} \tag{I.2}$$

with the assumption that the aircraft mass distribution is symmetrical with respect to the X_BOZ_B-plane (which leads to $J_{xy} = J_{yz} = 0$).

In this thesis the attitude of an aircraft is defined by the three Euler-angles of the frame $\mathcal{F}_B$ relative to the Earth-Fixed Frame of Reference $\mathcal{F}_E$, and they are defined as $[\psi, \theta, \varphi]^T$, or the yaw-angle, the pitch-angle and the roll-angle, respectively. These angles are the result of three subsequent rotations of the frame $\mathcal{F}_B$, starting from the attitude of the Earth-Fixed Frame of Reference and ending up with the desired attitude of the aircraft in three dimensional (3D) space. In the original situation, see figure I.1, the reference frames $\mathcal{F}_B$ ($O_{B_1}X_{B_1}Y_{B_1}Z_{B_1}$) and $\mathcal{F}_E$ coincide. Starting from this situation, $\mathcal{F}_B$ is rotated about the Z_{B_1}-axis over the yaw-angle ψ, see figure I.2, resulting in the body-axes $O_{B_2}X_{B_2}Y_{B_2}Z_{B_2}$. Next, $\mathcal{F}_B$ is rotated about the Y_{B_2}-axis over the pitch-angle θ, see figure I.3, resulting in the body-axes $O_{B_3}X_{B_3}Y_{B_3}Z_{B_3}$. Finally, $\mathcal{F}_B$ is rotated about the X_{B_3}-axis over the roll-angle φ, see figure I.4, resulting in the body-axes $O_{B_4}X_{B_4}Y_{B_4}Z_{B_4}$.

The Euler angles $[\psi, \theta, \varphi]^T$ are used to calculate the weight-components given in equation (I.1). The decomposition of an aircraft weight along the axes of $\mathcal{F}_B$ is given as (see also figure I.5),

$$\left.\begin{array}{rcl} W_x &=& -W\ sin\ \theta \\ W_y &=& W\ cos\ \theta\ sin\ \varphi \\ W_z &=& W\ cos\ \theta\ cos\ \varphi \end{array}\right\} \tag{I.3}$$

To complete the non-linear equations of motion given in equation (I.1), the kinematic relation between the rotational velocity components $[p, q, r]^T$ and the time derivatives of the Euler-angles $[\dot{\psi}, \dot{\theta}, \dot{\varphi}]^T$ is given in matrix notation (see also figure I.6),

$$\begin{bmatrix} p \\ q \\ r \end{bmatrix} = \begin{bmatrix} -sin\ \theta & 0 & 1 \\ +cos\ \theta\ sin\ \varphi & cos\ \varphi & 0 \\ +cos\ \theta\ cos\ \varphi & -sin\ \varphi & 0 \end{bmatrix} \begin{bmatrix} \dot{\psi} \\ \dot{\theta} \\ \dot{\varphi} \end{bmatrix} \tag{I.4}$$

with the inverse relation given as,

$$\begin{bmatrix} \dot{\psi} \\ \dot{\theta} \\ \dot{\varphi} \end{bmatrix} = \begin{bmatrix} 0 & +\frac{sin\ \varphi}{cos\ \theta} & +\frac{cos\ \varphi}{cos\ \theta} \\ 0 & +cos\ \varphi & -sin\ \varphi \\ 1 & +sin\ \varphi\ tg\ \theta & +cos\ \varphi\ tg\ \theta \end{bmatrix} \begin{bmatrix} p \\ q \\ r \end{bmatrix} \tag{I.5}$$

From equations (I.1) and (I.5) the Linear Time-Invariant (LTI) equations of motion are derived.

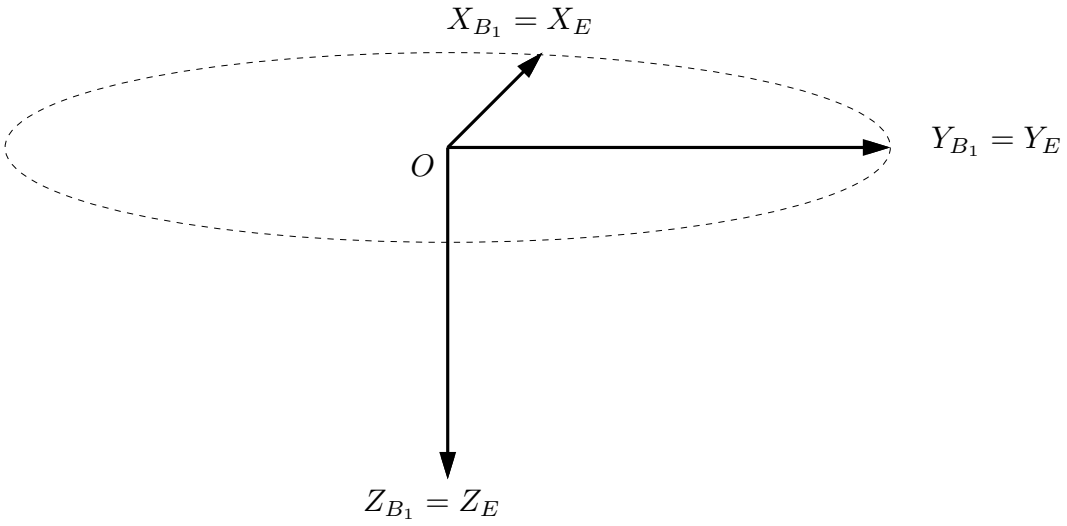


Figure I.1: The attitude of an aircraft ($\mathcal{F}_B$) relative to Earth ($\mathcal{F}_E$), initial position of a body-fixed frame of reference.

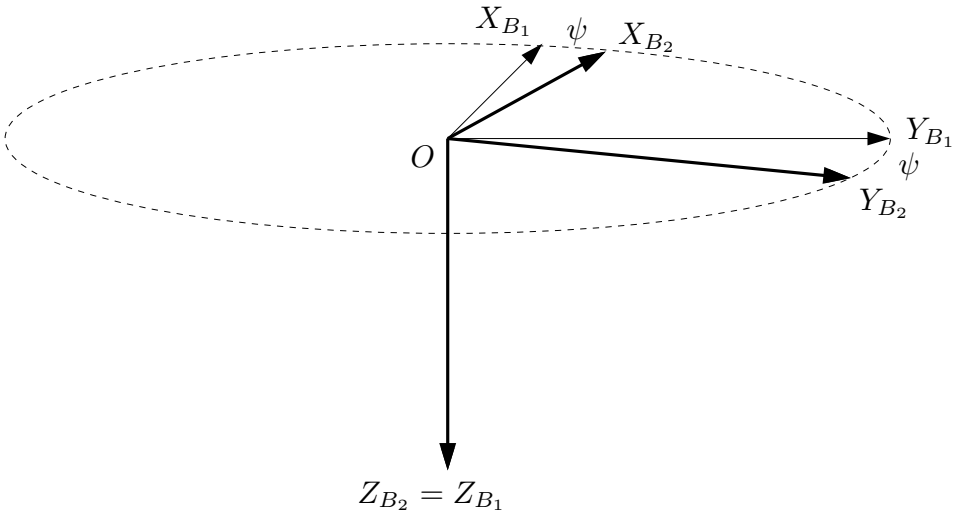


Figure I.2: The attitude of an aircraft ($\mathcal{F}_B$) relative to Earth ($\mathcal{F}_E$), rotation about the Z_B axis.

I.3 The linear time-invariant equations of motion

I.3.1 Linearization of the equations of motion

When the steady condition is characterized by the subscript 0, steady, straight flight is characterized by the following conditions,

$$\begin{array}{llll} \dot{u}_0 = 0 & u_0 \neq 0 & \dot{p}_0 = 0 & p_0 = 0 \\ \dot{v}_0 = 0 & v_0 = 0 & \dot{q}_0 = 0 & q_0 = 0 \\ \dot{w}_0 = 0 & w_0 \neq 0 & \dot{r}_0 = 0 & r_0 = 0 \end{array}$$

and,

$$\begin{array}{llll} \dot{\psi}_0 = 0 & \psi_0 \neq 0 & X_0 \neq 0 & L_0 = 0 \end{array}$$

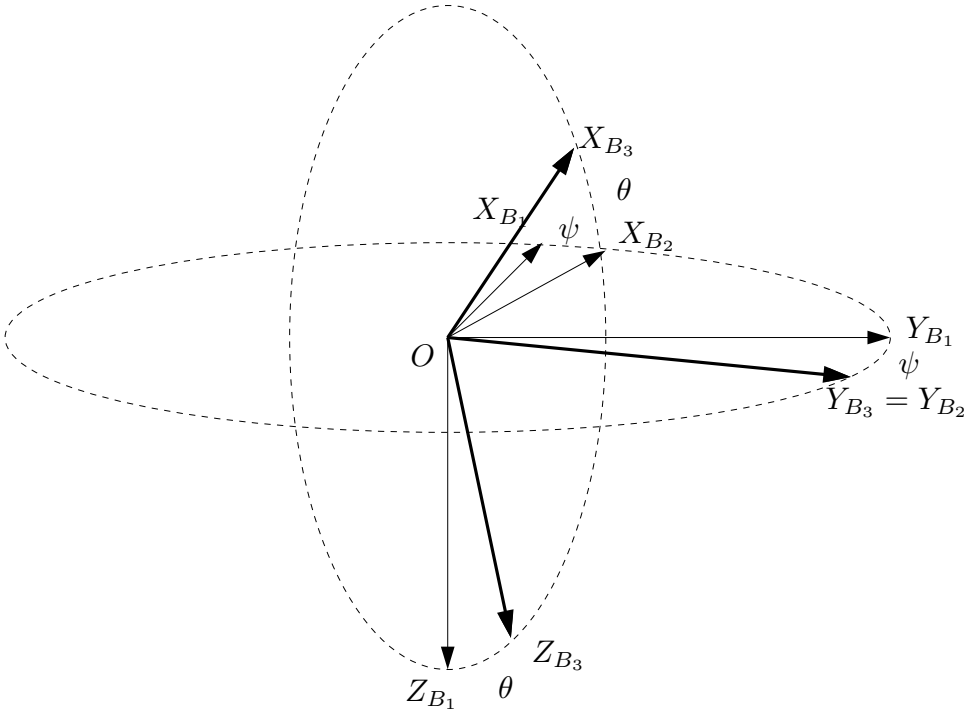


Figure I.3: The attitude of an aircraft ($\mathcal{F}_B$) relative to Earth ($\mathcal{F}_E$), rotation about the Y_B axis.

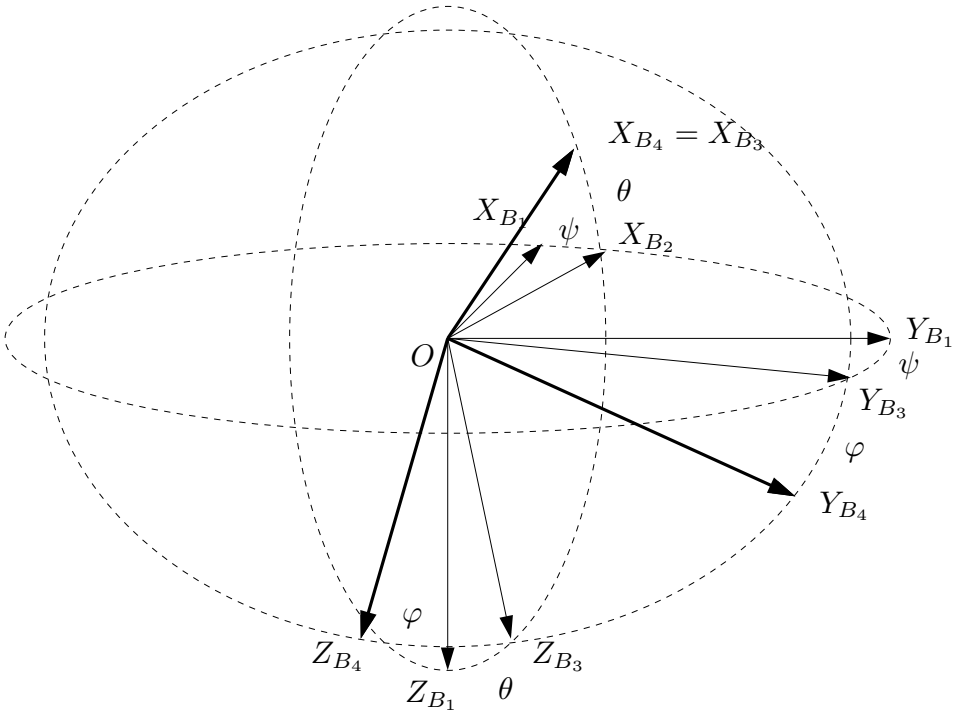


Figure I.4: The attitude of an aircraft ($\mathcal{F}_B$) relative to Earth ($\mathcal{F}_E$), rotation about the X_B axis.

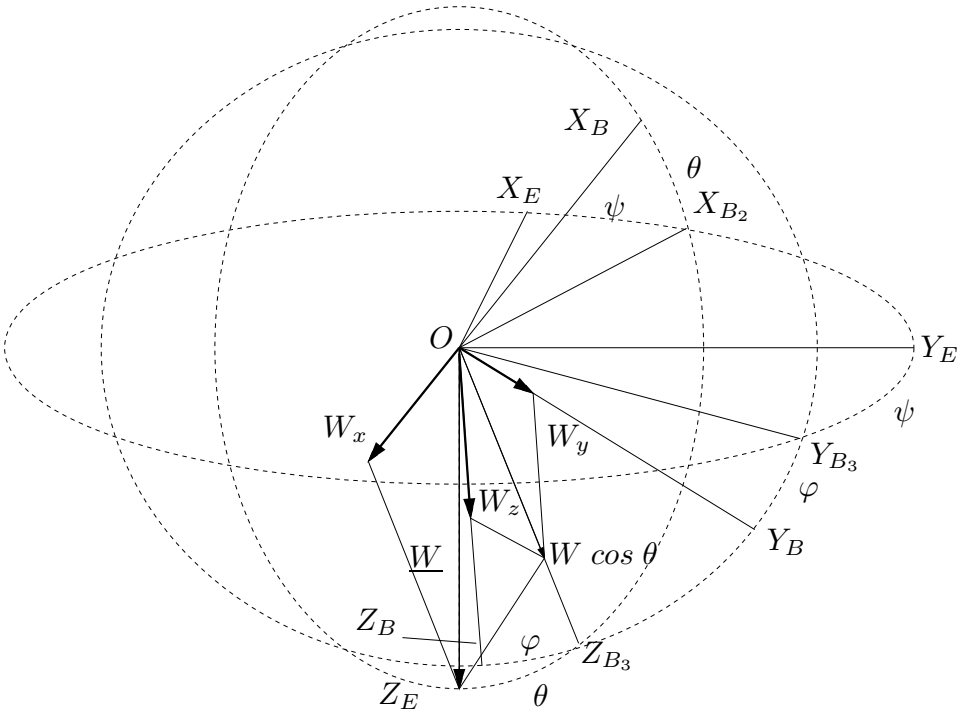


Figure I.5: Symmetric and asymmetric components of the aircraft weight.

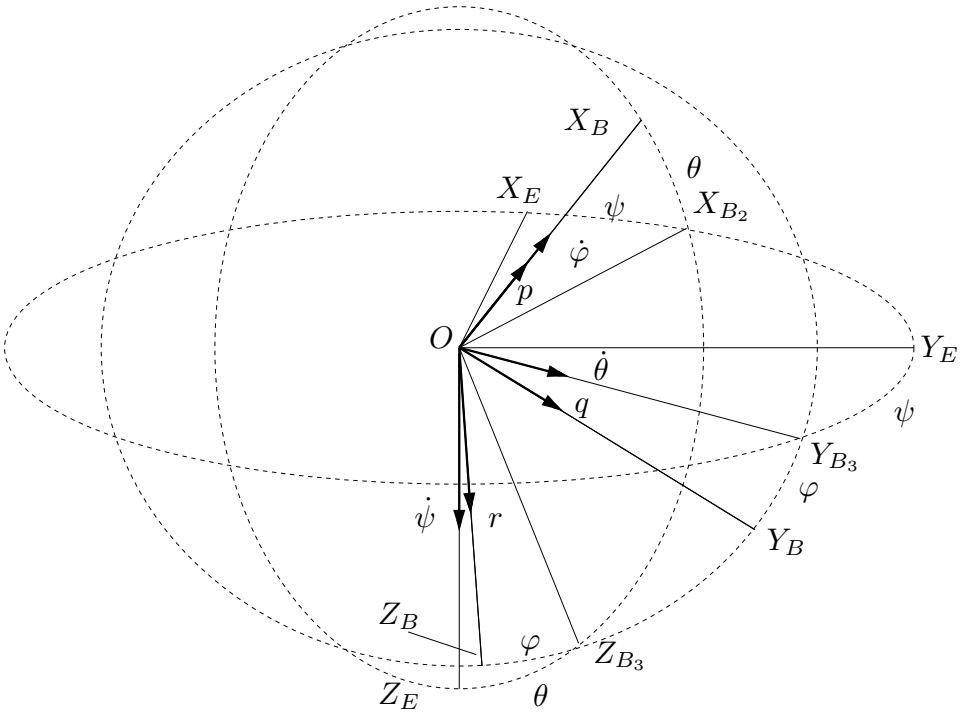


Figure I.6: Symmetric and asymmetric components of motion, relation between p, q, r and $\dot{\psi}$, $\dot{\theta}$, $\dot{\varphi}$.

$$\begin{array}{llll} \dot{\theta}_0 = 0 & \theta_0 \neq 0 & Y_0 = 0 & M_0 = 0 \\ \dot{\varphi}_0 = 0 & \varphi_0 = 0 & Z_0 \neq 0 & N_0 = 0 \end{array}$$

A state of aircraft motion perturbed slightly from this steady flight condition is described by,

$$\begin{array}{rclcrcl} u &=& u_0 + du & & p &=& dp \\ v &=& dv & & q &=& dq \\ w &=& w_0 + dw & & r &=& dr \end{array}$$

$$\begin{array}{rclcrclcrcl} \psi &=& \psi_0 + d\psi & & X &=& X_0 + dX & & L &=& dL \\ \theta &=& \theta_0 + d\theta & & Y &=& dY & & M &=& dM \\ \varphi &=& d\varphi & & Z &=& Z_0 + dZ & & N &=& dN \end{array}$$

Substitution of the above expressions in the non-linear equations of motion given in equation (I.1), results in,

$$\left.\begin{array}{rcl} -W\ sin(\theta_0 + d\theta) + X_0 + dX &=& m\,(\dot{u}\ +\ dq(w_0 + dw)\ -\ dr\ dv) \\ +W\ cos(\theta_0 + d\theta)\ sin\ d\varphi + dY &=& m\,(\dot{v}\ +\ dr(u_0 + du)\ -\ dp(w_0 + dw)) \\ +W\ cos(\theta_0 + d\theta)\ cos\ d\varphi + Z_0 + dZ &=& m\,(\dot{w}\ +\ dp\ dv\ -\ dq(u_0 + du)) \\ dL &=& I_x\ \dot{p}\ +\ (I_z - I_y)\,dq\ dr\ -\ J_{xz}\,(\dot{r} + dp\ dq) \\ dM &=& I_y\ \dot{q}\ +\ (I_x - I_z)\,dr\ dp\ +\ J_{xz}\left(dp^2 - dr^2\right) \\ dN &=& I_z\ \dot{r}\ +\ (I_y - I_x)\,dp\ dq\ -\ J_{xz}\,(\dot{p} - dr\ dq) \end{array}\right\} \quad \text{(I.6)}$$

The kinematic relations now become,

$$\begin{array}{rcccc} \dot{\psi} &=& dq\ \frac{sin\ d\varphi}{cos(\theta_0 + d\theta)} & & +dr\ \frac{cos\ d\varphi}{cos(\theta_0 + d\theta)} \\ \dot{\theta} &=& dq\ cos\ d\varphi & & -dr\ sin\ d\varphi \\ \dot{\varphi} &=& dp\ \ +(dq\ sin\ \varphi\ + dr\ cos\ d\varphi\ )\,tg\,(\theta_0 + d\theta) & & \end{array}$$

Neglecting the products of small variables, while also assuming that $cos\ d\theta = 1$, $cos\ d\varphi = 1$, $sin\ d\theta = d\theta$ and $sin\ d\varphi = d\varphi$, ánd considering that in the first force equation (X) and the third force equation (Z) the components of the aircraft weight are cancelled in the equilibrium state by the aerodynamic forces X_0 and Z_0, finally the linearized equations of motion become,

$$\left.\begin{array}{rcl} -W\ cos\theta_0 \cdot d\theta\ \ +dX &=& m\,(\dot{u}\ +\ dq \cdot w_0) \\ +W\ cos\theta_0 \cdot d\varphi\ \ +dY &=& m\,(\dot{v}\ +\ dr \cdot u_0\ -\ dp \cdot w_0) \\ -W\ sin\theta_0 \cdot d\theta\ \ +dZ &=& m\,(\dot{w}\ -\ dq \cdot u_0) \\ \\ dL &=& I_x\ \dot{p}\ -\ J_{xz}\dot{r} \\ dM &=& I_y\ \dot{q} \\ dN &=& I_z\ \dot{r}\ -\ J_{xz}\dot{p} \\ \\ \dot{\psi} &=& \frac{dr}{cos\ \theta_0} \\ \dot{\theta} &=& dq \\ \dot{\varphi} &=& dp + dr\ tg\ \theta_0 \end{array}\right\} \quad \text{(I.7)}$$

Next, assuming that small asymmetric aircraft motions and small asymmetric inputs have no influence on the symmetric aerodynamic forces X and Z and the symmetric aerodynamic moment M, ás well as small symmetric aircraft motions and small symmetric inputs have no influence on the asymmetric aerodynamic force Y and the asymmetric aerodynamic moments L and N, the aerodynamic forces and moments are decomposed in a Taylor series,

$$\left.\begin{array}{lcllllll}
dX &=& X_u du & +X_w dw & +X_{\dot{w}}\dot{w} & +X_q dq & +\sum_{i=1}^{i=N_s} X_{u_i} du_i \\
dY &=& Y_v dv & +Y_{\dot{v}}\dot{v} & +Y_p dp & +Y_r dr & +\sum_{j=1}^{j=N_a} Y_{u_j} du_j \\
dZ &=& Z_u du & +Z_w dw & +Z_{\dot{w}}\dot{w} & +Z_q dq & +\sum_{i=1}^{i=N_s} Z_{u_i} du_i \\
dL &=& L_v dv & +L_{\dot{v}}\dot{v} & +L_p dp & +L_r dr & +\sum_{j=1}^{j=N_a} L_{u_j} du_j \\
dM &=& M_u du & +M_w dw & +M_{\dot{w}}\dot{w} & +M_q dq & +\sum_{i=1}^{i=N_s} M_{u_i} du_i \\
dN &=& N_v dv & +N_{\dot{v}}\dot{v} & +N_p dp & +N_r dr & +\sum_{j=1}^{j=N_a} N_{u_j} du_j
\end{array}\right\} \quad \text{(I.8)}$$

with N_s the number of symmetrical inputs u_i (in this thesis being symmetrical atmospheric turbulence inputs), and N_a the number of asymmetrical inputs u_j (being now asymmetrical atmospheric turbulence inputs).
In equations (I.8) only the first order aerodynamic derivatives of the Taylor expansion are retained, that is the derivatives $\frac{\partial^2 X}{\partial u^2}$, $\frac{\partial^2 X}{\partial v^2}$, $\frac{\partial^2 X}{\partial w^2}$, $\frac{\partial^2 X}{\partial u \partial v}$, etc. are neglected, see also reference [29].

The combination of equations (I.7) and (I.8) results in the linearized equations of motion, which hold for small perturbations with respect to a steady, straight, symmetric flight-

condition, and they are summarized as,

$$
\begin{aligned}
-W\ cos\ \theta_0 \cdot d\theta + X_u du + X_w dw + X_{\dot{w}} \dot{w} + X_q dq + \sum_{i=1}^{i=N_s} X_{u_i} du_i &= m\,(\dot{u} + dq\ w_0) \\
+W\ cos\ \theta_0 \cdot d\varphi + Y_v dv + Y_{\dot{v}} \dot{v} + Y_p dp + Y_r dr + \sum_{j=1}^{j=N_a} Y_{u_j} du_j &= m\,(\dot{v} + dr\ u_0 - \\
& \quad - dp\ w_0) \\
-W\ sin\ \theta_0 \cdot d\theta + Z_u du + Z_w dw + Z_{\dot{w}} \dot{w} + Z_q dq + \sum_{i=1}^{i=N_s} X_{u_i} du_i &= m\,(\dot{w} - dq\ u_0) \\
\\
L_v dv + L_{\dot{v}} \dot{v} + L_p dp + L_r dr + \sum_{j=1}^{j=N_a} L_{u_j} du_j &= I_x\ \dot{p} - J_{xz} \dot{r} \\
M_u du + M_w dw + M_{\dot{w}} \dot{w} + M_q dq + \sum_{i=1}^{i=N_s} M_{u_i} du_i &= I_y\ \dot{q} \\
N_v dv + N_{\dot{v}} \dot{v} + N_p dp + N_r dr + \sum_{j=1}^{j=N_a} N_{u_j} du_j &= I_z\ \dot{r} - J_{xz} \dot{p} \\
\\
\dot{\psi} &= \tfrac{dr}{cos\ \theta_0} \\
\dot{\theta} &= dq \\
\dot{\varphi} &= dp + dr\ tg\ \theta_0
\end{aligned}
$$

If the aircraft is aerodynamically symmetric with respect to the $X_B O Z_B$-plane, only aircraft motions about a condition of steady, straight, symmetric flight ("the trim condition") are considered, and the perturbations and the subsequent deviations from the trim condition remain small enough to permit linearization of the equations of motion, the linearized equations of motion result in two independent sets of equations, i.e. the symmetric linear aircraft model and the asymmetric linear aircraft model.
For the symmetric aircraft motions the equations become,

$$
\left.
\begin{aligned}
-W cos\ \theta_0\ d\theta + X_u du + X_w dw + X_{\dot{w}} \dot{w} + X_q dq + \sum_{i=1}^{i=N_s} X_{u_i} du_i &= m\,(\dot{u} + dq\ w_0)) \\
-W sin\ \theta_0\ d\theta + Z_u du + Z_w dw + Z_{\dot{w}} \dot{w} + Z_q dq + \sum_{i=1}^{i=N_s} Z_{u_i} du_i &= m\,(\dot{w} - dq\ u_0) \\
M_u du + M_w dw + M_{\dot{w}} \dot{w} + M_q dq + \sum_{i=1}^{i=N_s} M_{u_i} du_i &= I_y\ \dot{q} \\
\dot{\theta} &= dq
\end{aligned}
\right\} \qquad \text{(I.9)}
$$

For the asymmetric aircraft motions the equations become,

$$\left.\begin{aligned} W cos\ \theta_0\ d\varphi + Y_v dv + Y_{\dot{v}}\dot{v} + Y_p dp + Y_r dr + \sum_{j=1}^{j=N_a} Y_{u_j} du_j &= m\,(\dot{v} + dr\ u_0 - dp\ w_0) \\ L_v dv + L_{\dot{v}}\dot{v} + L_p dp + L_r dr + \sum_{j=1}^{j=N_a} L_{u_j} du_j &= I_x\ \dot{p} - J_{xz}\ \dot{r} \\ N_v dv + N_{\dot{v}}\dot{v} + N_p dp + N_r dr + \sum_{j=1}^{j=N_a} N_{u_j} du_j &= I_z\ \dot{r} - J_{xz}\ \dot{p} \\ \dot{\psi} &= \tfrac{dr}{cos\ \theta_0} \\ \dot{\varphi} &= dp + dr\ tg\ \theta_0 \end{aligned}\right\} \quad \text{(I.10)}$$

I.3.2 Equations of motion in the stability frame of reference

In the previous sections the equations of motion have been given for the frame $\mathcal{F}_B$ $O_B X_B Y_B Z_B$. In this section the equations are given for the frame $\mathcal{F}_S$ ($O_S X_S Y_S Z_S$). The definition of these reference frames is given in appendix B.

In principle the frame $\mathcal{F}_S$ also is a body-fixed frame of reference, however, by choice of the orientation of the X_S-axis, the airspeed u_0 in $\mathcal{F}_S$ becomes $u_0 = Q_\infty$ and $w_0 = 0$, with Q_∞ the aircraft speed during steady, straight, symmetric flight (the "trim condition"). Additionally, the angle-of-attack during the trim condition is zero, $\alpha_0 = atan\left(\frac{w_0}{Q_\infty}\right) = 0$, resulting in $\theta_0 = \gamma_0$, with γ_0 the flightpath angle for the initial or trim condition. The new orientation of the reference frame $\mathcal{F}_S$ has consequences for the magnitude of the moments and product of inertia, see also reference [29].

Following the same lines as given in reference [29], the symmetric equations of motion become,

$$\left.\begin{aligned} -W cos\ \theta_0\ \theta \quad + X_u u + X_w w + X_{\dot{w}}\dot{w} + X_q q + \sum_{i=1}^{i=N_s} X_{u_i} u_i &= m\dot{u} \\ -W sin\ \theta_0\ \theta \quad\ + Z_u u + Z_w w + Z_{\dot{w}}\dot{w} + Z_q q + \sum_{i=1}^{i=N_s} Z_{u_i} u_i &= m\,(\dot{w} - q\ Q_\infty) \\ M_u u + M_w w + M_{\dot{w}}\dot{w} + M_q q + \sum_{i=1}^{i=N_s} M_{u_i} u_i &= I_y \dot{q} \\ \dot{\theta} &= q \end{aligned}\right\} \quad \text{(I.11)}$$

while the asymmetric equations of motion become,

$$\left.\begin{array}{rcl} W cos\,\theta_0\,\varphi \quad +Y_v v + Y_{\dot{v}}\dot{v} + Y_p p + Y_r r + \sum_{j=1}^{j=N_a} Y_{u_j} u_j & = & m\,(\dot{v} + r\,Q_\infty) \\ L_v v + L_{\dot{v}}\dot{v} + L_p p + L_r r + \sum_{j=1}^{j=N_a} L_{u_j} u_j & = & I_x\dot{p} - J_{xz}\dot{r} \\ N_v v + N_{\dot{v}}\dot{v} + N_p p + N_r r + \sum_{j=1}^{j=N_a} N_{u_j} u_j & = & I_z\dot{r} - J_{xz}\dot{p} \\ \dot{\psi} & = & \frac{r}{cos\,\theta_0} \\ \dot{\varphi} & = & p + r\,tg\,\theta_0 \end{array}\right\} \quad \text{(I.12)}$$

Both the moments and product of inertia for $\mathcal{F}_S$, as used in equations (I.11) and (I.12), are obtained from the following transformation, see reference [29],

$$\left.\begin{array}{rcl} I_x|_{\mathcal{F}_S} & = & I_x|_{\mathcal{F}_B}\,cos^2\alpha_0 + I_z|_{\mathcal{F}_B}\,sin^2\alpha_0 - J_{xz}|_{\mathcal{F}_B}\,sin(2\alpha_0) \\ I_y|_{\mathcal{F}_S} & = & I_y|_{\mathcal{F}_B} \\ I_z|_{\mathcal{F}_S} & = & I_x|_{\mathcal{F}_B}\,sin^2\alpha_0 + I_z|_{\mathcal{F}_B}\,cos^2\alpha_0 + J_{xz}|_{\mathcal{F}_B}\,sin(2\alpha_0) \\ J_{xz}|_{\mathcal{F}_S} & = & \frac{1}{2}\left(I_x|_{\mathcal{F}_B} - I_z|_{\mathcal{F}_B}\right)\,sin(2\alpha_0) + J_{xz}|_{\mathcal{F}_B}\,cos(2\alpha_0) \end{array}\right\} \quad \text{(I.13)}$$

with α_0 the aircraft trim angle-of-attack in $\mathcal{F}_B$, $I_x|_{\mathcal{F}_S}$, $I_y|_{\mathcal{F}_S}$, $I_z|_{\mathcal{F}_S}$ and $J_{xz}|_{\mathcal{F}_S}$ the moments and product of inertia in $\mathcal{F}_S$, and $I_x|_{\mathcal{F}_B}$, $I_y|_{\mathcal{F}_B}$, $I_z|_{\mathcal{F}_B}$ and $J_{xz}|_{\mathcal{F}_B}$ the moments and product of inertia in $\mathcal{F}_B$, as given in equation (I.2).

I.3.3 Non-dimensional equations of motion

In this section the non-dimensional linear equations of motion will be given.
For the symmetrical equations of motion, the force-equations are divided by the term $\frac{1}{2}\rho Q_\infty^2 S$ while the moment-equation is divided by the term $\frac{1}{2}\rho Q_\infty^2 S\bar{c}$, with ρ the air-density, Q_∞ the aircraft airspeed for the trim condition, S the wing-surface area and $\bar{c}$ the mean aerodynamic chord.
Similar to the symmetrical equations of motion, for the asymmetrical equations of motion the force-equation is divided by the term $\frac{1}{2}\rho Q_\infty^2 S$ while the moment-equations are now divided by the term $\frac{1}{2}\rho Q_\infty^2 Sb$, with b the aircraft span.

The non-dimensional symmetric equations of motion are written as, see reference [29],

$$2\mu_c\,D_c\hat{u} \quad = \quad C_{Z_0}\theta + C_{X_u}\hat{u} + C_{X_\alpha}\alpha + C_{X_{\dot{\alpha}}}D_c\alpha + C_{X_q}D_c\theta +$$

$$
\begin{aligned}
& & & + \sum_{i=1}^{i=N_s} C_{X_{u_i}} \hat{u}_i \\
2\mu_c \left(D_c\alpha - D_c\theta \right) &=& & -C_{X_0}\theta + C_{Z_u}\hat{u} + C_{Z_\alpha}\alpha + C_{Z_{\dot{\alpha}}} D_c\alpha + C_{Z_q} D_c\theta + \\
& & & + \sum_{i=1}^{i=N_s} C_{Z_{u_i}} \hat{u}_i \\
2\mu_c \, K_Y^2 \, D_c \frac{q\bar{c}}{Q_\infty} &=& & C_{m_u}\hat{u} + C_{m_\alpha}\alpha + C_{m_{\dot{\alpha}}} D_c\alpha + C_{m_q} D_c\theta + \\
& & & + \sum_{i=1}^{i=N_s} C_{m_{u_i}} \hat{u}_i \\
D_c\theta &=& & \frac{q\bar{c}}{Q_\infty}
\end{aligned}
\tag{I.14}
$$

with $C_{Z_0} = \frac{-W \, cos \, \theta_0}{\frac{1}{2}\rho Q_\infty^2 S}$, $C_{X_0} = \frac{W \, sin \, \theta_0}{\frac{1}{2}\rho Q_\infty^2 S}$, and the definition of all other parameters used in equations (I.14) summarized in table I.1. The non-dimensional inputs $\hat{u}_i$ are either the non-dimensional 1D longitudinal gust-component $\hat{u}_g = \frac{u_g}{Q_\infty}$, its non-dimensional time derivative $\frac{\dot{\hat{u}}_g \bar{c}}{Q_\infty}$, the non-dimensional 1D vertical gust-component $\alpha_g = \frac{w_g}{Q_\infty}$ or the latter non-dimensional time derivative $\frac{\dot{\alpha}_g \bar{c}}{Q_\infty}$. In tables I.2 and I.5 the definition of the symmetrical stability derivatives and the symmetrical gust derivatives are given. It should be noted that the unsteady derivatives are given with respect to $\frac{\dot{\alpha}\bar{c}}{Q_\infty}$, $\frac{\dot{\hat{u}}_g \bar{c}}{Q_\infty}$ and $\frac{\dot{\alpha}_g \bar{c}}{Q_\infty}$, instead of $\frac{\dot{\alpha}\bar{c}}{2Q_\infty}$, $\frac{\dot{\hat{u}}_g \bar{c}}{2Q_\infty}$ and $\frac{\dot{\alpha}_g \bar{c}}{2Q_\infty}$.

With $\theta_0 = \gamma_0$ (since now $\alpha_0 = 0$), the non-dimensional asymmetric equations of motion are written as, see reference [29],

$$
\begin{aligned}
2\mu_b \left(D_b\beta + 2\,\frac{rb}{2Q_\infty} \right) &=& C_L\varphi + C_{Y_\beta}\beta + C_{Y_{\dot{\beta}}} D_b\beta + C_{Y_p}\frac{pb}{2Q_\infty} + \\
& & + C_{Y_r}\frac{rb}{2Q_\infty} + \sum_{j=1}^{j=N_a} C_{Y_{u_j}} \hat{u}_j \\
4\mu_b \left(K_X^2 D_b \frac{pb}{2Q_\infty} - K_{XZ} D_b \frac{rb}{2Q_\infty} \right) &=& C_{\ell_\beta}\beta + C_{\ell_{\dot{\beta}}} D_b\beta + C_{\ell_p}\frac{pb}{2Q_\infty} + C_{\ell_r}\frac{rb}{2Q_\infty} + \\
& & + \sum_{j=1}^{j=N_a} C_{\ell_{u_j}} \hat{u}_j \\
4\mu_b \left(K_Z^2 D_b \frac{rb}{2Q_\infty} - K_{XZ} D_b \frac{pb}{2Q_\infty} \right) &=& C_{n_\beta}\beta + C_{n_{\dot{\beta}}} D_b\beta + C_{n_p}\frac{pb}{2Q_\infty} + C_{n_r}\frac{rb}{2Q_\infty} + \\
& & + \sum_{j=1}^{j=N_a} C_{n_{u_j}} \hat{u}_j \\
\frac{1}{2} D_b\psi &=& \frac{1}{cos \, \gamma_0}\frac{rb}{2Q_\infty}
\end{aligned}
$$

$$\frac{1}{2}D_b\varphi \quad = \quad \frac{pb}{2Q_\infty} + \frac{rb}{2Q_\infty}\ tg\ \gamma_0 \tag{I.15}$$

with $C_L = \frac{W\ cos\ \theta_0}{\frac{1}{2}\rho Q_\infty^2 S} = \frac{W\ cos\ \gamma_0}{\frac{1}{2}\rho Q_\infty^2 S}$, and the definition of all other parameters used in equations (I.15) summarized in table I.3. The non-dimensional inputs $\hat{u}_j$ are either the non-dimensional 1D lateral gust-component $\beta_g = \frac{v_g}{Q_\infty}$ or its non-dimensional time derivative $\frac{\dot{\beta}_g b}{Q_\infty}$. In tables I.4 and I.6 the definition of the asymmetrical stability derivatives and the asymmetrical gust derivatives are given. It should be noted that also for the asymmetrical equations of motion, the unsteady derivatives are given with respect to $\frac{\dot{\beta} b}{Q_\infty}$ and $\frac{\dot{\beta}_g b}{Q_\infty}$, instead of $\frac{\dot{\beta} b}{2Q_\infty}$ and $\frac{\dot{\beta}_g b}{2Q_\infty}$.

Also it should be noted that in this thesis the initial flight-condition (or trim condition) is always assumed to be level flight, that is the flightpath angle $\gamma_0 = 0$ [Rad.], thus resulting for the kinematic expressions in equations (I.15) in,

$$\begin{aligned} \frac{1}{2}D_b\psi &= \frac{rb}{2Q_\infty} \\ \frac{1}{2}D_b\varphi &= \frac{pb}{2Q_\infty} \end{aligned}$$

The assumption that $\gamma_0 = 0$ [Rad.] also results in $C_L = \frac{W}{\frac{1}{2}\rho Q_\infty^2 S}$.

I.3.4 The non-dimensional equations of motion in state-space form

In this thesis, similar to reference [29], both the symmetrical and asymmetrical equations of motion, equations (I.14) and (I.15), respectively, are often written in the form,

$$P\frac{d\underline{x}}{dt} = Q\ \underline{x} + R\ \underline{u} \tag{I.16}$$

For the symmetrical aircraft motions, the matrices P, Q and R in equation (I.16) are given as (denoted as P_s, Q_s and R_s),

$$P_s = \frac{\bar{c}}{Q_\infty}\begin{bmatrix} -2\mu_c & C_{X_{\dot{\alpha}}} & 0 & 0 \\ 0 & (C_{Z_{\dot{\alpha}}} - 2\mu_c) & 0 & 0 \\ 0 & 0 & -1 & 0 \\ 0 & C_{m_{\dot{\alpha}}} & 0 & -2\mu_c K_Y^2 \end{bmatrix}$$

and,

$$Q_s = \begin{bmatrix} -C_{X_u} & -C_{X_\alpha} & -C_{Z_0} & -C_{X_q} \\ -C_{Z_u} & -C_{Z_\alpha} & C_{X_0} & -\left(C_{Z_q} + 2\mu_c\right) \\ 0 & 0 & 0 & -1 \\ -C_{m_u} & -C_{m_\alpha} & 0 & -C_{m_q} \end{bmatrix}$$

and,

$$R_s = \begin{bmatrix} -C_{X_{u_i}} \\ -C_{Z_{u_i}} \\ 0 \\ -C_{m_{u_i}} \end{bmatrix}$$

respectively, with in equation (I.16) the aircraft state defined as $\underline{x} = \left[\hat{u}, \alpha, \theta, \frac{q\bar{c}}{Q_\infty}\right]^T$, and the input $\underline{u} = \hat{u}_i$. It should be noted that the fourth equation of equations (I.14) is now given as the third equation in equation (I.16).

For the asymmetrical aircraft motions, the matrices P, Q and R in equation (I.16) are given as (with the flightpath angle $\gamma_0 = 0$ [Rad.], and the matrices P, Q and R denoted as P_a, Q_a and R_a),

$$P_a = \frac{b}{Q_\infty} \begin{bmatrix} \left(C_{Y_{\dot{\beta}}} - 2\mu_b\right) & 0 & 0 & 0 \\ 0 & -\frac{1}{2} & 0 & 0 \\ C_{\ell_{\dot{\beta}}} & 0 & -4\mu_b K_X^2 & 4\mu_b K_{XZ} \\ C_{n_{\dot{\beta}}} & 0 & 4\mu_b K_{XZ} & -4\mu_b K_Z^2 \end{bmatrix}$$

and,

$$Q_a = \begin{bmatrix} -C_{Y_\beta} & -C_L & -C_{Y_p} & -\left(C_{Y_r} - 4\mu_b\right) \\ 0 & 0 & -1 & 0 \\ -C_{\ell_\beta} & 0 & -C_{\ell_p} & -C_{\ell_r} \\ -C_{n_\beta} & 0 & -C_{n_p} & -C_{n_r} \end{bmatrix}$$

and,

$$R_a = \begin{bmatrix} -C_{Y_{u_j}} \\ 0 \\ -C_{\ell_{u_j}} \\ -C_{n_{u_j}} \end{bmatrix}$$

respectively, with in equation (I.16) the aircraft state defined as $\underline{x} = \left[\beta, \varphi, \frac{pb}{2Q_\infty}, \frac{rb}{2Q_\infty}\right]^T$, and the input $\underline{u} = \hat{u}_j$. It should be noted that the fourth equation of equations (I.15) is left out of consideration since it merely has value for navigational aspects. Furthermore, the third equation of equations (I.15) is now given as the second equation in equation (I.16).

For both the symmetrical and asymmetrical equations of motion, the final state-space form in terms of the system-matrix A and the input-matrix B is obtained by premultiplying equation (I.16) by the inverse of matrix P,

$$\dot{\underline{x}} = P^{-1}\, Q\, \underline{x} + P^{-1}\, R\, \underline{u} = A\, \underline{x} + B\, \underline{u} \tag{I.17}$$

with A the system-matrix and B the input-matrix.

I.4 The linearized equations of motion in the frequency-domain

I.4.1 Introduction

In the previous section the matrices P, Q and R in equation (I.16) were considered to be constant, that is independent of the circular frequency ω [Rad./sec.]. However, in this section most of the matrix-elements in equation (I.16) are considered to be a function of the circular frequency ω [Rad./sec.]. Similar to equation (I.16), for the frequency-domain the equations of motion are written as,

$$P(\omega)\ j\omega\ \underline{x} = Q(\omega)\ \underline{x} + R(\omega)\ \underline{u} \tag{I.18}$$

with for the symmetrical motions the aircraft state defined as $\underline{x} = \left[\hat{u}, \alpha, \theta, \frac{q\bar{c}}{Q_\infty}\right]^T$, and the input defined as $\underline{u} = \hat{u}_i$. For the asymmetrical motions the aircraft state is defined as $\underline{x} = \left[\beta, \varphi, \frac{pb}{2Q_\infty}, \frac{rb}{2Q_\infty}\right]^T$, while the input is given as $\underline{u} = \hat{u}_j$.

For the symmetrical aircraft motions, the frequency-dependent matrix-elements of the matrices $P(\omega)$, $Q(\omega)$ and $R(\omega)$ in equation (I.18) are with respect to the airspeed perturbation $\hat{u}$, i.e. $\mathcal{C}_{\mathcal{X}_u}(\omega)$, $\mathcal{C}_{\mathcal{Z}_u}(\omega)$, $\mathcal{C}_{m_u}(\omega)$, $\mathcal{C}_{\mathcal{X}_{\dot{u}}}(\omega)$, $\mathcal{C}_{\mathcal{Z}_{\dot{u}}}(\omega)$ and $\mathcal{C}_{m_{\dot{u}}}(\omega)$. Also, the frequency-dependent matrix-elements are with respect to the angle-of-attack perturbation α, i.e. $\mathcal{C}_{\mathcal{X}_\alpha}(\omega)$, $\mathcal{C}_{\mathcal{Z}_\alpha}(\omega)$, $\mathcal{C}_{m_\alpha}(\omega)$, $\mathcal{C}_{\mathcal{X}_{\dot{\alpha}}}(\omega)$, $\mathcal{C}_{\mathcal{Z}_{\dot{\alpha}}}(\omega)$, and $\mathcal{C}_{m_{\dot{\alpha}}}(\omega)$ (the stability derivatives with respect to the pitch-rate q are assumed constant). Finally, the aerodynamic derivatives with respect to the symmetric (gust-) input $\hat{u}_i$ are considered to be frequency-dependent as well, see also chapters 5 to 12.

For the asymmetrical aircraft motions, the frequency-dependent matrix-elements of the matrices $P(\omega)$, $Q(\omega)$ and $R(\omega)$ in equation (I.18) are with respect to the side-slip angle β, i.e. $\mathcal{C}_{\mathcal{Y}_\beta}(\omega)$, $\mathcal{C}_{\ell_\beta}(\omega)$, $\mathcal{C}_{n_\beta}(\omega)$, $\mathcal{C}_{\mathcal{Y}_{\dot{\beta}}}(\omega)$, $\mathcal{C}_{\ell_{\dot{\beta}}}(\omega)$ and $\mathcal{C}_{n_{\dot{\beta}}}(\omega)$ (the stability derivatives with respect to both the roll-rate p and the yaw-rate r are assumed constant). Finally, the aerodynamic derivatives with respect to the asymmetric (gust-) input $\hat{u}_j$ are considered to be frequency-dependent as well, see also chapters 5 to 12.

The definition of the frequency-dependent stability- and gust derivatives is given in appendix D. However, it should be noted that the unsteady derivatives are now with respect to $\frac{\dot{u}\bar{c}}{Q_\infty}$ (instead of $\frac{\dot{u}\bar{c}}{2Q_\infty}$), $\frac{\dot{\alpha}\bar{c}}{Q_\infty}$ (instead of $\frac{\dot{\alpha}\bar{c}}{2Q_\infty}$), $\frac{\dot{\beta}b}{Q_\infty}$ (instead of $\frac{\dot{\beta}b}{2Q_\infty}$), etc..

I.4.2 Symmetrical equations of motion

For the symmetrical equations of motion, the now frequency-dependent matrices P, Q and R in equation (I.18) become, respectively,

$$P_s(\omega) = \frac{\bar{c}}{Q_\infty} \begin{bmatrix} \{\mathcal{C}_{\mathcal{X}_{\dot{u}}}(\omega) - 2\mu_c\} & \mathcal{C}_{\mathcal{X}_{\dot{\alpha}}}(\omega) & 0 & 0 \\ \mathcal{C}_{\mathcal{Z}_{\dot{u}}}(\omega) & \{\mathcal{C}_{\mathcal{Z}_{\dot{\alpha}}}(\omega) - 2\mu_c\} & 0 & 0 \\ 0 & 0 & -1 & 0 \\ \mathcal{C}_{m_{\dot{u}}}(\omega) & \mathcal{C}_{m_{\dot{\alpha}}}(\omega) & 0 & -2\mu_c K_Y^2 \end{bmatrix} \tag{I.19}$$

and,

$$Q_s(\omega) = \begin{bmatrix} -\mathcal{C}_{\mathcal{X}_u}(\omega) & -\mathcal{C}_{\mathcal{X}_\alpha}(\omega) & -C_{Z_0} & -C_{X_q} \\ -\mathcal{C}_{\mathcal{Z}_u}(\omega) & -\mathcal{C}_{\mathcal{Z}_\alpha}(\omega) & C_{X_0} & -\left(C_{Z_q} + 2\mu_c\right) \\ 0 & 0 & 0 & -1 \\ -\mathcal{C}_{m_u}(\omega) & -\mathcal{C}_{m_\alpha}(\omega) & 0 & -C_{m_q} \end{bmatrix} \tag{I.20}$$

and,

$$R_s(\omega) = \begin{bmatrix} -\mathcal{C}_{\mathcal{X}_{u_i}}(\omega) \\ -\mathcal{C}_{\mathcal{Z}_{u_i}}(\omega) \\ 0 \\ -\mathcal{C}_{m_{u_i}}(\omega) \end{bmatrix} \tag{I.21}$$

I.4.3 Asymmetrical equations of motion

For the asymmetrical equations of motion, the now frequency-dependent matrices P, Q and R in equation (I.18) become, respectively,

$$P_a(\omega) = \frac{b}{Q_\infty} \begin{bmatrix} \left\{\mathcal{C}_{\mathcal{Y}_{\dot{\beta}}}(\omega) - 2\mu_b\right\} & 0 & 0 & 0 \\ 0 & -\frac{1}{2} & 0 & 0 \\ \mathcal{C}_{\ell_{\dot{\beta}}}(\omega) & 0 & -4\mu_b K_X^2 & 4\mu_b K_{XZ} \\ \mathcal{C}_{n_{\dot{\beta}}}(\omega) & 0 & 4\mu_b K_{XZ} & -4\mu_b K_Z^2 \end{bmatrix} \tag{I.22}$$

and,

$$Q_a(\omega) = \begin{bmatrix} -\mathcal{C}_{\mathcal{Y}_\beta}(\omega) & -C_L & -C_{Y_p} & -\left(C_{Y_r} - 4\mu_b\right) \\ 0 & 0 & -1 & 0 \\ -\mathcal{C}_{\ell_\beta}(\omega) & 0 & -C_{\ell_p} & -C_{\ell_r} \\ -\mathcal{C}_{n_\beta}(\omega) & 0 & -C_{n_p} & -C_{n_r} \end{bmatrix} \tag{I.23}$$

and,

$$R_a(\omega) = \begin{bmatrix} -\mathcal{C}_{\mathcal{Y}_{u_j}}(\omega) \\ 0 \\ -\mathcal{C}_{\ell_{u_j}}(\omega) \\ -\mathcal{C}_{n_{u_j}}(\omega) \end{bmatrix} \tag{I.24}$$

Dimensional parameter	Dimension	Divisor	Non-dimensional parameter
t	$[t]$	$\frac{\bar{c}}{Q_\infty}$	$s_c = \frac{Q_\infty}{\bar{c}}\, t$
$\frac{d}{dt}$	$[t]^{-1}$	$\frac{Q_\infty}{\bar{c}}$	$D_c = \frac{\bar{c}}{Q_\infty}\, \frac{d}{dt} = \frac{d}{ds_c}$
$\frac{d^2}{dt^2}$	$[t]^{-2}$	$\frac{Q_\infty^2}{\bar{c}^2}$	$D_c^2 = \frac{\bar{c}^2}{Q_\infty^2}\, \frac{d^2}{dt^2} = \frac{d^2}{ds_c^2}$
u	$[\ell][t]^{-1}$	Q_∞	$\hat{u} = \frac{u}{Q_\infty}$
w	$[\ell][t]^{-1}$	Q_∞	$\alpha = \frac{w}{Q_\infty}$
q	$[t]^{-1}$	$\frac{Q_\infty}{\bar{c}}$	$\frac{q\bar{c}}{Q_\infty}$
$\dot{u}$	$[\ell][t]^{-2}$	$\frac{Q_\infty^2}{\bar{c}}$	$D_c\hat{u} = \frac{\dot{u}}{Q_\infty}\, \frac{\bar{c}}{Q_\infty} = \frac{\dot{\hat{u}}\bar{c}}{Q_\infty}$
$\dot{w}$	$[\ell][t]^{-2}$	$\frac{Q_\infty^2}{\bar{c}}$	$D_c\alpha = \frac{\dot{w}}{Q_\infty}\, \frac{\bar{c}}{Q_\infty} = \frac{\dot{\alpha}\bar{c}}{Q_\infty}$
$\dot{q}$	$[t]^{-2}$	$\frac{Q_\infty^2}{\bar{c}^2}$	$D_c\frac{q\bar{c}}{Q_\infty} = \dot{q}\frac{\bar{c}^2}{Q_\infty^2}$
m	$[m]$	$\rho S\bar{c}$	$\mu_c = \frac{m}{\rho S\bar{c}}$
I_Y	$[m][\ell]^2$	$\rho S\bar{c}\cdot\bar{c}^2$	$\mu_c K_Y^2 = \frac{I_Y}{\rho S\bar{c}^3}$
k_y	$[\ell]$	$\bar{c}$	$K_Y = \frac{k_y}{\bar{c}}$
X	$[m][\ell][t]^{-2}$	$\frac{1}{2}\rho S\bar{c}\cdot\bar{c}\cdot\frac{Q_\infty^2}{\bar{c}^2}$	$C_X = \frac{X}{\frac{1}{2}\rho Q_\infty^2 S}$
Z	$[m][\ell][t]^{-2}$	$\frac{1}{2}\rho S\bar{c}\cdot\bar{c}\cdot\frac{Q_\infty^2}{\bar{c}^2}$	$C_Z = \frac{Z}{\frac{1}{2}\rho Q_\infty^2 S}$
M	$[m][\ell]^2[t]^{-2}$	$\frac{1}{2}\rho S\bar{c}^2\cdot\bar{c}\cdot\frac{Q_\infty^2}{\bar{c}^2}$	$C_m = \frac{M}{\frac{1}{2}\rho Q_\infty^2 S\bar{c}}$

Table I.1: Non-dimensional parameters used in the non-dimensional symmetrical equations of motion.

	C_X	C_Z	C_m
$\hat{u}$	$\frac{1}{\frac{1}{2}\rho Q_\infty S}\cdot\frac{\partial X}{\partial u} = \frac{\partial C_X}{\partial\hat{u}}$	$\frac{1}{\frac{1}{2}\rho Q_\infty S}\cdot\frac{\partial Z}{\partial u} = \frac{\partial C_Z}{\partial\hat{u}}$	$\frac{1}{\frac{1}{2}\rho Q_\infty S\bar{c}}\cdot\frac{\partial M}{\partial u} = \frac{\partial C_m}{\partial\hat{u}}$
α	$\frac{1}{\frac{1}{2}\rho Q_\infty S}\cdot\frac{\partial X}{\partial w} = \frac{\partial C_X}{\partial\alpha}$	$\frac{1}{\frac{1}{2}\rho Q_\infty S}\cdot\frac{\partial Z}{\partial w} = \frac{\partial C_Z}{\partial\alpha}$	$\frac{1}{\frac{1}{2}\rho Q_\infty S\bar{c}}\cdot\frac{\partial M}{\partial w} = \frac{\partial C_m}{\partial\alpha}$
$\frac{\dot{\alpha}\bar{c}}{Q_\infty}$	$\frac{1}{\frac{1}{2}\rho S\bar{c}}\cdot\frac{\partial X}{\partial\dot{w}} = \frac{\partial C_X}{\partial\frac{\dot{\alpha}\bar{c}}{Q_\infty}}$	$\frac{1}{\frac{1}{2}\rho S\bar{c}}\cdot\frac{\partial Z}{\partial\dot{w}} = \frac{\partial C_Z}{\partial\frac{\dot{\alpha}\bar{c}}{Q_\infty}}$	$\frac{1}{\frac{1}{2}\rho S\bar{c}^2}\cdot\frac{\partial M}{\partial\dot{w}} = \frac{\partial C_m}{\partial\frac{\dot{\alpha}\bar{c}}{Q_\infty}}$
$\frac{q\bar{c}}{Q_\infty}$	$\frac{1}{\frac{1}{2}\rho Q_\infty S\bar{c}}\cdot\frac{\partial X}{\partial q} = \frac{\partial C_X}{\partial\frac{q\bar{c}}{Q_\infty}}$	$\frac{1}{\frac{1}{2}\rho Q_\infty S\bar{c}}\cdot\frac{\partial Z}{\partial q} = \frac{\partial C_Z}{\partial\frac{q\bar{c}}{Q_\infty}}$	$\frac{1}{\frac{1}{2}\rho Q_\infty S\bar{c}^2}\cdot\frac{\partial M}{\partial q} = \frac{\partial C_m}{\partial\frac{q\bar{c}}{Q_\infty}}$
$\hat{u}_i$	$\frac{1}{\frac{1}{2}\rho Q_\infty S}\cdot\frac{\partial X}{\partial u_i} = \frac{\partial C_X}{\partial\hat{u}_i}$	$\frac{1}{\frac{1}{2}\rho Q_\infty S}\cdot\frac{\partial Z}{\partial u_i} = \frac{\partial C_Z}{\partial\hat{u}_i}$	$\frac{1}{\frac{1}{2}\rho Q_\infty S\bar{c}}\cdot\frac{\partial M}{\partial u_i} = \frac{\partial C_m}{\partial\hat{u}_i}$
$\frac{\dot{\hat{u}}_i\bar{c}}{Q_\infty}$	$\frac{1}{\frac{1}{2}\rho S\bar{c}}\cdot\frac{\partial X}{\partial\dot{u}_i} = \frac{\partial C_X}{\partial\frac{\dot{\hat{u}}_i\bar{c}}{Q_\infty}}$	$\frac{1}{\frac{1}{2}\rho S\bar{c}}\cdot\frac{\partial Z}{\partial\dot{u}_i} = \frac{\partial C_Z}{\partial\frac{\dot{\hat{u}}_i\bar{c}}{Q_\infty}}$	$\frac{1}{\frac{1}{2}\rho S\bar{c}^2}\cdot\frac{\partial M}{\partial\dot{u}_i} = \frac{\partial C_m}{\partial\frac{\dot{\hat{u}}_i\bar{c}}{Q_\infty}}$

Table I.2: Definition of the constant symmetrical stability- and input derivatives for $\mathcal{F}_S$.

Dimensional parameter	Dimension	Divisor	Non-dimensional parameter
t	$[t]$	$\frac{b}{Q_\infty}$	$s_b = \frac{Q_\infty}{b}\, t$
$\frac{d}{dt}$	$[t]^{-1}$	$\frac{Q_\infty}{b}$	$D_b = \frac{b}{Q_\infty}\, \frac{d}{dt} = \frac{d}{ds_b}$
$\frac{d^2}{dt^2}$	$[t]^{-2}$	$\frac{Q_\infty^2}{b^2}$	$D_b^2 = \frac{b^2}{Q_\infty^2}\, \frac{d^2}{dt^2} = \frac{d^2}{ds_b^2}$
v	$[\ell][t]^{-1}$	Q_∞	$\beta = \frac{v}{Q_\infty}$
p	$[\ell][t]^{-1}$	$\frac{2Q_\infty}{b}$	$\frac{pb}{2Q_\infty}$
r	$[t]^{-1}$	$\frac{2Q_\infty}{b}$	$\frac{rb}{2Q_\infty}$
$\dot{v}$	$[\ell][t]^{-2}$	$\frac{Q_\infty^2}{b}$	$D_b\beta = \frac{\dot{v}}{Q_\infty}\, \frac{b}{Q_\infty} = \frac{\dot{\beta} b}{Q_\infty}$
$\dot{p}$	$[t]^{-2}$	$\frac{2Q_\infty^2}{b^2}$	$D_b \frac{pb}{2Q_\infty} = \frac{\dot{p} b^2}{2Q_\infty^2}$
$\dot{r}$	$[t]^{-2}$	$\frac{2Q_\infty^2}{b^2}$	$D_b \frac{rb}{2Q_\infty} = \frac{\dot{r} b^2}{2Q_\infty^2}$
m	$[m]$	$\rho S b$	$\mu_b = \frac{m}{\rho S b}$
I_X	$[m][\ell]^2$	$\rho S b \cdot b^2$	$\mu_b K_X^2 = \frac{I_X}{\rho S b^3}$
I_Z	$[m][\ell]^2$	$\rho S b \cdot b^2$	$\mu_b K_Z^2 = \frac{I_Z}{\rho S b^3}$
J_{XZ}	$[m][\ell]^2$	$\rho S b \cdot b^2$	$\mu_b K_{XZ} = \frac{J_{XZ}}{\rho S b^3}$
k_x	$[\ell]$	b	$K_X = \frac{k_x}{b}$
k_z	$[\ell]$	b	$K_Z = \frac{k_z}{b}$
Y	$[m][\ell][t]^{-2}$	$\frac{1}{2}\rho S b \cdot b \cdot \frac{Q_\infty^2}{b^2}$	$C_Y = \frac{Y}{\frac{1}{2}\rho Q_\infty^2 S}$
L	$[m][\ell]^2[t]^{-2}$	$\frac{1}{2}\rho S b^2 \cdot b \cdot \frac{Q_\infty^2}{b^2}$	$C_\ell = \frac{L}{\frac{1}{2}\rho Q_\infty^2 S b}$
N	$[m][\ell]^2[t]^{-2}$	$\frac{1}{2}\rho S b^2 \cdot b \cdot \frac{Q_\infty^2}{b^2}$	$C_n = \frac{N}{\frac{1}{2}\rho Q_\infty^2 S b}$

Table I.3: Non-dimensional parameters used in the non-dimensional asymmetrical equations of motion.

	C_Y	C_ℓ	C_n
β	$\frac{1}{\frac{1}{2}\rho Q_\infty S} \cdot \frac{\partial Y}{\partial v} = \frac{\partial C_Y}{\partial \beta}$	$\frac{1}{\frac{1}{2}\rho Q_\infty S b} \cdot \frac{\partial L}{\partial v} = \frac{\partial C_\ell}{\partial \beta}$	$\frac{1}{\frac{1}{2}\rho Q_\infty S b} \cdot \frac{\partial N}{\partial v} = \frac{\partial C_n}{\partial \beta}$
$\frac{\dot{\beta} b}{Q_\infty}$	$\frac{1}{\frac{1}{2}\rho S b} \cdot \frac{\partial Y}{\partial \dot{v}} = \frac{\partial C_Y}{\partial \frac{\dot{\beta} b}{Q_\infty}}$	$\frac{1}{\frac{1}{2}\rho S b^2} \cdot \frac{\partial L}{\partial \dot{v}} = \frac{\partial C_\ell}{\partial \frac{\dot{\beta} b}{Q_\infty}}$	$\frac{1}{\frac{1}{2}\rho S b^2} \cdot \frac{\partial N}{\partial \dot{v}} = \frac{\partial C_n}{\partial \frac{\dot{\beta} b}{Q_\infty}}$
$\frac{pb}{2Q_\infty}$	$\frac{2}{\frac{1}{2}\rho Q_\infty S b} \cdot \frac{\partial Y}{\partial p} = \frac{\partial C_Y}{\partial \frac{pb}{2Q_\infty}}$	$\frac{2}{\frac{1}{2}\rho Q_\infty S b^2} \cdot \frac{\partial L}{\partial p} = \frac{\partial C_\ell}{\partial \frac{pb}{2Q_\infty}}$	$\frac{2}{\frac{1}{2}\rho Q_\infty S b^2} \cdot \frac{\partial N}{\partial p} = \frac{\partial C_n}{\partial \frac{pb}{2Q_\infty}}$
$\frac{rb}{2Q_\infty}$	$\frac{2}{\frac{1}{2}\rho Q_\infty S b} \cdot \frac{\partial Y}{\partial r} = \frac{\partial C_Y}{\partial \frac{rb}{2Q_\infty}}$	$\frac{2}{\frac{1}{2}\rho Q_\infty S b^2} \cdot \frac{\partial L}{\partial r} = \frac{\partial C_\ell}{\partial \frac{rb}{2Q_\infty}}$	$\frac{2}{\frac{1}{2}\rho Q_\infty S b^2} \cdot \frac{\partial N}{\partial r} = \frac{\partial C_n}{\partial \frac{rb}{2Q_\infty}}$
$\hat{u}_j$	$\frac{1}{\frac{1}{2}\rho Q_\infty S} \cdot \frac{\partial Y}{\partial u_j} = \frac{\partial C_Y}{\partial \hat{u}_j}$	$\frac{1}{\frac{1}{2}\rho Q_\infty S b} \cdot \frac{\partial L}{\partial u_j} = \frac{\partial C_\ell}{\partial \hat{u}_j}$	$\frac{1}{\frac{1}{2}\rho Q_\infty S b} \cdot \frac{\partial N}{\partial u_j} = \frac{\partial C_n}{\partial \hat{u}_j}$
$\frac{\dot{\hat{u}}_j b}{Q_\infty}$	$\frac{1}{\frac{1}{2}\rho S b} \cdot \frac{\partial Y}{\partial \dot{u}_j} = \frac{\partial C_Y}{\partial \frac{\dot{\hat{u}}_j b}{Q_\infty}}$	$\frac{1}{\frac{1}{2}\rho S b^2} \cdot \frac{\partial L}{\partial \dot{u}_j} = \frac{\partial C_\ell}{\partial \frac{\dot{\hat{u}}_j b}{Q_\infty}}$	$\frac{1}{\frac{1}{2}\rho S b^2} \cdot \frac{\partial N}{\partial \dot{u}_j} = \frac{\partial C_n}{\partial \frac{\dot{\hat{u}}_j b}{Q_\infty}}$

Table I.4: Definition of the constant asymmetrical stability- and input derivatives for $\mathcal{F}_S$.

	Stability derivatives		
	C_X	C_Z	C_m
$\hat{u}$	$C_{X_u} = \frac{\partial C_X}{\partial \hat{u}}$	$C_{Z_u} = \frac{\partial C_Z}{\partial \hat{u}}$	$C_{m_u} = \frac{\partial C_m}{\partial \hat{u}}$
$\frac{\dot{\hat{u}}\bar{c}}{Q_\infty}$	$C_{X_{\dot{u}}} = \frac{\partial C_X}{\partial \frac{\dot{\hat{u}}\bar{c}}{Q_\infty}}$	$C_{Z_{\dot{u}}} = \frac{\partial C_Z}{\partial \frac{\dot{\hat{u}}\bar{c}}{Q_\infty}}$	$C_{m_{\dot{u}}} = \frac{\partial C_m}{\partial \frac{\dot{\hat{u}}\bar{c}}{Q_\infty}}$
α	$C_{X_\alpha} = \frac{\partial C_X}{\partial \alpha}$	$C_{Z_\alpha} = \frac{\partial C_Z}{\partial \alpha}$	$C_{m_\alpha} = \frac{\partial C_m}{\partial \alpha}$
$\frac{\dot{\alpha}\bar{c}}{Q_\infty}$	$C_{X_{\dot{\alpha}}} = \frac{\partial C_X}{\partial \frac{\dot{\alpha}\bar{c}}{Q_\infty}}$	$C_{Z_{\dot{\alpha}}} = \frac{\partial C_Z}{\partial \frac{\dot{\alpha}\bar{c}}{Q_\infty}}$	$C_{m_{\dot{\alpha}}} = \frac{\partial C_m}{\partial \frac{\dot{\alpha}\bar{c}}{Q_\infty}}$
$\frac{q\bar{c}}{Q_\infty}$	$C_{X_q} = \frac{\partial C_X}{\partial \frac{q\bar{c}}{Q_\infty}}$	$C_{Z_q} = \frac{\partial C_Z}{\partial \frac{q\bar{c}}{Q_\infty}}$	$C_{m_q} = \frac{\partial C_m}{\partial \frac{q\bar{c}}{Q_\infty}}$
	1D gust derivatives		
	C_X	C_Z	C_m
$\hat{u}_g$	$C_{X_{u_g}} = \frac{\partial C_X}{\partial \hat{u}_g}$	$C_{Z_{u_g}} = \frac{\partial C_Z}{\partial \hat{u}_g}$	$C_{m_{u_g}} = \frac{\partial C_m}{\partial \hat{u}_g}$
$\frac{\dot{\hat{u}}_g\bar{c}}{Q_\infty}$	$C_{X_{\dot{u}_g}} = \frac{\partial C_X}{\partial \frac{\dot{\hat{u}}_g\bar{c}}{Q_\infty}}$	$C_{Z_{\dot{u}_g}} = \frac{\partial C_Z}{\partial \frac{\dot{\hat{u}}_g\bar{c}}{Q_\infty}}$	$C_{m_{\dot{u}_g}} = \frac{\partial C_m}{\partial \frac{\dot{\hat{u}}_g\bar{c}}{Q_\infty}}$
α_g	$C_{X_{\alpha_g}} = \frac{\partial C_X}{\partial \alpha_g}$	$C_{Z_{\alpha_g}} = \frac{\partial C_Z}{\partial \alpha_g}$	$C_{m_{\alpha_g}} = \frac{\partial C_m}{\partial \alpha_g}$
$\frac{\dot{\alpha}_g\bar{c}}{Q_\infty}$	$C_{X_{\dot{\alpha}_g}} = \frac{\partial C_X}{\partial \frac{\dot{\alpha}_g\bar{c}}{Q_\infty}}$	$C_{Z_{\dot{\alpha}_g}} = \frac{\partial C_Z}{\partial \frac{\dot{\alpha}_g\bar{c}}{Q_\infty}}$	$C_{m_{\dot{\alpha}_g}} = \frac{\partial C_m}{\partial \frac{\dot{\alpha}_g\bar{c}}{Q_\infty}}$

Table I.5: Definition of the constant symmetrical stability- and 1D gust derivatives for $\mathcal{F}_S$.

	Stability derivatives		
	C_Y	C_ℓ	C_n
β	$C_{Y_\beta} = \frac{\partial C_Y}{\partial \beta}$	$C_{\ell_\beta} = \frac{\partial C_\ell}{\partial \beta}$	$C_{n_\beta} = \frac{\partial C_n}{\partial \beta}$
$\frac{\dot{\beta} b}{Q_\infty}$	$C_{Y_{\dot{\beta}}} = \frac{\partial C_Y}{\partial \frac{\dot{\beta} b}{Q_\infty}}$	$C_{\ell_{\dot{\beta}}} = \frac{\partial C_\ell}{\partial \frac{\dot{\beta} b}{Q_\infty}}$	$C_{n_{\dot{\beta}}} = \frac{\partial C_n}{\partial \frac{\dot{\beta} b}{Q_\infty}}$
$\frac{pb}{2Q_\infty}$	$C_{Y_p} = \frac{\partial C_Y}{\partial \frac{pb}{2Q_\infty}}$	$C_{\ell_p} = \frac{\partial C_\ell}{\partial \frac{pb}{2Q_\infty}}$	$C_{n_p} = \frac{\partial C_n}{\partial \frac{pb}{2Q_\infty}}$
$\frac{rb}{2Q_\infty}$	$C_{Y_r} = \frac{\partial C_Y}{\partial \frac{rb}{2Q_\infty}}$	$C_{\ell_r} = \frac{\partial C_\ell}{\partial \frac{rb}{2Q_\infty}}$	$C_{n_r} = \frac{\partial C_n}{\partial \frac{rb}{2Q_\infty}}$
	1D gust derivatives		
	C_Y	C_ℓ	C_n
β_g	$C_{Y_{\beta_g}} = \frac{\partial C_Y}{\partial \beta_g}$	$C_{\ell_{\beta_g}} = \frac{\partial C_\ell}{\partial \beta_g}$	$C_{n_{\beta_g}} = \frac{\partial C_n}{\partial \beta_g}$
$\frac{\dot{\beta}_g b}{Q_\infty}$	$C_{Y_{\dot{\beta}_g}} = \frac{\partial C_Y}{\partial \frac{\dot{\beta}_g b}{Q_\infty}}$	$C_{\ell_{\dot{\beta}_g}} = \frac{\partial C_\ell}{\partial \frac{\dot{\beta}_g b}{Q_\infty}}$	$C_{n_{\dot{\beta}_g}} = \frac{\partial C_n}{\partial \frac{\dot{\beta}_g b}{Q_\infty}}$

Table I.6: Definition of the constant asymmetrical stability- and 1D gust derivatives for $\mathcal{F}_S$.

References

[1] Robinson, P.A., *The modeling of turbulence and downbursts for flight simulators*, UTIAS report No. 339, University of Toronto, 1991.

[2] Batchelor, G.K., *Theory of homogeneous turbulence*, Cambridge University Press, Cambridge, 1953.

[3] Van Gool, P.C.A., *Rotorcraft Responses to Atmospheric Turbulence*, Delft University Press, 1997.

[4] Houbolt, J.C. and Steiner, R. and Pratt, K.G., *Dynamic Response of Airplanes to Atmospheric Turbulence Including Flight Data on Input and Response*, NASA TR-R-199, 1964.

[5] Etkin, B., *Dynamics of Atmospheric Flight*, John Wiley & Sons Inc., 1972.

[6] Van de Moesdijk, G.A.J., *The Description of Patchy Atmospheric Turbulence, Based on a Non-Gaussian Simulation Technique*, Delft University of Technology, Department of Aerospace Engineering, Report VTH-192, February 1975.

[7] Van der Spek, J.A., *Aerodynamic Model Identification, a CFD Approach*, Masters Thesis, Delft University of Technology, Faculty of Aerospace Engineering, Control and Simulation Division, 1998.

[8] Maskew, B., *Prediction of Subsonic Aerodynamic Characteristics; A Case for Low-Order Panel Methods*, Journal of Aircraft, Vol. 19, No. 2, February 1982.

[9] Maskew, B., *Program VSAERO Theory Document*, NASA Contractor Report 4023, NASA, 1987.

[10] Ashby, D.L., Dudley, M.R., Iguchi, S.K., Browne, L., Katz, J., *Potential Flow Theory and Operation Guide for the Panel Code PMARC*, NASA Technical Memorandum 102851, NASA, 1991.

[11] Katz, J., Plotkin, A., *Low-Speed Aerodynamics, From Wing Theory to Panel Methods*, McGraw-Hill, Inc., 1991.

[12] Katz, J., Plotkin, A., *Low-Speed Aerodynamics*, Cambridge University Press, 2001.

[13] Giesing, J.P., Rodden, W.P., Stahl, B., *Sears Function and Lifting Surface Theory for Harmonic Gust Fields*, Journal of Aircraft, Vol. 7, No. 3, May-June 1970.

[14] Horlock, J.H., *Fluctuating Lift Forces on Aerofoils Moving Through Transverse and Chordwise Gusts*, Journal of Basic Engineering, Transactions of the ASME, December 1968.

[15] Isaacs, R., *Airfoil Theory for Flows of Variable Velocity*, Journal of Aeronautical Sciences, Vol. 12, 1945.

[16] Jones, R.T., *Operational Treatment of the Non-Uniform Lift Theory in Airplane Dynamics*, NACA Technical Note 667, 1938.

[17] Jones, R.T., *The Unsteady Lift of a Wing of Finite Aspect Ratio*, NACA Report 681, 1940.

[18] Kármán, von, Th., Sears, W.R., *Airfoil Theory for Non-Uniform Motion*, Journal of the Aeronautical Sciences, Vol. 5, No. 10, August 1938.

[19] Katz, J., Maskew, B., *Unsteady Low-Speed Aerodynamic Model for Complete Aircraft Configurations*, Journal of Aircraft, Vol. 25, No. 4, April 1988.

[20] Küssner, H.G., *Zusammenfassender Bericht über den instationären Auftrieb von Flügeln*, Luftfahrtforschung, Bd. 13, 1936.

[21] Leishman, J.G., *Principles of Helicopter Aerodynamics*, Cambridge Aerospace Series, Cambridge University Press, 2000.

[22] Sears, W.R., *Some Aspects of Non-Stationary Airfoil Theory and Its Practical Application*, Journal of the Aeronautical Sciences, 1940.

[23] Sears, W.R., Sparks, D.O., *On the Reaction of an Elastic Wing to Vertical Gusts*, Journal of the Aeronautical Sciences, Vol. 9, No. 2, 1941.

[24] Theodorsen, T., *General Theory of Aerodynamic Instability and the Mechanism of Flutter*, NACA Technical Report No. 496, 1935.

[25] Van der Vaart, J.C., *The Calculation of the R.M.S. Value of an Aircraft's Normal Acceleration due to Gaussian Random Atmospheric Turbulence*, Delft University of Technology, Department of Aerospace Engineering, Report VTH-213, March 1976.

[26] Wagner, H., *Uber die Entstehung des Dynamischen Auftriebes von Tragflugeln*, Z.F.A.M.M., Vol. 5, No. 1, February 1925.

[27] Juliana, S., *Cessna Citation II Aircraft Aerodynamic Model Parameter Identification*, M.Sc. Thesis, Delft University of Technology, August 2001.

[28] Anon., *U.S. Airplane Flight Manual Model C550*, Model 550 Citation II Weight and Balance Data Sheets, Cessna Aircraft Company, Aircraft Division, Wichita, Kansas, USA.

[29] Mulder, J.A., van Staveren, W.H.J.J., van der Vaart, J.C., *Flight Dynamics*, Lecture Notes AE3-302, Delft University of Technology, Department of Aerospace Engineering, 2000.

[30] Mulder, J.A., van der Vaart, J.C., *Aircraft Responses to Atmospheric Turbulence*, Lecture Notes AE4-304, Delft University of Technology, Department of Aerospace Engineering, 1995.

[31] Bisplinghoff, R.L., Ashley, H., Halfman, R.L., *Aeroelasticity*, Addison-Wesley Publishing Co., Cambridge, Mass., USA, 1957.

[32] Broek, van den, P.Ph., Brandt, A.P., *Vliegeigenscahppen II*, DUT report D-34, Delft University of Technology, 1984.

[33] Gerlach, O.H., *Calculation of the Response of an Aircraft to Random Atmospheric Turbulence, Part I, Symmetric Motions*, DUT report VTH-138, Delft University of Technology, 1966.

[34] Gerlach, O.H., Baarspul, M., *Calculation of the Response of an Aircraft to Random Atmospheric Turbulence, Part II, Asymmetric Motions*, DUT report VTH-139, Delft University of Technology, 1968.

[35] Etkin, B., *The Turbulent Wind and its Effect on Flight*, UTIAS report No. 44, 1980.

[36] Lind, R., Brenner, M., *Robust Aero-Servo-Elastic Stability Analysis*, Springer-Verlag, printed in Germany, 1999.

Samenvatting

Vliegtuig responsies ten gevolge van atmosferische turbulentie spelen een belangrijke rol in het vliegtuig-ontwerp (het bepalen van belastingen), het ontwikkelen van regelsystemen en vlucht simulatie (bijvoorbeeld in het onderzoek naar vliegeigenschappen en de training van piloten). Het simuleren van deze vliegtuig responsies vereist een nauwkeurig mathematisch model. In dit proefschrift zullen twee klassieke methoden worden beschouwd, een methode ontwikkeld aan de Technische Universiteit Delft (het DUT-model) en het zogenaamde vier punts model (*Four Point Aircraft model* of FPA-model). Hoewel deze methoden in het verleden vaak zijn toegepast, blijft de nauwkeurigheid van deze modellen in het ongewisse. De oorzaak hiervan ligt bij één van de vereisten voor systeem identificatie; het is van fundamenteel belang dat zowel de ingangsignalen als de uitgangsignalen bekend zijn voor het te identificeren systeem. Gebruik makend van deze experimenteel vergaarde signalen is het mogelijk een mathematisch model op te stellen voor willekeurige systemen. Voor het opstellen van een dergelijk model, zoals een vliegtuig vliegend door stochastische atmosferische turbulentie, kunnen echter enige problemen ontstaan. Wanneer het ingangsignaal stochastische atmosferische turbulentie betreft, ontstaat het probleem hoe de turbulentie aangrijpt op het vliegtuig. Het meten van de vliegtuigresponsie in termen van de gemeten invalshoek, langshellinghoek, rolhoek, en dergelijke, blijkt in de praktijk een overkomelijk probleem te zijn. Echter, het probleem ligt nu bij het meten van de aan het vliegtuig toegekende ingangen of verstoringen; in dit proefschrift zijn deze stochastische atmosferische turbulentie velden. Het meten van de stroming rondom een vliegtuig tijdens vliegproeven blijft hedentendage een probleem. Het vergt een oneindig aantal sensoren om de stroming rondom het vliegtuig te bepalen, met tot gevolg dat de verdeling van de atmosferische turbulentie snelheids componenten rondom het vliegtuig in de praktijk ook niet te identificeren zal zijn.

In een poging meer duidelijkheid te verschaffen met betrekking tot de responsie van een vliegtuig ten gevolge van atmosferische turbulentie, het onderwerp van dit proefschrift, zullen in eerste instantie twee verschillende modellen worden gedefinieerd. Het eerste model heeft betrekking op de modellering van atmosferische turbulentie, terwijl het tweede betrekking heeft op de mathematische beschrijving van het vliegtuig onderhevig aan atmosferische verstoringen. Voor wat betreft de modellering van atmosferische turbulentie zal in dit proefschrift gebruik gemaakt worden van een stochastisch, stationair, homogeen, isotroop atmosferisch turbulentie model. Dit in de literatuur vaak gebruikte model zal wor-

den toegepast om de vliegtuig responsie te bepalen. Vervolgens zullen in dit proefschrift enige mathematische vliegtuigmodellen worden besproken. Vele van dergelijke modellen zijn in de literatuur voorgesteld, echter, de verifiëring ervan blijft problematisch vanwege het eerder genoemde identificatie probleem van de atmosferische turbulentie snelheids componenten. Als onderdeel van het mathematisch vliegtuig model, maakt het (parametrisch) aerodynamisch model daarvan deel uit. In de literatuur maakt dit model vaak gebruik van zogenaamde (quasi-) stationaire aerodynamische resultaten; dat wil zeggen dat de stationaire aerodynamische parameters worden bepaald met behulp van windtunnel experimenten, handboekmethoden, *Computational Aerodynamics* (CA) welke onder andere gebruik maken van gelineariseerde potentiaal stroming modellen, of *Computational Fluid Dynamics* (CFD) methoden welke gebruik maken van volledige potentiaal, Euler en Navier-Stokes modellen.
In dit proefschrift zal het meest eenvoudige model voor stroming simulaties worden toegepast om de op een vliegtuig werkende tijdsafhankelijke aerodynamische krachten en momenten te bepalen. Het model gaat uit van niet-stationaire gelineariseerde potentiaal theorie. Dit model resulteert in een zogenaamde "panelen-methode" welke toegepast zal worden als een virtuele windtunnel (of een virtuele vliegproef faciliteit) voor een gediscretizeerd vliegtuig (of vliegtuig grid). De toepassing van de methode zal uiteindelijk resulteren in stationaire en niet-stationaire stabiliteitsafgeleiden. Deze afgeleiden worden bepaald met behulp van harmonische simulaties. Eveneens worden de stationaire en niet-stationaire remousafgeleiden bepaald voor geïsoleerde atmosferische turbulentie velden (of remous velden). Enkel één-dimensionale longitudinale, laterale en vertikale remous velden zullen worden beschouwd, naast twee-dimensionale longitudinale en vertikale remous velden. De harmonische analyse resulteert in frequentie-afhankelijke stabiliteits- en remousafgeleiden welke gebruikt zullen worden ter bepaling van een aerodynamich model in termen van constante parameters (constante stabiliteits- en remousafgeleiden). Het nieuw geïntroduceerde model (het *Parametric Computational Aerodynamics model*, of PCA-model) zal vergeleken worden met het *Delft University of Technology model* (DUT-model) en het *Four Point Aircraft model* (FPA-model). Deze drie parametrische modellen zullen toegepast worden voor het bepalen van zowel de tijds- als frequentiedomein vliegtuigresponsies. De vliegtuigresponsies zullen zowel de responsie van het aerodynamisch model als de vliegtuigbewegingen bevatten ten gevolge van de eerder gemoemde remous velden. Naast de parametrische modellen zullen ook vliegtuigresponsies gegeven worden welke zijn verkregen door middel van toepassing van de niet-stationaire gelineariseerde potentiaal stroming methode. Voor deze toepassing zal het vliegtuig grid gevlogen worden door twee-dimensionale stochastische remous velden, resulterend in *Linearized Potential Flow model* oplossingen. Resultaten van deze simulaties zullen vergeleken worden met die verkregen uit de PCA-, DUT- en FPA-modellen.

Uit de gepresenteerde resultaten valt te concluderen dat het geïntroduceerde PCA-model het meest nauwkeurig is voor de beschouwde remous velden. Vergeleken met de *Linearized Potential Flow* oplossing (welke gezien wordt als het model dat de werkelijkheid het meest benadert) produceert het nieuwe parametrische model resultaten welke nauwkeuriger zijn

dan die verkregen met behulp van de klassieke parametrische modellen (het DUT- en FPA-model), en in het bijzonder voor de vliegtuig responsies ten gevolge van twee-dimensionale remous velden. Tevens is het model meer nauwkeurig in het bepalen van de vliegtuig responsies ten gevolge van één-dimensionale longitudinale remous velden.
Hoewel enkel resultaten gegeven zullen worden voor de Cessna Ce550 Citation II, zijn de aangegeven theorie en methoden toepasbaar op vliegtuigen van verscheidene grootte, dat will zeggen van de kleinste onbemande vliegtuigen (UAV's) tot de grootste straalverkeersvliegtuigen (zoals de Boeing B747 en de Airbus A380).

Aangezien het in dit proefschrift samengevat onderzoek meerdere disciplines bevat, worden enkele in detail besproken. Zo zullen, bijvoorbeeld, de ontwikkelde panelen-methoden uitvoerig worden beschreven in een volgorde welke ook is toegepast in de ontwikkelde software. Bovendien zal de procedure voor het bepalen van de model parameters van het nieuwe PCA-model uitvoerig worden weergegeven.

Acknowledgements

Although the list of persons to express my gratitude to will not be complete, I would like to thank a number of people by name for providing support over the past years.

First of all, I would like to thank my promotor Prof.dr.ir. J.A. Mulder for giving me the opportunity to do this research. Bob, thank you for your advice and your ongoing support over the past years.

Next, without whose help this thesis would have looked considerably different, my gratitude is extended to Dr.ir. J.C. van der Vaart. Hans, thank you for meticulously reading through all the drafts of this thesis (yes, I know, I always handed them in late, my apologies).

Also, for their support I would like to thank my colleagues and friends at the Disciplinary Group of Control and Simulation, Max Baarspul, Florin Barb, Samir Bennani, Richard Bennis, Chu Qi Ping, Cor Dam, Herman Damveld, Sinar Juliana, Alwin Kraeger, Peter Kraan, Henk Lindenburg, Gertjan Looije, Bertine Markus, Andries Muis, Max Mulder, René van Paassen, Adri Tak, Tom van der Voort and Kees van Woerkom. Furthermore, I would like to thank Steven Hulshoff, Martin Laban, Paolo Lisandrin and Leo Veldhuis for the numerous discussions we had on computational aerodynamic simulations, and Ronald Slingerland for his valuable inputs.

A special thanks to my friends Sunjoo Advani, Paul van Gastel, Paul van Gool, Coen van der Linden, Elischewah Basting and Marco Soijer. Thank you for your ongoing interest into my research and for the good times we spent together.

In the past years I was fortunate to have several students under my supervision, contributing to the Group research effort. In this period I was extremely lucky to work with very talented persons, of whom I would like to mention in particular: Bert Beuker, Bart Groenenboom, Marjolein Hermans, Erwin Kipperman, Joao-Pedro Mortagua, Christiaan Schoemaker, Jorrit van der Spek and Bauke Tilma. With Samir Bennani, Marjolein Hermans and Jorrit van der Spek we started the AMICAE-project (Aerodynamic Model Identification using Computational Aerodynamic Experiments) which ultimately resulted in the modeling of elastic aircraft, the Aero-Servo-Elasticity (ASE) project. This project

would not have existed without the help of Herman Damveld and Jan Hol, both true NASTRAN gurus. With Herman Damveld aboard in the Disciplinary Group of Control and Simulation/SIMONA, the ASE-project really got kick-started. Also, at the time, the ASE project would not have been initiated if Joao-Pedro Mortagua did not have the courage to start it with us (muito obrigado amigo).

Also, I have to mention my remote friends at the National Aerospace Laboratory (NLR). First of all, Louis Erkelens and Wim de Boer. Thank you for the interest you have shown into my research and into my position at the DUT in the past years, I sincerely appreciated it. I also thank the both of you for the NLR's financial support. My gratitude is also extended to Bart Eussen, Michel Hounjet and Jos Meijer. Thank you for all the discussions we had on flight-dynamics, unsteady aerodynamics, complex curve-fitting and the modeling of elastic aircraft. Furthermore, a special thanks to friends from the U.S.A., that is Gary Balas (University of Minnesota), Martin Brenner (NASA) and Rick Lind (NASA/University of Florida) for educating me in the field of aeroelasticity, flight-dynamics and control related topics.

When we started the AMICAE-project I was fortunate to have a friend in the USA who, on request and without hesitation, sent me numerous publications regarding Linearized Potential Flow simulations (publications which were very difficult to obtain in The Netherlands). Thank you Claudette Rietveld-Holden, you are a fantastic teacher, you are a fantastic friend.

Finally, I would like to thank my father, my mother, my sisters Barbara and Annemarie, my brother-in-law Bas Maring, my relatives and my friends, for their support and patience during my research.

This thesis is dedicated to my parents.

Jan-Willem van Staveren

Alphen aan den Rijn, November 7, 2003

Curriculum vitae

Jan-Willem van Staveren was born on August 6th, 1966, in Sittard, The Netherlands. From 1979 to 1984 he attended the "Albanianae Scholengemeenschap" in Alphen aan den Rijn where he obtained the Atheneum-β certificate.
In 1984 he started his studies at the Delft University of Technology, Faculty of Aerospace Engineering. In October, 1991, at the Disciplinary Group for Stability and Control, he obtained the M.Sc. degree in Aerospace Engineering for his study on the modeling of aircraft subjected to atmospheric turbulence and the design of control-systems to suppress the aircraft motion responses to it. This research was conducted under the supervision of Prof.dr.ir. J.A. Mulder and Dr.ir. J.C. van der Vaart.
In November, 1991, he joined the Disciplinary Group for Stability and Control as a Ph.D.-candidate, researching the modeling of aircraft subjected to atmospheric turbulence, the subject of this thesis.
From 1991 he has been co-responsible for the graduate course *Aircraft Responses to Atmospheric Turbulence* at the Faculty of Aerospace Engineering.